NEW ADVANCES IN GEOLOGY AND ENGINEERING TECHNOLOGY OF UNCONVENTIONAL OIL AND GAS

EDITED BY: Yuwei Li, Shengnan Chen and Jizhou Tang

PUBLISHED IN: Frontiers in Earth Science and Frontiers in Chemistry

frontiers Research Topics

frontiers

ISSN 1664-8714
ISBN 978-2-83250-005-7
DOI 10.3389/978-2-83250-005-7

About Frontiers

Frontiers is more than just an open-access publisher of scholarly articles: it is a pioneering approach to the world of academia, radically improving the way scholarly research is managed. The grand vision of Frontiers is a world where all people have an equal opportunity to seek, share and generate knowledge. Frontiers provides immediate and permanent online open access to all its publications, but this alone is not enough to realize our grand goals.

Frontiers Journal Series

The Frontiers Journal Series is a multi-tier and interdisciplinary set of open-access, online journals, promising a paradigm shift from the current review, selection and dissemination processes in academic publishing. All Frontiers journals are driven by researchers for researchers; therefore, they constitute a service to the scholarly community. At the same time, the Frontiers Journal Series operates on a revolutionary invention, the tiered publishing system, initially addressing specific communities of scholars, and gradually climbing up to broader public understanding, thus serving the interests of the lay society, too.

Dedication to Quality

Each Frontiers article is a landmark of the highest quality, thanks to genuinely collaborative interactions between authors and review editors, who include some of the world's best academicians. Research must be certified by peers before entering a stream of knowledge that may eventually reach the public - and shape society; therefore, Frontiers only applies the most rigorous and unbiased reviews.
Frontiers revolutionizes research publishing by freely delivering the most outstanding research, evaluated with no bias from both the academic and social point of view. By applying the most advanced information technologies, Frontiers is catapulting scholarly publishing into a new generation.

What are Frontiers Research Topics?

Frontiers Research Topics are very popular trademarks of the Frontiers Journals Series: they are collections of at least ten articles, all centered on a particular subject. With their unique mix of varied contributions from Original Research to Review Articles, Frontiers Research Topics unify the most influential researchers, the latest key findings and historical advances in a hot research area! Find out more on how to host your own Frontiers Research Topic or contribute to one as an author by contacting the Frontiers Editorial Office: frontiersin.org/about/contact

NEW ADVANCES IN GEOLOGY AND ENGINEERING TECHNOLOGY OF UNCONVENTIONAL OIL AND GAS

Topic Editors:
Yuwei Li, Liaoning University, China
Shengnan Chen, University of Calgary, Canada
Jizhou Tang, Tongji University, China

Citation: Li, Y., Chen, S., Tang, J., eds. (2022). New Advances in Geology and Engineering Technology of Unconventional Oil and Gas.
Lausanne: Frontiers Media SA. doi: 10.3389/978-2-83250-005-7

Table of Contents

frontiers in Earth Science

ORIGINAL RESEARCH
published: 28 May 2021
doi: 10.3389/feart.2021.693960

Immiscible CO_2 Flooding Efficiency in Low-Permeability Reservoirs: An Experimental Investigation of Residual Oil Distribution

Ying Yang[1], Xiao-Feng Zhou[2,3], Le-Yin Sun[4], An-Lun Wang[2,3], Jian-guang Wei[2,3], Chen-Xi Li[5] and Xiang Ke[6]*

[1]The Department of Gas and Condensate Field Development, National University of Oil and Gas "Gubkin University", Moscow, Russia, [2]Key Laboratory of Continental Shale Hydrocarbon Accumulation and Efficient Development (Northeast Petroleum University), Ministry of Education, Daqing, China, [3]Institute of Unconventional Oil and Gas, Northeast Petroleum University, Daqing, China, [4]The Ninth Oil Production Plant of Daqing Oilfield Co., Ltd., Daqing, China, [5]The Oil and Gas Production Engineering Service Center, Sinopec Zhongyuan Oilfield, Puyang, China, [6]China Petroleum Engineering and Construction Corporation South-West Branch, Chengdu, China

Residual oil distribution plays a critical role in understanding of the CO_2 flooding processes, but its quantitative research for reservoirs with different permeability levels rarely has been comprehensively conducted in the laboratory. This article presents the results of an experimental study on the immiscible CO_2 displacement efficiency in different permeability core samples and various oil distribution patterns prior to and after immiscible CO_2 flooding. Experiments were conducted on four core samples extracted from the selected oil field with a permeability range from 0.210–66.077 mD. The experimental results show that the immiscible CO_2 can mobilize oil in ultralow-permeability environment and achieve a reasonable displacement efficiency (40.98%). The contribution of different oil distribution patterns to displacement efficiency varies in reservoirs with different permeabilities. With the increase of core permeability, the contribution of cluster and intergranular pore oil distribution patterns to displacement efficiency increases. However, the oil displacement efficiency of corner and oil film patterns tends to increase with lower permeability. Therefore, immiscible CO_2 flooding is recommended for ultralow-permeability case, especially for reservoirs with larger amount of oil in corner and oil film distribution patterns. The oil displacement efficiency calculated by immiscible CO_2 flooding experiment results agrees reasonably well with the core frozen slices observation. The results of this study have practical significance that refers to the effective development of low-permeability reservoirs.

Keywords: residual oil distribution, immiscible CO_2 flooding, displacement efficiency, frozen slice technology, ultralow permeability

OPEN ACCESS

Edited by:
Yuwei Li,
Liaoning University, China

Reviewed by:
Zhaojie Song,
China University of Petroleum, China
Pengliang Yu,
The University of Auckland, New Zealand

****Correspondence:***
An-Lun Wang
969659914@qq.com

Specialty section:
This article was submitted to Economic Geology, a section of the journal Frontiers in Earth Science

Received: *12 April 2021*
Accepted: *10 May 2021*
Published: *28 May 2021*

Citation:
Yang Y, Zhou X-F, Sun L-Y, Wang A-L, Wei J-g, Li C-X and Ke X (2021) Immiscible CO_2 Flooding Efficiency in Low-Permeability Reservoirs: An Experimental Investigation of Residual Oil Distribution. Front. Earth Sci. 9:693960. doi: 10.3389/feart.2021.693960

INTRODUCTION

The onshore proven undeveloped oil reserves in China are mainly low-permeability and ultralow-permeability reservoirs (Zhao et al., 2011; Duan et al., 2014). There are many researches in this field with different focuses (Li et al., 2017; Zhang et al., 2020; Wang et al., 2021). Field tests show that CO_2 flooding is a potential option to improve the oil recovery of low-permeability sandstone reservoirs

(Zekri et al., 2006; Bourgeois et al., 2011; Wei et al., 2020a), which is the future development direction of enhanced oil recovery (EOR) in these reservoirs (Su et al., 2011; Hao et al., 2016; Li et al., 2019; Wu et al., 2020).

Determination of residual oil distribution is critically important for developers to identify the potential sweet point, which provides a reasonable basis for the optimum oil recovery method selection. Although residual oil distribution plays a critical role in understanding of the processes which take place within a reservoir during and after CO_2 flooding, and many laboratory studies have been performed to evaluate the residual oil distribution, very limited effort has been focused on its quantitative research at the core scale considering different permeability levels. Wang et al. (2013) studied the residual oil distribution in ultralow-permeability reservoir by using nuclear magnetic resonance (NMR) technique, and they considered wettability, pressure gradient, and different water cuts. Iglauer et al. (2014) imaged a sequence of surfactant EOR production steps with a microcomputed tomography, and they limited the study to microscopic sweep efficiency. Residual oil distribution on pore-scale during secondary and tertiary solvent injection was investigated by Shokrlu and Babadagli, (2015), and they studied the efficiency of a miscible-displacement process that is conducted in a cyclic form similar to water-alternating gas. Hu et al. (2017) conducted an experimental study on the mechanism of CO_2-immiscible flooding and residual oil distribution in a water-drive reservoir. Al-Bayati et al. (2019) presented the results of an experimental study on immiscible CO_2 flooding efficiency in sandstone porous media, but their research did not involve microscale investigation and they focused on the influence of permeability heterogeneity. Wei et al. (2020b) conducted an experimental study, in which the original oil–water distribution feature and that after fluid injection were revealed, and they only covered the case of tight oil reservoirs. Druetta and Picchioni (2020) developed a numerical model to investigate the mechanisms and effectiveness of polymer flooding on the residual oil after waterflooding, and they validated their results by comparing them with the experiments carried out by other authors. Although they conducted numerical simulation, it still provided some perspectives on the experimental investigation of residual oil distribution. Wang et al. (2020) conducted an investigation on the multiphase flow characteristics and EOR mechanism of water-alternating gas (WAG) injection after continuous CO_2 injection at the microscale using CT scanning and microelectronic photolithography. They concluded that WAG injection after continuous CO_2 injection increased oil recovery by 23.15%, which was dominated by the first and second WAG injection cycles. Wei et al. (2021) also applied the NMR technology to carry out experimental research, in which the microscopic oil displacement mechanism in low-permeability reservoirs was discussed, but they focused on five different EOR methods including CO_2 flooding. To our knowledge, the displacement efficiency of immiscible CO_2 flooding by considering the contribution of various oil distribution patterns to displacement efficiency in reservoirs with different permeabilities have not been investigated before. In this work, in order to represent different oil recovery scenarios, scales in the different permeability recovery process are considered: from the macro- to microscale systems. The core permeability range is from 0.210–66.077 mD. The efficiency of immiscible CO_2 flooding is evaluated by the field core drainage experiments, combined with the frozen slice technology the displacement process of oil by immiscible CO_2 is analyzed quantitatively. Thus, this research is dedicated to bridge the existing gap in our knowledge by following a systematic experimental approach and improve fundamental understanding with which it will be possible to develop better production techniques and improved CO_2 EOR models.

EXPERIMENTAL WORK AND METHODOLOGY

Coreflooding Equipment, Core Samples, and Chemicals

In immiscible CO_2 flooding experiments, we have followed a systematic approach. **Figure 1** shows a schematic diagram of the core flooding apparatus used in this study, which consists of the injection system, the displacement system, the pressure control system, and the fluid collection system. The advanced frozen slice technology and the laser confocal scanning microscopy have been applied in order to visualize oil distribution. Experiments were carried out on four core samples from the Daqing Oilfield, China. In the experiments, kerosene and synthetic brine with a salinity of 6778 mg/L were used to simulate oil and formation water. **Table 1** presents the results of measured properties of the sandstone core samples. The core sample G-2 with medium permeability was selected in order to be compared with other low-permeability cores.

Experimental Procedure

Specific experimental procedures are as follows: 1) prepare the formation water and oil as mentioned, 2) clean and dry the core sample, 3) put the core sample in the holder and maintain the confining pressure at 3 MPa; vacuum the core for 24 h, 4) inject formation water into the core by hand pump until the pressure at the end of the core remains at 0.5 MPa, 5) inject oil at a constant speed of 0.005 ml/min until no water flows out, 6) place the core in the 90°C thermotank for 48 h, 7) cut 1.5 cm core end to make a frozen slice, 8) set the temperature and the back pressure of the displacement system at 50°C and 6.5 MPa to ensure immiscible condition (Yang et al., 2015; Zhang et al., 2017; Dindoruk et al., 2020); flood the remaining core with a constant speed of 0.01 ml/min for three pore volume (PV) CO_2, 9) record injection pressure, oil and gas production every certain time until no oil comes out, 10) cut 1.5 cm core end to make another frozen slice, and 11) use the laser confocal scanning microscopy to visualize residual oil distribution.

The same procedure was applied to all core samples with different permeabilities.

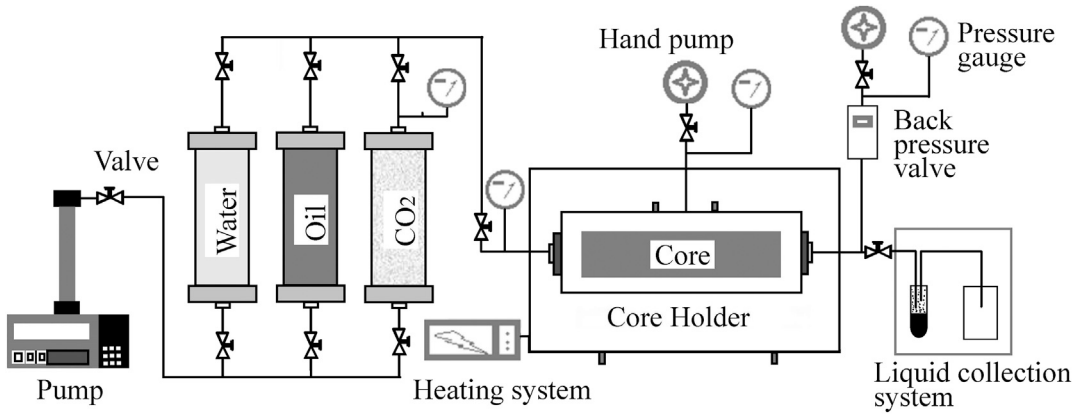

FIGURE 1 | Schematic of the experimental setup.

TABLE 1 | Petrophysical properties of the core samples.

Sample	Diameter, cm	Length, cm	Dry weight, g	Bulk volume, cm^3	Porosity, %	Permeability, mD	Permeability level
FY-1	2.54	4.93	55.9991	24.981	12.366	0.210	Ultra-low
FY-2	2.50	4.81	51.7287	23.631	16.617	7.047	Extra low
G-1	2.50	6.89	73.4510	33.841	15.399	21.751	Low
G-2	2.51	7.21	72.8497	35.676	21.998	60.077	Medium

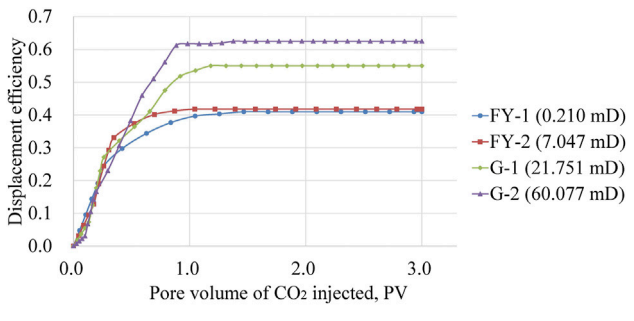

FIGURE 2 | Displacement efficiency vs. PV number of CO_2 injected for different cores.

RESULTS AND DISCUSSION

In this section, the flooding experiment results are analyzed in order to understand the macroscopic displacement efficiency relative to different permeabilities. The results of residual oil distribution visualization by laser confocal microscopy are discussed to shed some light on the microscale oil distribution and contribution of different distribution patterns to displacement efficiency with all mentioned permeability ranges.

Immiscible CO_2 Flooding Experiments: Macroscopic Displacement Efficiency

The displacement efficiency of immiscible CO_2 flooding as a function of PV number for core samples with different permeabilities was calculated and is presented in **Figure 2**. **Figure 3** shows the change of percent displacement efficiency and oil saturation post and prior to CO_2 flooding with permeability.

As expected, in all runs, displacement efficiency increased with the increasing of pore volume of CO_2 injected. At the initial stage of immiscible CO_2 flooding, the oil displacement efficiency of cores with different permeability levels did not change significantly, and the ultralow and extra low-permeability cores had even faster growth rate than that of the PV number. Injecting CO_2 as an immiscible agent at experimental conditions resulted in final oil displacement efficiency of 40.98 and 41.76% for ultralow and extra low permeability, respectively. There was only a slight change in displacement efficiency when the permeability increased from ultralow to extra low, but immiscible CO_2 flooding performance improved significantly at higher permeability. The following oil displacement efficiency was obtained: 54.98 and 62.49% corresponding to low and medium permeability, respectively. At the higher permeability, the injected CO_2 succeeded to contact more oil in place and managed to displace and/or extract much more oil than in the lower permeability case. The displacement efficiency of immiscible CO_2 flooding in medium permeability core was increased by 52.49, 49.64, and 13.66% compared with ultralow-, extra low-, and low-permeability core samples, respectively.

The increase of displacement efficiency began to slow down after about 0.35 PV of CO_2 had been injected for ultralow and extra low-permeability cores, and 0.9 PV for higher permeability cores. Moreover, in the case of medium permeability, higher oil saturation prior to CO_2 flooding and lower oil saturation post

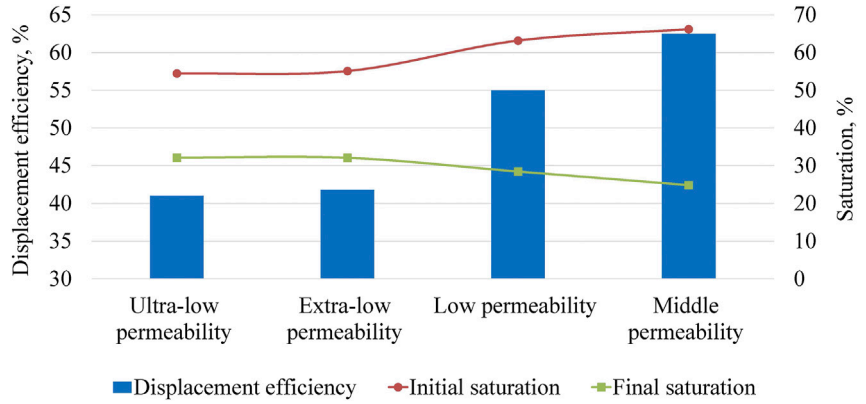

FIGURE 3 | Displacement efficiency and oil saturation post and prior to CO_2 flooding vs. permeabilities.

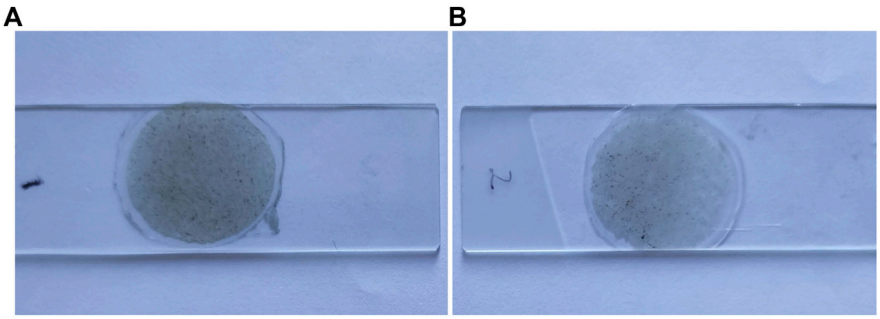

FIGURE 4 | Frozen slices of core FY-1 prior to **(A)** and post **(B)** CO_2 floods.

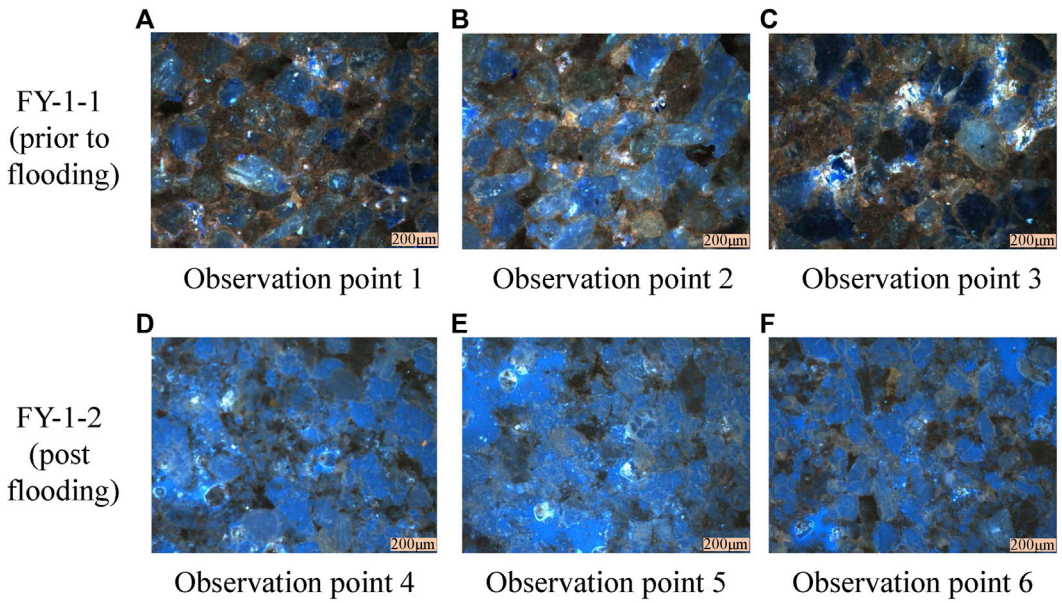

FIGURE 5 | Oil saturation prior to and post CO_2 floods in reservoir core with ultralow permeability. **(A–C:** observation points before the CO_2 flood, **D–F:** observation points after CO_2 flood).

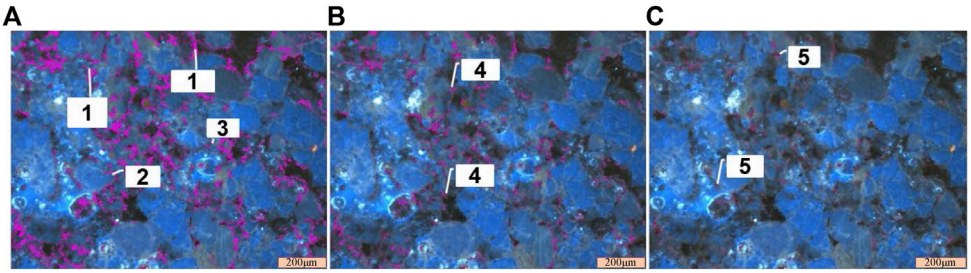

FIGURE 6 | Visualization of different residual oil distribution patterns of core sample FY-1 (**A**: 1—cluster; 2—pore-throat; 3—corner; **B**: 4—intergranular pore; **C**: 5—oil film).

flooding were observed. Nevertheless, experimental results show that the immiscible CO_2 can mobilize oil in ultralow-permeability environment with a reasonable recovery.

Quantitative Observation of Core-Frozen Slices: Microscopic Displacement Efficiency

We performed a series of experiments as mentioned above for quantitative observation of different residual oil distribution patterns on core frozen slices with different permeabilities. The frozen slices of ultralow-permeability core prior to and post-immiscible CO_2 flooding are shown in **Figure 4**. Three observation points were selected evenly on each of the slices. In order to determine the oil distribution patterns and analyze their contribution to displacement efficiency, microphoto images of oil saturation were taken prior to and after CO_2 flood, which are shown in **Figure 5**. **Figures 5A–C** show oil distribution of the three observation points before the CO_2 flood, and **Figures 5D–F** reveal three observation points oil distribution after CO_2 flood. We can see a significant decrease of oil saturation after CO_2 floods.

The image processing software developed by our team is used for quantitative analysis of oil distribution in different pore structures. In this study, we found five dominant oil distribution patterns, namely, cluster, pore-throat, corner, intergranular pore, and oil film. Cluster distribution pattern refers to the oil trapped in the large pores connected by small pores and narrow throats. In the pore-throat distribution pattern, oil is snapped off at the neck (narrow throat) and may become residual under the current displacement conditions. In corner distribution pattern, oil is trapped in the end of the pores (the dead corner) due to poor connectivity. In the intergranular pore distribution, oil is in the dispersed phase due to the existence of fine particles in pores. Oil film distribution pattern refers to the oil located on the particle surface of the channel wall in the form of thin layer.

Figure 6 presents the software processing result of the residual oil distribution in ultralow-permeability reservoirs. It can be seen that all the five oil distribution patterns (**Figure 6A**—cluster, pore-throat, and corner; **Figure 6B**—intergranular pore; **Figure 6C**—oil film) exist in ultralow-permeability reservoirs but with different proportions. Similarly, we can calculate the oil distribution pattern of other cores before and after displacement.

Figure 7 shows the proportions of different oil distribution patterns to total pore volume prior to and post CO_2 floods, then we can determine the production contribution from every oil distribution pattern.

From **Figures 6**, **7**, we can learn that various oil distribution patterns had different contributions to displacement efficiency in reservoirs with different permeabilities. The most common oil distribution pattern for all core samples was cluster, which had the biggest contribution to oil production. The distribution pattern of intergranular pore also had a higher production contribution. Oil did not tend to be stored in oil film pattern, which was mainly affected by the pore structure. Generally speaking, the larger the permeability was, the greater the contribution of cluster and intergranular distribution patterns to the oil production and the higher the ultimate oil displacement efficiency. The production contribution of the cluster distribution pattern in medium permeability core was increased by 32.89, 29.56, and 7.44% when compared with ultralow-, extra low-, and low-permeability core samples, respectively.

Compared with other core samples, the *in situ* oil saturation of core sample with extra low permeability was more concentrated in the corner and oil film distribution patterns, resulting in relatively low oil mobility. Therefore, although its permeability was much higher than that of ultralow-permeability core, only slight increase in displacement efficiency was observed, and this phenomenon should be studied on case-by-case basis using the formation fluids and rocks under reservoir conditions. In general, oil displacement efficiency of corner and oil film patterns tends to decrease with higher permeability. In core samples with ultralow permeability, CO_2 can enter into smaller pores, expand the sweep area, and improve the displacement efficiency of oil in pore-throat, corner, and oil film distribution pattern. There was no big change between cores with different permeabilities in the contribution of pore-throat oil distribution pattern to displacement efficiency.

The displacement efficiencies of immiscible CO_2 flooding in reservoir core samples with different permeabilities by microscopic oil distribution were 37.62% (ultralow), 41.52% (extra low), 56.86% (low), and 61.90% (medium). The average relative error of oil displacement efficiency calculated by immiscible CO_2 flooding experiment results and by frozen slices observation was 3.28%.

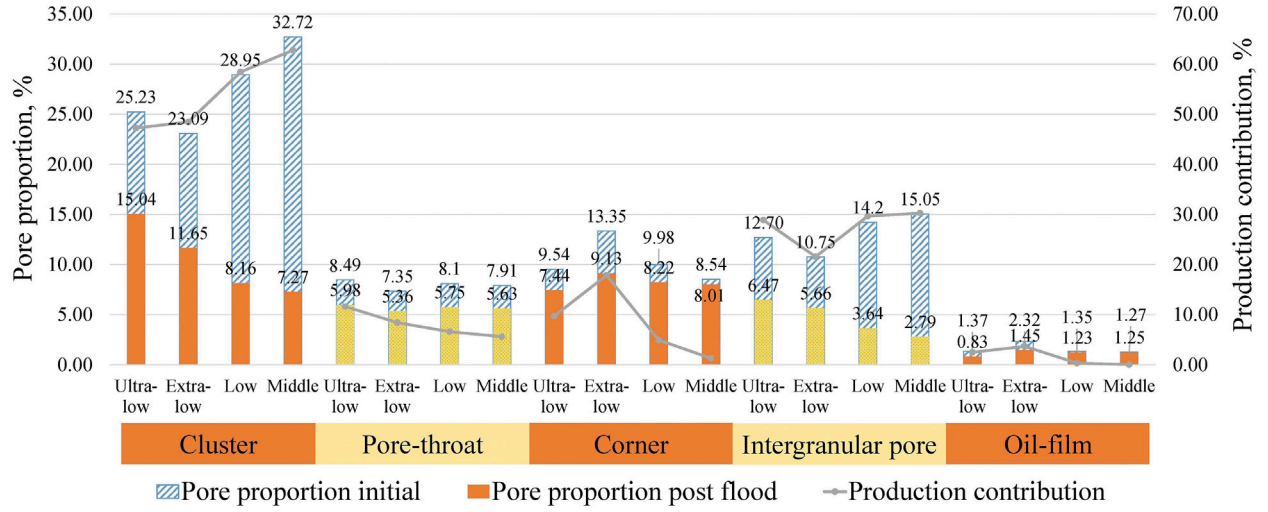

FIGURE 7 | Proportions of oil distribution patterns to total pore volume before and after CO_2 floods, their production contribution.

CONCLUSION

The experiments described in this article represent immiscible CO_2 floods on core samples with different permeabilities. From the experimental studies presented above, we can draw the following conclusions:

1. Immiscible CO_2 flooding performance on reservoir cores improves with the increase of permeability. Compared with ultralow-, extra low-, and low-permeability core samples from the target oilfield, the displacement efficiency of immiscible CO_2 flooding on medium permeability core was increased by 52.49, 49.64, and 13.66%, respectively.
2. In all core frozen slices, five oil distribution patterns with different proportions were observed. The experimental results showed that the production contribution of different oil distribution patterns varies in reservoirs with different permeability levels. Compared with other oil distribution patterns, there was no big change between cores with different permeabilities in the production contribution of pore-throat distribution pattern.
3. The contribution of cluster and intergranular pore-oil distribution patterns to displacement efficiency was more pronounced in cases with higher permeability. The production contribution of cluster distribution pattern in medium permeability core sample during immiscible CO_2 flooding was increased by 32.89, 29.56, and 7.44% when compared with ultralow-, extra low-, and low-permeability cores, respectively. Therefore, the pore proportion of cluster and intergranular pore oil distribution patterns is an important indicator for efficient development of higher permeability reservoirs.
4. The oil displacement efficiency of corner and oil film distribution patterns tends to increase with lower permeability, where CO_2 can enter the smaller pore structures and expand the sweep area. In ultralow-permeability reservoirs, the immiscible CO_2 can mobilize oil in all five distribution patterns and achieve reasonable displacement efficiency (40.98%). Therefore, immiscible CO_2 flooding is recommended for ultralow-permeability case, especially for reservoirs with larger amount of oil in corner and oil film distribution patterns.

DATA AVAILABILITY STATEMENT

The original contributions presented in the study are included in the article/Supplementary Material, further inquiries can be directed to the corresponding authors.

AUTHOR CONTRIBUTIONS

YY proposed the research. X-FZ, C-XL and XK prepared figures and tables, and interpreted the structural data. YY, A-LW and J-G W developed the main ideas. L-YS participated in the field work. X-FZ and A-LW participated in the lab work. YY, X-FZ, A-LW and J-G W contributed to writing the original manuscript. L-YS, C-XL and XK contributed to revising the manuscript. All co-authors actively contributed to the manuscript with comments, ideas, and suggestions.

FUNDING

This work was funded by the Youth Science Foundation of Northeast Petroleum University (Grant No2019QNL-22).

REFERENCES

Al-Bayati, D., Saeedi, A., Myers, M., White, C., and Xie, Q. (2019). An Experimental Investigation of Immiscible-CO2-Flooding Efficiency in Sandstone Reservoirs: Influence of Permeability Heterogeneity. *SPE Reservoir Eval. Eng.* 22 (3), 990–997. doi:10.2118/190876-PA

Bourgeois, M. J., Thibeau, S., and Guo, J. (2011). *Modelling Residual Oil Saturation in Miscible and Immiscible Gas Floods by Use of Alpha-Factors*. Vienna, Austria: Paper presented at the SPE EUROPEC/EAGE Annual Conference and Exhibition. doi:10.2118/143379-MS

Dindoruk, B., Johns, R., and Orr, F. M. (2020). *Measurement of Minimum Miscibility Pressure: A State of the Art Review*. Virtual: Paper presented at the SPE Improved Oil Recovery Conference. doi:10.2118/200462-MS

Druetta, P., and Picchioni, F. (2020). Influence of Physical and Rheological Properties of Sweeping Fluids on the Residual Oil Saturation at the Micro- and Macroscale. *J. Non-Newtonian Fluid Mech.* 286, 104444. doi:10.1016/j.jnnfm.2020.104444

Duan, B., Yin, Y., Hu, Y., Yao, W., Zhu, Z., and Nie, C. (2014). Study on the Fluid's Flowing Law in the Different-Level Pores of Low Permeability Reservoir. *Sci. Technol. Eng.* 14, 26–30. doi:10.3969/j.issn.1671-1815.2014.10.006 (in Chinese with English abstract).

Hao, H., Hou, J., Zhao, F., Hou, L., Wang, Z., and Song, Z. (2016). Experiments of Gas Channeling Control during CO_2 Immiscible Flooding in Low Permeability Reservoirs with Heterogeneity. *Pet. Geology. Recovery Efficiency* 23, 95–100. doi:10.3969/j.issn.1009-9603.2016.03.017 (in Chinese with English abstract).

Hu, W., Lu, C., Wang, R., Yang, Y., and Wang, X. (2017). Mechanism of CO_2 Immiscible Flooding and Distribution of Remaining Oil in Water Drive Oil Reservoir. *Pet. Geology. Recovery Efficiency* 24, 99–105. doi:10.13673/j.cnki.cn37-1359/te.2017.05.015 (in Chinese with English abstract).

Iglauer, S., Sarmadivaleh, M., Geng, C., and Lebedev, M. (2014). In-situ *Residual Oil Saturation and Cluster Size Distribution in Sandstones after Surfactant Flooding Imaged with X-ray Micro-computed Tomography*. Doha, Qatar: Paper presented at the International Petroleum Technology Conference. doi:10.2523/IPTC-17312-MS

Li, R., Liao, X., Zou, J., Zhang, H., Zhou, X., Mu, L., et al. (2019). *Experimental and Numerical Studies on Asphaltene Deposition Distribution during CO_2 Flooding in Ultra-low Permeability Reservoirs*. Houston, Texas, USA: Paper presented at the Carbon Management Technology Conference. doi:10.7122/CMTC-552770-MS

Li, Y., Jia, D., Rui, Z., Peng, J., Fu, C., and Zhang, J.(2017). Evaluation Method of Rock Brittleness Based on Statistical Constitutive Relations for Rock Damage. *J. Pet. Sci. Eng.*. 153, 123–132. doi:10.1016/j.petrol.2017.03.041

Shokrlu, Y. H., and Babadagli, T. (2015). Pore-scale Investigation of Phase Distribution and Residual-Oil Development during Secondary and Tertiary Solvent Injection. *SPE Reservoir Eval. Eng.* 18, 39–52. doi:10.2118/173180-PA

Su, Y., Wu, C., Zhang, Q., and Wu, X. (2011). Characteristics of Immiscible CO_2 Displacement in Extremely Low Permeability Reservoir. *J. Chongqing Univ.* 34, 53–57. doi:10.11835/j.issn.1000-582X.2011.04.010 (in Chinese with English abstract).

Wang, L., He, Y., Wang, Q., Liu, M., and Jin, X. (2020). Multiphase Flow Characteristics and EOR Mechanism of Immiscible CO2 Water-Alternating-Gas Injection after Continuous CO2 Injection: A Micro-scale Visual Investigation. *Fuel.* 282, 118689. doi:10.1016/j.fuel.2020.118689

Wang, X., Yang, Z., Li, H., and Li, Z. (2013). Microscopic Distribution of Remaining Oil of Ultra-low Permeability Reservoir by Using NMR Technique. *J. Basic Sci. Eng.* 21, 702–709. doi:10.3969/j.issn.1005-0930.2013.04.012 (in Chinese with English abstract).

Wang, Z., Zeng, L., Yu, J., Zhang, Z., Yang, S., and Liu, Y. (2021). Key Geological Factors Controlling Oil Displacement Efficiency of CO2 Injection in Low-Permeability Reservoirs. *Energy Explor. Exploit.* 39 (3), 993–1009. doi:10.1177/0144598721995609

Wei, J., Li, J., Zhou, X., and Zhang, X. (2020a). Effect of Pressure and CO2 Content on the Asphaltene Precipitation in the Light Crude Oil. *Pet. Sci. Technol.* 38 (2), 116–123. doi:10.1080/10916466.2019.1684947

Wei, J., Zhou, X., Zhou, J., Li, J., and Wang, A. (2020b). Recovery Efficiency of Tight Oil Reservoirs with Different Injection Fluids: An Experimental Investigation of Oil-Water Distribution Feature. *J. Pet. Sci. Eng.* 195, 107678. doi:10.1016/j.petrol.2020.107678

Wei, J., Zhou, J., Li, J., Zhou, X., Dong, W., and Cheng, Z., (2021). Experimental Study on Oil Recovery Mechanism of CO2 Associated Enhancing Oil Recovery Methods in Low Permeability Reservoirs. *J. Pet. Sci. Eng.* 197, 108047. doi:10.1016/j.petrol.2020.108047

Wu, S., Fan, T., Zhao, L., Peng, H., Wang, B., and Ma, X., (2020). *Miscible CO2 Flooding Simulation with a Compositional Model in Middle East Carbonate Reservoir*. Virtual: Paper presented at the SPE Asia Pacific Oil & Gas Conference and Exhibition. doi:10.2118/202259-MS

Yang, S., Lian, L., Yang, Y., Li, S., Tang, J., Ji, Z., et al. (2015). Molecular Optimization Design and Evaluation of Miscible Processing Aids Applied to CO_2 Flooding. *Xinjiang Pet. Geology.* 36, 555–559. doi:10.7657/XJPG20150510 (in Chinese with English abstract).

Zekri, A. Y., Almehaideb, R. A., and Shedid, S. A. (2006). *Displacement Efficiency of Supercritical CO2 Flooding in Tight Carbonate Rocks under Immiscible Conditions*. Vienna, Austria: Paper presented at the SPE Europec/EAGE Annual Conference and Exhibition. doi:10.2118/98911-MS

Zhang, F., An, M., Zhang, L., Fang, Y., and Elsworth, D. (2020). Effect of Mineralogy on Friction-Dilation Relationships for Simulated Faults: Implications for Permeability Evolution in Caprock Faults. *Geosci. Front.* 11 (02), 439–450. doi:10.1016/j.gsf.2019.05.014

Zhang, X., Chen, H., Li, B., Mei, Y., Yang, G., and Tang, H. (2017). Discussion on Controlling Conditions of Optimal Near-Miscible Flooding by Impure CO_2 in Low Permeability Reservoir. *China Offshore Oil and Gas* 29, 75–78. doi:10.11935/j.issn.1673-1506.2017.06.009 (in Chinese with English abstract).

Zhao, M., Li, J., and Wang, Z. (2011). The Study on CO_2 Immiscible Mechanism in Low Permeability Reservoir. *Sci. Technology Eng.* 11, 1438–1440. doi:10.3969/j.issn.1671-1815.2011.07.007 (in Chinese with English abstract).

Conflict of Interest: Author L-YS was employed by the company The Ninth Oil Production Plant of Daqing Oilfield Co., Ltd; author C-XL was employed by the company The Oil and Gas Production Engineering Service Center, Sinopec Zhongyuan Oilfield; author XK was employed by the company China Petroleum Engineering and Construction Corporation South-West Branch.

The remaining authors declare that the research was conducted in the absence of any commercial or financial relationships that could be construed as a potential conflict of interest.

frontiers in Earth Science

ORIGINAL RESEARCH
published: 11 August 2021
doi: 10.3389/feart.2021.712681

Calculation of Average Reservoir Pore Pressure Based on Surface Displacement Using Image-To-Image Convolutional Neural Network Model

Chaoyang Hu, Fengjiao Wang and Chi Ai*

Laboratory of Enhanced Oil Recovery of Education Ministry, Northeast Petroleum University, Daqing, China

The average pore pressure during oil formation is an important parameter for measuring the energy required for the oil formation and the capacity of injection–production wells. In past studies, the average pore pressure has been derived mainly from pressure build-up test results. However, such tests are expensive and time-consuming. The surface displacement of an oilfield is the result of change in the formation pore pressure, but no method is available for calculating the formation pore pressure based on the surface displacement. Therefore, in this study, the vertical displacement of the Earth's surface was used to calculate changes in reservoir pore pressure. We employed marker-stakes to measure ground displacement. We used an improved image-to-image convolutional neural network (CNN) that does not include pooling layers or full-connection layers and uses a new loss function. We used the forward evolution method to produce training samples with labels. The CNN completed self-training using these samples. Then, machine learning was used to invert the surface vertical displacement to change the pore pressure in the oil reservoir. The method was tested in a block of the Sazhong X development zone in the Daqing Oilfield in China. The results showed that the variation in the formation pore pressure was 83.12%, in accordance with the results of 20 groups of pressure build-up tests within the range of the marker-stake measurements. Thus, the proposed method is less expensive, and faster than existing methods.

Keywords: convolutional neural network, average pore pressure, surface displacement, inversion calculation, daqing oilfield

OPEN ACCESS

Edited by:
Jizhou Tang,
Tongji University, China

Reviewed by:
Xuyang Guo,
China University of Petroleum, China
Fengshou Zhang,
Tongji University, China

****Correspondence:***
Fengjiao Wang
Wangfengjiao8699@126.com

Specialty section:
This article was submitted to Economic Geology, a section of the journal Frontiers in Earth Science

Received: *21 May 2021*
Accepted: *02 August 2021*
Published: *11 August 2021*

Citation:
Hu C, Wang F and Ai C (2021) Calculation of Average Reservoir Pore Pressure Based on Surface Displacement Using Image-To-Image Convolutional Neural Network Model. Front. Earth Sci. 9:712681. doi: 10.3389/feart.2021.712681

INTRODUCTION

Oil reservoirs consist of porous media, and the formation pore pressure refers to the fluid pressure in the pores of a reservoir. The formation energy, development potential, rock type, and geological structure are reflected in the formation pore pressure and its variation law. Continental sandstone oilfield has entered the stage of ultra-high water cut development. With the long-term injection of foreign fluid and the continuous exploitation of oil and gas, the formation pressure is continuously supplemented and released, and the seepage law of formation fluid changes all the time. Formation pore pressure is the representation of reservoir energy and the direct embodiment of reservoir fluid seepage capacity. It also plays an important role in the adjustment of large-scale well pattern in the middle and late stage of oilfield development. The average formation pore pressure in a development block is an important parameter for adjusting the injection–production intensity and measuring the

injection–production capacity (Gao et al., 2018). Accurate prediction of the formation pressure is an important prerequisite for stable and seamless oil field development (Xu W. et al., 2019; Sheng et al., 2020). During the development of an oil field, continuous casing damage occurs frequently at the weakest horizontal structural surface of the reservoir. The main reason for this phenomenon has been proven to be the slip of the weak horizontal structural surface caused by the inter-regional pore pressure. Casing damage severely affects oil field development, forcing many injection–production wells to shut in. For instance, at the Daqing Oilfield in China, an area where casing damage is prevalent, the damage rates are as high as 50–80% (Cui 2015).

The section slip of a standard horizontal fossil layer is caused by uneven deformation induced by the inter-regional pore pressure (Hu et al., 2018; Xie et al., 2020; Zhao et al., 2020). It is necessary to control the difference in average inter-regional formation pressure to prevent expansion of the casing damage area in the Daqing Oilfield (Ai et al., 2015). The original cause of the casing damage was the pressure change of the formation. Pressure changes can induce stress changes of rock underground (Guo et al., 2019a). Therefore, monitoring and prediction of the formation pore pressure are important to ensure daily oilfield production (Tang et al., 2018; Xu X. Q. et al., 2019; Tang et al., 2021). However, the average pore pressure during formation cannot be directly obtained (Shen et al., 2014; Li et al., 2017; Ameh 2019). Additionally, the formation-pressure gradient near water injection and oil production wells is excessively large to be used as the basic parameter for calculating the average formation pressure (Wang and Sheng, 2018; Zhang et al., 2020). The technology for predicting formation pore pressure has been successfully employed in seismic data prediction research since the 1970s (Tipper 1976). The main forecasting methods include the equivalent depth formula (Yun 1996), Eaton method (Eaton 1972), ratio method, empirical formula, Fillippone method (Fillippone 1982), and some other methods (Sun and Sun, 2007; Wei et al., 2007; Yu et al., 2014; Xiong et al., 2019; Zhang et al., 2021). However, these methods are limited in terms of their accuracy in calculating the seismic layer velocity. Therefore, some scholars have proposed a prediction method for abnormal formation pressure based on acoustic impedance inversion and multi-seismic attribute joint inversion (Banik et al., 2013), and based on pre-stack velocity inversion (Dutta 2002; Dutta and Khazanehdari, 2006). Moreover, the seismic multi-elastic parameter pore fluid pressure prediction method has been developed for low permeability reservoirs, and satisfactory results have been obtained in practical applications of this method (Hou et al., 2019). In general, the average pore pressure has been observed to depend on the results of pressure build-up tests, which are both cost- and time-intensive. Moreover, the pressure build-up test data of a single well can reflect the average pore pressure of only formations near the test well. Consequently, it is difficult to evaluate the average formation pressure in several oilfields.

Several studies have confirmed that a correlation exists between surface displacement and formation pore pressure, which is not a simple linear one-to-one correspondence. In 2009, Rutqvist et al. (2010) conducted a series of rock mechanics simulation analyses of a reservoir–geomechanical coupling reservoir and the interaction between pore pressure and geological stress is considered. They reported that the surface displacement was consistent with the expansion in the volume of the injection area and adjacent strata caused by the pressure change, which was as a result of the change in the reservoir pore pressure. The surface displacement depended on the change in the reservoir pressure, volume of the injected fluid, and elastic properties of the reservoir cap. Xue et al. (2018) studied the abrupt transition of the coupled gas-stress behavior at the dilatancy boundary using a strain-based percolation model. Based on orthogonal triaxial stress experiments with CH_4 seepage, the complete stress–strain relationship and the corresponding evolution of the volumetric strain and permeability were obtained. Zhang et al. (2018) investigated the effect of pore-fluid pressure on normal deformation through laboratory experiments. The results indicated that the pore-fluid pressure significantly affects the normal deformation of a jointed sample. Moreover, the relative normal deformation of the host rock during fluid injection has a linear relationship with the pore-fluid pressure. Guo et al. (2019b) considered the mechanisms of the mixed responses of unconventional reservoir under inter well interference, used the finite element method to describe the poroelastic behaviors of multiphase-fluid diffusivity and rock deformation, and used the displacement discontinuity method to describe the numerical simulation work flow of multi-fracture propagation.

Evidently, past research has focused primarily on changes in the formation pore pressure to calculate the surface displacement. Recently, surface displacement has been predicted based on underground parameters (Qi et al., 2017). However, the present study represents the first attempt at calculating the pore pressure of underground oil reservoirs based on the surface displacement. Although positive evolution is possible, reverse evolution is challenging. According to the relationship between the formation pore pressure and surface displacement, forward calculation involves an explicit equation, whereas backward calculation involves a set of equations that cannot be calculated directly. When the number of grids is large, a large number of equations will be formed. When the number of equations is large, the accuracy of the constant term of the coefficient matrix, or the input of the model, will be improved.

In this study, the convolution method was simplified to a convolution algorithm based on the convolution characteristics of the linear-deformation stage. Artificial intelligence can assist in determining the relationship between two parameters. Machine learning can play a good role in images, or two-dimensional matrix; in this regard, convolutional neural networks (CNNs) are the most effective tool. An improved CNN was established in this study to determine pore pressure variation from surface displacement. The accuracy of the model was verified using marker-stake monitoring data and the average formation-pressure data obtained from pressure build-up tests conducted in the Sazhong Development Zone, Daqing Oilfield, China.

INVERSION OF CHANGES IN AVERAGE PORE PRESSURE

The relationship between the average pore pressure and surface displacement is critical for the inversion of the reservoir pore pressure. The surface deformation occurs only after the formation pore pressure changes. The calculation of formation pore pressure by surface deformation is an inverse calculation. The geological factors of oil layer are complex, and the formation pressure is influenced by many factors (Cipolla et al., 2018). If the value of a discrete cell in the forward calculation is the superposition of multiple equations, the inverse calculation is to solve these equations, but if the forward calculation is an iterative calculation, the reverse calculation needs multivariable iterative solution. Only forward calculation is simple enough, and inversion calculation can be carried out. The extent of the change in the reservoir volume caused by the change in reservoir pore pressure is within the range of linear elastic deformation of reservoirs. The deformation of the reservoir due to changes in pore pressure simultaneously causes deformation of the surrounding strata, and the resulting displacement is transferred to the surface. In this process, the deformation of the formation rock is still in the stage of linear elasticity. According to the superposition principle of stress and strain in the linear elastic stage, the final surface displacement is the linear superposition of the change in the pore pressure of each underground storage grid on the surface displacement generated by each grid. We assumed that there was no gradient in the plane and that the mechanical and seepage parameters were equal in the plane. Thus, if a single grid changes the surface deformation distribution due to a unit pressure, the surface displacement caused by any formation pressure can be linearly superposed based on the formation deformation generated by the unit pressure of a single grid. This method can be expressed by the convolution equation:

$$u(x,y) = k(x,y)^{*}\,\mathrm{p}(\mathrm{x},\mathrm{y}), \tag{1}$$

where u (x, y) is the vertical displacement of the surface at point (x, y) (m); k (x, y) is the convolution kernel (m), i.e., a storage grid changes the distribution of the surface displacement caused by a unit pressure (m/MPa); and p (x, y) is the formation-pore-pressure distribution (MPa).

The actual measured or calculated formation pore pressure and surface deformation parameters constituted a plane composed of limited data point planes. It is necessary to perform plane discretization in advance and discretize the stratum plane into a finite mesh with a length of M and a width of N. The two-dimensional discrete convolution equation is

$$u(x,y) = k(x,y)*p(x,y) = \sum_{i=0}^{M}\sum_{j=0}^{N} k(i,j)p(x+i,y+j) \tag{2}$$

.

The convolution kernel k (x, y) represents the vertical displacement of a formation with changes in the unit pressure of a single grid, which can be obtained through numerical simulation. Correspondingly, p (x, y) is the formation pore-pressure distribution. Therefore, the determination of surface displacement based on formation pore pressure involves forward modeling and explicit calculation, that is, for a vertical displacement u (x, y) at any surface location, there is no unknown number in the solution process.

To obtain the pore pressure distribution of the p (x, y) formation based on the vertical displacement u (x, y) of the surface, it is necessary to solve a large set of equations in which the number of unknowns is equal to the square of the convolution kernel. However, the position of the convolution core far away from the center was almost zero (the value of the far end of the convolution core caused by the change of unit displacement and unit pressure is almost zero). Thus, inversion of the equations is impossible because some unknown coefficients in some of the equations are close to 0, which significantly affects the solution accuracy (Hwang et al., 2019; Mohammady et al., 2020).

In the calculation for deconvolution, machine learning can be used to address the problem of convolution. Because the surface displacement field is a group of plane data, it is similar to a blurred image. CNN is the most effective type of machine learning algorithm, and it uses images as the input layer. However, the calculation of changes in formation pressure based on surface displacement inversion is deduced from one field to another, which requires some changes to the existing CNN structure. A traditional CNN model is shown in **Figure 1**.

The model can be explained as equations as:

$$\begin{aligned}&\text{Convolution: } h^{(1)} = I*k^{(1)} + b^{(1)}\\ &\text{Pooling: } p^{(1)} = \mathrm{AF}\{\mathrm{POOLING}\left[h^{(1)}\right]\}\\ &\text{Convolution: } h^{(2)} = h^{(1)}*k^{(2)} + b^{(2)}\\ &\text{Pooling: } p^{(2)} = \mathrm{AF}\{\mathrm{POOLING}\left[h^{(2)}\right]\}\end{aligned} \tag{3}$$

where $h^{(i)}$ is the i-th hidden image layer; $k^{(i)}$ is the convolution kernels of i-th layer; $b^{(i)}$ is the biases of i-th layer; I is the model inputs. AF is the activate function, POOLING is pooling calculation.

Pooling calculation is a computing method that divides a two-dimensional data into several regions, calculates a value from all grids in each region, and then recombines it into new two-dimensional data.

The same calculation method is used until the last convolution and pooling operation. Then each pixel of the last group of two-dimensional images is arranged into a variable $h_{\mathrm{F}}^{(1)}$ in one dimension as

$$\begin{aligned}&\text{Convert into one} - \text{dimensional} : h_{\mathrm{F}}^{(1)}(m) = p^{(L)}(x,y)\\ &\text{Full connection} : h_{\mathrm{F}}^{(2)} = \mathrm{AF}\left\{W^{(1)}h_{\mathrm{F}}^{(1)}(m) + b_{\mathrm{F}}^{(1)}\right\}\\ &\text{Output} : Y' = \mathrm{AF}\left\{W^{(2)}h_{\mathrm{F}}^{(2)}(m) + b_{\mathrm{F}}^{(2)}\right\}\end{aligned} \tag{4}$$

where L is the number of hidden layers; $h_{\mathrm{F}}^{(i)}$ is the i-th hidden layer in full connection; $b_{\mathrm{F}}^{(i)}$ is the biases of i-th layer in full connection; $W^{(i)}$ is the weights of i-th layer; Y' is the predicted values.

Traditional CNNs include an input layer, convolution layer, pooling layer, full-connection layer, and output layer. Through continuous convolution and pooling, the input image is

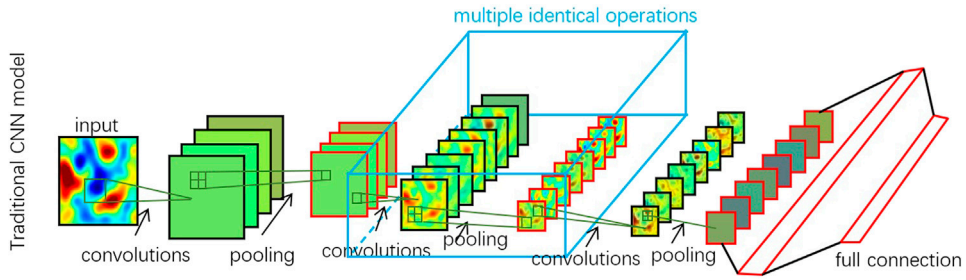

FIGURE 1 | Traditional CNN model.

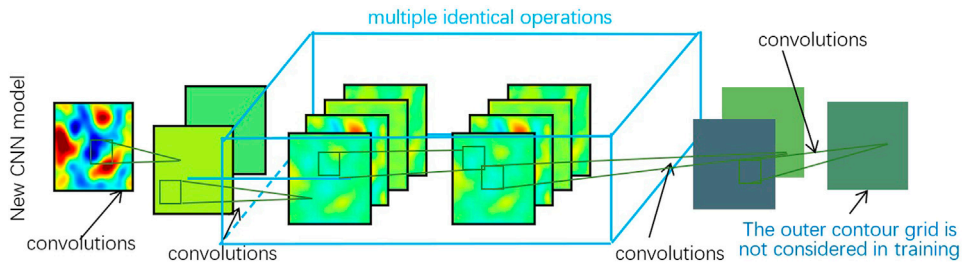

FIGURE 2 | Proposed image-to-image model.

abstracted into a number of low-pixel two-dimensional parameters, and the results are output through several fully connected neural networks. The output results are used for image recognition and other applications. The convolution layer is used to increase the thickness (number of images), the pooling layer is used to highlight features and reduce the number of intermediate parameters, and the full-connection layer is used to convert two-dimensional data to one-dimensional data.

For our application, the aforementioned structure must be modified. As the relationship between the fields of surface vertical displacement and formation pressure change depends on the displacement of the formation, the process is smooth and continuous. The relationship between the fields of surface vertical displacement and formation pressure change is the coupling relationship between fluid pressure and rock matrix stress in porous media. The change of rock matrix stress will cause the strain of rock, which shows macroscopic deformation and displacement on the surface. In the Seepage-solid coupling model of porous media, it can be seen from the compatibility equation derived from the geometric equation that the deformation and displacement of each point are continuous in the process of rock elastic deformation. Hence, no pooling layers are needed for image collection, and the layer thickness need not be large either. Since the output layer comprises two-dimensional data, it is an image-to-image issue, and no full-connection layer is needed to transform the dimensions of the data. Therefore, the proposed CNN does not include a pooling layer and or a full-connection layer. Pooling layer can effectively abstract and prevent overfitting in machine vision models. However, in this issue, the two functions of pooling layer are not effective. For practical physical problems, there are few features that can be abstracted as the surface deformation field does not have some contours like the image; The training data of this model comes from forward calculation, there are unlimited training samples, the training process will not encounter the same samples, so it will not overfit. At the same time, pooling computing can reduce the dimension of intermediate computing process and reduce the number of variables. However, for this problem, the number of grids becomes less after pooling, which is equivalent to a sudden doubling of the grid size, changing the corresponding relationship between the input and output layers at the same position. The proposed image-to-image model are shown in **Figure 1**.

The new model can be explained as:

$$\begin{aligned} h^{(1)} &= u * k^{(1)} + b^{(1)} \\ h^{(2)} &= h^{(1)} * k^{(2)} + b^{(2)} \end{aligned} \tag{5}$$

where u is the deformation on the ground surface, mm.

The same calculation method is used until the last convolution. The final predicted pressure change field is the final output image.

$$p'(x, y) = h^{(L-1)} * k^{(L)} + b^{(L)} \tag{6}$$

where p' is the predicted pressure change field in reservoir, MPa.

In addition to the aforementioned modifications, the loss function of the model was adjusted. The surface vertical displacement due to changes in pore pressure at a certain underground point includes not only the point with the same plane coordinate but also the area around this point. In contrast, the vertical displacement of a certain point on the surface is the

FIGURE 3 | Marker-stake for surface displacement measurement.

result of the joint action of pore pressure changes in a certain range of underground. The influence range of the boundary area of the underground pore pressure is larger than that of the surface vertical displacement observation area. Thus, the influence of the boundary pore pressure in the training sample cannot be fully reflected in the surface vertical displacement. In the loss function, the boundary pore pressure grid should be ignored to focus the CNN training on the relevant grid.

The CNN model requires millions of samples for training. As the surface vertical displacement can be calculated using the average formation pressure according to **Eq. 2**, machine learning samples can be easily obtained. The convolution kernel k (x, y) can be obtained using the finite-element method. Hence, when a certain formation pressure value is assumed, the surface vertical displacement is obtained using **Eq. 2**, and the corresponding average formation pore pressure and surface vertical displacement constitute a training sample. Thus, infinite training samples can be obtained by assuming different values of formation pressure and calculating the corresponding surface vertical displacements. The proposed CNN can be trained to handle practical problems using the samples thus obtained.

OILFIELD TEST

Forward Evolutionary Computation

In the Sazhong Development Zone of the Daqing Oilfield, the vertical displacement of the formation was measured using marker-stakes arranged on the ground and then by measuring the changes in the formation pore pressure. The marker-stakes protruded 1.5 m above the ground and extended 4.0 m into the stratum. The center of the marker-stakes was made of steel to prevent the displacement of the shallow soil. The height difference between two adjacent marker-stakes was measured using a precision level, and the vertical displacement of the stratum at each marker-stake position in the plane was calculated using four benchmark stakes in the nondevelopment area. One of the marker-stakes is shown in **Figure 3**.

The surface-monitoring network included 27 survey marker-stakes in the development zone and four benchmark stakes outside the development zone. The spacing between the marker-stake points was 700–1,000 m, and the stakes were more evenly arranged in the monitoring area. A Dini03 precision electronic level (Trimble, United States of America) was used to measure the height difference between two adjacent marker-stakes; the standard deviation of the round-trip measurement per kilometer was ± 0.3 mm. The marker-stakes were built in Block X of the Sazhong development zone. There are 2,499 oil and water wells in this block, covering three series of development well groups. The block area is 19.28 km^2, and the original formation pressure of the block is 10.13 MPa. The top depth of the oil layer is approximately 800 m, and the bottom depth is approximately 1,250 m (the total thickness of the interlayer between reservoirs is approximately 150 m). The total effective thickness of the oil layer is approximately 150 m. **Figure 4** shows the locations of the marker-stakes.

From November 2017 to April 2018, the vertical displacement measurement of the marker-stakes and the build-up tests for the average formation pressure were conducted for Block X (**Figure 4**). The vertical displacement, measured twice, was the surface vertical displacement at the marker-stake locations. The surface vertical displacement field measured based on the vertical position change at two time points is shown in **Figure 5**.

Because of the fewer monitoring times for formation pressure in the pressure build-up test, the grid size was expanded to 900 m × 900 m when using the formation pressure in the pressure build-up test. The change in the average pore pressure obtained from the well pressure build-up test from November 2017 to April 2018 is shown in **Figure 6**.

From November 2017 to April 2018, casing damage was serious in this block, and casing damage was found in most wells. At that time, it was thought that the casing damage was caused by over-high water injection amount. Therefore, hundreds of water injection wells were shut down during this period, but the oil well production was normal. Such a system leads to the decrease of injection production ratio. Because of less injection and more recovery, the average pressure of the formation decreases and the formation tends to be compacted. To measure the accuracy of the calculation results, the overall compliance degree is defined as follows:

$$C = 1 - \frac{\sum |p'_k - p_k|}{\sum |p_k|} \tag{7}$$

where p'_k is the vertical displacement of the surface, as calculated based on the positive evolution at each marker-stake (mm), and p_k is the measured vertical displacement of the surface at each marker-stake (mm).

According to **Eq. 7**, the overall degree of compliance was 82.51%. The main reason for the error was that there were few recovered logging data, few data points to be calculated, and an excessively large grid.

The matching relationship between the change in formation pore pressure and the surface vertical displacement was investigated. Using the COMSOL finite-element software, a

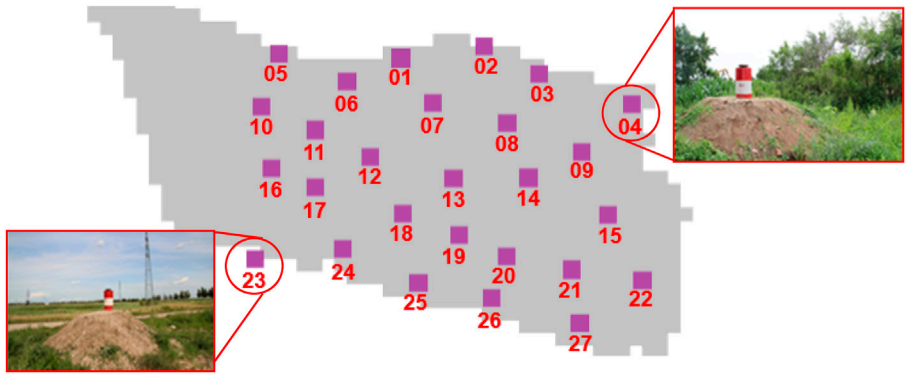

FIGURE 4 | Map showing locations of the surface displacement marker-stakes.

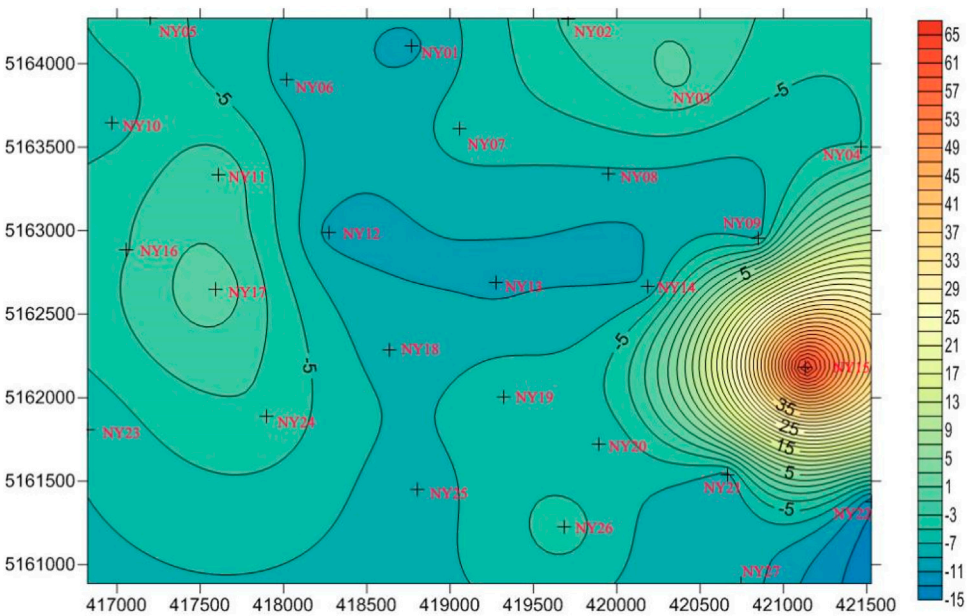

FIGURE 5 | Surface vertical displacement field measured based on vertical position change from November 2017 to April 2018[1].

geomechanical model with dimensions of 10,000 m × 10,000 m × 5,000 m was established to calculate the surface displacement caused by the unit grid pressure difference, that is, the convolution kernel for the test samples. The reservoir thickness was calculated as the total thickness of the vertical sandstone of the reservoir, which was 300 m. A geometric view of the finite-element model is shown in **Figure 7**.

In the COMSOL simulation, the poroelasticity model was applied. Poroelasticity describes the interaction between fluid flow and deformation in elastic porous media like reservoir. In the poroelasticity model, the relation of stress, strain, and pore pressure is defined as:

$$\boldsymbol{\sigma} = E\boldsymbol{\varepsilon} - \alpha_B p_f \mathbf{I} \tag{8}$$

where $\boldsymbol{\sigma}$ is the Cauchy stress tensor; E is the Young's modulus; $\boldsymbol{\varepsilon}$ is the strain tensor; α_B is the Biot coefficient, and p_f is the fluid pore pressure; $\mathbf{I}$ is the unit tensor.

As the change of pore pressure is not enough to make the reservoir plastic deformation, the stress-strain relationship adopts the classical linear elastic physical equation. Navier's equations for reservoir in equilibrium under purely gravitational load is

$$\nabla \cdot \boldsymbol{\sigma} = (\rho_f \phi + \rho_d) g \tag{9}$$

where ρ_f and ρ_d represent fluid and drained densities, respectively, and ϕ is the porosity of reservoir.

Darcy's law is used to describe the fluid flowing in reservoir pores.

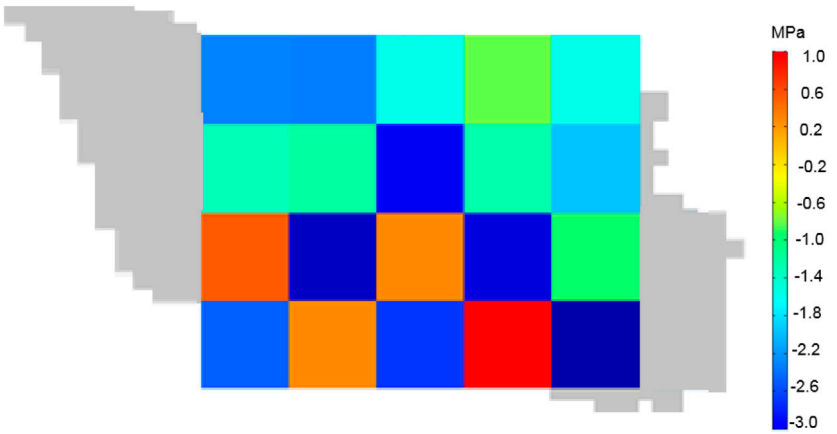

FIGURE 6 | Formation pressure change from November 2017 to April 2018.

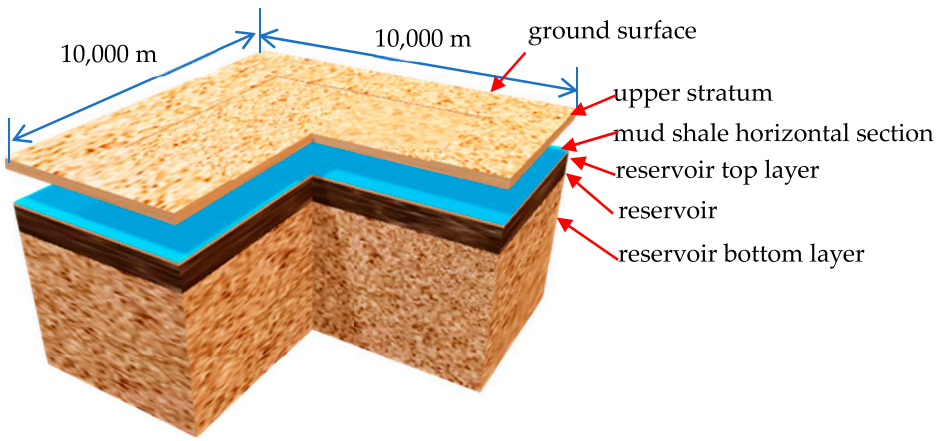

FIGURE 7 | Geometric view of the finite-element model.

TABLE 1 | Conditions and mechanical parameters of the strata in the geomechanical model.

Parameters	Unit	Value
Reservoir Biot coefficient	1	0.95
Side length of per unit grid	m	900
Top reservoir depth	m	800
Converted reservoir thickness	m	5,000
Converted reservoir length	m	10,000
Unit pressure difference	MPa	1.0
Reservoir Young's modulus	MPa	1,500
Poisson's ratio in reservoir	1	0.2
Elastic modulus of rock at reservoir top	MPa	1,300
Poisson's ratio at reservoir top	1	0.2
Elastic modulus of rock at reservoir bottom	MPa	2000
Poisson's ratio at reservoir bottom	1	0.2

$$\nabla \cdot (\rho_f \mathbf{u}_f) = Q_m \tag{10}$$

$$\mathbf{u}_f = -\frac{K}{\mu}(\nabla p + \rho_f g D) \tag{11}$$

where $\mathbf{u}_f$ is the fluid velocity in reservoir; K is the permeability of the reservoir; μ is the fluid's dynamic viscosity in reservoir; p is the fluid's pressure; ρ_f is its density; ∇D is a unit vector in the direction over which the gravity acts.

From top to bottom, the geological model is divided into the upper stratum (700 m), mud shale horizontal section (0 m, an interface with continuous vertical displacement and discontinuous horizontal displacement), a reservoir top layer (50 m), a reservoir (300 m), and a reservoir bottom layer (3,950 m). The other parameters are listed in **Table 1**.

Based on finite-element analysis, the distribution of the surface vertical displacement caused by the pressure difference in the center unit grid is shown in **Figure 8**.

The relationship between the surface displacement and pressure difference is represented by the convolution kernel k (x, y) for the analyzed block. For the finite element model, the

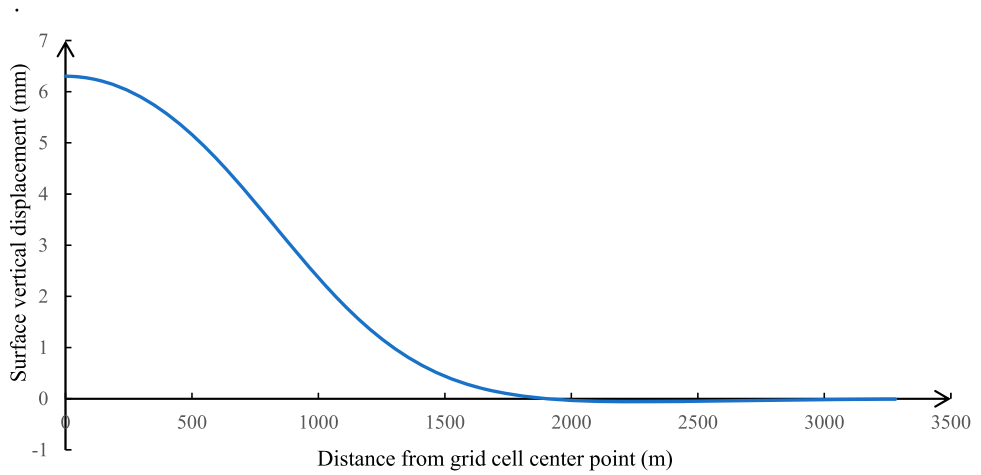

FIGURE 8 | Relationship between surface displacement and pressure difference in per-unit grid.

surface deformation under the given pore pressure field can be calculated by changing the pore pressure of the reservoir after selecting the poroelasticity model to realize the forward calculation process. But for the inversion calculation, the software can not calculate the origin of given surface deformation, or the pore pressure field. Using the convolution neural network model in this manuscript, the inversion calculation can be realized, but a large number of forward calculation results are needed as training samples to train the convolution neural network. The forward calculation results can be got by poromechanical mechanism. The relevant part has been added in the manuscript.

Backward Evolutionary Computation Using Improved CNN Model

To compare with the average pore pressure variation from the pressure build-up test, the formation pressure dispersion of a 900 m × 900 m block was conducted. Twenty such blocks (5 in the *x*-direction and 4 in the *y*-direction) in the range of the marker-stake measurements were used for the inversion of the formation pore pressure through the vertical displacement of the surface and of the formation pore pressure obtained via the pressure build-up test. Blocks outside the range of the marker-stake measurements were not considered.

The input and output of the improved image-to-image CNN are square matrices with the same length and width. Because the boundary grid was ignored in the training of the CNN model, the input and output matrices of the model should be larger than the actual grid. In accordance with the actual conditions in Block X, a 7 × 7 input and output layer model was established.

The improved image-to-image CNN model contained 10 hidden layers. There were two channels in the first and last hidden layers and four channels in the remaining hidden layers. As the grid sizes of the input and output layers were the same, the same padding convolutional method was used to calculate the intermediate results. The convolution kernels in the CNN had a size of 3 × 3. Thus, the total number of training variables was 1,225, and the number of intermediate variables was 6,468. An activation function was not used, because a physical causal relationship exists between the formation pore pressure and surface vertical displacement. The improved image-to-image CNN model is shown in **Figure 9**.

The convolution kernel for forward evolution represents the surface vertical displacement field of single grid formation pore unit pressure change, and its value was obtained using the curve shown in **Figure 4**. In the convolution kernel, only the grids near the center possess values, and the values of the three grids outside the center are all 0. The convolution kernel size for the forward evolution was 7 × 7. The test data were obtained by assuming a pressure field and forward calculating the surface vertical displacement. Each point of the 7 × 7 formation pressure field sample randomly assumes a pressure value from −0.5 MPa to +0.5 MPa. The surface vertical displacement field was obtained via a convolution calculation using **Eq. 2**. We loaded eight samples at a time for training. To reduce the time cost of creating training samples, the training sample batch was changed per 20 training cycles. An adaptive moment estimation method was used to train the CNN. The same method was also used to build 64 samples for testing, and the testing samples were not used for training; they were only used to test the accuracy of the predicted pressure field. The learning efficiency was set to 0.001. The loss function only considers the error of the 5 × 5 grids in the center and not the error of the outermost grids.

We used Python 3.6 with TensorFlow 2.14 to develop an improved image-to-image CNN program. The CNN was trained 100,000 times, and the average error of the formation pressure change based on the test samples with the number of training iterations is shown in **Figure 10**. **Figure 11** shows the formation pressure changes of the first 64 test samples compared with the prediction results of different training iterations. After 100,000

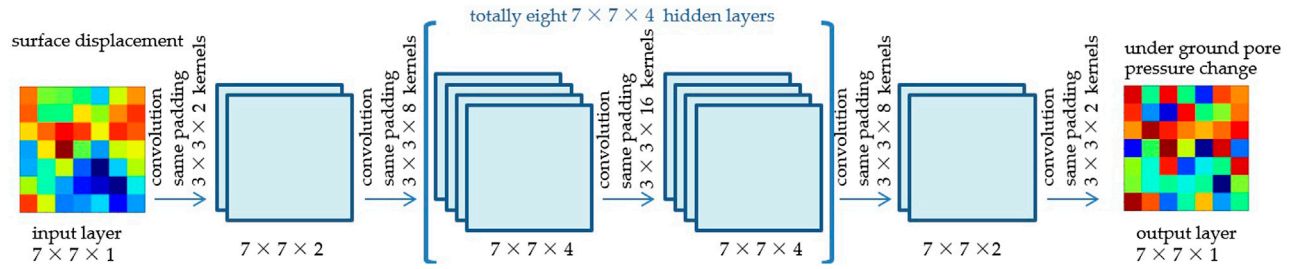

FIGURE 9 | Improved image-to-image CNN model for inversion of surface vertical displacement to calculate underground pore pressure change.

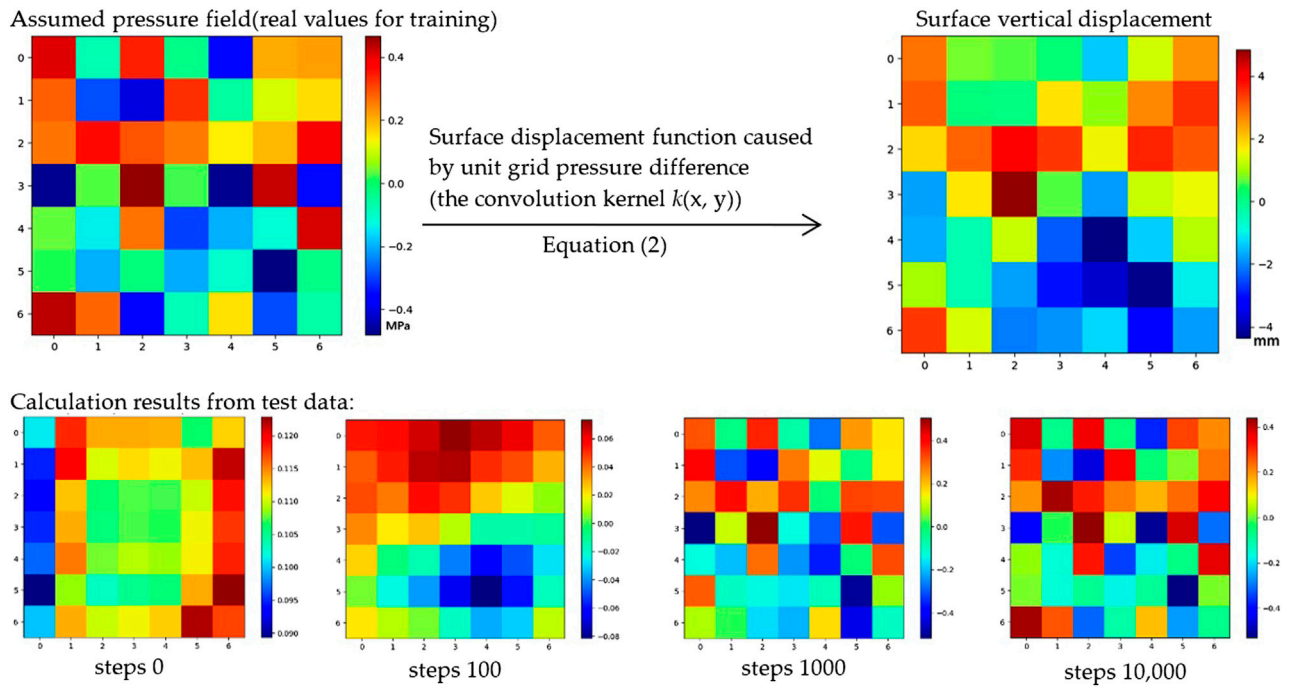

FIGURE 10 | Formation pressure changes of the first sample compared with the prediction of different training iterations. In step 100,000, the formation pressure change values of each grid in the figure are not different from the real values.

training cycles the average error of the formation pressure is 0.00495 MPa, and the formation pressure change values of each grid in the figure are not different from the real values. If the relationship between the underground pore pressure change and the surface vertical displacement measurement is completely accurate, an accurate distribution of the formation pore pressure can be obtained through the improved image-to-image CNN model.

Using the measured surface vertical displacement between November 2017 and April 2018 of Block X, we calculated the average formation pressure change of each grid within the coverage of the marker-stakes. During the period from November 2017 to April 2018, 102 wells were tested by pressure build-up test in this block, and the test was distributed in different positions in the block. The formation pressure results were averaged according to the divided in twenty 900 × 900 m blocks shown in **Figure 12**.

By comparing the average pore pressure changes shown in **Figures 6**, **12** in the same position, we found that the results were in good agreement; the coincidence rate of the pressure-change trend was 95%, and the overall coincidence degree was 83.12%.

The accuracy of the change in unit pressure change or convolution kernel is the most important factor affecting the final accuracy. In this method, the numerical simulation is mainly used to simulate the surface deformation field of a formation grid after changing the unit formation pressure. The surface deformation field is the convolution kernel used in forward calculation. The accuracy of the convolution kernel directly determines the prediction accuracy of the model in

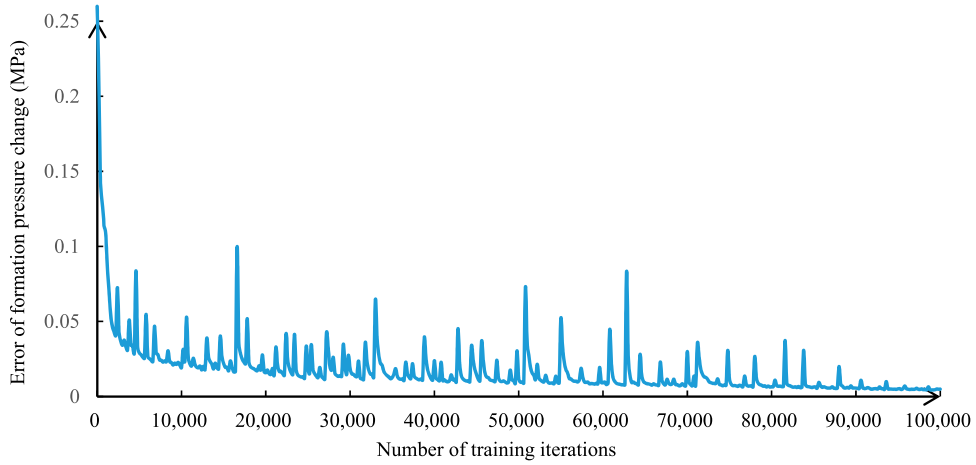

FIGURE 11 | Average error of formation pressure change based on test samples with the number of training iterations.

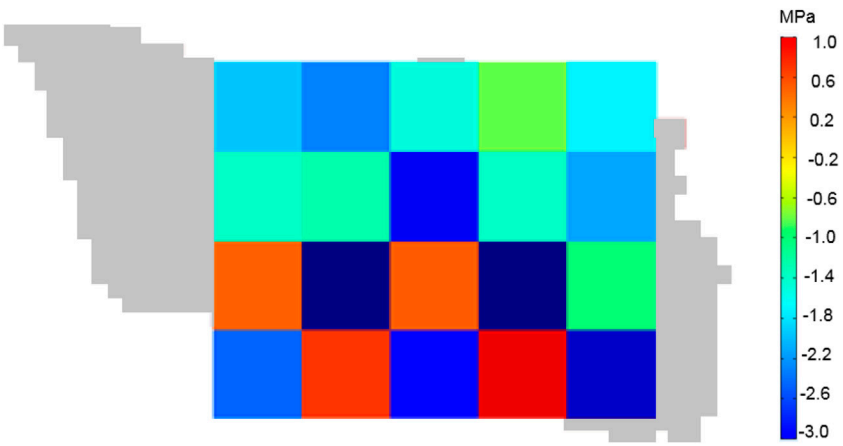

FIGURE 12 | Comparison of strata pressure change from November 2017 to April 2018 from surface displacement inversion.

practical block application. There are inevitable errors in numerical simulation. One error source is the accuracy of the finite element model, which can be reduced by increasing the number of finite element meshes and optimizing the finite element model. Another error comes from the accuracy of the stratigraphic model, which can be reduced by the improvement and fine description of the block geological model. The lithology distribution and mechanical parameters of the actual strata were not the same in the plane. The discontinuous interfaces such as faults in the formation also affect the convolution kernel. These effects cause the convolution kernel to vary with the plane position. However, this effect was not considered in the present study. This is the main reason for the calculation error. Furthermore, during this period, the surface displacement increased. The basic coverage of the marker-stake measurement parameters was larger, and the measurement error was much smaller than the measurement value. In addition, the average pore pressure difference considered for the correlation was derived from the pressure build-up test. In this case, the grid area was larger, and there were only 20 grids. The amount of data used was small. Nevertheless, such data density is sufficient to meet the needs of oilfield management. The method of inversion of the average formation pore pressure via surface displacement is faster, less expensive, and more accurate.

CONCLUSION

(1) Surface displacement is a reflection of the formation pore pressure change. The range of formation vertical displacement due to the change in formation pore pressure is within the range of linear elastic deformation of the formation rock, and the displacement per unit grid pressure difference can be used as a convolution kernel. The

distribution of the surface vertical displacement can be obtained through the convolution of the formation pore pressure and convolution kernel.

(2) Through forward evolution, the surface displacement field can be calculated using any formation pressure field. Infinite training samples can be obtained by constantly assuming the formation pressure field and calculating the corresponding surface vertical displacement.

(3) The improved CNN method adopts an image-to-image network mode instead of a pooling layer and a full connection layer. The new loss function ignores the error of the boundary grid and focuses the training of the CNN parameters on adjusting the output results. These model improvement methods effectively improved the accuracy of the model calculation.

(4) A field test in the Daqing Oilfield in China showed that the variation in the formation pore pressure obtained via inversion was 83.12%, in accordance with the results of 20 groups of pressure build-up tests within the range of marker-stake measurements. Overall, the inversion method of average formation pore pressure by surface displacement has a lower cost and is faster.

DATA AVAILABILITY STATEMENT

The original contributions presented in the study are included in the article/supplementary material, further inquiries can be directed to the corresponding author.

AUTHOR CONTRIBUTIONS

Conceptualization, CH and CA; methodology, FW and CA; validation, FW; formal analysis, CH; investigation, CH and CA; resources, CA; writing—original draft preparation, CH; writing—review and editing, FW; visualization, CH; supervision, CA.

FUNDING

This research was supported by National Natural Science Foundation of China (Grant No. 52074088, Grant No. 51804076). Heilongjiang Provincial Natural Science Foundation of China (Young Scientists) (Grant No. QC QC2018047).

REFERENCES

Ai, C., Hu, C. Y., and Cui, Y. M. (2015). Casing Optimization for Delaying Casing Damage in the Datum Bed of the Daqing Oilfield. *Pet. Drill. Tech.* 6, 7–12. doi:10.11911/syztjs.201506002

Ameh, E. G. (2019). Geochemistry and Multivariate Statistical Evaluation of Major Oxides, Trace and Rare Earth Elements in Coal Occurrences and Deposits Around Kogi East, Northern Anambra Basin, Nigeria. *Int. J. Coal Sci. Technol.* 6 (2), 260–273. doi:10.1007/s40789-019-0247-4

Banik, N., Koesoemadinata, A., Wagner, C., Inyang, C., and Bui, H. T. (2013). "Predrill Pore Pressure Prediction Directly from Seismically Derived Acoustic Impedance," in SEG Technical Program Expanded Abstracts, Houston, TX, September 2013, 2905–2909.

Cipolla, C., Motiee, M., and Kechemir, A. (2018). "Integrating Microseismic, Geomechanics, Hydraulic Fracture Modeling, and Reservoir Simulation to Characterize Parent Well Depletion and Infill Well Performance in the Bakken," in Paper presented at the SPE/AAPG/SEG Unconventional Resources Technology Conference, Houston, TX, July 2018. doi:10.15530/urtec-2018-2899721

Cui, Y. M. (2015). *Mechanism of Formation Slippage and Shear Casing Damage of the Marker Bed in Sazhong Development Area of Daqing Oilfield*. Daqing, Heilongjiang: Northeast Petroleum University.

Dutta, N. C., and Khazanehdari, J. (2006). Estimation of Formation Fluid Pressure Using High-Resolution Velocity from Inversion of Seismic Data and a Rock Physics Model Based on Compaction and Burial Diagenesis of Shales. *Lead. Edge* 25 (12), 1528–1539. doi:10.1190/1.2405339

Dutta, N. C. (2002). Deepwater Geohazard Prediction Using Prestack Inversion of Large offsetP-Wave Data and Rock Model. *Lead. Edge* 21 (2), 193–198. doi:10.1190/1.1452612

Eaton, B. A. (1972). The Effect of Overburden Stress on Geopressure Prediction from Well Logs. *J. Pet. Technol.* 24 (8), 929–934. doi:10.2118/3719-pa

Fillippone, W. R. (1982). "Estimation of Formation Parameters and the Prediction of Overpressures from Seismic Data," in SEG Technical Program of Expanded Abstracts, Dallas, TX, October 1982, 482–483.

Gao, D., Liu, Y., Guo, Z., Han, J., Lin, J., Fang, H., et al. (2018). A Study on Optimization of CBM Water Drainage by Well-Test Deconvolution in the Early Development Stage. *Water* 10 (7), 929. doi:10.3390/w10070929

Guo, X., Wu, K., Killough, J., and Tang, J. (2019a). Understanding the Mechanism of Interwell Fracturing Interference with Reservoir/Geomechanics/Fracturing Modeling in Eagle Ford Shale. *SPE Reservoir Eval. Eng.* 22 (3), 842–860. doi:10.2118/194493-pa

Guo, X., Wu, K., An, C., Tang, J., and Killough, J. (2019b). Numerical Investigation of Effects of Subsequent Parent-Well Injection on Interwell Fracturing Interference Using Reservoir-Geomechanics-Fracturing Modeling. *SPE J.* 24 (4), 1884–1902. doi:10.2118/195580-pa

Hou, Z., Yu, H., Liu, Y., Zhang, S., and Gu, H. (2019). High-Precision Seismic Prediction of 3D Pore-Pressure in Tight Sandstone Gas Reservoirs with Low Porosity and Permeability at M Gas Field in Xihu Sag. *Geol. Sci. Technol. Inf.* 38 (2), 267–274. doi:10.19509/j.cnki.dzkq.2019.0232

Hu, C. Y., Ai, C., and Wang, F. J. (2018). Optimization of Casing Design Parameters to Mitigate Casing Failure Caused by Formation Slippage. *SDHM* 2, 85–98. doi:10.3970/sdhm.2018.00115

Hwang, J. K., Seo, S., Castanon, J. S., and Kim, H.-C. (2019). DFT-based Identification of Oscillation Modes from PMU Data Using an Exponential Window Function. *Energies* 12, 4357. doi:10.3390/en12224357

Li, Y., Jia, D., Rui, Z., Peng, J., Fu, C., and Zhang, J. (2017). Evaluation Method of Rock Brittleness Based on Statistical Constitutive Relations for Rock Damage. *J. Pet. Sci. Eng.* 153, 123–132. doi:10.1016/j.petrol.2017.03.041

Mohammady, S., Farrell, R., Malone, D., and Dooley, J. (2020). Performance Investigation of Peak Shrinking and Interpolating the PAPR Reduction Technique for LTE-Advance and 5G Signals. *Information* 11, 20. doi:10.3390/info11010020

Qi, S., Zou, Y., Wu, F., Yan, C., Fan, J., Zang, M., et al. (2017). A Recognition and Geological Model of a Deep-Seated Ancient Landslide at a Reservoir under Construction. *Remote Sens.* 9, 383. doi:10.3390/rs9040383

Rutqvist, J., Vasco, D. W., and Myer, L. (2010). Coupled Reservoir-Geomechanical Analysis of CO2 Injection and Ground Deformations at in Salah, Algeria. *Int. J. Greenhouse Gas Control.* 4, 225–230. doi:10.1016/j.ijggc.2009.10.017

Shen, Z., Beck, F. E., and Ling, K. (2014). The Mechanism of Wellbore Weakening in Worn Casing-Cement-Formation System. *J. Pet. Eng.* 2014, 1–8. doi:10.1155/2014/126167

Sheng, Y.-N., Li, W., Guan, Z.-c., Jiang, J., Lan, K., and Kong, H. (2020). Pore Pressure Prediction in Front of Drill Bit Based on Grey Prediction Theory. *J. Petrol. Explor Prod. Technol.* 10 (6), 2439–2446. doi:10.1007/s13202-020-00896-3

Sun, W. L., and Sun, K. F. (2007). A Review of Seismic Formation Pressure Prediction. *Prog. Explor. Geophys.* 30 (6), 428–432 (In Chinese). doi:10.13809/j.cnki.cn32-1825/te.2007.06.005

Tang, J., Wu, K., Li, Y., Hu, X., Liu, Q., and Ehlig-Economides, C. (2018). Numerical Investigation of the Interactions between Hydraulic Fracture and Bedding Planes with Non-Orthogonal Approach Angle. *Eng. Fracture Mech.* 200, 1–16. doi:10.1016/j.engfracmech.2018.07.010

Tang, J., Fan, B., Xiao, L., Tian, S., Zhang, F., Zhang, L., Weitz, D., et al. (2021. A New Ensemble Machine Learning Framework for Searching Sweet Spots in Shale Reservoirs. *SPE J.* 26 (01), 482–497. doi:10.2118/204224-PA

Tipper, J. C. (1976). The Study of Geological Objects in Three Dimensions by the Computerized Reconstruction of Serial Sections. *J. Geol.* 84 (4), 476–484. doi:10.1086/628213

Wang, X., and Sheng, J. J. (2018). A Self-Similar Analytical Solution of Spontaneous and Forced Imbibition in Porous media. *Adv. Geo-energy Res.* 2 (3), 260–268. doi:10.26804/ager.2018.03.04

Wei, M. A., Chen, C., Wang, Y. J., and Ma, H. (2007). New Approach for Pore Pressure Prediction. *Oil& Gas Geol.* 28 (3), 395–400. (In Chinese). doi:10.3321/j.issn:0253-9985.2007.03.014

Xie, J., Tang, J., Yong, R., Fan, Y., Zuo, L., Chen, X., et al. (2020). A 3-D Hydraulic Fracture Propagation Model Applied for Shale Gas Reservoirs with Multiple Bedding Planes. *Eng. Fract. Mech.* 228, 106872. doi:10.1016/j.engfracmech.2020.106872

Xiong, X. J., Huang, J., Chen, R., Liao, Y., and Yuan, Y. (2019). Pore Pressure Prediction Method of Under-compacted Formation. *Comput. Tech. Geophys. Geochem. Explor.* 41 (1), 1–5. doi:10.3969/j.issn.1001-1749.2019.01.001

Xu, W., Liu, R., Yang, H., Zhang, L., and Yang, Y. (2019). "Investigation of Well Testing Reservoirs with Multiphase Flow in a Mature Field," in *SIMULATION: Transactions of the Society for Modeling and Simulation International*. doi:10.1155/2019/2847345

Xu, X.-q., and Zhou, H.-b. (2019). Study on the Influence of Pulse Current Cathodic Protection Parameters of Oil Well Casing. *Adv. Mater. Sci. Eng.* 2019, 1–9. doi:10.1155/2019/2847345

Xue, D., Zhou, J., Liu, Y., and Zhang, S. (2018). A Strain-Based Percolation Model and Triaxial Tests to Investigate the Evolution of Permeability and Critical Dilatancy Behavior of Coal. *Processes* 6, 127. doi:10.3390/pr6080127

Yu, F., Jin, Y., Chen, M., Lu, Y. H., Niu, C. C., and Ge, W. F. (2014). Discussion on a Formation Pore Pressure Detection Method for Carbonate Rocks Based on the Thin Plate Theory. *Pet. Drill. Tech.* (5), 57–61. doi:10.11911/syztjs.201405010

Yun, M. H. (1996). Formation Pressure Prediction Using Seismic Data. *Oil Geophys. Prospect.* 31 (4), 575–586. (In Chinese).

Zhang, Q., Li, X., Bai, B., Hu, S., and Shi, L. (2018). Effect of Pore Fluid Pressure on the Normal Deformation of a Matched Granite Joint. *Processes* 6, 107. doi:10.3390/pr6080107

Zhang, F., An, M., Zhang, L., Fang, Y., and Elsworth, D. (2020). Effect of Mineralogy on Friction-Dilation Relationships for Simulated Faults: Implications for Permeability Evolution in Caprock Faults. *Geosci. Front.* 11 (2), 439–450. doi:10.1016/j.gsf.2019.05.014

Zhang, J., Li, Y., Pan, Y., Wang, X., Yan, M., Shi, X., et al. (2021). Experiments and Analysis on the Influence of Multiple Closed Cemented Natural Fractures on Hydraulic Fracture Propagation in a Tight Sandstone Reservoir. *Eng. Geol.* 281, 105981. doi:10.1016/j.enggeo.2020.105981

Zhao, X., Zhou, L., Pu, X., Jin, F., Shi, Z., Han, W., et al. (2020). Formation Conditions and Enrichment Model of Retained Petroleum in Lacustrine Shale: A Case Study of the Paleogene in Huanghua Depression, Bohai Bay Basin, China. *Pet. Explor. Dev.* 47 (5), 916–930. doi:10.1016/s1876-3804(20)60106-9

Conflict of Interest: The authors declare that the research was conducted in the absence of any commercial or financial relationships that could be construed as a potential conflict of interest.

Publisher's Note: All claims expressed in this article are solely those of the authors and do not necessarily represent those of their affiliated organizations, or those of the publisher, the editors and the reviewers. Any product that may be evaluated in this article, or claim that may be made by its manufacturer, is not guaranteed or endorsed by the publisher.

frontiers in Earth Science

ORIGINAL RESEARCH
published: 01 September 2021
doi: 10.3389/feart.2021.718733

Seepage Behavior of Fractures in Paleogene Sandstone Reservoirs in Nanpu Sag, Bohai Bay Basin, Eastern China

Zhaosheng Wang[1,2], Meiri Muhtar[3], Donghao Xu[3], Jinchuan Fang[3], Jing Li[3], Daojie Liu[4], Zhenguo Zhang[1] and Lianfeng Gao[1]*

[1]College of Mining Engineering, Liaoning Technical University, Fuxin, China, [2]College of Mining Engineering, North China University of Science and Technology, Tangshan, China, [3]CNPC Logging Company Limited Xinjiang Branch, Karamay, China, [4]CNPC Jidong Oilfield, Tangshan, China

Natural fractures play an important role in the seepage system of Paleogene sandstone reservoirs at Nanpu Sag. Characteristics and formation mechanisms of natural fractures and stress-sensitivity permeability are comprehensively investigated and their impact on water injection is discussed based on core and log data (FMI and diplog data) as well as stress-sensitivity permeability measurement. Results show that high-angle shear fractures, including NE-SW strike fractures and NW-SE strike fractures, are widely developed in the study area, which were primarily developed during the late Paleogene and late Neogene. The present maximum horizontal principal stress is orientated at N60°–80°E, approximately parallel to the NE-SW fractures, contributing greatly to the seepage system at the early oilfield development stage. Fractures in the study area can be divided into three phases and are characterized by obvious stress-sensitivity permeability, which is closely related to fracture aperture and throat size. Since the fracture occurrence enhances stress sensitivity of permeability, it is necessary to regulate well pattern based on dynamic behaviors of fractured reservoirs at different development stages.

Keywords: fracture, formation mechanism, stress-sensitivity permeability, sandstone reservoirs, Nanpu sag

OPEN ACCESS

Edited by:
Yuwei Li,
Liaoning University, China

Reviewed by:
Lei Gong,
Northeast Petroleum University, China
Lingyun Kong,
University of North Dakota, United States
Kouqi Liu,
Central Michigan University, United States

****Correspondence:***
Zhaosheng Wang
zhaoshengw@126.com

Specialty section:
This article was submitted to Economic Geology, a section of the journal Frontiers in Earth Science

Received: *01 June 2021*
Accepted: *19 July 2021*
Published: *01 September 2021*

Citation:
Wang Z, Muhtar M, Xu D, Fang J, Li J, Liu D, Zhang Z and Gao L (2021) Seepage Behavior of Fractures in Paleogene Sandstone Reservoirs in Nanpu Sag, Bohai Bay Basin, Eastern China. Front. Earth Sci. 9:718733. doi: 10.3389/feart.2021.718733

INTRODUCTION

As oil and gas resource consumption continuously increases, identifying and producing reserves from wide-distributed low-permeability reservoirs has attracted increasing attention (Shanley and Cluff, 2015; Alhuraishawy et al., 2018; Qing et al., 2021). Sandstone reservoirs with permeability <50 $\times$ 10^{-3} μm^2 are defined as low-permeability reservoirs in China (Zeng et al., 2013). They are commonly compacted with intensive brittleness, which is beneficial for the development of fractured reservoirs under strong diagenesis and tectonic activities (Tamagawa and Pollard, 2008; Olorode et al., 2012; Nagel et al., 2013; Cao et al., 2020). Fractures with porosity are commonly less than 0.5% and generally contribute little to the storage capacity of low-permeability reservoirs (Zeng et al., 2016; Lin et al., 2020; Liu et al., 2020). However, they can improve permeability significantly and bring strong heterogeneity (Laubach et al., 2018; Wang Z. S. et al., 2020; Gong et al., 2021). Pressure drops can commonly induce stress sensitivity of fractures, sharply close fractures around wells, and significantly decrease permeability, exerting a negative impact on oil and gas development (Li et al.,

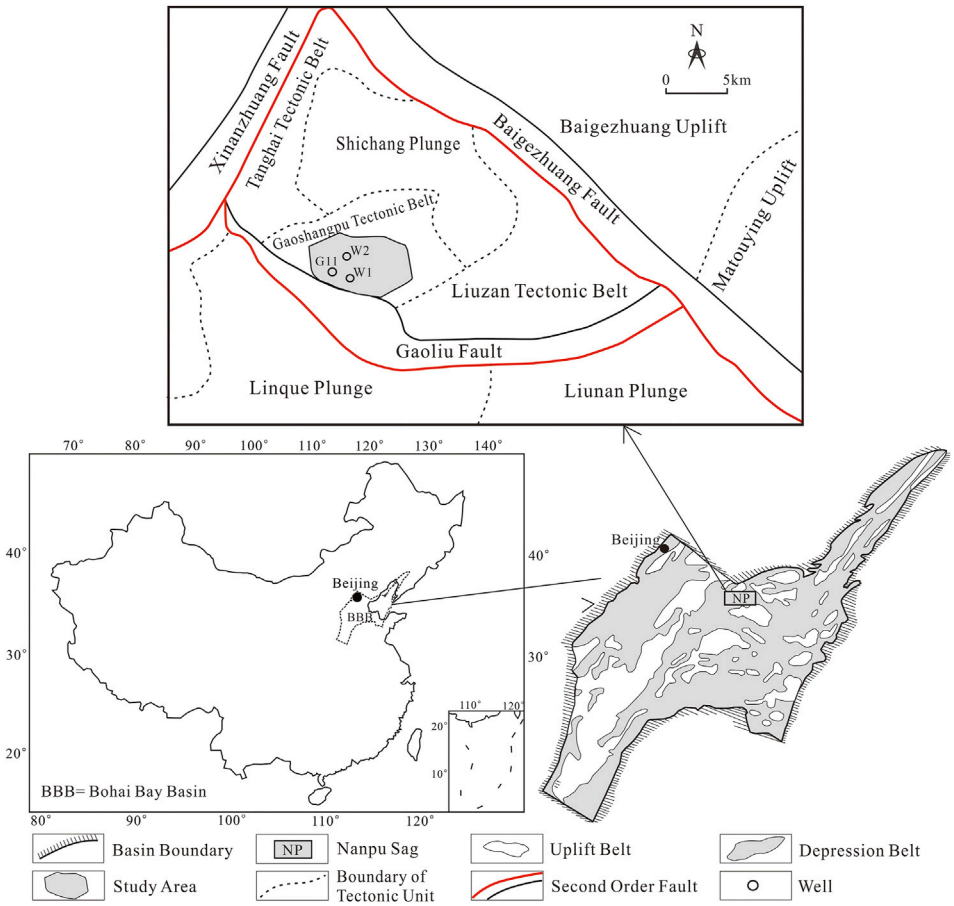

FIGURE 1 | Structure units and location of Nanpu Sag.

2021). Geologists and petroleum engineers are currently interested in fracture development in low permeability reservoirs, especially the variation of stress sensitivity of fractures, since fracture behaviors in low-permeability reservoirs is of great importance to improve production performance and enhance oil recovery (Khair et al., 2015; Babadagli, 2020; Zhang et al., 2021).

Nanpu Sag in Bohai Bay Basin has abundant hydrocarbon resources, while the latest oil and gas resource assessment shows that oil and gas resources are higher than 70×10^8 bbls (Jiang et al., 2018). The Gaoshangpu Oilfield at Nanpu Sag has not been well developed since being discovered in the late 1990s, even after a series of research and development deployments have been carried out. Specifically, production capacity was high at the initial stage with an average well yield of 371 bbls/day but declined fast at the later stage, e.g., it decreased to a low value with high water injection pressure after water injection. Continuous pressure boosting increased the water cut greatly, exhibiting the typical production behavior of fractured reservoirs (Zeng et al., 2012; Gong et al., 2019a). The current recovery rate and average well yield are only 8.1% and 13.3 bbls/day, respectively, whereas the water cut is up to 91.6%. The following problems, e.g., 1) insufficient understanding of natural fracture development, 2) poor investigation on stress sensitivity of natural fractures, and 3) uncertainty about the impact of natural fractures on the water injection, limit the efficient development of Gaoshangpu Oilfield at Nanpu Sag.

In this paper, taking the Paleogene Shahejie low-permeability sandstone reservoir in Gaoshangpu Oilfield, Nanpu Sag, as an example, we investigate the genetic mechanisms and growth features of natural fractures, and discuss their stress sensitivity as well as their influence on water injection through integrating core data, log data, and a stress-sensitivity permeability experiment.

GEOLOGICAL SETTING

Location and Structure

Nanpu Sag in Bohai Bay Basin, Eastern China (**Figure 1**), is a Meso Cenozoic rift basin with an area of 1932 km^2 (Pang et al., 2019). It is structurally characterized by faults in the east and north and overlaps in the west and south (Dong et al., 2010; Zhao et al., 2020). This study focuses on the Paleogene sandstone reservoir at Gaoshangpu Oilfield. This oilfield is located at the Gaoliu structural belt (on the upthrow of Gaoliu fault) in the

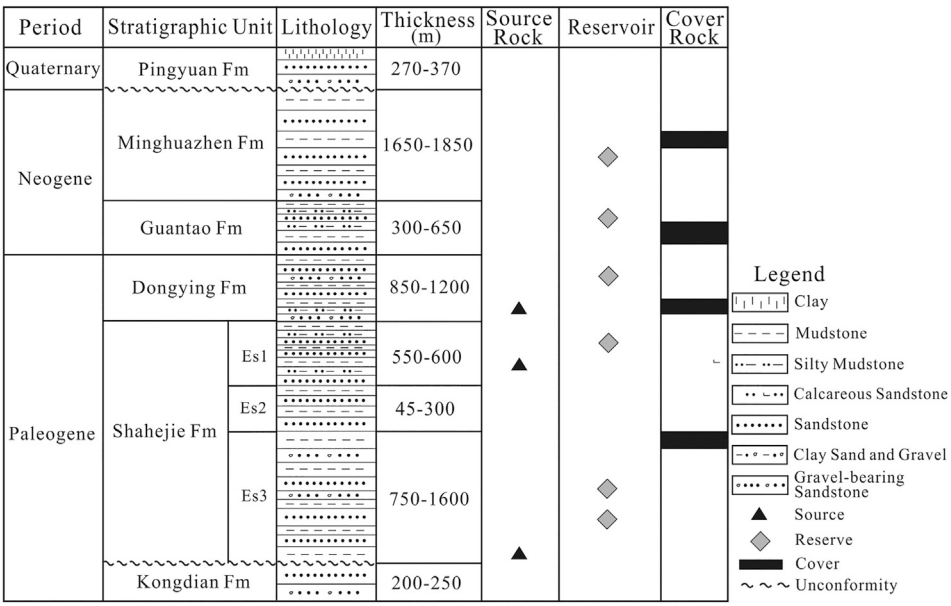

FIGURE 2 | The composite columnar section in Nanpu Sag.

north of Nanpu Sag, which is dominated by NE-SW, NW-SE, and near E-W faults, with an average length of 2.1 km and an average displacement of 100 m.

Stratum

The strata drilled in Gaoshangpu Oilfield are Paleogene Shahejie Formation (Es) and Dongying Formation (Ed), Neogene Guantao Formation (Ng) and Minghuazhen Formation (Nm), and Quaternary Pingyuan Formation from bottom to top (Zhang et al., 2018). Shahejie Formation uncomfortably connects with Kongdian Formation, and Quaternary Pingyuan Formation is in unconformity contact with Neogene Minghuazhen Formation (**Figure 2**). The Paleogene Shahejie Formation is one of the primary oil-bearing intervals at Nanpu Sag, which can be divided into Sha-3 Member (E_S^3), Sha-2 Member, and Sha-1 Member from bottom to top. The Sha-3 Member is the most

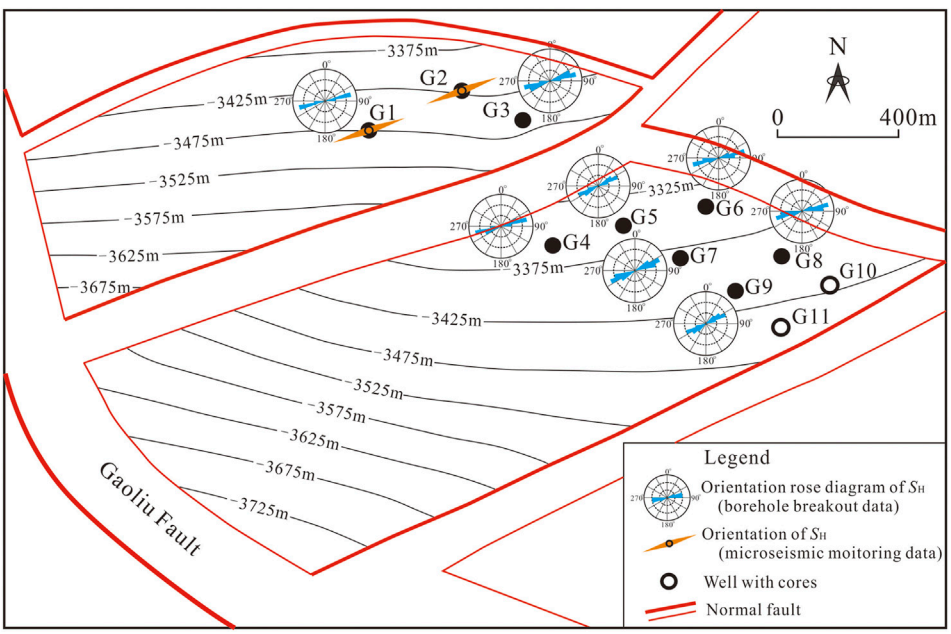

FIGURE 3 | The maximum horizontal stress (S_H) orientation of different wells.

TABLE 1 | Characteristic parameters of samples.

Sample No.	Diameter/cm	Length/cm	K/10^{-3}μm^2	Depth/m	Layer	Well
1	2.512	5.668	397.7	3414.63	Es 3	G11
2	2.522	5.544	26.3	3422.32	Es 3	G11
3	2.518	5.487	15.9	3483.65	Es 3	G10

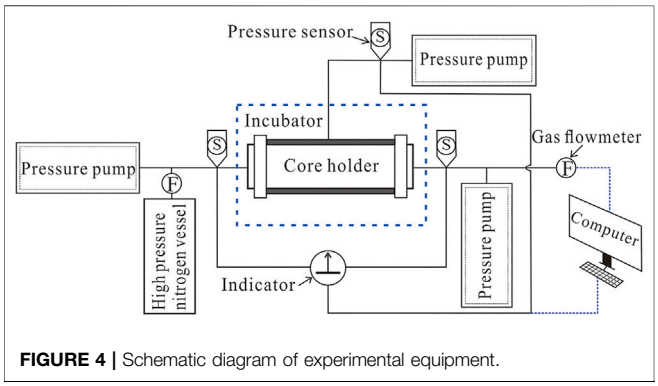

FIGURE 4 | Schematic diagram of experimental equipment.

important oil producer at Gaoshangpu Oilfield, with a thickness of 750–1,600 m (2,460.6–5,249.3 ft).

Reservoir

The Paleogene Shahejie Formation at Gaoshangpu Oilfield is characterized by a clastic deposition system dominated by fan delta deposits (Mu et al., 2003). The Sha-3 Member was deposited at fan delta front subfacies, which are dominated by underwater distributary channel sandbodies (Li et al., 2014). The reservoir is primarily medium sandstone and fine sandstone, followed by pebbly sandstone with low composition maturity and low structure maturity. The sandstones are mainly lithic feldspar sandstone and feldspar lithic sandstone, with argillaceous as matrix. The reservoir is dominated by secondary pores with average porosity and permeability of 10.3% and 11.4 × 10^{-3} μm^2, respectively.

In-situ Stress

The borehole breakout method can be used to determine maximum horizontal principal stress orientation with diplog data (Collett et al., 2011) and the assumption that the long axis of the elliptical borehole is perpendicular to the maximum horizontal principal stress (Barton et al., 2013), since uneven stress can result in borehole breakout during drilling (Scelsi et al., 2019). A series of microseismic waves generated by hydraulic fracturing can be received by microseismic monitoring and can be processed to determine fracture parameters, e.g., azimuth, length, and height, where the azimuth is commonly consistent with that of maximum horizontal principal stress (Maxwell et al., 2010; Stabile et al., 2013). The dominant orientation of the maximum horizontal principal stress at Shahejie Formation is determined based on the above two methods with value of N60°–80°E (**Figure 3**).

MATERIALS AND METHODS

Core samples from three wells with a total length of 245 m (804 ft) and log data were interpreted to describe natural fractures and the orientation of maximum horizontal principal stress (**Figure 1** and **Figure 3**). Three groups of samples were tested to analyze stress sensitivity.

Increasing effective stress or lithostatic pressure on the fracture surface due to decreasing formation pressure can lead to low fracture aperture and irreversibly decrease permeability, which is called stress-sensitivity permeability (Jelmert and Selseng, 1998). Samplings perpendicular to the formation orientation were carried out on the Paleogene sandstones. Three groups of samples were collected, namely samples with high-angle fracture (group 1), samples with micro fracture (group 2), and samples with no fracture (group 3) (**Table 1**). The experiment was performed on high pressure porosimeter based on single-phase flow (following Darcy's law) at room temperature to describe the stress-sensitivity fracture permeability. The equipment was mainly composed of core holder, inflator, pressure sensor, incubator, flowmeter, and a computer. (**Figure 4**). Fracture permeability variation with effective stress (confining pressure) was measured when loading axial pressure and keeping flow pressure. The effective stress and flow rate were assumed to be in a range of 3–40 MPa and 0.3–0.45 ml/min, respectively, based on rock-breaking test.

The variation of flow rate with pressure difference between two ends of the sample is measured through changing confining pressure under stable conditions, and thereby, the permeability can be determined based on Darcy's Law (Mackay et al., 2020).

$$Q = KA\,\Delta h/L \tag{1}$$

Where, Q is flow rate, *L/min*; A is cross-sectional area, cm^2; $\triangle h$ *is* pressure difference between two ends of the sample, MPa; L is length of the sample, cm; and K is permeability coefficient, *L/min.*

Stress-sensitivity of permeability can be expressed by stress sensitive coefficient (Bustin, 1997; Hu et al., 2020), which is defined as the decreased percentage of permeability within a certain variation of boundary conditions. The stress sensitive coefficient of permeability can be expressed as (Li, 2006):

$$I_P = (K_o - K_i)/K_o \tag{2}$$

Where, I_P is stress sensitive coefficient of permeability; K_i is permeability under certain effective stress Pi, 10^{-3} μm^2; and K_o is permeability under initial effective stress, 10^{-3} μm^2.

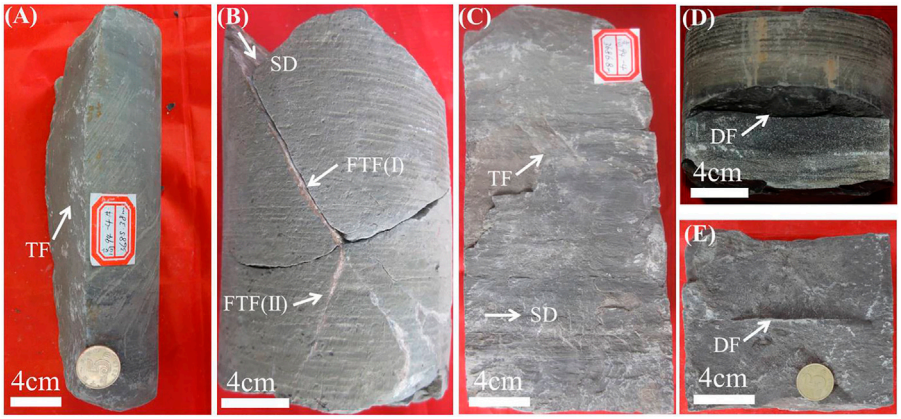

FIGURE 5 | Photos of tectonic fractures in cores of Es 3 Member **(A)** High dip-angle tectonic fracture. The fracture surface is smooth and flat. Well G10: depth 3,685.4 m (12,091.2 ft) **(B)** Two stages of fractures, set I and set II were filled with calcite, set II are terminated at set I. Well G11: depth 3,413.3 m (11,198.5 ft) **(C)** High dip-angle tectonic fracture. The fracture is perpendicular to the bedding planes and fracture surface shows horizontal striation. Well G10: depth 3,686.8 m (12,095.8 ft) **(D)** diagenetic fracture. Well G10: depth 3,684.0 m (12,086.6 ft) **(E)** diagenetic fracture. Well W2: depth 3,608.6 m (11,839.2 ft). TF is tectonic fracture, DF is diagenetic fracture, TFF is filled tectonic fracture, SD is striation direction. See **Figure 1** and **Figure 3** for wells location.

RESULTS

Core Fracture Characteristics

Core observation suggests that fractures can be originally classified into two types in the study area: structural fractures and diagenetic fractures. Structural fractures are the most popular ones, followed by diagenetic fractures. The structural fractures are dominated by shear ones with an average linear density of 1.3 m^{-1}. These fractures have straight and smooth surfaces and large penetration (**Figure 5A**). Two-stage fractures can be observed, while fractures at the early stage limit fracture extension at the late stage (**Figure 5B**). Also, two types of scorings can be found from fracture surface. The orientation of the first type is the same as the inclination of fracture surface (**Figure 5B**), while that of the second type, the popular one in the study area, is the same as the orientation of fracture surface (**Figure 5C**). It indicates a significant difference between their development conditions, i.e., the former was attributed to tensile

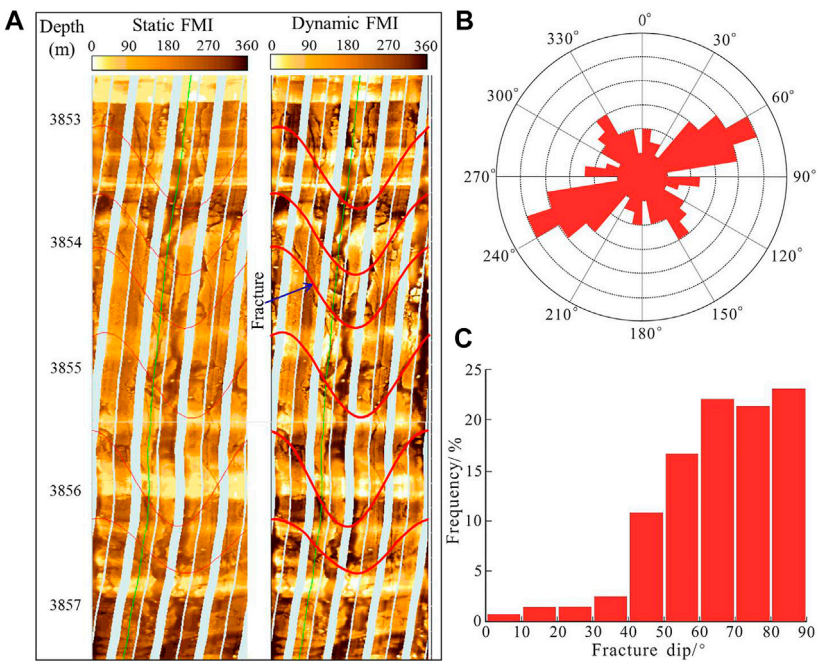

FIGURE 6 | Parameters of natural fractures **(A)** Fractures detected by formation microscanner image (FMI) in well W1 **(B)** Rose diagrams of natural fracture strike from FMI in the Paleogene sandstones (N = 161) **(C)** Dip of natural fracture from FMI and cores in the Paleogene sandstones (N = 297). See **Figure 1** for well W1 location.

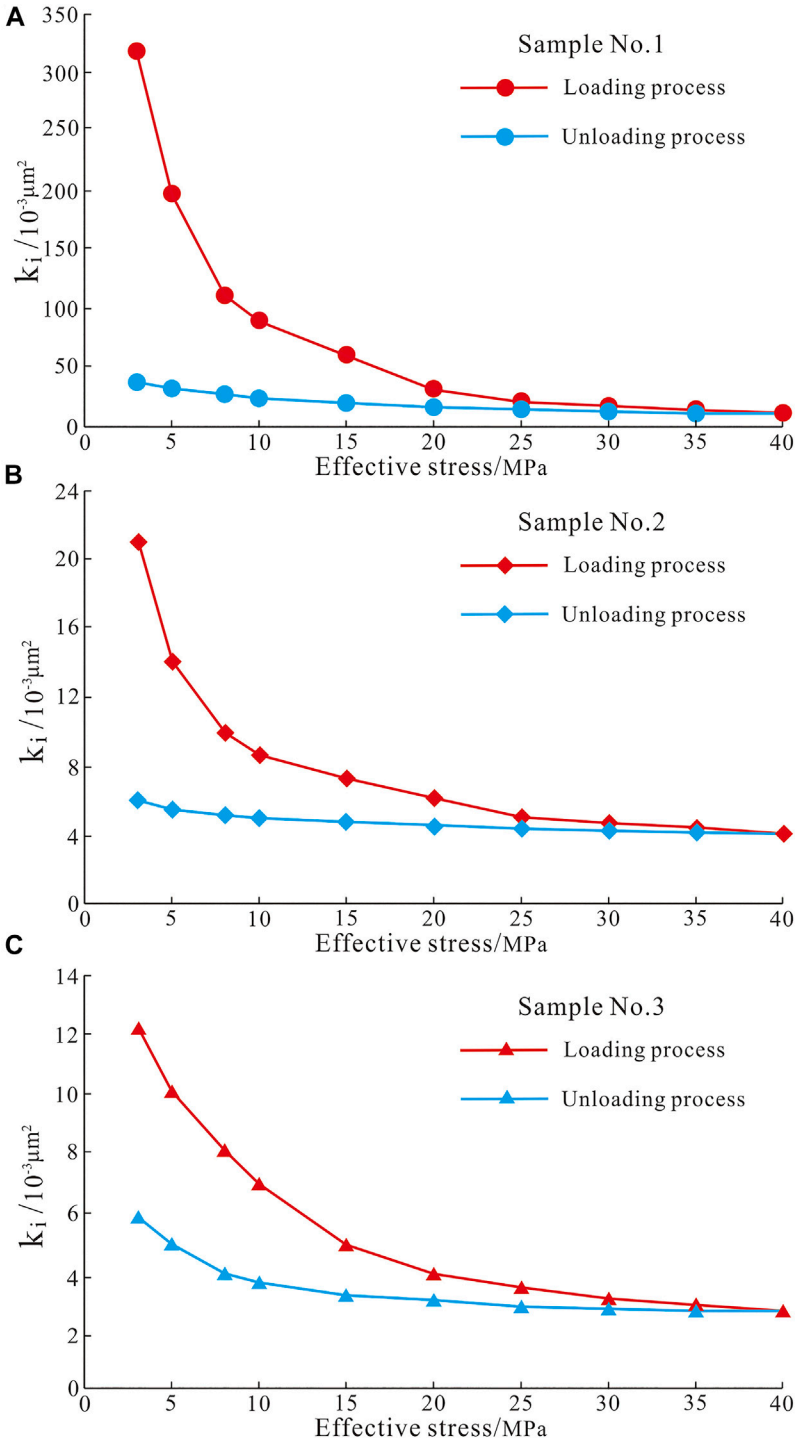

FIGURE 7 | Fracture permeability variation under different effective stress.

stress, while the latter was caused by strike-slip tectonic stress. Some fractures are filled by calcite, e.g., the partly-filled and fully-filled fractures account for 6.7 and 7.5%, respectively. while low-filling indicates high fracture valid. Diagenetic fractures are mainly developed in argillaceous rocks with low fracture density (average value of 0.3 m^{-1}), which are mainly low-angle fractures (<30°) (**Figures 5D,E**). Such fractures have small apertures and poor permeability under overlying pressure, exerting only a minor impact on oil and gas development (Zeng et al., 2010).

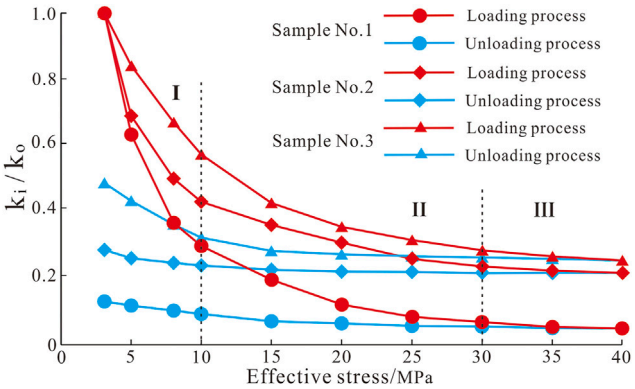

FIGURE 8 | Contrast chart of unitary experimental data of different samples.

FMI Fracture Characteristics

FMI log is an important approach to identify natural fractures (Genter et al., 1997; Jiu et al., 2013). Natural fractures are represented by a complete sinusoidal curve (**Figure 6A**) on FMI, where dark sinusoidal curves represent effective fractures due to low resistance (mud filtrate invasion), and light sinusoidal curves express filling fractures (Niu et al., 2008). Two groups of fractures can be identified from FMI in the study area, i.e., NE-SW strike fractures (with proportion of 45.9%, density of 1.0 m^{-1}, filling degree of 9.3%) and NW-SE strike fractures (with proportion of 28.1%, density of 0.6 m^{-1}, filling degree of 11.4%). Also, two groups of secondary fractures can be found: E-W strike and S-N strike fractures (**Figure 6B**). The dip angle primarily varies between 60–90° with a small group of low-angle fractures (**Figure 6C**).

Fracture Permeability Stress-Sensitivity

Measurements on three groups of samples show that permeability has a negative exponential correlation with increasing effective stress, which is poorly recovered with decreasing effective stress (**Figure 7**). The permeability of these samples share a similar variation trend, but have some differences in variation amplitude. The permeability of group 1 and group 2 samples decreases rapidly at the initial stage (with effective stress of 3–10 MPa). After that, it decreases slowly with confining pressure at 10–30 MPa, which is obvious in group 2 samples. Finally, it decreases slightly when the effective stress reaches 30 MPa (**Figures 7A,B**). In terms of the group 3 samples, the permeability also decreases rapidly at the initial stage, but has smaller decreased amplitude compared with the group 1 and group 2 samples. Its permeability can be well recovered with decreasing effective stress (**Figure 7C**). The stress sensitive coefficients of permeability are 0.894, 0.733, and 0.518, respectively, for these three groups. Consequently, the group 1 and group 2 samples have intensive stress-sensitivity permeability, and the group 3 samples have a medium one, according to the criterion proposed by Li (2006).

DISCUSSION

Mechanical mechanisms of structural fracture growth (Olsson et al., 2004; Gale and Gomez, 2007; Zhang et al., 2020) suggests that tensile stress field occurs when the orientation of the scoring is consistent with the inclination of fracture surface [where the maximum principal stress (σ_1) is vertical and the intermediate principal stress (σ_2) and the minimum principal stress (σ_3) are horizontal], and it is consistent with the tensile stress field at the late Paleogene of Nanpu Sag (Tong et al., 2013), where NE-SW horizontal compression and NW-SE tensile stress developed NE-SW direction shear fractures. Strike-slip tectonic stress occurs when the scoring shares the same orientation with fracture surface (where the σ_2 is vertical, the σ_1 and σ_3 are horizontal). Hence, it corresponds to the strike-slip tectonic stress field at the end of Neogene (Fan et al., 2010; Jiang et al., 2015), where the near E-W horizontal compression resulted in the NE-SW and NW-SE directions' structural fractures. Combined with the fracture pattern (**Figure 5**), these structural fractures in the study area can be determined to have been formed during the late Paleogene and late Neogene.

The stress-sensitivity permeability can be divided into three phases based on variation amplitude (**Figure 8**). In terms of the group 1 samples, the ratio of average amplitudes for three phases is about 4:2:1. Natural fracture, the primary seepage channel, decreases sharply in apertures with increasing effective stress at phase I. It results in a rapid decrease in permeability, which can be explained by the exponential relationship between fracture aperture and permeability (Alnoaimi and Kovscek, 2019). After that, the permeability decreases smoothly with slowly decreased fracture apertures. High effective stress falls off particles attached to the pore surface at phase III, which can plug narrow throats or pores and decrease matrix permeability (Jones et al., 2001; Zhang et al., 2015; Geng et al., 2017). The stress sensitive coefficient of group 2 basically shares the same variation trend and origin with group 1, who has a smaller variation amplitude (about 2.2:1.3:1). The ratio of average variation amplitude of stress sensitive coefficient in matrix rock is about 1.8:1.2:1, which is the lowest due to the increased stress sensitive coefficient involving fracture closure (Warpinski and Teufel,

1992; Zhang et al., 2019). Large throats in matrix rock, as main seepage channels, are typically the first to be narrowed with increasing effective stress, rapidly decreasing permeability. The remaining small throats and pores are difficult to be further closed and deformed when the rock sample is compressed to a certain degree, which can explain the slow decrease in permeability (Magdalena and Erling, 2013; Gowacki and Selvadurai, 2016). Hence, the stress-sensitivity permeability is closely related to fracture aperture and throat size.

Fractures govern well patterns in low-permeability oilfields through controlling the seepage system (Tamagawa and Pollard, 2008; Laubach et al., 2018). Fracture permeability varies as a function of fracture density, filling degree, and current *in-situ* stress (Baytok and Pranter, 2013; Gong et al., 2019b; Wang Z. et al., 2020). The NE-SW strike fractures in the study area are characterized by their high density, large aperture, being weakly-filled, and approximately parallel to the regional maximum horizontal principal stress (Connolly and Cosgrove, 1999). Therefore, these fractures have high permeability and are the dominant seepage system at the early development stage. However, flow velocity at these fractures is high and pressure drops sharply at the early stage, and fracture apertures and permeability also decrease at a high speed. The occurrence of stress-sensitivity decreases permeability of fractured reservoirs significantly at the Gaoshangpu Oilfield, which leads to high injection pressure when transferring into water flooding under the existing well pattern. Therefore, it is necessary to minimize the negative influence of stress sensitivity *via* maintaining formation energy and original pressure-seepage field. NW-SE strike fractures, secondary seepage system at the early stage, are slow in aperture decreasing and permeability declining, which works better in fluid flowing compared with other fractures. This can be confirmed by the well-connected injectors and producers along the NW-SE direction. Therefore, it is necessary to regulate well pattern based on fracture dynamic parameters at different stages, which is important to improve the performance of low-permeability fractured reservoirs.

CONCLUSION

Shear fractures in Paleogene sandstone reservoirs at Nanpu Sag chiefly assume the NE-SW direction; the second most common are the fractures of the NW-SE direction. They were formed due to tensile stress in the late Paleogene and the strike-slip stress at the late Neogene. The permeability is medium stress-sensitivity in matrix, but is intensive stress-sensitivity in fractures. The variation of permeability with increasing effective stress can be divided into three phases, which are closely related to fracture aperture and throat size. Therefore, paying attention to fracture dynamic parameters and adjusting corresponding well patterns is important to improving the performance of fractured reservoirs at different development stages.

DATA AVAILABILITY STATEMENT

The original contributions presented in the study are included in the article/supplementary materials, further inquiries can be directed to the corresponding author.

AUTHOR CONTRIBUTIONS

ZW: Methodology, Investigation, Writing - Original Draft; MM: Conceptualization; DX: Experiment; JF: Resources, Software; JL: Visualization, Data Curation; ZZ: Methodology, Funding acquisition; DL: Resources, Software; LG: Data Curation.

FUNDING

This study is financially supported by the National Natural Science Foundation of China (No: 41172015) and the National Major Science and Technology Projects of China (2017ZX05009001-002).

ACKNOWLEDGMENTS

The authors wish to thank Haigang Lao, doctor of China University of Petroleum (Huadong), for his sincere and generous help. This study is financially supported by the National Natural Science Foundation of China (No: 41172015) and the National Major Science and Technology Projects of China (2017ZX05009001-002).

REFERENCES

Abul Khair, H., Cooke, D., and Hand, M. (2015). Paleo Stress Contribution to Fault and Natural Fracture Distribution in the Cooper Basin. *J. Struct. Geology* 79, 31–41. doi:10.1016/j.jsg.2015.07.007

Alhuraishawy, A. K., Bai, B., Wei, M., Geng, J., and Pu, J. (2018). Mineral Dissolution and fine Migration Effect on Oil Recovery Factor by Low-Salinity Water Flooding in Low-Permeability sandstone Reservoir. *Fuel* 220, 898–907. doi:10.1016/j.fuel.2018.02.016

Alnoaimi, K. R., and Kovscek, A. R. (2019). Influence of Microcracks on Flow and Storage Capacities of Gas Shales at Core Scale. *Transp Porous Med.* 127, 53–84. doi:10.1007/s11242-018-1180-5

Babadagli, T. (2020). Unravelling Transport in Complex Natural Fractures with Fractal Geometry: A Comprehensive Review and New Insights. *J. Hydrol.* 587, 124937. doi:10.1016/j.jhydrol.2020.124937

Barton, C. A., Zoback, M. D., and Burns, K. L. (2013). *In-Situ* Stress Orientation and Magnitude at the Fenton Geothermal Site, New Mexico, Determined from Wellbore Breakouts. *Geophys. Res. Lett.* 15 (5), 467–470. doi:10.1029/GL015i005p00467

Baytok, S., and Pranter, M. J. (2013). Fault and Fracture Distribution within a Tight-Gas sandstone Reservoir: Mesaverde Group, Mamm Creek Field, Piceance Basin, Colorado, USA. *Pet. Geosci.* 19 (3), 203–222. doi:10.1144/petgeo2011-093

Cao, D., Wang, A., Ning, S., Li, H., Guo, A., Chen, L., et al. (2020). Coalfield Structure and Structural Controls on Coal in China. *Int. J. Coal. Sci. Technol.* 7 (2), 220–239. doi:10.1007/s40789-020-00326-z10.1007/s40789-020-00326-z

Collett, T. S., Lewis, R. E., Winters, W. J., Lee, M. W., Rose, K. K., and Boswell, R. M. (2011). Downhole Well Log and Core Montages from the Mount Elbert Gas Hydrate Stratigraphic Test Well, Alaska North Slope. *Mar. Pet. Geology* 28, 561–577. doi:10.1016/j.marpetgeo.2010.03.016

Dong, Y., Xiao, L., Zhou, H., Wang, C., Zheng, J., Zhang, N., et al. (2010). The Tertiary Evolution of the Prolific Nanpu Sag of Bohai bay basin, china: Constraints from Volcanic Records and Tectono-Stratigraphic Sequences. *Geol. Soc. America Bull.* 122, 609–626. doi:10.1130/B30041.1

Fan, B. J., Liu, C. L., Liu, G. D., and Zhu, J. (2010). Forming Mechanism of the Fault Systerm and Structural Evolution History of Nanpu Sag. *J. Xi,an Shiyou University(Natural Sci. Edition)* 25, 13–20. (in Chinese with English abstract).

Gale, J. F. W., and Gomez, L. A. (2007). Late Opening-Mode Fractures in Karst-Brecciated Dolostones of the Lower Ordovician Ellenburger Group, West texas: Recognition, Characterization, and Implications for Fluid Flow. *Bulletin* 91, 1005–1023. doi:10.1306/03130706066

Geng, Y., Tang, D., Xu, H., Tao, S., Tang, S., Ma, L., et al. (2017). Experimental Study on Permeability Stress Sensitivity of Reconstituted Granular Coal with Different Lithotypes. *Fuel* 202, 12–22. doi:10.1016/j.fuel.2017.03.093

Genter, A., Castaing, C., Dezayes, C., Tenzer, H., Traineau, H., and Villemin, T. (1997). Comparative Analysis of Direct (Core) and Indirect (Borehole Imaging Tools) Collection of Fracture Data in the Hot Dry Rock Soultz Reservoir (france). *J. Geophys. Res.* 102, 15419–15431. doi:10.1029/97jb00626

Gong, L., Fu, X., Wang, Z., Gao, S., Jabbari, H., Yue, W., et al. (2019b). A New Approach for Characterization and Prediction of Natural Fracture Occurrence in Tight Oil Sandstones with Intense Anisotropy. *Bulletin* 103, 1383–1400. doi:10.1306/12131818054

Gong, L., Su, X., Gao, S., Fu, X., Jabbari, H., Wang, X., et al. (2019a). Characteristics and Formation Mechanism of Natural Fractures in the Tight Gas Sandstones of Jiulongshan Gas Field, China. *J. Pet. Sci. Eng.* 175, 1112–1121. doi:10.1016/j.petrol.2019.01.021

Gong, L., Wang, J., Gao, S., Fu, X., Liu, B., Miao, F., et al. (2021). Characterization, Controlling Factors and Evolution of Fracture Effectiveness in Shale Oil Reservoirs. *J. Pet. Sci. Eng.* 203, 108655. doi:10.1016/j.petrol.2021.108655

Gowacki, A., and Selvadurai, A. P. S. (2016). Stress-induced Permeability Changes in indiana limestone. *Eng. Geol.* 215, 122–130. doi:10.1016/j.enggeo.2016.10.015

Hu, Z., Klaver, J., Schmatz, J., Dewanckele, J., Littke, R., Krooss, B. M., et al. (2020). Stress Sensitivity of Porosity and Permeability of Cobourg limestone. *Eng. Geology* 273, 105632. doi:10.1016/j.enggeo.2020.105632

Jelmert, T. A., and Selseng, H. (1998). Permeability Function Describes Core Permeability in Stress-Sensitive Rocks. *Oil Gas J.* 96 (49), 60–63. doi:10.1016/S1353-2561(99)00081-X

Jiang, F., Pang, X., Li, L., Wang, Q., Dong, Y., Hu, T., et al. (2018). Petroleum Resources in the Nanpu Sag, Bohai Bay Basin, Eastern China. *Bulletin* 102, 1213–1237. doi:10.1306/0906171608017148

Jiang, Y. L., Liu, P., Song, G. Q., Liu, H., Wang, Y. S., and Zhao, K. (2015). Late Cenozoic Faulting Activities and Their Influence upon Hydrocarbon Accumulations in the Neogene in Bohai Bay Basin. *Oil Gas Geology* 36 (4), 525–533. doi:10.11743/ogg20150401

Jiu, K., Ding, W., Huang, W., Zhang, Y., Zhao, S., and Hu, L. (2013). Fractures of Lacustrine Shale Reservoirs, the Zhanhua Depression in the Bohai bay basin, Eastern china. *Mar. Pet. Geology* 48, 113–123. doi:10.1016/j.marpetgeo.2013.08.009

Jones, C., Somerville, J. M., Smart, B. G. D., Kirstetter, O., Hamilton, S. A., and Edlmann, K. P. (2001). Permeability Prediction Using Stress Sensitive Petrophysical Properties. *Pet. Geosci.* 7, 211–219. doi:10.1144/petgeo.7.2.211

Laubach, S. E., Lamarche, J., Gauthier, B. D. M., Dunne, W. M., and Sanderson, D. J. (2018). Spatial Arrangement of Faults and Opening-Mode Fractures. *J. Struct. Geology* 108, 2–15. doi:10.1016/j.jsg.2017.08.008

Li, C. L. (2006). Evaluation Method for Stress Sensitivity of Reservoir Rock. *Pet. Geology. Oil Field Develop. Daqing* 25 (1), 40–43. (in Chinese with English abstract).

Li, J., Li, X.-R., Song, M.-S., Liu, H.-M., Feng, Y.-C., and Liu, C. (2021). Investigating Microscopic Seepage Characteristics and Fracture Effectiveness of Tight Sandstones: a Digital Core Approach. *Pet. Sci.* 18, 173–182. doi:10.1007/s12182-020-00464-8

Li, Y. H., Qi, L. X., Xia, Q. J., Yang, J. X., Chen, S. Y., and Cao, T. F. (2014). Reservoir Characteristics of Es_3^3 in Gaoshangpu Oilfield. *China Mining Mag.* 23 (9), 83–88. (in Chinese with English abstract).

Lin, K., Huang, W., Finkelman, R. B., Chen, J., Yi, S., Cui, X., et al. (2020). Distribution, Modes of Occurrence, and Main Factors Influencing lead Enrichment in Chinese Coals. *Int. J. Coal. Sci. Technol.* 7 (1), 1–18. doi:10.1007/s40789-019-00292-1

Liu, B., Yang, Y., Li, J., Chi, Y., Li, J., and Fu, X. (2020). Stress Sensitivity of Tight Reservoirs and its Effect on Oil Saturation: A Case Study of Lower Cretaceous Tight Clastic Reservoirs in the Hailar Basin, Northeast China. *J. Pet. Sci. Eng.* 184, 106484. doi:10.1016/j.petrol.2019.106484

Mackay, F., Toner, J., Morozov, A., and Marenduzzo, D. (2020). Darcy's Law without Friction in Active Nematic Rheology. *Phys. Rev. Lett.* 124 (18), 187801. doi:10.1103/PhysRevLett.124.187801

Maxwell, S. C., Rutledge, J., Jones, R., and Fehler, M. (2010). Petroleum Reservoir Characterization Using Downhole Microseismic Monitoring. *Geophysics* 75 (5), 75A129–75A137. doi:10.1190/1.3477966

Mu, L. H., Peng, S. M,, Yin, Z. J., and Lei, Y. L. (2003). Sequence Stratigraphy and Lithofacies Palaeography of the Shahejie Formation of Paleogene in Liuzan Oilfield, Eastern Hebei Province. *J. Palaeogeogr.* 5 (3), 304–315.

Nagel, N. B., Sanchez-Nagel, M. A., Zhang, F., Garcia, X., and Lee, B. (2013). Coupled Numerical Evaluations of the Geomechanical Interactions between a Hydraulic Fracture Stimulation and a Natural Fracture System in Shale Formations. *Rock Mech. Rock Eng.* 46 (3), 581–609. doi:10.1007/s00603-013-0391-x

Niu, H. L., Tian, Z. J., Hu, X., and Zhuang, S. (2008). Application of Imaging Log Interpretation Patterns in Fractured Basement Reservoirs. *Prog. Geophys.* 23 (5), 1544–1549. doi:10.1016/S1872-5791(08)60056-1

Olorode, O. M., Freeman, C. M., Moridis, G. J., and Blasingame, T. A. (2012). High-Resolution Numerical Modeling of Complex and Irregular Fracture Patterns in Shale Gas and Tight Gas Reservoirs. *SPE Reserv. Eval. Eng.* 16, 443–455. doi:10.2118/152482-MS

Olsson, W. A., Lorenz, J. C., and Cooper, S. P. (2004). A Mechanical Model for Multiply-Oriented Conjugate Deformation Bands. *J. Struct. Geology* 26, 325–338. doi:10.1016/s0191-8141(03)00101-9

Pang, B., Dong, Y. X., Chen, D., and Pang, X. Q. (2019). Main Controlling Factors and Basic Model for Hydrocarbon Enrichment in the sandstone Target Layer of Petroliferous basin: a Case Study of Neogene sandstone Reservoirs in Nanpu Sag, Bohai Bay Basin. *Acta Petrolei Sinica* 40 (5), 519–531. doi:10.7623/syxb201905002

Connolly, P., and Cosgrove, J. (1999). Prediction of Fracture-Induced Permeability and Fluid Flow in the Crust Using Experimental Stress Data. *Bulletin* 83, 757–777. doi:10.1306/e4fd2d75-1732-11d7-8645000102c1865d

Qing, F., Yan, J., Wang, J., Hu, Q., Wang, M., Geng, B., et al. (2021). Pore Structure and Fluid Saturation of Near-Oil Source Low-Permeability Turbidite sandstone of the Dongying Sag in the Bohai Bay Basin, east China. *J. Pet. Sci. Eng.* 196, 108106. doi:10.1016/j.petrol.2020.108106

Bustin, R. M. (1997). Importance of Fabric and Composition on The Stress Sensitivity of Permeability in Some Coals, Northern Sydney Basin, Australia: Relevance To Coalbed Methane Exploitation. *Bulletin* 81, 1894–1908. doi:10.1306/3B05C65E-172A-11D7-8645000102C1865D

Scelsi, G., De Bellis, M. L., Pandolfi, A., Musso, G., and Della Vecchia, G. (2019). A Step-by-step Analytical Procedure to Estimate the *In-Situ* Stress State from Borehole Data. *J. Pet. Sci. Eng.* 176, 994–1007. doi:10.1016/j.petrol.2019.01.100

Shanley, K. W., and Cluff, R. M. (2015). The Evolution of Pore-Scale Fluid-Saturation in Low-Permeability sandstone Reservoirs. *Bulletin* 99, 1957–1990. doi:10.1306/03041411168

Stabile, T. A., Iannaccone, G., Zollo, A., Lomax, A., Ferulano, M. F., Vetri, M. L. V., et al. (2013). A Comprehensive Approach for Evaluating Network Performance in Surface and Borehole Seismic Monitoring. *Geophys. J. Int.* 192, 793–806. doi:10.1093/gji/ggs049

Stroisz, A. M., and Fjær, E. (2013). Tracing Causes for the Stress Sensitivity of Elastic Wave Velocities in Dry Castlegate sandstone. *Geophys. J. Int.* 192 (1), 137–147. doi:10.1093/gji/ggs029

Tamagawa, T., and Pollard, D. D. (2008). Fracture Permeability Created by Perturbed Stress Fields Around Active Faults in a Fractured Basement Reservoir. *Bulletin* 92, 743–764. doi:10.1306/02050807013

Tong, H. M., Zhao, B. Y., Cao, Z., Liu, G. X., Dun, X. M., and Zhao, D. (2013). Structural Analysis of Faulting System Origin in the Nanpu Sag, Bohai Bay Basin. *Acta Geologica Sinica* 87 (11), 1647–1661.

Wang, Z. S., Dong, S. Q., Meng, N. N., Liu, D. J., and Gao, W. (2020a). Fracture Network and its Controlling Factors in the Low-Permeable Fault Block Reservoirs in Deep-Buried Gaoshangpu Oilfield, Bohai Bay Basin. *Oil Gas Geology* 41 (3), 534–542. doi:10.11743/ogg20200310

Wang, Z., Zeng, L., Luo, Z., Zu, K., Lao, H., and Meng, N. (2020b). Natural Fractures in the Triassic Tight Sandstones of the Dongpu Depression, Bohai Bay Basin, Eastern China: The Key to Production. *Interpretation* 8 (4), SP71–SP80. doi:10.1190/INT-2019-0252.1

Warpinski, N. R., and Teufel, L. W. (1992). Determination of the Effective-Stress Law for Permeability and Deformation in Low-Permeability Rocks. *SPE Formation Eval.* 7 (2), 123–131. doi:10.2118/20572-PA

Zeng, L., Jiang, J., and Yang, Y. (2010). Fractures in the Low Porosity and Ultra-Low Permeability Glutenite Reservoirs: A Case Study of the Late Eocene Hetaoyuan Formation in the Anpeng Oilfield, Nanxiang Basin, China. *Mar. Pet. Geology* 27, 1642–1650. doi:10.1016/j.marpetgeo.2010.03.009

Zeng, L., Lyu, W., Li, J., Zhu, L., Weng, J., Yue, F., et al. (2016). Natural Fractures and Their Influence on Shale Gas Enrichment in Sichuan Basin, China. *J. Nat. Gas Sci. Eng.* 30, 1–9. doi:10.1016/j.jngse.2015.11.048

Zeng, L., Su, H., Tang, X., Peng, Y., and Gong, L. (2013). Fractured Tight sandstone Oil and Gas Reservoirs: A New Play Type in the Dongpu Depression, Bohai Bay Basin, China. *Bulletin* 97, 363–377. doi:10.1306/O912121205710.1306/09121212057

Zeng, L., Tang, X., Wang, T., and Gong, L. (2012). The Influence of Fracture Cements in Tight Paleogene saline Lacustrine Carbonate Reservoirs, Western Qaidam Basin, Northwest China. *Bulletin* 96, 2003–2017. doi:10.1306/04181211090

Zhang, F., An, M., Zhang, L., Fang, Y., and Elsworth, D. (2020). Effect of Mineralogy on Friction-Dilation Relationships for Simulated Faults: Implications for Permeability Evolution in Caprock Faults. *Geosci. Front.* 11 (2), 439–450. doi:10.1016/j.gsf.2019.05.014

Zhang, H. Y., He, S. L., Luan, G. H., Men, C. Q., Mo, S. Y., and Liu, H. (2015). Experimental Study on Stress Sensitivity of Microfracture Ultra-low Permeability Reservoirs. *J. Xi'an Shiyou University(Nat. Sci. Edition)* 30 (1), 30–35. doi:10.3969/j.issn.1673-064X.2015.01.005

Zhang, J., Li, Y., Pan, Y., Wang, X., Yan, M., Shi, X., et al. (2021). Experiments and Analysis on the Influence of Multiple Closed Cemented Natural Fractures on Hydraulic Fracture Propagation in a Tight sandstone Reservoir. *Eng. Geology* 281, 105981. doi:10.1016/j.enggeo.2020.105981

Zhang, J., Wei, C., Ju, W., Yan, G., Lu, G., Hou, X., et al. (2019). Stress Sensitivity Characterization and Heterogeneous Variation of the Pore-Fracture System in Middle-High Rank Coals Reservoir Based on Nmr Experiments. *Fuel* 238, 331–344. doi:10.1016/j.fuel.2018.10.127

Zhang, K., Jiang, S. H., Yue, J. T., Wang, Y. Y., and Wang, Y. F. (2018). Sedimentary Micro-Facies of Fan Delta in Es_3^{2+3} Submember, Gaoshangpu Oilfield. *Periodical Ocean Univ. China* 48 (5), 86–94. doi:10.16441/J.cnki.hdxb.20160377

Zhao, X. X., Zhou, L., Pu, X., Jin, F., Shi, Z., Han, W., et al. (2020). Formation Conditions and Enrichment Model of Retained Petroleum in Lacustrine Shale: A Case Study of the Paleogene in Huanghua Depression, Bohai Bay Basin, Chinan. *Pet. Exploration Develop.* 47 (5), 916–930. doi:10.1016/S1876-3804(20)60106-9

Conflict of Interest: MM, DX, JF and JL are employed by CNPC Logging Company Limited Xinjiang Branch. DL is employed by CNPC Jidong Oilfield.

The remaining authors declare that the research was conducted in the absence of any commercial or financial relationships that could be construed as a potential conflict of interest.

Publisher's Note: All claims expressed in this article are solely those of the authors and do not necessarily represent those of their affiliated organizations, or those of the publisher, the editors and the reviewers. Any product that may be evaluated in this article, or claim that may be made by its manufacturer, is not guaranteed or endorsed by the publisher.

frontiers in Earth Science

ORIGINAL RESEARCH
published: 03 September 2021
doi: 10.3389/feart.2021.711695

The Effect of Formation Water Salinity on the Minimum Miscibility Pressure of CO_2-Crude Oil for Y Oilfield

Yanfu Pi[1], Jinxin Liu[1], Li Liu[1], Xuan Guo[2], Chengliang Li[3] and Zhihao Li[1]*

[1]Key Laboratory of Enhanced Oil and Gas Recovery of Ministry of Education, Northeast Petroleum University, Daqing, China, [2]China United Coalbed Methane Co, Ltd., Taiyuan, China, [3]CNOOC Safety Technology Service Co, Ltd., Shanghai, China

CO_2 miscible flooding is an important technology for enhancing oil recovery and greenhouse gas storage in the world. As a tertiary recovery technology, it is usually applied after water flooding. Therefore, the actual reservoirs usually contain a lot of injected water in addition to connate water. The salinity of these formation waters varies from place to place. CO_2 is an acid gas. After it is injected into the reservoir, it easily reacts with formation water and rock and affects the physical properties of the reservoir. However, no research results have been reported whether this reaction affects the minimum miscibility pressure (MMP) of CO_2-crude oil, a key parameter determining miscible flooding in formation water. Based on CO_2-formation water–rock interaction experiments, this paper uses the core flooding method to measure the CO_2-crude oil MMP under different salinity in formation water. Results show that CO_2 causes a formation water pH decrease from 7.4 to 6.5 due to its dissolution in formation water. At the same time, CO_2 reacts with formation water, albite, potassium feldspar, and carbonate minerals in the cores to generate silicate and carbonate precipitates, which could migrate to the pore throat together with the released clay particles. Overall, CO_2 increased core porosity by 5.63% and reduced core permeability by 7.43%. In addition, when the salinity of formation water in cores was 0, 4,767, and 6,778 mg/L, the MMP of CO_2-crude oil was 20.58, 19.85, and 19.32 MPa, respectively. In other words, the MMP of CO_2-crude oil decreased with the increase of salinity of formation water.

Keywords: CO_2 miscible flooding, minimum miscibility pressure, formation water salinity, core displacement experiment, CO_2-formation water-rock interaction experiment

OPEN ACCESS

Edited by:
Yuwei Li,
Liaoning University, China

Reviewed by:
Hui Pu,
University of North Dakota, United States
B. Bai,
Missouri University of Science and Technology, United States
Hongwei Yu,
Research Institute of Petroleum Exploration and Development (RIPED), China

****Correspondence:***
Jinxin Liu
1593254607@qq.com

Specialty section:
This article was submitted to Economic Geology, a section of the journal Frontiers in Earth Science

Received: *19 May 2021*
Accepted: *15 July 2021*
Published: *03 September 2021*

Citation:
Pi Y, Liu J, Liu L, Guo X, Li C and Li Z (2021) The Effect of Formation Water Salinity on the Minimum Miscibility Pressure of CO_2-Crude Oil for Y Oilfield. Front. Earth Sci. 9:711695. doi: 10.3389/feart.2021.711695

INTRODUCTION

CO_2 flooding is an effective method to improve oil recovery. There are two displacement modes: CO_2 miscible flooding and CO_2 immiscible flooding, depending on whether the reservoir pressure can reach the minimum miscible pressure (MMP) of CO_2-crude oil (Zhang et al., 2019; Syed et al., 2020; Han et al., 2018; Jishun et al., 2015). CO_2 miscible flooding can result in much higher oil recovery than CO_2 immiscible flooding because the miscible condition can reduce capillary pressure to zero, and residual oil can be significantly reduced in flooded areas/zones. Therefore, MMP, which determines whether the reservoir oil and CO_2 are miscible or not, is particularly important.

At present, studies on the influencing factors of MMP mainly focus on CO_2 purity (Cumicheo et al., 2014; Zhao et al., 2020; Cumicheo et al., 2014), oil composition (Dong et al., 2001; Hemmati-Sarapardeh et al., 2014; Yalcin and Faruk, 2020), temperature, and pressure (Zolghadr et al., 2013;

TABLE 1 | Compositional results of the oil sample.

Carbon no.	mol%	wt%	Carbon no.	mol%	wt%
C_1	46.35	6.16	C_{16}	1.74	2.46
C_2	5.42	1.56	C_{17}	0.82	1.73
C_3	3.35	1.32	C_{18}	0.67	2.41
C_4	1.88	0.92	C_{19}	0.78	2.02
C_5	1.26	0.74	C_{20}	0.83	2.05
C_6	2.85	1.32	C_{21}	1.36	4.13
C_7	3.42	1.42	C_{22}	0.31	3.86
C_8	3.96	3.11	C_{23}	0.36	4.02
C_9	3.31	2.76	C_{24}	0.24	2.83
C_{10}	1.95	2.31	C_{25}	0.41	1.85
C_{11}	2.36	1.46	C_{26}	0.3	1.49
C_{12}	2.86	2.68	C_{27}	0.23	0.89
C_{13}	2.05	2.97	C_{28}	0.15	0.74
C_{14}	0.71	1.42	C_{29}	0.34	1.66
C_{15}	2.35	2.55	C_{30+}	7.38	35.16

Jamiu, 2013; Jia et al., 2019; Moeini et al., 2014). In fact, the reservoir is usually flooded by water before CO_2 injection, and inevitably, there is connate and injected water with different salinity in formation. As a highly active gas, CO_2 easily reacts with formation water after being injected into a reservoir (Ampomah et al., 2017; Ren et al., 2019). It can impact the physico-chemical balance between reservoir rock and formation water and result in a change in the reservoir rock's physical properties. However, no research has been reported about whether and how the interactions affect the MMP for the formations with different water salinity.

Both theoretical calculation and laboratory experimental methods have been used to obtain the MMP of CO_2-crude oil (Zendehboudi et al., 2013; Ahmadi et al., 2015; Ahmadi et al., 2017; Ahmadi et al., 2018). Theoretical calculation methods mainly include empirical formulae (Yellig and Metcalfe, 1980), multiple contacts (Adekunle and Hoffman, 2016), numerical simulations (Ekechukwu et al., 2020), and equation of states (Karkevandi-Talkhooncheh et al., 2017), etc., because the application range of different calculation methods is different, and the results are greatly affected by parameters. The experimental measurement methods mainly include the slim tube test (STT) (Flock and Nouar, 1984; Mogensen, 2016), rising bubble apparatus (RBA) (Christiansen and Haines, 1987; Novosad et al., 1990; Czarnota et al., 2017), vanishing interfacial tension technique (VIT) (Rao, 1997; Saeedi Dehaghani and Soleimani, 2020), X-ray computerized scanner (Liu et al., 2015; Ahmad et al., 2016), magnetic resonance imaging technique (MRI) (Liu et al., 2016; Karkevandi-Talkhooncheh et al., 2018), core displacement experiment (Zhang and Gu, 2015; Ennin and Grigg, 2016), and so on. Among these methods, STT is the most common method that has been widely used because it usually has a long tube packed with sand or glass beads and can effectively simulate the fluid flow in porous media. However, core tubing cannot represent the mineral composition, porosity, permeability, and connate water saturation of real reservoir rocks. Therefore, it cannot be used for our study because our goal is to investigate formation the water salinity effect on the MMP of CO_2-crude oil in reservoirs. In this paper, we use CO_2-formation water–rock interaction experiments to reveal their interaction mechanisms using reservoir rock samples. On the basis of these experiments, MMP is measured using core displacement experiments in the formation water with different salinity. The results are of great significance to the optimization design of CO_2 miscible flooding.

EXPERIMENTS

Materials

The oil samples were taken from Y oilfield. Their components and related properties are shown in **Tables 1**, **2**, respectively, at reservoir pressure (22.05 MPa) and temperature (98.5°C).

Distilled water and synthetic formation water from different areas of Y oilfield were used for the experiments. The composition and salinity of the formation waters are shown in **Table 3**. The pH values of the two formation waters were 7, 7.4, and 7.8, respectively. CO_2 with purity of 99.99% was provided by United Gas Ltd. for CO_2-water–rock interaction and core displacement tests.

The wettability of four natural cores from Y oilfield is water wet. The length, diameter, porosity, and permeability of natural cores were 30 cm, 2.5 cm, 23%, and 50×10^{-3} μm^2, respectively. The core minerals are mainly composed of 53% quartz, 32% feldspar (plagioclase, potassium feldspar), and 15% lithic (clay minerals, a small amount of carbonate minerals). The carbonate minerals are mainly calcite and ankerite.

Experimental Apparatus

The core flooding apparatus shown in **Figure 1** was used to investigate the CO_2-water–rock interaction and obtain MMP. The apparatus is composed of an ISCO pump (260D, Teledyne ISCO Inc., United States), core holder (40 MPa), backpressure regulator, pressure gauges (OMEGA Engineering INC., Canada) with an accuracy of ±0.01 MPa, accumulators (40 MPa), and an oven. Both the accumulator and core holder were put in the oven to simulate reservoir temperatures. The changes in the porous throat before and after the CO_2-water–rock reaction were observed by Nano Voxel-4000 CT scanner (Sanying Precision Instrument Inc., China). The PH value of the produced water was tested by a PHB-4 pH detector (Sinameasure AOTumation Technology Inc., China).

Experimental Procedures

CO_2-formation Water–Rock Interaction Experiment

Through the CO_2-formation water–rock interaction experiment, the reaction mechanism of gas, water, and rock is revealed. The procedures are listed as follows in detail:

1) To compare the changes of core physical properties before and after displacement, the end face of the core is cut. The remaining core is put into the core holder or vacuum and then saturated with formation water.
2) CO_2 and formation water are injected into the container through the ISCO pump A, and the formation water is in the supersaturated state during the whole experiment.

TABLE 2 | Physical properties of the oil sample.

Parameter	Gas oil ratio (m^3/m^3)	Volume ratio of formation oil (m^3/m^3)	Saturation pressure (MPa)	Density of formation oil (g/cm^3)	Formation oil volume factor (mPa·s)
Value	22.8	1.106	4.95	0.9377	3.62

TABLE 3 | Compositions of formation water.

Compositions	$NaHCO_3$	NaCl	KCl	$MgSO_4$	Na_2SO_4	$CaCl_2$	Total
Formation Water 1	2,718	1789	20	62	114	64	4,767
Formation Water 2	3,866	2,545	28	88	161	90	6,778

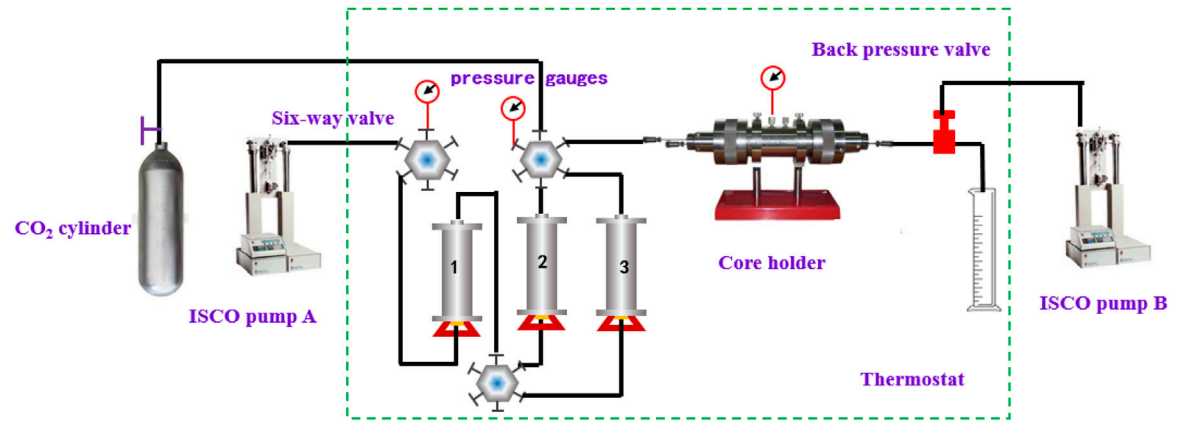

FIGURE 1 | Connection diagram of core displacement device.

3) The formation water is injected into the core at a flow rate of 0.3 ml/min. Effluent samples are taken at the outlet every 10 min. The pH value and ion concentration of these samples are measured by the PHB-4 pH detector and DiONEX 500 chromatograph.
4) After the core flooding test, the core is put into the oven for drying. When the mass of the core is no longer changed, the physical parameters of the core are measured, and the core and the original undergo CT scan.

CO_2 Miscible Flooding Experiment

The CO_2 miscible flooding experiment is used to measure the CO_2-crude oil MMP in the formation water with different salinity. The detailed procedures are as follows:

1) The core is placed into the core holder and vacuumed; then it is saturated with distilled water by manual pump.
2) The core is placed into the core holder and vacuumed; then it was saturated with distilled water by manual pump.
3) The pressure of the backpressure valve is set by ISCO pump B, and its value is below the injection-end pressure of 0.8–1 MPa. A constant pressure flow of 5 MPa is set by ISCO pump A. Then, the displacement experiment is carried out. When the volume of cumulative injection is greater than 1.5 PV, the displacement is stopped, and the oil recovery at this pressure is calculated.
4) The displacement experiment at the next pressure is carried out. CO_2 pressures were 5, 10, 15, 20, 25, 27, and 30 MPa. The pressure in the CO_2 cylinder is 5 MPa. Displacement pressure is adjusted by two containers.
5) After completion of the experiments at each pressure, the core and formation water were replaced to carry out the next experiment.

RESULTS AND DISCUSSION

Changes of pH and Ion Concentration of Produced Liquid

CO_2 is a kind of acidic gas, which easily reacts with formation water after being injected into the reservoir, breaking the physical-chemical balance between rock and formation water and then affecting the core physical parameters. To reveal the law of CO_2-water–rock interaction, the PH value of the produced liquid and the concentration of related ions were measured.

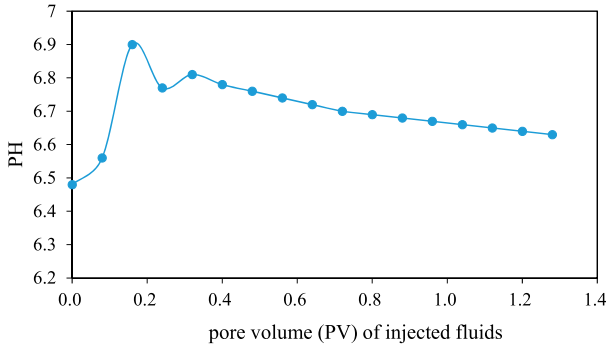

FIGURE 2 | Curve of pH values of produced water over the PV.

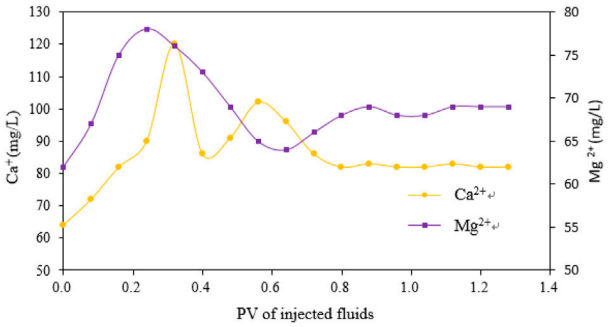

FIGURE 4 | Curve of Ca^{2+} and Mg^{2+} concentration of produced water over the PV.

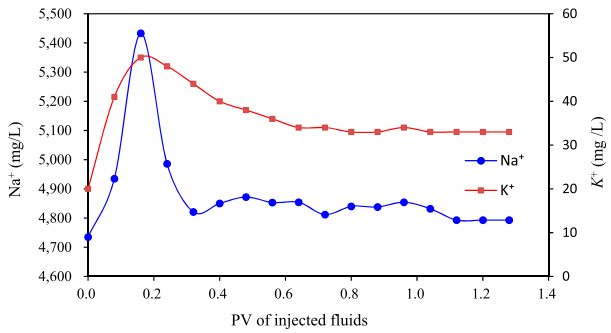

FIGURE 3 | Curve of Na^+ and K^+ concentration of produced water over the PV.

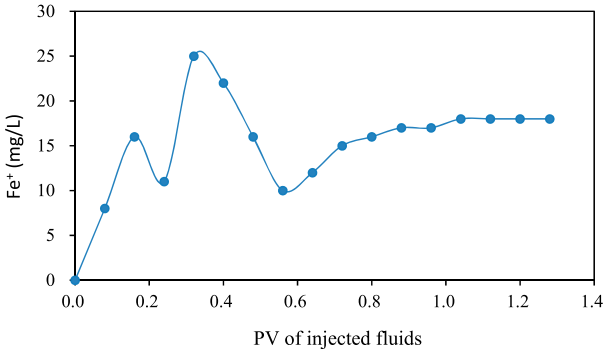

FIGURE 5 | Curve of Fe^{2+} concentration of produced water over the PV.

The test results of PH values of the produced liquid are shown in **Figure 2**. When the formation water is saturated with CO_2 in the container, the formation water is weakly acidic, and the pH value decreases from 7.4 to 6.48. After the formation water was injected into the core, the pH value of the solution increased significantly at the beginning of the experiment, and then decreased to a stable level with the increase of the injected PV. The analysis is as follows: The main reason for the formation water changing from alkaline to acidic is that CO_2 acidifies the water and forms free H_2CO_3. The reaction equation is as follows:

$$CO_2 + H_2O \Leftrightarrow H^+ + H_2CO_3^- \quad (1)$$

The variation curve of pH values with injected PV suggests that the reactions occurred between core, water, and CO_2, which significantly reduced the content of H^+ in the above equation, and then the pH value of the solution slowly decreased to a stable level as the reaction reached equilibrium.

Figure 3 shows the changed Na^+ and K^+ concentrations of produced water with the injected PV. The mass concentrations of Na^+ and K^+ increased first and then decreased to a stable level with the increase of injected PV. The chemical reactions between CO_2, core, and water depend on the mineral compositions of the core. The known mineral

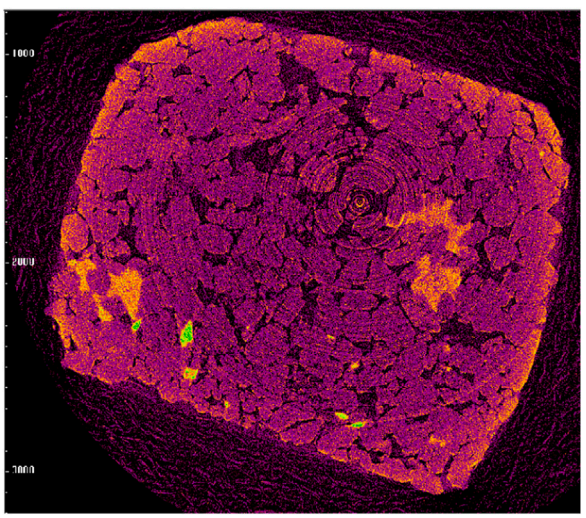

FIGURE 6 | T scan of original core.

compositions of the cores are mainly quartz, plagioclase, potassium feldspar, clay minerals, and carbonate minerals (ankerite and calcite). The change of mass concentrations of

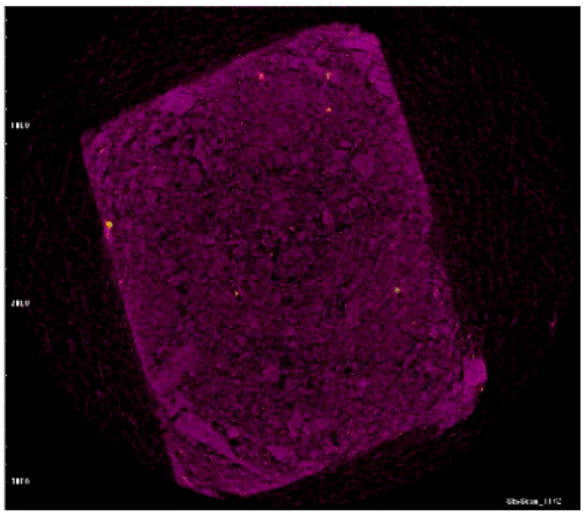

FIGURE 7 | T scan of core after experiment.

Na^+ and K^+ in produced effluent samples indicates that albite ($NaAlSi_3O_8$) and potassium feldspar ($KAlSi_3O_8$) in the core reacted with acidic formation water. The reaction equation is as follows:

$$2NaAlSi_3O_8 + H^+ + 9H_2O \Leftrightarrow Al_2Si_2O_5(OH)_4 + 2NA^+ + 4H_4SiO_4 \quad (2)$$

$$2KAlSi_3O_8 + H^+ + 9H_2O \Leftrightarrow Al_2Si_2O_5(OH)_4 + 2K^+ + 4H_4SiO_4 \quad (3)$$

These reactions generated silicate minerals and released Na^+ and K^+, leading to a significant increase in their mass concentration at the beginning of the experiment. With the progress of the experiment, albite ($NaAlSi_3O_8$) and potassium feldspar ($KAlSi_3O_8$) reached solve-precipitation equilibrium, and the ion concentration decreased to a stable level.

Figures 4, **5** show the changes of Mg^{2+}, Ca^{2+}, and Fe^{2+} concentrations. The concentrations of Mg^{2+}, Ca^{2+}, and Fe^{2+} increased first and then fluctuated to a stable level with the increase of injected PV. The change of the mass concentration of Mg^{2+}, Ca^{2+}, and Fe^{2+} in the reaction solution was mainly related to the dissolution and precipitation of calcite and ankerite. At the beginning of the experiment, the concentrations of Ca^{2+}, Fe^{2+}, and Mg^{2+} increased, which indicated that carbonate minerals (calcite and ankerite) were corroded by the CO_2 acid solution. The reaction consumes H+ in the solution, which leads to the increase of pH value in the solution. The calcite dissolution equation of the solution is shown in **Eq. 4**, and the ankerite dissolution equation is shown in **Eq. 5**.

$$CaCO_3 + H^+ \Leftrightarrow Ca^{2+} + HCO_3^- \quad (4)$$

$$Ca(Fe_{0.7}Mg_{0.3})(CO_3)_2 + H^+ \Leftrightarrow Ca^{2+} + 0.7Fe^{2+} + 0.3Mg^{2+} + 2HCO_3^- \quad (5)$$

TABLE 4 | Changes of core porosity and permeability before and after the experiment.

Porosity(%)		Rate of change in porosity(%)	Permeability($\times 10^{-3}\mu m^2$)		Rate of change in permeability(%)
Before the experiment	After the experiment		Before the experiment	After the experiment	
21.3	22.5	5.63	20.2	18.7	−7.43

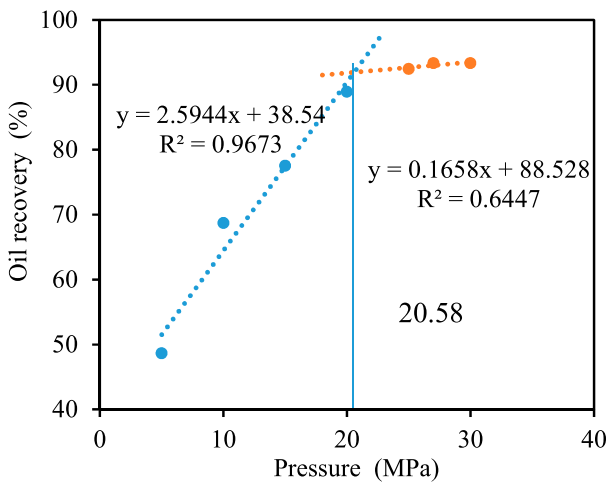

FIGURE 8 | Oil recovery under different displacement.

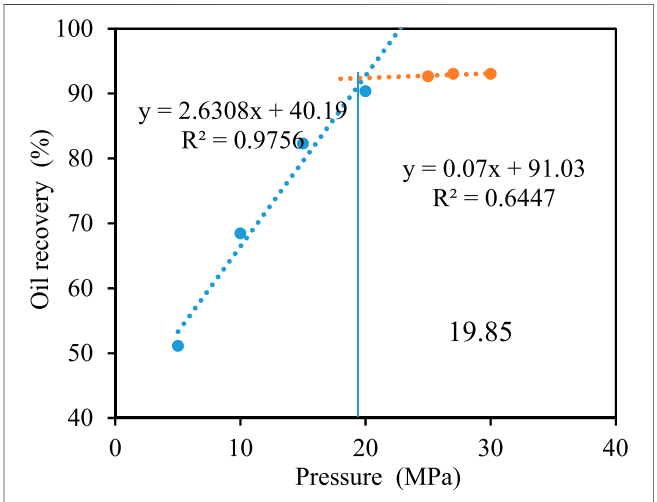

FIGURE 9 | Oil recovery under different displacement. Pressure when formation water salinity is 0 mg/L pressure when formation water salinity is 6778 mg/L.

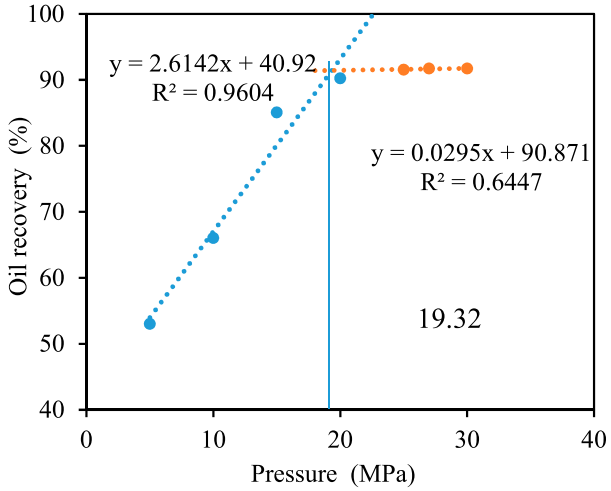

FIGURE 10 | Oil recovery under different displacement pressure when formation water salinity is 15,000 mg/L.

At the same time, with the progress of the experiment, the above reaction promoted the continuous ionization of H_2CO_3 and lowered the PH value of the solution. Meanwhile, some cations in the solution, such as Mg^{2+} and Ca^{2+}, react with bicarbonate to form insoluble carbonate. This reaction released a large amount of H^+, which reduced the concentration of metal cations in the solution. The reaction formulas are shown in **Eq. 1**, **Eqs 6–8**:

$$HCO_3^- \Leftrightarrow H^+ + CO_3^{-2} \quad (6)$$

$$Mg^{2+} + HCO_3^- \Leftrightarrow MgCO_3\downarrow + H^+ \quad (7)$$

$$Ca^{2+} + HCO_3^- \Leftrightarrow CaCO_3\downarrow + H^+ \quad (8)$$

Changes of Core Physical Properties

Figures 6, **7** show the CT scanning results of natural cores before and after the experiment. The pore volume of the core increases obviously after displacement. This is consistent with the core porosity measurement results after the experiment (**Table 4**). However, the core permeability decreases obviously after displacement. The relevant analysis is as follows: The formation water filled with saturated Ca^{2+} dissolves the core. At the same time, it generates corresponding precipitates ($Al_2Si_2O_5(OH)_4$, H_4SiO_4), and a lot of Mg^{2+} and Ca^{2+}. With the increase of the concentration of these divalent ions, they react with the bicarbonate in the formation water to generate $MgCO_3$ and $CaCO_3$ precipitates. The dissolution of these new mineral phases with carbonate cements releases clay particles that were transported by fluid to the pore throats, where the pores were blocked and the permeability of the core was reduced.

CO_2-Crude Oil MMP Under Formation Water of Different Salinity

To reveal the influence of formation water salinity on the MMP of CO_2 and crude oil, the core displacement method is used to measure the MMP under different formation water. It can be seen from **Figures 8–10** that the MMP is 20.80, 19.85, and 19.21. The MMP of CO_2-crude oil decreases. The analysis is as follows:

There is a spatial competition effect in the dissolution of CO_2 in formation water. Compared with CO_2, the ionic radius of inorganic salt is smaller, and it more easily fills the gap in water molecules (**Figure 11**). This reduces the dissolution space for CO_2, resulting in less CO_2 soluble in water and more CO_2 soluble in crude oil in the core saturated with high salinity, resulting in more miscibility. Therefore, the higher the salinity of the formation water, the smaller the MMP between CO_2 and crude oil.

When the pressure is greater than 7.38 MPa, CO_2 reaches supercritical state. Under the action of its extraction and pore-throat capillary force, NaCl in the formation water is pumped to the mineral surface. The precipitated NaCl crystals with mineral precipitation of CO_2-water–rock interaction are carried by CO_2 for blocking the pore throat.

This increases the pore volume and reduces the permeability of the core. The change of the physical properties of the core increase the gas breakout time and

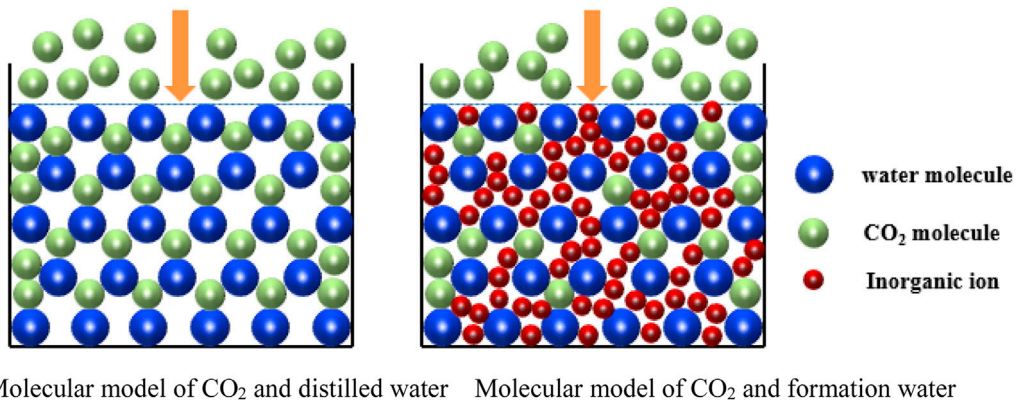

FIGURE 11 | Spatial competition between ions of inorganic salt and CO_2.

make the compositional exchange between CO_2 and crude oil more intense in the smaller pore space. Thus, the MMP between CO_2 and crude oil is lower.

Molecular model of CO_2 and distilled water Molecular model of CO_2 and formation water.

CONCLUSION

Based on CO_2-formation water–rock interaction and core displacement method experiments, the following conclusions are drawn in this paper:

1)CO_2 can react with formation water to decrease the formation water pH from 7.4 to 6.5.

2) CO_2 can react with minerals in the core to form insoluble silicate and carbonate precipitates. These new minerals migrate to the pore throat together with the released clay particles, resulting in the increase of the core porosity by 5.63% and the decrease of the core permeability by 7.43%.

3)Formation water salinity influences MMP. MMP of CO_2-crude oil decreased with the increase of formation water salinity in the cores.

DATA AVAILABILITY STATEMENT

The original contributions presented in the study are included in the article/Supplementary Material, further inquiries can be directed to the corresponding author.

AUTHOR CONTRIBUTIONS

YP conceived and designed the analysis JL wrote the paper and performed the analya CL collected the data ZL collected the data.

FUNDING

This work was supported by the National Natural Foundation of China (The influence mechanism and rules of low-permeability sandstone reservoir water shield on the minimum miscible pressure of CO_2-crude oil Project No.52174023), and the Natural Science Foundation of Heilongjiang Province of China (The Influence of Formation Water on CO_2-Crude Oil MMP under Reservoir Conditions Project No.E2018013).

REFERENCES

Adekunle, O., and Hoffman, B. T. (2016). Experimental and analytical methods to determine minimum miscibility pressure (MMP) for Bakken formation crude oil. *J. Pet. Sci. Eng.* 146, 170–182. doi:10.1016/j.petrol.2016.04.013

Ahmad, W., Vakili-Nezhaad, G., Al-Bemani, A. S., and Al-Wahaibi, Y. (2016). Experimental Determination of Minimum Miscibility Pressure. *Proced. Eng.* 148, 1191–1198. doi:10.1016/j.proeng.2016.06.629

Ahmadi, M. A., Zahedzadeh, M., Shadizadeh, S. R., and Abbassi, R. (2015). Connectionist model for predicting minimum gas miscibility pressure: Application to gas injection process. *Fuel* 148, 202–211. doi:10.1016/j.fuel.2015.01.044

Ahmadi, M. A., Zendehboudi, S., and James, L. A. (2017). A reliable strategy to calculate minimum miscibility pressure of CO2-oil system in miscible gas flooding processes. *Fuel* 208, 117–126. doi:10.1016/j.fuel.2017.06.135

Ahmadi, M. A., Zendehboudi, S., and James, L. A. (2018). Developing a robust proxy model of CO2 injection: Coupling Box-Behnken design and a connectionist method. *Fuel* 215, 904–914. doi:10.1016/j.fuel.2017.11.030

Ampomah, W., Balch, R. S., Cather, M., Will, R., Gunda, D., Dai, Z., et al. (2017). Optimum design of CO2 storage and oil recovery under geological uncertainty. *Appl. Energ.* 195, 80–92. doi:10.1016/j.apenergy.2017.03.017

Christiansen, R. L., and Haines, H. K. (1987). Rapid Measurement of Minimum Miscibility Pressure with the Rising-Bubble Apparatus. *SPE Reservoir Eng.* 2 (04), 523–527. doi:10.2118/13114-pa

Cumicheo, C., Cartes, M., Segura, H., Müller, E. A., and Mejía, A. (2014). High-pressure densities and interfacial tensions of binary systems containing carbon dioxide+n-alkanes: (n-Dodecane, n-tridecane, n-tetradecane). *Fluid Phase Equilibria* 380, 82–92. doi:10.1016/j.fluid.2014.07.039

Czarnota, R., Janiga, D., Stopa, J., and Wojnarowski, P. (2017). Determination of minimum miscibility pressure for CO 2 and oil system using acoustically monitored separator. *J. CO2 Utilization* 17, 32–36. doi:10.1016/j.jcou.2016.11.004

Dong, M., Huang, S., Dyer, S. B., and Mourits, F. M. (2001). A comparison of CO2 minimum miscibility pressure determinations for Weyburn crude oil. *J. Pet. Sci. Eng.* 31 (1), 13–22. doi:10.1016/s0920-4105(01)00135-8

Ekechukwu, G. K., Falode, O., and Orodu, O. D. (2020). Improved Method for the Estimation of Minimum Miscibility Pressure for Pure and Impure CO_2–Crude Oil Systems Using Gaussian Process Machine Learning Approach[J]. *J. Energ. Resour. Tech.* 142 (12), 132–138. doi:10.1115/1.4047322

Ennin, E., and Grigg, R. B. (2016). *CO_2 flooding and minimum miscibility pressure study in Texas Farnsworth Field[C]//SPE Trinidad and Tobago section energy resources conference*. Canada: Society of Petroleum Engineers.

Flock, D. L., and Nouar, A. (1984). Parametric Analysis on the determination of the minimum miscibility pressure in slim tube displacements[J]. *J. Can. Pet. Tech.* 23 (05), 80–88. doi:10.2118/84-05-12

Han, J., Han, S., Sung, W., and Lee, Y. (2018). Effects of CO2 miscible flooding on oil recovery and the alteration of rock properties in a carbonate reservoir. *J. CO2 Utilization* 28, 26–40. doi:10.1016/j.jcou.2018.09.006

Hemmati-Sarapardeh, A., Ayatollahi, S., Ghazanfari, M.-H., and Masihi, M. (2014). Experimental Determination of Interfacial Tension and Miscibility of the CO2-Crude Oil System; Temperature, Pressure, and Composition Effects. *J. Chem. Eng. Data* 59 (1), 61–69. doi:10.1021/je400811h

Jamiu, M. (2013). Ekundayo. Minimum Miscibility Pressure Measurement with Slim Tube Apparatues-How Unique is the Value? [J]. *SPE*, 165966.

Jia, B., Tsau, J.-S., and Barati, R. (2019). A review of the current progress of CO2 injection EOR and carbon storage in shale oil reservoirs. *Fuel* 236, 404–427. doi:10.1016/j.fuel.2018.08.103

Jishun, Q. I. N., Haishui, H. A. N., and Xiaolei, L. I. U. (2015). Application and enlightenment of carbon dioxide flooding in the United States of America[J]. *Pet. Exploration Dev.* 42 (2), 232–240.

Karkevandi-Talkhooncheh, A., Hajirezaie, S., Hemmati-Sarapardeh, A., Husein, M. M., Karan, K., and Sharifi, M. (2017). Application of adaptive neuro fuzzy interface system optimized with evolutionary algorithms for modeling CO 2 -crude oil minimum miscibility pressure. *Fuel* 205, 34–45. doi:10.1016/j.fuel.2017.05.026

Karkevandi-Talkhooncheh, A., Rostami, A., Hemmati-Sarapardeh, A., Ahmadi, M., Husein, M. M., and Dabir, B. (2018). Modeling minimum miscibility pressure during pure and impure CO2 flooding using hybrid of radial basis function neural network and evolutionary techniques. *Fuel* 220, 270–282. doi:10.1016/j.fuel.2018.01.101

Liu, Y., Jiang, L., and Tang, L. (2015). Minimum miscibility pressure estimation for a CO_2/n-decane system in porous media by X-ray CT[J]. *Experiments in Fluids* 56 (7), 1–9. doi:10.1007/s00348-015-2025-4

Liu, Y., Jiang, L., Song, Y., Zhao, Y., Zhang, Y., and Wang, D. (2016). Estimation of minimum miscibility pressure (MMP) of CO2 and liquid n-alkane systems

using an improved MRI technique. *Magn. Reson. Imaging* 34 (2), 97–104. doi:10.1016/j.mri.2015.10.035

Moeini, F., Hemmati-Sarapardeh, A., Ghazanfari, M.-H., Masihi, M., and Ayatollahi, S. (2014). Toward mechanistic understanding of heavy crude oil/brine interfacial tension: The roles of salinity, temperature and pressure. *Fluid phase equilibria* 375, 191–200. doi:10.1016/j.fluid.2014.04.017

Mogensen, K. (2016). A novel protocol for estimation of minimum miscibility pressure from slimtube experiments. *J. Pet. Sci. Eng.* 146, 545–551. doi:10.1016/j.petrol.2016.07.013

Novosad, Z., Sibbald, L. R., and Costain, T. G. (1990). Design of miscible solvents for a rich gas drive-comparison of slim tube and rising bubble tests[J]. *J. Can. Pet. Tech.* 29 (01), 54–57. doi:10.2118/90-01-03

Rao, D. N. (1997). A new technique of vanishing interfacial tension for miscibility determination[J]. *Fluid phase equilibria* 139 (1), 311–324. doi:10.1016/s0378-3812(97)00180-5

Ren, M., Sevilla, M., Fuertes, A. B., Mokaya, R., Tour, J. M., and Jalilov, A. S. (2019). Pore Characteristics for Efficient CO2 Storage in Hydrated Carbons. *ACS Appl. Mater. Inter.* 11 (47), 44390–44398. doi:10.1021/acsami.9b17833

Saeedi Dehaghani, A. H., and Soleimani, R. (2020). Prediction of CO 2 -Oil Minimum Miscibility Pressure Using Soft Computing Methods. *Chem. Eng. Technol.* 43 (7), 1361–1371. doi:10.1002/ceat.201900411

Syed, F. I., Neghabhan, S., Zolfaghari, A., and Dahaghi, A. K. (2020). Numerical Validation of Asphaltene Precipitation and Deposition during CO2 miscible flooding. *Pet. Res.* 5 (3), 235–243. doi:10.1016/j.ptlrs.2020.04.002

Yalcin, Erik. Nazan, and Faruk, Ay (2020). Use of petrological and organic geochemical data in determining hydrocarbon generation potential of coals: miocene coals of Malatya Basin (Eastern Anatolia-Turkey). *Int. J. Coal Sci. Technol.* doi:10.1007/s40789-020-00376-3

Yellig, W. F., and Metcalfe, R. S. (1980). Determination and Prediction of CO2 Minimum Miscibility Pressures (includes associated paper 8876). *J. Pet. Tech.* 32 (01), 160–168. doi:10.2118/7477-pa

Zendehboudi, S., Ahmadi, M. A., Bahadori, A., Shafiei, A., and Babadagli, T. (2013). A developed smart technique to predict minimum miscible pressure-eor implications. *Can. J. Chem. Eng.* 91 (7), 1325–1337. doi:10.1002/cjce.21802

Zhang, K., and Gu, Y. (2015). Two different technical criteria for determining the minimum miscibility pressures (MMPs) from the slim-tube and coreflood tests. *Fuel* 161, 146–156. doi:10.1016/j.fuel.2015.08.039

Zhang, N., Yin, M., Wei, M., and Bai, B. (2019). Identification of CO2 sequestration opportunities: CO2 miscible flooding guidelines. *Fuel* 241, 459–467. doi:10.1016/j.fuel.2018.12.072

Zhao, X., Zhou, L., Pu, X., Jin, F., Shi, Z., Han, W., et al. (2020). Formation conditions and enrichment model of retained petroleum in lacustrine shale: A case study of the Paleogene in Huanghua depression, Bohai Bay Basin, China. *Pet. Exploration Dev.* 47 (5), 916–930. doi:10.1016/s1876-3804(20)60106-9

Zolghadr, A., Riazi, M., Escrochi, M., and Ayatollahi, S. (2013). Investigating the Effects of Temperature, Pressure, and Paraffin Groups on the N2 Miscibility in Hydrocarbon Liquids using the Interfacial Tension Measurement Method. *Ind. Eng. Chem. Res.* 52 (29), 9851–9857. doi:10.1021/ie401283q

Conflict of Interest: XG was employed by the China United Coalbed Methane Co., Ltd. CL was employed by CNOOC Safety Technology Service Co., Ltd. Shanghai Branch.

The remaining authors declare that the research was conducted in the absence of any commercial or financial relationships that could be construed as a potential conflict of interest.

Publisher's Note: All claims expressed in this article are solely those of the authors and do not necessarily represent those of their affiliated organizations, or those of the publisher, the editors and the reviewers. Any product that may be evaluated in this article, or claim that may be made by its manufacturer, is not guaranteed or endorsed by the publisher.

frontiers in Earth Science

ORIGINAL RESEARCH
published: 20 September 2021
doi: 10.3389/feart.2021.746071

Comparison of Nanomaterials for Enhanced Oil Recovery in Tight Sandstone Reservoir

Chenjun Zhang[1], Xu Jin[1], Jiaping Tao[1,2], Bo Xiong[1]*, Zhijian Pan[1], Siwei Meng[1], Bin Ding[1], Ying Wang[1] and Lihao Liang[2]*

[1]Research Institute of Petroleum Exploration & Development, PetroChina, Beijing, China, [2]School of Petroleum Engineering, China University of Petroleum (East China), Qingdao, China

With dwindling conventional oil resources, the development of high-performance oil-displacing agents to exploit unconventional oil and gas resources has become a research focus, and new technical ideas have been proposed for petroleum engineering with the advancement of nanomaterials and technology. This study characterized the microscopic pore throat structure of the unconventional tight sandstone reservoir of Ordos Basin in China comprehensively by using high-resolution scanning electron microscopy, image panoramic mosaic technology, mineral quantitative scanning system, and 3D image of pore. A new nanofluid with diphenyl ether surfactants as shell and C_{10}–C_{14} straight-chain hydrocarbon compounds as kernel was prepared according to the features of tight sandstone reservoirs. The basic physical properties of the nanofluid were evaluated and compared with those of three other generic oil-displacing agents to understand the oil-displacement effect and mechanism. Results show that this nanofluid remains relatively stable and dispersible with aging and its average particle size matches well with the pore throat size of the target reservoir, which increases the sweep volume effectively. Additionally, the change from oil-wet to water-wet can exert capillary imbibition. And the oil-water interfacial tension can be greatly reduced to the level of 10^{-2} mN/m because of nanofluid's excellent interfacial activity, which improves the efficiency of oil washing in nano-scale pore throats. Finally, the core imbibition experiment further demonstrated the superiority of the nanofluid. Using the nanofluid in optimal concentration with cores of approximately 0.1 mD can achieve a recovery rate of 37.5%, which is higher than generic oil-displacing agents by up to 9%. This study demonstrates that the excellent performance of nanofluid in enhancing oil recovery and provides a reference for the development of unconventional reservoirs, which are difficult to function with generic agents.

Keywords: unconventional reservoir, tight sandstone, oil-displacing agent, nanofluid, enhanced oil recovery

OPEN ACCESS

Edited by:
Jizhou Tang,
Tongji University, China

Reviewed by:
Lihua Zuo,
Texas A&M University Kingsville, United States
Hua Zhang,
Buckman Laboratories, United States

****Correspondence:***
Xu Jin
jinxu@petrochina.com.cn
Bo Xiong
xiongb69@petrochina.com.cn

Specialty section:
This article was submitted to Economic Geology, a section of the journal Frontiers in Earth Science

Received: *23 July 2021*
Accepted: *24 August 2021*
Published: *20 September 2021*

Citation:
Zhang C, Jin X, Tao J, Xiong B, Pan Z, Meng S, Ding B, Wang Y and Liang L (2021) Comparison of Nanomaterials for Enhanced Oil Recovery in Tight Sandstone Reservoir. Front. Earth Sci. 9:746071. doi: 10.3389/feart.2021.746071

INTRODUCTION

As non-renewable resources, oil and gas have limited underground reserves. Due to constraints in geological conditions and development technology, most crude oil still remains underground. Various technologies for enhanced oil recovery (EOR) have gradually become important technologies for oil and gas field development. Unconventional tight oil and gas resources have

become the main oil and gas resources for increasing reserves and production nowadays and have currently been the research hotspot in EOR and economic development. The recoverable resources of unconventional oil and gas are mainly distributed in the four major regions of North America, Asia-Pacific, Latin America, and Russia (Zou et al., 2015). The median porosity of tight sandstone reservoirs in China ranges from 3.2 to 9.1%, with an average of 1.5–9.04%, and a median permeability of 0.03 to 0.455 mD, with an average of 0.01 to 1.0 mD (Zou et al., 2012). Aside from their thin pore throat structure, vast heterogeneity, strong capillary force, and non-Darcy flow, tight sandstone reservoirs have tremendously different characteristics, including oil and gas occurrence law and fluid flow mechanism, when compared with conventional oil reservoirs. Therefore, tight sandstone reservoirs are faced with the problems of rapid increase in water content, rapid decline in production, and generally low recovery factors. Generic chemical agents are difficult to sweep effectively. Thus, the development of key materials for EOR and technological innovation warrants investigation.

Various EOR methods can be considered in the initial stage to fit in unconventional reservoir conditions. Chemical flooding is an important branch of enhanced oil recovery, and its technology development has been relatively mature. Injecting chemical agents into the formation improves not only the flow characteristics of the fluid in the microscopic pores of the formation but also the interface characteristics among the oil-displacing agents, the rock surface, and the crude oil to achieve EOR. However, applying those techniques in unconventional oil reservoirs is challenging because of the different flooding theories and exploitation technologies between conventional and unconventional oil reservoirs. Among chemical flooding methods, polymers feature poor salt tolerance or high temperature resistance in oil reservoirs, high material consumption, and serious chemical loss, and they cannot drive the residual oil in small pores; alkaline flooding affects the demulsification of crude oil, causing serious scaling and formation damage; meanwhile, surfactants easily adhere to the rock surface, which increases the amount of oil-displacing agents and the cost; the application of chemical compound flooding is also limited because of the lack of high-temperature-resistance and corrosion-resistance polymers and surfactants (Jay et al., 1999; Chang et al., 2006; Muggeridge et al., 2014). Therefore, innovative research on the modification and development of oil-displacing agents is necessary in response to the above-mentioned problems.

With the further integration of nanotechnology and petroleum engineering, the application of nanomaterials in oilfield EOR has become a research focus of scientists worldwide (Fletcher and Davis, 2010; Shamsijazeyi et al., 2014; Liu et al., 2018; Zhang F. et al., 2020; Zhang L. et al., 2020; Ledyastuti and Jason, 2020; Al-Anssari et al., 2021; Keykhosravi et al., 2021). Nanomaterials are ultrafine materials with at least one dimension in the range of 1–100 nm in the 3D space (Das et al., 2008). Owing to the small particle size and large specific surface area of nanomaterials, the number of surface-active atoms, surface free energy, and interfacial tension of nanoparticles (NPs) increases sharply as the particle size decreases. Compared with generic chemical agents, nanomaterials agents have certain advantages in the aspects of rheology, wettability, surface effects, particle migration, and so on (Liu et al., 2016). The pore diameter of tight sandstone reservoirs is generally in micrometers, and nanomaterials can pass through the pores easily. Nanomaterial agents form a constitutionally stable interfacial film between the continuous phase and the dispersed phase; thus, they have strong adsorption capacity at the interface and require high energy to separate from the interface. Compared with common surfactant emulsions, nanomaterials have good stability. Therefore, in view of the development problems of tight sandstone reservoirs, the use of nano-scale chemical agents for flooding has become a new method for EOR and provides a new idea for the development of improving oil recovery.

In the past decade of research, scientists have developed many nanomaterials for oil displacement. Silica nanoparticles (SNPs) are commonly used among all nanomaterials because of their excellent dynamic and rheological properties, and many studies have shown that SNPs exert a good effect on EOR (Ju et al., 2006; Ju and Fan, 2009; Sadeghpour et al., 2013; Zhang et al., 2014). Ragab produced nanosilica of different sizes from the white sand and considered that 78 nm nanosilica particles coated with xanthan gum polymer could achieve the highest ultimate recovery factor of 80% (Ragab and Hannora, 2015). The stability of CO_2 foam stabilized by silica and nanoclay NPs was studied and its oil recovery was investigated by performing modified bulk foam tests and flow experiments (Guo and Aryana, 2016). Dai prepared new self-dispersing SNPs, tested them by spontaneous imbibition experiment of low-permeability cores (Dai et al., 2017), and then explained the potential EOR mechanism of silica nanofluids from the aspects of interfacial tension, contact angle, structural disjoining pressure mechanism (Wasan et al., 2011; Zhang et al., 2016, 2018), and so on. Although the interfacial tension and contact angle decrease with the increase in nanofluid concentration, Hendraningrat also found that high concentrations (e.g., 0.1 wt % or more) of SNPs block the pore network and will not give additional oil recovery in low-permeability reservoirs (Hendraningrat, 2013; Hendraningrat and Torsater, 2014). Therefore, optimizing the nanofluid concentration can maximize the recovery factor. As for the potential agents based on metal nanomaterials, such as zirconium dioxide (ZrO_2), titanium dioxide (TiO_2), aluminum oxide (Al_2O_3), iron oxide (Fe_3O_4), and cerium oxide (CeO_2), their mechanism is mainly to increase the viscosity of the agents and reduce the interfacial tension between oil and water. Giraldo used alumina-based nanofluid as a wettability modifier in sandstone cores (Giraldo et al., 2013); Hamide Ehtesabi investigated the behavior of low-concentration TiO_2 NPs in core plug porous media and its transport and retention in the oilfield reservoir through studying the diffusion, adsorption, and deposition of NPs in different parts of the core plug (Ehtesabi et al., 2014, 2015).

Despite all reported studies, many studies have focused on conventional oil reservoirs. There are very few experiments

TABLE 1 | Physical parameters of cores.

Core number	Length, cm	Diameter, cm	Permeability, md	Porosity, %	Pore volume, cm^3
A	5.993	2.528	0.102	5.894	1.774
B	5.662	2.527	0.107	7.162	2.019
C	5.499	2.498	0.078	8.437	2.274
D	5.853	2.524	0.117	8.446	2.474
E	5.477	2.529	0.116	9.222	2.536
F	5.837	2.525	0.033	5.662	1.655
G	4.752	2.533	0.087	7.161	1.715
H	5.276	2.529	0.109	9.325	2.471
I	6.627	2.535	0.174	8.639	2.890
J	6.449	2.514	0.768	9.769	3.126
a	4.863	2.528	0.647	10.350	2.526
b	4.829	2.524	0.662	9.240	2.232
c	4.939	2.525	0.678	10.070	2.492
d	4.805	2.519	0.630	9.090	2.177
e	4.905	2.519	0.654	9.060	2.215
f	4.932	2.533	0.662	12.900	3.208
g	4.821	2.531	0.015	7.370	1.787
h	4.941	2.540	0.012	6.230	1.559
i	4.919	2.528	0.014	7.090	1.750

comparing the oil displacement effects of different types of micro-nano materials in unconventional tight sandstone reservoirs on the basis of the geological background and reservoir structure has yet to be conducted (Nassar et al., 2014; Nazari Moghaddam et al., 2015). In addition, relevant experimental data about continental sandstone reservoirs in China are lacking. Therefore, selecting suitable oil-displacing agents for tight sandstone reservoirs with the complex micro-nano pore throat structure and studying its displacement mechanism are challenging and meaningful.

Nanoparticles have been the subject of the majority of published studies, and their solid form may cause particle aggregation. However, this study focuses on nanofluids, contrasts several micro-nano oil displacement materials, and analyzes their characteristics theoretically. It also summarizes the physical properties and oil displacement behavior in porous media, evaluates the oil displacement effect from multiple factors, and reveals the oil displacement mechanism. This study provides theoretical and experimental basis for the application of nanofluids in unconventional oil reservoirs to enhance oil recovery.

MATERIALS AND METHODS

Materials

Core Samples

The core samples (A–J) used in this study are tight sandstone taken from Yanchang Formation, Ordos Basin, China with characteristics of low porosity, low permeability, and poor cementation. These samples were used for rock characterization experiments, such as electron microscope observation and imbibition experiments. In addition, some man-made tight cores (a–i) composed of quartz sand were used in some experiments to avoid reservoir heterogeneity and stratigraphic interference, and their parameters are shown in **Table 1**.

TABLE 2 | Composition of formation brine.

Ion	Na^+/K^+	Ca^{2+}	Mg^{2+}	Cl^-	SO_4^{2-}	HCO_3^-
Concentration, mg/L	9,283	3,296	468	17,462	251	73

Simulated Oil and Water

Simulated oil used in the experiment is crude oil taken from the oil field with a viscosity of 3.89 mPa·s at 70°C and a density of 0.826 g/cm^3. The salinity of the simulated brine used to stimulate formation water in the experiment is 30, 800 mg/L, and its ion content is shown in **Table 2**.

Oil-Displacing Agents

A new nanofluid with diphenyl ether surfactants as shell and C_{10}–C_{14} straight-chain hydrocarbon compounds as kernel was prepared, and the concentration of the original solution used in following experiments is 35%. Three other oil-displacing agents, betaine, cationic surfactant (cetyl trimethyl ammonium chloride), and anionic surfactant (petroleum sulfonate) with good effect and certain representativeness in previous experiments, were selected for the comparative experiments, and they are all available on the market.

Synthesis of Nanofluid: The diphenyl ether surfactants, C_{10}–C_{14} straight-chain hydrocarbon compounds, and remaining water were mixed at an optimal proportion and stirred under low energy conditions (30–400 r/min, 20–50°C) until the mixture was completely dissolved to become a homogeneous solution. The homogeneous solution was diluted to low concentration with deionized water or inorganic salt water to prepare the nanofluid permeation flooding system with a shell–kernel structure.

Reservoir Characteristics Test

The tight sandstone reservoir of the Yanchang Formation in the Ordos Basin, China, was selected as the research site, and scanning electron microscopy (SEM) was used to observe the microscopic pore throat structure in the study area. The experimental operations are as follows: *1*) High-resolution SEM and double beams of field-emission SEM with image panoramic mosaic technology (MAPS) were used to observe the surface of rock samples and the abundance and form of pores and fractures. In the experiment, the accelerating voltage was 10 kV, and the beam current was 40 nA, which can effectively identify the micro-nano pores in the reservoir. The scanning area of MPS was 2.48 mm × 2.15 mm, and the resolution was 2048 × 1768. It is composed of 1369 (37 × 37) pictures. *2*) The rock samples observed using scanning electron microscope mineral quantitative evaluation system (QEMSCAN) were consistent with the samples of MAPS, and QEMSCAN provided the mineral content of the study area. *3*) For focused ion beam scanning electron microscopy (FIB-SEM), the surface was marked with the ion gun and plate platinum to protect the target area first; then, three sides of the target area were carved to form an observation pit with a depth of 10–20 μm and a width of about two times the width of the target area; finally, automatic denudation imaging was started after repeated corrections (Sun et al., 2016). 3D images of the pore structure were obtained using FIB-SEM to analyze the pore distribution and distinguish different pore types in the sandstone samples. A precise characterization of the microscopic properties of the reservoir can be achieved by using these techniques, and pore volume and pore connectivity were evaluated to determine crude oil flow eventually. The apparatus used included Helios 650 and FEI Quanta 650 from Thermo Fisher Scientific, United States.

Measurement of Physical Properties of Agents

Interfacial Tension Tests

The spinning drop method (Cayias et al., 1975) was used to determine the interfacial tension between crude oil and different oil-displacing agent solutions. The experiment was operated as follows: *1*) Four oil-displacing agent samples were prepared at five gradient concentrations of oil-displacing agent solutions and injected into the sample tube of the interfacial tension meter. *2*) A small amount of crude oil was injected into the sample cell under the condition that no air bubble exists. *3*) The sample cell was placed into a spin-dropping device at 70°C, the instrument speed (6000 rpm) was adjusted to make the oil drop rotate, and the diameter of the oil drop was elongated under the action of centrifugal force and interfacial tension. *4*) The diameter of the oil droplets was measured by video image analysis to obtain the interfacial tension. The apparatus used is a rotating droplet interfacial tensiometer produced by DataPhysics Instruments GmbH, German.

Wettability Alteration Test

Wettability is an important property of solid surfaces, which is usually characterized by contact angle. The experimental operations are as follows:

1) After heating and drying the core extracted with dichloromethane, the core was cut into 3–4 mm-thick uniform thin sections, and the thin sections were saturated by simulated formation water for later use. *2*) The treated thin sections were placed into crude oil for aging at 70°C for 7 days, and oil-displacing agents of different concentrations were prepared at the same time. Then, the sections were placed into the agents and reacted at 70°C for 7 days. *3*) The core sections fixed with water droplets were placed in a quartz ark containing different oil-displacing agents, and the contact angle was measured before and after treatment by using the optical contact angle measuring instrument DSA100 from Krüss, Germany.

Particle Size Measurement

The oil-displacing agents were prepared into solutions with various concentrations and aged at formation temperature. The oil-displacing agents in different aging time were placed in an ultrasonic device for 10 min to make the particles dispersed and then placed into a size analyzer to test the particle size. The apparatus used was Zeta PALS, a zeta potential and NP size analyzer developed by Malvern, United Kingdom.

Spontaneous Imbibition Experiment

Man-made cores were selected for the imbibition experiments to avoid the negative influence of differences in the mineral composition and anisotropy of field cores on the results. The permeability of the man-made cores had two ranges of about 0.1 mD and about 1 mD. The steps of the experiment are as follows: *1*) After measuring the core porosity and permeability parameters required for the experiment, the core (without initial water) was evacuated for 4 h to remove air and saturate the oil. *2*) After aging the saturated-oil cores, we weighted the cores and measured their NMR T_2 spectrum. *3*) The oil-saturated core was immersed in liquid filled with oil-displacing agents in 70°C (**Figure 1**). The volume of oil removed from the core was monitored over time, with frequent recordings at the initial stage and once every 24 h afterward. The NMR T_2 spectrum was measured again after the imbibition. In addition, a certain concentration of $MnCl_2$ must be added to the water used in the experiment to shield the hydrogen signal in the water and make the NMR results more accurate.

RESULTS

Characteristics of Reservoir Rock

Mineral Composition

QEMSCAN test results indicate that the minerals with the highest content are quartz, albite, illite, and K-feldspar, which are also the main constituent minerals of tight sandstone reservoirs, and their average mineral proportions can reach 50.86, 13.59, and 7.34, and 5.33%, respectively; the contents of mica, calcite, dolomite, and kaolinite followed closely, and their average proportions are distributed between 1 and 4% (**Figure 2**). Illite with a high content is a weakly

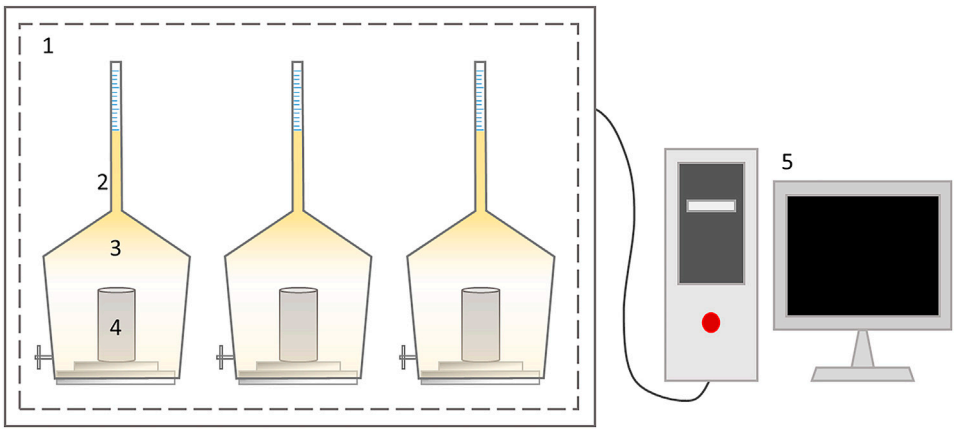

FIGURE 1 | Schematic of the imbibition assembly: (1) temperature control system, (2) imbibition apparatus, (3) oil-displacing agent, (4) core, (5) data entry system.

expansive clay mineral, and its crystal layer is not easy to separate even in the presence of water molecules, thus preventing the throat plugging. Kaolinite is also a relatively stable non-expansive mineral, which has weak adhesion to sandstone particles and is prone to particle migration. Thus, the flow rate of the injected fluid should be controlled. In general, the type, content, and form of minerals affect pore abundance and EOR implementation to some degree.

Pore Throat Structure

Pore throat structure is relevant to mineralogy, which can be partially explained by the crystalline structure of minerals, as well as practical reservoir conditions like humidity, temperature, and applied stresses (Zhang F. et al., 2020). In addition to clastic particles, organic matter, impurities, and cements, the rock composition of tight sandstone reservoirs also includes many types of pores. SEM observation shows that the reservoir pores in the studied area are underdeveloped with low porosity and the reservoir space can be divided into primary and secondary pores according to genesis. Primary pores include intergranular and intercrystalline pores; secondary pores include intergranular dissolved pores, intragranular dissolved pores, and a few micro-fractures. *1*) Intergranular pores: mainly composed of residual intergranular pores, which have regular shape and smooth boundary with a relatively regular shape in triangle or polygon. The average diameters of the pores and throats are 10–50 μm (**Figures 3A,E**). *2*) Intercrystalline pores: micropores mainly exist in authigenic clay minerals, such as kaolinite, chlorite, and illite. The small pores are mainly micro-nano-scale with certain connectivity, and their average diameters are generally 0.1–3 μm (**Figures 3C,D,F,I**). *3*) Intergranular dissolved pores: caused by the erosion of the edges of debris particles and cements, with irregular shapes and a wide range of pore size distribution. When the dissolution is strong, these pores often communicate with other pores to form super-large composite pores with diameters ranging from 1 to 30 μm (**Figure 3B**). *4*) Intragranular dissolved pores: mainly include feldspar dissolved pores and lithic dissolved pores. Feldspar dissolved pores generally develop along joints, and lithic dissolved pores have honeycomb structure, with relatively isolated distribution and poor connectivity. The average pore size distribution is 0.5–3 μm (**Figure 3G**). *5*) Micro-fractures: the pores are mainly connected by micro-fractures, such as cracks, joints, and natural deflects abounded in rock material, and closely connected to the rupture, failure, and loss of stability (Li et al., 2017). Its width is generally a few nanometers to tens of nanometers (**Figure 3H**).

SEM and FIB-SEM results show that the pores in the micro-nano porous reservoirs are generally small, and the pore diameter is basically below 30 μm, dominated by 50 nm–10 μm nanometer-micrometer pores. Intergranular dissolved pores, intragranular dissolved pores, and micro-fractures are relatively well developed, and the pores are comparatively isolated, unevenly distributed, and poorly connected. FIB shows the 3D perspective of pore throat structure more directly (**Figure 4**). The characteristics of tight reservoir rocks have resulted in complex oil and gas occurrence and migration mechanisms. The research of microscopic pore throat structure, pore throat types, and mineral composition from the side confirm that injecting a suitable oil-displacing flooding system is necessary and pave the way for the subsequent work of the microscopic oil displacement mechanism in tight sandstone reservoir.

Properties of Oil-Displacing Agents

Dispersed Stability

The particle size distribution range of all the tested oil-displacing agents is at the micro-nano level according to the size measurement. A higher concentration of the agent intensifies Brownian motion of the droplets, which rise the collision probability and slightly increase the initial particle size. As shown in **Figure 5**, the initial average particle diameters of the nanofluid with the concentrations of 0.1, 0.5 and 0.9 wt% are respectively 15.7, 17.8 and 25.0 nm. The microemulsion state of the system with a concentration of 0.1 and 0.5 wt% remains

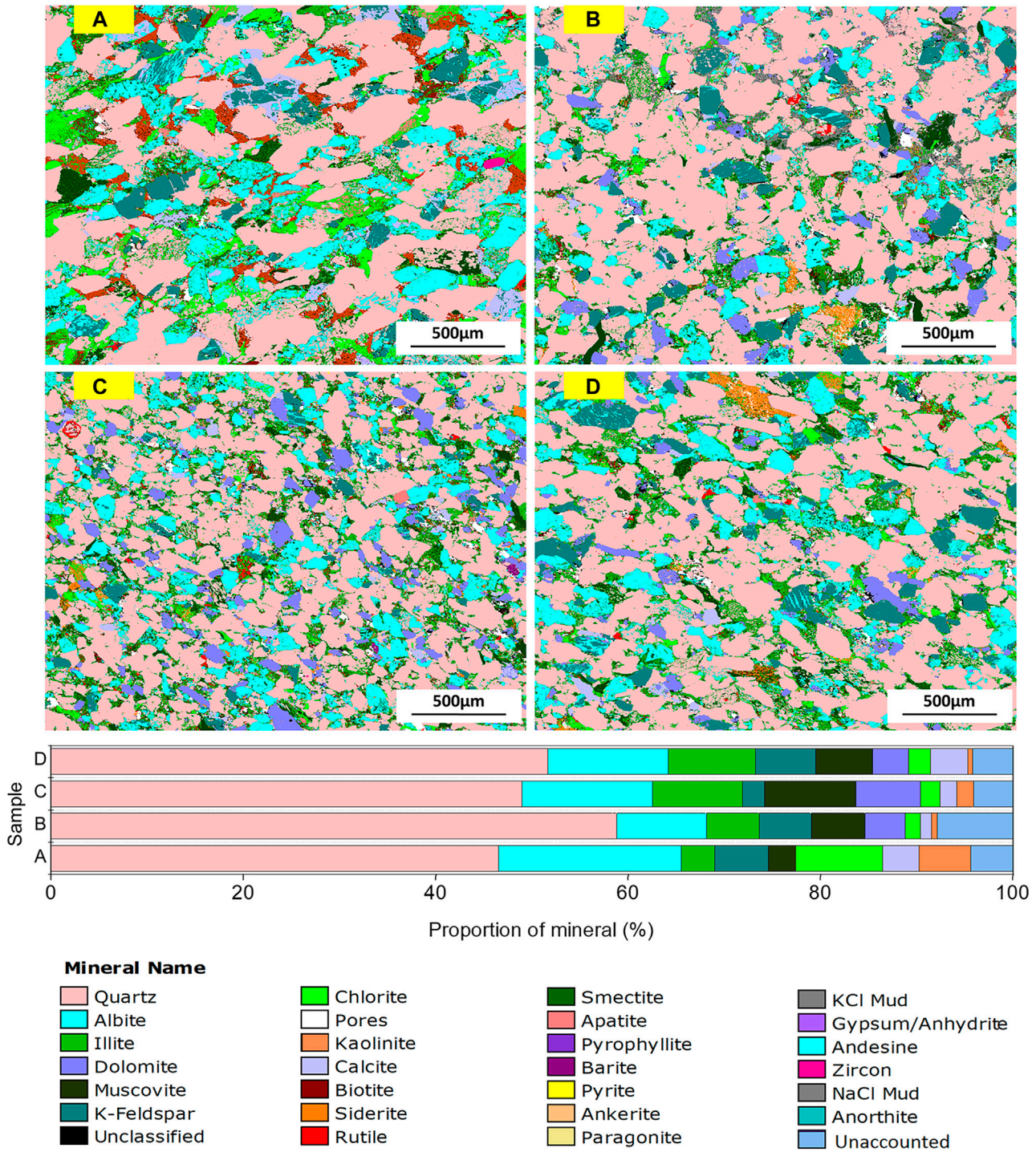

FIGURE 2 | Mineral composition of core sample A, B, C and D tested by QEMSCAN.

stable over time, with the average particle size maintain at 20 nm or so; in a system with a concentration of 0.9 wt%, the particle size increases over time until it reaches equilibrium, and finally stabilizes at about 60 nm. These results indicate that the nanofluid has the greatest advantage over size, and it matches with the small throats very well. The particle of the nanofluid in microemulsion state is relatively stable and dispersible with aging, unaffected by temperature and salinity, which means it can fully adapt to the reservoir conditions.

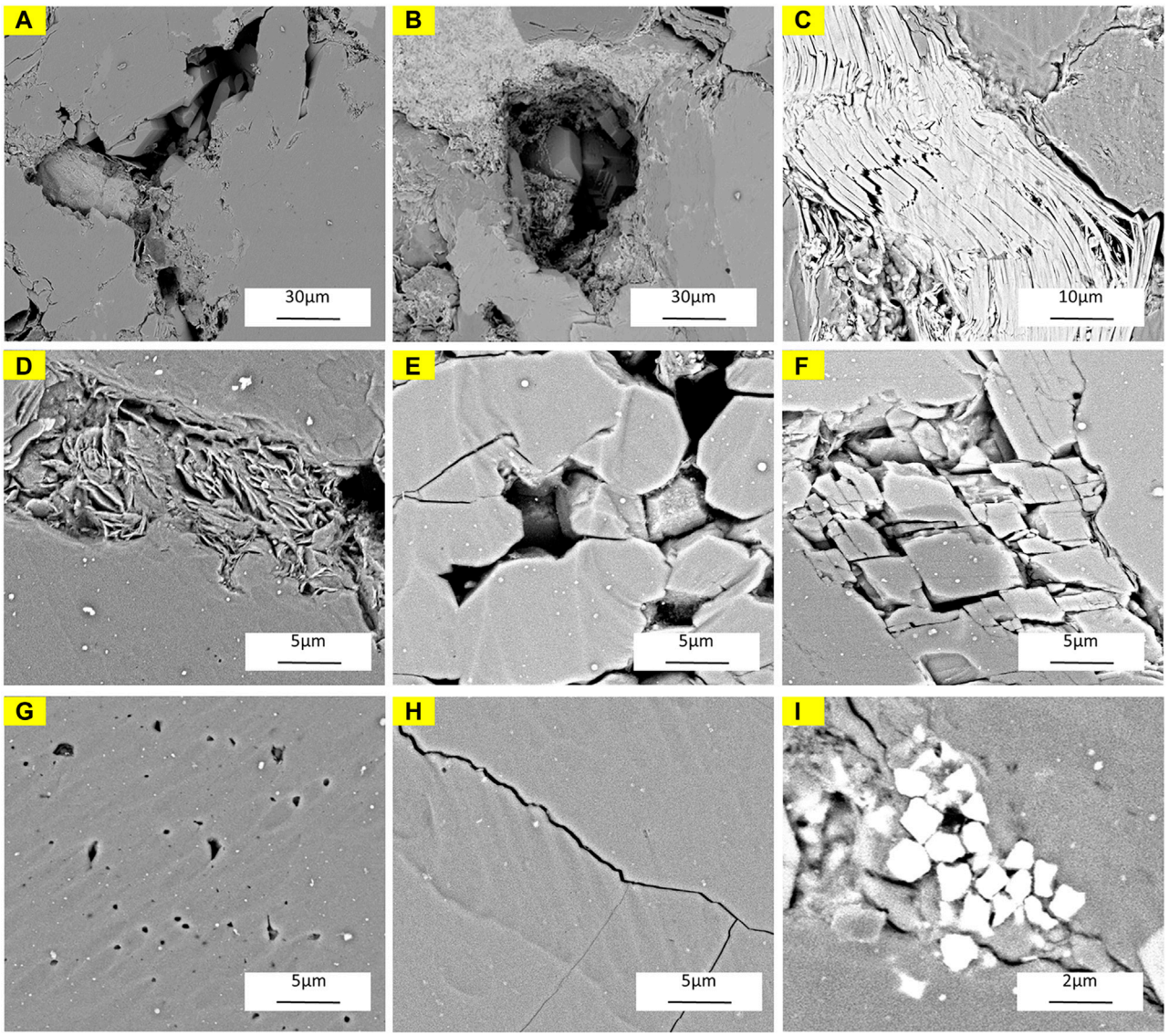

FIGURE 3 | Typical SEM photos of pore throat structures: **(A)** Intergranular pores; **(B)** Intergranular dissolved pores; **(C)** Intercrystalline pores (Inter-mica pores); **(D)** Intercrystalline pores (Inter-illite pores), **(E)** Intergranular pores (Inter-quartz-feldspathic pores); **(F)** Intercrystalline pores (Inter-calcite pores); **(G)** Intragranular dissolved pores; **(H)** Micro-fractures; **(I)** Intercrystalline pores (Inter-pyrite pores).

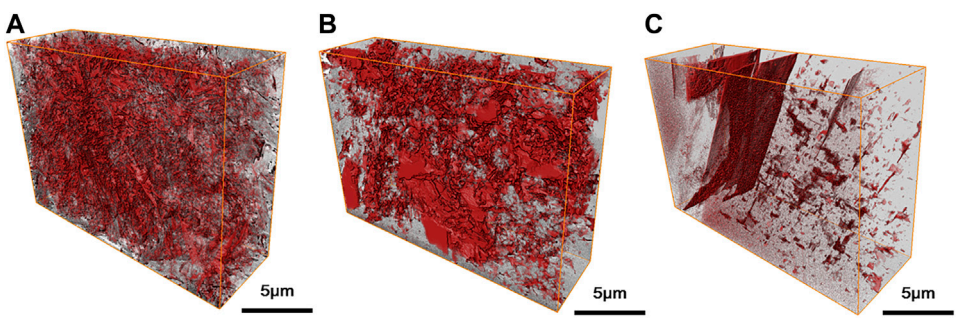

FIGURE 4 | 3D pore throat structure of core sample A, B and C (FIB-SEM).

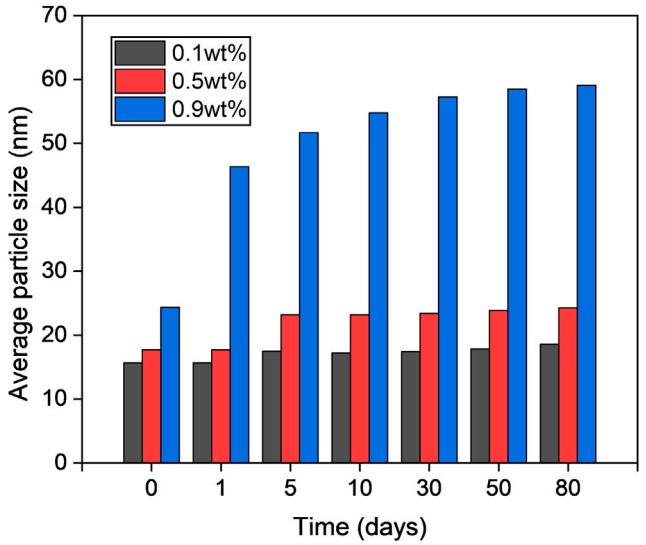

FIGURE 5 | Particle size distribution of the nanofluid at the test temperature of 70°C.

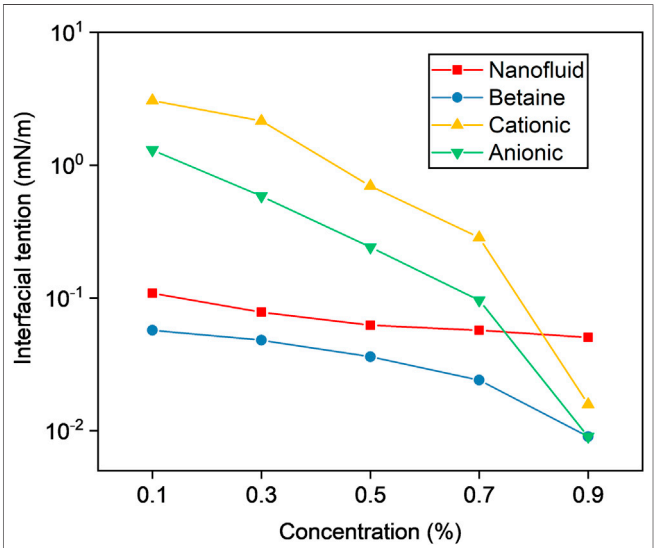

FIGURE 6 | Interfacial tension of four oil-displacing agents with different concentration.

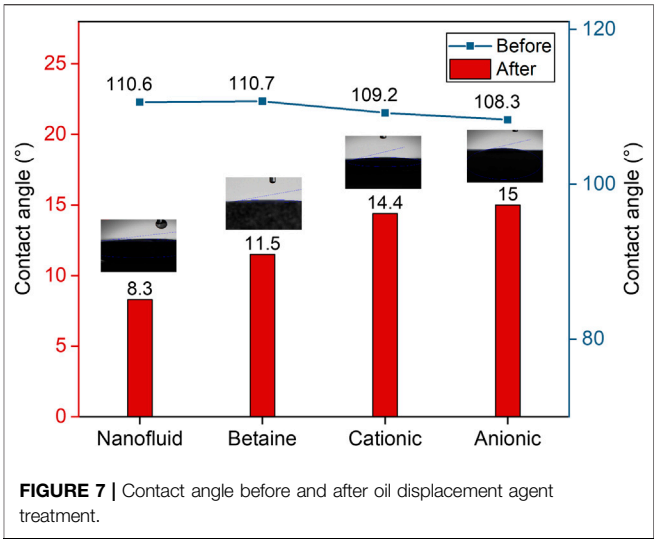

FIGURE 7 | Contact angle before and after oil displacement agent treatment.

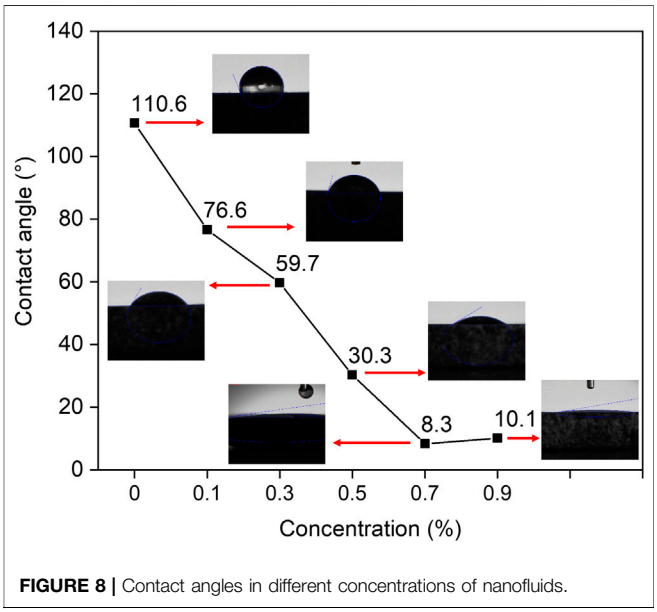

FIGURE 8 | Contact angles in different concentrations of nanofluids.

Interfacial Tension

The interfacial tension test results of the four oil-displacing agents at five concentrations show that the interfacial tension of each oil-displacing agent gradually decreases as the concentration is increased (**Figure 6**). The cationic surfactant gradually decreases from 3.080 to 0.016 mN/m, and the anionic surfactant gradually decreases from 1.30 to 0.009 mN/m. The low interfacial tension of the cationic surfactant and anionic surfactant could only be maintained at a very high concentration; the line tendency of nanofluid and betaine is flatter and more gently changing, and its values are much lower than those of the anionic and cationic surfactants, which range within 1×10^{-2}–1×10^{-1} mN/m. After the interfacial tension is in the order of 1×10^{-2} mN/m, the effect of increasing the concentration to reduce the interfacial tension is not obvious.

The decreasing tendency of interfacial tension is not evident in **Figure 6** when the concentration is high (0.7 wt%, 0.9 wt%). Nevertheless, underground oil-displacing agents are diluted to an extremely low concentration in the practical flooding process, and the high concentration also represent high costs, so ignore the negative effects in high concentrations and control the concentration accurately in a low value.

Wettability Alteration

Considering the interfacial tension, the nanofluid, betaine, cation surfactant, and anion surfactant have the optimal concentration

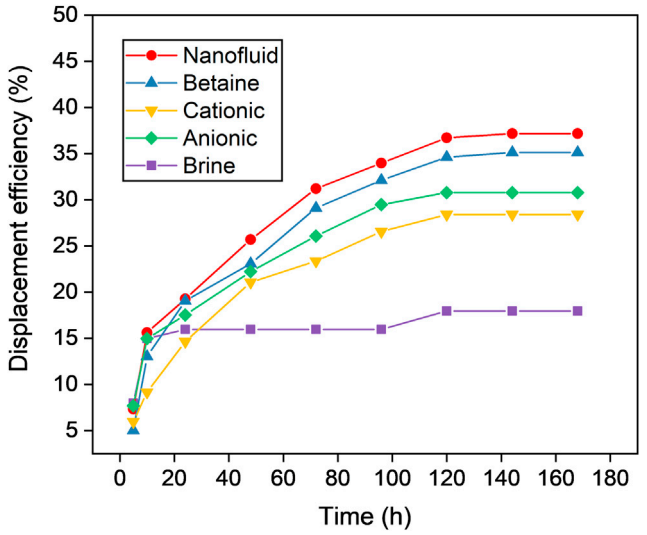

FIGURE 9 | Displacement efficiency of different oil displacement agents (1 mD).

values for wettability modification of 0.5, 0.1, 0.9, and 0.7 wt%, respectively. The contact angles of the rock thin sections before and after treatment by the oil-displacing agents and the optimum concentration determined by the interfacial tension of different oil-displacing agents were measured. **Figure 7** shows that betaine decreases from the initial 110.7° to 11.5°, cationic surfactant decreases from the initial 109.2° to 14.4°, and the anionic surfactant decreases from the initial 108.3° to 15.0°. As shown in **Figure 8**, the nanofluid's contact angle of the two phases before treatment is 110.6°, and the contact angle gradually decreases as the concentration is increased, which reaches a minimum of 8.3° at 0.7 wt%. Then, the contact angle increases slightly as the concentration is increased. Although different oil-displacing agents change the wettability to different degrees, the wettability of the rock interface is reversed from lipophilic to strong-hydrophilic after treatment with these four oil-displacing agents.

Oil-displacement Capacity

Spontaneous Imbibtion

All core samples are subject to the spontaneous imbibition test. In different imbibition devices, cores were immersed in different liquid phases. Compared with the contact angle measurement experiment in which only one water droplet is in contact with the outer surface of the core sample, the self-absorption test involves a large amount of water entering the interconnected porous space of the rock and contacting the inner surface of the rock.

The cores used in this experiment are *sample a*, *sample b*, *sample c*, *sample d*, *sample e* and *sample f*, undergoing imbibition using nanofluid, betaine, cationic surfactant, anionic surfactant, and brine, respectively. The permeabilities of these cores are distributed below 1 mD (0.64–0.68 mD), as shown in **Table 2**. **Figure 9** displays the curve of the spontaneous imbibition displacement efficiency over time. The figure shows that the replacement rate is very high in the initial stage of imbibition, and the displacement efficiency increases rapidly because the core absorbs water and removes oil under the function of capillary force; as time goes by, the water saturation of the core continues to increase, the capillary action weakens, and the imbibition rate gradually slows down until the curve is flat. Ultimately, the cumulative recovery rate does not change after reaching the maximum value. After the imbibition tests, 37.2, 35.1, 28.4, 34.2, and 18.0% of oil are extracted in cores immersed in nanofluid, betaine, cationic surfactant, anionic surfactant, and brine, respectively.

Lines in **Figure 10** show the measurement results of the cores with permeability about 0.1 mD (*sample g*, *sample h* and *sample i* are used). Only nanofluid and betaine were tested in this experiment because of the poor effects of the cationic and anionic surfactants. The corresponding recovery factors of the nanofluid and betaine systems are 37.5 and 31.3%. Results show that in tight sandstone cores, nanofluid has the best oil displacement effect in the imbibition experiment because of its low interfacial tension and wettability alteration.

NMR T_2 Analysis

The NMR T_2 spectra corresponding to different oil-displacing agents in the same permeability interval are drawn to the same coordinate system to elucidate the mechanism, and the changes in the NMR T_2 spectrum during imbibition are shown in **Figures 11**, **12**, which further visually verify the total displacement efficiency of the imbibition experiment. **Figure 11** shows the crude oil production degree of the 1 mD cores treated by different fluids before and after the imbibition experiment, and **Figure 12** shows the results of 0.1 mD cores. Although the curve shape and the corresponding peak value differ during imbibition, their change trends are the same (Lowden et al., 1998; Y; Volokitin et al., 2001). The analysis suggests that the curve characterizes the oil distribution in different cores because Mn^{2+} shields the hydrogen signal in the water. Therefore, the mechanism of

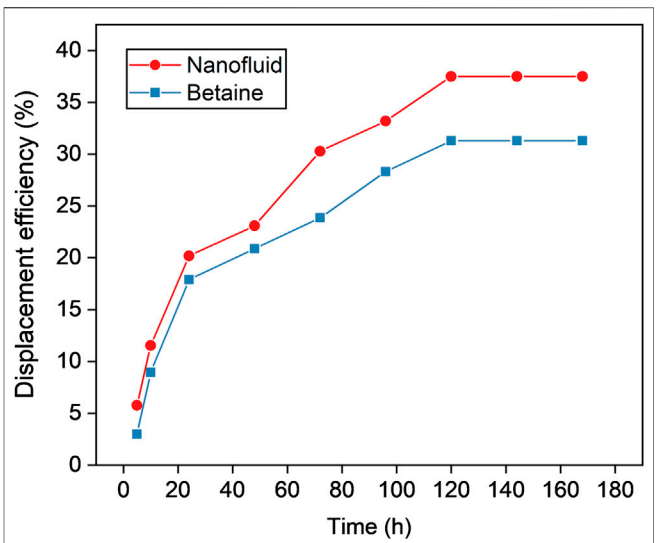

FIGURE 10 | Displacement efficiency of different oil displacement agents (0.1 mD).

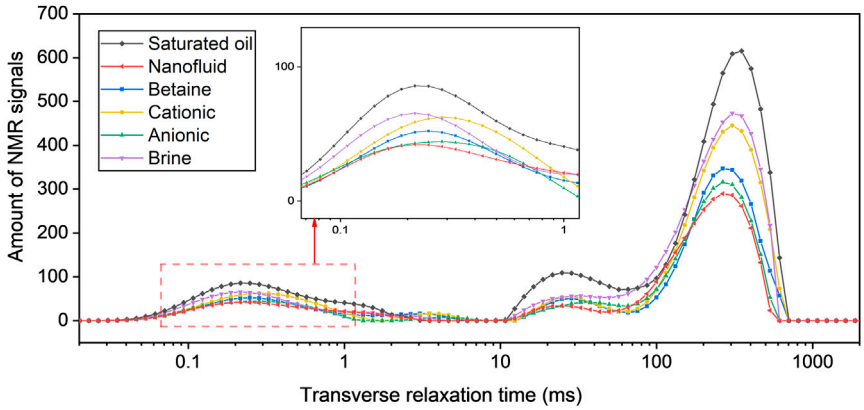

FIGURE 11 | The T_2 curves of the cores before and after imbibition (1 mD).

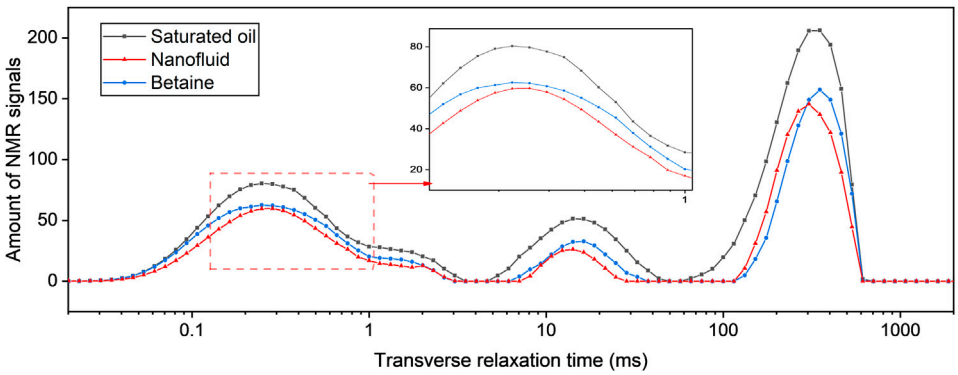

FIGURE 12 | The T_2 curves of the cores before and after imbibition (0.1 mD).

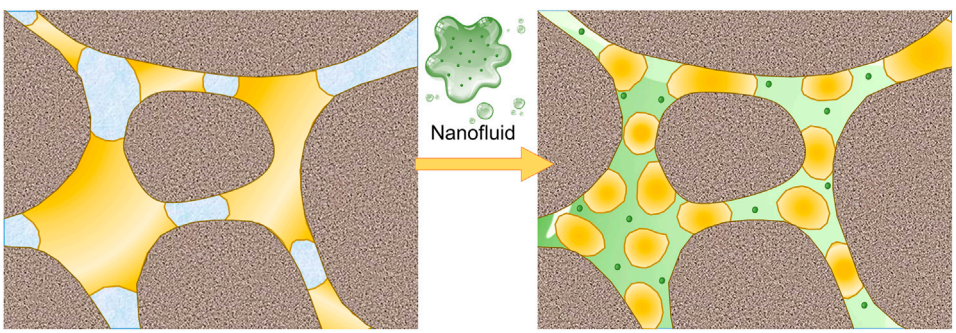

FIGURE 13 | Mechanism of nanofluid's enhancing oil permeation capacity.

imbibition to replace the oil can be understood directly through the changes in the area enclosed by the curve.

The principle is shown in the following formula:

$$\frac{1}{T_2} = \rho_2 \frac{S}{V} = C\frac{1}{r}$$

Where T_2 is the relaxation time indicated by nuclear magnetic resonance, *ms*; ρ_2 is the relaxation rate, *μm/ms*; S/V is the pore comparison area, dimensionless; C is the conversion coefficient, dimensionless, and r is the pore radius, *μm*.

Therefore, the larger the pore radius, the longer the relaxation time. The NMR T_2 spectrum obtained by the experiment shows an obvious multi-peak shape, indicating the presence of small pores (0.1–1 ms), medium pores (10–100 ms), and large pores (100–1000 ms) from left to right. The integral area of each curve in the figure represents the total amount of remaining oil, and

comparing the areas of different sizes pores can directly indicate their contribution to the oil recovery factor of the imbibition test. During the imbibition of the nanofluid acting on the core of 0.1 mD (**Figure 12**), the total recovery degree is 37.5%, which includes 36.95% of the large pores' absolute recovery, 62.91% of the medium pores' absolute recovery, and 32.47% of the small pores' absolute recovery. The recovery ratio of remaining oil in the medium and small pores is quite considerable, accounting for a certain proportion of the overall recovery rate.

DISCUSSION

Studies (Zhu et al., 2013) have shown that micro-nano pore space is an important storage space for unconventional oil and gas, and its pore structure is an important factor affecting the physical properties of the reservoir. Precise characterization of the micro-nano pore structure has become an important content of unconventional reservoir research. Several obvious differences exist between tight sandstone reservoirs and conventional oil reservoirs. In specific, sandstone reservoirs have tight lithology, low porosity, and low permeability, especially in the micro-scale with small pore volume, small throat radius, complex connectivity, and heterogeneity. These characteristics cause the mechanism of oil and gas occurrence and migration to be significantly different from those of conventional reservoirs and induce problems such as difficulty in injection and production using generic oil-displacing agents. The size of the pore throat affects the storage performance of tight oil to a certain extent. **Figure 13** illustrates the nanofluid's mechanism for increasing oil permeation, which will be explained in following paragraphs.

Because of the oil-displacing agents' characteristic of small size, their transport through the rock near the well bore would be greatly enhanced, allowing the nanofluid to be used for conformance control deeper in the reservoir (Zhang L. et al., 2020). When the concentration of nanofluid exceeds a certain limit, it will cause coalescence and aggregation phenomena, which will rise the particle size into micron range. The agglomerated large-size particles that exceed the pore throat diameter can clog or plug the pore and throat structure, damaging the reservoir. The oil-displacing agent with stable state and good dispersibility can maintain the nano-level particle size, which is beneficial to reduce the injection pressure and allow agent to pass through the small pore throats of tight sandstone reservoirs smoothly. The small particle size also increases the specific surface area of the nanofluid particles and increases the surface activity to provide energy for the oil-water interface better.

The results of interfacial tension experiments show that the use of nano-oil-displacing agents can provide extremely low interfacial tension between the crude oil and oil-displacing agents. In the chemical flooding of tight sandstone reservoirs, the crude oil and the injection flooding system form two-phase seepage in the micro-nano capillary pores with complex morphology. Oil droplets deform when passing through the capillary pores of reservoirs because of the surface activity acting on the oil-water interface and reducing the oil–water interfacial tension. When the crude oil comes in contact with nanofluids, it is dispersed into smaller oil droplets, thereby reducing the resistance of oil droplets passing through the narrow pore throats and forming a smoother oil displacement system. Therefore, the inference here is that the change in interfacial tension will significantly influence the effect of EOR.

As the main driving factor for imbibition, the capillary effect increases the intrusion capacity of the wetting phase. Tight sandstone reservoirs have small pore throats and high capillary force inversely proportional to the pore size. The contact angle experiment proves that the capillary changes from resistance to driving force when the wettability of the rock surface changes from lipophilic to hydrophilic. It can effectively exert the capillary imbibition effect, allowing the crude oil to peel off easily from the rock formations. As a result, the crude oil continuously peels off during the driving process and is pushed forward by the displacement fluid, which enhances the oil reservoir recovery. The wettability of the rock interface is reversed from lipophilic to strong hydrophilic after being treated with different oil-displacing agents. The change in contact angle is slightly different from the nanofluid to the others, but the overall extent of change is similar. Therefore, the change in wettability promotes the production of crude oil, but it is not a unique oil displacement mechanism for nanofluids.

The results of the imbibition experiment intuitively demonstrate the actual effects of several types of oil-displacing agents. The nanofluid more easily enters the core micro-nano pore throat than the others, and the effect is still excellent under the conditions of ultra-low permeability of 0.1–1 mD, which proves that the nanofluid can improve the flow performance of crude oil in the matrix and effectively improve the oil displacement efficiency of the micro-nano pore throat. Moreover, oil-displacing agents enter into cores and displace saturated oil quickly, whereas the imbibition speed of the untreated samples (oil-wet samples) is slow, which concurs with the above-mentioned hydrophilic properties.

NMR T_2 shows that the nanofluid effectively drives a large part of the residual oil in the small pores of tight cores. The small and medium pores play important roles in imbibition, and the medium pores have the highest recovery rate. Although the capillary force, which is the main force of imbibition, is the largest in small pores, the viscous force of the non-wetting phase is also becoming larger, and it leads to a lower recovery rate. Therefore, comprehensively considering the capillary force and the viscous force of the non-wetting phase, the medium pores are more conducive to the progress of imbibition.

Based on the preliminary evaluation of the nanofluid's effectiveness in this paper, we will conduct further studies to explore the undiscovered problems of nanofluids, which involve improving stability, reducing formulation loss underground, and researching more potential oil displacement mechanisms.

CONCLUSION

This paper discusses the effects of several oil-displacing agents on unconventional tight sandstone reservoirs and explores the potential oil displacement mechanism of nanomaterials under specific reservoir conditions. The following conclusions can be drawn:

1) The pores and throats of unconventional tight sandstone reservoirs are generally small and not abundant. The reservoir space mainly includes intergranular and intercrystalline pores, intergranular and intragranular dissolved pores, and a small number of fractures. The diameters of main pores and throats are in the range of below 30 μm, dominated by 50 nm–10 μm micro-nano pores. Nano oil-displacing agent has good particle size distribution and stable performance, which is beneficial for crude oil to pass nano-pore throats during displacement, and has good matching with the target reservoir pore size distribution. It can effectively enter the nano-scale pore throats in the reservoir matrix. It can also reduce the injection pressure while effectively expanding the swept volume.
2) All four oil-displacing agents can alter the core wettability from lipophilic to strong hydrophilic, and can effectively exert capillary imbibition during the imbibition process, allowing the crude oil to peel off easily from the rock formations. Both nanofluid and betaine have excellent interfacial activity, which can reduce the oil–water interfacial tension reduced to 1×10^{-2} mN/m under the conditions of reservoir temperature and salinity, making the oil droplets easier to deform and disperse into smaller oil droplets when passing through the capillary pore throat, improving the sweep efficiency in the nano throat pore effectively.
3) Imbibition experiments further confirmed the superiority of the newly prepared nanofluid. Compared with other oil-displacing agents, the remaining oil in medium and small pores can be recovered under the simulated condition of tight sandstone reservoirs. In the case of 0.1 mD core, the absolute imbibition efficiency of small pore throat can reach 32.47%, and the total efficiency can reach 37.5%, which shows the great application prospects of this nanofluid.

This study serves as a reference for tight continental sandstone reservoirs with micro-nano pore throat systems, which are difficult to treat with generic oil-displacing agents. The new nanofluid can act on formation energy replenishment, displacement, cyclic injection, and other technical methods effectively, achieving effective crude oil removal and EOR. The development and utilization of nano-scale oil displacement materials are expected to become a disruptive technology for the efficient production of unrecoverable reserves.

DATA AVAILABILITY STATEMENT

The original contributions presented in the study are included in the article/Supplementary Material, further inquiries can be directed to the corresponding authors.

AUTHOR CONTRIBUTIONS

XJ provided the idea of this study and designed the paper framework. J-PT and L-HL investigated 491 the background and proposed the methodology. BD prepared the nanofluid. C-JZ performed experiments, processing, and data analysis, and wrote original draft. Z-JP and S-WM conceptualized and validated the conclusion. BX and YW provided relevant references and made corrections to the manuscript. All authors contributed to the article and approved the submitted version.

FUNDING

This work was supported by the National Key Research and Development Program of China (Grant No. 2019YFA0708701).

REFERENCES

Al-Anssari, S., Ali, M., Alajmi, M., Akhondzadeh, H., and Keshavarz, A. (2021). Synergistic Effect of Nanoparticles and Polymers on the Rheological Properties of Injection Fluids: Implications for Enhanced Oil Recovery. *Energy Fuels* 35, 6125. doi:10.1021/acs.energyfuels.1c00105

Cayias, J. L., Schechter, R. S., and Wade, W. H. (1975). The Measurement of Low Interfacial Tension via The Spinning Drop Technique. *Adsorption at Interfaces* 17, 234–247. doi:10.1021/bk-1975-0008.ch017

Chang, H. L., Zhang, Z. Q., Wang, Q. M., Xu, Z. S., Guo, Z. D., Sun, H. Q., et al. (2006). Advances in Polymer Flooding and Alkaline/Surfactant/Polymer Processes as Developed and Applied in the People's Republic of China. *J. Pet. Techn.* 58, 84–89. doi:10.2118/89175-jpt

Dai, C., Wang, X., Li, Y., Lv, W., Zou, C., Gao, M., et al. (2017). Spontaneous Imbibition Investigation of Self-Dispersing Silica Nanofluids for Enhanced Oil Recovery in Low-Permeability Cores. *Energy Fuels* 31, 2663–2668. doi:10.1021/acs.energyfuels.6b03244

Das, S. K., Choi, S., Yu, W., and Pradeep, T. (2008). *Nanofluids: Science and Technology*. Hoboken, NJ: John Wiley & Sons.

Ehtesabi, H., Ahadian, M. M., and Taghikhani, V. (2015). Enhanced Heavy Oil Recovery Using TiO2 Nanoparticles: Investigation of Deposition During Transport in Core Plug. *Energy Fuels* 29, 1–8. doi:10.1021/ef5015605

Ehtesabi, H., Ahadian, M. M., Taghikhani, V., and Ghazanfari, M. H. (2014). Enhanced Heavy Oil Recovery in Sandstone Cores Using TiO2 Nanofluids. *Energy Fuels* 28, 423–430. doi:10.1021/ef401338c

Fletcher, A., and Davis, J. (2010). "How EOR Can Be Transformed by Nanotechnology," in Spe Improved Oil Recovery Symposium, Tulsa, OK, April 24–28, 2010. doi:10.2118/129531-ms

Giraldo, J., Benjumea, P., Lopera, S., Cortés, F. B., and Ruiz, M. A. (2013). Wettability Alteration of Sandstone Cores by Alumina-Based Nanofluids. *Energy Fuels* 27, 3659–3665. doi:10.1021/ef4002956

Guo, F., and Aryana, S. (2016). An Experimental Investigation of Nanoparticle-Stabilized CO 2 Foam Used in Enhanced Oil Recovery. *Fuel* 186, 430–442. doi:10.1016/j.fuel.2016.08.058

Hendraningrat, L. (2013). A Coreflood Investigation of Nanofluid Enhanced Oil Recovery. *J. Pet. Sci. Eng.* 111, 128. doi:10.1016/j.petrol.2013.07.003

Hendraningrat, L., and Torsæter, O. (2014). Effects of the Initial Rock Wettability on Silica-Based Nanofluid-Enhanced Oil Recovery Processes at Reservoir Temperatures. *Energy Fuels* 28, 6228–6241. doi:10.1021/ef5014049

Jay, V., Jim, T., Bob, V., Pitts, M. J., and David, P. (1999). "Alkaline-Surfactant-Polymer Flooding of the Cambridge Minnelusa Field," in SPE Rocky Mountain Regional Meeting, Gillette, WY, May 15–18, 1999.

Ju, B., and Fan, T. (2009). Experimental Study and Mathematical Model of Nanoparticle Transport in Porous Media. *Powder Techn.* 192, 195–202. doi:10.1016/j.powtec.2008.12.017

Ju, B., Fan, T., and Ma, M. (2006). Enhanced Oil Recovery by Flooding with Hydrophilic Nanoparticles. *China Particuol.* 4, 41–46. doi:10.1016/s1672-2515(07)60232-2

Keykhosravi, A., Vanani, M. B., Daryasafar, A., and Aghayari, C. (2021). Comparative Study of Different Enhanced Oil Recovery Scenarios by Silica Nanoparticles: An Approach to Time-dependent Wettability Alteration in Carbonates. *J. Mol. Liquids* 324, 115093. doi:10.1016/j.molliq.2020.115093

Ledyastuti, M., and Jason, J. (2020). Molecular Dynamics Simulation of Nanocellulose-Oil-Water Interaction in Enhanced Oil Recovery Application. *IOP Conf. Ser. Mater. Sci. Eng.* 980, 012008. doi:10.1088/1757-899x/980/1/012008

Li, Y., Jia, D., Rui, Z., Peng, J., Fu, C., and Zhang, J. (2017). Evaluation Method of Rock Brittleness Based on Statistical Constitutive Relations for Rock Damage. *J. Pet. Sci. Eng.* 153, 123–132. doi:10.1016/j.petrol.2017.03.041

Liu, H., Jin, X., and Ding, B. (2016). Application of Nanotechnology in Petroleum Exploration and Development. *Pet. Exploration Develop.* 43, 1107–1115. doi:10.1016/s1876-3804(16)30129-x

Liu, H., Jin, X., Zhou, D., Yang, Q., and Longqiu, L. I. (2018). Potential Application of Functional Micro-nano Structures in Petroleum. *Pet. Exploration Develop.* 45, 745. doi:10.1016/s1876-3804(18)30077-6

Lowden, B. D., Porter, M. J., and Powrie, L. S. (1998). "T2 Relaxation Time versus Mercury Injection Capillary Pressure: Implications for NMR Logging and Reservoir Characterisation," in 1998 SPE European Petroleum Conference, The Hague, Netherlands, October 20–22, 1998. doi:10.2118/50607-ms

Muggeridge, A., Cockin, A., Webb, K., Frampton, H., Collins, I., Salino, P., et al. (2014). Recovery Rates, Enhanced Oil Recovery and Technological Limits Recovery Rates, Enhanced Oil Recovery and Technological Limits. *Philos. Trans. A. Math. Phys. Eng. Sci.* 372, 20120320. doi:10.1098/rsta.2012.0320

Nassar, N. N., Hassan, A., and Vitale, G. (2014). Comparing Kinetics and Mechanism of Adsorption and Thermo-Oxidative Decomposition of Athabasca Asphaltenes onto TiO2, ZrO2, and CeO2 Nanoparticles. *Appl. Catal. A Gen.* 484, 161–171. doi:10.1016/j.apcata.2014.07.017

Nazari Moghaddam, R., Bahramian, A., Fakhroueian, Z., Karimi, A., and Arya, S. (2015). Comparative Study of Using Nanoparticles for Enhanced Oil Recovery: Wettability Alteration of Carbonate Rocks. *Energy Fuels* 29, 2111–2119. doi:10.1021/ef5024719

Ragab, A. M. S., and Hannora, A. E. (2015). "An Experimental Investigation of Silica Nano Particles for Enhanced Oil Recovery Applications," in SPE North Africa Technical Conference and Exhibition (Cairo, Egypt: Society of Petroleum Engineers). doi:10.2118/175829-ms

Sadeghpour, A., Pirolt, F., and Glatter, O. (2013). Submicrometer-Sized Pickering Emulsions Stabilized by Silica Nanoparticles with Adsorbed Oleic Acid. *Langmuir* 29, 6004–6012. doi:10.1021/la4008685

Shamsijazeyi, H., Miller, C. A., Wong, M. S., Tour, J. M., and Verduzco, R. (2014). Polymer-Coated Nanoparticles for Enhanced Oil Recovery. *J. Appl. Polym. Sci.* 131, 4401–4404. doi:10.1002/app.40576

Sun, L., Wang, X., Jin, X., Jianming, L. I., and Songtao, W. U. (2016). Three Dimensional Characterization and Quantitative Connectivity Analysis of Micro/nano Pore Space. *Pet. Exploration Develop.* 43, 537. doi:10.1016/S1876-3804(16)30063-5

Volokitin, Y., Looyestijn, W. J., Sli J Kerman, W., and Hofman, J. P. (2001). A Practical Approach to Obtain Primary Drainage Capillary Pressure Curves from NMR Core and Log Data. *Petrophysics* 42.

Wasan, D., Nikolov, A., and Kondiparty, K. (2011). The Wetting and Spreading of Nanofluids on Solids: Role of the Structural Disjoining Pressure. *Curr. Opin. Colloid Interf. Sci.* 16, 344–349. doi:10.1016/j.cocis.2011.02.001

Zhang, F., An, M., Zhang, L., Fang, Y., and Elsworth, D. (2020a). Effect of Mineralogy on Friction-Dilation Relationships for Simulated faults: Implications for Permeability Evolution in Caprock Faults. *Geosci. Front. V.* 11, 79–90. doi:10.1016/j.gsf.2019.05.014

Zhang, H., Nikolov, A., and Wasan, D. (2014). Enhanced Oil Recovery (EOR) Using Nanoparticle Dispersions: Underlying Mechanism and Imbibition Experiments. *Energy Fuels* 28, 3002–3009. doi:10.1021/ef500272r

Zhang, H., Ramakrishnan, T. S., Nikolov, A., and Wasan, D. (2018). Enhanced Oil Displacement by Nanofluid's Structural Disjoining Pressure in Model Fractured Porous media. *J. Colloid Interf. Sci.* 511, 48–56. doi:10.1016/j.jcis.2017.09.067

Zhang, H., Ramakrishnan, T. S., Nikolov, A., and Wasan, D. (2016). Enhanced Oil Recovery Driven by Nanofilm Structural Disjoining Pressure: Flooding Experiments and Microvisualization. *Energy Fuels* 30, 2771–2779. doi:10.1021/acs.energyfuels.6b00035

Zhang, L., Abbaspourrad, A., Parsa, S., Tang, J., Cassiola, F., Zhang, M., et al. (2020b). Core-Shell Nanohydrogels with Programmable Swelling for Conformance Control in Porous Media. *ACS Appl. Mater. Inter.* 12, 34217–34225. doi:10.1021/acsami.0c09958

Zhu, R., Bai, B., and Cui, J. (2013). Research Advances of Microstructure in Unconventional Tight Oil and Gas Reservoirs. *J. Palaeogeogr* 15, 615–623. doi:10.7605/gdlxb.2013.05.049

Zou, C., Zhai, G., Zhang, G., Wang, H., Zhang, G., Li, J., et al. (2015). Formation, Distribution, Potential and Prediction of Global Conventional and Unconventional Hydrocarbon Resources. *Pet. Exploration Develop.* 42, 14–28. doi:10.1016/s1876-3804(15)60002-7

Zou, C., Zhu, R., Wu, S., Yang, Z., Tao, S., Yuan, X., et al. (2012). Types, Characteristics, Genesis and Prospects of Conventional and Unconventional Hydrocarbon Accumulations: Taking Tight Oil and Tight Gas in China as an Instance. *Acta Petrol. Sin.* 33, 173–187. doi:10.7623/syxb201202001

Conflict of Interest: Authors C-JZ, XJ, J-PT, Z-JP, S-WM, BD, YW, and BX were employed by the company PetroChina.

The remaining authors declare that the research was conducted in the absence of any commercial or financial relationships that could be construed as a potential conflict of interest.

Publisher's Note: All claims expressed in this article are solely those of the authors and do not necessarily represent those of their affiliated organizations, or those of the publisher, the editors and the reviewers. Any product that may be evaluated in this article, or claim that may be made by its manufacturer, is not guaranteed or endorsed by the publisher.

frontiers in Earth Science

ORIGINAL RESEARCH
published: 27 September 2021
doi: 10.3389/feart.2021.735208

Experimental and Numerical Investigation of Characteristics of Highly Heterogeneous Rock Mechanical Responses in Tight Sandy Conglomerate Reservoir Rock Under Tri-axial Compression

Bin Chen[1], Jiaqi Ji[1], Jingqi Lin[1], Huayong Chen[1], Xueliang Wang[1], Xuyang Guo[2,3], Wentao Yang[4] and Jiaying Lin[2,3]*

[1]China Petroleum Logging Company Limited Xinjiang Branch, Karamay, China, [2]Department of Petroleum Engineering, China University of Petroleum, Karamay, China, [3]College of Petroleum Engineering, China University of Petroleum, Beijing, China, [4]College of Chemistry, Nankai University, Tianjin, China

OPEN ACCESS

Edited by:
Yuwei Li,
Liaoning University, China

Reviewed by:
Peng Tan,
CNPC Engineering Technology R and D Company Limited, China
Lei Gong,
Northeast Petroleum University, China

***Correspondence:**
Xuyang Guo
xguo@cup.edu.cn

Specialty section:
This article was submitted to Economic Geology, a section of the journal Frontiers in Earth Science

Received: *02 July 2021*
Accepted: *10 September 2021*
Published: *27 September 2021*

Citation:
Chen B, Ji J, Lin J, Chen H, Wang X, Guo X, Yang W and Lin J (2021) Experimental and Numerical Investigation of Characteristics of Highly Heterogeneous Rock Mechanical Responses in Tight Sandy Conglomerate Reservoir Rock Under Tri-axial Compression. Front. Earth Sci. 9:735208. doi: 10.3389/feart.2021.735208

Due to the use of horizontal wells and hydraulic fracturing, commercial tight oil production from some tight sandy conglomerate reservoirs has been achieved. Since the widely distributed gravels in the sandy matrix in conglomerate reservoir rocks are harder than the matrix, the rock mechanical response in conglomerates under compression is highly heterogeneous. This increases the complexity of understanding the hydraulic fracturing behaviors in conglomerate reservoirs. Previous tri-axial compression tests provided the stress-strain relationships of conglomerate samples as a whole, and the stress and strain in the gravels and in the sandy matrix were not investigated due to the limitation of the compression test lab. This study presents tri-axial test results for a conglomerate sample cored from a reservoir that has been economically developed. Lab results are then used to calibrate the numerical model for the simulation of the tri-axial compression process. Numerical results indicate that the elastic modulus and size of gravels have significant impacts on the axial stresses and axial strains in the conglomerate. Stress concentrations are observed in gravels due to the heterogeneous mechanical properties in the conglomerate. The reorientation of the maximum horizontal principal stress is quantified to study the mechanisms of the interaction types between hydraulic fractures and gravels embedded in the tight sandy matrix.

Keywords: tight oil reservoirs, numerical simulation, tri-axial compression, stress and strain, hydraulic fracture

INTRODUCTION

Unconventional oil and gas resources in low permeability reservoirs have attracted tremendous attention in the upstream in the petroleum industry (Xie et al., 2020; Zhao et al., 2020). Due to the low permeability in such reservoirs, it usually requires horizontal wells with hydraulic fracturing technologies to obtain commercial production (Zhang et al., 2017; Tang et al., 2018; Cheng et al., 2019; Dong et al., 2021). Recently, the high potential of hydrocarbon production in tight

FIGURE 1 | Conglomerate rock sample used for the compression test.

FIGURE 2 | Rapid triaxial testing system (China University of Petroleum 2021).

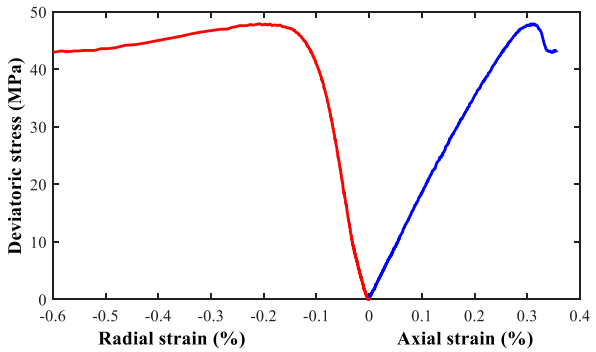

FIGURE 3 | Results of the tri-axial compression test.

sandy conglomerate reservoirs has been proved by large-scale field production involving horizontal wells with hydraulic fracturing in several locations such as the Junggar Basin and Songliao Basin in China (Feng et al., 2013; Xiang and Zhang 2015). However, due to the presence of gravels in the tight sandy matrix, the rock mechanical characteristics are rather heterogeneous. Since the hydraulic fracturing quality is closely related to the complex mechanical behaviors in conglomerates, it is important to understand how the conglomerates deform under the compression induced by reservoir stimulation processes.

Experimental tests are widely used in rock mechanical analyses. In such tests, the exertion of confining pressure and axial stress can establish the *in-situ* stress conditions in the subsurface. They help to obtain essential rock mechanical parameters and constitutive relationships using rock samples, which are especially critical for the optimization of hydraulic fracturing parameters. Kluge et al. (2020) proposed a novel shear test strategy to correlate the permeability evolution and micro-faults. Their test was established based on an MTS 815 tri-axial compression cell and concluded that the induced fractures increase the permeability by two–three orders of magnitude. Based on a modified tri-axial compression test with changing confining pressure and axial stress, it is found out that stress paths of loading and unloading directly govern the brittleness, elastoplasticity, and tensile and shear failure mechanisms in tight rocks (Guo et al., 2019). The anisotropy of deformation in tri-axial tests is discussed by Togashi et al. (2017), where a novel method with only a single test on one sample is proposed. Thus, it is more economical and convenient to quantify the deformation anisotropy. The advantage of this method is that there is no need to carry out multiple tests on various samples. Similarly, Aghababaei et al. (2019) also proposed a multi-stage strategy to obtain key strengths and failure behaviors using reduced numbers of samples to decrease the time and cost involved in tri-axial compression tests. However, they pointed out that the newly developed experimental method yields lower strength measurements than the single stage method. In order to understand the fracture patterns, Baumgarten and Konietzky (2013) conducted conventional single stage compression tests, multi-stage tests and continuous failure state tests. Both uni-axial and tri-axial tests were employed. They indicated that the combination of lab tests and numerical simulations helped to improve the understanding of post-failure behaviors.

The presence of gravels in a relatively homogeneous matrix leads to complexity in evaluating the rock mechanical behaviors, which have attracted attention from many researchers. Kumara et al. (2013) carried out a study on the stress and strain relationships in sand-gravel mixtures. This study provides insight into the deformation characteristics in sandy conglomerate reservoirs. They found out that the shape of gravels and the percentage of sand in the mixture both affect the stress-strain curves, and 30% of sand leads to the highest stress-strain curve indicating the highest strength. Akram et al. (2019) employed uni-axial, tri-axial, and Brazilian tests to investigate the effects of specimen size, clast size, cement matrix, and clast properties on the strength and deformation

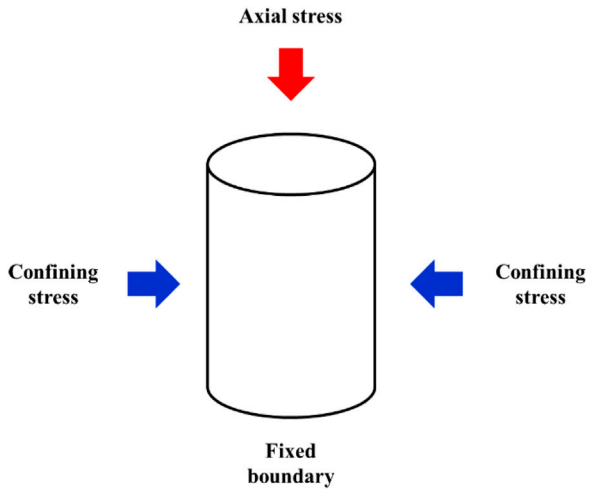

FIGURE 4 | Three-dimensional geometry of the model.

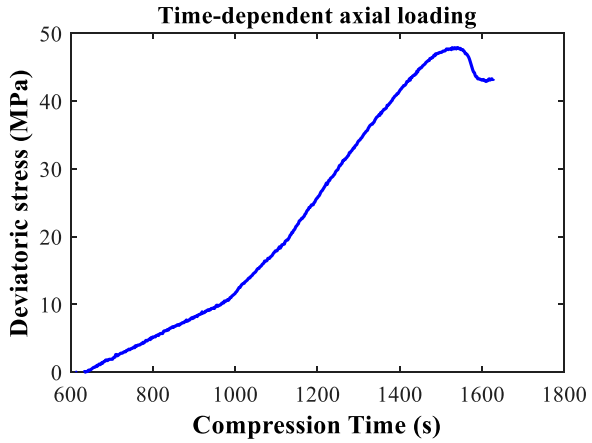

FIGURE 5 | Axial loading in the compression test.

patterns in conglomerate rocks. They concluded that with the increase of particle size, peak strength and Young's modulus decrease. Zhou et al. (2020) further experimentally investigated the effects of sphericity, where sphericity is negatively related to gravel content and the plasticity of the rock is positively correlated with heterogeneity. They emphasized the effect of gravel on the emergence of micro-cracks on the edges of gravels. In a rock mechanical test, Shi et al. (2013) reported elastic parameters based on acoustic measurements in 80 samples from the Triassic and Permian Formations in the conglomerate reservoirs in the Mahu Sag, Junggar Basin in Xinjiang, China. The dynamic modulus range is between 28.4 and 32.21 GPa while the dynamic Poisson's ratios are between 0.2055 and 0.2858. The correlation between P and S waves is good while the correlation between dynamic and static parameters is poor.

A major importance of tri-axial tests is that they provide strengths, elastic parameters, and failure patterns for rock samples. It is widely accepted that the quality of hydraulic fracturing in tight and heterogeneous is jointly governed by stress shadows, *in-situ* stress, brittleness, fracability, clay and organic matter, and fracturing parameters (Guo et al., 2018a; Guo et al., 2018b; Dahi Taleghani et al., 2018; Li et al., 2018; Lecampion et al., 2018; Guo et al., 2019; Mao et al., 2020; Hou et al., 2019; Wang et al., 2019; Chen et al., 2021). To better characterize the hydraulic fracture network, tri-axial tests can provide essential measurements for rock mechanical properties (Guo et al., 2020; Duan et al., 2021). In addition, gravels in conglomerates introduce heterogeneities and increase the complexity of hydraulic fracture propagation. Some efforts were made to investigate these phenomena. Heterogeneities related to topology and geometry were discussed and it was observed that structured fracture networks have less dispersion than disordered networks, and the corresponding production performance can also be affected (Hyman and Jimenez-Martinez 2018; Zhi et al., 2021). The layered formation is deemed as a typical mechanical heterogeneity that leads to complex fracture propagation behaviors (Yue et al., 2019; Tan et al., 2020; Tan et al., 2021). For mechanical heterogeneities characterized by stratified formations, fracture tip locations, modulus values, and each layer's height percentage are the key parameters affecting hydraulic fracture paths and geometries.

Based on the literature review, it is noted that tri-axial tests have been widely studied, while the mechanical responses within the highly heterogeneous sandy conglomerates require further investigation. In this study, a novel workflow including tri-axial testing and the finite element analysis of mechanical responses within the testing sample is proposed. Then, this study provides lab-calibrated distributions of stresses and strains in the sandy matrix, in the gravels, and in the interface between gravels and matrix. The effects of gravel size, gravel spacing, and gravel stiffness on stress concentration are also quantified. The heterogeneity of mechanical responses discussed in this article provides a reference for the hydraulic fracturing interaction with gravels and insights for hydraulic fracture parameter design and optimization.

TRI-AXIAL COMPRESSION TEST

In the experimental study, a tight sandy conglomerate rock sample taken from the Lower Triassic Baikouquan Formation in Mahu Sag, Junggar Basin in northwestern China is used for the tri-axial compression test. 1×10^8 tons of reserves were already reported in the low-porosity and low-permeability reservoirs. Continuous and commercialized tight oil production has been achieved in this area after the use of horizontal wells and hydraulic fracturing. To further improve the recovery in this area, optimization of drilling and hydraulic fracturing parameters is required where rock mechanical tests can provide necessary data for the optimization. Due to the fan-deltaic sedimentary environment in the sag, large-scale accumulation is favorable. Tight sandy matrix and gravels are the main components of the reservoir rock, and the clastic gravels are generally quartz and feldspar. Therefore, the stiffness of the gravels is higher than the tight matrix. Gravels in this area have a maximum diameter of 24.8 mm and have good sphericity. Correlations between P wave velocity and S wave velocity are good, and one established correlation

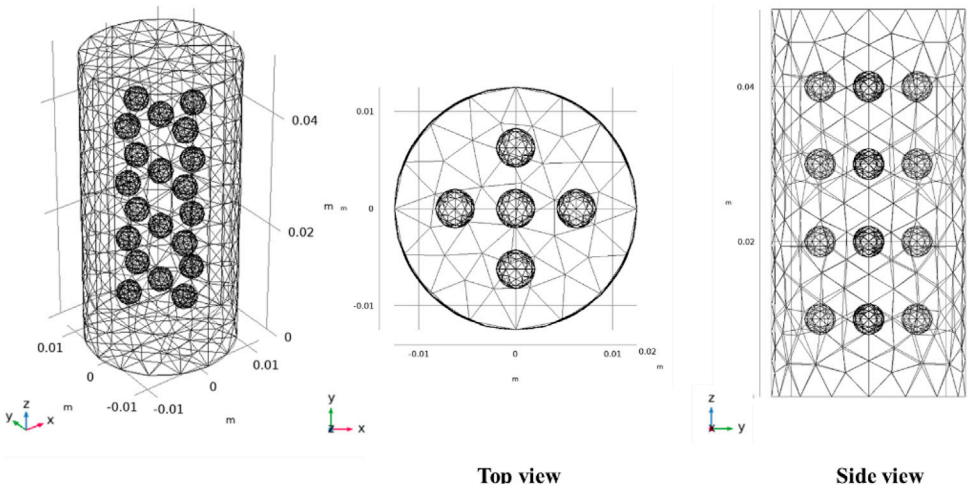

FIGURE 6 | Schematic of the simplified geometry for conglomerate compression simulation.

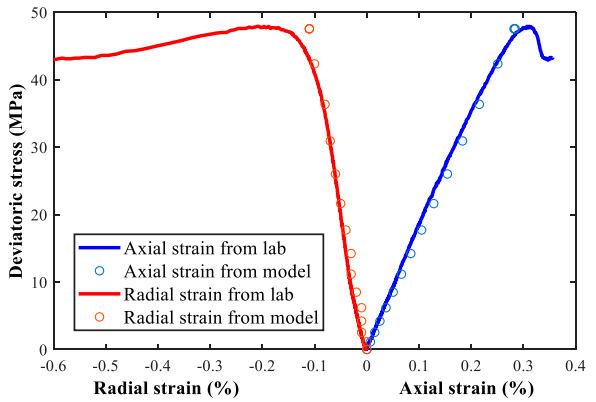

FIGURE 7 | Matching between lab and modeling results for linear elasticity. Note that only linear regimes are studied.

is $V_s = 0.3692\,V_p + 851.3$ (Shi et al., 2018; Qin and Yang, 2019; Zhou et al., 2020; Qian et al., 2021). **Figure 1** is the tight sandy conglomerate sample taken from the formation, where strong heterogeneity can be observed with gravels embedded in the matrix. In the sample, the gravel sizes range between 2 and 12 mm. The tight sandy sample is from a reservoir containing sandstones, mudstones, and conglomerates. Gavels show relatively good roundness and mainly contain feldspars and quartzes. The support mode is a combination of the matrix and gravels (Zhou et al., 2020).

The tri-axial compression test is conducted in the Rapid Triaxial Testing System GCTS RTR-1500 (**Figure 2**). This platform can provide a maximum pressure of 140 MPa, a maximum compressive force of 1,500 kN, a maximum tensile force of 820 kN, and a maximum temperature of 150 °C. A confining pressure of 40 MPa is used in the test with continuous increases in the axial loading. **Figure 3** presents the experimental results of the relationship between deviatoric stress, radial strain, and axial strain. Before reaching the peak strength, a linear correlation is observed. The size of the core is a standard sample with a diameter of 25 mm and a length of 50 mm. The weight is 53.5 g. They are the essential parameters to be used in the following finite element analysis.

NUMERICAL STUDY

The tri-axial compression test is capable of providing key elastic parameters. However, the parameters are obtained based on the compression of the entire conglomerate while the distribution of stress and strain in the rock cannot be directly examined by the compression test. Since the heterogeneity in the conglomerate sample is strong, it is not reasonable to assume homogeneous and uniform mechanical responses to compression in the sample. Therefore, a numerical model based on finite element methods and momentum balance in the stress tensor is introduced to quantify the mechanical behaviors in the sample.

Mathematical Model

Cauchy stress tensors are used to describe the stress components in the 3D domain. The momentum balance between stress components and traction boundaries is expressed as:

$$\nabla \cdot \sigma = t \tag{1}$$

where σ is the stress tensor; t is the traction boundary.

Since the compression test results exhibit strong linear elasticity, linear elastic materials are used for the sandy matrix and the gravels. Based on Hooke's law:

$$\sigma = \sigma_0 + \mathrm{C}: \varepsilon_{el} \tag{2}$$

$$\varepsilon_{el} = \varepsilon - \varepsilon_{inel} \tag{3}$$

where σ_0 is the initial stress; C is the elasticity tensor; ε_{el} is the elastic strain; ε is the total strain; ε_{inel} is the inelastic strain.

The total strain can also be expressed as:

$$\varepsilon = \frac{1}{2}\left[(\nabla \mathrm{u})^T + (\nabla \mathrm{u})\right] \tag{4}$$

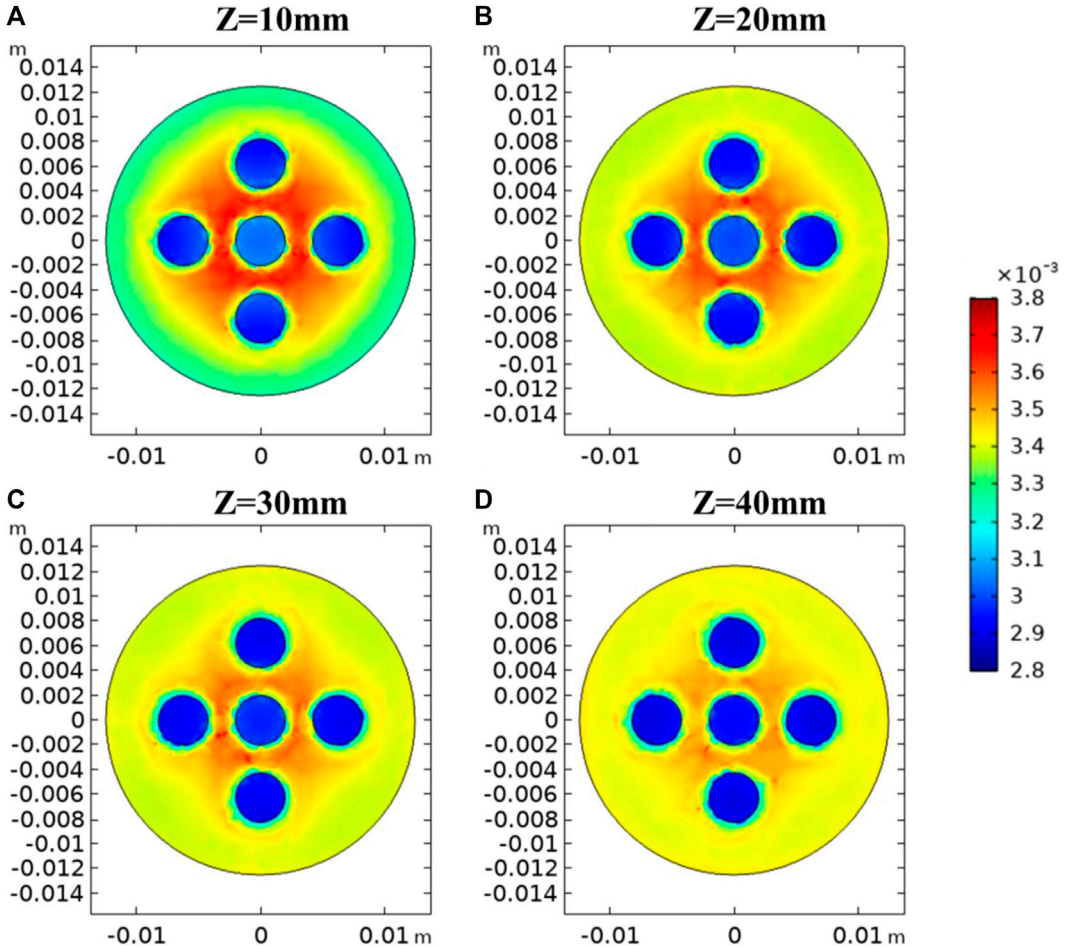

FIGURE 8 | Distribution of axial strains in X-Y planes of **(A)** Z = 10 mm, **(B)** 20 mm, **(C)** 30 mm, and **(D)** 40 mm in the base case.

The elasticity tensor is related to Young's modulus and Poisson's ratio as:

$$\mathrm{C} = \mathrm{C}(E, \nu) \tag{5}$$

Although heterogeneity in the rock mechanical properties is considered in this study, isotropy is used in the assumption. Therefore, a highly symmetric elasticity matrix is obtained:

$$\mathrm{D} = \frac{E}{(1+\nu)(1-2\nu)} \begin{bmatrix} 1-\nu & \nu & \nu & & & & \\ \nu & 1-\nu & \nu & & & & \\ \nu & \nu & 1-\nu & & & & \\ & & & \frac{1-2\nu}{2} & & & \\ & & & & \frac{1-2\nu}{2} & & \\ & & & & & \frac{1-2\nu}{2} & \end{bmatrix} \tag{6}$$

where E is the Young's modulus; ν is the Poisson's ratio.

In order to simulate the tri-axial compression process in the laboratory, a three-dimensional geometry is established as in **Figure 4**. Three types of boundary conditions are used in the geometry. The first type is the axial stress exerted at the top of the cylindrical domain. It is used to represent the time-dependent axial load in the GCTS testing system. The second type is the confining stress or confining pressure exerted radially. This is used to represent the confinement in the testing system. The third type is the fixed bottom boundary.

For the first and second types of stress boundaries, their effects are written as:

$$\sigma \cdot \mathrm{n} = t \tag{7}$$

$$t = -P \cdot \mathrm{n} \tag{8}$$

where n is the normal vector and P is the nominal stress.

For the third type of fixed boundary, the effect is written as:

$$\mathrm{u} = 0 \tag{9}$$

Note that the boundary tractions are time-dependent as functions of time. They represent the loading process in the testing system during the compression test.

To build up the numerical model, three-dimensional tetrahedral cells are used in the mesh. Local grid refinements

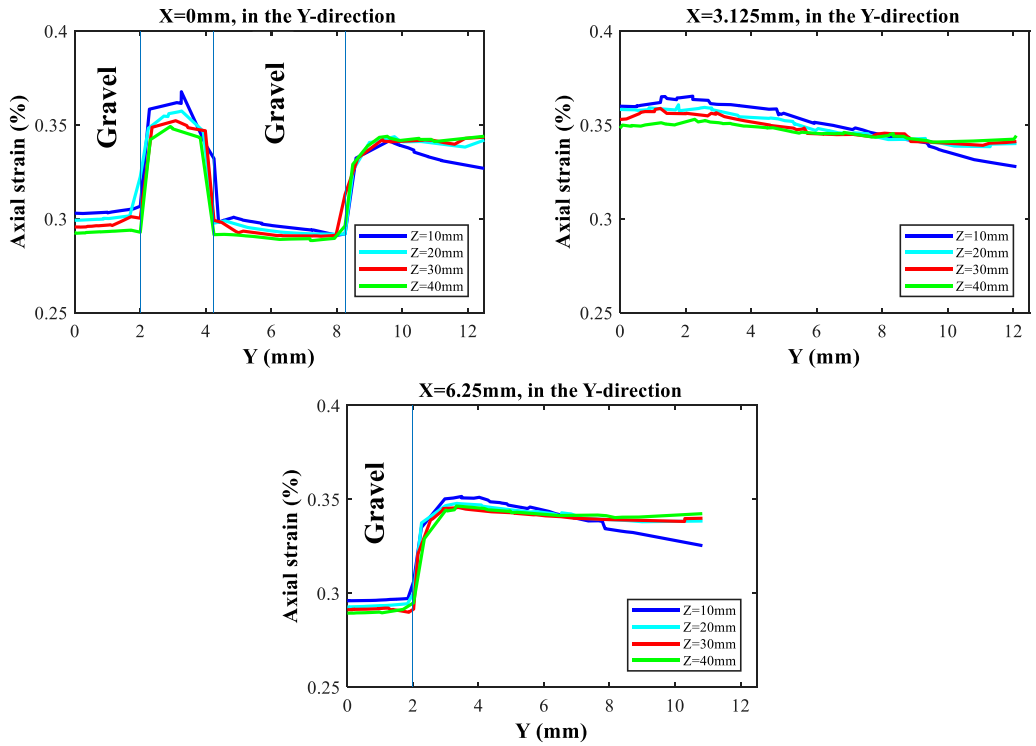

FIGURE 9 | Distribution of axial strains at X = 0, 3.125, and 6.25 mm in the Y-direction in planes of Z = 10, 20, 30, and 40 mm in the base case. Vertical lines denote the gravel-matrix interfaces.

are employed in and near gravels to improve the convergence and stability of numerical solutions. Totally 39,081 elements are used in the mesh and the degrees of freedom is 141,762. A direct solver is used and the simulation time for the base case is 474 s. To solve for displacements in the mechanical problem, quadratic serendipity shape functions are used in space discretization.

Base Case

In the base case, the mathematical model is calibrated with lab data. In the model, the time-dependent axial stress and confining stress boundaries are from the tri-axial compression test records as in **Figure 5**. Note that it only reports loading after the confining stress is fully increased to the target of 40 MPa and the process for the increase in loading for the confining stress is not plotted. This is used in **Eqs 7**, **8** in the model.

An assumption is made in the simulation to reasonably simplify the process to quantify the heterogeneity. Based on the observation of the tight conglomerate core and statistical review carried out by Liu et al. (2018) in the same formation, uniformly distributed spheres as in **Figure 6** are used to represent the gravels in the sandy matrix. Therefore, quantitative analyses can be better focused on the size, spacing, and elastic parameters of the gravels.

In general, four layers of gravels are uniformly distributed vertically. In each layer, five gravels are uniformed placed. In the base case, the diameter of each spherical gravel is 2 mm. In each layer, the spacing between two neighboring gravels is 4.25 mm. The vertical spacing between two neighboring layers is 8 mm.

Before detailed numerical analyses, a calibration of the parameters used in the model is carried out. After the calibration of rock mechanical parameters of the gravels and matrix, axial and radial strains from the model are used for matching purposes. In **Figure 7**, the matching between the lab results and the modeling results for axial strain, radial strain, and deviatoric stress is achieved. Note that only the results in the linear deformation regimes are used as this study does not consider failure mechanisms. Only results before the peak strength are used. Based on the match, the linear elastic assumption used in the modeling study can be verified.

The mechanical parameters used in the numerical model are calibrated in the matching process. In the calibration, the Young's modulus of the sandy matrix is 17 GPa; the Poisson's ratio of the sandy matrix is 0.41; the Young's modulus of the gravel is 47 GPa; the Poisson's ratio of the gravel is 0.31.

Distributions of the axial strain, the axial stress, and the orientation of the maximum principal stress in the horizontal direction in the base case are plotted. They are plotted at the end of the elastic deformation when the axial strain is at its maximum. In **Figure 8**, the two-dimensional distributions of axial strains in planes Z = 10, 20, 30, and 40 mm are presented. The deformation in gravels is generally smaller than that in the matrix, as gravels have higher stiffnesses. Distinct strains are observed as the effects of the boundaries between gravels and the matrix are dominant.

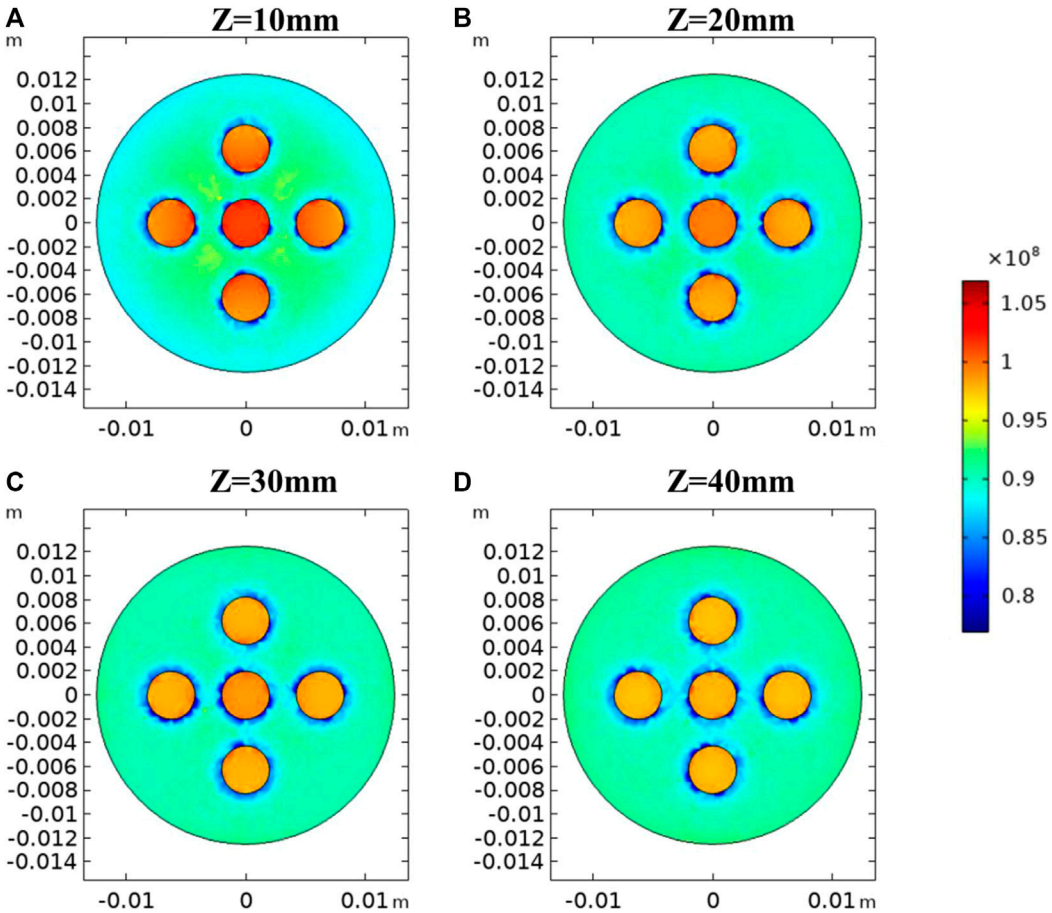

FIGURE 10 | Distribution of axial stresses in X-Y planes of **(A)** Z = 10 mm, **(B)** 20 mm, **(C)** 30 mm, and **(D)** 40 mm in the base case.

In the sandy matrix, areas between neighboring gravels also experience relatively higher axial strains compared to areas near the boundary of the rock sample. This is the stress concentration caused by non-uniform deformation in gravels and in the matrix during the tri-axial compression process. Therefore, it is found out that the stress concentration is only observed in between gravels. The strain magnitudes are higher at areas closer to the fixed bottom boundary of the rock sample. This is because the fixed bottom leads to higher changes in deformation at nearby areas, while the top and the confining boundaries are traction boundaries that allow for movements.

In **Figure 9**, one-dimensional distributions of axial strains along X = 0, 3.125, and 6.25 mm at four X-Y planes in **Figure 8** are plotted. These lines are selected as they penetrate the three gravels, zero gravels, and one gravels as it moves away from the center of the sample. Vertical lines in the one-dimensional plots represent the boundaries between gravels and the sandy matrix. Note that in **Figure 9**, only half of the lines are presented due to symmetry. At X = 0mm, it is clear that the axial strain magnitudes are lower in the gravels than in the matrix. The strains in the gravels and between gravels are positively correlated with the distance to the bottom boundary, while the differences in strains near the boundary of the sample are not distinct except for Z = 10 mm. At X = 3.125mm, the strain distributions between gravels are discussed. Areas closer to the center of the sample have higher axial strains. This indicates that the stress concentration is more noticeable in areas more surrounded by gravels. At X = 6.25mm, the effect of gravels on decreased axial strains is again exhibited. The changes in the strain are relatively sharp at the gravel-matrix boundary due to the changes in elastic parameters. The axial strains outside the gravels are around 0.35%.

Figure 10 plots the axial stress distributions at X-Y planes with different Z values. Strong heterogeneities in axial stresses are also observed. In general, stress concentrations are located within the gravels as they are typically harder than the sandy matrix and have greater elastic moduli. The elevated axial stresses in gravels at Z = 10 mm are the greatest as they are closer to the fixed bottom boundary which allows for limited space for deformation. Another observation is that the interfaces between gravels and the matrix endure decreases in axial stresses, which is caused by the sharp differences in elastic moduli between two different materials.

To better present the heterogeneity in axial stresses, **Figure 11** describes the one-dimensional axial stress distributions at X = 0, 3.125, and 6.25 mm at four different X-Y planes. Due to symmetry, only half of the domain is plotted. It is noticed that

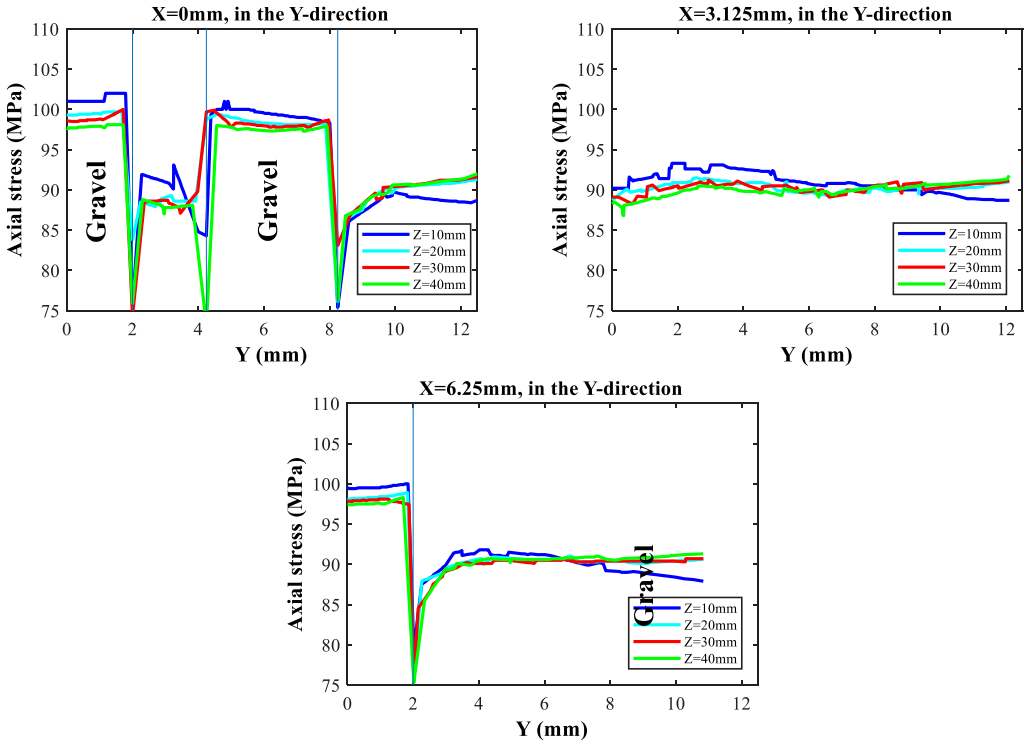

FIGURE 11 | Distribution of axial stresses at X = 0, 3.125, and 6.25 mm in the Y-direction in planes of Z = 10, 20, 30, and 40 mm in the base case. Vertical lines denote the gravel-matrix interfaces.

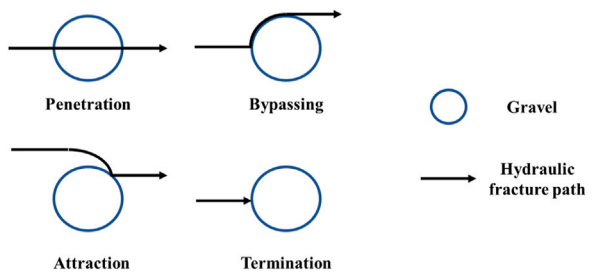

FIGURE 12 | Types of interactions between gravels and hydraulic fractures in tight sandy conglomerates.

the axial stress at and near the center of the gravel in the plane tends to be greater than that in the outer gravel. Significant decreases in axial stresses are observed at the boundaries between gravels and the matrix. The magnitudes of the decreases can be as great as 15 MPa. For the one-dimensional distribution at X = 3.125 mm with no presence of gravels, oscillations in stresses are observed due to the presence of gravels at nearby areas, while the general trends are flat compared to X = 0 and 6.25 mm.

In addition to axial strains and axial stresses in the matrix and gravels, the orientation of the maximum horizontal stresses is quantitatively analyzed. This is of special significance as previous studies have indicated that the interaction between heterogeneous gravels and hydraulic fractures is complicated, and hydraulic fractures in tight sandy conglomerate reservoirs can penetrate the gravels, bypass the gravels, be attracted by the gravels, or be terminated by the gravels (Zhu et al., 2005). **Figure 12** shows conceptual interaction types between hydraulic fractures and gravels. The underlying mechanisms are complicated due to the heterogeneity in rock mechanical parameters.

To understand the mechanisms behind the interaction types presented above, in **Figure 13**, the effect of compression on stress reorientation in the rock sample is studied based on numerical modeling. The compression effect here resembles the tensile failure caused by the net pressure in hydraulic fracture. To calculate the reorientation of the principal stress in the horizontal plane presented in **Figure 13**, **Eq. 10** is used as below:

$$\tan 2\theta = \frac{2\tau_{xy}}{\sigma_x - \sigma_y} \tag{10}$$

where θ is the change in the orientation; τ_{xy} is the shear stress; σ_x and σ_y are stresses in two directions.

Since the rock sample is under a conventional tri-axial compression state $(\sigma_1 > \sigma_2 = \sigma_3)$ with uniform confining pressure and an eternal axial load, the initial direction of S_{Hmax} is strictly radial. However, due to the heterogeneity introduced by gravels, it is noted that at various X-Y planes, S_{Hmax} orientations are no longer strictly radial, and highly non-uniform reorientations are observed. In general, the S_{Hmax} directions along the X axis and the Y axis are still largely radial, which is closer to the initial condition. At the circular interfaces between gravels and the matrix, S_{Hmax} directions

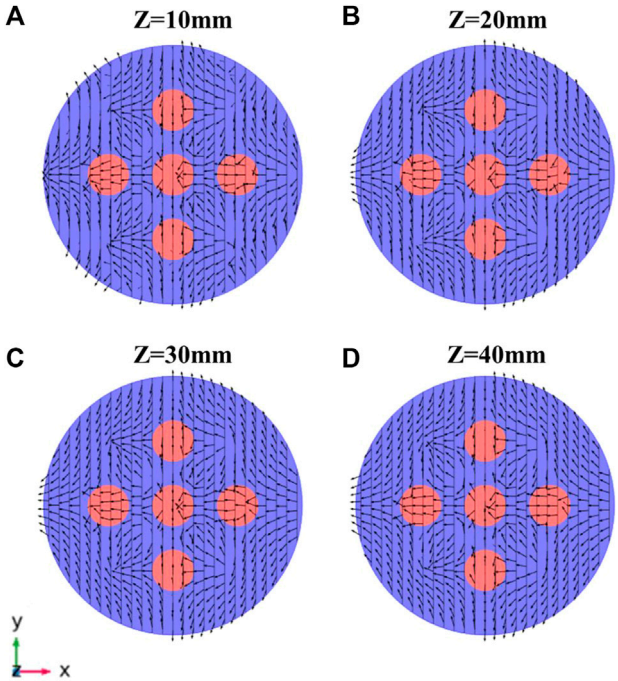

FIGURE 13 | Orientation of maximum horizontal principal stress S_{Hmax} in X-Y planes. Arrows denote directions of S_{Hmax} and red circles denote gravels. Results are for X-Y planes of **(A)** Z = 10 mm, **(B)** 20 mm, **(C)** 30 mm, and **(D)** 40 mm.

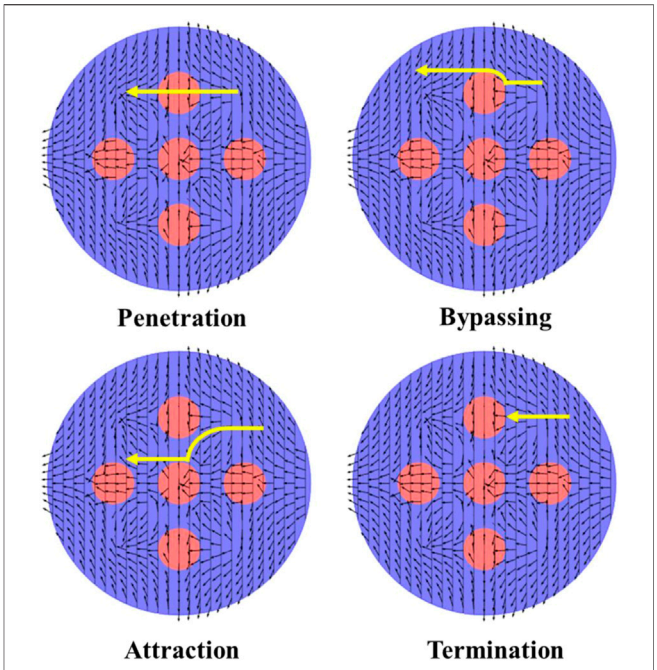

FIGURE 14 | Effects of principal stress reorientation on gravel-hydraulic fracture interaction types. Arrows denote directions of S_{Hmax} and red circles denote gravels.

are observed to be circled around the gravels. This is due to the non-uniform changes in the normal stresses and shear stresses around the gravels. The most prominent shear stress changes are in sandy matrix areas near the gravels, and this is the major reason for stress reorientations and stress reversals.

Based on the non-uniform reorientation of S_{Hmax} in **Figure 13**, the different types of interactions between gravels and hydraulic fracturing propagations in the conglomerate can be explained. A hydraulic fracture initially propagating in the X-direction is used in the analysis as in **Figure 14**.

Firstly, for the penetration type, when the hydraulic fracture propagates in the direction of S_{Hmax} since the directions of S_{Hmax} in the gravel and in the matrix along the path do not change, the gravel-matrix interface does not change the fracture propagation direction. Although the hydraulic fracture propagates orthogonally with the direction of S_{Hmax} in the gravel, the totally reversed S_{Hmax} usually does not change the fracture path. This phenomenon of the effect of totally reversed S_{Hmax} on fracture path is also verified in Safari et al. (2017). Secondly, for the bypassing type, the intersection between the gravel-matrix boundary and the hydraulic fracture has a S_{Hmax} orientation that is nearly tangential with regard to the gravel-matrix boundary. Thus, the initial fracture propagation is diverted in the directions tangential to the gravel-matrix boundary. Except for the yellow fracture path in the plot, the fracture can also be captured by the gravel-matrix boundary and then be diverted by the reoriented S_{Hmax} and move past the gravel. Thirdly, for the attraction type, the initial hydraulic fracture is governed by the S_{Hmax} pointing in the radial direction. Note that the S_{Hmax} pointing in the radial direction between the outer gravels is not affected by the existence of gravels. After the initial fracture propagation contacts the gravel-matrix boundary, the tangential S_{Hmax} on the boundary diverts the fracture along the boundary. This explains the scenarios where a fracture propagating near a gravel is attracted to the gravel. Fourthly, it is also possible that a hydraulic fracture is terminated by the gravel-matrix boundary. This cannot solely be explained by the reorientation of S_{Hmax}, as the different strengths between gravels and the sandy matrix can also affect the propagation of fractures. Since gravels usually have higher strengths, it is possible that the fracture can penetrate through the sandy matrix while the net pressure within the fracture cannot provide enough tensile traction to induce failures in the gravels. Also, modeling results indicate that there are stress concentrations in gravels, which makes it more difficult for the hydraulic fracture to propagate within the gravels with higher stresses. Thus, the propagation path of the hydraulic fracture is terminated by the interface between the gravel and the matrix.

Effects of Size and Elastic Modulus of Gravels on Heterogeneous Mechanical Responses

In the base case, a gravel elastic modulus of 27 GPa and a gravel radius of 2 mm are employed. To investigate the effects of gravel elastic modulus and gravel size on the deformation of the conglomerate sample, two sets of sensitivity analyses are carried out to show how the changes in elastic modulus and size of the spherical gravels affect the stress distributions in the conglomerate. In the analysis of elastic modulus of gravels, elastic modulus values of 35 and 19 GPa are used. In the analysis of gravel size, radii of 1 and 3 mm are used.

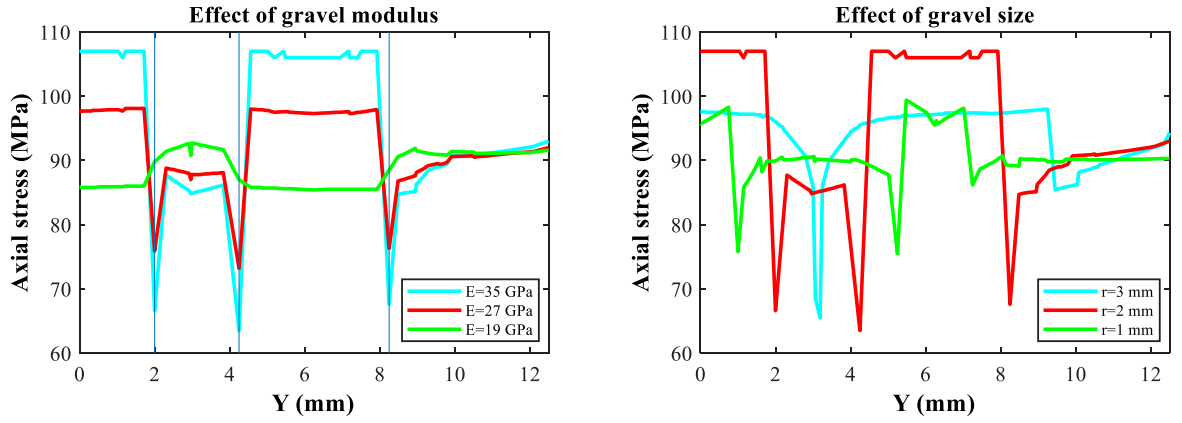

FIGURE 15 | Axial stress in the Y-direction at X = 0 mm for Z = 40 mm with various elastic moduli and radii of gravels.

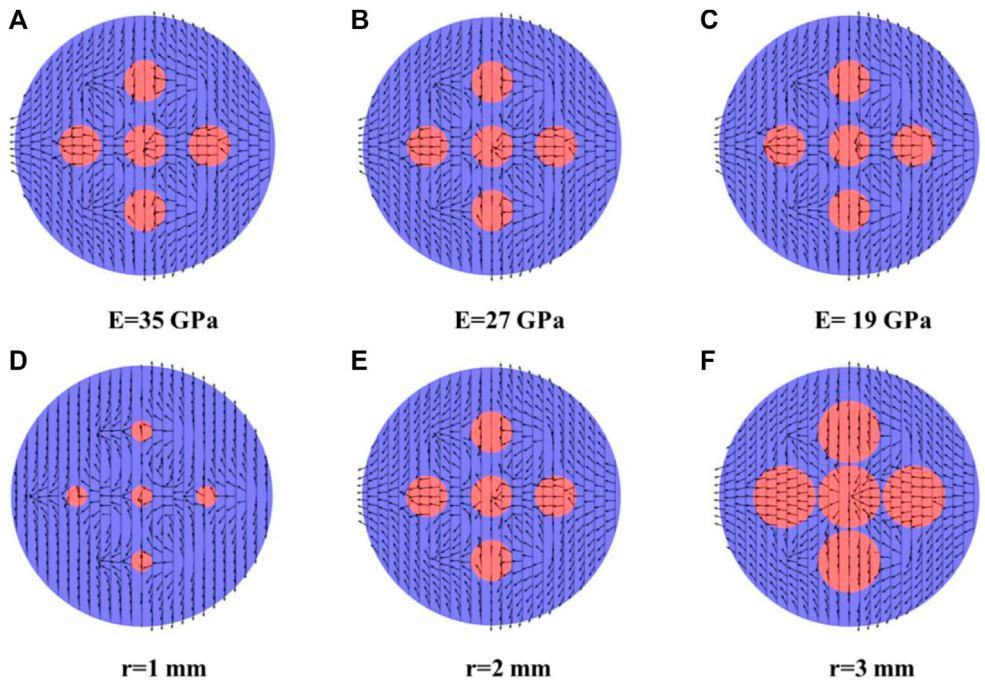

FIGURE 16 | S_{Hmax} reversal at Z = 40 mm with various elastic moduli and radii of gravels. Arrows denote directions of S_{Hmax} and red circles denote gravels. **(A)** E = 35 GPa, **(B)** E = 27 GPa, **(C)** E = 19 GPa, **(D)** r = 1 mm, **(E)** r = 2 mm, and **(F)** r = 3 mm.

In **Figure 15**, axial stress distributions in the Y-direction for X = 0 mm at Z = 40 mm are plotted. The effect of gravel elastic modulus and gravel size is exhibited. Based on the results with various gravel elastic moduli on the left, it is noted that the interfaces between gravels and the sandy matrix still denote the sharps changes in axial stresses. In general, a higher gravel elastic modulus leads to higher axial stress magnitudes in the gravels. However, when the elastic modulus is decreased to 19 GPa which is very close to the elastic modulus of the sandy matrix, axial stresses in gravels are no longer elevated. In contrast, increases in axial stresses in the sandy matrix between neighboring are observed. Therefore, when the elastic modulus of gravels is decreased from 35 to 19 GPa, the stress concentrations move from the gravels to the matrix between gravels. When the difference in elastic moduli between gravels and the matrix is relatively large (e.g., 35 GPa for gravels and 17 GPa for the matrix), it is harder for gravels to deform under tri-axial compression. When the difference is small (e.g., 19 GPa for gravels and 17 GPa for the matrix), it is easier for gravels to deform under tri-axial compression. However, in general, the average axial stresses in all elastic modulus simulation cases are very close. This indicates that although gravels and the matrix have their own moduli, the overall mechanical responses in the conglomerate to tri-axial compression do not change much. This is because the tri-axial compression parameters of axial loading and confining pressure are the same in all sensitivity cases.

When gravel radii of 1 mm, 2 mm, and 3 mm are simulated, it is noted that the peak axial stresses for a radius of 1 mm and a radius of 3 mm are at very similar levels of around 98 MPa in gravels. When the radius changes, the corresponding axial stress distribution drastically changes. In general, axial stresses in gravels are higher and axial stresses in the matrix are lower. The profile shapes are directly governed by sizes of spherical gravels. Regardless of the gravel size, sharp decreases in stresses are observed at the interfaces between gravels and matrices. However, there are no clear correlations between gravel radius and the axial stresses in either gravels or the matrix.

Since the stress reorientation around gravels is a key parameter to determine the interaction between hydraulic fracturing and gravels, **Figure 16** plots the comparison of S_{Hmax} reversals in the conglomerate at Z = 40 mm for all the elastic modulus cases and gravel size cases. Results with elastic moduli of 35 GPa, 27 GPa, and 19 GPa indicate that the gravel modulus does not significantly alter the reorientation patterns of the maximum principal stress in the horizontal plane. Generally, S_{Hmax} directions are circled around the gravel-matrix interfaces. For results with gravel radii of 1 mm, 2 mm, and 3 mm, the effect of gravel radius on reorientation of S_{Hmax} directions is more pronounced. For the case of radius = 3 mm, S_{Hmax} in gravels generally points to the radial direction which is the direction caused by the loading of confining pressure. As the radius decreases from 3 to 1 mm, the radius of the circled S_{Hmax} reorientation around gravels also decreases. Since S_{Hmax} reorientations are circled around the gravels, changing the size of the gravels alters the reorientation patterns of S_{Hmax}. Based on the observations in **Figure 13**, changing the size or modulus of gravels consequently alters the hydraulic fracturing patterns in the conglomerate.

CONCLUSION

In this study, the heterogeneous rock mechanical responses in a tight sandy conglomerate sample cored from a Lower Triassic Formation under tri-axial compression are experimentally and numerically investigated. The stress-strain relationships are first obtained from the lab. The lab data are then used to calibrate the finite element model for the simulation of the tri-axial compression process. Then, detailed numerical results for axial strain, axial stress, and S_{Hmax} reorientation in the sandy matrix and gravels are presented and discussed.

In Conclusion

1) Before reaching peak strengths, the deformation of the tight sandy conglomerate sample exhibits linear elasticity. Consequently, the constitutive relationship in the numerical model is also determined as linear elastic.
2) Since the tri-axial compression test in the lab can only demonstrate the overall response of the conglomerate sample and cannot quantify the spatial distribution of stress and strain in the sample, it is meaningful to develop a three-dimensional finite element model with a reasonable and lab-calibrated parameterization for the quantification of the stress and strain evolutions in the heterogeneous sample.
3) In general, axial strains in the gravels are lower than those in the matrix, while axial stresses in the gravels are higher than those in the matrix. This phenomenon of stress concentration is explained by higher elastic moduli in the gravels, which makes it more difficult to deform.
4) The elastic modulus and size of gravels both affect the distribution of stresses and strains. Increased elastic moduli in gravels lead to more heterogeneous distributions of stresses and strains among the conglomerate, while their effects on S_{Hmax} reorientation are not significant. The pattern of S_{Hmax} reorientation is primarily governed by the size of gravels.
5) The nonuniformly reoriented S_{Hmax} in the conglomerate is one of the reasons why hydraulic fracturing can have various interaction types with gravels. The interaction types include penetrating the gravels, bypassing the gravels, being attracted by the gravels, and being terminated by the gravels

DATA AVAILABILITY STATEMENT

The raw data supporting the conclusion of this article will be made available by the authors, without undue reservation.

AUTHOR CONTRIBUTIONS

BC, JJ, JL, HC, and XW contributed to the conception, design, and data interpretation for this study. XG and JL conducted the experimental and numerical study. XG wrote the draft of the manuscript. JJ, WY, and JL modified the manuscript.

ACKNOWLEDGMENTS

The authors acknowledge support from the Research Foundation of China University of Petroleum-Beijing at Karamay (No. XQZX20200009), the National Natural Science Foundation of China (No. 51904314, No. 51991362) and the Fundamental Research Funds for the Central Universities and the Science Foundation of China University of Petroleum, Beijing (No. 2462018YJRC031).

REFERENCES

Aghababaei, M., Behnia, M., and Moradian, O. (2019). Experimental Investigation on Strength and Failure Behavior of Carbonate Rocks under Multistage Triaxial Compression. *Int. J. Rock Mech. Mining Sci.* 123 (123), 104099. doi:10.1016/j.ijrmms.2019.104099

Akram, M. S., Sharrock, G. B., and Mitra, R. (2019). Investigating Mechanics of Conglomeratic Rocks: Influence of Clast Size Distribution, Scale and Properties of Clast and Interparticle Cement. *Bull. Eng. Geol. Environ.* 78, 2769–2788. doi:10.1007/s10064-018-1274-x

Baumgarten, L., and Konietzky, H. (2013). Investigations on the Fracture Behaviour of Rocks in a Triaxial Compression Test. Paper presented at the ISRM International Symposium - EUROCK 2013. Wroclaw, Poland, October 2013. doi:10.1201/b15683-148

Chen, A., Guo, X., Yu, H., Huang, L., Shi, S., and Cheng, N. (2021). A Parametric Study of Hydraulic Fracturing Interference between Fracture Clusters and Stages Based on Numerical Modeling. *Energy Exploration & Exploitation* 39 (1), 65–85. doi:10.1177/0144598720953257

Cheng, W., Jiang, G.-S., Xie, J.-Y., Wei, Z.-J., Zhou, Z.-D., and Li, X.-D. (2019). A Simulation Study Comparing the Texas Two-step and the Multistage Consecutive Fracturing Method. *Pet. Sci.* 16, 1121–1133. doi:10.1007/s12182-019-0323-9

China University of Petroleum (2021). Photo of the GCTS RTR-1500 Rapid Triaxial Testing System. Available at: http://www.cup.edu.cn/prplab.

Dahi Taleghani, A., Gonzalez-Chavez, M., Yu, H., and Asala, H. (2018). Numerical Simulation of Hydraulic Fracture Propagation in Naturally Fractured Formations Using the Cohesive Zone Model. *J. Pet. Sci. Eng.* 165, 42–57. doi:10.1016/j.petrol.2018.01.063

Dong, J.-N., Yuan, G.-J., Wang, X.-Y., Chen, M., Jin, Y., Zeng, C., et al. (2021). Experimental Study of Multi-Timescale Crack Blunting in Hydraulic Fracture. *Pet. Sci.* 18, 234–244. doi:10.1007/s12182-020-00479-1

Duan, W., Sun, B., Pan, D., Wang, T., Guo, T., and Wang, Z. (2021). Experimental Study on Fracture Propagation of Hydraulic Fracturing for Tight sandstone Outcrop. *Energy Exploration & Exploitation* 39 (1), 156–179. doi:10.1177/0144598720972513

Feng, Z., Yin, C., Lu, J., and Zhu, Y. (2013). Formation and Accumulation of Tight sandy Conglomerate Gas: A Case from the Lower Cretaceous Yingcheng Formation of Xujiaweizi Fault Depression, Songliao Basin. *Pet. Exploration Develop.* 40 (6), 696–703. doi:10.1016/s1876-3804(13)60094-4

Guo, X., Wu, K., An, C., Tang, J., and Killough, J. (2019). Numerical Investigation of Effects of Subsequent Parent-Well Injection on Interwell Fracturing Interference Using Reservoir-Geomechanics-Fracturing Modeling. *SPE J.* 29 (4), 1884–1902. doi:10.2118/195580-pa

Guo, X., Wu, K., Killough, J., and Tang, J. (2018a). Understanding the Mechanism of Interwell Fracturing Interference Based on Reservoir-Geomechanics-Fracturing Modeling in Eagle Ford Shale. *SPE Reservoir Eval. Eng.* 22 (03), 842–860. SPE-194493-PA. doi:10.15530/urtec-2018-2874464

Guo, X., Wu, K., and Killough, J. (2018b). Investigation of Production-Induced Stress Changes for Infill-Well Stimulation in Eagle Ford Shale. *SPE J.* 23 (04), 1372–1388. doi:10.2118/189974-pa

Guo, Y., Hou, L., Yao, Y., Zuo, L., Wu, Z., and Wang, L. (2020). Experimental Study on Influencing Factors of Fracture Propagation in Fractured Carbonate Rocks. *J. Struct. Geology.* 131, 103955. doi:10.1016/j.jsg.2019.103955

Hou, B., Chang, Z., Fu, W., Muhadasi, Y., and Chen, M. (2019). Fracture Initiation and Propagation in a Deep Shale Gas Reservoir Subject to an Alternating-Fluid-Injection Hydraulic-Fracturing Treatment. *SPE J.* 24 (4), 1839–1855. doi:10.2118/195571-pa

Hyman, J. D., and Jiménez-Martínez, J. (2018). Dispersion and Mixing in Three-Dimensional Discrete Fracture Networks: Nonlinear Interplay between Structural and Hydraulic Heterogeneity. *Water Resour. Res.* 54, 3243–3258. doi:10.1029/2018wr022585

Kluge, C., Blöcher, G., Barnhoorn, A., and Bruhn, D. (2020). Hydraulic-mechanical Properties of Microfaults in Granitic Rock Using the Punch-Through Shear Test. *Int. J. Rock Mech. Mining Sci.* 134 (134), 104393. doi:10.1016/j.ijrmms.2020.104393

Kumara, J., Hayano, K., Shigekuni, Y., and Sasaki, K. (2013). Physical and Mechanical Properties of Sand-Gravel Mixtures Evaluated from DEM Simulation and Laboratory Triaxial Test. *Int. J. GEOMATE* 4 (2), 546–551.

Lecampion, B., Bunger, A., and Zhang, X. (2018). Numerical Methods for Hydraulic Fracture Propagation: A Review of Recent Trends. *J. Nat. Gas Sci. Eng.* 49, 66–83. doi:10.1016/j.jngse.2017.10.012

Li, J., Yu, W., Guerra, D., and Wu, K. (2018). Modeling wettability alteration effect on well performance in Permian basin with complex fracture networks. *Fuel* 224, 740–751. doi:10.1016/j.fuel.2018.03.059

Liu, X., Xiong, J., Liang, L., and You, X. (2018). Rock Mechanical Characteristics and Fracture Propagation Mechanism of Sandy Conglomerate Reservoirs in Baikouquan Formation of Mahu Sag. *Xinjiang Pet. Geology.* 39 (1), 83–91. doi:10.7657/XJPG20180108

Mao, S., Siddhamshetty, P., Zhang, Z., Yu, W., Chun, T., Kwon, J. S. I., et al. (2020). Impact of proppant pumping schedule on well production for slickwater fracturing. *SPE J.* 26 (01), 342–358. doi:10.2118/204235-PA

Qin, H., and Yang, X. (2019). Log Interpretation Methods for Measuring the Brittleness of Tight Reservoir. *Well Log. Technol.* 43 (5), 509–513. doi:10.16489/j.issn.1004-1338.2019.05.013

Qian, Y., Wang, W., Lin, L., Zhang, H., Hou, Z., and Cheng, J. (2021). Calculation and Application of Transversely Isotropic formation Rock Mechanical Parameters. *Well Log. Technol.* 45(1), 62–67. doi:10.16489/j.issn.1004-1338.2021.01.011

Safari, R., Lewis, R., Ma, X., Mutlu, U., and Ghassemi, A. (2017). Infill-Well Fracturing Optimization in Tightly Spaced Horizontal wells. *SPE J.* 22 (2), 582–514. doi:10.2118/178513-pa

Shi, S., Zhao, C., Liu, H., Ding, K., Li, J., Chen, J., et al. (2018). Experimental Study on Rock Mechanics Parameters-A Case of the Sand Conglomerate Reservoir in M2 Well Area. 3rd International Conference on Advances in Energy and Environment Research (ICAEER 2018), Aug 10–12, Guilin, China.

Tan, P., Jin, Y., and Pang, H. (2021). Hydraulic Fracture Vertical Propagation Behavior in Transversely Isotropic Layered Shale Formation with Transition Zone Using XFEM-Based CZM Method. *Eng. Fracture Mech.* 248, 107707. doi:10.1016/j.engfracmech.2021.107707

Tan, P., Pang, H., Zhang, R., Jin, Y., Zhou, Y., Kao, J., et al. (2020). Experimental Investigation into Hydraulic Fracture Geometry and Proppant Migration Characteristics for southeastern Sichuan Deep Shale Reservoirs. *J. Pet. Sci. Eng.* 184, 106517. doi:10.1016/j.petrol.2019.106517

Tang, J., Wu, K., Li, Y., Hu, X., Liu, Q., and Ehlig-Economides, C. (2018). Numerical Investigation of the Interactions between Hydraulic Fracture and Bedding Planes with Non-orthogonal Approach Angle. *Eng. Fracture Mech.* 200, 1–16. doi:10.1016/j.engfracmech.2018.07.010

Togashi, Y., Kikumoto, M., and Tani, K. (2017). An Experimental Method to Determine the Elastic Properties of Transversely Isotropic Rocks by a Single Triaxial Test. *Rock Mech. Rock Eng.* 50, 1–15. doi:10.1007/s00603-016-1095-9

Wang, J., Ge, H., Wang, X., Shen, Y., Liu, T., Zhang, Y., et al. (2019). Effect of clay and Organic Matter Content on the Shear Slip Properties of Shale. *J. Geophys. Res. Solid Earth* (124), 9505–9525. doi:10.1029/2018jb016830

Xiang, C., and Zhang, X. (2015). Conglomerate Reservoirs Characteristics and Main Controlling Factors of Kexia Formation in Liuzhong Area of Kelamayi Oilfield. *Electron. J. Geotechnical Eng.* 20 (12), 5061–5073.

Xie, J., Tang, J., Yong, R., Fan, Y., Zuo, L., Chen, X., et al. (2020). A 3-D Hydraulic Fracture Propagation Model Applied for Shale Gas Reservoirs with Multiple Bedding Planes. *Eng. Fracture Mech.* 228, 106872. doi:10.1016/j.engfracmech.2020.106872

Yue, K., Olson, J. E., and Schultz, R. A. (2019). The Effect of Layered Modulus on Hydraulic-Fracture Modeling and Fracture-Height Containment. *SPE Drilling & Completion* 34 (04), 356–371. doi:10.2118/195683-pa

Zhang, F., Dontsov, E., and Mack, M. (2017). Fully Coupled Simulation of a Hydraulic Fracture Interacting with Natural Fractures with a Hybrid Discrete-Continuum Method. *Int. J. Numer. Anal. Meth. Geomech.* 41 (13), 1430–1452. doi:10.1002/nag.2682

Zhao, X., Zhou, L., Pu, X., Jin, F., Shi, Z., Han, W., et al. (2020). Formation Conditions and Enrichment Model of Retained Petroleum in Lacustrine Shale: A Case Study of the Paleogene in Huanghua Depression, Bohai Bay Basin, China. *Pet. Exploration Develop.* 47 (5), 916–930. doi:10.1016/S1876-3804(20)60106-9

Zhi, D., Guo, X., Wang, W., Jin, Y., Liu, C., Chen, G., et al. (2021). Fracturing and Production Analysis of the Efficacy of Hydraulic Fracture Stage Reduction in the Improvement of Cost-effectiveness in Shale Oil Development: A Case Study of Jimsar Shale Oil, China. *Energy Sci Eng* 9, 1337–1348. doi:10.1002/ese3.940

Zhou, B., Ge, H., Zhou, W., Wang, J., Hao, H., Wang, X., et al. (2020). Experimental Study of the Main Influencing Factors in Mechanical Properties of Conglomerate. *Earthquake Res. China* 34 (3), 430–451.

Conflict of Interest: Authors BC, JJ, JL, HC, and XW were employed by the company China Petroleum Logging Company Limited.

The remaining authors declare that the research was conducted in the absence of any commercial or financial relationships that could be construed as a potential conflict of interest.

Publisher's Note: All claims expressed in this article are solely those of the authors and do not necessarily represent those of their affiliated organizations, or those of the publisher, the editors, and the reviewers. Any product that may be evaluated in this article, or claim that may be made by its manufacturer, is not guaranteed or endorsed by the publisher.

frontiers in Earth Science

ORIGINAL RESEARCH
published: 07 October 2021
doi: 10.3389/feart.2021.694729

Research on Minimum Miscible Pressure Between Crude Oil and Supercritical Carbon Dioxide System in Ultra-Low Permeability Reservoir by the Long-Slim-Tube Experiment Method

Guangjuan Fan[1,2], Yuejun Zhao[3,4], Xiaodan Zhang[3], Yilin Li[3] and Hao Chen[3]*

[1]School of Earth Sciences, Northeast Petroleum University, Daqing, China, [2]Key Laboratory of Oil and Gas Reservoir Formation Mechanism and Resource Evaluation of Heilongjiang Province, Northeast Petroleum University, Daqing, China, [3]Department of Petroleum Engineering, Northeast Petroleum University, Daqing, China, [4]Key Laboratory of Enhanced Oil Recovery (Northeast Petroleum University), Ministry of Education, Daqing, China

OPEN ACCESS

Edited by:
Shengnan Chen,
University of Calgary, Canada

Reviewed by:
Zhezi Zhang,
University of Western Australia, Australia
Liguo Zhong,
China University of Petroleum, China
Yousef Kazemzadeh,
University of Tehran, Iran
Milad Arabloo,
Sharif University of Technology, Iran

***Correspondence:**
Yuejun Zhao
89645472@qq.com

Specialty section:
This article was submitted to Economic Geology, a section of the journal Frontiers in Earth Science

Received: 13 April 2021
Accepted: 08 September 2021
Published: 07 October 2021

Citation:
Fan G, Zhao Y, Zhang X, Li Y and Chen H (2021) Research on Minimum Miscible Pressure Between Crude Oil and Supercritical Carbon Dioxide System in Ultra-Low Permeability Reservoir by the Long-Slim-Tube Experiment Method. Front. Earth Sci. 9:694729. doi: 10.3389/feart.2021.694729

Carbon dioxide (CO_2) injection has become an important technology to enhance oil recovery in ultra-low permeability reservoirs. Compared with other CO_2 flooding technologies, CO_2 miscible flooding has a better development effect, and the minimum miscible pressure (MMP) is a key parameter to realize miscible flooding. Therefore, it is very important to accurately predict the MMP. The prediction methods of MMP generally include laboratory experiment method and theoretical calculation method. In this study, a long-slim-tube displacement experiment method was used to determine the MMP in the study area, and the experimental temperature and pressure were consistent with those under reservoir conditions. The research results show that the recovery ratio increased gradually with the increase of experimental pressure, but the increase amplitude gradually decreased. According to the relation curve between crude oil recovery ratio and experimental displacement pressure, when the experimental pressure was larger than 29.6 MPa, the recovery ratio did not increase significantly with the increase of displacement pressure, which indicates that the interfacial tension between crude oil and CO_2 disappeared under this pressure and they reached a miscible state. It is speculated that the MMP between crude oil and CO_2 system in the study area predicted by the long-slim-tube displacement experiment method was 29.6 MPa. The results of this study help to realize miscible flooding in ultra-low permeability reservoirs and thus enhance oil recovery.

Keywords: supercritical carbon dioxide, carbon dioxide flooding, long-slim-tube displacement experiment, minimum miscible pressure, enhanced oil recovery

INTRODUCTION

Enhanced oil recovery (EOR) by carbon dioxide (CO_2) injection has been widely applied by the U.S., Russia, Canada, China, and other countries (Mogensen, 2016; Azizkhani and Gandomkar, 2020). CO_2 injection applies to most ultra-low permeability oilfields. Compared to other gas injection technologies, CO_2 injection has the merits of significantly enhanced oil recovery and low cost, so it is widely used (Jalilov et al., 2017; Kolster et al., 2017; Oschatz and Antonietti, 2018; Zhou et al., 2018; Chen et al., 2020). At the same time, some CO_2 can be stored underground by CO_2 flooding to reduce greenhouse gas emissions (Qin et al., 2015; Ahmadi et al., 2017; Birdja et al., 2019; Zhang et al., 2020a). In this regard, CO_2 flooding has a broad application prospect in the context of energy shortage, energy conservation, and emission reduction (Guo et al., 2017; Berneti and Varaki, 2018; Mutailipu et al., 2019; Gong et al., 2020). Laboratory and field tests have shown that CO_2 miscible flooding is superior to immiscible flooding in enhancing oil recovery for light oil and middle viscosity crude oil (Wu et al., 2015; Shao et al., 2020; Wu et al., 2020), and the minimum miscible pressure (MMP) is a key parameter to realize miscible flooding. Therefore, it is very important to accurately predict the MMP.

The determination methods of MMP generally include laboratory experiment method and theoretical calculation method. Laboratory experiment methods cover long-slim-tube displacement experiment method, interfacial tension method, rising bubble apparatus (RBA) method, and vapor density method. Theoretical calculation methods are mainly empirical formula method, equation of state method, and simulation calculation method (Zhang et al., 2008; Yang et al., 2019; Zhang et al., 2020b; Kaufmann and Connelly, 2020).

Long-Slim-Tube Displacement Experiment Method

This method is an effective one-dimensional flow displacement experimental model. When the pore size of the porous medium is very small, viscous fingering will be offset by lateral diffusion. The repeated accurate results can be given by the slim-tube experiment method. Ultimate recovery factors obtained from the displacement experiments are plotted into a curve, and the turning point in the curve is determined as the pressure at which dynamic miscibility appears for the first time (Han et al., 1989; Zuo et al., 1993; Yi, 2000; Li et al., 2002; Hao et al., 2005).

Interfacial Tension Method

From 1965 to 1989, Benham, Stalkup, Holm, Lake, and other scholars believed according to their research results that when the fluids mix at any ratio and reach miscibility, interface between fluids will disappear, that is, the interfacial tension becomes zero. When the interfacial tension under different gas components and different pressures is determined by an interfacial tension tester, and the interfacial tension is extrapolated as zero, the corresponding pressure is the minimum miscible pressure (MMP) (Zhang et al., 2006; Peng et al., 2007; Gunde et al., 2010; Ghorbani et al., 2014; Li et al., 2016).

RBA Method

Determining the MMP with this method was proposed by Christiansen and Kim in 1986. This method has the characteristics of short determination period and relatively low instrument requirements, allowing direct observation of the miscible process; the MMP is determined based on the shape and movement distance of the bubble, rather than the pressure associated with recovery ratio (Elsharkawy et al., 1996; Dong et al., 2001).

Vapor Density Method

This is a dynamic test method proposed by Harmon and Grigg in 1988 (Richard and Reid, 1988). It has the characteristics of short time and low cost. It directly determines the relationship between the density and pressure of injected gas-rich phase and confirms the MMP of miscible gas and crude oil using the dissolution characteristics of gas and oil.

Empirical Formula Method

It is a simple and fast theoretical method for calculation and often used to predict the MMP. Scholars have proposed many empirical formulas according to different applicable conditions (Yuan et al., 2005; Ye, 2009; Li et al., 2012), including MMP (p_{mm}) correlation (Ye, 2009), National Petroleum Council (NPC) method (Ye, 2009), Holm and Josendal correlation (Li et al., 2012), Mungan correlation (Yuan et al., 2005), Glaso empirical formula (Glaso, 1985), Johnson and Pollin (JP) empirical formula (Johnson and Pollin, 1981), the Petroleum Recovery Institute empirical formula (Johnson and Pollin, 1981), Cronquist empirical formula (Cronquist, 1978), Yellig–Metcalfe correlation (Yellig and Metcalfe, 1980), empirical formula by ORR and SILVA (1987), empirical formula by Alston et al. (1985), and so on. The empirical formula method is simple and fast in calculation, but because the parameters examined are different and have their respective applicable scope, there are differences in prediction accuracy. In the practical application, the appropriate formula should be selected according to the actual situation of the reservoir.

Equation of State Method

This is a numerical method based on the system phase equilibrium theory and the equation of state. By studying the relationship between phase behavior and miscible function of the CO_2–crude oil system, we can get the bubble point value of the system and then obtain the MMP value of the system (Guo et al., 1999; Sun et al., 2006; Ye et al., 2012; Fazlali et al., 2013). The equations of state for calculating the MMP include Peng–Robinson equation of state (PR-EOS) (Guo et al., 1999; Ye et al., 2012), Nasrifar–Moshfeghian equation of state (NM-EOS) (Fazlali et al., 2013) and modified statistical associating fluid theory equation of state (mSSAFT-EOS) (Sun et al., 2006). The MMP can be calculated quickly and accurately with the equation of state method, but there is no clear judgment criterion for the miscible function, so it needs to be considered comprehensively according to the actual reservoir conditions and fluid characteristics in calculation.

TABLE 1 | The composition data of crude oil components.

Component	Mole fraction (%)	Component	Mole fraction (%)
CO_2	0.025	n-C_4	1.220
N_2	0.971	i-C_5	0.166
C_1	28.739	n-C_5	1.417
C_2	1.035	C_6	2.318
C_3	0.809	C_{7+}	63.178
i-C_4	0.122		

Simulation Calculation Method

The method includes phase behavior simulation calculation method and artificial intelligence algorithm (Chen, 2016). In the phase behavior simulation calculation method, the effect of CO_2 gas injected into the reservoir on crude oil properties is investigated by the phase behavior simulation technology, then the parameters of equation of state are adjusted by fitting PVT experimental data to establish a phase state model that conforms to the real fluid, and finally the MMP of oil and gas system is calculated by simulating the multistage contact experiment process. Artificial intelligence algorithm is a new MMP predicting method in recent years, which mainly includes artificial neural network (ANN) method, genetic algorithm (GA), particle swarm optimization (PSO), ant colony algorithm (ACA), simulated annealing algorithm (SAA), least-squares support vector machine (LSSVM) (Shokrollahi et al., 2013; Alomair and Iqbal, 2014; Rostami et al., 2018), and gene expression programming (GEP) (Tatar et al., 2013; Kamari et al., 2015; Tian et al., 2020). Compared with other numerical methods, the artificial intelligence method has the unique ability to identify the implicit linear or nonlinear relationship between input variables and target output values and a large number of parallel operations; it has a high prediction accuracy and is capable of processing large amounts of data in parallel. However, as the prediction process is realized by multiple conversion calculations and programming of input parameters, the internal correlation between each input parameter and MMP cannot be intuitively observed.

Among all the prediction methods, the long-slim-tube displacement experiment method has been widely used and recognized by researchers and scholars (Han et al., 1989; Zuo et al., 1993; Yi, 2000; Li et al., 2002; Hao et al., 2005; Zhang et al., 2008; Ekundayo and Ghedan, 2013; Zhang and Gu, 2015; Yang et al., 2019). The long-slim-tube displacement experiment can be operated repeatedly. Compared with other methods, this method is more aligned with the characteristics of oil and gas displacement process in the porous medium of crude oil reservoir. Moreover, it can greatly eliminate the influence of unfavorable factors such as heterogeneity, mobility ratio, viscous fingering, and gravity separation of lithology. Therefore, the long-slim-tube displacement experiment method was chosen to determine the MMP in the study area.

DETERMINATION OF MINIMUM MISCIBLE PRESSURE

Experimental Material

The crude oil used in the experiment was the simulated crude oil prepared with the ground crude oil and natural gas in the study area according to formation conditions and fluid characteristics. The experiment temperature was 108.5°C. When the temperature and pressure of the formation were 108.5°C and 23.8 MPa, the viscosity of crude oil was 1.88 mPa s. The molecular weight of C_{7+} in crude oil composition was 347.29 g/mol, and the density of C_{7+} was 0.8971 g/cm^3. The composition data of crude oil components are shown in **Table 1**. The purity of CO_2 gas was 99.9%, and its properties were exactly the same as the gas injected in the study area.

Preparation of the Formation Oil Sample

The experimental formation oil was prepared with ground oil and natural gas. Preparation process: pour a certain amount of ground oil into the high pressure physical instrument PVT barrel, seal it and heat it up to the formation temperature, then add the gas into the PVT barrel at the saturation pressure, stir and increase pressure to the formation pressure, and measure the saturation pressure of crude oil and the dissolved gas–oil ratio. If the saturation pressure and the actual formation oil saturation pressure are not equal, we should adjust the amount of dissolved gas in the PVT barrel until the saturation pressure and gas–oil ratio measured are equal to that of the formation oil (Li, 2006; Lewis, 2008; Abdalla et al., 2014; Adekunle, 2014).

Experimental Apparatus

The experimental apparatus mainly included (Yang et al., 2015; Han et al., 2016; Fathinasab et al., 2018) the piston container of simulated crude oil, the piston container of CO_2, the piston container of formation water, slim tube filled with quartz sand particles, back pressure control valve, gas flowmeter, liquid flowmeter, etc. The sketch of experimental apparatus and flow chart are shown in **Figure 1**.

The injection pump was ISCO full automatic pump, with working pressure between 0 and 70 MPa and accuracy of 0.01 ml. The working pressure range of back pressure control valve was −70 MPa. The long slim tube was a one-dimensional artificial porous medium spiral stainless steel coil tightly filled with approximately 200 meshes of pure quartz sand. The accuracy of gas flowmeter was 1 ml. The highest temperature of thermostat was 200°C. The experimental parameters are shown in **Table 2**.

Experimental Procedure

The experiment was carried out in accordance with the petroleum and natural gas industry standard of the People's Republic of China (Measurement Method For Minimum Miscibility Pressure By Slim Tube Test, 2016) (SY/T 6573-2016).

(1) Experiment preparation

Temperature setting: turn on the power switch of the thermostat to heat up. When the temperature is close to the formation temperature, start the constant temperature controller. After 3 h, the temperature can be completely maintained at the predetermined value.

Tube cleaning: saturate the slim tube model adequately with petroleum ether, and use high-pressure air to dry the petroleum ether.

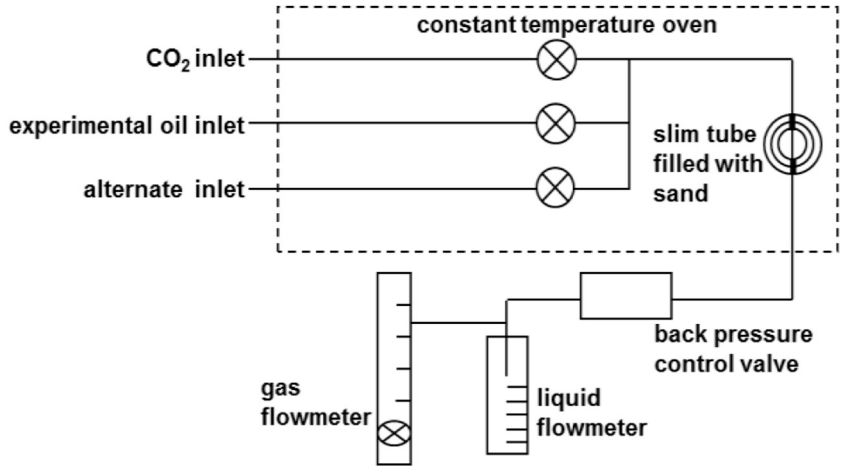

FIGURE 1 | The sketch of long-slim-tube displacement experimental apparatus.

TABLE 2 | Basic parameters of the long-slim-tube displacement experimental model.

Main parameters	Numerical values
Length (cm)	2000
Maximum temperature (°C)	200
Maximum pressure (MPa)	70
Inner diameter (cm)	0.387
Outer diameter (cm)	0.637
Porosity (%)	43.26
Permeability measured with gas (mD)	5,970
Filler (pure quartz sand) (mesh)	185–230

CO_2 introduction: open the pump and push the piston back to the top of the piston container to vent the gas in the container; inject the displacing gas CO_2 into the piston container and close the valve.

Vacuumize the long slim tube, then fill the sand filling slim tube with formation water, and calculate the porosity.

Clean the formation water in the sand filling slim tube with toluene, and dry it in a thermostat to evaporate the toluene.

Fill the sand filling slim tube with simulated oil, inject the simulated oil into the slim tube model with the ISCO pump, and stop injection when 1.5 PV simulated oil was injected. Then, the injection and output of simulated oil were calculated, and the saturated oil injected into the tube was determined according to the volume difference, which is the end of the preparation process. Get ready for a displacement experiment.

2) Start the ISCO constant-pressure and constant-speed pump and increase the pressure of gas in the piston container to be 1~3 MPa lower than the displacement pressure.
3) Raise the back pressure to the predetermined displacement pressure with a manual pump.
4) Open the pump at constant speed to inject CO_2 for displacement, open the slim tube outlet valve, and adjust the gas pressure to make it equal to or slightly higher than the displacement pressure.
5) In the process of displacement, determine oil production, gas volume, and pump reading regularly as required and check oil sample saturation. When the cumulative volume injected into the pump is greater than 1.2 PV, stop the displacement and calculate the recovery ratio at this pressure.
6) At the end of the displacement process, start the cleaning process, inject the petroleum ether directly injected into the slim tube model, and keep the appropriate back pressure. Control the flow rate of petroleum ether in the slim tube properly, so as not to affect the cleaning effect. Close the outlet for 1–2 h, allow petroleum ether to fully contact with residual oil under high pressure dissolve residual oil in petroleum ether, and release it from the outlet. Repeat several times and discharge the mixture of petroleum ether and residual oil. When the components of the mixture and pure petroleum ether were basically the same, the residual oil in the model was determined to have been completely removed and fully saturated by petroleum ether. Then, high-pressure air was injected from the inlet to blow the remaining petroleum ether in the slim tube into the oil–gas separator, and dry the tube for next experiment.
7) Follow the abovementioned steps for displacement at the next pressure point.

In general, the MMP of a gas can be analyzed by measuring the recovery ratio at more than five pressure points. The experimental back pressures in experiment were 20, 25, 30, 35, 40, and 45 MPa. Then, the MMP was calculated according to the relationship between the recovery ratio and the experimental displacement pressure.

Experimental Result

Through the above experimental process, the data and relation curve of recovery ratio and CO_2 injection amount at different experimental pressures are shown in **Table 3** and **Figure 2**.

TABLE 3 | The long-slim-tube displacement experimental data under different pressures.

CO_2 injection amount (PV)	Recovery (%)					
	20 MPa	25 MPa	30 MPa	35 MPa	40 MPa	45 MPa
0	0	0	0	0	0	0
0.13	6.33	7.22	8.90	7.89	8.02	9.30
0.25	15.11	17.23	19.10	20.58	20.91	21.50
0.39	24.51	27.96	30.92	32.93	33.50	35.00
0.51	33.68	38.42	43.10	46.00	47.60	51.20
0.64	42.92	48.95	59.30	61.80	63.00	66.70
0.77	52.19	59.53	73.20	79.20	80.50	80.50
0.9	61.26	69.88	83.70	86.00	88.20	89.00
1.04	66.74	76.50	88.00	89.40	90.20	91.20
1.14	69.30	79.00	89.40	90.30	91.10	91.70
1.2	69.90	80.35	90.15	90.50	91.22	91.90

As seen from **Table 3** and **Figure 2**, the recovery ratio increased with the increase of CO_2 injection amount at different experimental pressures. When the experimental pressure was 20 and 25 MPa, the recovery ratio increased slightly after the CO_2 injection amount was greater than 1.0 PV. When the experimental pressure was 30, 35, 35, and 40 MPa, the recovery ratio increased insignificantly after the CO_2 injection amount was greater than 0.9 PV.

According to the experimental results, the recovery ratio by CO_2 flooding under different experimental pressures can be obtained (**Table 4**).

The generally accepted criterion for miscible flooding in slim tube displacement experiment is that the recovery ratio is greater than 90% when the injection volume is 1.2 times the pore volume, and the displacement efficiency does not increase significantly with the increase of displacement pressure (Choubineh et al., 2016; KarimanMoghaddam and SaeediDehaghani, 2017; Ma et al., 2018; Ghorbani et al., 2019; Li et al., 2019; Yu et al., 2020). In **Table 4**, when the injected CO_2 volume was 1.2 PV, the recovery ratio increased with increasing experimental pressure. When the experimental pressure was 20 and 25 MPa, the corresponding recovery ratio was lower than 90%, indicating that the CO_2 flooding under these pressures was immiscible; when the experimental pressure was above 30 MPa, the corresponding recovery ratio was above 90%, indicating that the miscible flooding can be formed by CO_2 flooding under the pressure of more than 30 MPa. According to the experimental results in **Table 4**, the relation curve between crude oil recovery ratio and experimental pressure when CO_2 of 1.2 PV was injected was plotted (**Figure 3**). It can be seen from **Figure 3** that the immiscible flooding stage and miscible flooding stage intersected at 29.6 MPa. When the experimental pressure was higher than 29.6 MPa, the recovery ratio did not increase significantly, which indicates that the interfacial tension between crude oil and CO_2 disappeared under this pressure and they reached a miscible state. Therefore, the MMP between crude oil and CO_2 system in the study area predicted by the long slim tube displacement experiment method was 29.6 MPa.

CONCLUSION

The crude oil used in the experiment was the simulated crude oil prepared with the ground crude oil and natural gas in the study area according to the formation conditions and fluid characteristics. The experiment was carried out in accordance with the petroleum and natural gas industry standard of the People's Republic of China "Measurement Method for Minimum Miscible Pressure by Slim Tube Test" (SY/T 6573-2016). The experimental results show the recovery ratio increased with the increase of CO_2 injection amount at different experimental pressures. When the experimental pressure was 20 and 25 MPa, the recovery ratio increased slightly after the CO_2 injection amount was greater than 1.0 PV. When the experimental pressure was 30, 35, 35, and 40 MPa, the recovery ratio increased insignificantly after the CO_2 injection amount was greater than 0.9 PV. When the experimental pressure was 20 and 25 MPa, the corresponding recovery ratio was lower than 90%, indicating that the CO_2 flooding under these pressures was immiscible; when the experimental pressure was above 30 MPa, the corresponding recovery ratio was above 90%, indicating that the miscible flooding can be formed by CO_2 flooding under the pressure of more than 30 MPa. The relation curve between recovery ratio and experimental pressure was plotted, and it shows that the oil recovery at CO_2 injection of 1.2 PV increased with the increase of experimental pressure, and the immiscible flooding stage and miscible flooding stage intersected at 29.6 MPa. When the experimental pressure was higher than 29.6 MPa, the oil recovery did not increase significantly. Therefore, the MMP between crude oil and CO_2 system in the study area determined by the long-slim-tube displacement experiment was 29.6 MPa. The results show that miscible flooding can be formed in the study area when the reservoir pressure is greater than 29.6 MPa; otherwise, it is

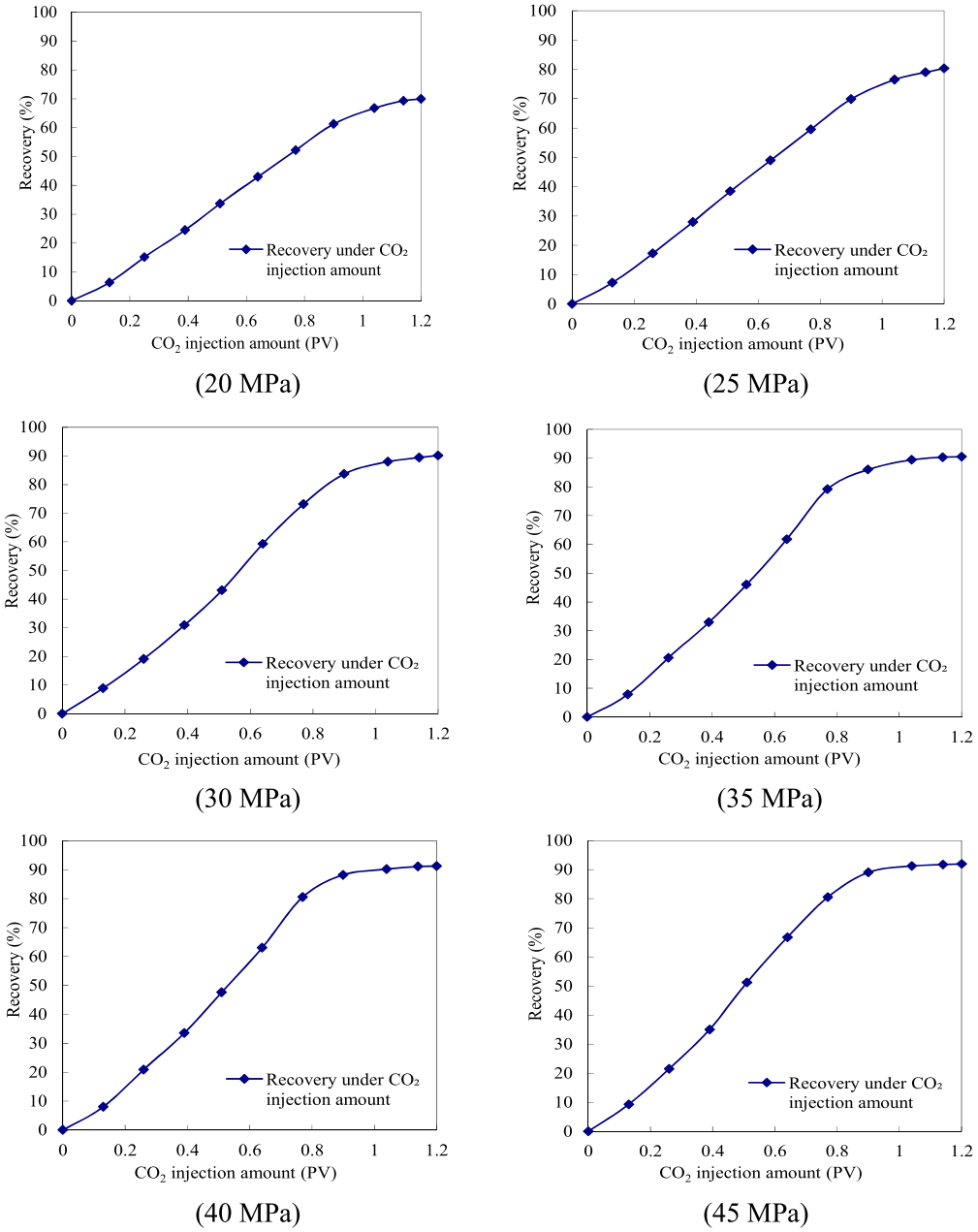

FIGURE 2 | Relationship diagram between recovery ratio and CO_2 injection amount under different pressures.

TABLE 4 | The long-slim-tube displacement experiment results of crude oil for injecting CO_2.

Experimental temperature (°C)	Experimental pressure (MPa)	Recovery ratio at 1.2 PV (%)	Miscible evaluation
108.5	20	69.90	Immiscible
108.5	25	80.35	Immiscible
108.5	30	90.15	Miscible
108.5	35	90.50	Miscible
108.5	40	91.22	Miscible
108.5	45	91.90	Miscible

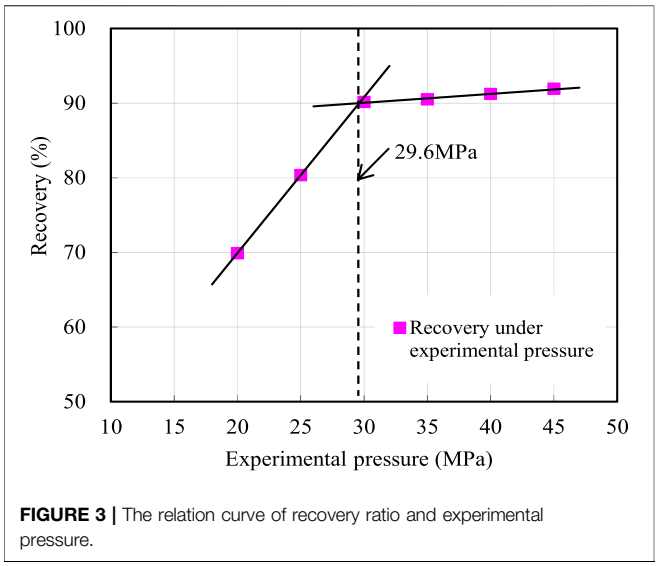

FIGURE 3 | The relation curve of recovery ratio and experimental pressure.

impossible to achieve miscible flooding. The research results are applicable to oilfields with similar crude oil properties and CO_2 properties.

DATA AVAILABILITY STATEMENT

The original contributions presented in the study are included in the article/Supplementary Material; further inquiries can be directed to the corresponding author.

AUTHOR CONTRIBUTIONS

GF and YZ contributed to conception and design of the study. XZ and YL organized the database. YZ, XZ, YL, and HC carried out the long-slim-tube displacement experiment. XZ, YL, and HC performed the statistical analysis. GF and YZ wrote the first draft of the manuscript. GF, YZ, XZ, YL, and HC wrote sections of the manuscript. All authors contributed to manuscript revision and read and approved the submitted version.

FUNDING

This work was financially supported by the National Natural Science Foundation of China (42002154 and 51834005), the Natural Science Foundation of Heilongjiang Province (E2016008 and QC2016055), the PetroChina Innovation Foundation (2020D-5007-0213), the Youths Science Foundation of Northeast Petroleum University (2019QNL-15), and the Open Fund Project of Heilongjiang Key Laboratory of Oil and Gas Reservoir Formation Mechanism and Resource Evaluation (KL20190101).

ACKNOWLEDGMENTS

The authors would like to thank the editor and the reviewers of this paper for their valuable comments that helped improve the quality of the paper.

REFERENCES

Abdalla, A. M. A., By, Zulkefli., and Abdurahman, H. N. (2014). Enhanced Oil Recovery Techniques Miscible and Immiscible Flooding. *J. Appl. Sci.* 14 (10), 1016–1022.

Adekunle, O. (2014). Master Thesis of the Colorado School of Mines. Experimental Approach to Investigate Minimum Miscibility Pressures in the Bakken

Ahmadi, M. A., Zendehboudi, S., and James, L. A. (2017). A Reliable Strategy to Calculate Minimum Miscibility Pressure of CO_2-oil System in Miscible Gas Flooding Processes. *Fuel* 208, 117–126. doi:10.1016/j.fuel.2017.06.135

Alomair, O., and Iqbal, M. (2014). *SPE Saudi Arabia Section Technical Symposium and Exhibition*. Saudi Arabia: Al-Khobar. CO_2 Minimum Miscible Pressure MMP Estimation Using Multiple Linear Regression MLR Technique. doi:10.2118/172184-MS

Alston, R. B., Kokolis, G. P., and James, C. F. (1985). CO_2 Minimum Miscibility Pressure: A Correlation for Impure CO_2 Streams and Live Oil Systems. *Soc. Pet. Eng. J.* 25 (02), 268–274. doi:10.2118/11959-pa

Azizkhani, A., and Gandomkar, A. (2020). A Novel Method for Application of Nanoparticles as Direct Asphaltene Inhibitors during Miscible CO_2 Injection. *J. Pet. Sci. Eng.* 185, 106661. doi:10.1016/j.petrol.2019.106661

Berneti, S. M., and Varaki, M. A. (2018). Development of ε-insensitive Smooth Support Vector Regression for Predicting Minimum Miscibility Pressure in CO_2 Flooding. *Songklanakarin J. Sci. Technol.* 40 (1), 53–59.

Birdja, Y. Y., Pérez-Gallent, E., Figueiredo, M. C., Göttle, A. J., Calle-Vallejo, F., and Koper, M. T. M. (2019). Advances and Challenges in Understanding the Electrocatalytic Conversion of Carbon Dioxide to Fuels. *Nat. Energ.* 4, 732–745. doi:10.1038/s41560-019-0450-y

Chen, G., Gao, H., Fu, K., Zhang, H., Liang, Z., and Tontiwachwuthikul, P. (2020). An Improved Correlation to Determine Minimum Miscibility Pressure of CO_2-oil System. *Green. Energ. Environ.* 5, 97–104. doi:10.1016/j.gee.2018.12.003

Chen, G. Y. (2016). *Simulation Prediction and Experimental Determination of CO_2-oil Minimum Miscibility Pressure*. Changsha, China: Doctoral dissertation of Hunan University.

Choubineh, A., Mousavi, S. R., Vafaee Ayouri, M., Ahmadinia, M., Choubineh, D., and Baghban, A. (2016). Estimation of the CO_2-oil Minimum Miscibility Pressure for Enhanced Oil Recovery. *Pet. Sci. Tech.* 34 (22), 1847–1854. doi:10.1080/10916466.2016.1238936

Cronquist, C. (1978). *Carbon Dioxide Dynamic Miscibility with Light Reservoir Oils. Proc*. Tulsa: Fourth Annual US DOE Symposium, 28–30.

Dong, M., Huang, S., Dyer, S. B., and Mourits, F. M. (2001). A Comparison of CO_2 Minimum Miscibility Pressure Determinations for Weyburn Crude Oil. *J. Pet. Sci. Eng.* 31 (1), 13–22. doi:10.1016/s0920-4105(01)00135-8

Ekundayo, J. M., and Ghedan, S. G. (2013). Minimum Miscibility Pressure Measurement with Slim Tube Apparatus - How Unique Is the Value. *SPE* 165966. doi:10.2118/165966-ms

Elsharkawy, A. M., Poettmann, F. H., and Christiansen, R. L. (1996). Measuring CO_2 Minimum Miscibility Pressures: Slim-Tube or Rising-Bubble Method? *Energy Fuels* 10 (2), 443–449. doi:10.1021/ef940212f

Fathinasab, M., Ayatollahi, S., Taghikhani, V., and Shokouh, S. P. (2018). Minimum Miscibility Pressure and Interfacial Tension Measurements for N2 and CO_2 Gases in Contact with W/O Emulsions for Different Temperatures and Pressures. *Fuel* 225, 623–631. doi:10.1016/j.fuel.2018.03.134

Fazlali, A., Nikookar, M., Agha-Aminiha, A., and Mohammadi, A. H. (2013). Prediction of Minimum Miscibility Pressure in Oil Reservoirs Using a Modified SAFT Equation of State. *Fuel* 108, 675–681. doi:10.1016/j.fuel.2012.12.091

Ghorbani, M., Gandomkar, A., and Montazeri, G. (2019). Describing a Strategy to Estimate the CO_2-heavy Oil Minimum Miscibility Pressure Based on the Experimental Methods. *Energy Sourc. A: Recovery, Utilization, Environ. Effects* 41 (17), 2083–2093. doi:10.1080/15567036.2018.1549170

Ghorbani, M., Momeni, A., Safavi, S., and Gandomkar, A. (2014). Modified Vanishing Interfacial Tension (VIT) Test for CO_2-oil Minimum Miscibility Pressure (MMP) Measurement. *J. Nat. Gas Sci. Eng.* 20, 92–98. doi:10.1016/j.jngse.2014.06.006

Glaso, O. (1985). Generalized Minimum Miscibility Pressure Correlation (Includes Associated Papers 15845 and 16287). *Soc. Pet. Eng. J.* 25 (06), 927–934. doi:10.2118/12893-pa

Gong, H., Qin, X., Shang, S., Zhu, C., Xu, L., San, Q., et al. (2020). Enhanced Shale Oil Recovery by the Huff and Puff Method Using CO_2 and Cosolvent Mixed Fluids. *Energy Fuels* 34, 1438–1446. doi:10.1021/acs.energyfuels.9b03423

Gunde, A. C., Bera, B., and Mitra, S. K. (2010). Investigation of Water and CO_2 (Carbon Dioxide) Flooding Using Micro-CT (Micro-computed Tomography) Images of Berea sandstone Core Using Finite Element Simulations. *Energy* 35 (12), 5209–5216. doi:10.1016/j.energy.2010.07.045

Guo, P., Hu, Y., Qin, J., Li, S., Jiao, S., Chen, F., et al. (2017). Use of Oil-Soluble Surfactant to Reduce Minimum Miscibility Pressure. *Pet. Sci. Tech.* 35 (4), 345–350. doi:10.1080/10916466.2016.1259630

Guo, X. Q., Rong, S. X., Yang, J. T., and Guo, T. M. (1999). The Viscosity Model Based on PR Equation of State. *Acta Petrolei Sinica* 20 (3), 56–61.

Han, H. S., Li, S., and Chen, X. L. (2016). Main Control Factors of Carbon Dioxide on Swelling Effect of Crude Hydrocarbon Components. *Acta Petrolei Sinica* 37 (3), 392–398.

Han, P. H., Jiang, Y. L., and Zhang, J. C. (1989). Prediction of CO_2 Minimum Miscibility Pressure for Daqing Petroleum. *Oilfield Chem.* 6 (4), 309–316.

Hao, Y. M., Chen, Y. M., and Yu, H. L. (2005). Determination and Prediction of Minimum Miscibility Pressure in CO_2 Flooding. *Pet. Geology. Recovery Efficiency* 12 (6), 64–66.

Jalilov, A. S., Li, Y., Kittrell, C., and Tour, J. M. (2017). Increased CO_2 Selectivity of Asphalt-Derived Porous Carbon through Introduction of Water into Pore Space. *Nat. Energ.* 2, 932–938. doi:10.1038/s41560-017-0030-y

Johnson, J. P., and Pollin, J. S. (1981). Measurement and Correlation of CO_2 Miscibility Pressures. *SPE/DOE* 9790, 269–274.

Kamari, A., Arabloo, M., Shokrollahi, A., Gharagheizi, F., and Mohammadi, A. H. (2015). Rapid Method to Estimate the Minimum Miscibility Pressure (MMP) in Live Reservoir Oil Systems during CO 2 Flooding. *Fuel* 153, 310–319. doi:10.1016/j.fuel.2015.02.087

Kariman Moghaddam, A., and Saeedi Dehaghani, A. H. (2017). Modeling of Asphaltene Precipitation in Calculation of Minimum Miscibility Pressure. *Ind. Eng. Chem. Res.* 56, 7375–7383. doi:10.1021/acs.iecr.7b00613

Kaufmann, R. K., and Connelly, C. (2020). Oil price Regimes and Their Role in price Diversions from Market Fundamentals. *Nat. Energ.* 5, 141–149. doi:10.1038/s41560-020-0549-1

Kolster, C., Masnadi, M. S., Krevor, S., Mac Dowell, N., and Brandt, A. R. (2017). CO_2 Enhanced Oil Recovery: a Catalyst for Gigatonne-Scale Carbon Capture and Storage Deployment? *Energy Environ. Sci.* 10, 2594–2608. doi:10.1039/c7ee02102j

Lewis, E. (2008). *Sweep Efficiency in Miscible Enhanced Oil Recovery Processes*. Houston, TX: Doctoral Degree Dissertation of University of Houston.

Li, B. F., Ye, J. Q., Li, Z. M., Ji, Y. M., and Liu, W. (2016). Phase Interaction of CO_2-oil-water System and its Effect on Interfacial Tension at High Temperature and High Pressure. *Acta Petrolei Sinica* 37 (10), 1265–1272.

Li, D., Li, X., Zhang, Y., Sun, L., and Yuan, S. (2019). Four Methods to Estimate Minimum Miscibility Pressure of CO 2 -Oil Based on Machine Learning. *Chin. J. Chem.* 37, 1271–1278. doi:10.1002/cjoc.201900337

Li, H., Qin, J., and Yang, D. (2012). An Improved CO_2-Oil Minimum Miscibility Pressure Correlation for Live and Dead Crude Oils. *Ind. Eng. Chem. Res.* 51 (8), 3516–3523. doi:10.1021/ie202339g

Li, M. T. (2006). Laboratory Researches on Gas Injection and Porous Flow Mechanics for Low Permeability Reservoirs. Beijing, China: Doctoral Degree Dissertation of Chinese Academy of Science.

Li, X. L., Guo, P., Li, H. C., and Li, X. S. (2002). Determination of Minimum Miscibility Pressure between Formation Crude and Carbon Dioxide in Fan 124 Block of Daluhu Oilfield. *Pet. Geology. Recovery Efficiency* 9 (6), 62–63.

Ma, M., Liu, K., Shen, J., Kas, R., and Smith, W. A. (2018). *In Situ* Fabrication and Reactivation of Highly Selective and Stable Ag Catalysts for Electrochemical CO_2 Conversion. *ACS Energ. Lett.* 3, 1301–1306. doi:10.1021/acsenergylett.8b00472

Measurement Method For Minimum Miscibility Pressure By Slim Tube Test (2016). Petroleum and Natural Gas Industry Standard of the People's Republic of China, 6573–2016.

Mogensen, K. (2016). A Novel Protocol for Estimation of Minimum Miscibility Pressure from Slimtube Experiments. *J. Pet. Sci. Eng.* 146, 545–551. doi:10.1016/j.petrol.2016.07.013

Mutailipu, M., Jiang, L., Liu, X., Liu, Y., and Zhao, J. (2019). CO_2 and Alkane Minimum Miscible Pressure Estimation by the Extrapolation of Interfacial Tension. *Fluid Phase Equilibria* 494, 103–114. doi:10.1016/j.fluid.2019.05.002

Orr, F. M., and Silva, M. K. (1987). Effect of Oil Composition on Minimum Miscibility Pressure-Part 2: Correlation. *SPE* 2, 479–491. doi:10.2118/14150-pa

Oschatz, M., and Antonietti, M. (2018). A Search for Selectivity to Enable CO_2 Capture with Porous Adsorbents. *Energ. Environ. Sci.* 11, 57–70. doi:10.1039/c7ee02110k

Peng, B. Z., Luo, H., Chen, G. J., and Zhang, C. Y. (2007). Determination of the Minimum Miscibility Pressure of CO_2 and Crude Oil System by Vanishing Interfacial Tension Method. *Acta Petrolei Sinica* 28 (3), 93–95.

Qin, J. S., Han, H. S., and Liu, X. L. (2015). Application and Enlightenment of Carbon Dioxide Flooding in the United States of America. *Petrol. Explor. Dev.* 42 (2), 209–216. doi:10.1016/s1876-3804(15)30010-0

Richard, A. H., and Reid, B. G. (1988). Vapor-density Measurement for Estimating Minimum Miscibility Pressure. *SPE* 15403.

Rostami, A., Arabloo, M., Lee, M., and Bahadori, A. (2018). Applying SVM Framework for Modeling of CO_2 Solubility in Oil during CO_2 Flooding. *Fuel* 214, 73–87. doi:10.1016/j.fuel.2017.10.121

Shao, Y., Luo, C., Deng, B.-w., Yin, B., and Yang, M.-b. (2020). Flexible Porous Silicone Rubber-Nanofiber Nanocomposites Generated by Supercritical Carbon Dioxide Foaming for Harvesting Mechanical Energy. *Nano Energy* 67, 104290. doi:10.1016/j.nanoen.2019.104290

Shokrollahi, A., Arabloo, M., Gharagheizi, F., and Mohammadi, A. H. (2013). Intelligent Model for Prediction of CO_2 - Reservoir Oil Minimum Miscibility Pressure. *Fuel* 112, 375–384. doi:10.1016/j.fuel.2013.04.036

Silva, M. K., and Orr, F. M. (1987). Effect of Oil Composition on Minimum Miscibility Pressure-Part 1: Solubility of Hydrocarbons in Dense CO_2. *SPE* 2, 468–478. doi:10.2118/14149-pa

Sun, Y. H., Lv, G. Z., Wang, Y. F., and Dong, A. Q. (2006). A Method of State Equation for Determining Minimum Miscibility Pressure of CO_2. *Pet. Geology. Recovery Efficiency* 13 (1), 82–84.

Tatar, A., Shokrollahi, A., Mesbah, M., Rashid, S., Arabloo, M., and Bahadori, A. (2013). Implementing Radial Basis Function Networks for Modeling CO_2-reservoir Oil Minimum Miscibility Pressure. *J. Nat. Gas Sci. Eng.* 15, 82–92. doi:10.1016/j.jngse.2013.09.008

Tian, Y., Ju, B., Yang, Y., Wang, H., Dong, Y., Liu, N., et al. (2020). Estimation of Minimum Miscibility Pressure during CO_2 Flooding in Hydrocarbon Reservoirs Using an Optimized Neural Network. *Energy Exploration & Exploitation* 38 (6), 2485–2506. doi:10.1177/0144598720930110

Wu, S., He, J., and Li, Z. Z. (2015). Studies on the Chemical Agent System for Reducing in the Minimal Miscibility Pressure of CO_2 Flooding. *China Sciencepaper* 10 (18), 2161–2164.

Wu, S., Li, Z., and Sarma, H. K. (2020). Influence of Confinement Effect on Recovery Mechanisms of CO_2-enhanced Tight-Oil Recovery Process Considering Critical Properties Shift, Capillarity and Adsorption. *Fuel* 262, 116569. doi:10.1016/j.fuel.2019.116569

Yang, Z. M., Liu, X. W., and Zhang, Z. H. (2015). Physical Simulation of Staged-Fracturing Horizontal wells Using CO_2 Huff and Puff in Tight Oil Reservoirs. *Acta Petrolei Sinica* 36 (6), 724–729.

Yang, Z., Wu, W., Dong, Z., Lin, M., Zhang, S., and Zhang, J. (2019). Reducing the Minimum Miscibility Pressure of CO_2 and Crude Oil Using Alcohols. *Colloids Surf. A: Physicochemical Eng. Aspects* 568, 105–112. doi:10.1016/j.colsurfa.2019.02.004

Ye, A. P. (2009). Experience Formula of Determining Minimum Miscibility Pressure in CO_2 Flooding. *Fault-block Oil & Gas Field* 16 (5), 75–76.

Ye, A. P., Guo, P., Wang, S. P., Cheng, Z. Z., and Jian, R. (2012). Determination of Minimum Miscibility Pressure for CO_2 Flooding by Using PR Equation of State. *Lithologic Reservoirs* 24 (6), 125–128.

Yellig, W. F., and Metcalfe, R. S. (1980). Determination and Prediction of CO_2 Minimum Miscibility Pressures (Includes Associated Paper 8876). *J. Pet. Tech.* 32 (1), 160–168. doi:10.2118/7477-pa

Yi, R. (2000). A New Method for Determining the Minimum Miscibility Pressure. *Oil Drilling Prod. Tech.* 22 (4), 72.

Yu, H., Lu, X., Fu, W., Wang, Y., Xu, H., Xie, Q., et al. (2020). Determination of Minimum Near Miscible Pressure Region during CO_2 and Associated Gas Injection for Tight Oil Reservoir in Ordos Basin, China. *Fuel* 263, 116737. doi:10.1016/j.fuel.2019.116737

Yuan, H., Johns, R. T., Egwuenu, A. M., and Dindoruk, B. (2005). Improved MMP Correlation for CO_2 Floods Using Analytical Theory. *SPE Reservoir Eval. Eng.* 8 (05), 418–425. doi:10.2118/89359-pa

Zhang, A., Fan, Z., and Zhao, L. (2020). An Investigation on Phase Behaviors and Displacement Mechanisms of Gas Injection in Gas Condensate Reservoir. *Fuel* 268, 117373. doi:10.1016/j.fuel.2020.117373

Zhang, C. Y., Wang, W. Q., Chen, G. J., and Ma, C. F. (2006). Interfacial Tension experiment of Oil and Water, Oil and Gas for CO_2 Injected Reservoir Fluid System. *J. China Univ. Pet.* 30 (5), 109–112.

Zhang, G. D., Li, Z. Y., Liu, J. Y., Zhang, X., Xu, J. J., and Gao, P. (2008). Study on Determine Methods of Minimum Miscibility Pressure of Hydrocarbon Injection Miscible Flooding. *Drilling Prod. Tech.* 31 (3), 99–102.

Zhang, J., Zhang, H. X., Ma, L. Y., Liu, Y., and Zhang, L. (2020). Performance Evaluation and Mechanism with Different CO_2 Flooding Modes in Tight Oil Reservoir with Fractures. *J. Pet. Sci. Eng.* 188, 106950. doi:10.1016/j.petrol.2020.106950

Zhang, K., and Gu, Y. (2015). Two Different Technical Criteria for Determining the Minimum Miscibility Pressures (MMPs) from the Slim-Tube and Coreflood Tests. *Fuel* 161, 146–156. doi:10.1016/j.fuel.2015.08.039

Zhou, N., Khanna, N., Feng, W., Ke, J., and Levine, M. (2018). Scenarios of Energy Efficiency and CO_2 Emissions Reduction Potential in the Buildings Sector in China to Year 2050. *Nat. Energ.* 3, 978–984. doi:10.1038/s41560-018-0253-6

Zuo, Y.-x., Chu, J.-z., Ke, S.-l., and Guo, T.-m. (1993). A Study on the Minimum Miscibility Pressure for Miscible Flooding Systems. *J. Pet. Sci. Eng.* 8 (4), 315–328. doi:10.1016/0920-4105(93)90008-3

Conflict of Interest: The authors declare that the research was conducted in the absence of any commercial or financial relationships that could be construed as a potential conflict of interest.

frontiers in Earth Science

ORIGINAL RESEARCH
published: 25 October 2021
doi: 10.3389/feart.2021.752954

Characteristics and Origin of Organic Matter in Triassic Lacustrine Shale From Fuxian Oilfield

*Fan Bojiang**

School of Petroleum Engineering and Environmental Engineering, Yan'an University, Yan'an, China

Along with the successful exploitation of shale oil, organic-rich shale has attracted great attention to the geologists. However, quantitatively differentiating the origin of organic matter in shale is still challenging due to the nature of its complex depositional processes. Organic matter in lacustrine shales could be derived from both lake water (produced by lake water column) and land input (transported into the lake by rivers). The Triassic Chang-7 shale in the Yanchang Formation is a typical lacustrine shale deposited in the central part of the Ordos Basin. It is rich in organic matter (TOC of 0.52–9.37%) and consists primarily of type II_1 kerogen. The Chang-7 shale is thermally mature and currently in the stage of generating oil and gas, with more structured than organic matter. In this study, quantitative models of organic matter in the Chang-7 shale with sources from both lake water and land is established using geochemical and carbon isotopes data and the results show that lake water and land input have the almost equal contribution to the organic enrichment in the study area.

Keywords: lacustrine shale, organic matters, different origins, mathematical model, fuxian oilfield

OPEN ACCESS

Edited by:
Yuwei Li,
Liaoning University, China

Reviewed by:
Yangyang Li,
C&C Reservoirs, United States
Bo Liu,
Northeast Petroleum University, China
Yingchun Guo,
Chinese Academy of Geologi-cal Sciences (CAGS), China

***Correspondence:**
Fan Bojiang
632258611@qq.com

Specialty section:
This article was submitted to Economic Geology, a section of the journal Frontiers in Earth Science

Received: *04 August 2021*
Accepted: *20 September 2021*
Published: *25 October 2021*

Citation:
Bojiang F (2021) Characteristics and Origin of Organic Matter in Triassic Lacustrine Shale From Fuxian Oilfield. Front. Earth Sci. 9:752954. doi: 10.3389/feart.2021.752954

INTRODUCTION

Along with the successful exploitation of shale oil, organic-rich shale has attracted more and more attention to the petroleum geologists (Fink et al., 2018; Awan et al., 2020). Previous researchers have done a lot of investigation on the conditions of organic matter enrichment, and established corresponding interpretational models. The most popular models include: 1) organic matter is easy to be preserved in reducing environments, thus the enrichment of organic matter is related to reducing environment (Awan et al., 2020); 2) the higher the paleo-productivity is, the more organic matter can be provided, thus the enrichment of organic matter is related to paleo-productivity (Liu et al., 2017); 3) the enrichment of organic matter depends on both reducing environment and paleo-productivity (Demaison and Moore, 1980).

There is little doubt that the development of organic-rich shale is mainly controlled by sedimentary environments. Organic-rich shale tends to be deposited and preserved under conditions of anoxic water column, high primary productivity and rapid burial rate (Henderson, 2004; Piper and Perkins, 2004; Keighley et al., 2018). However, if a stable supply of organic matter exists, organic-rich shale can also be deposited in a relatively oxidized environment (Abaturov et al., 2018).

In the central part of the Ordos Basin, the Triassic Yanchang Formation was deposited in a lacustrine environment, and a set of organic-rich shales are developed within the Chang-7 member (i.e., Chang-7 shale) (**Figure 1**) (Fan and Shi, 2019). The Chang-7 shale is characterized by high organic matter content and good hydrocarbon generation potential. However, it is relatively thin,

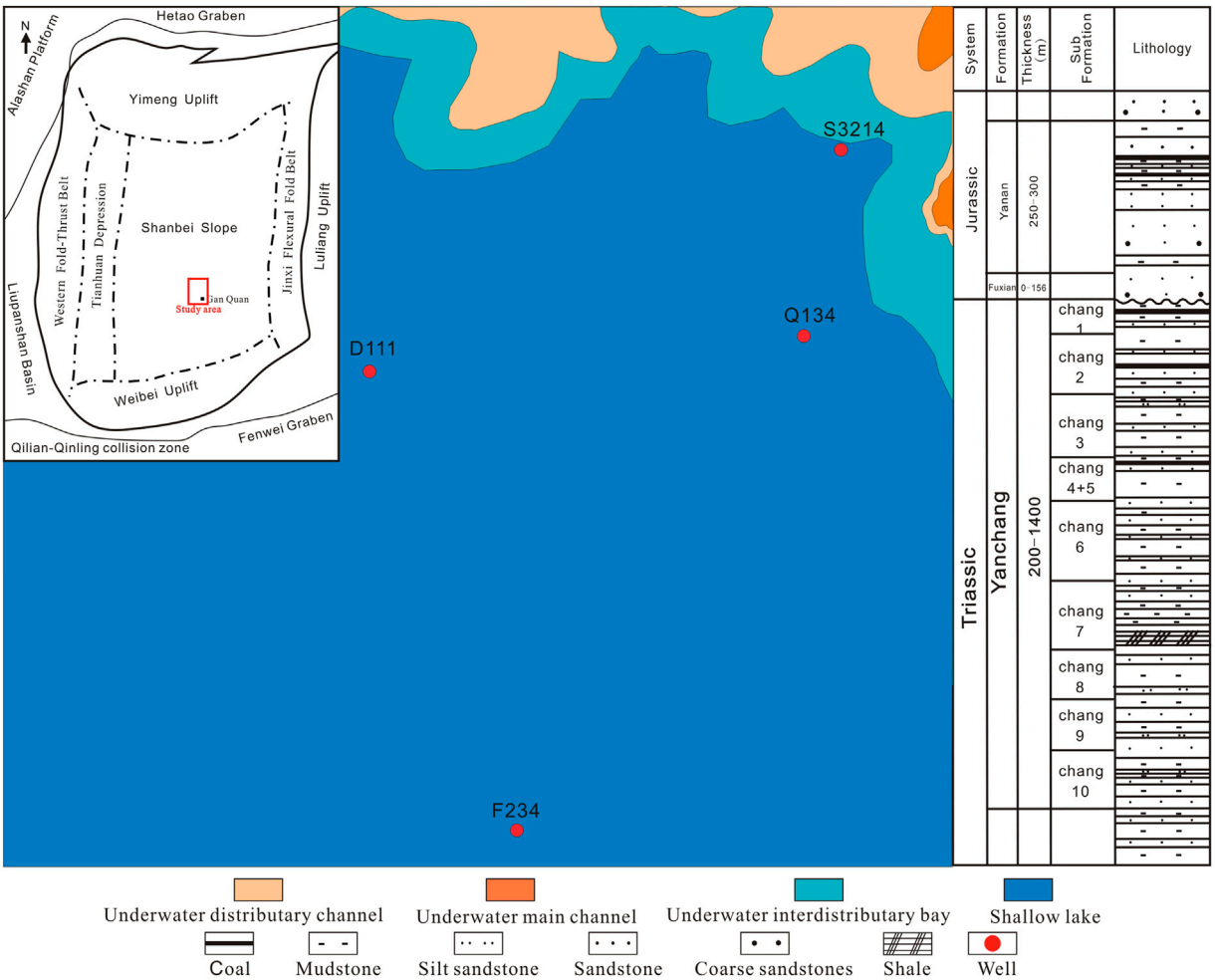

FIGURE 1 | Map showing the location and paleogeography of the study area. A stratigraphic and lithological column of Triassic Chang-7 shale as part of the Yanchang Formation is also shown on the right.

having thicknesses of only 2–10 m). Since 2016, three exploration wells in the study area have obtained industrial oil flow in the Chang-7 shale, and the average daily production rate is > 7 BOPD. Organic matter in the Chang-7 shale are sourced from both the lake-water column and terrestrial input transported by rivers. Therefore, to determine the contributions from each of the sources in a quantitative way, a mathematical model is established to characterized organic matter in the Chang-7 shale in the central part of the Ordos Basin (**Figure 1**).

Whole rock X-ray diffraction (XRD) measurements are carried out to obtain the mineral compositions of the Chang-7 shale, and the measured values of 17 samples vary greatly (**Table 1**). Clay minerals in the Chang-7 shale ranges 27.8–70.3% (average 54.95%). Quartz ranges 12.9–29.3%, (average 19.7%). K-feldspar content ranges 1.1–5.3% (average 3.3%). Plagioclase ranges 4.9–27.9% (average 12.5%). Pyrite ranges 0.5–16.2% (average 3.6%). These figures indicate that the Chang-7 shale contains a high content of clay minerals but low content of brittle minerals (e.g., quartz, feldspar and plagioclase).

CHARACTERISTICS OF ORGANIC MATTERS

Microscopic Characteristics

Organic matter in the Chang-7 shale can be classified into two types based on their morphology through microscopic observations: morphological organic matter and amorphous organic matter. Among the 27 samples in the study area, 24 have morphological organic matter and only 3 have amorphous organic matter. The morphological organic matter often develops in the homogeneous pure shale, while the amorphous organic matter often develops in the sandy shales. Analysis of the energy spectrum images shows that there are great differences in their compositions within different types of organic matter. In morphological organic matter, carbon content is always higher than that of other elements (**Figures 2A,B**), while in amorphous organic matter, the contents of Si, Al and other elements can be higher than that of carbon element (**Figures 2C,D**).

TABLE 1 | Mineral compositions of Chang-7 shale.

Well	Burial depth (m)	Minerals (%)						
		Quartz	K-feldspar	Plagioclase	Calcite	Pyrite	Clay	Others
Q71	1,434.9	29.3	5.2	27.9	9	—	27.8	30.1
D199	1,365.98	21.5	—	17.8	7	0.5	49	25.7
D199	1,372.83	13.1	1.8	13	1.5	16.2	45.8	21.7
D199	1,334.28	14	2.7	6.9	—	—	70.3	20.1
D199	1,352.98	19.5	5.3	16.4	1.9	—	54.5	21.9
Q71	1,422.22	19	3.1	13.1	3.1	3.2	51.3	26.2
Q71	1,429.82	24.6	3.4	14.5	0.4	4.4	45.3	32
D199	1,373.15	19.1	1.5	4.9	—	1.7	69.7	22.2
Q71	1,427.26	19.1	3.6	15	—	1.7	52.6	27.1
Q71	1,428.45	20	4.8	11.2	0.5	1.2	57.9	24.4
Q71	1,429.5	20.4	4.4	11.6	5.6	1.3	55.7	21.4
Q71	1,430.5	17.6	4	11.1	4.6	1.2	57.2	21.9
Q129	1,657.58	23.9	5.3	10.5	0.4	—	56.5	27.3
Q129	1,658.66	15.8	1.9	13	—	0.7	64.8	19.6
Q129	1,664.78	23.2	2.5	9.2	—	1.5	59.7	27.1
W100	2,009.43	12.9	1.6	7.1	1.7	7.5	63.9	18.2
W100	2,009.9	22.1	1.1	10	—	5.3	52.1	31.5

As the organic matter in the study area is mainly morphological, this study will focus on the morphological organic matter. Organic matter deposited in between brittle minerals is commonly filled with pyrite, some of which has organic pores (**Figures 3A–C**). However, organic pores are overall poorly developed in the 27 samples in the study area. Previous studies show that organic matter is commonly associated with pyrite in the Chang-7 shale of Ordos Basin as in this study, which is interpreted to have been mainly controlled by the paleo-water column (Er et al., 2016; Yuan et al., 2017). Organic matter deposited in between clay minerals has well-developed organic pores and no pyrite is observed (**Figures 3D–F**).

Organic matter can be highly enriched where brittle minerals and clay minerals are both in place (**Figures 3G–I**). It should be noted that organic matter in these places has the most developed organic pores compared with the organic matter in solely brittle mineral particles or clay minerals. In addition, intergranular pores and intragranular pores are better developed in places where brittle mineral particles and clay minerals are both developed (**Figures 3G–I**). Some scholars have explained this phenomenon using the hydrocarbon generation and expulsion processes (Tagiyev et al., 1997; Giliazetdinova et al., 2017). However, the current viewpoints on hydrocarbon generation and expulsion is highly controversial due to the complexity of this process (Mann, 1989; Huo et al., 2015). For example, the evolution process of organic matter during hydrocarbon generation has not been described in detail and the hydrocarbon expulsion processes have not been proved (Siddiqui and Lake, 1992; Rong, 2003; Alaug, 2011; Dong et al., 2014).

Organic Matter Abundance, Type and Maturity

A total of 25 shale samples were collected from 11 exploration wells in the study area for testing and analysis. The tests include measuring organic carbon content, rock pyrolysis parameters, and carbon isotope of shale carbonate. The organic carbon content was measured using Automatic Organic Carbon Analyzer (Vario TOC); the rock pyrolysis parameters were measured using Rock-eval 6 Pyrometer; the carbon isotopes were measured using Gas Isotope Ratio Mass Spectrometer (Thermo-finngan MAT253). The test results are shown in **Table 2**.

Total organic carbon in the study area ranges from 0.52 to 9.37% with an average of 2.85%. The samples with TOC < 2.00% account for 48.00% of the total samples; the samples with TOC < 4.00% account for 32.00% of the total samples; the samples with TOC > 4.00% account for 20.00% of the total samples.

Source rock with higher abundance of organic carbon commonly has higher ability in generating hydrocarbons. Therefore, total organic carbon content (TOC) is normally correlated positively with pyrolysis parameters such as free hydrocarbon (S_1) and pyrolytic hydrocarbon (S_2). A positive correlation between TOC and S_2 is also observed in the Chang-7 shale, and the value of S_2 increases along with the increase of TOC (**Figure 4**). However, S_1 has a poor correlation with TOC (**Figure 4**). Many researchers speculate that this is related to hydrocarbon migration within the source rock (Curtis, 2002) and argue that during the process of hydrocarbon generation and expulsion, free hydrocarbon migrates in a short distance, and the S_1 obtained in experiment cannot represent all the hydrocarbons generated *in-situ* (Zeng et al., 2006).

The organic matter in the Chang-7 shale contains type I, type II_1 and type II_2 kerogen. Among the total 25 samples, 16 of them (64%) contains type II_1 organic matter; while the other 9 samples (36%) contain type I and type II_2 organic matter. The maximum pyrolysis temperature of the Chang-7 shale in the study area ranges from 435 to 453°Cwith an average of 444°C, indicating that Chang-7 shale has entered mature stage and is generating oil and gas. Based on the cross plot of Hydrogen Index and Maximum Pyrolysis Temperature, the corresponding vitrinite reflectance is determined to be 0.5–1.2%, which confirms that the Chang-7 shale is in thermal maturity stage and generating oil and gas (**Figure 5**).

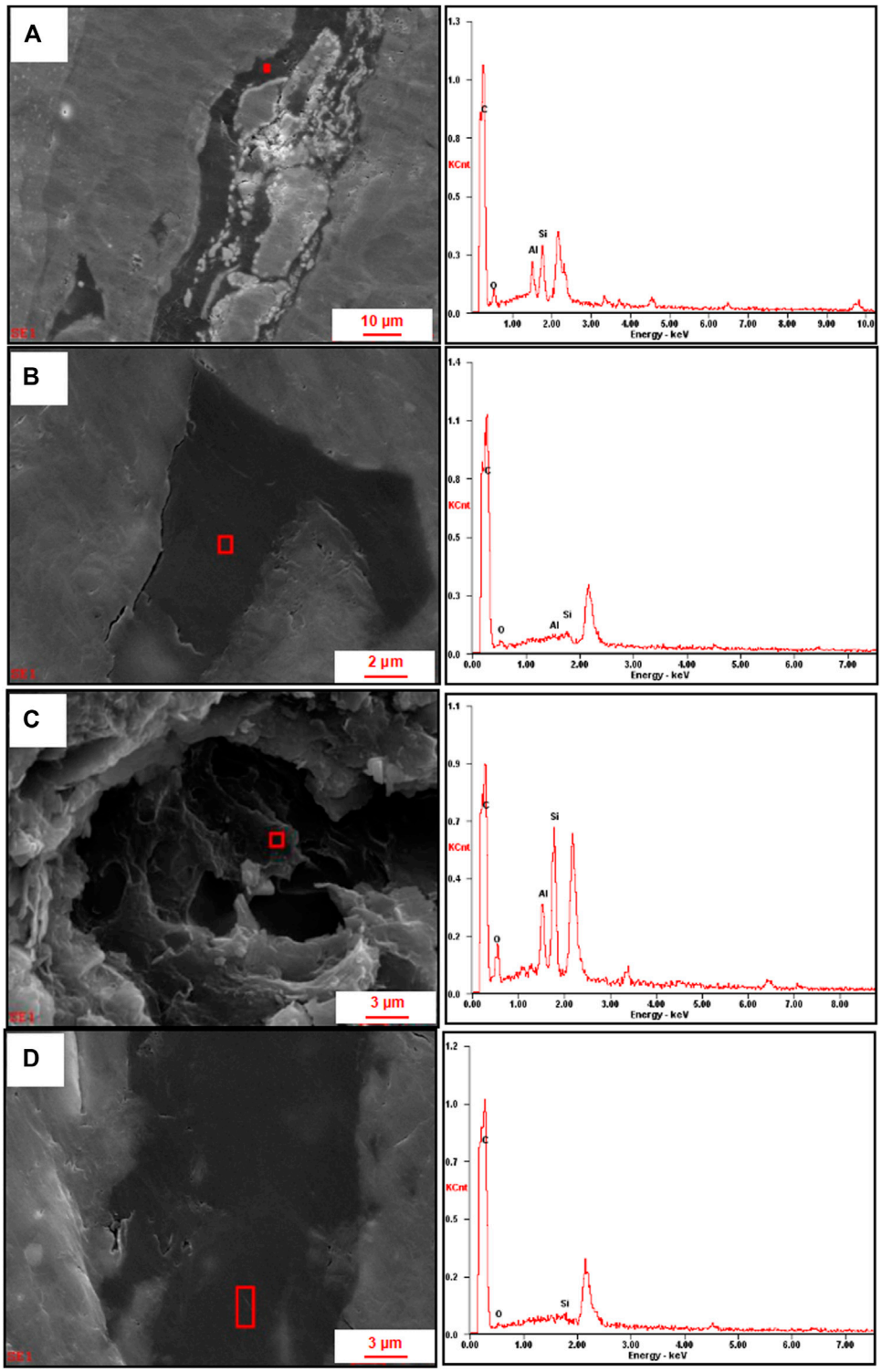

FIGURE 2 | SEM and EDS characteristics of organic matter **(A)** SEM and energy spectrum photos, showing morphological organic matter is filled with strawberry pyrite, Q129 well, 1667.48 m; **(B)** SEM and energy spectrum photos, showing morphological organic matter is filled with organic pores, Q129 well, 1667.48 m; **(C)** SEM and energy spectrum photos, showing coexistence of kaolinite and amorphous organic matter, D19 well, 1369.93 m; **(D)** SEM and energy spectrum photos, showing amorphous organic matter with organic pores, Q12 well, 1667.48 m.

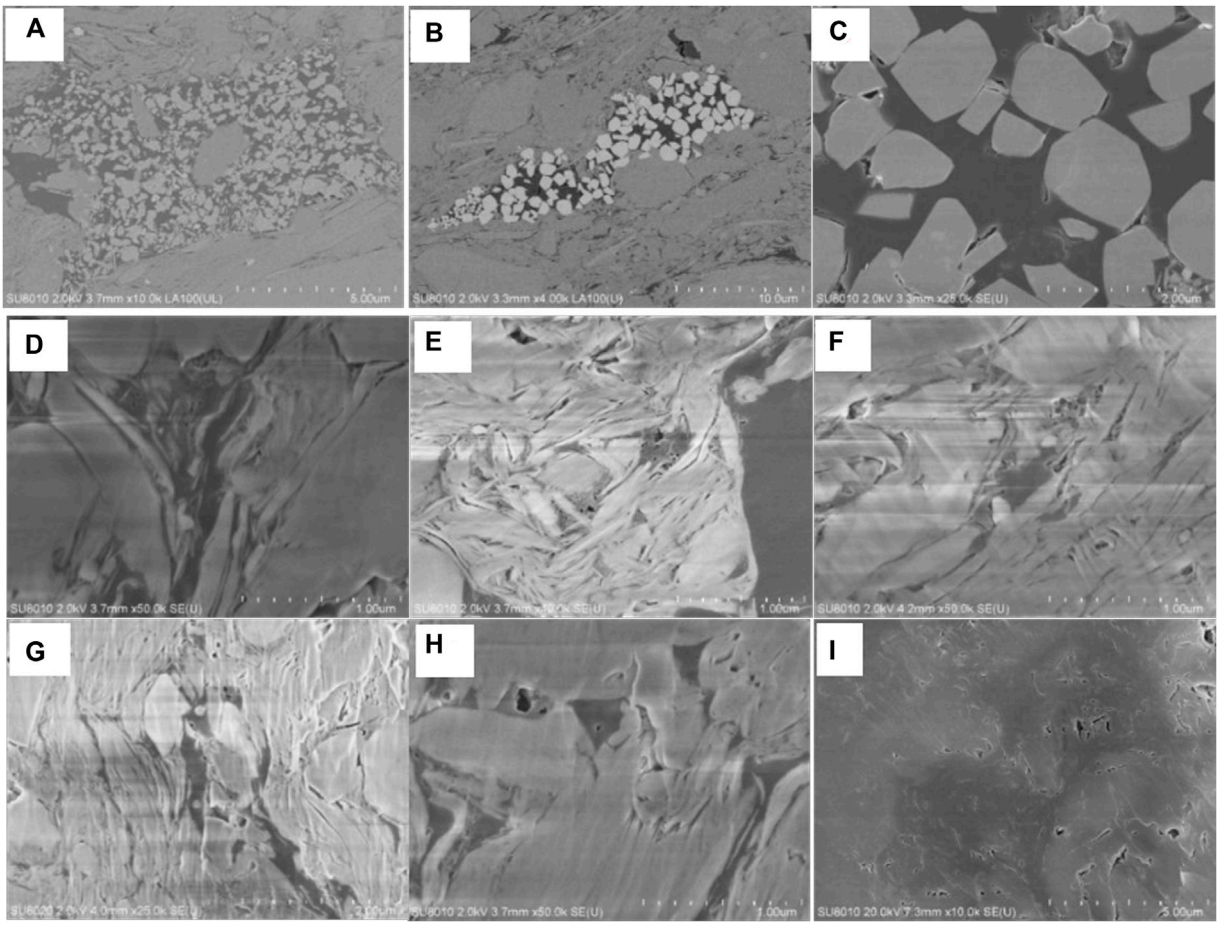

FIGURE 3 | Field emission SEM characteristics of organic matter **(A)** FE-SEM image showing pyrite and organic pores in organic matter, Q71 well, 1428.84 m; **(B)** FE-SEM image showing strawberry pyrite in organic matter, Q129 well, 1661.18 m; **(C)** FE-SEM image showing pyrite and organic pores in organic matter, Q129 well, 1661.18 m; **(D)** FE-SEM image showing organic matter with organic pores in clay minerals, Q71 well, 1428.84 m; **(E)** FE-SEM image showing organic matter with organic pores in clay minerals, Q71 well, 1428.84 m; **(F)** FE-SEM image showing organic matter with organic pores in clay minerals, Q71 well, 1427.94 m; **(G)** FE-SEM image showing organic matter in between clay minerals and brittle minerals, with highly developed intergranular pores, intragranular pores and organic pores, D199 well, 1372.59 m; **(H)** FE-SEM image showing organic matter in between clay minerals and brittle minerals, with highly developed intergranular pores, intragranular pores and organic pores, Q71 well, 1428.84 m; **(I)** FE-SEM image showing organic matter in between clay minerals and brittle minerals, with highly developed intergranular pores, intragranular pores and organic pores, W104 well, 1363.96 m.

Soluble hydrocarbons range 0.48–11.27 mg/g (average of 3.77 mg/g). Pyrolysis hydrocarbons range 1.66–18.75 mg/g (average 7.63 mg/g). Total hydrocarbon ranges 2.14–25.40 mg/g (average 11.40 mg/g). The hydrogen index ranges 117.51–678.85 mg/g (average 332.81 mg/g). Based on the organic matter abundance and type, thermal maturity, and pyrolysis parameters, the Chang-7 shale in the study area is regarded as a high-quality source rock.

Origins of Organic Matters

Organic matter in lacustrine shale could be derived from a lake water origin or terrestrial origin, or more commonly from both. Lake water contains a lot of nutrients, which feeds a large number of aquatic organisms that can reproduce in water. These aquatic organisms provide an important organic matter supply to the shale deposits (Liu et al., 2017; Liu et al., 2021). As fluvial and alluvial facies developed around the lake, a large number of terrestrial higher plants can be transported through rivers into the lake, which provides another important source of organic matter for lake sediments (Awan et al., 2020).

Based on core data and microscopic observations, the organic matter in the Chang-7 shale the study area are derived from both lake water and land input through river transportation. Core analysis shows that a large number of higher plant debris can be observed, which is a direct indicator of a terrestrial origin of the organic material (**Figures 6A,B**). Most of the higher plant debris in the Chang-7 shale is continuously distributed, which is probably due to the transportation of plants into the lake (**Figures 6C,D**). A large number of fish scale fossils can be found in the Chang-7 shale. These fish scales are mainly fan-shaped and angular-shaped, and their distribution tends to be clustered and patchy (**Figures 6E**). Complete fish fossils are also found occasionally in the Chang-7 shale (**Figures 6F**). The existence of fish, which require a large number of planktons

TABLE 2 | Geochemical parameters of organic matter in the Chang-7 shale.

Well	Burial depth (m)	TOC (%)	S_1 (mg/g)	S_2 (mg/g)	Tmax (°C)	HI (mg/g)	R	Q_1	Q_2	Q
D111	1,762.17	9.37	0.72	12.35	449	131.80	0.33	0.98	1.98	2.96
D314	1,107.23	2.57	2.83	3.02	452	117.51	0.51	0.91	0.87	1.78
S3214	1,143.27	5.14	1.14	6.12	453	119.07	0.43	0.89	1.18	2.08
D299	1,371.15	2.91	2.78	7.29	441	250.52	0.38	0.75	1.22	1.97
F234	1,557.24	1.63	2.36	4.14	442	253.99	0.47	0.88	0.99	1.86
D214	1,253.14	7.62	6.65	18.75	441	246.06	0.36	0.99	1.77	2.76
D121	1,149.36	2.17	4.73	6.73	438	310.14	0.42	0.89	1.23	2.13
Q200	1,380.68	6.69	2.65	16.42	439	245.44	0.36	0.79	1.41	2.20
D328	1,082.86	2.26	2.9	7.56	435	334.51	0.45	0.97	1.19	2.16
F234	1,561.54	3.42	1.93	12.37	439	361.70	0.55	0.96	0.79	1.75
F234	1,557.27	1.14	5.88	6.3	441	552.63	0.74	0.89	0.31	1.21
G178	1,609.24	2.59	1.26	10.85	437	418.92	0.6	0.85	0.57	1.42
D111	1,762.68	0.88	6.46	5.81	446	660.23	0.91	0.88	0.09	0.97
W436	1,960.57	1.67	2.65	9.06	447	542.51	0.87	0.86	0.13	0.99
F234	1,562.39	1.79	3.39	12.06	448	673.74	0.93	0.91	0.07	0.98
G178	1,609.19	2.67	9.65	10.82	436	405.24	0.6	0.85	0.57	1.42
Q200	1,378.78	0.74	0.48	1.66	439	224.32	0.57	0.90	0.68	1.58
D299	1,353.12	1.82	4.05	7.18	444	394.51	0.68	0.80	0.38	1.18
D299	1,364.78	0.84	1.65	3.74	447	445.24	0.72	0.92	0.36	1.27
F234	1,596.4	4.71	7.39	9.71	446	206.16	0.42	0.92	1.28	2.20
F234	1,560.78	2.56	3.74	4.74	449	185.16	0.63	0.92	0.54	1.47
Q301	1,699.73	1.33	2.93	2.63	445	197.74	0.52	0.93	0.86	1.79
Q246	1,646.76	0.52	11.27	3.53	446	678.85	0.93	0.86	0.06	0.92
W200	1,891.36	1.96	1.74	2.45	445	125.00	0.35	0.92	1.70	2.61
Q134	1,231.26	2.34	2.93	5.6	446	239.32	0.56	0.98	0.77	1.75

Abbreviations: TOC, Total Organic Carbon; S1, Free Hydrocarbon; S2, Pyrolytic Hydrocarbon; Tmax, Maximum Pyrolysis Temperature; HI, Hydrogen Index; R, Water Organic Matter Ratio; Q_1, Water Organic Matter Index; Q_2, Land Organic Matter Index; Q, Total Organic Matter Index.

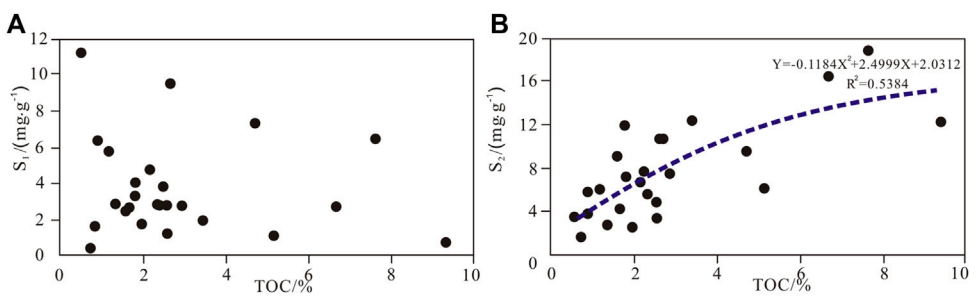

FIGURE 4 | Plots showing the relationship between TOC and pyrolysis parameters **(A)** TOC versus S_1; **(B)** TOC versus S_2.

and algae for survival, indicates that the paleo lake is rich in nutrients (Rowe et al., 2012).

A large number of sporophytes, molluscs and microfauna fossils are observed under the microscope in the Chang 7 shale (**Figures 6G,H**). Sporophytes and molluscs are characterized by 'dark in the middle and bright in the periphery' under orthogonal polarized light. This is because sporophytes and mollusks have a thin-walled structure, and difference exits between the calcification in the thin crust and the internal portion. Mollusks are typical aquatic organisms. Mollusk fossils are widely observed in the Chang-7 shale and are characterized by a long strip shape (**Figures 6G,H**). Sporophyte comes from higher plants, and it is an important sign of terrestrial input. Sporophytes in the Chang-7 shale are nearly circular in shape, and their occurrence is either clustered (**Figures 6I**) or isolated (**Figures 6J**). The skeleton fossils of microfauna are mainly small remnants of fish scales (**Figures 6H,K**). Other fossils exist in Chang-7 shale. However, due to the complete destruction of the paleontological morphology, it is almost impossible to identify their original forms based on the remnant fossils (**Figure 6L**).

More detailed organic matter origins are revealed by biomarker parameters. **Figures 2A–C** represent the samples cellected from type I, type II_1, type II_2 organic matters respectively (**Figure 7**). According to biogeochemical studies, the carbon distribution of n-alkanes is relatively complete. The TICs exhibit a typical oil-window n-alkane distribution with a peak at n-C_{15} to n-C_{22}, and the n-alkanes of most samples show a single peak distribution with no odd-over-even predominance. Compared with large molecule n-alkanes (above C_{20}), the content of small molecule n-alkanes (C_{20} and below C_{20}) is relatively low, with the ratio of 0.59–1.17 and average ratio of 0.79, indicating a significant contribution of higher plant input.

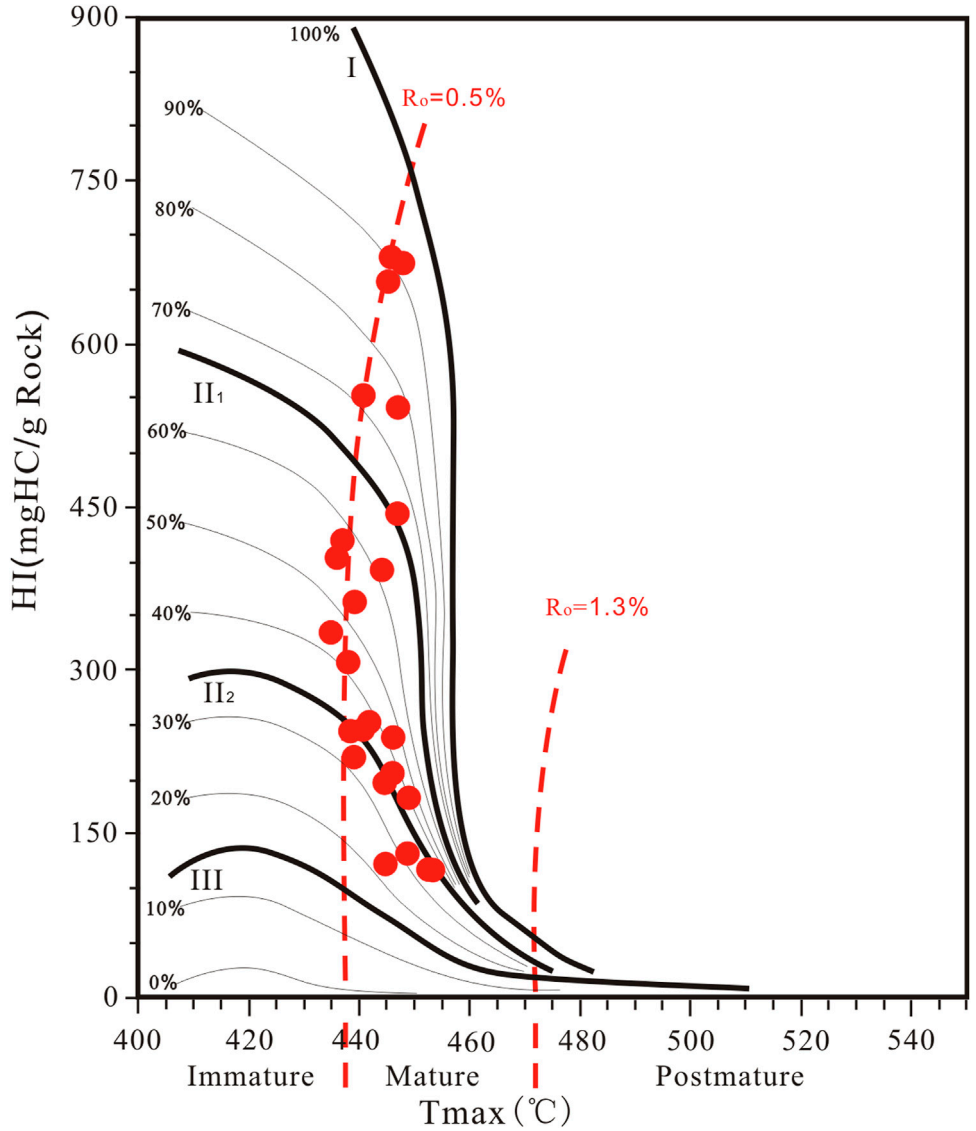

FIGURE 5 | Cross plot of hydrogen Index and maximum pyrolysis temperature, which indicates that the Chang-7 shale is in a mature stage.

Sterane usually originates from higher plants and algae. Thus, the origins of organic matter can also be effectively identified using sterane parameters. The most commonly used method is to determine the origins according to the relative content of regular steranes. C_{28} regular steranes are closely related to the development of diatoms; C_{27} regular steranes mainly come from algae; C_{29} regular steranes come from both algae and higher plants. For lacustrine systems, most of C_{27}, C_{28} and C_{29} regular steranes in liquid hydrocarbons are V-shaped (i.e. $C_{27} > C_{28} < C_{29}$), indicating a significant contribution of higher plant input. According to the samples in the study area, the distribution of regular steranes generally meets the above rules (**Figure 7**). The composition characteristics of C_{27}, C_{28} and C_{29} regular steranes show that the origins of organic matter in shale in the study area is composed of terrestrial plants and lake plankton (**Figure 8**).

Hydrocarbons formed through thermal maturation of terrestrial organic matter (especially higher plant-derived organic matter) are generally characterized by high ratio of Pr/Ph. Therefore, it is reliable to use Pr/Ph, C_{27}/C_{29} sterane, Pr/n-C_{17}, Ph/n-C18 to investigate sedimentary environment (Bushnev et al., 2017; Chiadikobi and Chiaghanam, 2018). Based on the analysis of 38 samples in the study area, there is only a minor variation in the values of Pr/n-C_{17} and Ph/n-C18, proving that the organic matter in Chang-7 shale has a mixed origin (**Figure 9**). In addition, Pr/Ph and C_{27}/C_{29} Sterane values also fall into a narrow range (**Figure 9B**), indicating that organic matter in Chang-7 shale is derived from both aquatic algae and terrestrial plants, and the Chang-7 shale was deposited under weakly reducing and weakly oxidizing conditions (**Figure 9**).

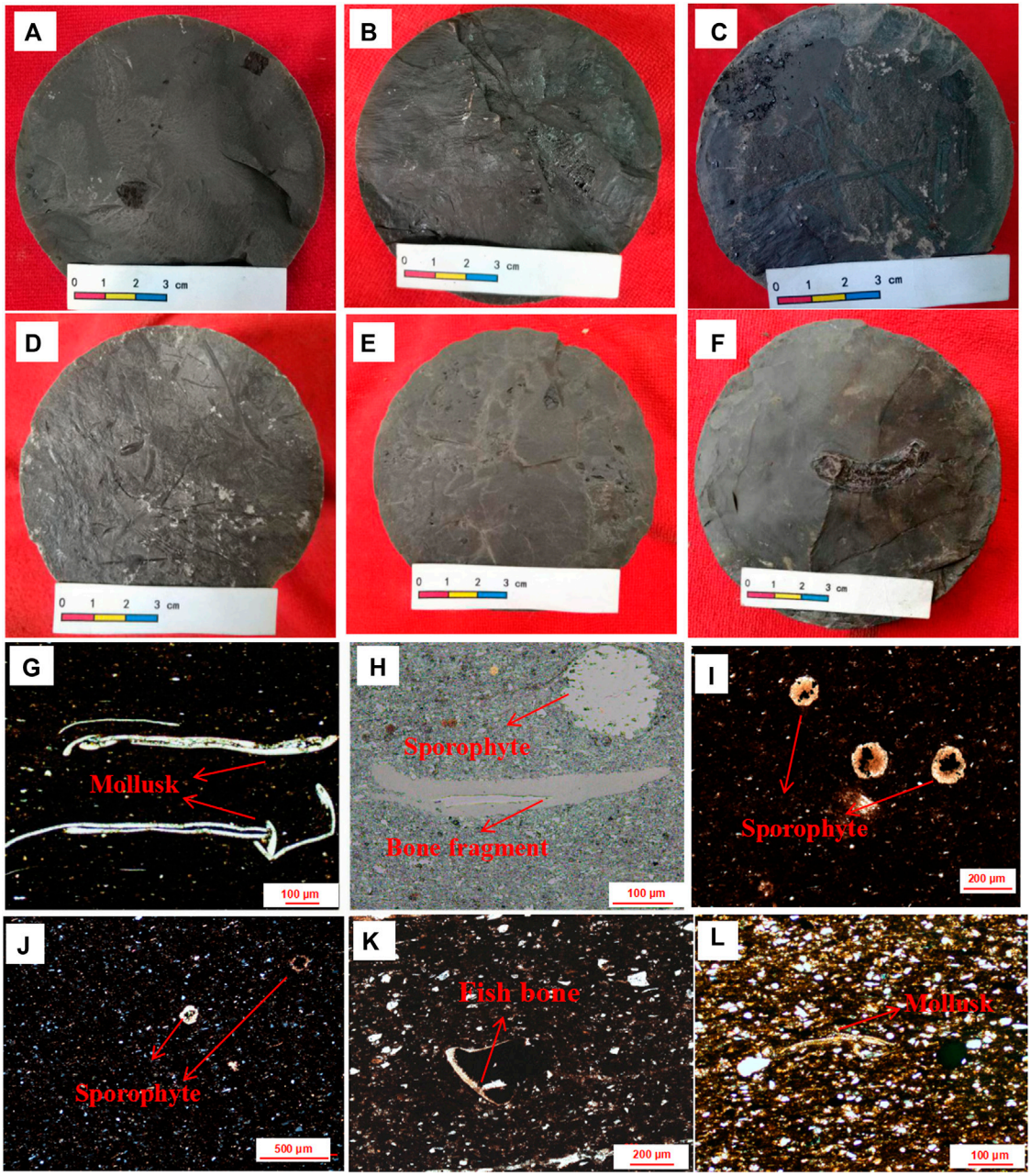

FIGURE 6 | Core and microscopic characteristics of source input **(A)** core photo showing plant debris (fossils), Z22 well, 1223.91 m; **(B)** core photo showing abandant plant debris (fossils) and carbonized particles, S31 well, 1152.35 m; **(C)** core photo showing abandant plant debris (fossils) and carbonized particles, D19 well, 1369.91 m; **(D)** core photo showing abandant plant debris (fossils), Q208 well, 1080.89 m; **(E)** core photo showing a large number of fish scales (fossils), Q100 well, 1383.07 m; **(F)** core photo showing an intact fish (fossils), S31-14 well, 141.16 m; **(G)** cast thin section, Plane-polarized light (10X) showing thin walled calcitic skeletal fragments, possible mollusks. YY1 well, 1315.12 m; **(H)** cast thin section, right-field reflected light (10X) showing bone fragment (center) and possible spore (upper right), YY1 well, 1374.24 m; **(I)** cast thin section, single polarization (10X) showing a black shale with sporophyte, YCCV1245 well, 1555.6 m; **(J)** cast thin section, single polarization (5X) showing a black shale with sporophyte, D11 well, 1762.08 m; **(K)** cast thin section, single polarization (10X) showing a sandy laminated shale with fossilized fish bone, YCCV1245 well, 1562.63 m; **(L)** cast thin section, single polarization (10X) showing a thin walled calcitic skeletal fragments, possible mollusk, YY1 well, 1397.66 m.

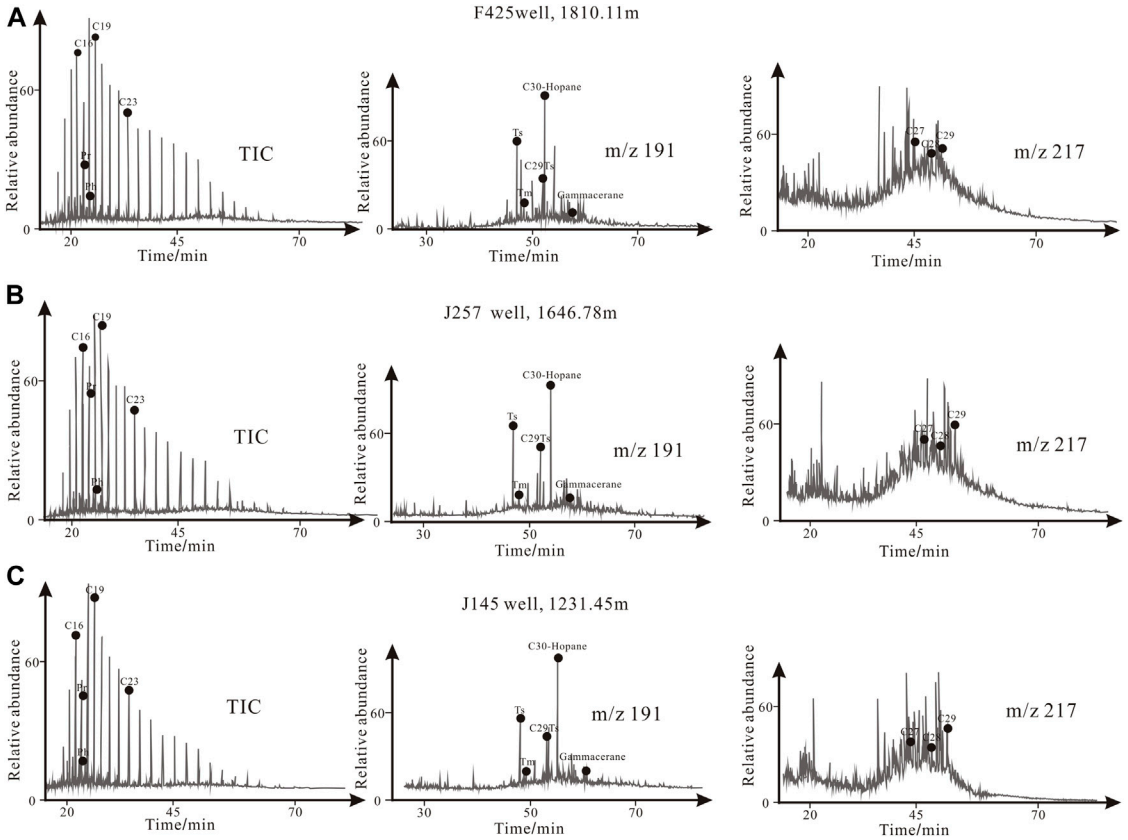

FIGURE 7 | The n-alkane gas chromatograms of saturated hydrocarbon in different organic matters.

QUANTITATIVE STUDY OF MIXED-ORIGIN ORGANIC MATTERS

Principles of Quantitative Characterization

Quantitative Characterization of Organic Matter Originated From Lake Water

Two stable carbon isotopes exist in natural conditions (i.e., ^{12}C and ^{13}C) (Li et al., 2017; Ogrinc et al., 2016; Faiz et al., 2018). Through photosynthesis, the concentration of ^{12}C and ^{13}C changes, which is called isotopic fractionation (Li et al., 2017; Ogrinc et al., 2016; Faiz et al., 2018). However, the precipitation of inorganic carbonates is not affected by isotopic fractionation. (Li et al., 2017; Ogrinc et al., 2016; Faiz et al., 2018). Lake water tends to be enriched in ^{13}C as plankton, especially phytoplankton preferably taking ^{12}C during photosynthesis. The enrichment of ^{13}C would result in high $\delta\ ^{13}C$ in carbonates (McKenzie, 1985; Weissert et al., 2008). $\delta\ ^{13}C$ in carbonates is calculated using the following equation:

$$\delta^{13}C = \left[\frac{\left(\frac{^{13}C}{^{12}C}\right)_{\text{sample value}}}{\left[\left(\frac{^{13}C}{^{12}C}\right)\right]_{\text{sample value}}} - 1 \right] \quad (1)$$

In this Formula, the standard value of ($^{13}C/^{12}C$) is the International PDB Standard (Pee Dee belemnite), $(^{13}C/^{12}C)_{\text{standard value}} = 1123.7 \times 10^{-5}$.

The concept of "aquatic organic index" is used to characterize the organic matter originated from lake water. aquatic organic index refers to the relative contribution of all kinds of aquatic organisms to the total organic matter within the sediments. The value of aquatic organic index ranges 0–1 and can be calculated as follows:

$$Q_1 = (\delta^{13}C\text{measured value} - \delta^{13}C\text{minimum value})/(\delta^{13}C\text{maximum value} - \delta^{13}C\text{minimum value}) \quad (2)$$

Q_1: aquatic organic index; $\delta\ ^{13}C_{\text{measured value}}$: carbon isotopic values of carbonate from the measured samples; $\delta\ ^{13}C_{\text{maximum value}}$: Maximum value of carbonate carbon isotopes; $\delta^{13}C_{\text{minimum value}}$: Minimum value of carbonate carbon isotopes.

According to the statistics of carbon isotope in lacustrine shales in China, the average value of $\delta\ ^{13}C_{\text{maximum value}}$ is 10.435, and the average value of $\delta\ ^{13}C_{\text{minimum value}}$ is −9.003.

Quantitative Characterization of Organic Matter Originated From Land Input

The type of organic matter provides qualitative information about their sources. Type I organic matter is primarily produced *in situ* in the water; type III organic matter is mainly from terrestrial sources, and type II organic matter commonly has a mixed

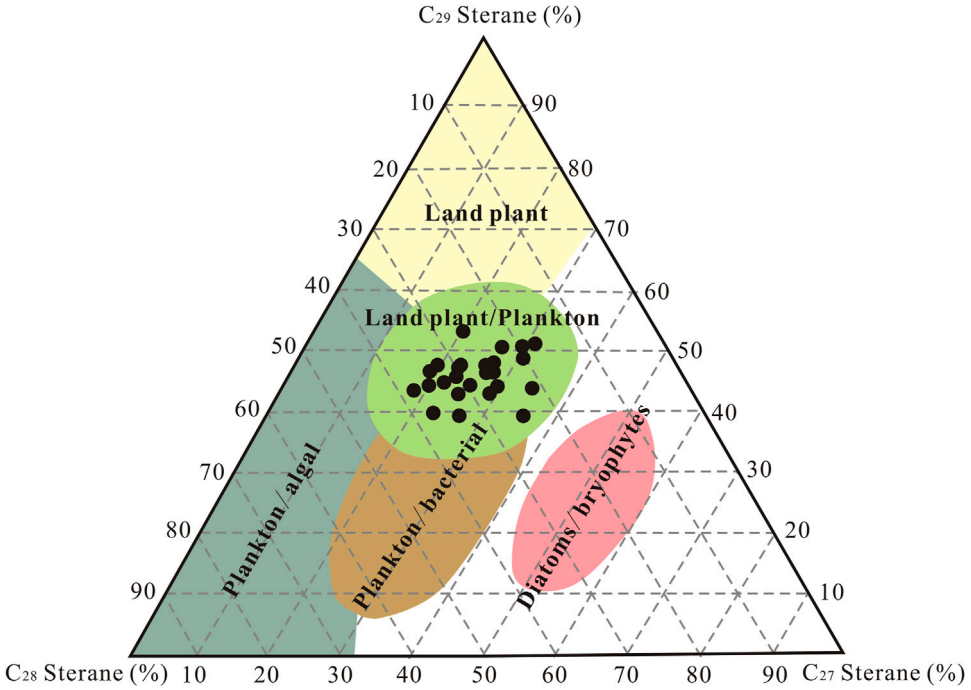

FIGURE 8 | Sedimentary environment of shale in study area **(A)** The relationship between Pr/n-C_{17} and Ph/n-C_{18}; **(B)** The relationship between Pr/Ph and C_{27}/C_{29}.

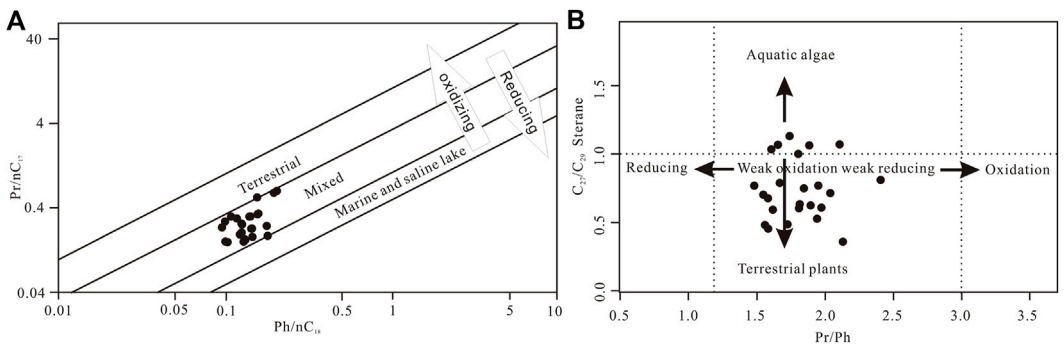

FIGURE 9 | Cross plots: **(A)** Q1 versus TOC; **(B)** Q2 versus TOC; **(C)** Q versus TOC; and **(D)** R versus HI, giving an indication for the origins of organic matter in the Chang-7 shale in the study area.

source. Recently, many researchers promoted the use of aquatic organic ratio (AOR) to quantitatively evaluate the source of organic matter (Pang et al., 2003; Hu et al., 2018; Awan et al., 2020). AOR is defined as the percentage of organic matter generated *in situ* in the water body to the total organic matter in the sediments. This method is based on the following assumptions: 1) type I organic matter is 100% from *in situ* water body; 2) type III organic matter is 100% from terrestrial input. Others fall in between 0 and 100% through interpolation.

With aquatic organic index (Q_1) and aquatic organic ratio (R), terrigenous organic index (Q_2) as defined by the organic matter contributed by terrestrial input can be calculated using the following equation:

$$Q_2 = Q_1 \times (1 - R)/R \quad (3)$$

Total organic index Q as the total organic matter productivity in the sediments can be calculated by the sum of Q_1 and Q_2 using the following equation:

$$Q = Q_1 + Q_2 \quad (4)$$

Quantitative Analysis of Organic Origins in the Study Area

The terrigenous organic index changes greatly in the study area, ranging from 0.06 to 1.98 (**Table 2**). The reason lies in that the input

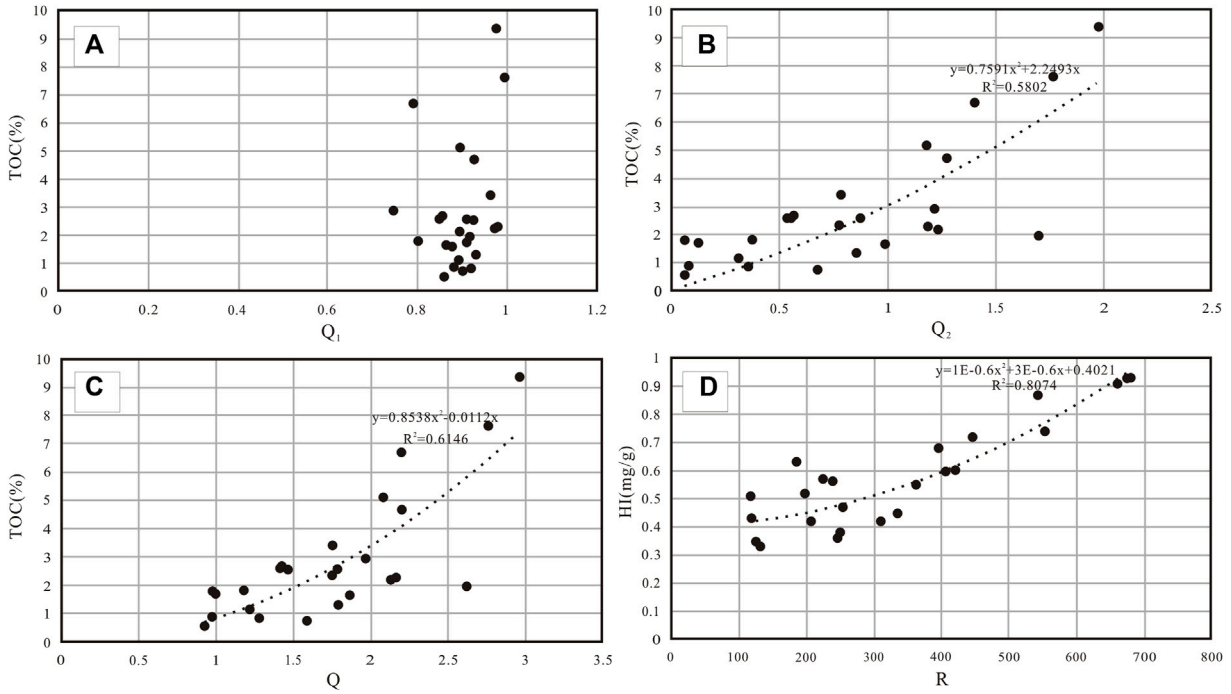

FIGURE 10 | Cross plots: **(A)** Q1 versus TOC, **(B)** Q2 versus TOC, **(C)** Q versus TOC, and **(D)** R versus HI, giving an indication for the origins of organic matter in the Chang-7 shale in the study area.

of terrigenous materials is controlled by an extremely complex process, which is affected by factors such as volume, rate and sources. Therefore, organic matter originated from terrigenous input commonly have significant variations in geochemical properties. In contrast, the aquatic organic index has little variations in the study area, ranging from 0.75 to 0.99 (only two samples are less than 0.8). This is probably due to the simple chemical nature and weak carbon isotope fractionation in the shallow lake where the Chang-7 shale was deposited (**Figure 10**).

Calculation based on data from the Chang-7 shale in the study area shows that the average aquatic organic index is 0.89 and the average terrigenous organic index is 0.84. The terrigenous organic index is very close to that of aquatic organic index. The data and analysis mentioned above indicate that paleo-water column and terrestrial input contributed equally to the enrichment of organic matter in the Chang-7 shale in the study area.

Using data from tests and calculation from 25 samples, a strong positive correlation between the total organic carbon content and total organic matter index can be seen, having a coefficient of 0.6146. There is also a strong positive correlation between the total organic carbon content and the terrestrial organic index, having a correlation coefficient of 0.5802 (**Figure 10**). The above observations indicate that the change of total organic index is primarily controlled by terrigenous organic index because there is no significant variations in aquatic organic index. The more input of organic matter from land, the more enriched in organic matter the shale is.

The quantitative analysis mentioned above has its own limitations. Two parameters, maximum value of carbonate carbon isotopes and minimum value of carbonate carbon isotopes, are difficult to be obtained, which limits its feasibility to be applied in other areas or scenarios.

CONCLUSION

This study shows that the Triassic Chang-7 shale in the central part of the Ordos Basin has high organic abundance. It is thermally mature and is currently generating oil and gas. It contains predominantly type II_1 organic matter. The organic matter in the Chang-7 shale is mostly structured other than amorphous. Terrestrial input and paleo-water column contributed equally to the enrichment of organic matter in the Chang-7 shale in the study area.

DATA AVAILABILITY STATEMENT

The original contributions presented in the study are included in the article/Supplementary Material, further inquiries can be directed to the corresponding author.

AUTHOR CONTRIBUTIONS

The author confirms being the sole contributor of this work and has approved it for publication.

FUNDING

This paper is financially supported by National Natural Science Foundations of Shaanxi Province (Grant No. 2019JQ-308).

ACKNOWLEDGMENTS

The authors wish to acknowledge Shaanxi Yanchang Petroleum for providing samples and data.

REFERENCES

Abaturov, A. L., Moskalev, I. V., Kiselkov, D. M., and Strelnikov, V. N. (2018). Production of Isotropic Coke from Shale: Microstructure of Coke from the Thermally Oxidized Distillation Residue of Shale Tar. *Coke Chem.* 61, 433–446. doi:10.3103/s1068364x18110029

Alaug, A. S. (2011). Source Rocks Evaluation, Hydrocarbon Generation and Palynofacies Study of Late Cretaceous Succession at 16/G-1 Offshore Well in Qamar Basin, Eastern Yemen. *Arab J. Geosci.* 4, 551–566. doi:10.1007/s12517-010-0182-6

Awan, R. S., Liu, C. L., GongChao, H. W. D., and Chamssidini, L. G. (2020). Paleo-sedimentary Environment in Relation to Enrichment of Organic Matter of Early Cambrian Black Rocks of Niutitang Formation from Xiangxi Area China. *Mar. Pet. Geology.* 112, 1–20. doi:10.1016/j.marpetgeo.2019.104057

Bushnev, D. A., Burdel'naya, N. S., and Zhuravlev, A. V. (2017). Organic Matter in Upper Devonian Deposits of the Chernyshev Ridge. *Geochem. Int.* 55, 548–558. doi:10.1134/s0016702917060027

Chiadikobi, K., and Chiaghanam, O. I. (2018). Biomarker Distributions of the Campano-Maastrichtian Nkporo Group of Anambra Basin, Southeastern Nigeria. *Pet. Coal* 60, 1161–1175.

Curtis, J. B. (2002). Fractured Shale-Gas Systems. *AAPG Bull.* 86, 1921–1938. doi:10.1306/61eeddbe-173e-11d7-8645000102c1865d

Demaison, G. J., and Moore, G. T. (1980). Anoxic Environments and Oil Source Bed Genesis. *AAPG Bull.* 64, 1179–1209. doi:10.1306/2f91945e-16ce-11d7-8645000102c1865d

Dong, T., He, S., Wang, D., and Hou, Y. (2014). Hydrocarbon Migration and Accumulation in the Upper Cretaceous Qingshankou Formation, Changling Sag, Southern Songliao Basin: Insights from Integrated Analyses of Fluid Inclusion, Oil Source Correlation and basin Modelling. *J. Asian Earth Sci.* 90, 77–87. doi:10.1016/j.jseaes.2014.04.002

Er, C., Li, Y., Zhao, J., Wang, R., Bai, Z., and Han, Q. (2016). Pore Formation and Occurrence in the Organic-Rich Shales of the Triassic Chang-7 Member, Yanchang Formation, Ordos Basin, China. *J. Nat. Gas Geosci.* 1, 435–444. doi:10.1016/j.jnggs.2016.11.013

Faiz, M., Zoitsas, A., Altmann, C., Baruch-Jurado, E., and Close, D. (2018). Carbon Isotope Fractionation in Coal and Marine Source Rocks and Implications for Exploration. *ASEG Extended Abstr.* 2018, 1. doi:10.1071/ASEG2018abP001

Fan, B., and Shi, L. (2019). Deep-Lacustrine Shale Heterogeneity and its Impact on Hydrocarbon Generation, Expulsion, and Retention: A Case Study from the Upper Triassic Yanchang Formation, Ordos Basin, China. *Nat. Resour. Res.* 28, 241–257. doi:10.1007/s11053-018-9387-2

Fink, R., Amann-Hildenbrand, A., Bertier, P., and Littke, R. (2018). Pore Structure, Gas Storage and Matrix Transport Characteristics of Lacustrine Newark Shale. *Mar. Pet. Geology.* 97, 525–539. doi:10.1016/j.marpetgeo.2018.06.035

Giliazetdinova, D. R., Korost, D. V., and Gerke, K. M. (2017). *Studying of Shale Organic Matter Structure and Pore Space Transformations during Hydrocarbon Generation//Advances in Laboratory Testing & Modelling of Soils & Shales*. Cham: Springer.

Henderson, R. A. (2004). A Mid-cretaceous Association of Shell Beds and Organic-Rich Shale: Bivalve Exploitation of a Nutrient-Rich, Anoxic Sea-Floor Environment. *PALAIOS* 19, 156–169. doi:10.1669/0883-1351(2004)019<0156:amaosb>2.0.co;2

Huo, Z., Pang, X., Ouyang, X., Zhang, B., Shen, W., Guo, F., et al. (2015). Upper Limit of Maturity for Hydrocarbon Generation in Carbonate Source Rocks in the Tarim Basin Platform, China. *Arab J. Geosci.* 8, 2497–2514. doi:10.1007/s12517-014-1408-9

Keighley, D., Mcfarlane, C., and Vanden Berg, M. (2018). Diagenetic Sequestration of Rare Earths and Actinides in Phosphatic Oil Shale from the Lacustrine Green River Formation (Eocene), Utah, USA: an SEM and LA-ICP-MS Study. *J. Paleolimnol* 59, 81–102. doi:10.1007/s10933-016-9905-3

Li, Y., Wang, H., Wang, M. L. P., Duan, T., and Ji, B. (2017). Automatic Identification of Carbonate Sedimentary Facies Based on PCA and KNN Using Logs. *Well Logging Technol.* 41, 57–63. doi:10.16489/j.issn.1004-1338.2017.01.010

Liu, B., Bechtel, A., Sachsenhofer, R. F., Gross, D., Gratzer, R., and Chen, X. (2017). Depositional Environment of Oil Shale within the Second Member of Permian Lucaogou Formation in the Santanghu Basin, Northwest China. *Int. J. Coal Geology.* 175, 10–25. doi:10.1016/j.coal.2017.03.011

Liu, B., Sun, J., Zhang, Y., He, J., Fu, X., Yang, L., et al. (2021). Reservoir Space and Enrichment Model of Shale Oil in the First Member of Cretaceous Qingshankou Formation in the Changling Sag, Southern Songliao Basin, NE China. *Pet. Exploration Develop.* 48, 608–624. doi:10.1016/s1876-3804(21)60049-6

Mann, U. (1989). Revealing Hydrocarbon Migration Pathways. *Geol. Rundsch* 78, 337–348. doi:10.1007/bf01988368

McKenzie, J. A. (1985). "Carbon Isotope and Productivity in the Lacustrine and marine Environment," in *Chemical Processes in Lakes*. Editor W. Stumm (New York: Wiley), 99–118.

Ogrinc, N., Kanduč, T., Krajnc, B., Vilhar, U., Simončič, P., and Jin, L. (2016). Inorganic and Organic Carbon Dynamics in Forested Soils Developed on Contrasting Geology in Slovenia-a Stable Isotope Approach. *J. Soils Sediments* 16, 382–395. doi:10.1007/s11368-015-1255-7

Pang, X., Li, M., Li, S., and Jin, Z. (2003). Geochemistry of Petroleum Systems in the Niuzhuang South Slope of Bohai Bay Basin. Part 2: Evidence for Significant Contribution of Mature Source Rocks to "Immature Oils" in the Bamianhe Field. *Org. Geochem.* 34, 931–950. doi:10.1016/s0146-6380(03)00032-9

Piper, D. Z., and Perkins, R. B. (2004). A Modern vs. Permian Black Shale—The Hydrography, Primary Productivity, and Water-Column Chemistry of Deposition. *Chemical Geology.* 206, 0–197. doi:10.1016/j.chemgeo.2003.12.006

Rong, L. X. (2003). Review of Hydrocarbon Migration and Accumulation Dynamics. *Nat. Gas Geoence* 31, 320–325. (in Chinese with Englsih abstract). doi:10.3969/j.issn.1672-1926.2003.05.002

Rowe, H., Hughes, N., and Robinson, K. (2012). The Quantification and Application of Handheld Energy-Dispersive X-ray Fluorescence (ED-XRF) in Mudrock Chemostratigraphy and Geochemistry. *Chem. Geology.* 324-325, 122–131. doi:10.1016/j.chemgeo.2011.12.023

Siddiqui, F. I., and Lake, L. W. (1992). A Dynamic Theory of Hydrocarbon Migration. *Math. Geol.* 24, 305–327. doi:10.1007/bf00893752

Tagiyev, M. F., Nadirov, R. S., Bagirov, E. B., and Lerche, I. (1997). Geohistory, thermal History and Hydrocarbon Generation History of the north-west South Caspian basin. *Mar. Pet. Geology.* 14, 363–382. doi:10.1016/s0264-8172(96)00053-0

Yuan, W., Liu, G., Stebbins, A., Xu, L., Niu, X., Luo, W., et al. (2017). Reconstruction of Redox Conditions during Deposition of Organic-Rich Shales of the Upper Triassic Yanchang Formation, Ordos Basin, China. *Palaeogeogr. Palaeoclimatol. Palaeoecol.* 486, 158–170. doi:10.1016/j.palaeo.2016.12.020

Zeng, Q., Qian, L., and Liu, D. (2006). Organic Petrological Study on Hydrocarbon Generation and Expulsion from Organic-Rich Black Shale and Oil Shale. *ACTA SEDIMENTOLOGICA SINICA* 24, 113–122. doi:10.3969/j.issn.1000-0550.2006.01.015

Conflict of Interest: The author declares that the research was conducted in the absence of any commercial or financial relationships that could be construed as a potential conflict of interest.

Publisher's Note: All claims expressed in this article are solely those of the authors and do not necessarily represent those of their affiliated organizations, or those of the publisher, the editors and the reviewers. Any product that may be evaluated in this article, or those of the publisher, the editors and the reviewers. Any product that may be evaluated in this article, or claim that may be made by its manufacturer, is not guaranteed or endorsed by the publisher.

frontiers in Chemistry

ORIGINAL RESEARCH
published: 05 November 2021
doi: 10.3389/fchem.2021.738717

Syntheses of a Hyperbranched Polymer and Its Performance on Enhanced Oil Recovery

Sanyuan Qiao[1], *Qingwang Liu*[1]*, *Xian Zhang*[1] and *Hongchang Che*[2]

[1]Petroleum Engineering, Northeast Petroleum University, Daqing, China, [2]Wells and Operation Department, PetroChina International Middle East, Beijing, China

A hyperbranched carboxylate-type polymer was synthesized through esterification and carboxymethylation, and its performance on enhanced oil recovery was experimentally evaluated. The optimum condition for esterification was 8 h at 120°C, where 3% PTSA as the catalyst and 9:1 mol ratio of the AB_2 intermediate and trimethylolpropane were used. The optimum condition for carboxymethylation was 4 h at 80°C. The critical micelle concentration of the hyperbranched polymer was 433.63 mg/L, the Krafft point was 5°C, and the surface tension was lowered to 28 mN/m. In the range of 400–500 mg/L concentration, the adsorption onto the oil sand surface achieved equilibrium, and micellar solubilization reached 600 ml/mol. The interfacial tension can be lowered to a level of 10^{-2} mN/m by the single use of the hyperbranched polymer, and the value further decreased to a level of 10^{-3} mN/m while being formulated with sodium dodecylsulfate or NaOH. Oil recovery of water flooding was further enhanced by the single use of a hyperbranched polymer or the combination of hyperbranched polymer/sodium dodecylsulfate. The latter exhibited more prosperous advantages in low-permeability reservoirs.

Keywords: syntheses, hyperbranched polymer, surfactant, core flooding, enhanced oil recovery

OPEN ACCESS

Edited by:
Shengnan Chen,
University of Calgary, Canada

Reviewed by:
Sadafara Anand Pillai,
School of Sciences, P P Savani University, India
Nilanjan Pal,
King Abdullah University of Science and Technology, Saudi Arabia

***Correspondence:**
Qingwang Liu
liuqingwang@163.com

Specialty section:
This article was submitted to Polymer Chemistry, a section of the journal Frontiers in Chemistry

Received: *09 July 2021*
Accepted: *30 September 2021*
Published: *05 November 2021*

Citation:
Qiao S, Liu Q, Zhang X and Che H (2021) Syntheses of a Hyperbranched Polymer and Its Performance on Enhanced Oil Recovery. Front. Chem. 9:738717. doi: 10.3389/fchem.2021.738717

INTRODUCTION

Polymer flooding is an economic and efficient method for enhanced oil recovery and is used worldwide (Zhao et al., 2020; Sieberer et al., 2017). Saboorian-Jooybari et al. presented a detailed review of the application of polymers in heavy oil flooding since the 1960s and concluded that polymer flooding can contribute to a range of 2.2–44% incremental oil recovery (Saboorian-Jooybari et al., 2016). Sheng et al. discussed the status of polymer flooding technology and highlighted some associated problems such as formation damage and low injectivity of polymers (Sheng et al., 2015). Brattekås and Seright investigated improved polymer gel conformance control during water flooding in fractured low-permeability carbonates and found that gel-blocking efficiency was dependent on water salinity, core materials, and oil presence (Brattekås and Seright, 2018; Wang and Zhang, 2019). Algharaib et al. experimentally investigated the impact of various parameters on polymer performance on enhanced oil recovery and found pre-flush and polymer characteristics having various degrees of influence (Algharaib et al., 2014). Cardoso et al. discussed the importance of chemical characteristics of polymers in enhanced oil recovery processes and concluded that more profitable results can be gained using polymers of higher average molar mass in the semidilute regime (Cardoso et al., 2016).

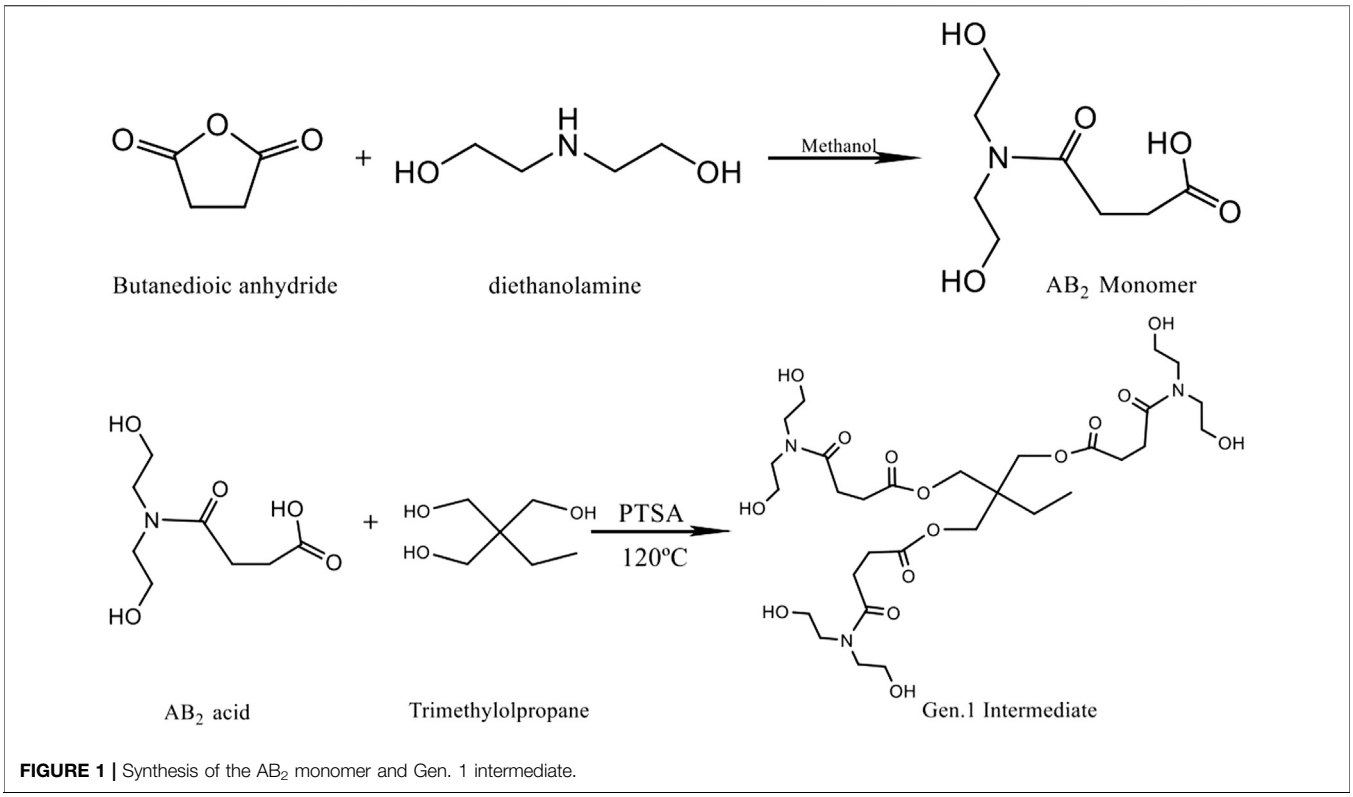

FIGURE 1 | Synthesis of the AB_2 monomer and Gen. 1 intermediate.

Hyperbranched polymers (HBPs) are highly branched macromolecules with a three-dimensional dendritic architecture, and a wide range of applications have been reported due to their well-defined structures, unique properties, and facile synthesis (Gurunathan et al., 2016). They usually have a large degree of functional terminal groups and intramolecular cavities presenting high solubility and low viscosities (Frey, 2003; Caminade et al., 2015).

Flory discussed the possibility of HBP syntheses by polycondensation of the AB_x-type monomer, to which attention was not paid at the time (Flory, 1941; Flory, 1952). The studies on the topic have thrived since 1990s, and their applications have been extended to enhanced oil recovery (Algharaib et al., 2014; Sun et al., 2016; Yin and Zhao, 2017). Addition of HBPs leads to greater oil recovery than conventional polymers in core flooding experiments (Luo et al., 2019; Jianbo et al., 2020; Chen et al., 2020).

Carboxylate surfactants, derived from petroleum, have been widely used in tertiary oil recovery due to their low adsorption onto sands, strong emulsifying property, and ability of lowering interfacial tension (Ziyuan et al., 2021). HBPs have high interfacial activity and low critical micelle concentration (CMC) and can be modified through abundant terminal groups in the unique structures (Clarke et al., 2016; Khorsandi et al., 2017).

This article is intended to synthesize a hyperbranched carboxylate–type polymer and evaluate its performance on enhanced oil recovery.

MATERIALS AND METHODS

Synthesis of Branched Monomers

A wide variety of polymer types can be synthesized, and special properties can be imparted via different routes and suitable end capping reactions. In this article, the hyperbranched macromolecules were synthesized by the polymerization of an intermediate (AB_x or latent AB_x monomers). First, a diethanolamine methanol solution was prepared by dissolving diethanolamine in a methanol solution. Then, succinic anhydride was added into anhydrous methanol and stirred until it was completely dissolved. Then, the diethanolamine solution was added to the succinic anhydride solution, and the final molar ratio of diethanolamine to succinic anhydride was found to be 1:1. The solution was placed in a cold water bath and maintained for 6 h, and then the methanol solution was removed using a rotary evaporator to obtain the AB_2-type monomer intermediate. Its molecular structure is shown in **Figure 1**.

Synthesis of a Gen.1 Intermediate

TMP (trimethylolpropane) is esterified with the AB_2 monomer at 120°C in the presence of *p*-toluenesulfonamide (PTSA) as the catalyst. The three terminal hydroxyl groups of TMP are equally replaced by the AB_2 monomer in the reactions, and then the Gen. 1 intermediate is obtained. When each hydroxyl group of TMP is substituted by esterification, two hydroxyl groups are introduced

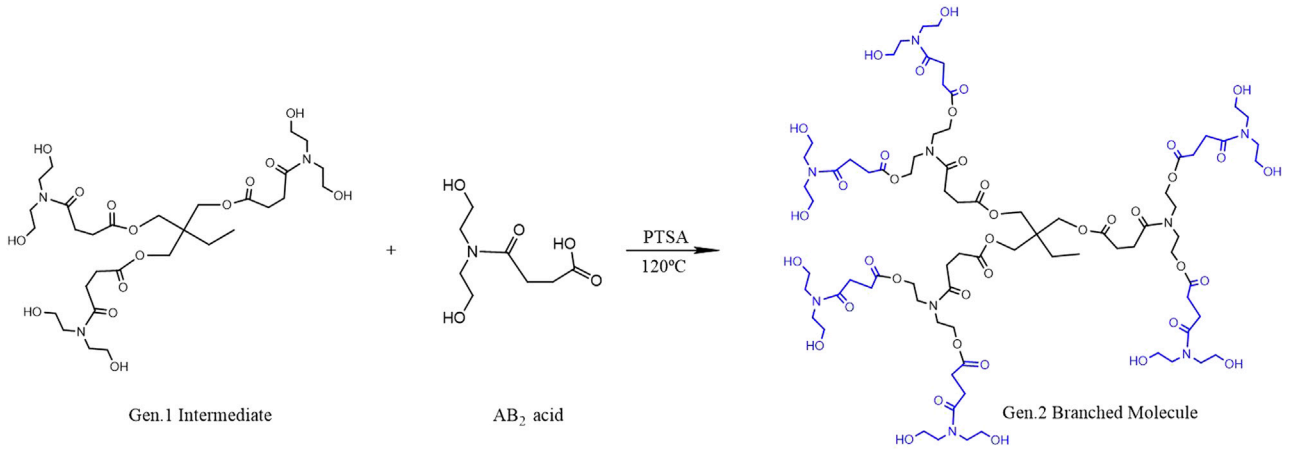

FIGURE 2 | Synthesis of Gen. 2 hyperbranched polyurethane (HPAE).

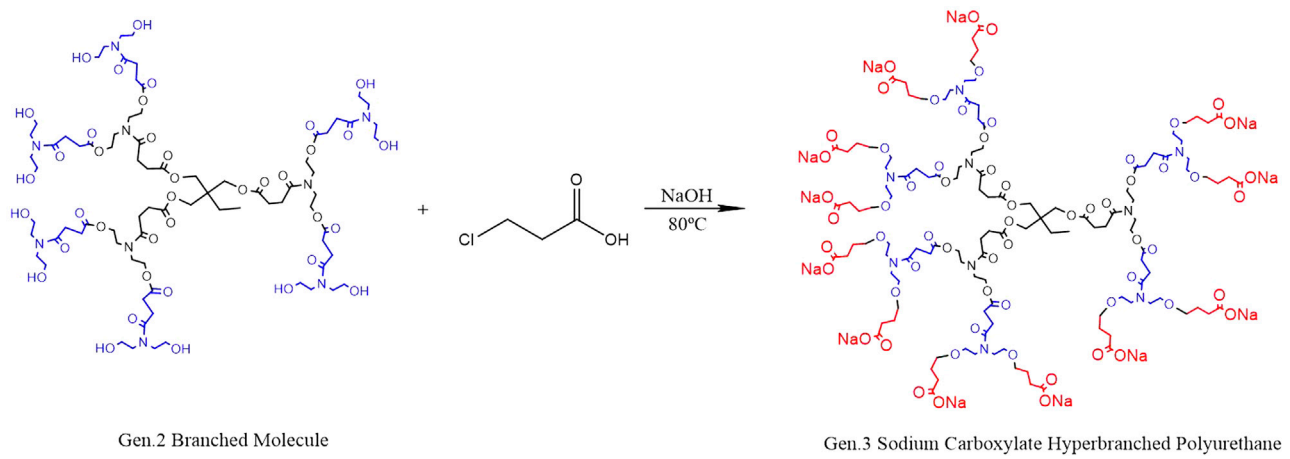

FIGURE 3 | Synthesis of HPAE with sodium carboxylate at the end of Gen.2 (*m*-HPAE).

into the end position, and the esterification reactions continue to proceed with the monomer. In order to minimize the consumption of the Gen.1 intermediate by the AB_2 monomer and assure the equal substitution of terminal hydroxyl groups in TMP, a molar ratio of 1:3 (TMP to the intermediate) is used, and the yield is about 75%. The reaction scheme is shown in **Figure 1**.

Synthesis of a Gen.2 Hyperbranched Molecule

The Gen.1 intermediate is esterified with the AB_2 monomer at 120°C in the presence of PTSA as the catalyst. The six terminal hydroxyl groups of the Gen.1 intermediate are esterified with the AB_2 intermediate, and then the second generation hyperbranched polyurethane (Gen.2 HPAE) is obtained. In the experiments, the molar ratio of 1:6 (Gen.1 intermediate to AB_2 monomer) is used to minimize the side reactions, and the yield is about 65%. The reaction scheme is shown in **Figure 2**.

Synthesis of HBP With Sodium Carboxylate at the End of Gen.2

Modified hyperbranched polyurethane (*m*-HPAE) and NaOH were put into a four-port bottle and heated to 80–100°C under magnetic stirring. A 3-chloropropionic acid solution (80 wt%) was vacuumed for 30–50 min and then poured into the bottle, leaving the reaction to proceed for 4–6 h. The solvent in the system was removed, and the product was washed using anhydrous ethanol and then filtered. The residues with low boiling point were removed using a rotary evaporator and

sodium carboxylate–terminated HPAE (SCHP) was obtained. The reaction scheme is shown in **Figure 3**. In the process of synthesis, the molar ratio (hyperbranched polyurethane to 3-chloropropionic acid and NaOH) was determined to be 1:12:12 to replace 12 terminal hydroxyl groups in the synthesized HPAE.

Evaluation of the Synthesized HBP

Fourier Transform Infrared Spectroscopy

Fourier transform infrared spectroscopy (FT-IR) analyses of the original polymer and the modified HPAE were performed using a VERTE70 (Germany) device. The samples were scanned in the mid-infrared region of wavenumbers (400–4,000 cm^{-1}) to record the FT-IR spectra.

Surface Tension

Surface tension was determined using the ring method where a ring attached to a torsion meter was dipped into the hyperbranched carboxylate surfactant solution. The liquid level was lowered after slow pull-up, and the force on the ring was measured before the liquid film tore off. The surface tension was calculated based on the diameter of the ring and the tear-off force.

Critical Micelle Concentration and Krafft Point

The CMC was determined by a conductivity method where a conductimeter was used to measure the conductivity of the solution. The Krafft point is the minimum temperature at which surfactants form micelles, that is, micelles cannot be formed below this critical micelle temperature. At the Krafft point, the solubility is equal to the CMC. The Krafft point was measured in the experiment. The solution of *m*-HPAE with a concentration of 1% was prepared and poured into a test tube which was heated in a water bath and stirred until the solution became clear and transparent. Then, it was placed in a cold water bath to allow the temperature to drop under continuous stirring until the precipitation was observed. The measurements were repeated, and the temperature was recorded.

Adsorption Property

The adsorption property of *m*-HPAE is a significant parameter to determine its suitability for enhanced oil recovery, relevant to its ability and effectiveness to reduce surface tension at the oil–water interface and strip off oil drops from the rock surface. *m*-HPAE varying from 100 mg/L to 900 mg/L was prepared and mixed with 2 g oil sands (from Daqing Oilfield in China) at the liquid/solid ratio of 60:1. The container was placed at 45°C and was continuously shaken for 8 h. The clear solution was obtained after separation and still stratification, and the concentration of the hyperbranched surfactants was determined by phase titration using Bromocresol green based on the following equation.

$$M = \frac{(C_1 - C_2) * V}{m},$$

where m is the weight of the oil sands, g; C_1 is the concentration before adsorption, mg/L; C_2 is the concentration after adsorption, mg/L; V is the volume of *m*-HPAE, mL; and M is the adsorption capacity, mg/L.

Micellar Solubilization

Micellar solubilization is the process of taking the solubilizate onto or into micelles as a part of the whole system. In the experiment, the hyperbranched surfactant solution was prepared with a concentration greater than the CMC. 10 ml distilled water was added into seven 50-ml bottles containing benzene with various volumes (10, 20, 30, 40, 50, 60, and 70 μl). The bottles were placed in the water bath at 40°C for 15 min, then taken out, and cooled down to atmospheric temperature. The absorbance value of each solution was measured using a spectrophotometer, and the solubilization value was calculated based on the following equation.

$$Z = \frac{1000A}{cV},$$

where Z is the solubilizing ability, mL/mol; c is the hyperbranched molecule solution concentration, mol/L; V is the hyperbranched molecule solution volume, mL; and A is the benzene content when reaching the solubilization limit, mL.

Wettability

Liquid droplets on the solid surface will form droplets under the action of the interfacial tension at the gas–liquid–solid three-phase interface, and the droplets will form a contact angle θ at the gas–liquid–solid three-phase interface. When equilibrium is reached, the wetting formula can be obtained.

$$\sigma_{g-s} = \sigma_{l-s} + \sigma_{g-l}cos\theta.$$

The contact angle θ can judge the wetting of the surface. The smaller the contact angle, the better the hydrophilic performance. The *m*-HPAE solution was prepared with a concentration of 400 mg/L to fully soak the rock sample and then dried to obtain the processed rock sample, and a contact angle tester was used to measure the contact angle of the rock sample surface before and after the treatment.

In the process of water flooding, the migration of oil and water in the rock pores will be affected by the wettability of the rock. The wettability of the pores directly affects the efficiency of water flooding. The capillary resistance formed by the lipophilic pores will reduce the recovery. The capillary force formed by hydrophilic pores can be used as a driving force to improve oil recovery. When the oil-in-water emulsion system flows through the bottom layer, the more hydrophilic the surface of the rock, the lower will be the flow resistance. If the surfactant can change the originally hydrophobic rock surface into a hydrophilic rock surface, it will convert the capillary force from resistance to motive force and increase the oil recovery.

Rheology

There are polymer chains in the *m*-HPAE structure, which will affect the extension structure in a high-concentration salt

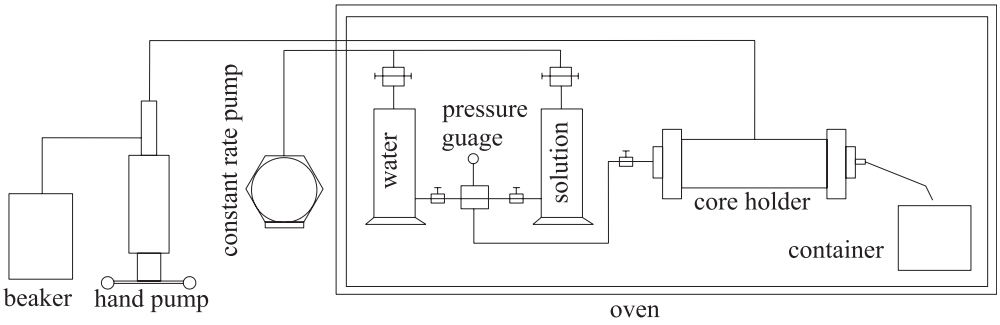

FIGURE 4 | Core flooding experiment system.

solution, and the formation environment is often accompanied by high salinity. This experiment explores the influence of salinity on the rheology of *m*-HPAE. An *m*-HPAE solution was prepared with a concentration of 400 mg/L, and NaCl was added to make its concentration reach 1000 mg/L and 10000 mg/L. The viscosity at different shear rates was measured by using a Brookfield rotary viscometer.

Core Flooding Experiment

Two binary surfactant systems, namely, *m*-HPAE/sodium dodecylsulfate (LAS) and *m*-HPAE/NaOH, were prepared, and the interfacial tension was measured prior to the core flooding experiments. The viscosity of the crude oil (obtained from Daqing Oilfield) is 10cP at 45°C, and the salinity of the formation water is 3×10^3 mg/L. The interfacial tension was measured using a TX-500C interfacial tensiometer at 500 rpm, and the data were recorded every 30 mins until the difference between the two consecutive readings was less than 0.001.

The core flooding experimental setup is composed of pressure sensors, the core holder and the sample collecting container, and the hand pump and the constant rate pump (**Figure 4**).

All components were placed in an oven with the temperature set at 65°C, except the hand pump and the constant rate pump. The core was vacuumed and saturated with formation water at the atmospheric temperature and then with the crude oil at 65°C. The core was flooded by water at the same temperature until 98% water cut and the oil recovery factor by water flooding were calculated. Then, 0.3 pore volume of the surfactant solution was injected followed by water flooding until 98% water cut and the oil recovery factor by surfactant flooding were calculated. The injection rate was constant at 0.3 ml/min, and pressure data were recorded every 30 min.

RESULTS AND DISCUSSION

Influential Factors on Syntheses

The processes where the intermediate and the final product are produced belong to the esterification and carboxymethylation reactions, respectively. The conversion rate in the esterification reaction is evaluated by the acid number which is the mass of potassium hydroxide (mg) required to neutralize the chemical (1 g). The conversion rate in the carboxymethylation reaction is calculated based on the hydroxyl value, which is potassium hydroxide (mg) required to neutralize the acetic acid taken up on acetylation of the chemical substance (1 g) that contains free hydroxyl groups.

As esterification reaction proceeds slowly at low temperature, and we recorded the data from the reaction conducted at 100°C. More intermediates are produced as the temperature increases. When the temperature was elevated to 115°C, the color of the product is light yellow, close to the color of the intermediate. The color of the product turns dark at a temperature above 130°C, indicating that the structure of the intermediate is broken, and an unexpected substance is produced.

There were no catalysts required in the carboxymethylation reaction, while various concentrations of PTSA (1, 2, 3, 4, and 5%) were used to accelerate the esterification reaction, since it is a reversible reaction. The reaction temperature was set at 120°C, reaction time was 8 h, and molar ratio of the intermediate and TMP was 9:1. The relationship between the acid number and concentration of PTSA is demonstrated in **Figure 5A**. The acid number decreases when PTSA concentration is increased till 3%. The acid number is determined to be 26.62 mg/g at 3% concentration, and in the meanwhile, the product exhibits light yellow color and viscous property. The reaction proceeds toward the AB_2 intermediate, and the carboxyl groups are continuously consumed. The effects of PTSA itself on the acid number are neglected, considering its relatively small usage. The acid number of the system is abnormal when PTSA concentration is more than 4%. It indicates that some unexpected byproducts are produced by increasing the concentration of the catalyst. PTSA concentration is determined to be 3% in the esterification reaction to avoid byproducts during the syntheses of *m*-HPAE.

Figure 5B shows the influence of temperature and reaction time on the acid number in the esterification reaction. Acid number can be used to indirectly demonstrate the extent of the reaction. It decreases with the increasing temperature due to the fact that the hydroxyl groups are reacting with the carboxylic acid in the previously formed monomer. The stabilized acid number indicates reaction equilibrium at 120°C, which is also the temperature limit of the light-yellow intermediate being produced. The influence of various reaction times was also evaluated at 120°C, where

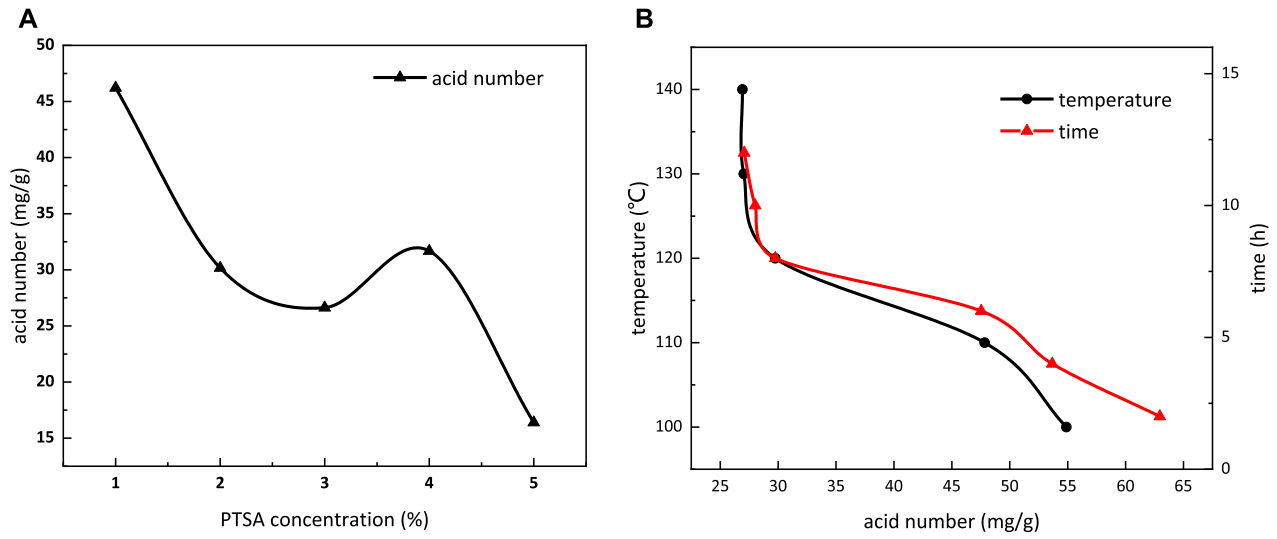

FIGURE 5 | Influence of PTSA concentration **(A)** and temperature and reaction time **(B)** on the acid number in the esterification reaction.

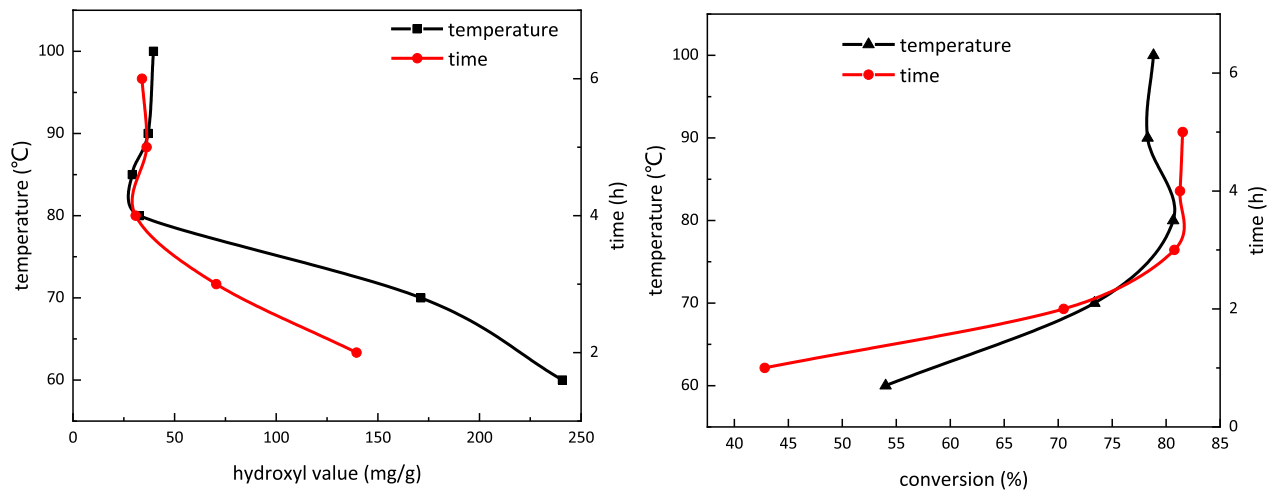

FIGURE 6 | Influence of temperature and reaction time on the hydroxyl value **(A)** and conversion **(B)** in the carboxymethylation reaction.

3% PTSA as the catalyst and 9:1 M ratio of the intermediate and TMP were used. The acid number presents a stabilized trend after the 8-h reaction, which indicates that the esterification reaction achieves equilibrium at 8 h. Therefore, in the esterification reaction, the temperature is determined to be 120°C, and the reaction time is 8 h.

Figure 6A depicts the influence of temperature and reaction time on the hydroxyl value in the carboxymethylation reaction. The hydroxyl value decreases with the increasing temperature and becomes stable at temperature above 80°C. With extended reaction time, the hydroxyl value also decreases and becomes stable when the reaction time is more than 4 h. Therefore, in the carboxymethylation reaction, the temperature is determined to be 80°C, and the reaction time is 4 h.

Figure 6B shows the influence of temperature and reaction time on conversion in the carboxymethylation reaction. When the temperature is above 80°C and reaction time is over 4 h, the conversion trend in the carboxymethylation reaction does not present obvious change, which is in line with the conclusion given in **Figure 7**. The conversion at 80°C reaction for 4 h is 80.77%.

FT-IR

The spectral data of HPAE and the modified HPAE (*m*-HPAE) were recorded by using a FT-IR spectrometer in a wide spectral range, as is shown in **Figure 7**.

The strong absorbance bands at 3,420 cm^{-1} (*m*-HPAE)and 3,386 cm^{-1} (HPAE) indicate that the -OH group is present in the molecular structure. In the process of the hydroxylation reaction

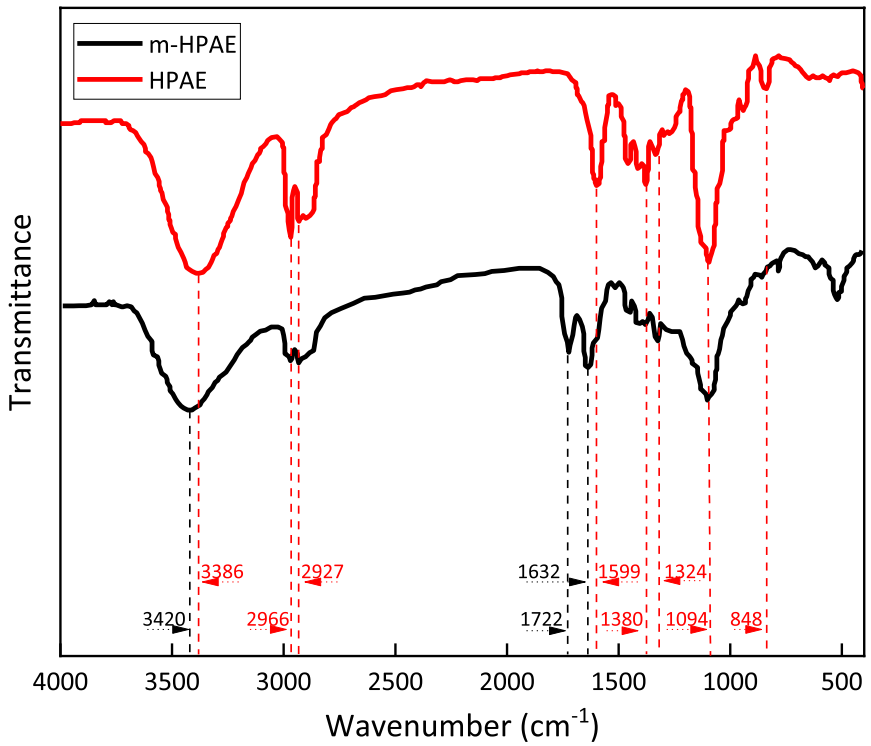

FIGURE 7 | FT-IR of HPAE and modified HPAE (*m*-HPAE).

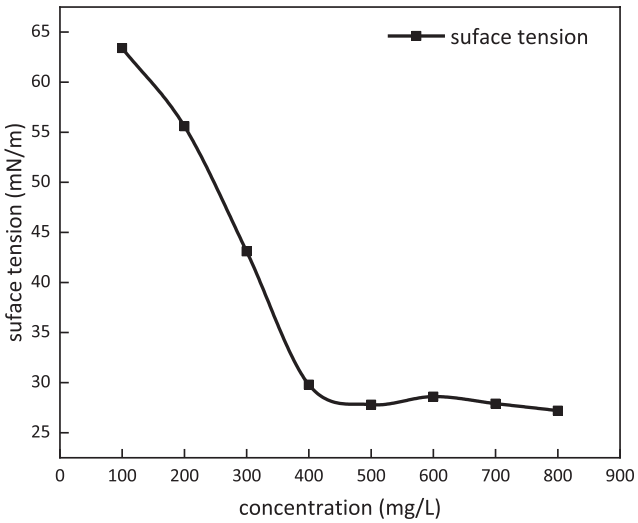

FIGURE 8 | Surface tension dependence on the concentration of *m*-HPAE.

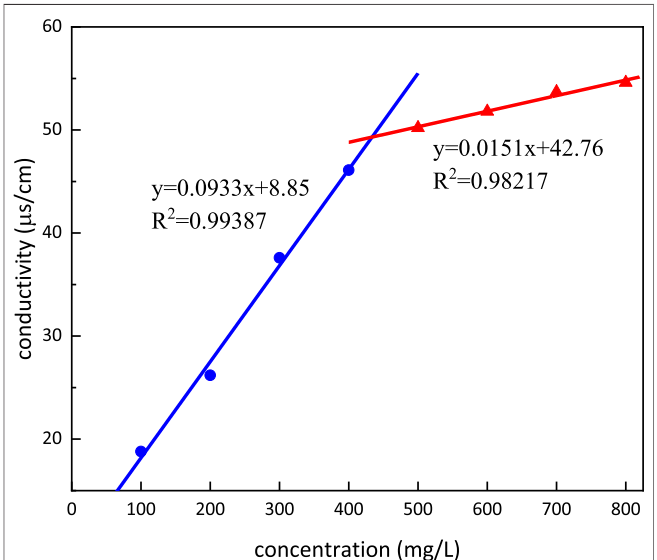

FIGURE 9 | Conductivity dependence on the concentration of *m*-HPAE.

of HPAE, -COONa is formed, and the terminal–OH is consumed, resulting in a less-intense absorption band. Meanwhile, it is normal that the amide–hydroxyl bonding peak appears in this region. The saturated carbon chain is elongated as a result of the hydroxylation of HPAE. This largely weakens the electron-withdrawing effect of adjacent–OH on amide groups, resulting in the enhanced inductive effect of adjacent carbon carbonyl C=O oxygen atoms on amide groups. That explains why the absorption peak has shifted to a higher wavenumber (3,420 cm^{-1}).

The absorption bands at 2,966 cm^{-1} and 2,927 cm^{-1} correspond to CH^{3-} and CH_2- in the molecule, respectively. The C–H absorption band at 2,890 cm^{-1} with low intensity is

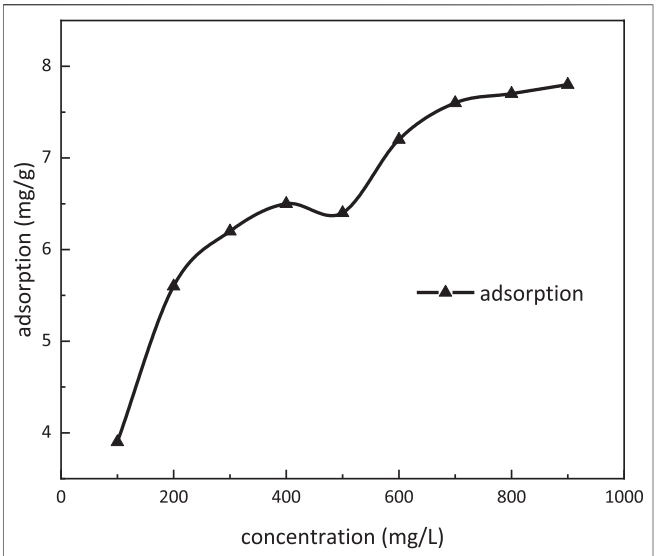

FIGURE 10 | Adsorption dependence on the concentration of *m*-HPAE.

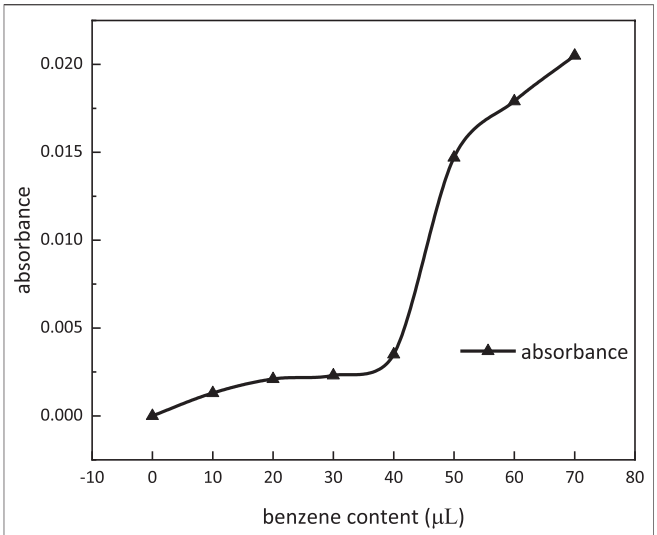

FIGURE 11 | Absorbance dependence on benzene content.

associated with the saturated carbon chain structure in the molecule.

Both HPAE and *m*-HPAE molecules show strong -COO- antisymmetric stretching vibration at 1,599 cm^{-1}. This absorption band is not associated to the amino acid (-CONH-) -COO- structure because the intensity is not highest. The presence of the -COO- structure in HPAE molecules throughout the modification processes is a strong evidence that the branched structure is built from the esterification reaction of HPAE and *m*-HPAE.

There are multiple strong absorption bands in the *m*-HPAE spectrum. 1722 cm^{-1} and 1,632 cm^{-1} correspond to ester carbonyl and tertiary amide carbonyl groups, respectively, which proves that the molecular structure at the position of the end group is modified to be –CO–N–COO-. Meanwhile, the carboxylic acid radical is present as indicated by the weak but characteristic absorption band at 550 cm^{-1} (-COO- vibration).

Multiple weak absorption bands are detected in the range of 1,500–1,000 cm^{-1} for both HPAE and *m*-HPAE, respectively. 1,380 cm^{-1} and 1,324 cm^{-1} correspond to amide C–N, while the broad absorption band at 1,094 cm^{-1} is connected to the aliphatic amide and C–O–C structure. The broad shape of the absorption band results from the increased contents of C–O–C by *m*-HPAE modification.

In theory, the products synthesized in this experiment can only be hyperbranched products or monomeric self-polymerized products. HPAE and *m*-HPAE are successfully obtained, and the expectation of the product design is met, as verified by infrared spectroscopy. The presence of hyperbranched and carboxymethylated products indicates the success of the branching and the carboxymethylation reactions. This is also confirmed by the increase in the value of the hydroxyl group.

Surface Tension

Surface tension dependence on the concentration of *m*-HPAE at 25°C is given in **Figure 8** *m*-HPAE is able to lower surface tension to around 28 mN/m, exhibiting excellence compared to the conventional surfactants such as OP-10 (around 31 mN/m) and LAS (around 32 mN/m).

Critical Micelle Concentration and Krafft Point

Conductivity dependence on the concentration of *m*-HPAE is shown in **Figure 9**. The conductivity was increasing with the increasing concentration of *m*-HPAE; however, the rate of the increase was different presenting a turning point (intersection of both lines) in the trend. This turning point, namely, CMC, is calculated to be 433.63 mg/L. The Krafft point is determined to be 5°C, which means that it can be used under room temperature conditions.

Adsorption Property

Adsorption dependence on the concentration of *m*-HPAE is given in **Figure 10**. The adsorption was increasing with increasing concentration of *m*-HPAE. In the range of 400–500 mg/L concentration, the adsorption onto the oil sand surface achieved a stable value. The CMC was also within this range, indicating that the adsorption equilibrium was achieved at the CMC. When the concentration was above 500 mg/L, the adsorption started to increase, breaking the stabilization. It is well-known that the dual layers of electrodiffusion were formed at the surface of the oil sands when contacting an aqueous solution. The negative ions in the surfactant solution were opposite to the electric charge on the surface of the oil sands, resulting in reduction in electrostatic action and weakening in the dual layers of electrodiffusion.

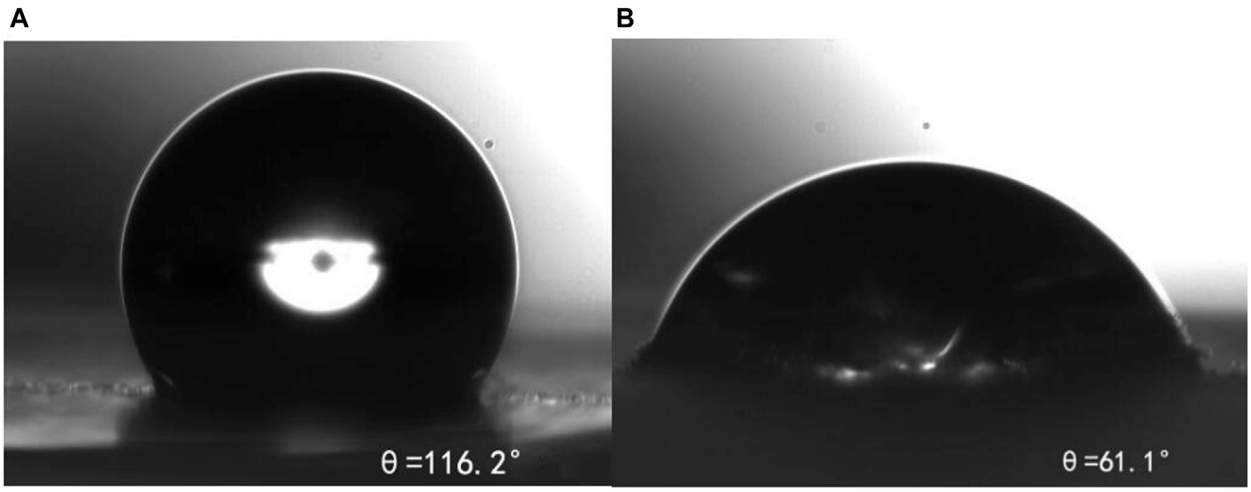

FIGURE 12 | Contact angle of hydrophobic formation of the rock sample **(A)** and rock sample after *m*-HPAE treatment **(B)**.

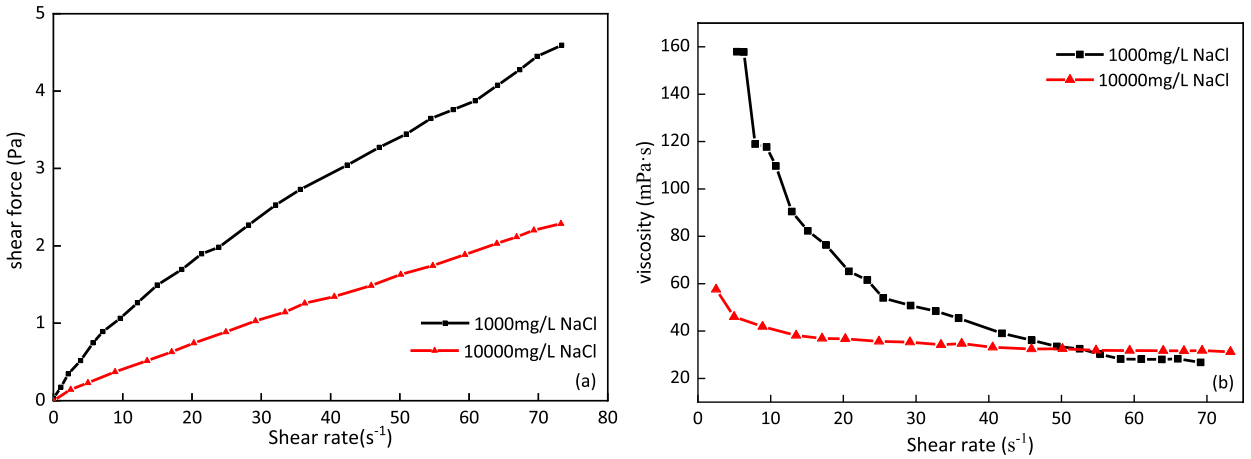

FIGURE 13 | Rheology of the *m*-HPAE solution in 1,000 mg/L and 10,000 mg/L salt solution.

More surfactant monomers tend to seek adsorption vacancy at higher concentration.

Micellar Solubilization

Absorbance dependence on benzene content at a wave number of 560 nm is shown in **Figure 11**. When benzene content was more than 40 μl, the absorbance of the solution was increasing dramatically. Micellar solubilization was determined to be 600 ml/mol at 40 μl of benzene content.

Wettability

Figure 12 shows that the contact angle (a) of the untreated rock sample is 116.2°, and the contact angle (b) after treatment is reduced to 61.1°, indicating that *m*-HPAE adsorbed on the rock surface can effectively improve the hydrophilicity of the rock surface, reduce the flow resistance of oil in water fluid in the water flooding system, reduce the possibility of blockage during the migration of formation of lipophilic particles, and achieve the purpose of improving formation permeability and enhancing oil recovery.

Rheology

Figure 13 shows that the apparent viscosity of the *m*-HPAE solution decreases with the increase in salinity. After the -COONa group is ionized in the solution, the -COO^- group is found to be electronegative. The mutual exclusion between groups results in the molecular chain being more stretched, the flow resistance increases, and the viscosity increases. When the high-concentration salt solution is added to the system, the cations gather around the electronegative groups, shielding the

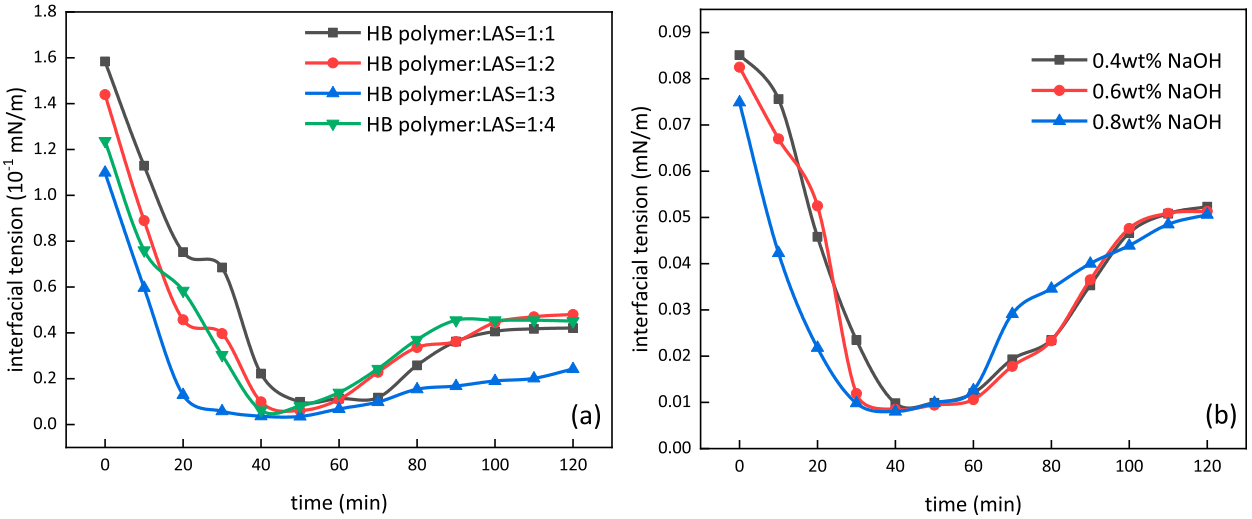

FIGURE 14 | Interfacial tension in various formulations of *m*-HPAE/LAS **(A)** and *m*-HPAE/NaOH **(B)**.

TABLE 1 | *m*-HPAE flooding results.

Core No	K (mD)	S_w (%)	E_w (%)	E_1 (%)	E (%)
1	129.85	60.87	31.98	10.40	42.38
2	269.65	42.55	29.84	13.87	43.71
3	604.91	58.46	31.94	21.58	53.52
4	701.55	52.69	38.05	20.64	58.69
5	819.68	68.87	34.99	18.98	53.97
6	921.66	62.35	32.69	22.58	55.27
7	1,021.87	70.15	41.58	25.15	66.73

TABLE 2 | *m*-HPAE/LAS flooding results.

Core No	K(mD)	S_w (%)	E_w (%)	E_1 (%)	E (%)
8	127.23	57.26	18.65	27.69	46.34
9	268.97	60.21	22.64	22.34	44.98
10	603.42	74.98	28.23	21.35	49.58
11	713.52	69.31	39.43	19.36	58.79
12	823.65	72.12	34.86	29.64	64.50
13	918.85	63.86	27.86	32.21	60.07
14	1,054.36	70.23	43.32	27.56	70.88

effective charge, reducing the anion mutual exclusion, shrinking the molecular chain structure, and reducing the flow resistance and viscosity. The m-HPAE solution maintains the shear thinning characteristic when adding the low-concentration salt solution (1000 mg/L), while after adding the high concentration salt solution (10000 mg/L), the shear thinning effect decreases with the increase of the shear rate, which is similar to Newtonian fluid, and the viscosity is maintained near 31 MPa s.

Core Flooding

The formulation of *m*-HPAE/LAS and *m*-HPAE/NaOH with various ratios was prepared, and the interfacial tension was measured using a TX-500C interfacial tensiometer, as shown in **Figure 14**. **Figure 14A** demonstrates the interfacial tension trend with various mass ratios of *m*-HPAE/LAS. The interfacial tension can be lowered to a level of 10^{-2} by individual *m*-HPAE or LAS; however, this value was further lowered to a level of 10^{-3} using the formulation of *m*-HPAE/LAS due to the synergistic effect exerted by petroleum sulfonate and the HB carboxylate surfactant. The negatively charged oxygen atoms in sulfonic groups enhanced the interaction with crude oil by making full use of anionic surfactants' advantage of maximum interfacial adsorption, leading to a lower interfacial tension at a relatively low usage. Being formulated with *m*-HPAE, this advantage was further exhibited to achieve the optimum effect with least usage. The interfacial tension was lowered to 3.5×10^{-3} mN/m at 1:3 mass ratio of *m*-HPAE/LAS.

Figure 14B depicts the interfacial tension change with different mass fraction of NaOH in 0.04 wt% *m*-HPAE. The interfacial tension was also lowered to a level of 10^{-3} using the formulation of *m*-HPAE/NaOH, and the three mass fractions of NaOH did not present obvious difference. The reduction in interfacial tension was caused by competitive adsorption of *m*-HPAE and the alkali. The active materials were also produced by the reaction between the alkali and the acid in the crude oil, resulting in further reduction in interfacial tension.

Due to the well-known reservoir damage caused by alkali, it is not recommended to be used for flooding. The LAS was proven to be able to lower interfacial tension to the same level as NaOH when being formulated with *m*-HPAE; therefore, only the binary surfactant system of *m*-HPAE/LAS was used in core flooding experiments. The *m*-HPAE flooding and water flooding experiments were also conducted for comparison. The permeability of heterogeneous cores ranged from 100 mD to 1000 mD. 0.04 wt% *m*-HPAE and 1:3 mass ratio of *m*-HPAE/LAS were used in the flooding experiments. The results of

m-HPAE flooding and *m*-HPAE/LAS flooding are listed in **Table 1** and **Table 2**, respectively.

As shown in **Table 1**, the oil recovery was further enhanced by *m*-HPAE flooding after 98% water cut was observed in water flooding. The increment was ranging from 10.4 to 25.15% in the group experiments. Two aspects of the HPB contribute to enhanced oil recovery. On the one hand, *m*-HPAE, as described above being a surfactant, is able to lower interfacial tension to a great extent and on the other hand, the *m*-HPAE structure with an inward lipophilic group and many outward hydrophilic groups creates the perfect space for the migration of the oil drops.

As is given in **Table 2**, oil recovery was further enhanced by *m*-HPAE/LAS following water flooding, ranging from 19.36 to 32.21%. The formulation made full use of the combined chemicals, namely, polymer, for water inflow profile modification to enhance sweep efficiency and surfactants for lowering interfacial tension. The synergistic effect resulted in the formulation being more efficient, especially in low permeability cores, than the single use of *m*-HPAE.

CONCLUSION

M-HPAE was synthesized through two-step reactions, namely, esterification and carboxymethylation, to form the intermediate and the final product, respectively. The optimum condition for esterification was 8 h at 120°C, where 3% PTSA as the catalyst and 9:1 mol ratio of the AB_2 monomer and TMP were used. The optimum condition for carboxymethylation was 4 h at 80°C, and the ratio of the carboxymethylation reagent to HPAE was 1:12.

The properties of *m*-HPAE were evaluated experimentally and determined to be more excellent than the conventional surfactants. The CMC was 433.63 mg/L, the Krafft point was 5°C, and the surface tension was lowered to 28 mN/m. In the range of 400–500 mg/L concentration, the adsorption onto the oil sand surface achieved equilibrium and micellar solubilization reached 600 ml/mol.

The contact angle of core samples treated with *m*-HPAE decreased from 116.2° to 61.1°, which can change from the hydrophobic surface to the hydrophilic surface, indicating that *m*-HPAE can promote the migration of oil in water emulsion.

Rheological experiments show that the *m*-HPAE solution maintains the characteristics of shear thinning in the environment of the low-concentration salt solution, while its apparent viscosity further decreases under the action of the high-concentration salt solution. With the increase in the shear rate, the viscosity tends to a fixed value and the property is close to Newtonian fluid.

The interfacial tension can be lowered to a level of 10^{-2} mN/m by the single use of *m*-HPAE, and the value further decreased to a level of 10^{-3} mN/m while being formulated with LAS or NaOH. The oil recovery of water flooding was further enhanced by the single use of *m*-HPAE or the combination of *m*-HPAE/LAS. The latter exhibited more prosperous advantages in low-permeability reservoirs.

DATA AVAILABILITY STATEMENT

The original contributions presented in the study are included in the article/Supplementary Material; further inquiries can be directed to the corresponding author.

AUTHOR CONTRIBUTIONS

SQ: substantial contributions to conception and design, acquisition of data, and analysis and interpretation of data; QL: drafting the article or revising it critically for important intellectual content; XZ: final approval of the version to be published; and HC: agreement to be accountable for all aspects of the study in ensuring that questions are related to the accuracy.

FUNDING

The study was funded by National Natural Science Foundation of China, Fund no. 51774089, and NEPU Youth Nursing Program for Natural Science Fund, 2018GPQZ-04.

REFERENCES

Algharaib, M., Alajmi, A., and Gharbi, R. (2014). Improving Polymer Flood Performance in High Salinity Reservoirs. *J. Pet. Sci. Eng.* 115, 17–23. doi:10.1016/j.petrol.2014.02.003

Brattekås, B., and Seright, R. S. (2018). Implications for Improved Polymer Gel Conformance Control during Low-Salinity Chase-floods in Fractured Carbonates. *J. Pet. Sci. Eng.* 163, 661–670. doi:10.1016/j.petrol.2017.10.033

Caminade, A.-M., Yan, D., and Smith, D. K. (2015). Dendrimers and Hyperbranched Polymers. *Chem. Soc. Rev.* 44 (12), 3870–3873. doi:10.1039/c5cs90049b

Cardoso, O. R., Lima Vidal, R. R., de Lima, B. V., and de Carvalho Balaban, R. (2016). Polymer Flooding: The Influence of Polymer Chemical Structure and the Porous Medium. *Macromol. Symp.* 367, 30–41. doi:10.1002/masy.201500129

Chen, Q., Ye, Z., Tang, L., Wu, T., Jiang, Q., and Lai, N. (2020). Synthesis and Solution Properties of a Novel Hyperbranched Polymer Based on Chitosan for Enhanced Oil Recovery. *Polymers (Basel)* 12 (09), 2130. doi:10.3390/polym12092130

Clarke, A., Howe, A. M., Mitchell, J., Staniland, J., and Hawkes, L. A. (2016). How Viscoelastic-Polymer Flooding Enhances Displacement Efficiency. *SPE J.* 21 (03), 0675–0687. doi:10.2118/174654-pa

Flory, P. J. (1941). Molecular Size Distribution in Three Dimensional Polymers. II. Trifunctional Branching Units. *J. Am. Chem. Soc.* 63 (11), 3091–3096. doi:10.1021/ja01856a062

Flory, P. J. (1952). Molecular Size Distribution in Three Dimensional Polymers. VI. Branched Polymers Containing A R Bf-1 Type Units. *J. Am. Chem. Soc.* 74 (11), 2718–2723. doi:10.1021/ja01856a062

Frey, H. (2003). Degree of Branching in Hyperbranched Polymers Enhancement of the DB: Scope and Limitations. *Acta Polymer.* 48 (8), 298–309. doi:10.1002/masy.201500129

Gurunathan, T., Mohanty, S., and Nayak, S. K. (2016). Hyperbranched Polymers for Coating Applications: A Review. *Polymer-Plastics Techn. Eng.* 55 (1), 92–117. doi:10.1080/03602559.2015.1021482

Jianbo, H., Kui, Z., Bin, X., Xiaodong, H., Jinlong, W., Haibo, S., et al. (2020). Classification and Log Evaluation to Low Permeability Conglomerate Reservoir of Baikouquan Formation in Mahu Depression Junggar Basin. *Well Logging Technol.* 44 (3), 305–311.

Khorsandi, S., Qiao, C., and Johns, R. T. (2017). Displacement Efficiency for Low-Salinity Polymer Flooding Including Wettability Alteration. *SPE J.* 22 (02), 417–430. doi:10.2118/179695-pa

Luo, S., Zhao, W., Lin, W., Liu, Y., Zhou, L., and Yang, C. (2019). Complex Gas and Water Identification Based on Lithologic Analysis. *Well Logging Technol.* 43 (3), 252–256.

Saboorian-Jooybari, H., Dejam, M., and Chen, Z. (2016). Heavy Oil Polymer Flooding from Laboratory Core Floods to Pilot Tests and Field Applications: Half-century Studies. *J. Pet. Sci. Eng.* 142, 85–100. doi:10.1016/j.petrol.2016.01.023

Sheng, J. J., Leonhardt, B., and Azri, N. (2015). Status of Polymer-Flooding Technology. *J. Pet. Sci. Eng.* 54, 116–126. doi:10.2118/174541-pa

Sieberer, M., Jamek, K., and Clemens, T. (2017). Polymer-Flooding Economics, from Pilot to Field Implementation. *SPE Econ. Manage.* 9, 51–60. doi:10.2118/179603-pa

Sun, C., Hou, J., Pan, G. M., and Xia, Z. Z. (2016). Optimized Polymer Enhanced Foam Flooding for Ordinary Heavy Oil Reservoir after Cross-Linked Polymer Flooding. *Adv. Mater. Sci. Eng.* 2017, 777–815. doi:10.1155/2017/5247305

Wang, J., and Zhang, C. (2019). Pore Structures and Classification of Carbonate Reservoirs in the Middle East. *Well Logging Technol.* 43 (6), 631–635.

Yin, D., and Zhao, D. (2017). Main Controlling Factor of Polymer-Surfactant Flooding to Improve Recovery in Heterogeneous Reservoir. *Adv. Mater. Sci. Eng.* 2017, 1–8. doi:10.1155/2017/5247305

Zhao, W., Liu, T., and Meng, H. (2020). Analysis of the Effects of Effective Pressure on Permeability and Formation Factor. *Well Logging Technol.* 44 (1), 32–37.

Ziyuan, C., Yuwei, L., Yishan, P., Bo, L., Ying, S., Jianguang, W., et al. (2021). Study on CO_2 Foam Fracturing Model and Fracture Propagation Simulation. *Energy* 238, 121778.

Conflict of Interest: Author HC is employed by PetroChina.

The remaining authors declare that the research was conducted in the absence of any commercial or financial relationships that could be construed as a potential conflict of interest.

Publisher's Note: All claims expressed in this article are solely those of the authors and do not necessarily represent those of their affiliated organizations, or those of the publisher, the editors, and the reviewers. Any product that may be evaluated in this article, or claim that may be made by its manufacturer, is not guaranteed or endorsed by the publisher.

NOMENCLATURE

HBP Hyperbranched polymer

HPAE Hyperbranched polyurethane

sCMC Critical micelle concentration

K Permeability

P Porosity

$\mathbf{S_w}$ Water saturation

$\mathbf{E_w}$ Oil recovery by water flooding

$\mathbf{E_1}$ Oil recovery by *m*-HPAE flooding

$\mathbf{E_2}$ Oil recovery by *m*-HPAE/LAS

E Overall oil recovery

frontiers in Earth Science

ORIGINAL RESEARCH
published: 16 November 2021
doi: 10.3389/feart.2021.759538

Experimental Investigation on the Crack Evolution of Marine Shale with Different Soaking Fluids

Lei Wang[1], Zhenhui Bi[1,3], Yijin Zeng[2], Guangguo Yang[2], Yintong Guo[1] and Hanzhi Yang[3]*

[1]State Key Laboratory of Geomechanics and Geotechnical Engineering, Institute of Rock and Soil Mechanics, Chinese Academy of Sciences, Wuhan, China, [2]Sinopec Research Institute of Petroleum Engineering, Beijing, China, [3]State Key Laboratory for Coal Mine Disaster Dynamics and Control, Chongqing University, Chongqing, China

Hydration induced cracks could promote the complexity of hydraulic fractures in marine shale gas reservoir. But the evolution process and forming mechanism has not been fully investigated. In this paper, Longmaxi marine shale were collected and immersed in three types of fluids (distilled water, fracturing fluid, and mineral oil) for more than 10 days. The spatial-temporal evolution of soaking fractures was recorded and analyzed. A fracture mechanical model was established, considering the effects of *in-situ* stress, fluid pressure, hydration stress, and capillary force. The promotion mechanism of hydration cracks in forming complex fracking network was discussed. Results showed that hydration fractures were extremely developed and evenly distributed in a state of network for specimens immersed in distilled water. For specimens soaked in fracturing fluid, the hydration cracks were moderately developed for the addition of anti-swelling agent. Fractures were rarely developed for specimens treated in mineral oil. The hydration fractures were mainly formed in the first 5 h and showed strong anisotropy. Cracks parallel to the bedding planes accounted for the vast majority, with a small proportion developed in vertical direction. Theoretical calculations indicated that the stress intensity factor (SIF) caused by hydration stress and capillary force was greater than the measured fracture toughness. The micro crack would probably propagate along bedding planes and grow up into macro horizontal fractures, which promoted the formation of crisscrossing fracture network in shale gas formation.

Keywords: marine shale, hydration fracture, spatial-temporal evolution, fracture mechanical model, fracture network

OPEN ACCESS

Edited by:
Yuwei Li,
Liaoning University, China

Reviewed by:
Tianshou Ma,
Southwest Petroleum University, China
Bing Hou,
China University of Petroleum, China
Ada Huang,
University of Alberta, Canada

****Correspondence:***
Zhenhui Bi
bzh199511998@163.com

Specialty section:
This article was submitted to Economic Geology, a section of the journal Frontiers in Earth Science

Received: *16 August 2021*
Accepted: *08 October 2021*
Published: *16 November 2021*

Citation:
Wang L, Bi Z, Zeng Y, Yang G, Guo Y and Yang H (2021) Experimental Investigation on the Crack Evolution of Marine Shale with Different Soaking Fluids. Front. Earth Sci. 9:759538. doi: 10.3389/feart.2021.759538

INTRODUCTION

Marine organic-rich shales deposited in oceanic and continental margin basins are the most important source rocks of both conventional and unconventional oil and gas resources all over the world (Zou et al., 2019). During the past decade, marine shale gas exploration in China has acquired rapid progress. With the discovery of Fuling, Weiyuan, Changning, Fushun, Yongchuan

Abbreviations: $K_I^{(1)}$, Stress intensity factor (SIF) induced by *in-situ* stress MPa•m$^{1/2}$; σ, Remote *in-situ* stress perpendicular to fracture face MPa; aHalf-length of the micro fracture m; $K_I^{(2)}$SIF induced by fluid pressure MPa•m$^{1/2}$; p_fFluid pressure in fracture MPa; bHalf-length of infiltration area m.; $K_I^{(3)}$SIF induced by hydration stress MPa•m$^{1/2}$; σ_wHydration stress MPa; FCapillary force, N; γSurface tension of water N/m; θContact angle °; WFracture width m; $K_I^{(4)}$SIF induced by capillary force MPa•m$^{1/2}$; K_ITotality of SIF MPa•m$^{1/2}$; σ_VVertical principal stress MPa; σ_hHorizontal minimum principal stress MPa.

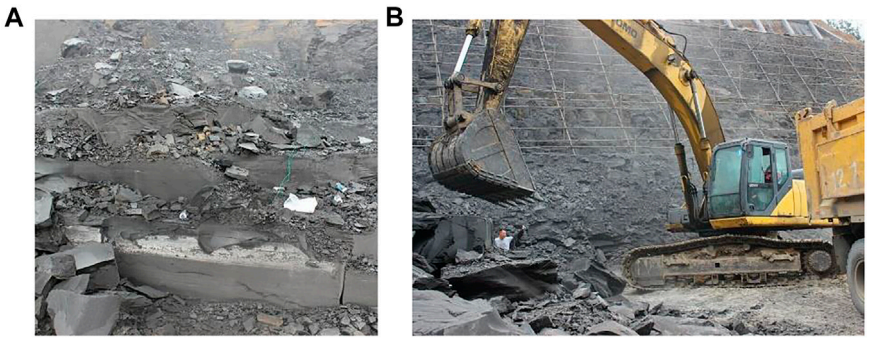

FIGURE 1 | Sampling process: **(A)** Longmaxi shale outcrop, and **(B)** field sampling.

Block in Sichuan Basin, the proved reserves of marine shale gas in China were up to 544.1 billion cubic meters, and the output of shale gas in 2020 reached 20 billion cubic meters (Cnr, 2021). Consequently, China has become the fourth country that achieved large scale commercial development of shale gas resources, and the other three countries are America, Canada and Argentina (Wang, 2017).

Shale hydration is a key factor that leads to wellbore instability problems in hard-brittle shale formation (Ma et al., 2021). Most researchers focused on revealing hydration mechanism (CHENEVERT ME, 1970; DARLEY HCH, 1969; Dokhani et al., 2015; Roshan et al., 2015; Wen et al., 2015; Liang et al., 2015; Kang et al., 2017) and developing effective anti-hydration drilling fluids to guarantee wellbore stability (Deville et al., 2011; Riley et al., 2012; An et al., 2015; Zhong et al., 2016; Barati et al., 2017). However, in the view of reservoir stimulation, it might be a positive effect on improving recovery ratio in shale gas reservoir (Dehghanpour et al., 2013; Ji and Geehan, 2013; Morsy and Sheng, 2014), because hydration induced fractures could enhance the formation permeability.

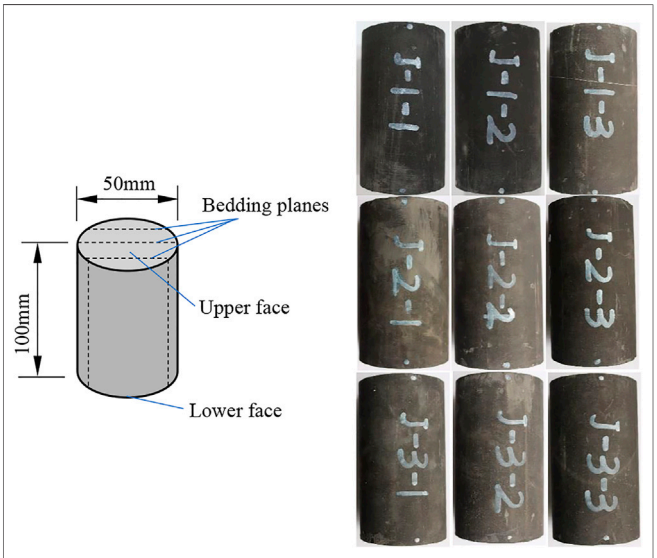

FIGURE 2 | Prepared standard specimens.

Field practice of shale gas exploration in Jiaoshiba block, Fuling Distict, Chongqing, China showed that it consumed about 3 h to fracturing one stage, preparation time between two adjacent stages was about 3–4 h, so fracturing 2 stages would cost nearly 1 day. Supposing that a well needs to fracture 16 stages, 8 days were needed (Wang et al., 2017). Typically, during the whole process of hydraulic fracturing, tens of thousands cubic meter fluid were injected in the reservoir, with very small proportion returning to the ground (Yuyang et al., 2021). So, shale reservoir was in a state of fluid immersion environment and hydration process would fully develop. Zhang and Sheng (2017) studied of the propagation of hydration-induced fractures in Mancos shale using computerized tomography. Ma and Chen (2014) investigated on the meso-damage characteristics of shale hydration. However, previous studies mainly focused on the certain or final hydration state to evaluate hydration effect. The detailed spatial-temporal evolution process of hydration fractures in marine shale was rarely reported and still need systematic study, which was valuable for reservoir engineers to design more abundant and effective permeable fractures.

This paper presents a detailed study on the fracture evolution of Longmaxi marine shale, soaked in three different types of fluids. The distribution and total length of hydration fractures were observed and analyzed from the time of immersion to more than 10 days. A mechanical model, considering the effects of *in-situ* stress, fluid pressure, hydration stress, and capillary force, was established to reveal the propagation mechanism of hydration fracture. Results could enlighten us about the formation mechanism of complex hydraulic fractures in shale gas reservoir.

EXPERIMENTAL DESIGN

Sample Preparation

The main shale gas reservoirs range from the upper Ordovician Wufeng Formation to lower Silurian Longmaxi Formation (Yi et al., 2019). Large shale blocks were collected from Longmaxi shale outcrop in Jiaoshiba Block, Fuling District, Chongqing, China (**Figure 1**). Then, cylindrical specimens with a diameter of

TABLE 1 | Mineral composition and mechanical properties of sampled marine shale.

Mineral composition									
Mineral type	Quartz	Cristobalite	Albite	Calcite	Muscovite	Pyrite	Annite	Ankerite	Clay mineral
Content (%)	50.23	4.75	17.60	2.60	5.71	5.80	3.83	4.21	5.26
Mechanical properties									
Loading direction VS Bedding plane			Strength (MPa)		Young's modulus (GPa)			Poisson's ratio	
Vertical			116.5		15.26			0.275	
Horizontal			86.2		15.95			0.320	

TABLE 2 | Allocation of specimens according to three types of soaking fluids.

Soaking fluids	**Distilled water**	**Fracturing fluid**	**Mineral oil**
Serial numbers of the specimens	J-1-1	J-2-1	J-3-1
	J-1-2	J-2-2	J-3-2
	J-1-3	J-2-3	J-3-3

50 mm were cored from shale blocks with the direction parallel to the bedding plane. These cored cylinders were cut and polished into standard specimens (ϕ50 mm × 100 mm) (Ulusay and Hudson, 2007). As shown in **Figure 2**, nine specimens were prepared ready for experiment. The mineral composition and general mechanical properties were provided in **Table 1** (Guo et al., 2018).

Experiment Scheme

Three kinds of soaking fluids (distilled water, fracturing fluid, and mineral oil) were selected to study the crack induced by hydration in shale. Mineral oil is a kind of liquid that contains no water. So, hydration effect would not occur for specimens soaking in it, which could be regarded as a control group. The fracturing fluid was a kind of slick water applied on site, where some additives (0.1% drag reducer, 0.2% anti-swelling agent, 0.1% synergistic agent, 0.02% anti-foaming agent) were added. MOBIL NUTO H46 was selected as mineral oil. As listed in **Table 2**, all nine specimens were divided into three groups and put into each of the three soaking fluids.

Test procedures are as follow:

1) Photograph the upper and lower faces of each specimen by high resolution camera to record the initial state of crack distribution.
2) Put each group of specimens into three vessels that contain different soaking fluids, guarantee all specimens are completely submerged.
3) After soaking for a certain time, take specimens out of the fluids and photograph the upper and lower faces of each specimen, then put specimens into the liquid again and keep on soaking. The time-points of taking out and photographing are set to 0, 2, 5, 12 and 23 h, 1D01, 1D09, 2D09, 4D, 7D01, 8D07 and 10D09 h from the test start time (h denotes hour, D represents day). The number of time-points are 12, and the whole observation period exceeds 10 days.
4) Import all photographs shot at different time-points into the AutoCAD software, draw and analyze the crack distribution of the upper and lower faces of all specimens.

EXPERIMENTAL RESULT AND ANALYSIS

Crack Evolution

Soaking in Distilled Water

After soaking in distilled water, the hydration fractures in the end faces of shale specimens were fully developed into a state of fracture network. Take the lower face of specimen J-1-2 for example (**Figure 3**). Before soaking, no fractures could be spotted by naked eyes. 2 h later, several fractures appeared parallel to the bedding planes. We called these horizontal fractures. After 5 h, the preexisting fractures continued propagating and new fractures were also formed. It was worthwhile to note that a new fracture was approximately vertical to the bedding planes and link up two horizontal fractures. We called it vertical fracture. Fractures were spread all over the end face. In the subsequent period, hydration fractures developed in two patterns: propagating parallel to the bedding planes and fracturing perpendicular to the bedding planes. After soaking 10 days and 9 h (10D09 h), the end face of the specimen showed a state of crisscrossing fracture network.

Soaking in Fracturing Fluid

For specimens soaking in fracturing fluid, hydration fractures were developed moderately and mainly paralleled to the bedding planes. Take the lower face of specimen J-2-3 for example (**Figure 4**). Originally, there were no obvious fractures in the end face. After soaking 2 h, several horizontal fractures were formed in the middle and lower part of the surface. Although continue soaking, rare new fractures were formed in other regions, instead, preexisting fractures kept on propagating and branching. Because of the addition of anti-swelling agent in fracturing fluid, the free swelling of clay minerals was restrained, leading to the relatively moderately developed hydration fractures compared with that immersed in distilled water.

Soaking in Mineral Oil

Entirely different from the specimens immersed in distilled water and fracturing fluid, fractures were rarely developed for specimens soaking in mineral oil. Take the specimen J-3-2 for

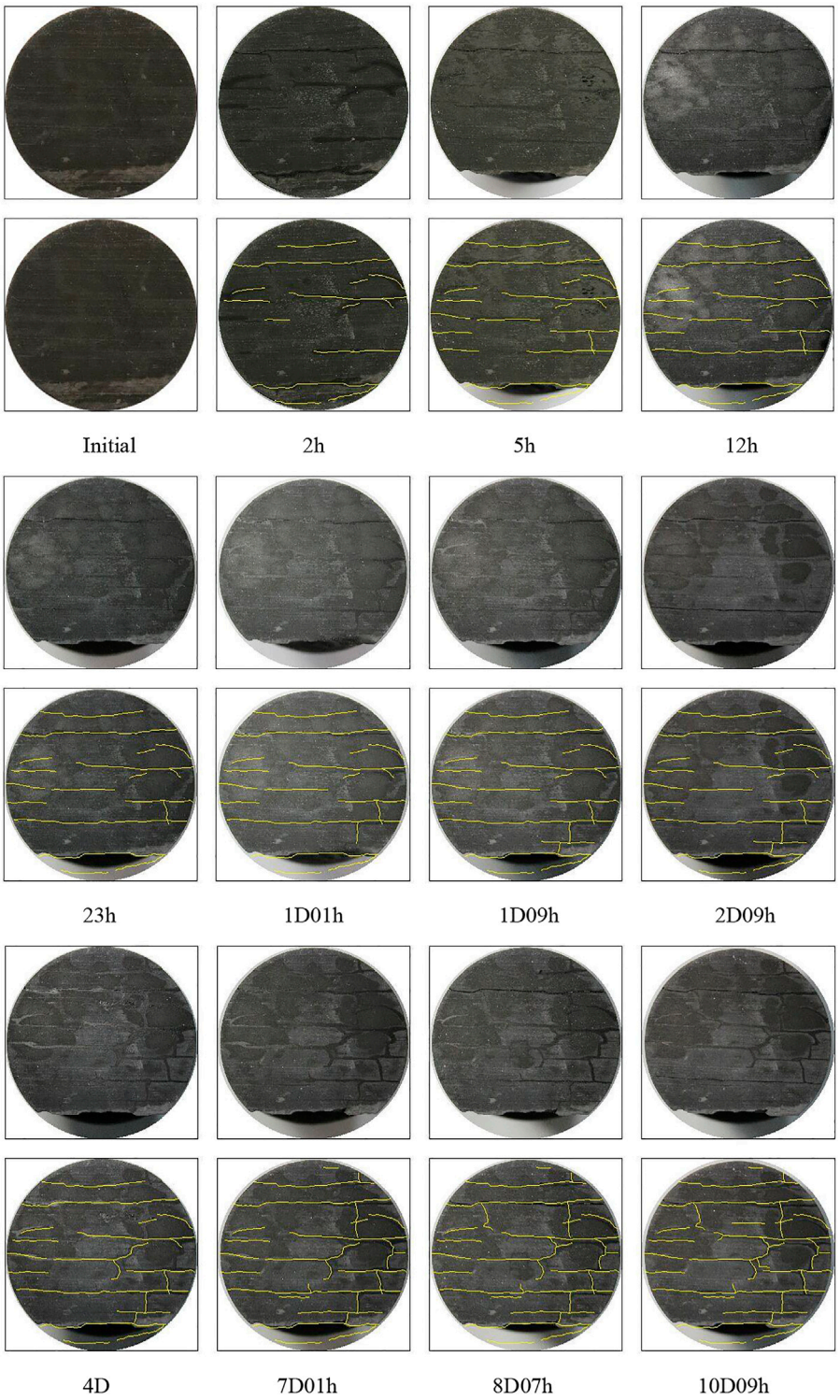

FIGURE 3 | Crack evolution process in distilled water **(lower face of J-1-2)** (In first line, original photos were showed; in second line, hydration fractures were highlighted by yellow lines in original photos).

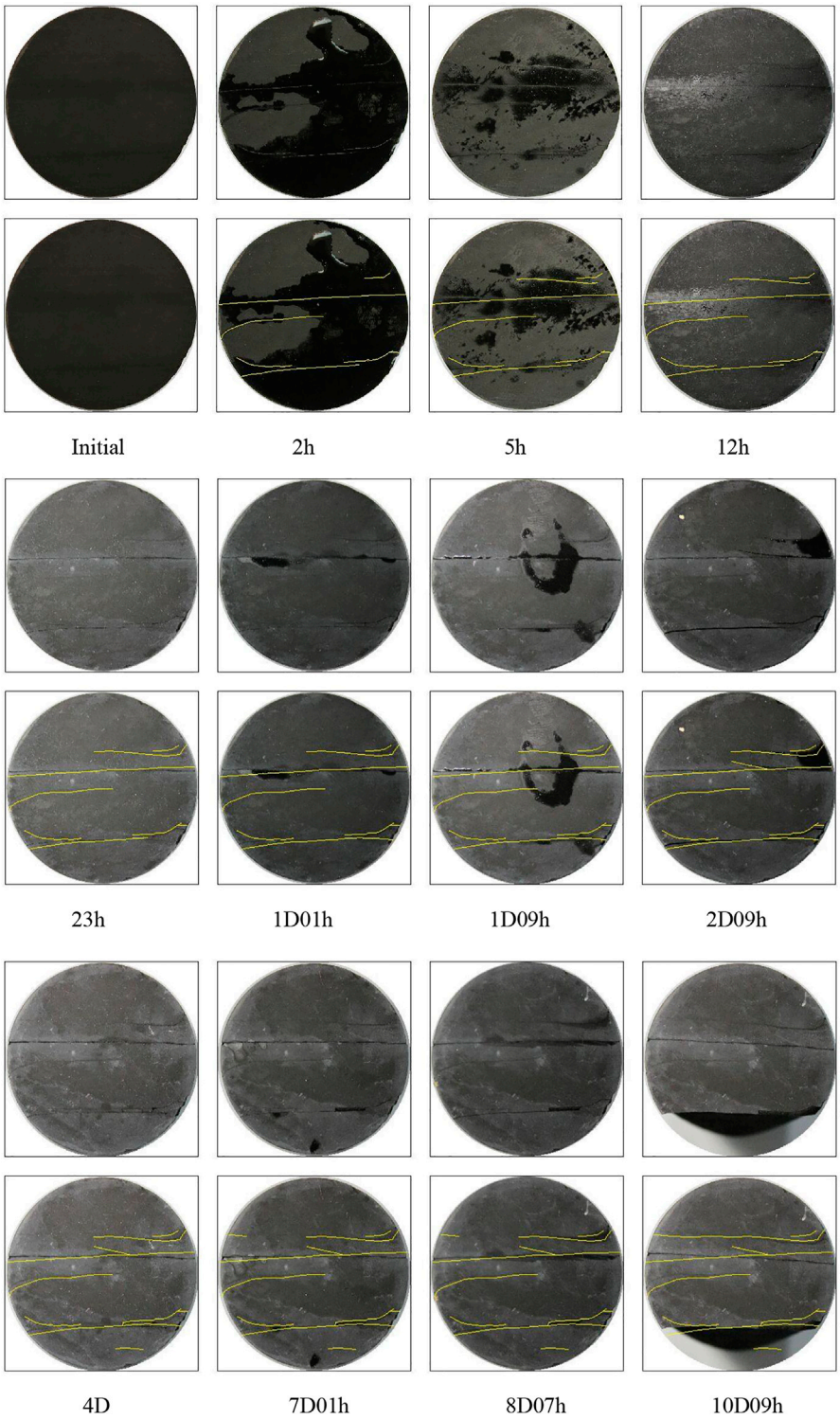

FIGURE 4 | Crack evolution process in fracturing fluid **(lower face of J-2-3)**.

example (**Figure 5**). There was one fracture in the upper face before soaking. After soaking 10D09 h, only one fracture developed in the middle part of the section and failed to reach the border. For the lower face, no fractures were spotted before test, and only three small fractures were formed after soaking 10D09 h.

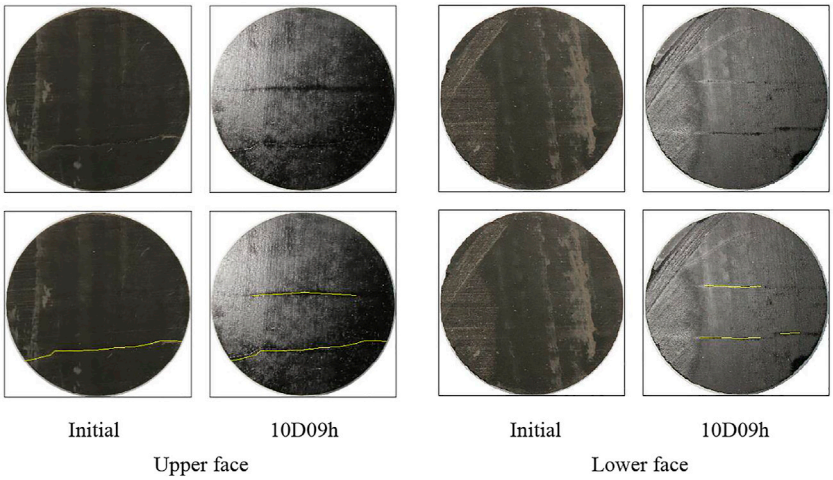

FIGURE 5 | Crack evolution process in mineral oil (J-3-2).

TABLE 3 | Statistics of length of all hydration crack of specimens soaking in distilled water and fracturing fluid (Unit: mm).

Time points number		0 h	2 h	5 h	12 h	23 h	1D01 h	1D09 h	2D09 h	4D	7D01 h	8D07 h	10D09 h
J-1-1	Upper	0	128	128	144	144	147	147	226	226	229	229	229
	Lower	0	163	163	210	215	216	216	230	306	331	337	340
J-1-2	Upper	0	106	119	128	140	140	163	188	190	190	202	205
	Lower	0	223	295	308	308	313	330	330	342	390	404	420
J-1-3	Upper	0	189	207	218	225	225	225	269	276	292	292	301
	Lower	49	193	237	237	258	258	266	281	287	287	293	301
J-2-1	Upper	11	169	186	186	186	186	186	211	211	214	214	214
	Lower	0	233	245	258	262	274	274	274	276	276	282	282
J-2-2	Upper	30	207	211	232	239	239	239	263	264	268	271	271
	Lower	23	191	233	233	248	251	251	255	259	259	266	266
J-2-3	Upper	0	145	166	166	170	179	179	188	199	203	203	219
	Lower	49	76	129	142	145	145	155	163	163	163	179	181

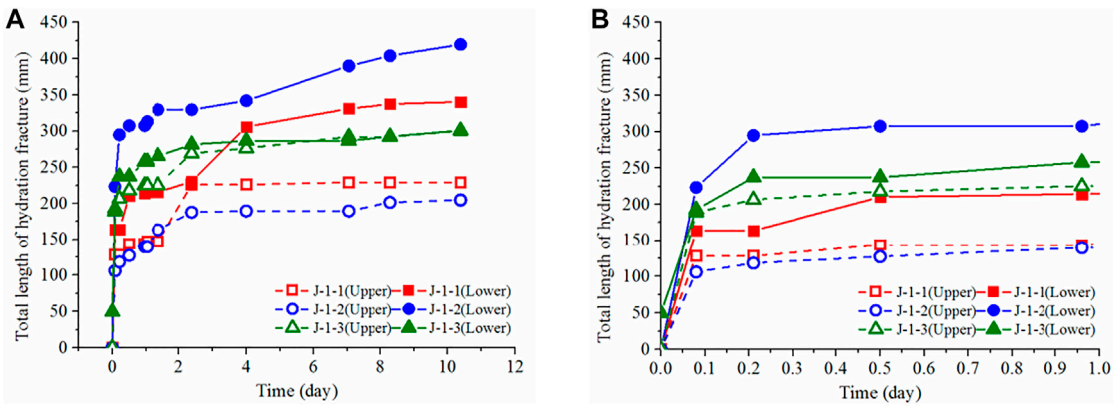

FIGURE 6 | Increase of the length of hydration fractures soaking in distilled water with time: **(A)** complete period, and **(B)** the first day.

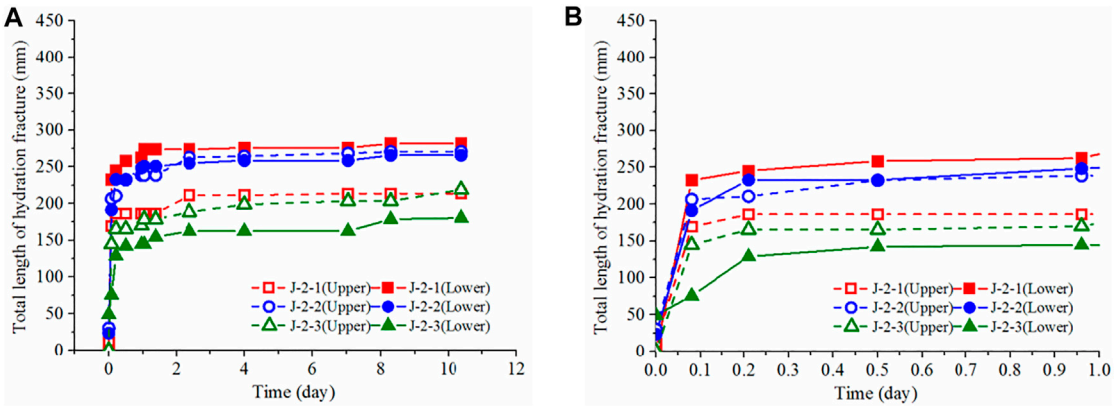

FIGURE 7 | Increase of the length of hydration fractures soaking in fracturing fluid with time: **(A)** complete period, and **(B)** the first day.

TABLE 4 | Statistics of length of vertical hydration crack of specimens soaking in purified water and fracturing fluid (Unit: mm).

Number		Soaking fluids	Vertical fractures			Total length of all fractures	Proportion of vertical fractures
			Whether occur	Occurrence time	Length		
J-1-1	Upper	Distilled water	No	---	---	229	---
	Lower		Yes	2D09 h	37	340	11%
J-1-2	Upper		No	---	---	205	---
	Lower		Yes	5 h	56	420	13%
J-1-3	Upper		Yes	23 h	23	301	8%
	Lower		Yes	4D	11	301	4%
J-2-1	Upper	Fracturing fluid	No	---	---	214	---
	Lower		No	---	---	282	---
J-2-2	Upper		No	---	---	271	---
	Lower		Yes	2D09 h	9	266	3%
J-2-3	Upper		No	---	---	219	---
	Lower		No	---	---	181	---

Statistical Analysis of Hydration Fractures

Evolution of the Total Fracture Length

The total length of end face hydration fractures at each soaking time-points were measured in AutoCAD. All data were collected in **Table 3**. Considering only a few fractures were formed in specimens submerging in mineral oil, fractures in these specimens were not included here.

For specimens soaking in distilled water, the length of hydration fractures grew rapidly in the early 5 h, then slowed down, and gradually reached a plateau. Finally, the total length of hydration fractures distributed between 150 and 450 mm (**Figure 6**). The average value of the six end faces was 299 mm. This indicated that the major part of hydration fractures was formed in the early period.

As illustrated in **Figure 7**, the evolution of the length of hydration fractures soaking in fracturing fluid was similar to those submerging in distilled water. The length of hydration fractures grew rapidly in the early 5 h, then slowed down, and finally became stable. The final hydration fracture length was distributed between 150 and 300 mm. The average value of the six end faces was 239 mm, decreased by 20% compared with that soaking in distilled water.

Evolution of the Vertical Fractures

It is worth considering that vertical fractures (fractures perpendicular to bedding planes) developed in some end faces of specimens and made the fracture system more complicated. Therefore, it was valuable to count and analyze the evolution of vertical fractures. Statistical data of vertical fractures were listed in **Table 4**. For specimens soaking in distilled water, four out of six end faces developed vertical fractures and the total fracture length were greater than those not forming vertical fractures. For specimens submerging in fracturing fluid, only one out of six end faces developed vertical fractures. The occurrence time of vertical fractures distributed between 5 h and 4 days. The proportion of length of vertical fractures was 3–13%, which was relatively small.

PROPAGATING MODEL OF THE HYDRATION FRACTURE

By investigating microstructure change during shale hydration, Shi et al. (2012) argued that capillary force induced by microfractures in shale promoted the hydration of clay

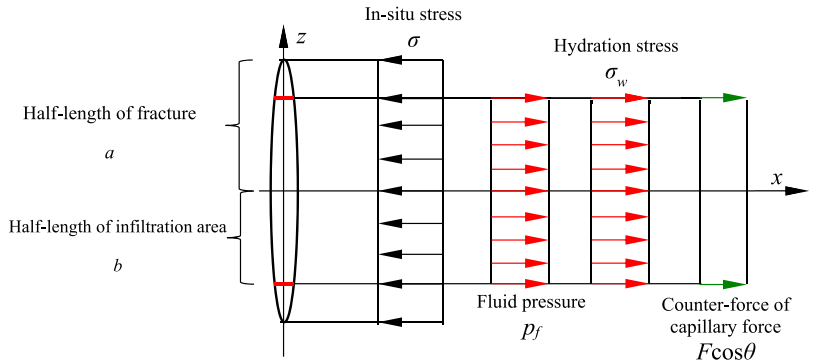

FIGURE 8 | Force analysis of hydration fracture.

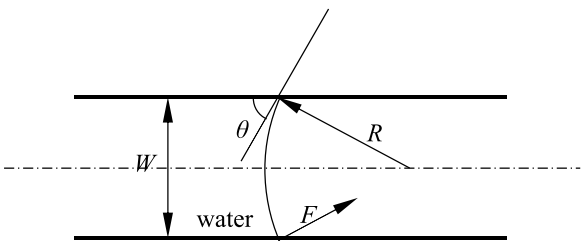

FIGURE 9 | Force analysis of capillary effect.

mineral. Meanwhile, hydration in turn accelerated the propagation of microfractures. This mutual promotion mechanism leads to the rapid evolution of hydration cracks. For this reason, a fracture propagation model considering hydration and capillary effect were established based on the theory of fracture mechanics (Anderson, 2005), and the promoting mechanism of hydration and capillary effect to fracture propagation were analyzed in a mechanical view.

The mechanical model is based on the following assumptions:

1) An infinite homogeneous medium contains a finite fracture;
2) The medium behaves in a linear elastic response to loading;
3) The fracture width is small enough to cause notable capillary effects;
4) Fluid pressure and hydration stress both distribute uniformly along fracture surface.

By considering hydration and capillary effects, the stress intensity factor (SIF) at fracture tip is determined by remote *in-situ* stress, fluid pressure, hydration stress and capillary force (see **Figure 8**).

1) SIF induced by *in-situ* stress

$$K_I^{(1)} = -\sigma\sqrt{\pi a} \tag{1}$$

Where σ is the remote *in-situ* stress perpendicular to fracture face, MPa; a is the half length of the micro fracture, m.

2) SIF induced by fluid pressure

$$K_I^{(2)} = 2p_f\sqrt{\frac{a}{\pi}}\arcsin\frac{b}{a} \tag{2}$$

Where p_f is the fluid pressure in fracture, MPa; b is the half length of infiltration area, m.

3) SIF induced by hydration stress

Hydration force are the result of swelling of clay mineral. Assume the clay mineral is distributed evenly in shale, and the hydration stress σ_w spread uniformly in fracture surface, the model I SIF can be described by

$$K_I^{(3)} = 2\sigma_w\sqrt{\frac{a}{\pi}}\arcsin\frac{b}{a} \tag{3}$$

4) SIF induced by capillary force

By simplifying the micro-fracture faces as parallel-plate, capillary force could be calculated by

$$F = \frac{2\gamma\cos\theta}{W} \tag{4}$$

Where F is capillary force, N; θ is contact angle, °; W is fracture width, m; γ is surface tension of water, N/m (**Figure 9**).

Fracture surface would bear the counter force of capillary force, $F\cos\theta$. SIF induced by this counter force is

$$K_I^{(4)} = \frac{4\gamma\cos^2\theta}{W}\sqrt{\frac{a}{\pi a^2 - b^2}} \tag{5}$$

The superposition of the above 4 parts results in the final mode I SIF.

$$\begin{aligned} K_I &= K_I^{(1)} + K_I^{(2)} + K_I^{(3)} + K_I^{(4)} \\ &= -\sigma\sqrt{\pi a} + 2p_f + \sigma_w\sqrt{\frac{a}{\pi}}\arcsin\frac{b}{a} + \frac{4\gamma\cos^2\theta}{W}\sqrt{\frac{a}{\pi a^2 - b^2}} \end{aligned} \tag{6}$$

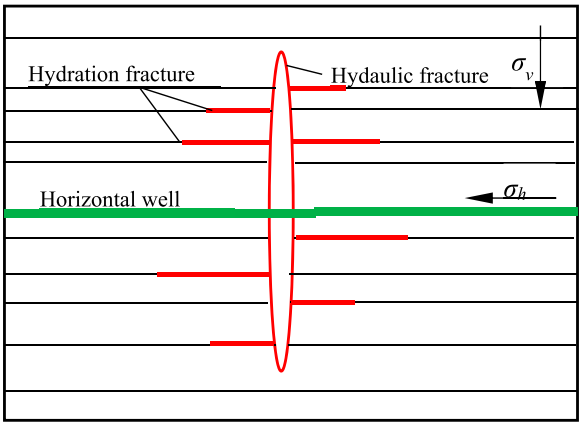

FIGURE 10 | Influence of hydration fracture to hydraulic fracturing.

Without considering the influence of *in-situ* stress and fluid pressure, assume the half length of micro-fracture is 0.005 m, half-length of infiltration area is 0.004 m, fracture with is 0.001 m, contact angle is 15°, surface tension is 0.0728 N/m, hydration stress is 1 MPa, the SIF induced by hydration and capillary effects is 3.613 MPa $m^{1/2}$. Heng et al. (2015) got the fracture toughness of shale (0.566 MPa $m^{1/2}$ along the bedding plane and 1.146 MPa $m^{1/2}$ perpendicular the bedding plane) by performing three-point bending test. By comparing this with previous study, it is apparently that the SIF caused by hydration stress and capillary force is greater than the measured fracture toughness and the micro-fracture would probably propagate.

DISCUSSION

Fracture propagation caused by hydration might play a key role in the formation of fracture network in shale gas extraction. As the major hydraulic fracture extends in the vertical or transverse direction, hydration fracture would form along the direction of bedding plane in the face of fracture. High fluid pressure and capillary induced hydration effect promotes fracture propagation along bedding-plane to the deeper shale reservoir. Micro hydration fracture would gradually develop into macro-crack which is a part of the whole hydraulic fractures. Finally, a 3-D stimulated volume would form, where major hydraulic fractures propagate along the direction of fracture height and length and secondary fractures extend along the direction of bedding planes (**Figure 10**).

Another import change is the reservoir stiffness. Shale formation that has been hydro-fractured is no longer an intact rock mass. Its strength, Youngs Modulus would reduce to some extent, and the permeability might increase. All these would bring critical influence on the follow-up fracturing and refracturing Wang et al., 2020.

It is a very interesting phenomenon that vertical cracks (fractures perpendicular to the bedding planes) occurred with horizontal (along bedding) fractures. Further analysis indicated that the occurrence time of vertical fractures distributed between 5 h and 4 days, at which the horizontal fractures had already been fully developed. It seems the horizontal and vertical fractures appeared in chronological order. As shown in **Figure 11**, the clay minerals usually arranged directionally along shale bedding planes. During the initial hydration process, the water absorption of clay minerals could induce great swelling stress to open the bedding planes. So, horizontal fractures along bedding planes would occur first and fully develop. Furthermore, the fully developed horizontal cracks promoted continuous hydration and swelling of clay minerals. This process could produce tensile stress along horizontal fracture surface and then induce the crack initiation and propagation perpendicular to the bedding planes, which contributed to forming the vertical cracks.

The application of water based fracturing fluid could induce abundant hydration cracks to increase the fracture complexity of fracking. But complex fractures would not surely represent high conductivity. The permeability damage caused by the swelling of clay mineral should also be evaluated, which is one of the critical disadvantages of the application of water based fracturing fluid Cong et al., 2022. Extra permeability tests should be conducted. The ideal water based fracturing fluid should not only create complex fractures, but also keep good fracture conductivity.

Although the evolution of hydration cracks was studied in this experiment, several limitations should be clarified to guide future research. Firstly, the test was conducted at room temperature and pressure, which ignored the high temperature and high pressure formation environment (Wang et al., 2021). Secondly, we only described the surface crack evolution, and failed to present the crack propagation inside the sample, which could be revealed by CT scanning (Ma and Chen, 2014; (Ma et al., 2016; Zhang and Sheng, 2017). Finally, the anisotropic bedding structure of shale

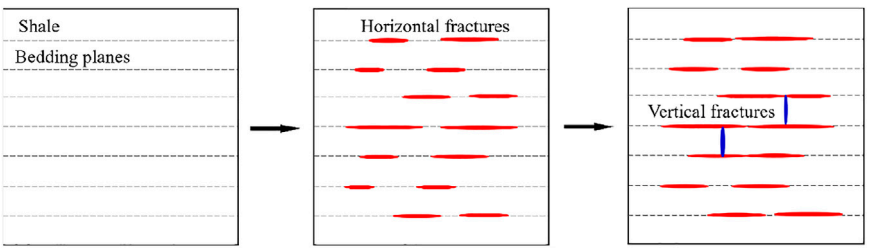

FIGURE 11 | Sketch map of the evolution of hydration fractures.

was not considered in theoretical analysis (Gui et al., 2018; (Ma et al., 2021). Restricted to experiment condition, the above aspects were not realized and would be paid attention in future study.

CONCLUSION

Shale hydration fractures not only threaten wellbore stability, but also influence the effect of reservoir stimulation. By performing shale soaking experiment in three different fluids, conclusions are as follows:

1) For specimens soaking in distilled water, hydration fractures were extremely developed and evenly distributed in a state of network, and their final average cumulative length were 299 mm.
2) For specimens soaking in fracturing fluid, hydration fractures were moderately developed and local accumulated, the final average cumulative length were 239 mm. The addition of anti-swelling agent remarkably restrained the free swelling of clay minerals. Fractures were rarely developed for specimens soaking in mineral oil.
3) The hydration fractures were mainly formed in the first 5 h and showed strong anisotropy. Cracks parallel to the bedding plane accounted for the vast majority, with a small proportion developed in vertical direction.
4) Theoretical calculations indicated that the stress intensity factor (SIF) caused by hydration stress and capillary force was greater than the measured fracture toughness. The micro crack would probably propagate along bedding plane and grow up into macro horizontal fractures, which promoted the formation of crisscrossing fracture network in shale gas formation

DATA AVAILABILITY STATEMENT

The original contributions presented in the study are included in the article/Supplementary Material, further inquiries can be directed to the corresponding author.

AUTHOR CONTRIBUTIONS

LW: Formal analysis; Writing—original draft. ZB: Writing—review and; editing. YZ: Acquisition and analysis of data. GY: Data curation. YG: Conceptualization; Methodology. HY: Design of the experiment.

FUNDING

This work was sponsored by the "Sinopec Science and Technology Department Project" (P21056). The open access publication fees is provided by this fund.

REFERENCES

An, Y., Jiang, G., Ren, Y., Zhang, L., Qi, Y., and Ge, Q. (2015). An Environmental Friendly and Biodegradable Shale Inhibitor Based on Chitosan Quaternary Ammonium Salt. *J. Pet. Sci. Eng.* 135, 253–260. doi:10.1016/j.petrol.2015.09.005

Anderson, T. L. (2005). *Fracture Mechanics-Fundamentals and Applications*. Boca Raton: CRC Press.

Barati, P., Shahbazi, K., Kamari, M., and Aghajafari, A. (2017). Shale Hydration Inhibition Characteristics and Mechanism of a New Amine-Based Additive in Water-Based Drilling Fluids. *Petroleum* 3, 476–482. doi:10.1016/j.petlm.2017.05.003

CHENEVERT ME (1970). Shale Alteration by Water Adsorption. *J. Pet. Tech.* 22, 1141–1148. doi:10.2118/2401-pa

Cnr (2021). The Growth Rate of Shale Gas Production in China Exceeded 30% in 2020. Available at: http://baijiahao.baidu.com/s?id=1691230280447523341&wfr=spider&for=pc.

Cong, Z., Li, Y., Pan, Y., Liu, B., Shi, Y., and Wei, J. (2022). Study on CO2 foam fracturing model and fracture propagation simulation. *Energy* 338, 121778. doi:10.1016/j.energy.2021.121778

DARLEY HCH (1969). A Laboratory Investigation of Borehole Stability. *J. Pet. Tech.* 21, 883–892. doi:10.2118/2400-pa

Dehghanpour, H., Lan, Q., Saeed, Y., Fei, H., and Qi, Z. (2013). Spontaneous Imbibition of Brine and Oil in Gas Shales: Effect of Water Adsorption and Resulting Microfractures. *Energy Fuels* 27, 3039–3049. doi:10.1021/ef4002814

Deville, J. P., Fritz, B., and Jarrett, M. (2011). Development of Water-Based Drilling Fluids Customized for Shale Reservoirs. *SPE Drilling and Completion* 26, 484–491. doi:10.2118/140868-PA

Dokhani, V., Yu, M., Takach, N. E., and Bloys, B. (2015). The Role of Moisture Adsorption in Wellbore Stability of Shale Formations: Mechanism and Modeling. *J. Nat. Gas Sci. Eng.* 27, 168–177. doi:10.1016/j.jngse.2015.08.056

Gui, J., Ma, T., Chen, P., Yuan, H., and Guo, Z. (2018). Anisotropic Damage to Hard Brittle Shale with Stress and Hydration Coupling. *Energies* 11, 1–15. doi:10.3390/en11040926

Guo, Y., Yang, C., Wang, L., and Xu, F. (2018). Effects of Cyclic Loading on the Mechanical Properties of Mature Bedding Shale. *Adv. Civil Eng.* 2018, 9. doi:10.1155/2018/8985973

Heng, S., Yang, C., Guo, Y., Wang, C., and Wang, L. (2015). Influence of Bedding Planes on Hydraulic Fracture Propagation in Shale Formations. *Chin. J. Rock Mech. Eng.* 34, 228–237. doi:10.13722/j.cnki.jrme.2015.02.002

Ji, L., and Geehan, T. (2013). "Shale Failure Around Hydraulic Fractures in Water Fracturing of Gas Shale," in SPE Canadian Unconventional Resources Conference 2013 - Unconventional Becoming Conventional: Lessons Learned and New Innovations (Calgary, Alberta, Canada: Society of Petroleum Engineers), 406–416. doi:10.2118/167155-ms

Kang, Y., Yang, B., Li, X., Yang, J., You, L., and Chen, Q. (2017). Quantitative Characterization of Micro Forces in Shale Hydration and Field Applications. *Pet. Exploration Develop.* 44, 328–335. doi:10.1016/S1876-3804(17)30038-1

Liang, L., Xiong, J., and Liu, X. (2015). Experimental Study on Crack Propagation in Shale Formations Considering Hydration and Wettability. *J. Nat. Gas Sci. Eng.* 23, 492–499. doi:10.1016/j.jngse.2015.02.032

Ma, T., and Chen, P. (2014). Study of Meso-Damage Characteristics of Shale Hydration Based on CT Scanning Technology. *Pet. Exploration Develop.* 41, 249–256. doi:10.1016/S1876-3804(14)60029-X

Ma, T., Gui, J., and Chen, P. (2021). Logging Evaluation on Mechanical-Damage Characteristics of the Vicinity of the Wellbore in Tight Reservoirs. *J. Petrol. Explor Prod. Technol.* 11, 3213–3224. doi:10.1007/s13202-021-01200-7

Ma, T., Yang, C., Chen, P., Wang, X., and Guo, Y. (2016). On the Damage Constitutive Model for Hydrated Shale Using CT Scanning Technology. *J. Nat. Gas Sci. Eng.* 28, 204–214. doi:10.1016/j.jngse.2015.11.025

Morsy, S., and Sheng, J. J. (2014). Effect of Water Salinity on Shale Reservoir Productivity. *Adv. Pet. Exploration Develop.* 8, 9–14. doi:10.3968/5604

Riley, M., Stamatakis, E., Young, S., Price Hoelsher, K., De Stefano, G., Ji, L., Guo, Q., and Friedheim, J. (2012). "Wellbore Stability in Unconventional Shale - The Design of a Nano-Particle Fluid," in Oil and Gas India Conference and Exhibition 2012, OGIC - Further, Deeper, Tougher: The Quest Continues. (Mumbai, India: Society of Petroleum Engineers - SPE), 416–423. doi:10.2118/153729-ms

Roshan, H., Ehsani, S., Marjo, C. E., Andersen, M. S., and Acworth, R. I. (2015). Mechanisms of Water Adsorption into Partially Saturated Fractured Shales: An Experimental Study. *Fuel* 159, 628–637. doi:10.1016/j.fuel.2015.07.015

Shi, B., Xia, B., Lin, Y., and Xu, J. (2012). CT Imaging and Mechanism Analysis of Crack Development by Hydration in Hard-Brittle Shale Formations. *Acta Petrolei Sinica* 33, 137–142.

Ulusay, R., and Hudson, J. A. (2007). *The Complete ISRM Suggested Methods for Rock Characterization, Testing and Monitoring; 1974–2006*. Cham, Switzerland: International Society for Rock Mechanics.

Wang, L., Guo, Y., Zhou, J., Yang, H., Yang, C., and Xiao, J. (2021). Rock Mechanical Characteristics of Deep marine Shale in Southern China, a Case Study in Dingshan Block. *J. Pet. Sci. Eng.* 204, 108699. doi:10.1016/j.petrol.2021.108699

Wang, L., Tang, K., Chen, F., Guo, T., Ren, G., and Dai, C. (2017). Technology of Bridge Plug and Multi-cluster Perforation and Its Application in Shale Gas of Sichuan and Chongqing Area. *Well Logging Technol* 41, 373-377.

Wang, S., Sun, D., Du, W., Geng, B., Bai, R., and Wang, Y. (2020). Evaluation Method of Shale Brittleness Index. *Well Logging Technol* 44, 294-299. doi:10.16489/j.issn.1004-1338.2017.03.023

Wang, S. (2017). Shale Gas Exploitation: Status, Issues and Prospects. *Nat. Gas Industry* 37, 115–130. doi:10.3787/j.issn.1000-0976.2017.06.016

Wen, H., Chen, M., Jin, Y., Zhang, Y., Ge, W., Du, J., et al. (2015). Water Activity Characteristics of Deep Brittle Shale from Southwest China. *Appl. Clay Sci.* 108, 165–172. doi:10.1016/j.clay.2015.02.015

Yi, J., Bao, H., Zheng, A., Zhang, B., Shu, Z., Li, J., et al. (2019). Main Factors Controlling marine Shale Gas Enrichment and High-Yield wells in South China: A Case Study of the Fuling Shale Gas Field. *Mar. Pet. Geology.* 103, 114–125. doi:10.1016/j.marpetgeo.2019.01.024

Yuyang, L., Xinhua, M., Xiaowei, Z., Wei, G., Lixia, K., Rongze, Y., et al. (2021). Shale Gas Well Flowback Rate Prediction for Weiyuan Field Based on a Deep Learning Algorithm. *J. Pet. Sci. Eng.* 203, 108637. doi:10.1016/j.petrol.2021.108637

Zhang, S., and Sheng, J. J. (2017). Study of the Propagation of Hydration-Induced Fractures in mancos Shale Using Computerized Tomography. *Int. J. Rock Mech. Mining Sci.* 95, 1–7. doi:10.1016/j.ijrmms.2017.03.011

Zhong, H., Qiu, Z., Zhang, D., Tang, Z., Huang, W., and Wang, W. (2016). Inhibiting Shale Hydration and Dispersion with Amine-Terminated Polyamidoamine Dendrimers. *J. Nat. Gas Sci. Eng.* 28, 52–60. doi:10.1016/j.jngse.2015.11.029

Zou, C., Zhu, R., Chen, Z.-Q., Ogg, J. G., Wu, S., Dong, D., et al. (2019). Organic-matter-rich Shales of China. *Earth-Science Rev.* 189, 51–78. doi:10.1016/j.earscirev.2018.12.002

Conflict of Interest: Authors YZ and GY were employed by Sinopec.

The remaining authors declare that the research was conducted in the absence of any commercial or financial relationships that could be construed as a potential conflict of interest.

Publisher's Note: All claims expressed in this article are solely those of the authors and do not necessarily represent those of their affiliated organizations, or those of the publisher, the editors, and the reviewers. Any product that may be evaluated in this article, or claim that may be made by its manufacturer, is not guaranteed or endorsed by the publisher.

frontiers in Earth Science

METHODS
published: 19 November 2021
doi: 10.3389/feart.2021.730080

Parameter Optimization of Segmental Multicluster Fractured Horizontal Wells in Extremely Rich Gas Condensate Shale Reservoirs

Wei Zhipeng, Wang Jinwei, Liu Rumin, Wang Tao and Han Guannan*

China Oilfield Services Limited, Tianjin, China

For economic and efficient development of extremely high-condensate shale gas reservoirs, a numerical model of segmental multicluster fractured horizontal well was established considering the effect of condensate and desorption, and the optimization of fracturing segments, fracturing clusters, half-length of main fracture, fracture permeability, fracture mesh density, and fracture distribution patterns were studied. It is indicated that the horizontal well whose design length is 2,700 m performs best when it has 43 fracturing segments with three clusters in each segment and the fracture permeability is 300 mD. The production capacity of horizontal wells is positively linearly correlated with the half-length of fractures. Increasing fracture half-length would be an effective way to produce condensate oil near wellbore. An effective fractured area can be constructed to remarkably improve productivity when the half-length of the fracture is 50 m and the number of secondary fractures is four in each segment. On the basis of reasonable fracture parameters, the staggered type distribution pattern is beneficial to the efficient development of shale gas-condensate reservoirs because of its large reconstruction volume, far pressure wave, small fracture interference, and small precipitation range of condensate.

Keywords: extremely high condensate, shale gas reservoir, segmental multicluster fractured, fracture parameter, horizontal wells

OPEN ACCESS

Edited by:
Yuwei Li,
Liaoning University, China

Reviewed by:
Xuyang Guo,
China University of Petroleum, China
Shaowen Mao,
Texas A&M University, United States
Jesse Williams-Kovacs,
University of Calgary, Canada

****Correspondence:***
Wei Zhipeng
282610988@qq.com

Specialty section:
This article was submitted to Economic Geology, a section of the journal Frontiers in Earth Science

Received: *24 June 2021*
Accepted: *27 October 2021*
Published: *19 November 2021*

Citation:
Zhipeng W, Jinwei W, Rumin L, Tao W and Guannan H (2021) Parameter Optimization of Segmental Multicluster Fractured Horizontal Wells in Extremely Rich Gas Condensate Shale Reservoirs. Front. Earth Sci. 9:730080. doi: 10.3389/feart.2021.730080

INTRODUCTION

Extremely high-condensate shale gas reservoirs, whose content of condensate can be as much as 600 g/m^3, undergo more sophisticated phase behavior compared with ordinary shale gas reservoirs, where issues such as low porosity, low permeability, adsorption, and desorption are investigated. Liquid phase would first precipitate and then reversely gasify during continuous isothermal depressurization (Ali et al., 1993).

This kind of gas reservoir is mainly distributed in North America. The exploration of this kind of liquid-rich shale condensate gas reservoir is still in initial stage. In recent years, scholars have carried out researches on different aspects (Behmanesh et al., 2013; Labed et al., 2015; Xu, 2016; Di et al., 2019; Guo et al., 2019; Qian et al., 2021; Zhi et al., 2021). Taylor et al. (2014) constructed an all-component dual-permeability model to simulate the flow after fracturing in the well group and studied the contribution of primary and secondary fracture systems to the production of liquid-rich shale gas reservoirs while ignoring the optimization of artificial fracture systems. Haghshenas et al. (2014) applied commercial numerical simulators to study the effects of factors such as recombination decomposition and absorption, pore structure and connectivity, fluid composition, and production

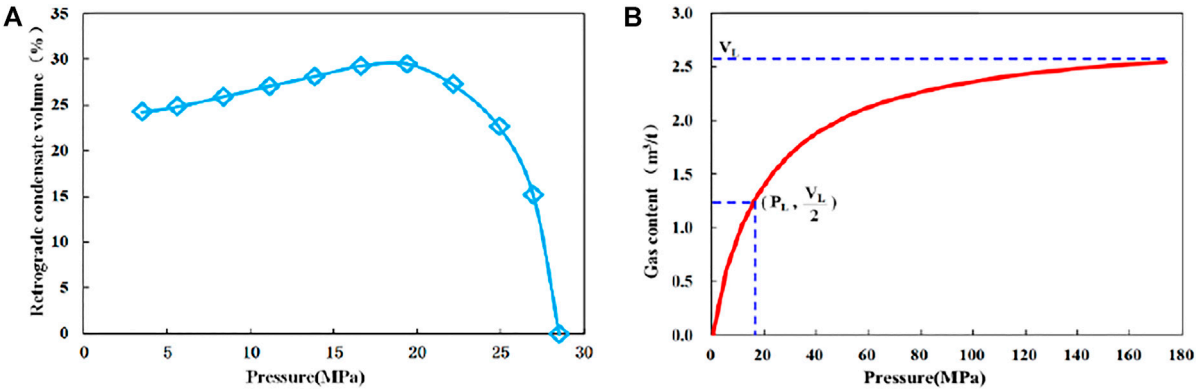

FIGURE 1 | Volume fraction change of condensate oil in CVD experiment **(A)** and Langmuir equilibrium absorption curve **(B)**.

conditions on the production of liquid-rich shale condensate gas reservoirs, without taking fracture systems into account. Jiang and Younis (2016) established a multicomponent model of complex fractured shale condensate gas reservoir and studied the productivity of CO_2 huff and puff. Labed (2016) conducted a numerical study on the flow of condensate gas in shale matrix using a pore network model, revealing the flow characters of the condensate shale gas. Multicluster fracturing of horizontal well is an effective means to develop shale gas condensate gas reservoir. Complex fracture network is generated during hydraulic fracturing process, bringing with it multiscale flow of matrix, natural fracture, and artificial fracture. Current investigations on extremely high-condensate shale gas reservoirs hardly consider the complex fracture system brought by segmental multicluster fracturing on the productivity of shale gas. In this article, the flow behavior in complex fracture systems is investigated, with the effect of adsorption–desorption and condensation. A numerical model of segmental multicluster fractured horizontal well is established based on Duvernay shale gas formation. The impact of parameters, including the number of fracturing segments, number of clusters in each segment, the half-length and permeability of a fracture, the fracture mesh density, and the distribution pattern of fractures, on the productivity of shale gas is then investigated based on the model. An optimized set of parameters is proposed in order to maximize the productivity.

INTRODUCTION OF DUVERNAY SHALE RESERVOIR

The effective thickness of the Duvernay shale reservoir in Simonette block of Western Canada Basin is 30 to 45 m, TOC is 2% to 6%, effective porosity is 3% to 6%, and permeability is 0.0001 to 0.0003 mD. The content of condensate of this block is 630 to 1,125 g/m^3, which is an ultrahigh-condensate gas reservoir by the international standard. The formation pressure is 77,000 kPa, and temperature is 116°C, so the reservoir fluid in the original state is gaseous, making it an unsaturated condensate gas reservoir. The dew point pressure is 28,550 kPa, and the maximum liquid precipitation is 29.51% (**Figure 1A**). The Langmuir isothermal adsorption curve is shown in **Figure 1B**. The average content of brittle minerals such as quartz and feldspar reaches 53%. Natural and induced fractures are easily formed under the action of external forces. As a result, complex fracture network probably dominates the pore system here. Large-scale multistage fractured horizontal wells were the main methods to produce the shale gas. Reasonable fracturing parameters of horizontal Wells are not clear yet.

NUMERICAL SIMULATION MODEL

At present, numerical simulation models of shale gas include dual-media model (Bustin et al., 2008; Ozkan et al., 2010), multimedia model (Wu et al., 2009), and equivalent-media model (Moridis et al., 2010). Among them, the dual-media model is the most widely used. The model assumes that shale is composed of two kinds of medium: matrix and fracture. Gas exists in shale in two forms: free state and adsorbed state, only free gas exists in fractures, and not only free gas exists in matrix, but also some gas is adsorbed on the matrix pore surface (Sun et al., 2012). The types of hydraulic fractures generated by staged fracturing vary from simple to complex, as shown in **Figure 2**. They are simple fractures, complex fractures, and fracture clusters (Fisher et al., 2004), among which the fracture cluster model is more consistent with the distribution of fracture network in the formation after hydraulic fracturing (Li et al., 2017; Li et al., 2018; Xie et al., 2020; Zhang et al., 2021a; Zhang et al., 2021b).

It is a very effective method to treat complex fracture network into equivalent fracturing reconstruction volume (SRV). SRV is composed of artificial main fracture and inner and outer areas of fracturing reconstruction. The inner zone is a complex fracture network system formed by fracturing transformation, which is treated as dual medium. The outer zone is treated as a single pore medium because it is not subject to fracturing transformation. In each region, the fluid flow is treated as a linear flow (Wu et al., 2017). Other basic assumptions are as follows:

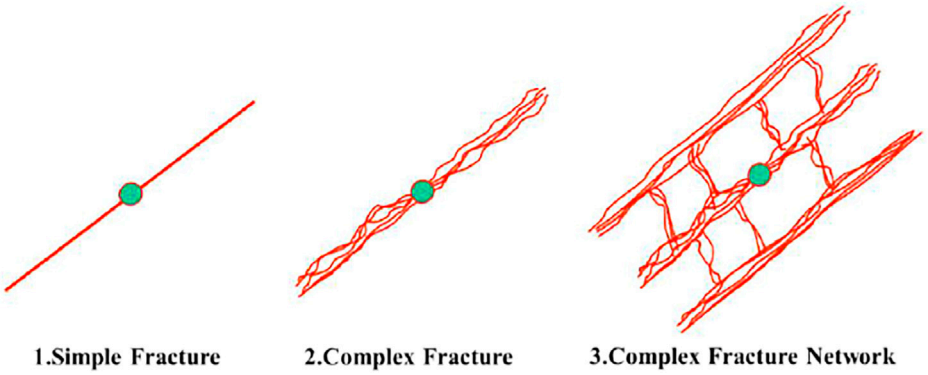

FIGURE 2 | Types of hydraulic fracture.

1) The reservoir is horizontally equal in thickness, the horizontal well is located in the center of the reservoir, and the fracture runs through the whole reservoir.
2) Consider the compressibility of oil and gas and ignore the compressibility of rock.
3) The adsorption and desorption of gas follows the Langmuir monolayer adsorption model. As the adsorption mechanism of condensate is not clear, it will not be considered separately.
4) The fluid is composed of oil and gas. The gas component exists only in the gas phase. The oil component can exist in both oil and gas phases at the same time. The content of dissolved condensate in the gas phase is characterized by Rv.

The outer region is the matrix region, and the adsorption and desorption of gas are described by Langmuir theory.

$$V = \frac{V_L p}{p_L + p} \tag{1}$$

where V_L is Langmuir volume (m^3/m^3); p_L is Langmuir pressure (MPa); p is pressure (MPa); V is the gas adsorption capacity in unit volume rock (m^3/m^3).

Therefore, the gas phase seepage equation of the outer zone (subscript A indicates the outer zone) is as follows:

$$\frac{\partial}{\partial y}\left(\frac{k_{Arg}}{\mu_g B_g}\cdot\frac{\partial p_A}{\partial y}\right) = \frac{\phi_A}{0.0864 k_A}\cdot\frac{\partial}{\partial t}\left[\frac{S_{Ag}}{B_g} + \frac{V_L p_A}{\phi_A (p_L + p_A)}\right] \tag{2}$$

where k is absolute permeability (10-3 μm^2); k_{rg} is relative permeability (decimal); μg is gas viscosity (mPa · s); B_g is volume factor (rm^3/sm^3); φ is porosity (decimal); S_g is gas saturation (decimal).

Initial condition: $p_A|_{t=0} = p_i$

Consider closed outer boundary conditions : $\frac{\partial p_A}{\partial y}|_{y=y_e} = 0$

The inner boundary is coupled with the fractured medium in the inner region, and the inner boundary condition is $p_A|_{y=y_F} = p_f$

where p_i is the original pressure (MPa); subscript f indicates the fracture in the inner area); y is the half-length of artificial fracture (m); y_e is the outer boundary range (m).

The inner region is a dual medium, which is characterized by Kazemi model of unsteady mass transfer. Then, the gas phase seepage equation in the matrix of the inner area (expressed by subscript m) is:

$$\frac{\partial}{\partial z}\left(\frac{k_{mrg}}{\mu_g B_g}\cdot\frac{\partial p_m}{\partial z}\right) = \frac{\phi_m}{0.0864 k_m}\cdot\frac{\partial}{\partial t}\left[\frac{S_{mg}}{B_g} + \frac{V_L p}{\phi_m (p_L + p)}\right] \tag{3}$$

Initial condition: $p_m|_{t=0} = p_i$

Consider closed outer boundary conditions : $\frac{\partial p_m}{\partial z}|_{z=0} = 0$

The inner boundary is coupled with the fractured medium, and the inner boundary condition is: $p_m|_{z=\frac{h_m}{2}} = p_f$, where h_m is the width of matrix block (m).

$$q_{gmf} = -\frac{2 k_m k_{mrg}}{h_m \mu_g}\cdot\left.\frac{\partial p_m}{\partial z}\right|_{z=\frac{h_m}{2}} \tag{4}$$

Considering that there is gas exchange between the fractures in the outer area and the inner area. The gas phase flow from the outer area is as follows:

$$q_{gAf} = \frac{k_A k_{Arg}}{\mu_g y_F}\cdot\left.\frac{\partial p_A}{\partial y}\right|_{y=y_F} \tag{5}$$

Considering the fluid supply from the inner matrix and the outer zone to the fracture medium in the inner zone, the gas-phase seepage equation in the fracture (expressed by subscript f) can be obtained as follows:

$$\frac{\partial}{\partial x}\left(\frac{k_{frg}}{\mu_g B_g}\cdot\frac{\partial p_f}{\partial x}\right) + \frac{q_{gmf} + q_{gAf}}{B_g k_f} = \frac{\phi_f}{0.0864 k_f}\cdot\frac{\partial}{\partial t}\left(\frac{S_{fg}}{B_g}\right) \tag{6}$$

Initial condition: $p_f|_{t=0} = p_i$

Outer boundary condition : $\frac{\partial p_f}{\partial x}|_{x=0} = 0$

The inner boundary is coupled with the artificial fracture, so the inner boundary condition is $p_f|_{x=\frac{L_f}{2}} = p_F$.

Considering the fluid exchange from the inner fracture to the artificial fracture (expressed by subscript F), the gas phase exchange capacity can be obtained as follows:

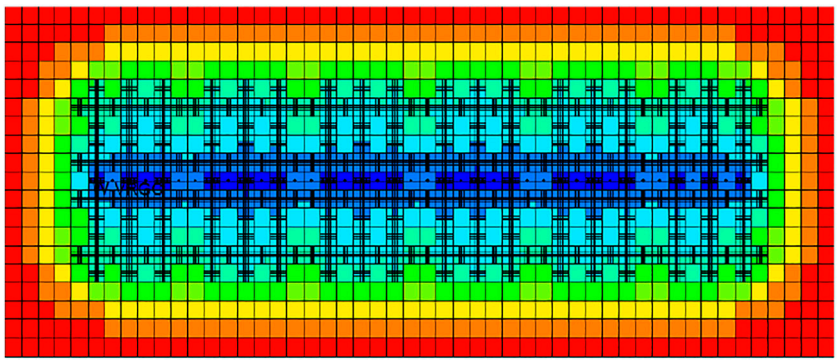

FIGURE 3 | Fracture distribution diagram of segmental fractured horizontal well mechanism model.

$$q_{gfF} = -\frac{2k_f k_{frg}}{w_F \mu_g} \cdot \left.\frac{\partial p_f}{\partial x}\right|_{x=\frac{L_F}{2}} \tag{7}$$

Therefore, the gas phase seepage equation in artificial fracture can be obtained as follows:

$$\frac{\partial}{\partial x}\left(\frac{k_{Frg}}{\mu_g B_g} \cdot \frac{\partial p_F}{\partial x}\right) + \frac{q_{gfF}}{B_g k_F} = \frac{\phi_F}{0.0864 k_F} \cdot \frac{\partial}{\partial t}\left(\frac{S_{Fg}}{B_g}\right) \tag{8}$$

Initial condition: $p_F|_{t=0} = p_i$

Outer boundary closure: $\frac{\partial p_F}{\partial y}|_{y=y_F} = 0$

If the gas well is produced under constant bottom-hole pressure, the inner boundary condition is as follows: $p_F|_{y=0} = p_{wf}$, where p_{wf} is the bottom-hole pressure (MPa).

Then, the gas production of the well can be obtained as follows:

$$q_{gsc} = 2 \times 0.0864 w_F H \frac{k_F k_{Frg}}{\mu_g B_g} \left.\frac{\partial p_F}{\partial y}\right|_{y=0} \tag{9}$$

GOR can be used to predict the output of oil phase. At the initial stage of production, the pressure has not spread to the reservoir boundary, and the gas oil ratio is constant, and GOR can be predicted with the data at the initial stage of production. When the pressure spreads to the boundary, GOR can be predicted by the material balance method.

Based on the DK-LS-LGR (dual permeability–logarithmic spacing change–local grid refinement) method of commercial numerical simulation software CMG, the complex fracture network generated by staged fracturing was characterized, and a mechanism model of staged multicluster fractured horizontal well in dual-media shale gas condensate reservoir considering the effects of condensate and desorption was established (**Figure 3**). A locally infilled double-permeability mesh with logarithmic spacing variation was used within the staged fracture zone to simulate the primary and secondary fractures generated by fracturing near the wellbore zone, whereas a common double-permeability mesh was used outside the zone to simulate the effects of natural fractures.

Based on the implementation of a large number of microseismic monitoring in the target block, it is clear that the effective half-length of fracture in the segmental fractured horizontal well is 50 to 75 m (**Figure 4**). The historical matching process of the model shows that the fitting effect is the best when the half-length of the fracture is 50 m. The permeability of hydraulic fractures is high in the near-well zone and low in the far-well zone. The fractures in each fracture stage are described as the fracture model in **Figure 5**, and the fracture permeability is set to decrease along the half-length of the fracture from the near-well to the far-well to further describe the actual situation of fractures in the formation.

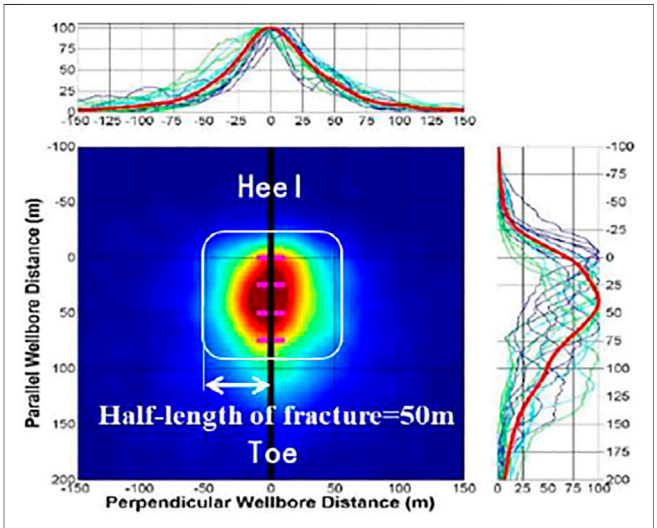

FIGURE 4 | Microseismic interpretation map.

WinProp module was used to process the PVT experimental data of the original well fluid, and the equation of state was fitted to generate the fluid model. Considering the influence of parameters such as fracture permeability, porosity, and water saturation decreasing along the half-length of fracture, the single-well history matching is carried out for bottom-hole pressure and daily oil and gas production, so as to make the model truly conform to the actual performance of gas reservoir. The fracture stress sensitivity is introduced into the simulation, and the fitting formula is as follows:

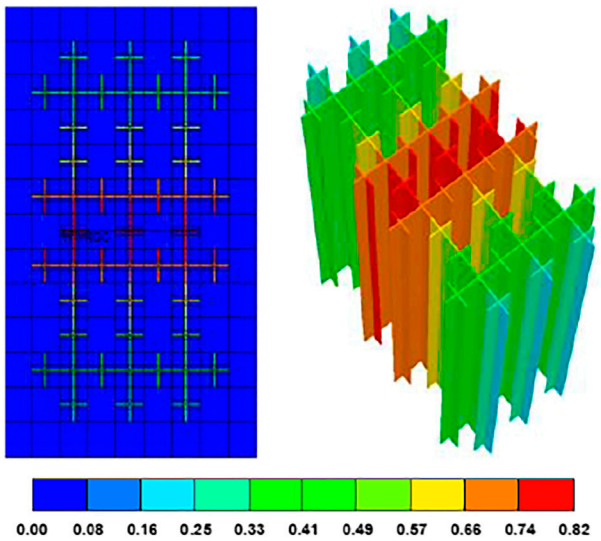

FIGURE 5 | Permeability distribution of hydraulic fractures in fracturing segment.

$$K_{mult} = 0.046e^{4\times10^{-5}P} \quad (10)$$

where K_{mult} is dimensionless permeability multiplication coefficient, and P is formation pressure (kPa). Fracture permeability will decrease with the decrease in formation pressure, which can further improve the fitting accuracy of bottom-hole pressure. During the model prediction, the half-length of fractures is set to be 50 m, with two to four clusters of fractures in each fracture stage, and the cluster spacing is 18 m. The production at constant pressure of 20,000 kPa was carried out under the combined action of condensate and desorption for 25 years.

FRACTURE PARAMETER OPTIMIZATION

The typically designed well length in ultrahigh condensate zone is 2,700 m. In order to develop shale condensate gas reservoir economically and efficiently, reasonable fracturing parameters of horizontal well should be determined. Based on the single-well model, the effects of the number of fracture stages, the number of clusters in the fracture stage, the half-length and permeability of the main fracture, the fracture network density, and the fracture distribution pattern on the development effect were studied.

Number of Fracture Stages and Number of Clusters in Each Stage

By keeping the length of horizontal wells constant, the numerical simulation study was carried out on horizontal wells with different number of fracture stages including two cluster fractures, three cluster fractures, and four cluster fractures. The variation curves of accumulated gas and accumulated condensate under different number of fractures were obtained (**Figure 6**).

It can be seen from **Figure 6** that the number of fractures has a great influence on the amount of accumulated condensate oil and gas. When the number of fractures is small, the growth range of accumulated gas and accumulated condensate oil is large with the increase in the number of fractures, and the lower the number of clusters within the interval, the higher the accumulated oil production. This is because under the same number of fractures, the fewer clusters per stage, the more fracture stages, and the larger the transformation range, which is conducive to the communication of more natural fractures, so as to improve the seepage conditions and increase the production rate. When the total number of fractures reaches a certain number, the change of accumulated gas and accumulated condensate with the increase in fracture number is not significant, and the difference between different cluster numbers becomes small. This is due to the decrease in reservoir pressure during depletion development of shale gas reservoirs as production progresses. The more the number of fractures, the faster the formation pressure drops. On the one hand, it is advantageous to the adsorption of shale gas desorption, increasing the reservoir gas. On the other hand, when the pressure is lower than the dew point, the condensate oil precipitates, and two-phase flow begins to appear in the formation, which leads to the increase in seepage resistance, the decrease in gas and oil production speed, and the loss of a large amount of condensate oil in the formation. It is the contradiction between fracturing stimulation and fluid resistance reduction. At the same time, the increase in fracture number leads to the decrease in interval spacing, bringing with it the interfracture interference, which restrains the production of each fracture and the overall effect of fracturing stimulation. Because of the large number of fractures, the difference of fracture treatment range with different cluster numbers becomes smaller, so the difference of cumulative production becomes smaller too. The comparison shows that 129 fractures is the optimal value, corresponding to a reasonable number of fracturing stages of 43, with three clusters of fractures in each stage. In this way, the shale reservoir can be fully stimulated to significantly increase oil and gas production, and the cumbersome situation caused by too many fracturing stages due to the small number of clusters in a single stage can be avoided.

Half-Length of Primary Fracture

Artificial fracture half-length affects the control range of single horizontal well to some extent. Increasing the half-length can improve the contact area between fracture and reservoir. Based on the optimized number of fracturing stages and the number of clusters within the stages, the fracture half-lengths were set as 20, 50, 80, 110, and 140 m, and the relationship curve between the accumulated oil and gas volume and the fracture half-length was obtained through simulation (**Figure 7A**). As can be seen from the figure, horizontal well productivity basically goes positively linear with fracture half-length. For shale reservoirs with very poor permeability, increasing artificial main fracture half-length can significantly expand the scope of reservoir reconstruction, thus increasing gas well productivity. In the production process, there will be two phase zones and condensate accumulation around the fracture surface, which leads to the decrease in gas

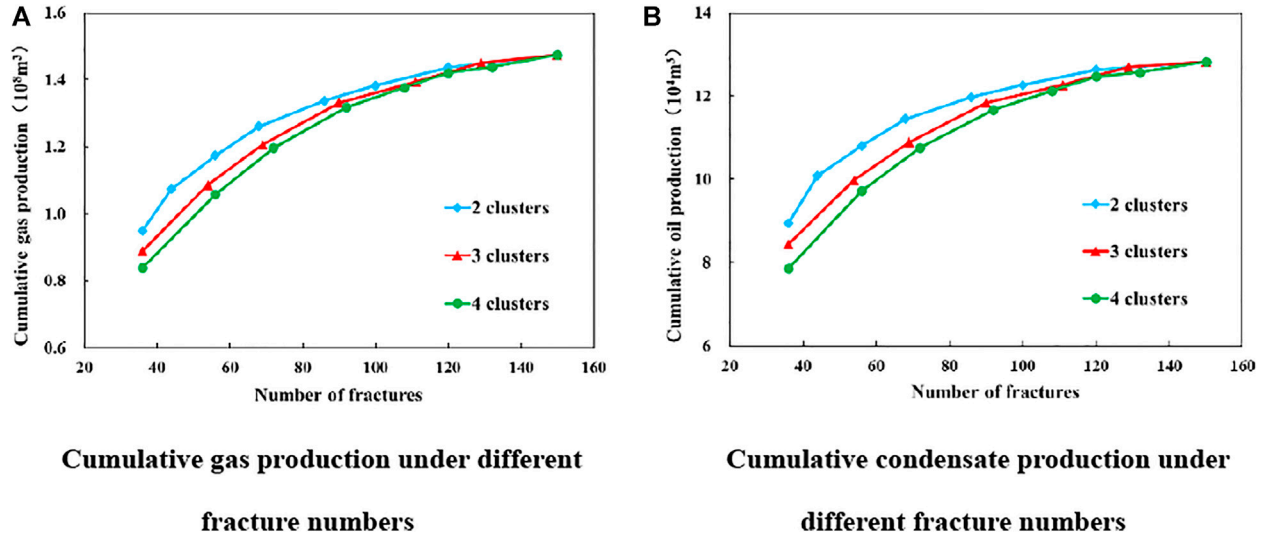

FIGURE 6 | Cumulative gas and condensate production curves of different numbers of fractures.

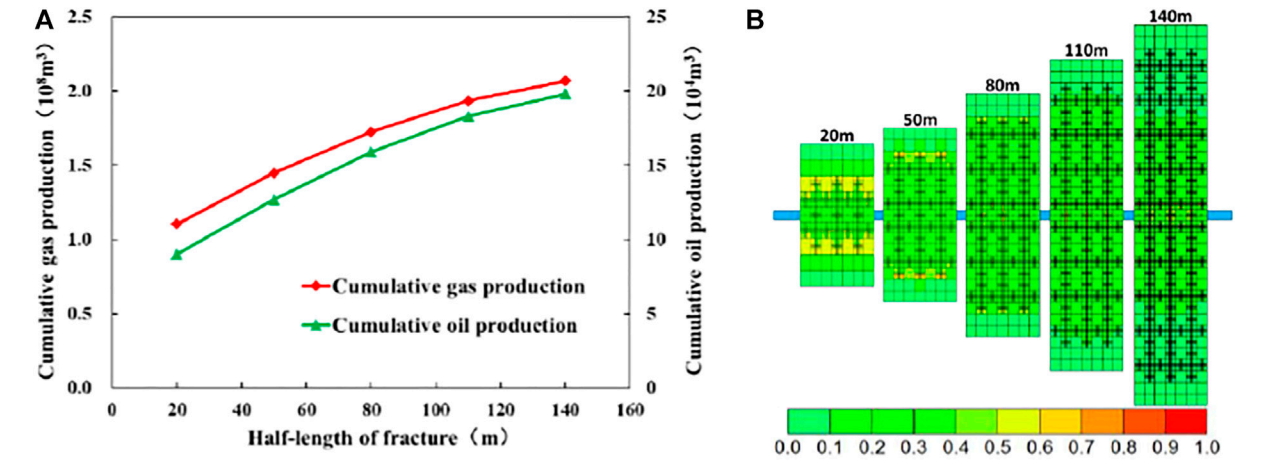

FIGURE 7 | Cumulative condensate and gas production curves **(A)** and condensate saturation distribution of fracturing segment **(B)** under different half-length of fracture.

and liquid permeability and the decrease in production. As can be seen from the condensate saturation distribution diagram (**Figure 7B**) in the fracturing stage under different fracture half-lengths, as the fracture half-length increases, the condensate saturation in the fracturing stage gradually decreases, so the seepage resistance will decrease correspondingly and the flow state of the fluid will be significantly improved. It can be concluded that increasing the fracture half-length is an effective way to exploit the potential of condensate near the well. However, in the actual fracturing process, fracturing equipment cannot meet the construction requirements of excessively high fracture half-length, so the economic and technical constraints can be fully considered to optimize the economic and optimal main fracture half-length.

Primary Fracture Permeability

Domestic and foreign experience in the transformation of ultralow permeability reservoirs by staged fractured horizontal wells shows that such reservoirs do not require high conductivity of artificial fractures (Yin et al., 2014). **Figure 8** shows the productivity prediction curves of horizontal Wells with different fracture permeability. The simulation results also confirm this view. **Figure 9A** shows that increasing the main fracture permeability has limited ability to improve the production status of shale condensate gas wells. When the main fracture permeability increases to a certain extent, the productivity of gas Wells does not increase significantly.

The permeability of shale gas condensate reservoir is very poor, and the conductivity between the fractures and the

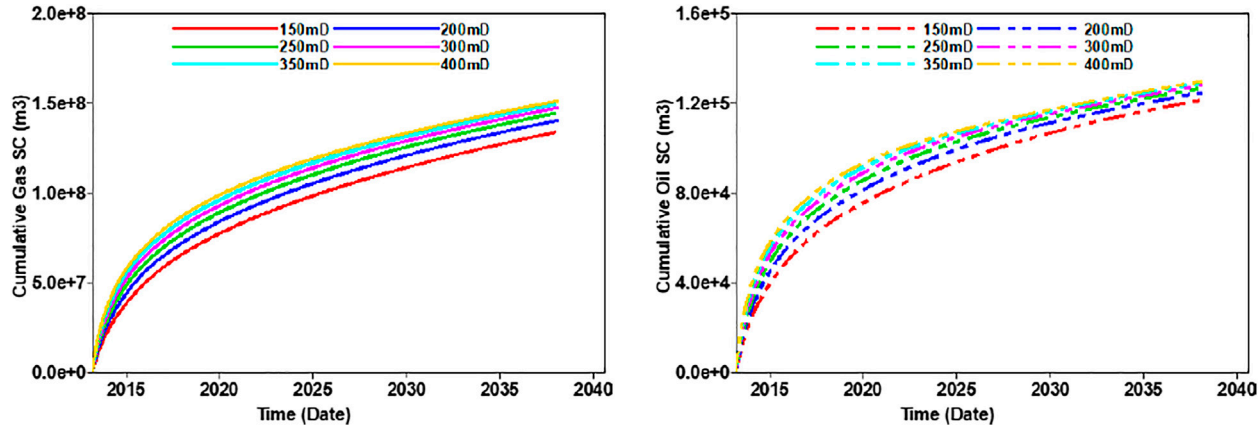

FIGURE 8 | Productivity of segmental fractured horizontal well with different fracture permeability.

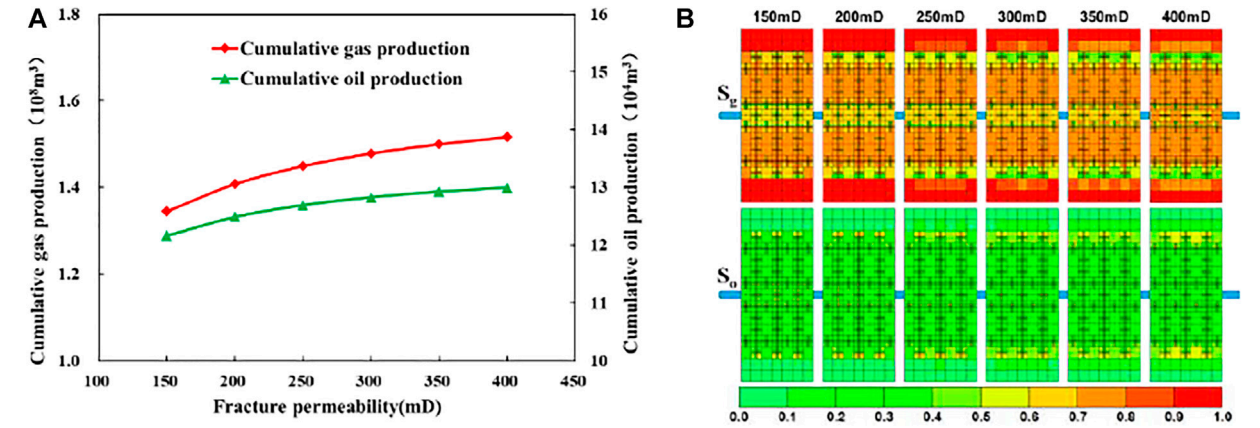

FIGURE 9 | Cumulative condensate and gas production curves **(A)** and oil and gas saturation distribution of fracturing segment **(B)** under different fracture permeability.

surrounding reservoir after fracturing is an important factor restricting the productivity of horizontal wells. Insufficient fluid supply from unmodified reservoirs to artificial fractures restricts the high seepage capacity of artificial fractures. As can be seen from the oil–gas saturation distribution in **Figure 9B**, when the permeability of the main fracture increases to a certain extent, there is no significant effect on oil and gas stimulation. When the number and half-length of fractures remain unchanged, the pursuit of excessive seepage capacity will inevitably lead to the increase in the difficulty of construction and the increase in fracturing cost (Mao et al., 2020). Therefore, it is reasonable to set the main fracture permeability as 300 mD.

Fracture Mesh Density

Fracture mesh density means the number of secondary fractures in each half-fracture. On the basis of the above fracture parameter optimization results, the half-length of the fracture in the model is set to be 50 m. Numerical simulations in which the number of secondary fractures in a single fracture stage is 0, 2, 4, 6, 8, and 10 are conducted, respectively, to simulate the development effect of staged fractured horizontal wells in shale condensate gas reservoir under different fracture network densities. It can be seen from the cumulative oil and gas volume curves of different numbers of secondary fractures (**Figure 10A**) that when the number of secondary fractures increases from 0 to 2, the cumulative oil and gas volume does not increase significantly. This is because there are few secondary fractures at this time, and no effective fracturing area has been formed. The amount of oil and gas production increased dramatically when the number of secondary fractures increases to 4. While the fracture mesh density continues to increase, oil and gas production increment is slow, which is due to the overlapping waste of transformation volume when fracture mesh density increases to a certain degree.

Figure 10B shows the local pressure distribution of staged fractured horizontal wells with different fracture network densities during 1 year of production. The analysis shows that when there are fewer than two secondary fractures, the fracture

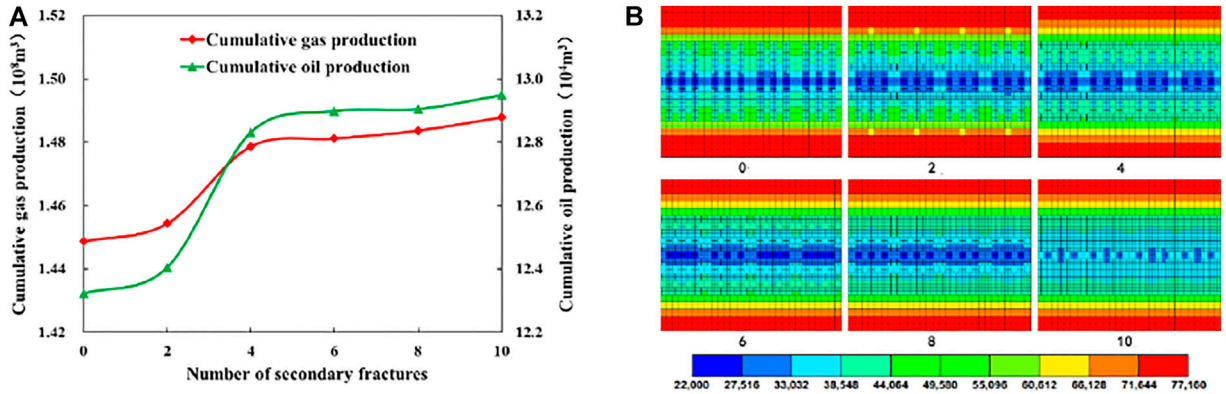

FIGURE 10 | Cumulative condensate and gas production curves **(A)** and local pressure distribution map of horizontal wells **(B)** under different number of secondary fractures.

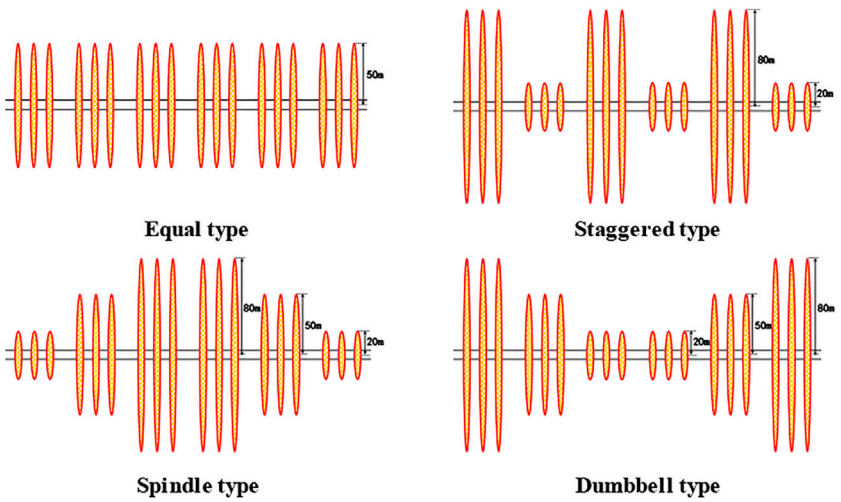

FIGURE 11 | Different fracture laying patterns.

network density is small, the pressure wave propagation is slow, and the spread range is small. When the number of secondary fractures reaches four, the main fractures and secondary fractures are staggered and connected, forming a complex fracture network. The reservoir between fractures is fully reformed, the pressure swept area increases, the pressure drop range is wide, and the stimulation effect is significant. As the fracture network density continues to increase, the pressure swept area does not change significantly, so the stimulation effect is no longer obvious.

Fracture Distribution Patterns

After optimizing the fracture parameters of segmented multicluster fractured horizontal wells, the effect of fracture distribution pattern on the productivity of shale gas condensate wells is further studied. In this case, a local horizontal well is fractured with six fractured sections, three clusters of fractures in each section, and main fracture permeability of 300 mD. Four fracture distribution patterns are designed (**Figure 11**) under the condition of maintaining the same total fracture length, which are of equal length type, staggered type, spindle type, and dumbbell type. Through simulation, the cumulative production figure (**Figure 12**) and the relationship curve between cumulative production and production time (**Figure 13**) were obtained under different fracture laying patterns.

It can be illustrated from **Figure 12** that the total fracture length is the same, and the final production of different fracture distribution pattern is different. The cumulative oil and gas production of staggered pattern is significantly higher than that of the other three types. It can be demonstrated from **Figure 13** that the initial outputs of the four fracture laying patterns are the same, and the production capacity of the staggered type in the middle and later stages of production is

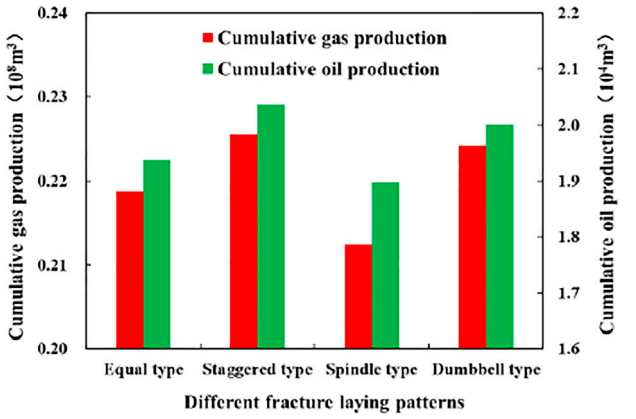

FIGURE 12 | Cumulative condensate and gas production of different fracture laying patterns.

obviously different from the other three types. This is because in the early stages of production, production is largely controlled by artificial fractures. Because the total fracture length is the same, the oil and gas productions are the same. With the extension of production time, the influence of pressure spread and the interference between fractures on productivity is greater. As can be seen from the pressure distribution diagram (**Figure 14**) of horizontal wells with different distribution methods after 5 years of production, the staggered type has a higher productivity due to more long fractures, larger volume of transformation, and longer range of pressure spread. At the same time, there is little interference between long and short cross-fractures, avoiding large scale of low pressure zones, and condensate precipitating (**Figure 15**), which reduces the reservoir damage, thus effectively improving the fluid flow state of the reservoir and achieving better stimulation effect.

DISCUSSION

A numerical model of segmental multicluster fractured horizontal wells is composed to discuss the flow of extremely rich gas condensate in complex fracture systems. The impact of factors including fracturing segments, fracturing clusters, half-length of main fracture, fracture permeability, fracture mesh density, and fracture distribution patterns on productivity were studied. The conclusions may provide meaningful support to the economic and efficient development of Duvernay gas-condensate shale reservoirs. However, some issues are still valuable to be further investigated and listed below.

1) The optimized fracture parameters are discussed via numerical simulation on the Duvernay formation, whereas those parameters have not yet been coupled with the field fracturing process. Whether the values of the parameters are applicable in the field practice needs to be further discussed.
2) In the optimization process, the parameters are discussed on the basis of other optimized values. Therefore, the interactions between parameters are not investigated. Further study could discuss the interaction between fracturing parameters by an orthogonal designed test.
3) The fracture patterns in this article are just in a theoretical way; the applicability of the fracture pattern should be discussed on the basis of field fracturing practice. The relationship between pump procedure and fracture patterns on the basis of stress interference is a significant issue.

CONCLUSION

For economic and efficient development of extremely high-condensate shale gas reservoirs, a numerical model of segmental multicluster fractured horizontal well was established considering the effect of condensate and desorption, and the optimization of fracturing segments, fracturing clusters, half-length of main fracture, fracture permeability, fracture mesh density, and fracture distribution patterns were studied. The results are as follows:

1) Based on the DK-LS-LGR method of CMG, the complex fracture network generated by staged fracturing is characterized with a single-well mechanism model of dual media staged multicluster fracturing horizontal well to simulate the multiscale flow of matrix, natural fractures, and artificial fractures in ultrahigh-condensate shale gas reservoir under the joint action of condensate and desorption. Considering the effect of fracture stress sensitivity and the decline of fracture permeability, porosity, and water saturation along the half-length of

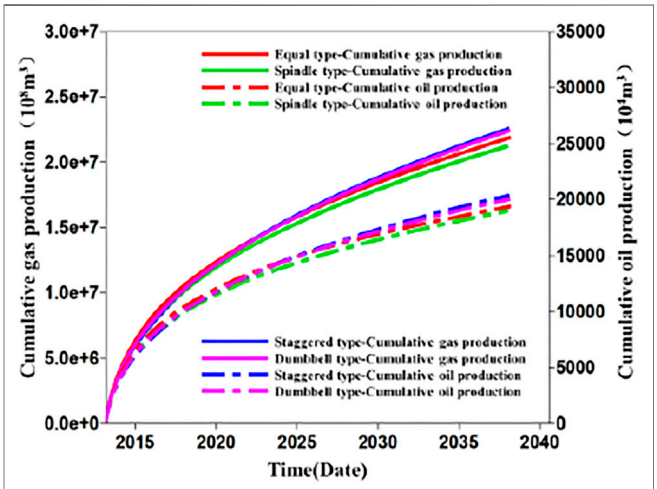

FIGURE 13 | Cumulative condensate/gas–time curves of different fracture laying patterns.

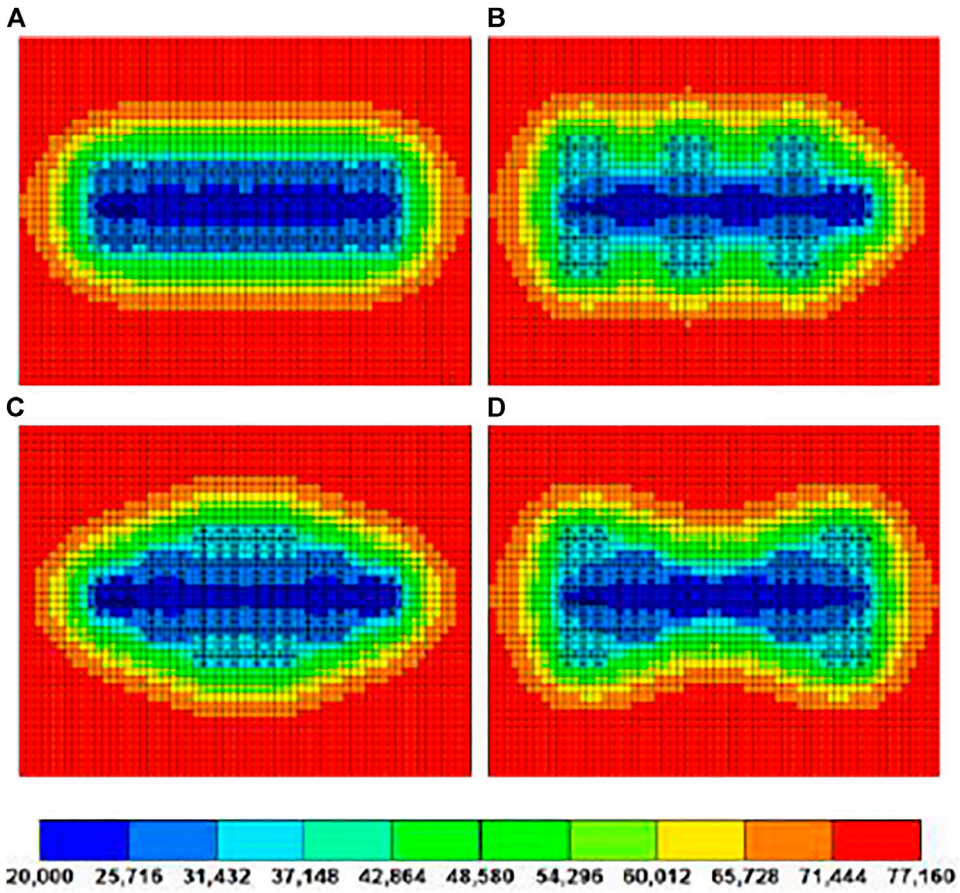

FIGURE 14 | Pressure distribution map of horizontal wells with different fracture laying patterns.

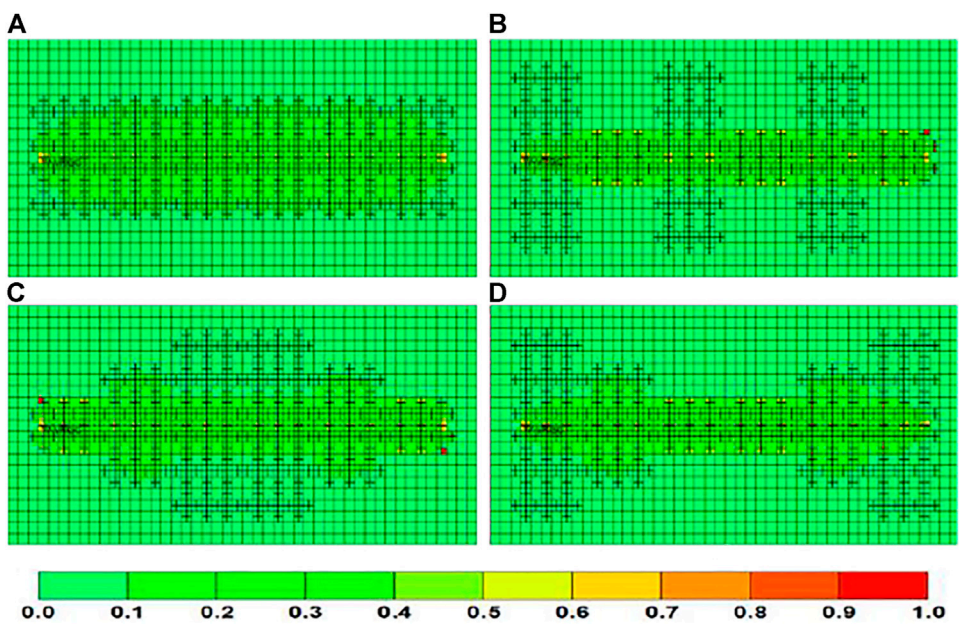

FIGURE 15 | Oil saturation distribution map of horizontal wells with different fracture laying patterns.

fracture, the accuracy of the history matching of the model can be further improved.

2) The fracture parameters of horizontal wells with a designed length of 2,700 m in the ultrahigh condensate area of Duvernay shale reservoir in the Simonette block of Western Canada Basin are simulated and optimized. The results show that the best development effect can be obtained when 43 stages are fractured with three clusters in each stage and 300 mD of the permeability. It not only can fully transform the shale reservoir and significantly increase the oil and gas production, but also can avoid the complicated situation caused by too many fracturing stages due to the small number of clusters in a single stage. There is a linear positive correlation between horizontal well productivity and fracture half-length. Increasing fracture half-length is an effective way to tap the potential of condensate near the well.
3) When the half-length of the fracture is 50 m, and the number of secondary fractures in a single fracturing stage reaches four, an effective fracturing area can be formed, with a large pressure sweep area, wide pressure drop range, and significant stimulation effect. As the fracture network density continues to increase, further increment of oil and gas production is slow, hindered by the overlapping waste of transformed volume.
4) On the basis of reasonable fracture parameters of staged multicluster fractured horizontal wells, the staggered fracture distribution method has the characteristics of a large reformation volume, far spread of pressure, small interference between fractures, and small range of condensate oil precipitation, which is conducive to the efficient development of shale condensate gas reservoir.

DATA AVAILABILITY STATEMENT

The original contributions presented in the study are included in the article/Supplementary Material, further inquiries can be directed to the corresponding author.

AUTHOR CONTRIBUTIONS

WZ and WJ contributed to conception and design of the study. WZ Conduct numerical simulation work. WJ performed the statistical analysis. LR wrote the first draft of the article. LR and WT wrote sections of the article. All authors contributed to article revision, read, and approved the submitted version.

REFERENCES

Ali, J. K., Butler, S., Allen, L., and Wardle, P. (1993). *The Influence of Interfacial Tension on Liquid Mobility in Gas Condensate Systems*. Aberdeen, United Kingdom: Society of Petroleum Engineers.

Behmanesh, H., Hamdi, H., and Clarkson, C. R. (2013). "Production Data Analysis of Liquid Rich Shale Gas Condensate Reservoirs," in SPE Unconventional Resources Conference Canada, Calgary, Alberta, Canada, November, 2013.

Bustin, A., Bustin, R. M., and Cui, X. (2008). "Importance of Fabric on the Production of Gas Shales," in SPE Unconventional Reservoirs Conference, February 10–12, 2008.

Di, S., Hong, J., Lyu, P., Ye, W., Li, H., Zhang, J., et al. (2019). Method for Fracturability Evaluation of Tight Oil Reservoirs in the Shulu Sag. *Well Logging Techn.* 43 (5), 536–541. doi:10.16489/j.issn.1004-1338.2019.05.018

Fisher, M. K., Heinze, J. R., Harris, C. D., Davidson, B. M., Wright, C. A., and Dunn, K. P. (2004). "Optimizing Horizontal Completion Techniques in the Barnett Shale Using Microseismic Fracture Mapping," in Proceedings of the Paper SPE 90051 presented at the SPE Annual Technical Conference and Exhibition, Houston, Texas, USA, 26 September, 2004 (Society of Petroleum Engineers), 26–29. doi:10.2118/90051-ms

Guo, X., Wu, K., An, C., Tang, J., and Killough, J. (2019). Numerical Investigation of Effects of Subsequent Parent-Well Injection on Interwell Fracturing Interference Using Reservoir-Geomechanics-Fracturing Modeling. *SPE J.* 24, 1884–1902. doi:10.2118/195580-pa

Haghshenas, B., Soroush, M., Brohi, I., and Clarkson, C. R. (2014). "Simulation of Liquids Rich Shale Gas Reservoirs with Heavy Hydrocarbon Fraction Desorption," in SPE Unconventional Resources Conference, April 1–3, 2014.

Jiang, J., and Younis, R. M. (2016). Compositional Modeling of Enhanced Hydrocarbons Recovery for Fractured Shale Gas-Condensate Reservoirs with the Effects of Capillary Pressure and Multicomponent Mechanisms. *J. Nat. Gas Sci. Eng.* 34, 1262–1275. doi:10.1016/j.jngse.2016.08.006

Labed, I., Oyeneyin, B., and Oluyemi, G. (2015). "Hydraulic Fracture Spacing Optimisation for Shale Gas-Condensate Reservoirs Development," in Proceedings of the SPE Offshore Europe Conference and Exhibition, Aberdeen, Scotland, UK, 8 September, 2015 (Society of Petroleum Engineers). doi:10.2118/175475-ms

Labed, I. (2016). Gas-condensate Flow Modelling for Shale Gas Reservoirs. PhD thesis. Robert Gordon University.

Li, J., Yu, W., Guerra, D., and Wu, K. (2018). Modeling Wettability Alteration Effect on Well Performance in Permian basin with Complex Fracture Networks. *Fuel* 224, 740–751. doi:10.1016/j.fuel.2018.03.059

Li, Y., Jia, D., Rui, Z., Peng, J., Fu, C., and Zhang, J. (2017). Evaluation Method of Rock Brittleness Based on Statistical Constitutive Relations for Rock Damage. *J. Pet. Sci. Eng.* 153, 123–132. doi:10.1016/j.petrol.2017.03.041

Mao, S., Siddhamshetty, P., Zhang, Z., Yu, W., Chun, T., Kwon, J. S.-I., et al. (2020). Impact of Proppant Pumping Schedule on Well Production for Slickwater Fracturing. *SPE J.* 26, 342–358. doi:10.2118/204235-pa

Moridis, G. J., Blasingame, T. A., and Freeman, C. M. (2010). "Analysis of Mechanisms of Flow in Fractured Tight-Gas and Shale-Gas Reservoirs," in Proceedings of the SPE Latin American and Caribbean Petroleum Engineering Conference, Lima, Peru, 1 December, 2010 (Society of Petroleum Engineers). doi:10.2118/139250-ms

Ozkan, E., Raghavan, R. S., and Apaydin, O. G. (2010). "*Modeling of Fluid Transfer from Shale Matrix to Fracture Network*," in SPE Annual Technical Conference and Exhibition, September 19–22, 2010 (Society of Petroleum Engineers).

Qian, Y., Wang, W., Lin, L., Zhang, H., Hou, Z., and Cheng, J. (2021). Calculation and Application of Transversely Isotropic Formation Rock Mechanical Parameters. *Well Logging Techn.* 45 (1), 62–67. doi:10.16489/j.issn.1004-1338.2021.01.011

Sun, H., Yao, J., Sun, Z., and Fan, D. (2012). Recent Development and prospect on Numerical Simulation of Shale Gas Reservoirs. *PGRE* 19 (1), 46–49. doi:10.13673/j.cnki.cn37-1359/te.2012.01.013

Taylor, R. S., Stobo, B., Niebergall, G., Aguilera, R., Walter, J., and Hards, E. (2014). "Optimization of Duvernay Fracturing Treatment Design Using Fully Compositional Dual Permeability Numeric Reservoir Simulation," in Proceedings of the SPE/CSUR Unconventional Resources Conference-Canada, Calgary, Alberta, Canada, 30 September, 2014 (Society of Petroleum Engineers), 7586–7590. doi:10.2118/171602-ms

Wu, Y. S., Moridis, G., Bai, B., and Zhang, K. (2009). "A Multi-Continuum Model for Gas Production in Tight Fractured Reservoirs," in Proceedings of the SPE Hydraulic Fracturing Technology Conference, The Woodlands, Texas, US, 19 January 2009 (Society of Petroleum Engineers). doi:10.2118/118944-ms

Wu, Y., Cheng, L., Huang, S., Bai, Y. H., Xu, B. X., and Ding, G. Y. (2017). A Tri-linear Model for Production Prediction in Retrograde Shale Gas Reservoirs. *Nat. Gas Geosci.* 28 (11), 1745–1754. doi:10.11764/j.issn.1672-1926.2017.09.009

Xie, J., Tang, J., Yong, R., Fan, Y., Zuo, L., Chen, X., et al. (2020). A 3-D Hydraulic Fracture Propagation Model Applied for Shale Gas Reservoirs with Multiple Bedding Planes. *Eng. Fracture Mech.* 228, 106872. doi:10.1016/j.engfracmech.2020.106872

Xu, B. (2016). New Production Data Analysistechniquefor Gas Condensate Wellin Shale Reservoirs. *Nat. Gas Geosci.* 27 (5), 905–909. doi:10.11764/j.issn.1672-1926.2016.05.0905

Yin, H., Yang, C., Tang, P., Mingyong, G., and Jing, F. (2014). Optimization of Multi-Stage Fracturing of Well YP1 with Super-long Horizontal Section in Changyuan, Daqing Oilfield. *Special Oil Gas Res.* 21 (5), 68.

Zhang, F., Wang, X., Tang, M., Du, X., Xu, C., Tang, J., et al. (2021a). Numerical Investigation on Hydraulic Fracturing of Extreme Limited Entry Perforating in Plug-And-Perforation Completion of Shale Oil Reservoir in Changqing Oilfield, China. *Rock Mech. Rock Eng.* 54, 2925–2941. doi:10.1007/s00603-021-02450-x

Zhang, J., Li, Y., Pan, Y., Wang, X., Yan, M., Shi, X., et al. (2021b). Experiments and Analysis on the Influence of Multiple Closed Cemented Natural Fractures on Hydraulic Fracture Propagation in a Tight Sandstone Reservoir. *Eng. Geology.* 281, 105981. doi:10.1016/j.enggeo.2020.105981

Zhi, D., Guo, X., Wang, W., Jin, Y., Liu, C., Chen, G., et al. (2021). Fracturing and Production Analysis of the Efficacy of Hydraulic Fracture Stage Reduction in the Improvement of Cost-effectiveness in Shale Oil Development: A Case Study of Jimsar Shale Oil, China. *Energy Sci Eng* 9, 1337–1348. doi:10.1002/ese3.940

Conflict of Interest: Authors WZ, WJ, LR, WT, and HG was employed by the company China Oilfield Services Limited.

frontiers in Earth Science

METHODS
published: 25 November 2021
doi: 10.3389/feart.2021.722787

Progress on Modeling of Dynamic Productivity of Fractured Gas Condensate Reservoir Based on a Fluid-Solid Coupling Method

Shuai Wang, Xianhong Tan, Yang Xia, Bo Tian and Bin Liang*

China National Offshore Oil Corporation Research Institute, Beijing, China

Bozhong 19-6 gas field is the first discovered large-scale gas condensate field in eastern China, which is also one of the largest metamorphic rock gas condensate fields in the world. It is a buried hill type, low permeability reservoir, with ultra-high condensate content where the fluid is nearly at its dew point pressure. No similar experience with such reservoirs have previously been reported in the context of gas field development in China and step-by-step progresses is been made to characterize this reservoir. Overall, documentation concerning this type of reservoir is rarely seen worldwide. This paper includes key successful results from multiple perspectives including experiments correlations, numerical modeling and the significance of incorporating certain details. Based on a fluid-solid coupling method, the simulations consider several factors including the fracture distribution, low permeability, medium deformation, and condensate characteristics, as well as their effects on the gas productivity. In the laboratory experiments, the stress sensitivity of the rock was tested using representative core samples. Here, experiment-based correlations of the starting pressure gradient of the gas condensate reservoir are proposed. The starting pressure gradient of different fluid types, such as black oil and gas condensate are highlighted as accurately simulating the reservoir. As a result, the numerical model to predict the dynamic productivity of a single well was successfully established considering all those factors. This paper can serve as a reference for studying other studies of metamorphic, fractured gas condensate reservoirs.

Keywords: fractured gas condensate reservoir, dynamic productivity of gas wells, fluid-solid coupling, numerical simulation, prediction

OPEN ACCESS

Edited by:
Yuwei Li,
Liaoning University, China

Reviewed by:
Zhao Hailong,
China University of Petroleum (Huadong), China
Qianru Qi,
University of Southern California, United States
Daiyin Yin,
Northeast Petroleum University, China

****Correspondence:***
Shuai Wang
408207747@qq.com

Specialty section:
This article was submitted to Economic Geology, a section of the journal Frontiers in Earth Science

Received: *09 June 2021*
Accepted: *11 October 2021*
Published: *25 November 2021*

Citation:
Wang S, Tan X, Xia Y, Tian B and Liang B (2021) Progress on Modeling of Dynamic Productivity of Fractured Gas Condensate Reservoir Based on a Fluid-Solid Coupling Method. Front. Earth Sci. 9:722787. doi: 10.3389/feart.2021.722787

INTRODUCTION

Fractured gas reservoirs are widely distributed in China (Jiang and Wang, 2009; Huang et al., 2021), such as Ke Shen-8 gas reservoir in Tarim Basin and Mo Xijia-2 gas reservoir in Sichuan Basin. The Bozhong 19-6 gas condensate field is the first discovered buried hill, large condensate field with low permeability, extremely high condensate content in eastern China, which fluid is nearly at its dew point pressure. It is also one of the largest condensate fields of metamorphic rock in the world. The geological reserve has a volume of nearly 1 billion cubic meters. While it is challenging to develop the gas field, there was no similar experience domestically for reference purposes. In the development of this type of condensate gas reservoir, condensate oil will be precipitated after the local formation pressure is lower than the dew point pressure. In addition, the reservoir has low permeability; the

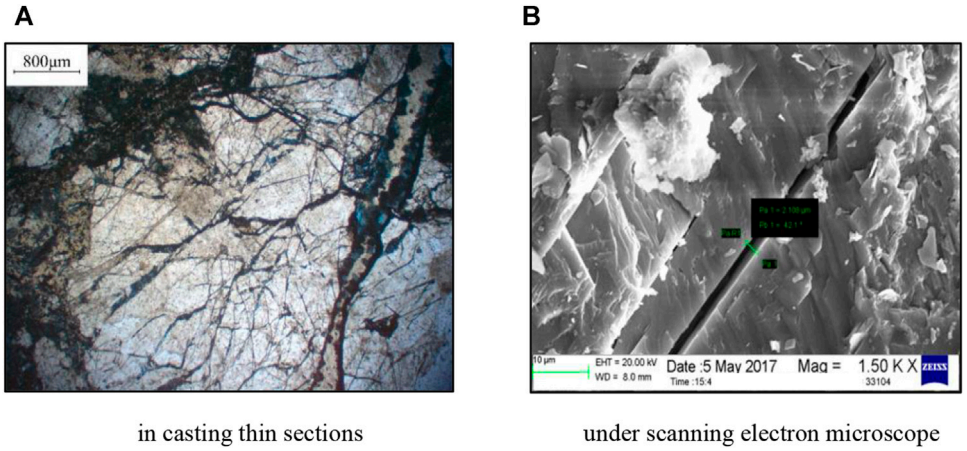

FIGURE 1 | Demonstrations of microfracture distribution. **(A)** In casting a thin sections, **(B)** Under a scanning electron microscope.

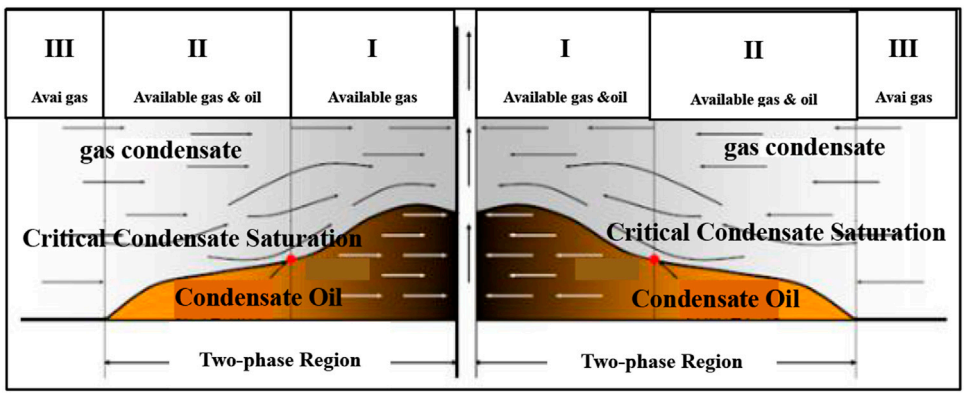

FIGURE 2 | Distribution of condensate near the wellbore zone.

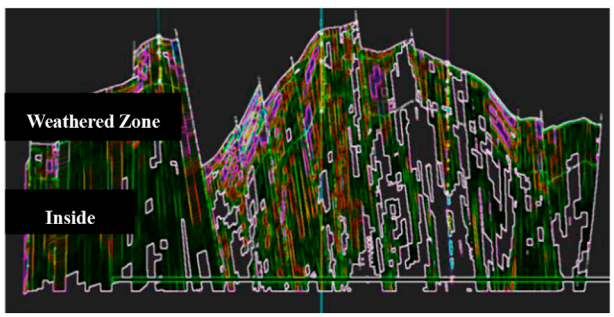

FIGURE 3 | Geological model of fractured reservoir in buried hill. Experiments on testing stress sensitivity of the fracture–matrix system.

matrix permeability is only 0.3 mD. Both condensate oil and gas are difficult to be recover after precipitation, resulting in low single well productivity and recovery. Accurate prediction of production capacity of this specific type of reservoir are needed, because such predictions form foundation for planning the gas field development to achieve the optimized recovery.

A lot of research work has been done on fractured reservoirs. In 1963, Warren J. E. took the established theoretical model for natural fractured reservoirs, which was the first one to study the characteristics of fracture–matrix structure (Warren and Root, 1963). In 1987, Ozkan E. proposed a way to predict the productivity from a single well in a natural fractured reservoir, under the constant pressure boundary condition, using the real production data. The model defined five different flow mechanisms and preliminarily proposed a method for estimating the reservoir parameters (Ozkan et al., 1987). At present, the equivalent continuum theory is mostly adopted in calculating the productivity of fractured gas reservoirs (Li et al., 2016). The method simplifies the fracture distribution within the reservoir, but does not consider the geometry and location of fractures. Assuming the steady state for gas condensate reservoir, Guo et al. proposed an equation to predict the productivity for the case of gas–liquid multiphase

TABLE 1 | Core parameters of different permeability and fracture distribution.

Core no	Length (cm)	Diameter (cm)	Porosity (%)	Permeability (mD)	Existence of fracture
1	10.30	6.57	9.76	3.38	Fractured
2	9.25	9.36	7.54	2.95	Fractured
3	7.82	9.51	6.30	4.39	Fractured
4	11.28	6.59	8.14	0.71	Crack-free
5	8.30	6.00	3.66	0.07	Crack-free
6	10.85	6.00	8.20	0.71	Crack-free

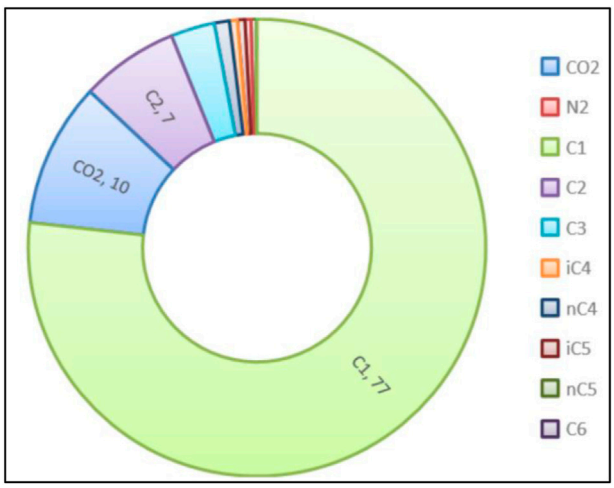

FIGURE 4 | Composition distribution of flash gas sampled from BZ19-6-X gas condensate well.

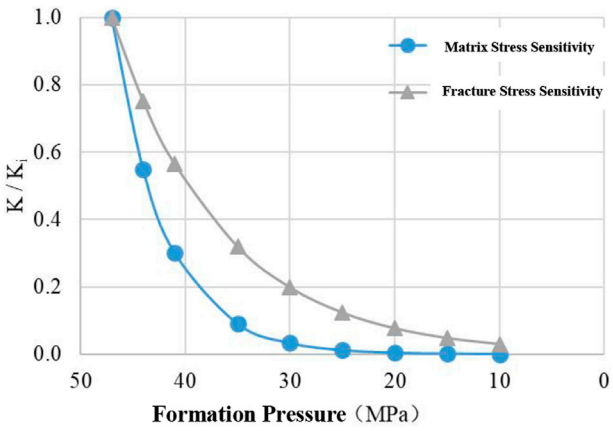

FIGURE 5 | Assignment of stress sensitivity parameters for dual media.

flow, where the open flow rate of gas well can be calculated by software (Guo, 2007). Li established a three-dimensional non-Darcy flow model for the system of oil and water. However, because of its high computational demand, this method has not been widely adopted.

In this paper, a numerical model is developed based on previous progress, incorporating specifically stress sensitivity and starting pressure gradient distributions (Lu et al., 2018). The model uses the fluid-solid coupling method and considers several factors, including the fracture distribution, medium variation in the low permeability, fractured gas reservoir, and reverse condensate volume. The incorporation of the starting pressure gradient of the gas condensate reservoir is highlighted here, and the relationship between pressure and permeability is correlated with experimental data.

METHODOLOGY

The Productivity of Fractured Gas Reservoirs

Buried hill gas condensate reservoir is a very complex type of reservoir with higher productivity than that of low permeability sandstone gas condensate reservoir. **Eq. 1** is the conventional method to calculate gas well productivity (Sun et al., 2012). The gas well production capacity is affected by not only rock and fluid properties but also well condition such as skin factor of a well.

$$q_g = \frac{0.07852Kh\left(p_R^2 - p_{wf}^2\right)}{\mu_g ZT\left(ln\,\frac{r_e}{r_w} + S_a\right)}, \tag{1}$$

where q_g is gas production rate (m^3/day), K is the permeability (mD), p_R is reservoir pressure (MPa), p_{wf} is bottom hole flowing pressure (MPa), Z is gas compression factor, T is temperature of reservoir (℃), and S_a is skin factor of the well.

Diagenesis of the Reservoir Rock

The Bozhong 19-6 reservoir is deeply bedded and highly heterogeneous, as which has experienced several tectonic movement periods and stress mode changes. **Figure 1** shows the morphology of micro-fractures from a thin section of the rock sample from the reservoir. Influenced by its depth and high compaction, generally the openings of macro-fractures are small. From imaging logging, those fracture openings are within 100~400 μm. From the thin section, the openings of micro-fractures are about 20~30 μm. Fractures cut through each other, and their distributions have multi-stage fracture characteristics. It is concluded that the fracture distribution is the most important factor controlling the physical properties of

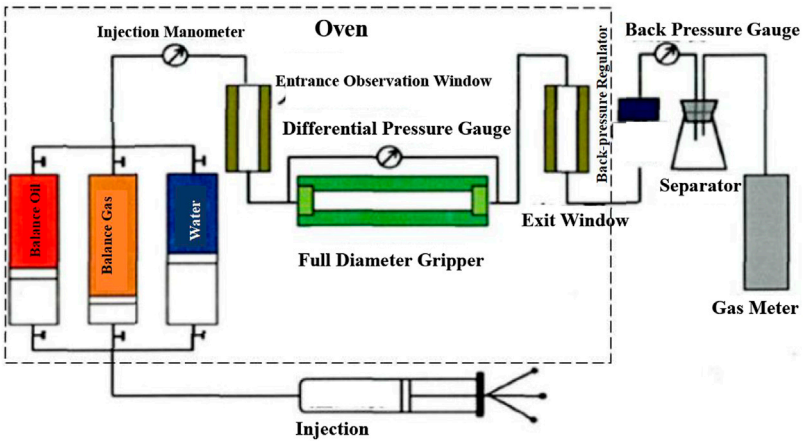

FIGURE 6 | Illustration of equipment measuring starting pressure gradient of the gas condensate reservoir (Chen et al., 2019).

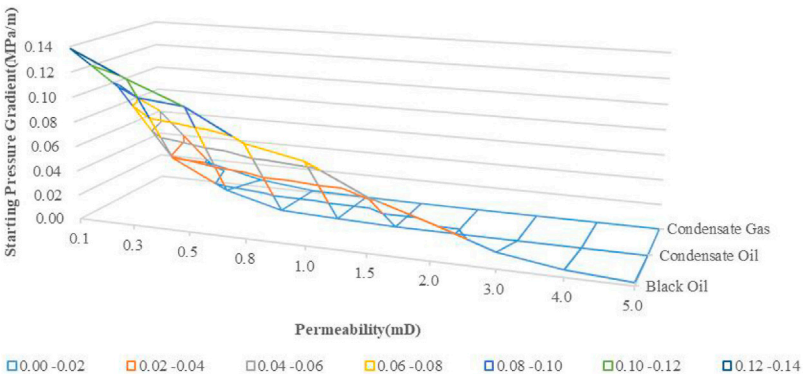

FIGURE 7 | Starting pressure gradient with respect to permeability and different fluid types (Wang et al., 2017).

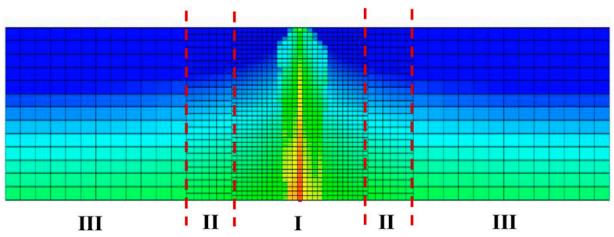

FIGURE 8 | Equivalent characterization of condensation radius by numerical simulation method (Wang et al., 2017).

the reservoir, that is, the fractures contribute the most of fluid flow. In the matrix, the radii of pore throats are less than 1 μm. Small pores and their poor connectivity result in low permeability. Overall, the flow velocity of the fluid is very low and the flow is highly nonlinear.

The starting pressure gradient is closely related to the permeability of the porous media. Generally speaking, the lower the permeability corresponds to the higher the starting pressure gradient. In addition, the influence of pressure change on permeability of the fracture–matrix structure cannot be ignored. The formation pressure decline along the gas field development process changes the effective confining stresses. As the permeability decreases continuously, this process is irreversible. The aforementioned factors all lead to a decrease in productivity as the recovery continues. Therefore, the productivity is dynamic and must be modeled.

Effect of Fluid Phase Changes

The change of fluid phase state in gas condensate reservoir is a very important factor affecting the dynamic productivity. Compared with dry gas well, gas condensate well has a faster productivity decline. This is because when the bottom hole flowing pressure is lower than the dew point pressure, condensate forms in the area around the well, which leads to additional pressure losses, and negatively affects the movement of gas. When the critical saturation for condensate fluid is exceeded, the condensate begins to flow in the reservoir. **Figure 2** shows the hydrocarbon two-phase flow in the near-wellbore zone.

TABLE 2 | Gas condensate parameters of well BZ19-6-X (Liang et al., 2020).

Sampling horizon	GOR m^3/m^3	Dew point pressure < MPa	Dew pressure difference MPa	Condensate content g/m^3	Maximum amount of reverse condensate %	Surface condensate density t/m^3	Gaseous Z-factor	Gas volume coefficient
Ar	1,095	45.61	1.9	710.67	40.97	0.798	1.217	0.00381

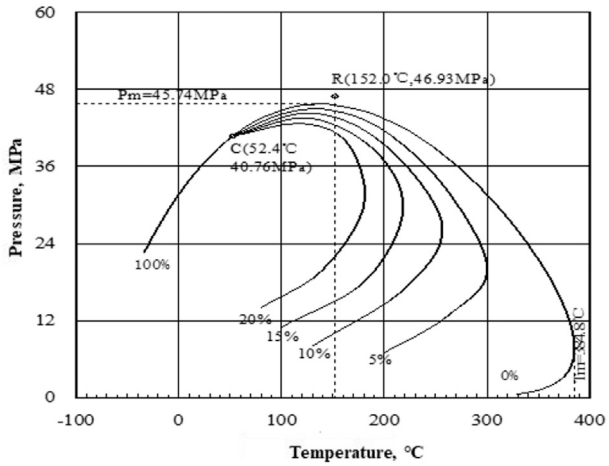

FIGURE 9 | Phase envelope of Bozhong 19-6 gas condensate field (Liang et al., 2020).

Predictive Model of Dynamic Productivity

Based on the Petrel integrated software platform, a three-dimensional geological model of the fracture–matrix system was established, which adopts the technology of DFN stochastic modeling. Combined with the sensitive seismic attributes, the model considered various factors such as paleogeomorphology, fault and micro-geomorphology, to make a quantitative prediction of the fractured reservoir. **Figure 3** shows the matrix–fracture coupling geological model of Bozhong 19-6 reservoir. It includes the dual geological framework and shows the layering of weathering zone in details.

1) Modeling of the matrix

Multiple parameters such as fracture density, net–gross ratio, matrix porosity, and permeability were calibrated by micro-seismic data. Those parameters are used to identify the characteristics of the matrix, according to the scheme in matrix classification. Through probabilistic simulation with constraints representing various types of matrices, distribution of different matrix types can be established.

2) Modeling of fracture

For the fractures of different scales, the combined deterministic simulation and probabilistic simulation were used to model the fracture network. For large fractures at fault level, the fracture distribution detected by seismic attributes such as maximum curvature and refined probabilistic fault volume were used for input, which can be directly transformed into the large-scale fracture network through deterministic simulation. For medium-sized fractures, fracture distribution interpreted with imaging logging was used.

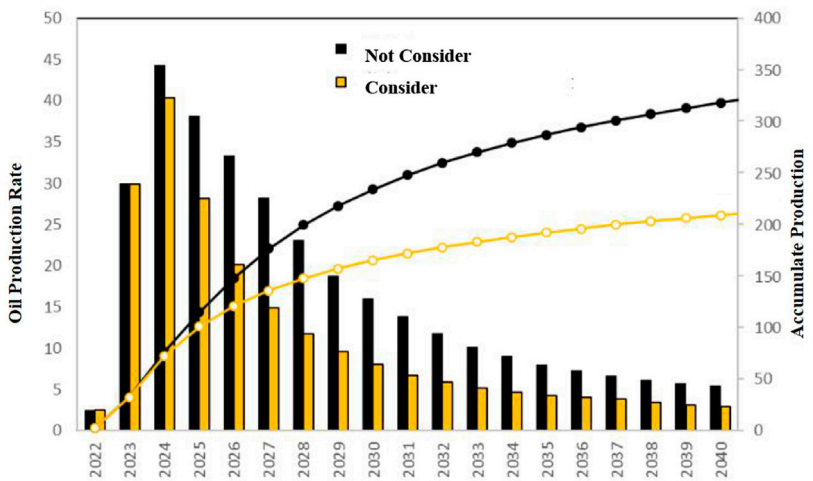

FIGURE 10 | Effect of stress sensitivity on oil production prediction.

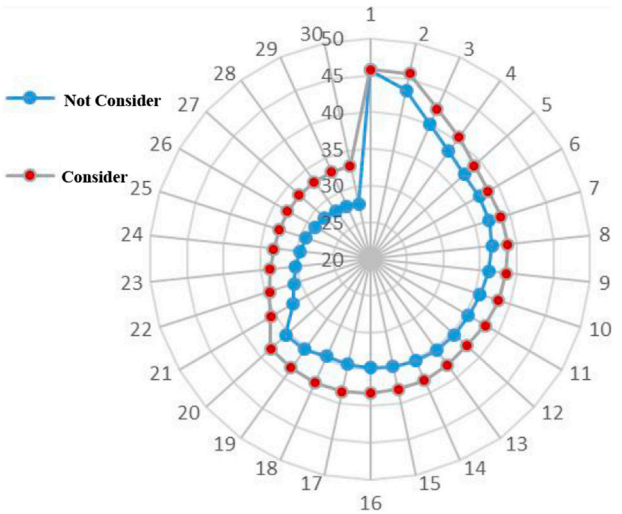

FIGURE 11 | Effect of stress sensitivity on bottom hole pressure.

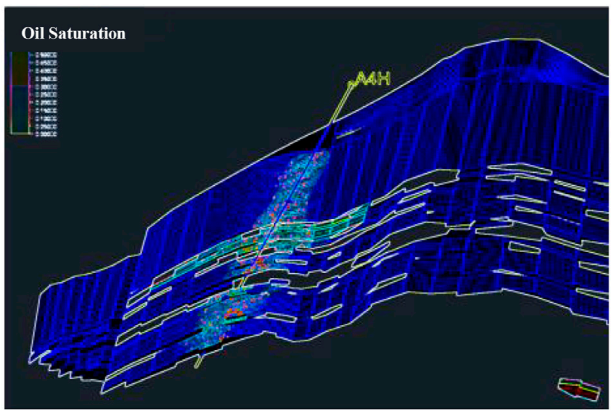

FIGURE 12 | Prediction result of condensate precipitation in well BZ19-6-X (Gao et al., 2020).

Experiments Testing the Stress Sensitivity

As the numerical modeling requires a pressure–permeability curve, experiments on stress sensitivity were conducted, using cores of different fracture distributions and *in situ* fluid sample. Six core samples with different levels in permeability and fracture distribution were selected to conduct the experiments testing stress sensitivity, using high-temperature and high-pressure core displacement device. The fracture density was 4 per meter. Core parameters are shown in **Table 1**, in which cores 1~3 represent fractured rock and cores 4~6 represent crack-free rock. The condensate fluid sampled from well BZ19-6-X, as shown in **Figure 4**, was used in the experiments.

The experimental procedure under unsteady-state condition is as follows:

1) Place the sample into core holder and maintain a constant pressure drop;
2) Change the confining pressure through a manual pump, and test the core permeability when the confining pressure reaches 10, 20, 30, 40, and 50 MPa, respectively;
3) Correlate the core permeability changes with respect to effective stress.

Based on the experimental results, deformation coefficient of the fractured rock was obtained, as shown in **Eq. 2**. Considering the stress-sensitive effect, the relationship between permeability and formation pressure is shown in **Eq. 3**. The pressure–permeability curves for both fracture and matrix are shown in **Figure 5**.

$$\alpha_K = 0.153K_i^{-0.34}, \tag{2}$$

$$K = K_i e^{-\alpha_K (p_i - p)}, \tag{3}$$

where α_k is the medium deformation coefficient, K is the permeability of reservoir (mD), K_i is the initial permeability of reservoir (mD), p is the reservoir pressure (mD), and p_i is the initial reservoir pressure (mD).

Starting Pressure Gradient

The actual fluid flow in the formation is under high temperature and pressure. To better describe the non-Darcy flow, the starting pressure gradient of the gas condensate flow under high temperature and pressure was studied through experimental work (Chen et al., 2019). Under the pressure of 50 MPa and temperature of 152°C, the cores (with fractures) with permeability of 2.51 and 2.58 mD, respectively, were used in testing with different fluid samples. The experimental set was composed of an injection pump system, core gripper, back pressure regulator, differential pressure gauge, temperature control system, liquid fraction collector, and gas meter. The flow velocity of the gas condensate through the cores was controlled by changing the pressure drop rate at the outlet, using the back pressure regulator. Illustration of the experimental equipment is shown in **Figure 6**.

Characterization of starting pressure gradient in the gas condensate reservoir had also been done through numerical simulation (Wang et al., 2017). In the study, black oil and gas condensate were studied, as shown in **Figure 7**. **Figure 8** shows the estimated distribution of liquid condensate, which honored the theoretical condensate distribution around the wellbore.

RESULTS AND DISCUSSIONS

Bozhong 19-6 gas condensate reservoir was characterized for both matrix and fracture system. The fracture analysis was conducted for various magnitudes, including macro-fractures, medium and small fractures, and micro-fractures (Kang et al., 2021). The total porosity of the reservoir rock in Bozhong 19-6 ranges from 2 to 4%, and the permeability ranges from 0.3 to 4 mD, showing the characteristics of low porosity and low permeability. The Bozhong 19-6 gas condensate reservoir is characterized by high condensate content, and its maximum

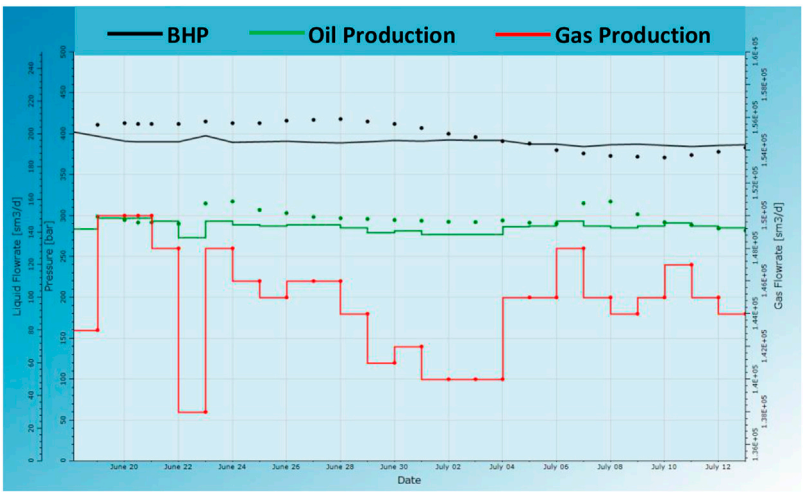

FIGURE 13 | Historical matching effect of well BZ19-6-X (Gao et al., 2020).

reversed condensate volume can be as high as 40.97%, as shown in **Table 2**, and small ground-dew pressure difference of 1.9 MPa (Liang et al., 2020). When the pressure drop increases, precipitated liquid will clog the near-wellbore area in the formation, resulting in reduced production, as shown in **Figure 9**.

Incorporating the stress sensitivity and starting pressure gradient mentioned previously in the numerical simulation, it was noticed that as the reservoir development continues, the influence of stress sensitivity and starting pressure gradient on the performance becomes more significant, as shown in **Figure 10** and **Figure 11**. Their effects are mainly manifested as rapid production decline and increased loss in bottom hole flowing pressure. Compared with the case not including the stress sensitivity, the difference on estimated average pressure drop is 10%; therefore, the difference on cumulative production estimation is much more. Comparing the cases that do and do not including the starting pressure gradient curves, the difference predicted oil production can as high as 72%. Therefore, stress sensitivity and starting pressure gradient cannot be neglected in modeling the specific type of reservoir.

Based on the fluid-solid coupling model (Gao et al., 2020) established, the productivity of BZ19-6-X well was predicted, and historical fitting was performed. **Figure 12** and **Figure 13** show the history match and prediction of retrograde condensate production in Well BZ19-6-X. The well was managed by controlling gas production rate and pressure drawdown. Through fitting the condensate production data, the accuracy in prediction of the single well production history was more than 90%.

CONCLUSION

1) Based on fluid-solid coupling numerical model and relevant experimental work, this paper comprehensively reviewed the key factors that must be incorporated into such a model, including fracture distribution, permeability changes for gas condensate reservoirs, condensate volume, non-Darcy flow, and other factors affecting well productivity.
2) A comparison with experimental data indicates that the starting pressure gradient of different fluid types of black oil and gas condensate, as well as the stress sensitivity, are key factors that should be included in numerical simulation of the fractured gas condensate reservoir.
3) According to validation with real data, the numerical model was able to predict the performance of a single well, with a fitting accuracy of more than 90%.

In the review of the key progress made toward characterizing this rare type of reservoir from various perspectives and scales, the final developed model was able to predict the performance of a single well. Studies that have been done on the metamorphic, fractured gas condensate reservoir have resulted in significant progress. This paper may serve as a reference for other reserves of the same type.

DATA AVAILABILITY STATEMENT

The original contributions presented in the study are included in the article/Supplementary Material. Further inquiries can be directed to the corresponding author.

AUTHOR CONTRIBUTIONS

All authors listed have made a substantial, direct, and intellectual contribution to the work and approved it for publication.

ACKNOWLEDGMENTS

This paper is supported by CNOOC Research Institute.

REFERENCES

Chen, J., Li, J., Zhou, Z., and Wang, Y. B. (2019). Establishment and Application of Production Capacity Formula of Wenchang Low Permeability Gas Condensate Well [J]. *SHANDONG CHEMICAL INDUSTRY* 48 (19).

Gao, Z. N., Geng, Z. G., Zhang, F. Y., Yu, Y. Z., and Wu, T. T. (2020). Numerical Simulation of Metamorphis Buried-Hill Fractured Gas Condensate Reservoir Based on Fluid-Sloid Coupling [J]. *Spec. Oil Gas Reservoirs* 02 (20). doi:10.3969/j.issn.1006-6535.2020.01.018

Guo, K. L., Guo, Q., and Cheng, S. Q. (2007). Study on Productivity Calculation Model and Method of Horizontal Well in Condensate Gas Reservoir [J]. *Lithologic Reservoir* 07 (01).

Huang, L., Kang, Y., and Xu, C. (2021). Comprehensive Evaluation of Gas Condensate Reservoir Productivity Based on Fracture Characteristic Parameters [J]. *Petrochemical Appl.* 21 (03).doi:10.1016/j.jngse.2014.03.016

Jiang, W. K., and Wang, J. M. (2009). Productivity Evaluation of Gas Well in Fractured Carbonate Reservoir [J]. *Nat. Gas Industry* 29 (9), 103–105. doi:10.3787/j.issn.1000-0976.2009.09.029

Kang, B. T., Zhang, Y. C., Chen, G. N., Li, C. X., Jiang, B., and Zuo, J. Y. (2021). A New Development Index Prediction Method for Confined Gas Condensate Reservoirs [J]. *Petrochemical Appl.* (01), 21. doi:10.3969/j.issn.1673-5285.2021.01.007

Li, Q., Guo, Y., Tian, C., Qian, L., and Cheng, Y. (2016). Different Angle Crack Defects on the Influence of Dynamic Fracture Behavior of Materials [J]. *Sci. Tech. Eng.* 18 (28), 1–5.

Liang, B., Tan, X. H., Zhu, G. J., Tian, B., Wang, S., Li, N., et al. (2021). *Study on Improving Recovery of Condensate Oil in Low Perm and High Condensate Gas Reservoir*. Singapore: Springer. doi:10.1007/978-981-16-0761-5_293

Lu, J. L., Zhang, H., Chang, B. H., Cao, W., and Sun, H. D. (2018). A New Method for Productivity Evaluation of Gas Condensate Well in Gas-Liquid Two-phase State [J]. *Nat. Gas Industry* 18 (04).

Ozkan, E., Ohaeri, U., and Raghavan, R. (1987). Unsteady Flow to a Well-Produced at a Constant Pressure in a Fractured Reservoir [J]. *SPE Formation Eval.* 2 (2), 186–200. doi:10.2118/9902-pa

Sun, E. H., Li, X. P., and Wang, W. D. (2012). Study on Productivity Analysis Method of Gas-Water Two-phase Flow Well in Low Permeability Gas Reservoir [J]. *Lithologic Reservoir* 12 (06). doi:10.3969/j.issn.1673-8926.2012.06.025

Wang, S., Zhang, S., Tan., X., Jiang, H., and Zhang, X. (2017). *Numerical Simulation Method and Laboratory Experiments of Starting Pressure Gradient in Tight Sandstone Oil Reservoirs*. SPE/IATMI Asia pacific Oil Gas Conference and Exhibition. doi:10.2118/186349-MS

Warren, J. E., and Root, P. J. (1963). The Behavior of Naturally Fractured Reservoirs [J]. *Soc. Pet. Eng. J.* 3 (3), 245–255. doi:10.2118/426-pa

Conflict of Interest: The authors declare that the research was conducted in the absence of any commercial or financial relationships that could be construed as a potential conflict of interest.

Publisher's Note: All claims expressed in this article are solely those of the authors and do not necessarily represent those of their affiliated organizations, or those of the publisher, the editors, and the reviewers. Any product that may be evaluated in this article, or claim that may be made by its manufacturer, is not guaranteed or endorsed by the publisher.

frontiers in Earth Science

METHODS
published: 23 December 2021
doi: 10.3389/feart.2021.797405

Nanoindentation-Based Three-Parameter Fracability Evaluation Method for Continental Shales

Siwei Meng[1], Dongxu Li[2], Qi Wang[3], Jiaping Tao[1], Jian Su[1], Hanqi Li[4], Xu Jin[1] and Liu Yang[5]**

[1]Research Institute of Petroleum Exploration and Development, Beijing, China, [2]PetroChina Daqing Oilfield Co., Ltd., Daqing, China, [3]Petrochina Foreign Cooperation Administration Department, Beijing, China, [4]University of Texas at Austin, Austin, TX, United States, [5]China University of Mining and Technology (Beijing), Beijing, China

Shale fracturing evaluation is of great significance to the development of shale oil and gas resources, but the commonly used shale evaluation methods (e.g., the method using the brittleness index based on mineral composition or elastic parameters) have certain limitations. Fractures and beddings affecting fracturing are not considered in these methods. Therefore, it is necessary to develop a new method to evaluate fracturing more comprehensively. The samples used in this research were taken from four typical continental shale basins of China, namely the Bohai Bay Basin, the Ordos Basin, the Songliao Basin, and the Junggar Basin. From a microscopic point of view, a three-parameter evaluation method involving multi-dimensional factors has been developed based on the nanoindentation method. Then, the fracturing coefficient K_2 is obtained by combining the ratio β of the fracture indentation to the total indentation and the uneven coefficient m. After that, the fracability coefficient K_3 is the ratio of the elastic modulus parallel to bedding to that perpendicular to bedding. Finally, the correlation between fracability coefficients K_1, K_2, and K_3 is used to evaluate the overall fracturing performance of shale. The results of this evaluation method are in good agreement with the actual fracturing performance. It can be concluded that this method is highly reliable and practical and well worthy of promoted applications.

Keywords: nanoindentation, shale, brittleness index, fracability, mechanical properties

OPEN ACCESS

Edited by:
Yuwei Li,
Liaoning University, China

Reviewed by:
Jiawei Li,
Texas A&M University, United States
Jun Zhang,
Northeast Petroleum University, China

****Correspondence:***
Xu Jin
jinxu@petrochina.com.cn
Liu Yang
shidayangliu@126.com

Specialty section:
This article was submitted to Economic Geology, a section of the journal Frontiers in Earth Science

Received: *18 October 2021*
Accepted: *01 December 2021*
Published: *23 December 2021*

Citation:
Meng S, Li D, Wang Q, Tao J, Su J, Li H, Jin X and Yang L (2021) Nanoindentation-Based Three-Parameter Fracability Evaluation Method for Continental Shales. Front. Earth Sci. 9:797405. doi: 10.3389/feart.2021.797405

INTRODUCTION

With the increasing demand for oil and gas resources all around the world, shale oil has become a key field for the exploration and development of unconventional oil and gas resources globally. The fracturing evaluation is of great significance to the development of shale oil and gas resources. Previous practice of shale fracability evaluation mostly uses the brittleness index to reflect the degree of difficulties in creating complex fracture networks (Ai et al., 2016; Li et al., 2017; Qin and Yang, 2019; Tang et al., 2019; Zhang et al., 2020). At present, two types of brittleness indexes are commonly used for shale, namely the mineral composition-based and rock mechanical parameter-based ones. However, during actual fracturing, the *in-situ* stress, the natural fracture development degree, bedding, and

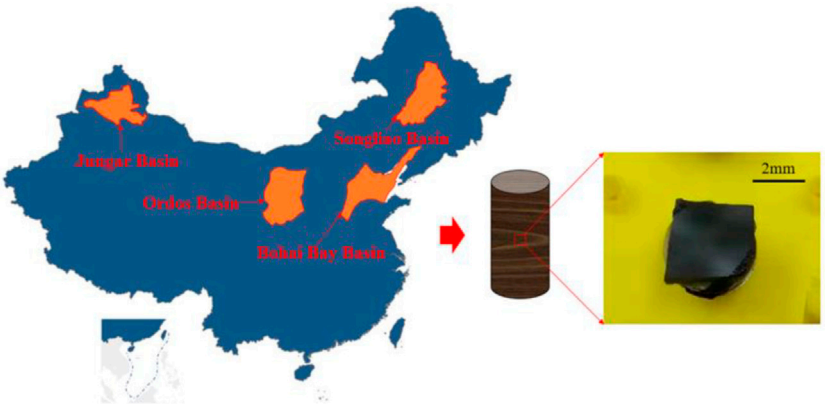

FIGURE 1 | Distribution of samples.

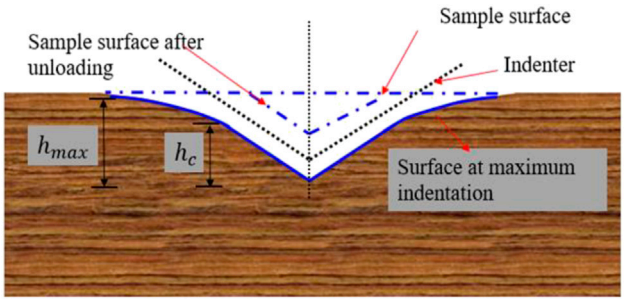

FIGURE 2 | Principle of nanoindentation.

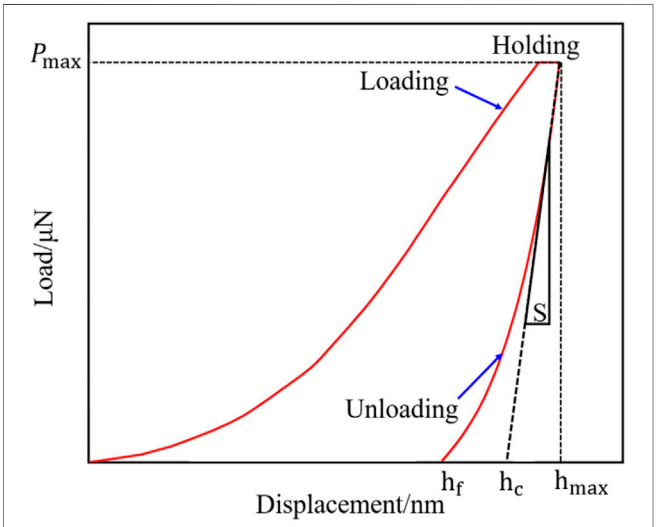

FIGURE 3 | Load vs. displacement for nanoindentation.

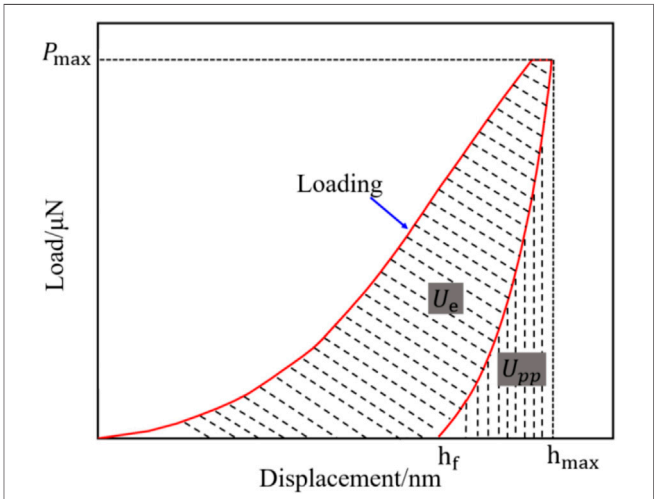

FIGURE 4 | U_e and U_p in the diagram of load vs. displacement.

internal structure all have significant impacts on the shale fracability (Zhang et al., 2018a; Xie et al., 2020; Yang et al., 2020; Mao et al., 2021; Zhang et al., 2021).

In 2013, some scholars developed a fracability evaluation method using three rock mechanical parameters, namely the Young's modulus, Poisson's ratio, and uniaxial tensile strength, as the independent variables, and the fracability coefficient as a dependent variable, which yet ignored the impact of mineral composition (Yuan et al., 2013). In 2014, some scholars proposed a comprehensive evaluation method for shale gas fracability, which uses a radar chart of six geomechanical parameters to rank the fracability of shale gas reservoirs. However, this method cannot be used for quantitative analysis (Zhao et al., 2015). In 2015, some scholars proposed an evaluation method for shale gas fracability by integrating three features of shale (the brittleness, fracture toughness, and natural weak plane), but the impact of rock mechanical parameters was not addressed (Chen et al., 2017). In 2017, some scholars set up an evaluation system for shale fracability comprising five factors—the brittleness index, rock mineral content, cohesion, natural fractures, and porosity to evaluate the fracability of the Niutitang Formation. Nonetheless,

TABLE 1 | Composition of bulk minerals.

Samples	Quartz	Plagioclase	Potash feldspar	Apatite	Calcite	Dolomite	Pyrite	Clay minerals
Junggar	25.4	26.2	4.9	8.5	0.8	22.1	0	12.1
Bohai	14.6	28.8	4.5	1.8	20.2	23.9	0	6.2
Ordos	30.8	14.8	5.4	0	0	0	0	49.0
Songliao	27.9	11.7	1.8	0	0	3.3	5.2	50.1

TABLE 2 | Composition of clay minerals.

Samples	Smectite	I/S	Illite	Kaolinite	Chlorite	C/S
Junggar	72	0	21	3	4	0
Bohai	0	0	24	5	13	58
Ordos	0	57	27	1	15	0
Songliao	0	68	29	0	3	0

"I/S" is illite/smectite mixed-layer, ""C/S ""is chlorite/smectite mixed-layer.

TABLE 3 | Calculation of the fracability coefficient K_1.

Sample	E/GPa	H/GPa	Kc/ $(MPa \cdot m^{1/2})$	K_1
Junggar	35.23	3.46	15.65	0.49
Bohai	26.78	3.23	12.66	0.54
Ordos	26.88	2.76	13.64	0.39
Songliao	22.26	2.19	10.39	0.45

TABLE 4 | Calculation of the fracability coefficient K_2.

Sample	β	m	K_2
Junggar	23	3.44	6.68
Bohai	35	4.99	7.01
Ordos	28	4.17	6.71
Songliao	18	1.99	6.01

TABLE 5 | Calculation of the fracability coefficient K_3.

Sample	E_h	E_v	K_3
Junggar	35.23	21.07	1.67
Bohai	32.78	18.91	1.73
Ordos	26.88	13.34	2.01
Songliao	22.26	17.58	1.27

this research neglected the impact of organic matter and *in-situ* stress difference (Di et al., 2019).

The evaluation methods mentioned above mostly evaluate the fracability from a macro point of view, and rarely perform evaluation from a micro point of view. Over the past few years, many researchers have gradually applied the nanoindentation technique to studying the mechanical properties of rocks. Some scholars calibrated the indentation position by integrating the nanoidentation with the backscattered electron diffraction (BSE) and measured the mechanical property of kerogen at the nano scale. They found out that the elastic modulus of kerogen was 5–9 GPa, and higher kerogen content would reduce the overall elastic modulus of rock (Kumar et al., 2012; Shukla et al., 2015). Some scholars proposed a nanoindentation-based evaluation model for the fracture toughness of coal, which estimates the fracture energy and fracture area according to the brittle failure theory and the pop-in feature on the loading curve (Manjunath and Birendra, 2019). Some scholars obtained the mechanical properties of dry and saltwater-saturated coal samples at the nano scale through nanoindentation tests and compared them with the results of the traditional acoustic testing, based on which the limitations of the traditional acoustic testing are concluded (Zhang et al., 2018b).

The study addresses the typical continental shale of the Bohai Bay Basin, the Ordos Basin, the Songliao Basin, and the Junggar Basin in China. With the X-ray diffraction (XRD) test, scanning electron microscopy (SEM), and the nanoindentation test of the grid identation mode, the mechanical parameters of rocks such as elastic modulus, hardness, and fracture toughness are obtained. The evaluation results are in good agreement with the actual fracturing treatment performance and fracturing numerical simulation result. It is shown that this method is highly reliable and practical, and thus well worthy of promoted applications. This study provides an idea and technical method for evaluation of the continental shale and is valuable for revealing the mechanical behavior of shale and realizing efficient development of shale gas.

TESTING METHODS

Test Samples

The test samples were obtained from the Bohai Bay, Ordos, Songliao, and Junggar Basins, respectively (**Figure 1**). The Bohai Bay Basin is a faulted basin composed of a series of Paleogene half-graben sags. The Paleogene is a typical lacustrine sedimentary system having experienced two secondary cycles of lake transgression and regression. Located in the north of Xinjiang, the Junggar Basin covers an area of about $13 \times 10^4\ km^2$, which is a multi-stage superimposed basin occurring on an amalgamation block. Located in Northeast China, the Songliao Basin crosses over three provinces, Heilongjiang, Jilin, and Liaoning, and extends from NE to SW, with a NS length of about 820 km, a EW width of 350 km, and an area of about $26 \times 10^4\ km^2$, bounded by the Nenjiang Fault in the west and the Mudanjiang Fault in the east. It is a large Mesozoic-Cenozoic continental sedimentary basin. Located in the west of the North China Platform, the Ordos Basin covers an area of about $25 \times 10^4\ km^2$ developing the Paleozoic and Mesozoic two petroleum systems. In this article, shale samples with parallel bedding and vertical bedding are prepared respectively. The

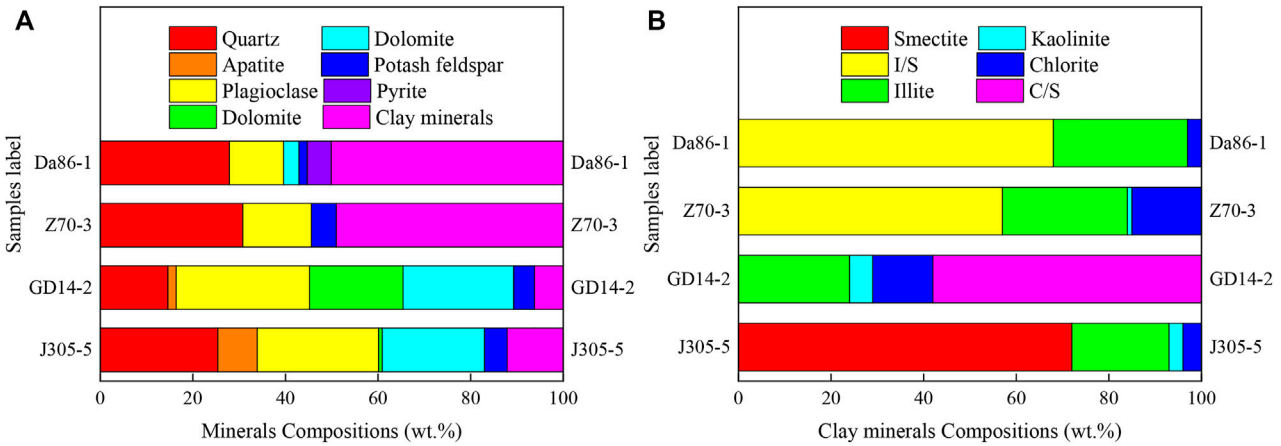

FIGURE 5 | Histograms for compositions of **(A)** bulk minerals and clay minerals **(B)**.

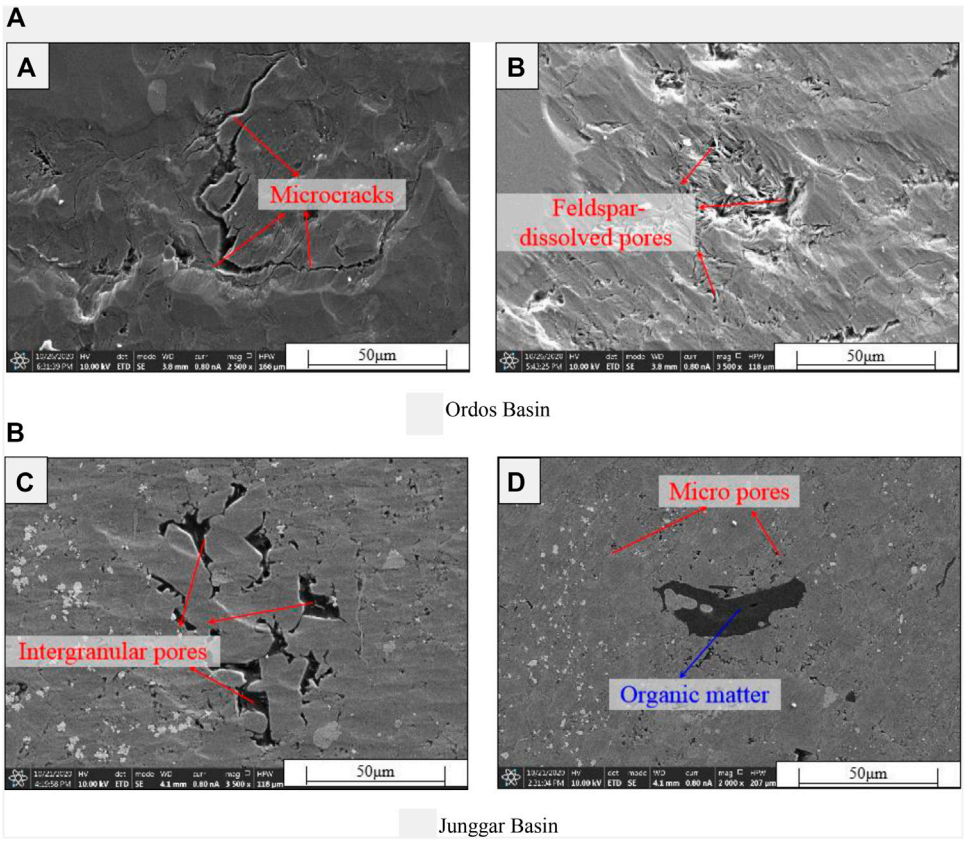

FIGURE 6 | SEM images. **(A)** Ordos Basin. **(B)** Junggar Basin. **(C)** Bohai Bay Basin. **(D)** Songliao Basin.

tested shale sample is mixed curing with epoxy resin and curing agent, whose size is set as length of 5mm, width of 5 mm and thickness of 3 mm. Then, the cured samples will be polished by using the polished section with 15, 9, 3 and 0.5 μm to ensure the smoothness of sample.

Testing Methods

XRD

The TTR III multifunctional X-ray diffractometer manufactured by Rigaku (Japan) was used for mineral composition analysis. Each mineral crystal has its specific X-ray diffraction spectrum,

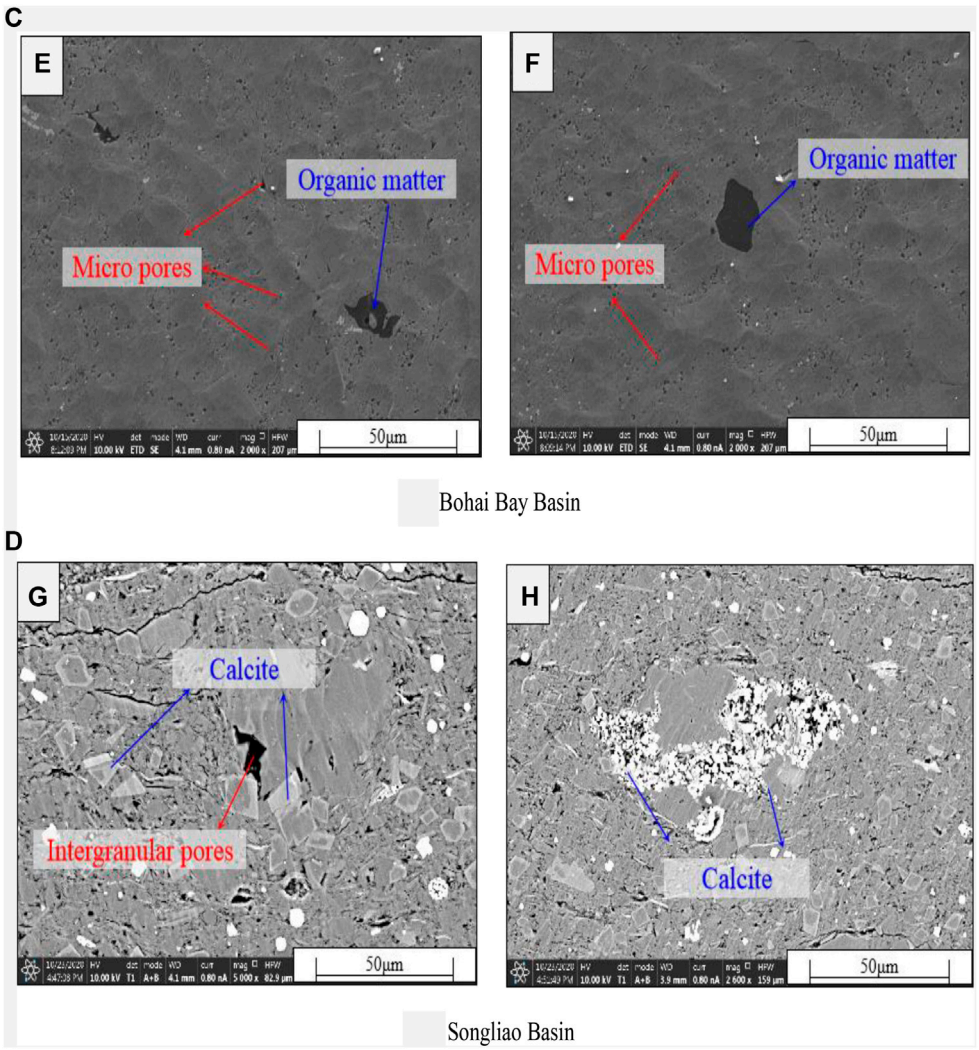

FIGURE 6 | SEM images. **(A)** Ordos Basin. **(B)** Junggar Basin. **(C)** Bohai Bay Basin. **(D)** Songliao Basin.

whose characteristic peak intensity is positively related to the mineral content in a sample. The positive correlation (the K value) between the content of a mineral and the intensity of its characteristic diffraction peak can be determined as a prior by testing. Subsequently, the content of this mineral can be obtained by measure the intensity of its characteristic peak in an unknown sample.

SEM

The Apreo field-emission scanning electron microscope (FE-SEM), manufactured by FEI (America), was used for SEM, which is able to perform a fast qualitative or quantitative micro analysis for the multi-element composition by electron beam scanning. In the process of testing, information such as the sample number, accelerating voltage, scale, amplification factor, date, time, and working distance can be obtained. Researcher has established the correlation between shale pore structure, pore size distribution, and rock mechanical properties at the nano scale by the methodology based on the FE-SEM and digital image processing (Liu and Ostadhassan, 2017).

Nanoindentation Technique

Testing Principles and Steps

The nanoindentation technique uses the high-precision sensor to control the indenter to press into and out of a sample and record the changes in load and displacement during this process. **Figure 2** illustrates the mechanism of indentation. As shown in **Figure 3**, a typical process of nanoindentation has three stages: loading, holding, and unloading. In the loading stage, the press-in depth increases with the increase in the pressing load, which is associated with elastic and plastic deformation. The holding stage is designed to eliminate the effect of the sudden force change on the calculation of mechanical parameters. In the unloading stage, the indentation partially recovers, with the reduction in load. It is assumed that only elastic deformation occurs in this stage, based on which the mechanical properties at the indentation point is calculated.

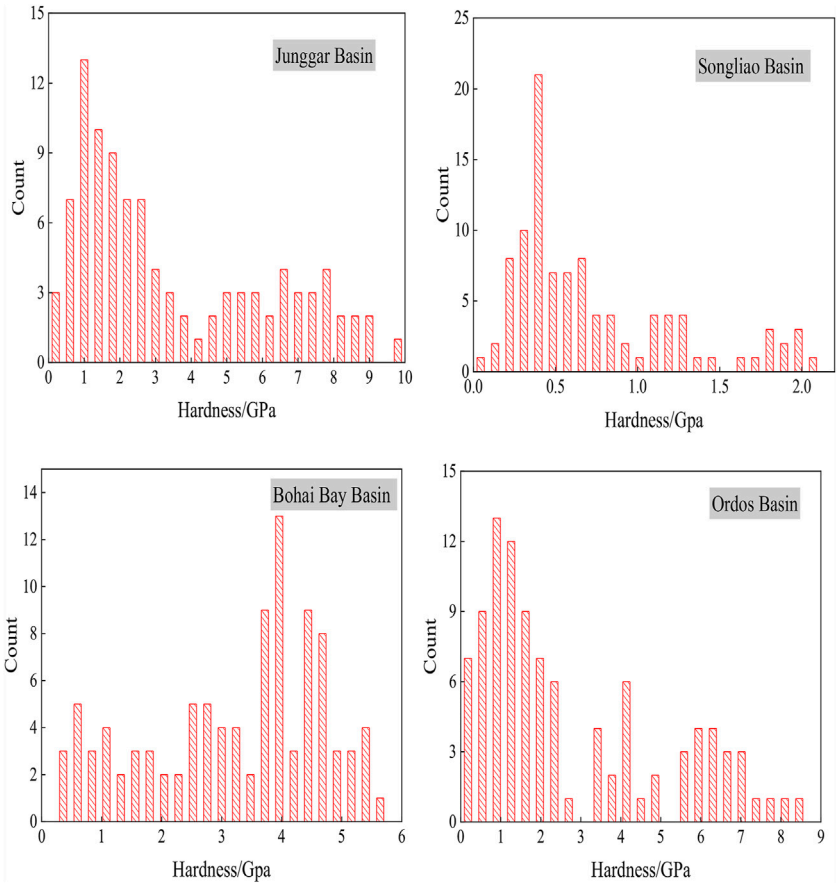

FIGURE 7 | Statistical results of hardness.

In this study, the quasi-static nanoindentation test with a fixed maximum load was carried out, and the grid indentation method is used, with a total of 100 indentation points for each sample. Due to the high heterogeneity across the rock surface, a great number of indentation points were measured using the grid indentation mode, which allows for statistical analysis of the rock microscopic mechanical properties. During the test, the nanoindenter was pressed into the shale surface at a loading rate of 100 μN/s, held in place for 5 s as soon as the load reaches the maximum value of 1 mN, and then gradually popped out of the shale surface at an unloading rate of 100 μN/s. Its displacement-load path is shown in **Figure 3**.

Theory

According to the relationship between indentation and load (specifically, the proportional relationship between the maximum load $F_{\max}$ adopted in the test and the contact area A_c of sample) (Oliver and Pharr, 1992), the rock hardness H can be expressed as:

$$H = \frac{F_{\max}}{A_c} \tag{1}$$

where, $F_{\max}$ is the maximum load in N, and A_c is the projected contact area in m^2.

The contact stiffness S of the sample can be obtained from the initial slope of the unloading section as:

$$E_r = \frac{\sqrt{\pi}}{2\beta\sqrt{A_c}} S \tag{2}$$

where S is the contact stiffness in kN/mm.

Fracture toughness can be determined *via* the energy analysis (Cheng et al., 2002). In the operation process of nanoindentation, the total energy U is composed of elastic energy U_e and plastic energy U_p. As irreversible energy, U_p can be further decomposed into pure plastic energy U_{pp} and fracture energy U_{frac}. Therefore, the following equation is obtained:

$$U = U_e + U_{pp} + U_{frac} \tag{3}$$

where U is the total energy in J; U_e is the elastic energy in J; U_p is the plastic energy in J; U_{pp} is the pure plastic energy in J; U_{frac} is the fracture energy in J. U_e and U_p can be obtained from the diagram of load vs. displacement, as shown in **Figure 4**.

The relationship between U_{PP} and U is as follows:

$$\frac{U_{frac}}{U} = 1 - \left[\frac{1 - 3\left(h_f/h_{\max}\right)^2 + 2\left(h_f/h_{\max}\right)^3}{1 - \left(h_f/h_{\max}\right)^2}\right] \tag{4}$$

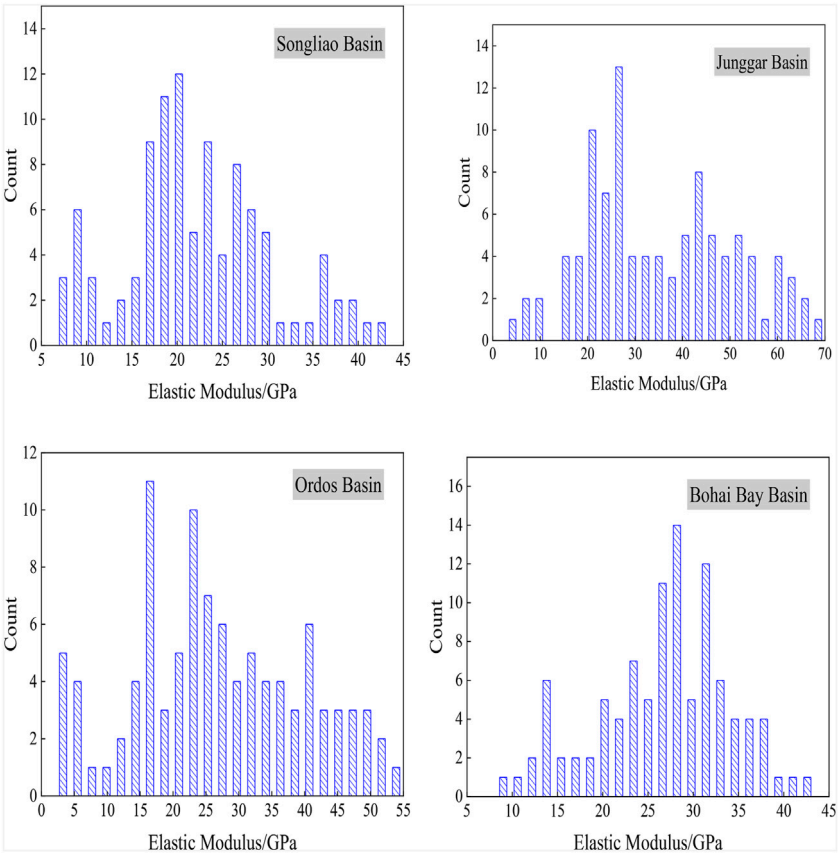

FIGURE 8 | Statistical results of elastic moduli.

The propagation of fractures generates U_{frac}, and the corresponding critical energy release rate G_c can be obtained using the following equation:

$$G_c = \frac{\partial U_{frac}}{\partial A} = \frac{U_{frac}}{A_m} \tag{5}$$

where, G_c is the critical energy release rate in N/m; A_m is the maximum fracture area in m^2, calculated using the relationship between the indenter depth and area.

The fracture toughness K_{ic} can be calculated using the following equation:

$$K_{ic} = \sqrt{G_c E_r} \tag{6}$$

TEST RESULTS

Mineral Analysis Results

The bulk mineral composition is listed in **Table 1**, which varies greatly among different samples. Quartz and clay minerals are two main mineral component, with the content of 14.6–30.8% and 6.2–50.1%, respectively. Other minerals include apatite, plagioclase, calcite, dolomite, etc. The samples from the Bohai Bay Basin presents the calcite content as high as 20.2%, while other samples almost contain no calcite. **Table 2** shows that there are remarkable differences in the relative composition of clay minerals. The samples from the Ordos and Songliao Basins have high relative content of I/S, while the samples from the Junggar Basin have smectite content high up to 72%. As for the samples from the Bohai Bay Basin, the C/S is the main component for clay minerals, reaching 58%.

Figure 5 presents the histograms of the compositions of bulk minerals and clay minerals. The samples from the Songliao and Ordos Basins have similar compositions, which are greatly different from those of the samples from the other two basins.

Microscopic Pore Characteristics

SEM analysis is used to study different pore sizes, pore types, and micro-fractures. **Figure 6** shows the typical SEM images of rock samples from four basins. Most of the pore sizes are at the micro/nano scale and some organic matter also occurs. The pore types include residual intergranular pores and feldspar dissolution pores. There is also locally-developed calcite. There are prominent micro-fractures in some reservoir rocks. In addition to the initial pores on the surface of shale, there are also many pores caused by the whole or partial exfoliation of massive minerals. And beyond that, there are also microscopic fissures

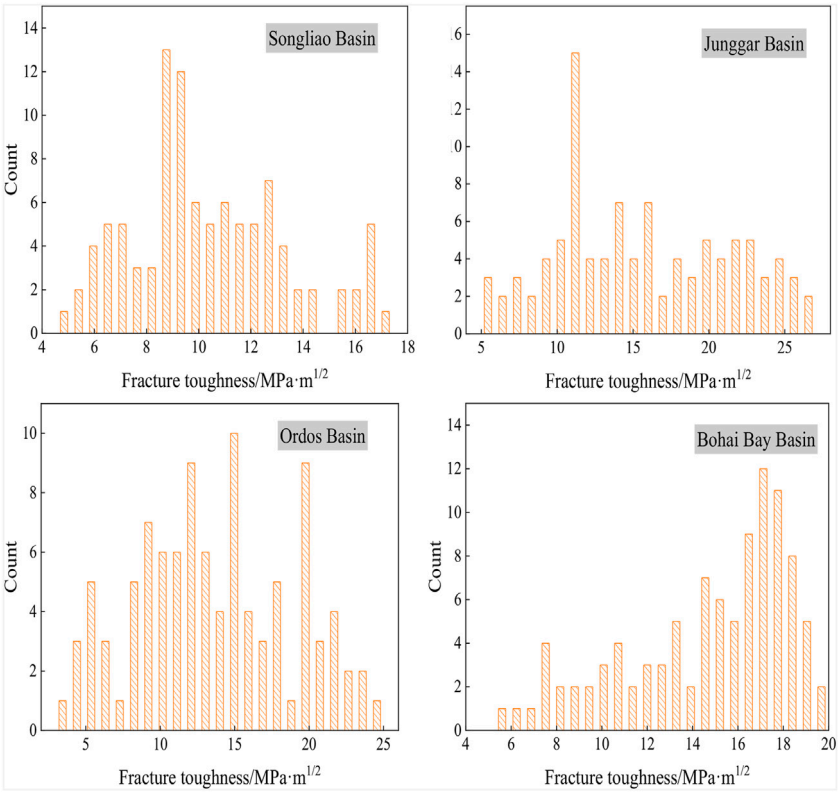

FIGURE 9 | Statistical results of fracture toughness.

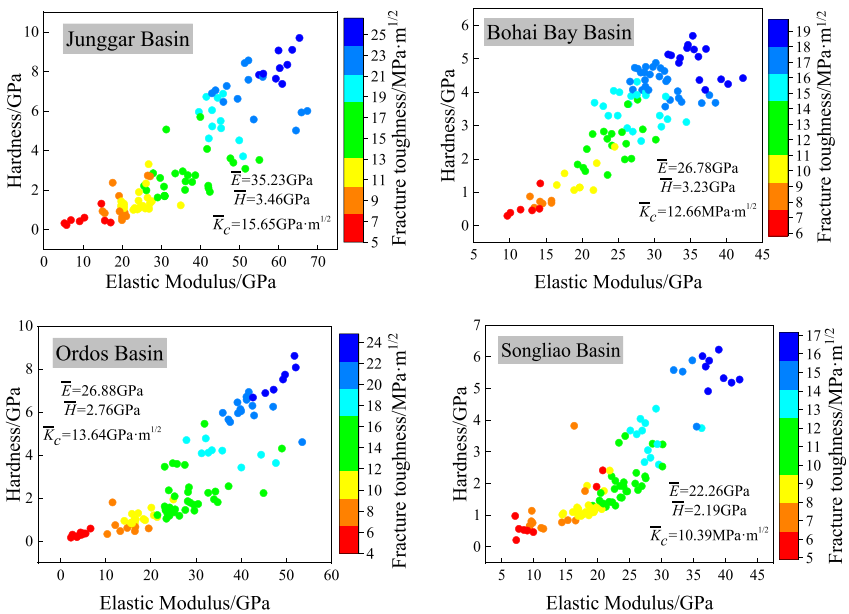

FIGURE 10 | Distribution of mechanical parameters for the four basins.

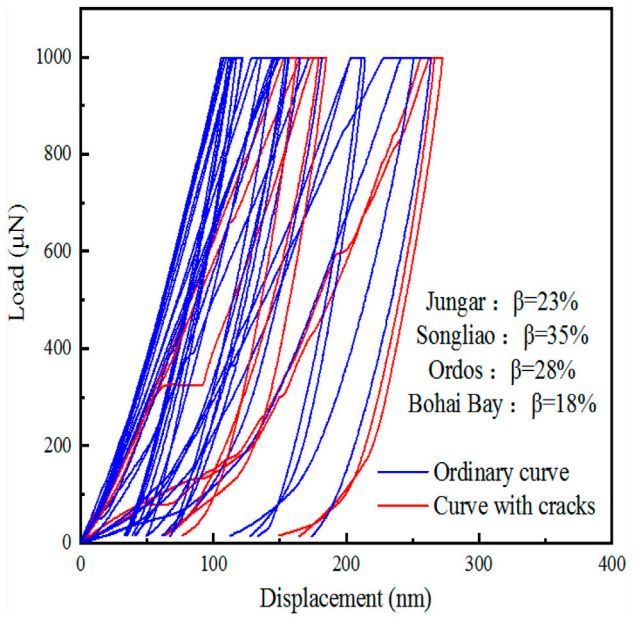

FIGURE 11 | Heterogeneity coefficient β for the four basins.

developed at the edges of the mineral grains and pores throughout the mineral grains. The pore structure is affected by the sedimentary environment, and the geological structure has a great impact on the pore structure (Yang et al., 2016; Lin et al., 2017).

Results of Nanoindentation

Figure 7 shows the calculated frequency distribution of the grid hardness for the four basins. For the Junggar Basin, the maximum hardness is 9.704 GPa, the minimum is 0.232 GPa, averaging 3.466 GPa, and the hardness is mainly distributed in the range of 0.232–4 GPa. For the Songliao Basin, the hardness presents a maximum of 6.231 GPa, and a minimum of 0.217 GPa, averaging 2.215 GPa, and is mainly distributed in the range of 0.2–1 GPa. For the Bohai Bay Basin, the maximum hardness is 5.692 GPa, the minimum is 0.296 GPa, averaging 3.225 GPa, and the hardness is mainly distributed in the range of 3.5–5 GPa. For the Ordos Basin, the maximum and minimum hardness is 8.614 and 0.176 GPa, respectively, with an average of 2.796 GPa, and the hardness is mainly distributed in the range of 0.176–3 GPa. It can be concluded that the Junggar Basin has the largest average hardness, while the Songliao Basin has the smallest average value.

Figure 8 shows the calculated frequency distribution of the grid elastic moduli for the four basins. For the Junggar Basin, the elastic modulus presents a maximum of 67.289 GPa and a minimum of 5.244 GPa, averaging 35.252 GPa; the elastic moduli are mainly distributed in the range of 15–30 GPa. For the Songliao Basin, the elastic modulus presents a maximum of 42.207 GPa and a minimum of 7.118 GPa, averaging 22.128 GPa; the elastic moduli are mainly distributed in the range of 20–50 GPa. For the Bohai Bay Basin, the elastic modulus presents a maximum of 42.287 GPa and a minimum of 9.649 GPa, averaging 26.783 GPa; the elastic moduli are mainly distributed in the range of 20–35 GPa. For the Ordos Basin, the elastic modulus presents a maximum of 53.535 GPa and a minimum of 2.281 GPa, averaging 26.903 GPa; the elastic moduli are mainly distributed in the range of 15–40 GPa. It can be concluded that the Junggar Basin has the largest average elastic modulus, while the Songliao Basin has the smallest average value.

Figure 9 shows the calculated frequency distribution of the grid fracture toughness for the four basins. For the Junggar Basin, the fracture toughness is associated with a maximum of 26.773 MPa $m^{1/2}$ and a minimum of 5.291 MPa $m^{1/2}$, averaging 15.659 MPa $m^{1/2}$; the fracture toughness is mainly distributed in the range of 10–20 MPa $m^{1/2}$. For the Songliao Basin, the fracture toughness is associated with a maximum of 17.117 MPa $m^{1/2}$ and a minimum of 4.913 MPa $m^{1/2}$, averaging 10.396 MPa $m^{1/2}$; the fracture toughness is mainly distributed in the range of 5–13 MPa $m^{1/2}$. For the Bohai Bay Basin, the fracture toughness is associated with a maximum of 19.707 MPa $m^{1/2}$ and a minimum of 5.832 MPa $m^{1/2}$, averaging 14.624 MPa $m^{1/2}$; the fracture toughness is mainly distributed in the range of 14–20 MPa $m^{1/2}$. For the Ordos Basin, the fracture toughness is associated with a maximum of 24.379 MPa $m^{1/2}$ and a minimum of 3.616 MPa $m^{1/2}$, averaging 13.646 MPa $m^{1/2}$; the fracture toughness is mainly distributed in the range of 8–18 MPa $m^{1/2}$. It can be concluded that the Bohai Bay Basin has the largest average fracture toughness, while the Songliao Basin has the smallest average value.

DISCUSSION

Brittleness Index K_1

In the elastic deformation stage of materials, the stress is directly proportional to the strain, which conforms to the Hooke's Law. The ratio of the two is termed the elastic modulus E_r of the material. The greater the E_r value is, the higher the shale fracability is, which indicates a positive correlation between the two. Hardness H refers to the ability of shale to resist hard materials pressing into its local surface. The greater the H value is, the higher the shale fracability (also a positive correlation). Fracture toughness K_c refers to the ability of shale to prevent the crack from progagating and is a quantitative indicator to measure the toughness of materials. The greater the K_c value is, the lower the shale fracability is (a negative correlation). According to the relationships between the above relevant variables and shale fracability, the shale fracability is positively correlated with the brittleness index K_1 defined as below:

$$K_1 = \frac{E_r H}{K_c^2} \tag{7}$$

As shown in **Eq. 6**, the dimension of the fracability coefficient K_1 is m^{-1}. For convenience of the subsequent analysis and discussion, K_1 has multiplied with a unit length to obtain a

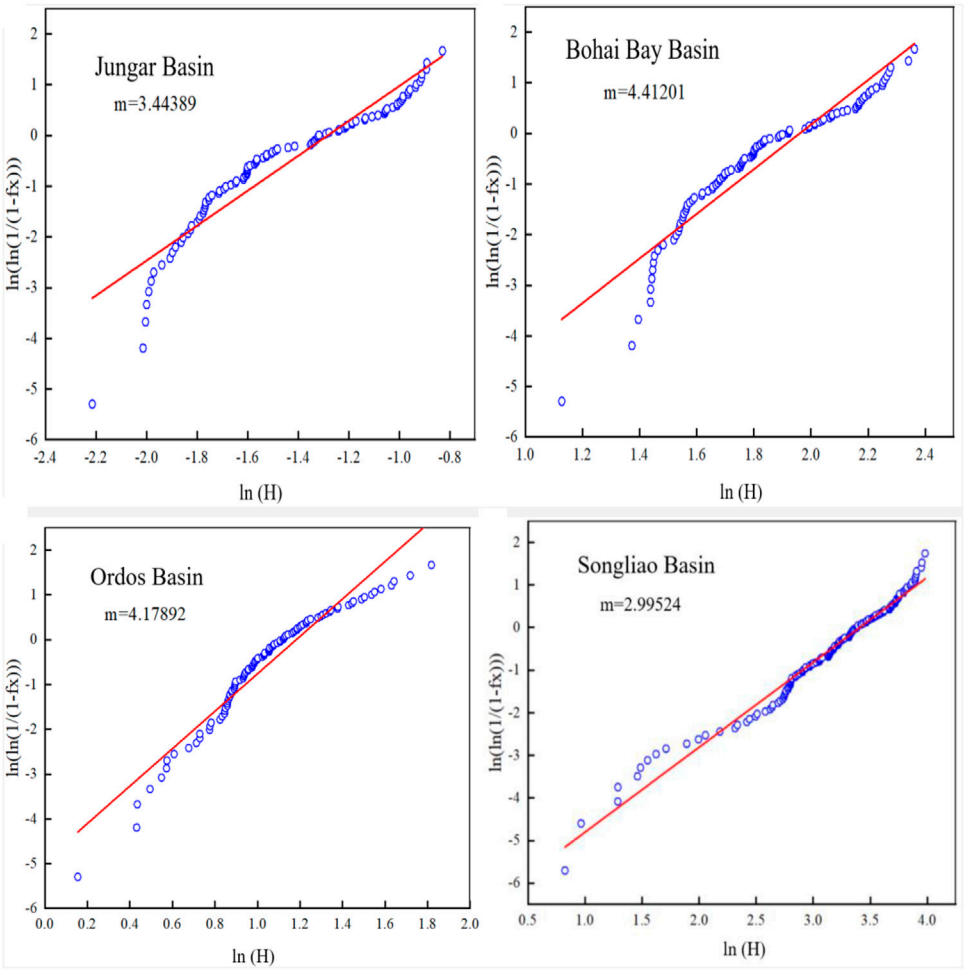

FIGURE 12 | Heterogeneity coefficient m for the four basins.

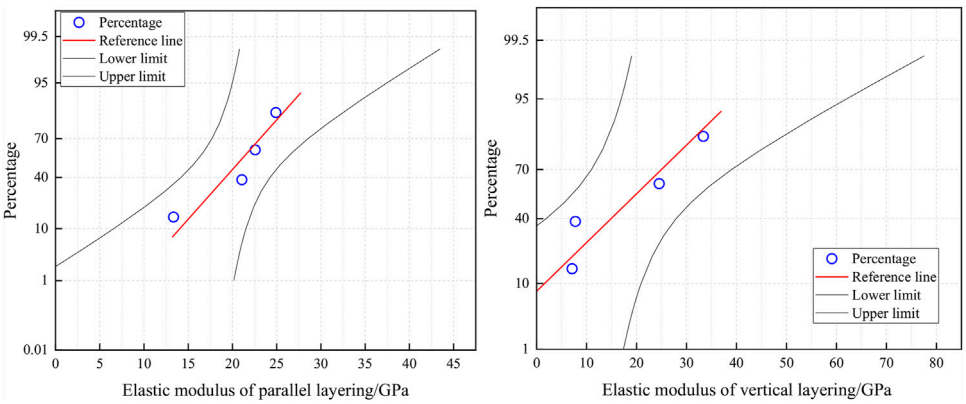

FIGURE 13 | Normal distribution of elastic moduli parallel to and perpendicular to beddings.

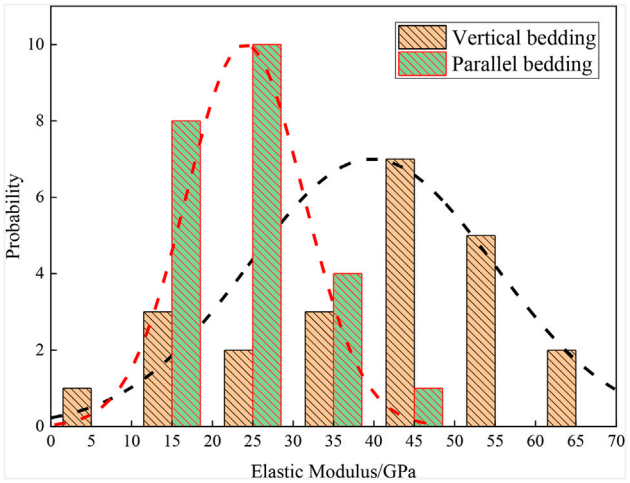

FIGURE 14 | Distribution of elastic moduli parallel and perpendicular to beddings.

dimensionless index. **Figure 10** shows the distribution of mechanical parameters for the four basins. The K_1 values for all of the four basins are obtained, which are shown in **Table 3**.

Based on the brittleness index K_1 calculated using the above equation, a comprehensive evaluation was made for the fracability of the shale in the four basins. The shale in the Junggar Basin has high fracability coefficient K_1 values mainly of 0.4–0.6 (averaging 0.49), due to that it has the largest elastic modulus and hardness. The shale in the Bohai Bay Basin has low fracability coefficient K_1 values mainly of 0.3–0.5 (averaging 0.4), owing to its lower elastic modulus and hardness. The shale in the Songliao Basin is associated with the fracability coefficient K_1 of 0.3–0.8 (averaging 0.45), and that in the Ordos Basin has the fracability coefficient K_1 values of 0.3–0.5 (averaging 0.39, the lowest). However, the average K_1 values of the shale in the four basins are found with only minor differences.

TABLE 6 | Fracability in cases of different values of weight factors.

	Junggar	Bohai	Ordos	Songliao
Case 1 (α_1 = 0.75, α_2 = 0.05, α_3 = 0.2)	1.0355	1.1015	1.03	0.892
Case 2 (α_1 = 0.85, α_2 = 0.03, α_3 = 0.12)	0.8173	0.8769	0.774	0.7152
Case 3 (α_1 = 0.7, α_2 = 0.1, α_3 = 0.2)	1.345	1.425	1.346	1.17
Case 4 (α_1 = 0.6, α_2 = 0.05, α_3 = 0.35)	1.2125	1.28	1.273	1.015

Brittleness Index K_2

m is a parameter for the Weibull distribution, known as the Weibull modulus. In this research, the higher the m values of

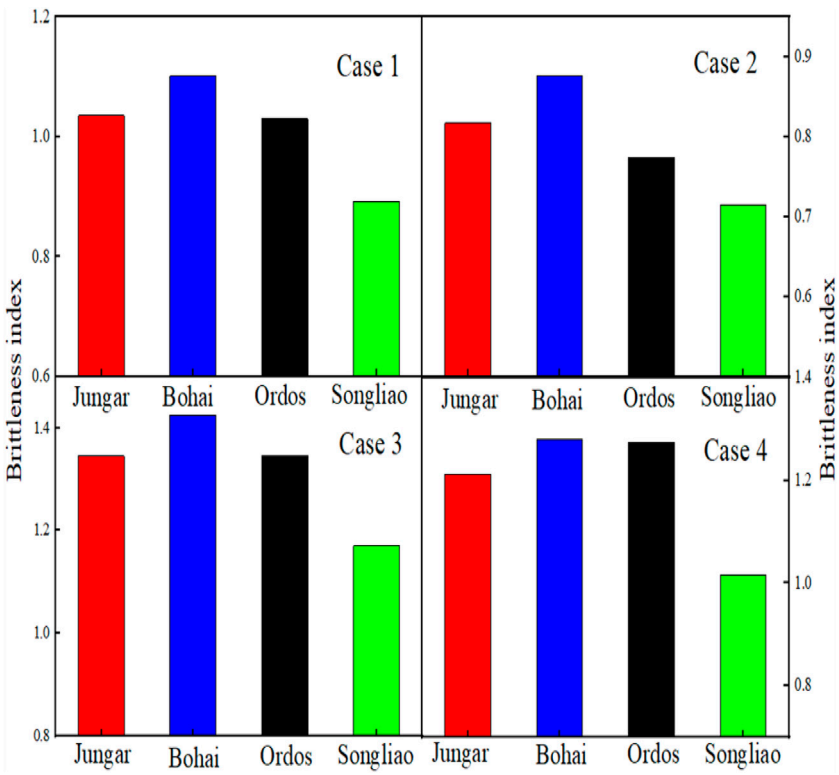

FIGURE 15 | Overall fracability for all the four basins in the four cases.

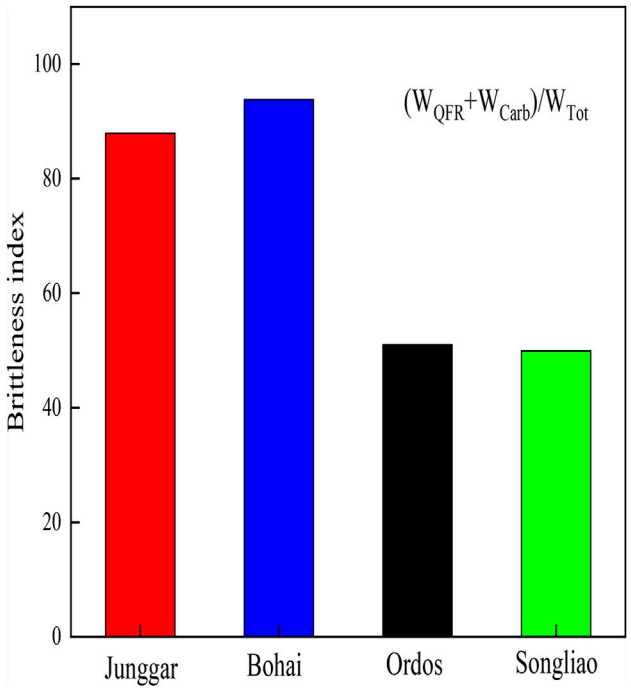

FIGURE 16 | Fracability based on mineral composition.

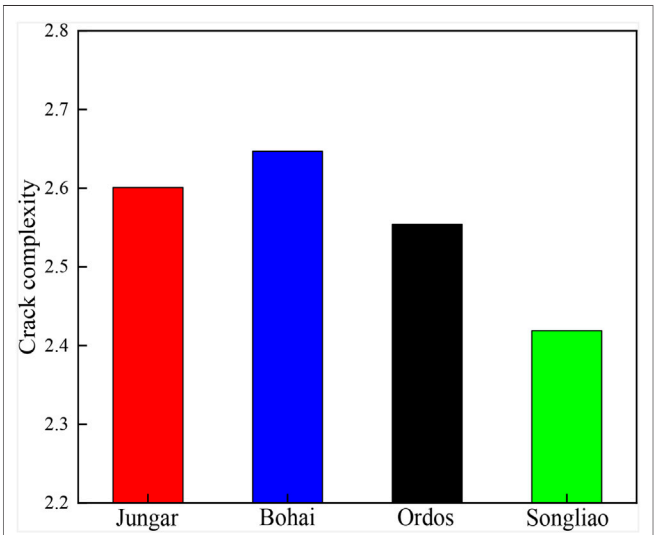

FIGURE 17 | Microscopic comprehensive evaluation for shale oil producibility (Jin et al., 2021).

corresponding mechanical parameters (such as elastic modulus and hardness) are, the less the discreteness of parameter x is, which implies less discreteness of corresponding mechanical parameters of rock and thus lower rock heterogeneity. Therefore, the higher the 1/m value is, the higher the heterogeneity is. β represents the proportion of special load-displacement curves featuring fractures and pores to the total curves. The larger the β value is, the stronger the heterogeneity is.

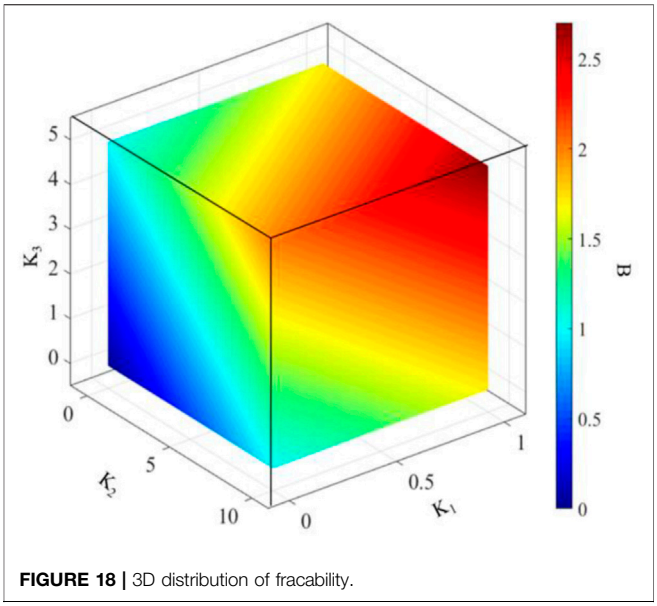

FIGURE 18 | 3D distribution of fracability.

Hence, β/m is used to evaluate the heterogeneity—the larger the β/m value is, the greater the heterogeneity is.

$$K_2 = \frac{\beta}{m} \tag{8}$$

Figures 11 and **12** show the heterogeneity coefficient β and m for the four regions, respectively. And then the brittleness index K_2 is calculated, as shown in **Table 4**. The samples from the Bohai Bay Basin have the largest proportion of curves featuring fractures and pores, and thus higher heterogeneity. The calculated fracability coefficient K_2 of the shale is the highest in the Bohai Bay Basin (7.01) and the lowest in the Songliao Basin (4.08).

Brittleness Index K_3

The brittleness index characterizes the difficulties in creating complex fracture networks by hydraulic fracturing. With a higher brittleness index, the reservoir is more sensitive to fracturing and the resultant fractures are more complex. The elastic modulus reflects the ability of shale to preserve the fractures after being fractured. Some researchers analyzed the kerogen morphology and nanomechanical properties of oil shale cored in different directions (parallel and perpendicular to the bedding plane) (Alstadt et al., 2016).

As shown in **Figures 13**, **14**, there is usually a great difference between the elastic moduli in the horizontal and vertical bedding directions. A greater difference is preferred for fractures to propagate along the bedding plane.

The ratio between the elastic moduli in the directions in relation to the bedding plane is directly related to the fracability, so the ratio of the elastic modulus parallel to the bedding plane to that perpendicular to the bedding plane can be used to represent brittleness. Therefore, the fracability coefficient K_3 is defined as below:

$$K_3 = \frac{E_h}{E_v} \tag{9}$$

where E_h is the elastic modulus along the bedding plane, and E_v is the elastic modulus perpendicular to the bedding.

Based on upscaling and analysis of the nanoindentation test data, the elastic moduli of shale parallel and perpendicular to beddings at the centimeter scale were obtained, and a new model to calculate the brittleness index was established. The calculated brittleness index K_3 is shown in **Table 5**. For samples from the Ordos Basin, there is a great difference between samples parallel and perpendicular to beddings, and the fracability coefficient K_3 is the largest (2.01). For samples from the Songliao Basin, the difference between samples parallel and perpendicular to beddings is the smallest, and the fracability coefficient K_3 is thus the lowest (1.27).

Three-Parameter Evaluation

The three fracability coefficients K_1, K_2, and K_3 based on the nanoindentation test are all dimensionless and the sum of them can characterize the overall fracability of shale. In addition, weight factors α_1, α_2 and α_3 should be defined for the summation to represent the impact degree of each fracability coefficient on the overall fracability. To this end, four cases are discussed in this research. First, assuming $\alpha_1+\alpha_2+\alpha_3 = 1$ and all the three indexes produce the same impact (in other words, $\alpha_1\overline{K_1} = \alpha_2\overline{K_2} = \alpha_3\overline{K_3}$), then $\alpha_1 = 0.75$, $\alpha_2 = 0.05$ and $\alpha_3 = 0.2$. When the impact of K_1 is more significant, we have $\alpha_1\overline{K_1} = 2\alpha_2\overline{K_2} = 2\alpha_3\overline{K_3}$ and thus $\alpha_1 = 0.85$, $\alpha_2 = 0.03$, and $\alpha_3 = 0.12$. When the impact of K_2 is more significant, we have $2\alpha_1\overline{K_1} = \alpha_2\overline{K_2} = 2\alpha_3\overline{K_3}$ and then $\alpha_1 = 0.7$, $\alpha_2 = 0.1$, and $\alpha_3 = 0.2$. When the impact of K_3 is more significant, we have $2\alpha_1\overline{K_1} = 2\alpha_2\overline{K_2} = \alpha_3\overline{K_3}$ and then $\alpha_1 = 0.6$, $\alpha_2 = 0.05$, and $\alpha_3 = 0.35$. Rational weight factors can be determined in accordance with the field conditions, to characterize the impact degree of the three indexes on the fracability. Thus, the ultimate brittleness index is obtained as:

$$B = \alpha_1 K_1 + \alpha_2 K_2 + \alpha_3 K_3 \tag{10}$$

The calculated brittleness index B with different α_1, α_2, and α_3 values for each basin is shown in **Table 6** and **Figure 15**. Except for Case 4, the Bohai Bay Basin has the most distinctive fracability. In Cases 1 and 3, there is little difference in fracability between the Junggar and Ordos Basins. In **Figure 16**, the fracability based on the mineral composition analyzed from the rock cutting are compared. **Figure 17** shows the microscopic comprehensive evaluation for the producibility of the continental shale oil in the four basins by previous research (Jin et al., 2021). Comparison shows that Case 2 is more consistent with the field conditions. Therefore, $\alpha_1 = 0.85$, $\alpha_2 = 0.03$, and $\alpha_3 = 0.12$ are used, and the above equation is rewritten as:

$$B = 0.85K_1 + 0.03K_2 + 0.12K_3 \tag{11}$$

As shown in **Figure 18**, the fracability of the shale reservoir is determined from the perspectives of the point (K_1), area (K_2), and volume (K_3) parameters and the 3D distribution of fracability is obtained. The redder the color in the figure is, the greater the fracability is; the bluer the color is, the lower the fracability is.

CONCLUSION

This research addresses the typical continental shale of the Bohai Bay, Ordos, Songliao, and Junggar Basins in China. *via* the XRD mineral analysis, SEM, and nanoindentation test using the grid indentation testing mode, the elastic modulus, hardness, and fracture toughness of rocks are obtained. Furthermore, the three fracability parameters K_1, K_2, and K_3 are obtained by analyzing the measured mechanical parameters, resulting in the ultimate fracability coefficient $B = 0.7K_1+0.1K_2+0.2K_3$.

1) The point fracability coefficient is obtained: $K_1 = E_r H/K_c^2$. In the Junggar Basin, the average fracability coefficient K_1 of shale is 0.49, indicating the highest point fracability among the four basins. In the Bohai Bay Basin, the average fracability coefficient K_1 of shale is 0.4, and the point compressibility K_1 shows no great difference from the other three basins.
2) The area fracability coefficient is obtained: $K_2 = \beta/m$. Among the four regions, the samples from the Bohai Bay Basin have the largest proportion of curves featuring fractures and pores, and a high degree of heterogeneity. The calculated fracability coefficient K_2 of the shale is the highest (7.01) in the Bohai Bay Basin, and the lowest (4.08) in the Songliao Basin.
3) The volume fracability coefficient is obtained: $K_3 = E_h/E_v$. For the samples from the Ordos Basin, there is a great difference between the elastic moduli parallel and perpendicular to beddings, and the fracability coefficient K_3 is the largest (2.01). For the samples from the Songliao Basin, the difference between the elastic moduli parallel and perpendicular to beddings is the smallest, and the fracability coefficient K_3 is also the lowest (1.27).
4) With the sum of the three subordinate fracability coefficients, the overall fracability of shale is characterized. In addition, weight factors α_1, α_2, and α_3 should be defined for the summation to represent the impact degrees of the three parameters on fracability. With the composition of minerals taken into account, the weight factors are finally determined as: $\alpha_1 = 0.85$, $\alpha_2 = 0.03$, and $\alpha_3 = 0.12$, and in other words, the ultimate fracability index $B = 0.85K_1+0.03K_2+0.12K_3$.

DATA AVAILABILITY STATEMENT

The raw data supporting the conclusions of this article will be made available by the authors, without undue reservation.

AUTHOR CONTRIBUTIONS

All authors contributed to the conceptualization, methodology and manuscript preparation.

FUNDING

The research was funded by National Key R&D Program of China (2018YFE0196000) and Foundation Program for Directly Affiliated Institutions of CNPC (2019D-500808).

REFERENCES

Ai, C., Zhang, J., Li, Y.-w., Zeng, J., Yang, X.-l., and Wang, J.-g. (2016). Estimation Criteria for Rock Brittleness Based on Energy Analysis during the Rupturing Process. *Rock Mech. Rock Eng.* 49 (12), 4681–4698. doi:10.1007/s00603-016-1078-x

Alstadt, K. N., Katti, K. S., and Katti, D. R. (2016). Nanoscale Morphology of Kerogen and *In Situ* Nanomechanical Properties of Green River Oil Shale. *J. Nanomech. Micromech.* 6 (1), 04015003. doi:10.1061/(ASCE)NM.2153-5477.0000103

Chen, J., Cao, H., and Sun, P. (2017). Fracability Evaluation of Shale in the Niutitang Formation in Northwestern Hunan. *Earth Sci. Front.* 24 (6), 390–398. doi:10.13745/j.esf.yx.2017-2-50

Cheng, Y., Li, Z., and Cheng, C. (2002). Scaling Relationships for Indentation Measurements. *Philos. Magazine A* 82, 1821–1829. doi:10.1080/01418610208235693

Di, S., Hong, J., Lv, P., Ye, W., Li, H., Zhang, J., et al. (2019). Method for Fracturability Evaluation of Tight Oil Reservoirs in the Shulu Sag. *Well Logg. Technol.* 43 (5), 536–541. doi:10.16489/j.issn.1004-1338.2019.05.018

Jin, X., Li, G., Meng, S., Wang, X., Liu, C., Tao, J., et al. (2021). Microscale Comprehensive Evaluation of continental Shale Oil Recoverability. *Pet. Exploration Develop.* 40 (01), 256–268. doi:10.1016/s1876-3804(21)60021-6

Kumar, V., Curtis, M. E., Gupta, N., Sondergeld, C. H., and Rai, C. S. "Estimation of Elastic Properties of Organic Matter and Woodford Shale through Nano-Indentation Measurements," in Proceedings of the Society of Petroleum Engineers - SPE Canadian Unconventional Resources Conference 2012, Calgary, Alberta, Canada, October-November 2012. doi:10.2118/162778-MS

Li, Y., Jia, D., Rui, Z., Peng, J., Fu, C., and Zhang, J. (2017). Evaluation Method of Rock Brittleness Based on Statistical Constitutive Relations for Rock Damage. *J. Pet. Sci. Eng.* 153, 123–132. doi:10.1016/j.petrol.2017.03.041

Lin, D., Wang, J., Yuan, B., and Shen, Y. (2017). Review on Gas Flow and Recovery in Unconventional Porous Rocks. *Adv. Geo-energ. Res.* 1 (1), 39–53. doi:10.26804/ager.2017.01.04

Liu, K., and Ostadhassan, M. (2017). Microstructural and Geomechanical Analysis of Bakken Shale at Nanoscale. *J. Pet. Sci. Eng.* 153, 133–144. doi:10.1016/j.petrol.2017.03.039

Manjunath, G. L., and Jha, B. (20192038). Nanoscale Fracture Mechanics of Gondwana Coal. *Int. J. Coal Geology.* 204, 102–112. doi:10.1016/j.coal.2019.02.007

Mao, S., Zhang, Z., Chun, T., and Wu, K. (2021). Field-Scale Numerical Investigation of Proppant Transport Among Multicluster Hydraulic Fractures. *SPE J.* 26 (1), 307–323. doi:10.2118/203834-PA

Oliver, W. C., and Pharr, G. M. (1992). An Improved Technique for Determining Hardness and Elastic Modulus Using Load and Displacement Sensing Indentation Experiments. *J. Mater. Res.* 7 (6), 1564–1583. doi:10.1557/JMR.1992.1564

Shukla, P., Taneja, S., Sondergeld, C., and Rai, C. (2015). Nanoindentation Measurements on Rocks. *Fracture, Fatigue, Fail. Damage Evol.* 5, 99–105. doi:10.1007/978-3-319-06977-7_13

Qin, H., and Yang, X. (2019). Study on Interpretation Method of Brittleness Logging in Tight Reservoir. *Well Logg. Technol.* 43 (5), 509–513 & 530. doi:10.16489/j.issn.1004-1338.2019.05.013

Tang, J., Wu, K., Zuo, L., Xiao, L., Sun, S., and Ehlig–Economides, C. (2019). Investigation of Rupture and Slip Mechanisms of Hydraulic Fractures in Multiple-Layered Formations. *SPE J.* 24 (5), 2292–2307. doi:10.2118/197054-PA

Xie, J., Tang, J., Yong, R., Fan, Y., Zuo, L., Chen, X., et al. (2020). A 3-D Hydraulic Fracture Propagation Model Applied for Shale Gas Reservoirs with Multiple Bedding Planes. *Eng. Fracture Mech.* 228, 106872. doi:10.1016/j.engfracmech.2020.106872

Yang, L., Chen, C., Liu, Y., and Zheng, Y. (2020). A Comparative Study of Ion Diffusion during Water Imbibition in Shale, sandstone and Volcanic Rock. *Capillarity* 3 (2), 16–27. doi:10.46690/capi.2020.02.01

Yang, L., Ge, H., Shi, X., Cheng, Y., Zhang, K., Chen, H., et al. (2016). The Effect of Microstructure and Rock Mineralogy on Water Imbibition Characteristics in Tight Reservoirs. *J. Nat. Gas Sci. Eng.* 34, 1461–1471. doi:10.1016/j.jngse.2016.01.002

Yuan, J., Deng, J., Zhang, D., Li, D., Yan, W., Chen, C., et al. (2013). Fracability Evaluation of Shale-Gas Reservoirs. *Acta Pertolei Sinica* 34 (3), 523–527. doi:10.7623/syxb201303015

Zhang, F., An, M., Zhang, L., Fang, Y., and Elsworth, D. (2020). Effect of Mineralogy on Friction-Dilation Relationships for Simulated Faults: Implications for Permeability Evolution in Caprock Faults. *Geosci. Front.* 11 (2), 439–450. CNKI:SUN:GSFT.0.2020-02-008. doi:10.1016/j.gsf.2019.05.014

Zhang, J., Ai, C., Li, Y.-w., Che, M.-G., Gao, R., and Zeng, J. (2018a). Energy-based Brittleness index and Acoustic Emission Characteristics of Anisotropic Coal under Triaxial Stress Condition. *Rock Mech. Rock Eng.* 51, 3343–3360. doi:10.1007/s00603-018-1535-9

Zhang, J., Li, Y., Pan, Y., Wang, X., Yan, M., Shi, X., et al. (2021). Experiments and Analysis on the Influence of Multiple Closed Cemented Natural Fractures on Hydraulic Fracture Propagation in a Tight sandstone Reservoir. *Eng. Geology.* 281, 105981. doi:10.1016/j.enggeo.2020.105981

Zhang, Y., Lebedev, M., Al-Yaseri, A., Yu, H., Xu, X., Sarmadivaleh, M., et al. (2018b). Nanoscale Rock Mechanical Property Changes in Heterogeneous Coal after Water Adsorption. *Fuel* 218, 23–32. doi:10.1016/j.fuel.2018.01.006

Zhao, J., Xu, W., Li, Y., and Hu, J. (2015). A New Method for Fracability Evaluation of Shale-Gas Reservoirs. *Nat. Gas Geosci.* 26 (6), 1165–1172. doi:10.11764/j.issn.1672-1926.2015.06.1165

Conflict of Interest: DL was employed by the PetroChina Daqing Oilfield Co., Ltd.

The remaining authors declare that the research was conducted in the absence of any commercial or financial relationships that could be construed as a potential conflict of interest.

frontiers in Earth Science

ORIGINAL RESEARCH
published: 17 January 2022
doi: 10.3389/feart.2021.807788

Flow Simulation and Influence Factors Analysis of CO_2 Foam Fracturing in Annulus Injection

*Hao Li and Genbo Peng**

Department of Petroleum Engineering, Northeast Petroleum University, Daqing, China

CO_2 foam fracturing fluid is widely used in unconventional oil and gas production because of its easy flowback and low damage to the reservoir. Nowadays, the fracturing process of CO_2 foam fracturing fluid injected by coiled tubing is widely used. However, the small diameter of coiled tubing will cause a large frictional pressure loss in the process of fluid flow, which is not beneficial to the development of fracturing construction. In this paper, the temperature and pressure calculation model of gas, liquid, and solid three-phase fluid flow in the wellbore under annulus injection is established. The model accuracy is verified by comparing the calculation results with the existing gas, solid, and gas and liquid two-phase model of CO_2 fracturing. The calculation case of this paper shows that compared with the tubing injection method, the annulus injection of CO_2 foam fracturing fluid reduces the friction by 3.06 MPa, and increases the wellbore pressure and temperature by 3.06 MPa and 5.77°C, respectively. Increasing the injection temperature, proppant volumetric concentration, and foam quality will increase the wellbore fluid temperature and make the CO_2 transition to the supercritical state while increasing the mass flow rate will do the opposite. The research results verify the feasibility of the annulus injection of CO_2 foam fracturing fluid and provide a reference for the improvement of CO_2 foam fracturing technology in the field.

Keywords: CO_2 foam, temperature distribution, pressure distribution, multi-field coupling, annulus injection

OPEN ACCESS

Edited by:
Jizhou Tang,
Tongji University, China

Reviewed by:
Meng Wang,
University of Houston, United States
Chunkai Fu,
University of Louisiana at Lafayette, United States
Wan Cheng,
China University of Geosciences Wuhan, China

****Correspondence:***
Genbo Peng
1173736517@qq.com

Specialty section:
This article was submitted to Economic Geology, a section of the journal Frontiers in Earth Science

Received: *02 November 2021*
Accepted: *29 November 2021*
Published: *17 January 2022*

Citation:
Li H and Peng G (2022) Flow Simulation and Influence Factors Analysis of CO_2 Foam Fracturing in Annulus Injection. Front. Earth Sci. 9:807788. doi: 10.3389/feart.2021.807788

INTRODUCTION

With the development of the economy, the exploitation of conventional oil and gas resources has been unable to meet the energy consumption required by scientific and technological progress. Therefore, the development focus has gradually shifted to low permeability and dense unconventional oil and gas resources (Song et al., 2017; Li C et al., 2017; Tang et al., 2021; Tang et al., 2020; Tan and Qiao, 2020; Zhang et al., 2021). Due to the low permeability of unconventional reservoirs (Tang et al., 2019; Xie et al., 2020; Shao et al., 2019; Wang et al., 2020), application of hydraulic fracturing technology for unconventional oil and gas production has many problems, such as low flowback and damage to the reservoir, which has been unable to meet the technical requirements of unconventional oil and gas development. CO_2 fracturing is widely recognized by engineers, experts, and scholars because it can achieve several times higher permeability than hydraulic fracturing (Wang et al., 2012; He et al., 2016; Wanniarachchi et al., 2018; Cong et al., 2022), and has little damage to the reservoir and easy flowback during fracturing (Gupta et al., 2005; Wang et al., 2011; Yi et al., 2019). Nowadays, CO_2 fracturing technology is mainly divided into CO_2 foam fracturing, CO_2 dry fracturing, supercritical CO_2 fracturing, CO_2 dry foam fracturing, and the other

special CO_2 fracturing (Sun F et al., 2017). Compared with CO_2 dry fracturing, CO_2 foam fracturing has many advantages, such as low construction difficult and technical equipment requirements, and has been widely used. He et al. (2018) found through fracturing tests that Supercritical CO_2 can obtain lower breakdown pressure than freshwater under the same pressure. Carter et al. (1996), McAndrew et al. (2017), and Tong et al. (2017, 2019) found through experiments that CO_2 foam fracturing fluid has a greater sand-carrying capacity than water. Gu and Mohanty (2014) simulated the effect of foam quality on fracture morphology by using the PKN model and found that the length of cracks decreases with the increase of foam quality, while the width increases. Friehauf and Sharma (2009b) found through simulation that the foam quality is between 0.3 and 0.5, and the optimal fracturing effect will be obtained. A large number of studies have shown that CO_2 foam fracturing can effectively improve the fracturing effect of unconventional reservoirs. However, when CO_2 foam fracturing is used, there is an interaction between the rheological parameters of fracturing fluid in the wellbore and the pressure and temperature (Guo and Zeng 2015; Friehauf and Sharma 2009a; Song et al., 2017a; 2017b). How to accurately calculate the rheological parameters of CO_2 foam fracturing fluid in wellbore and fracture and determine the fracturing fluid phase has become an important prerequisite for accurately predicting the shape of fracturing fractures. A lot of theoretical and experimental studies have been done on CO_2 foam fluids (Sherif et al., 2016; Ahmed et al., 2017; Faroughi et al., 2018; Moridis 2018; Yekeen et al., 2018). Li et al. (2008) established a coupled mathematical model of density, pressure, and temperature distribution of foam fluid flowing in the wellbore. The analysis showed that foam quality had a great influence on fluid parameters. However, although this model has a wider range of application than previous models, the effect of proppant on CO_2 foam fracturing fluid flow in the wellbore is not considered. An et al. (2014), Li Y et al. (2017), Luo et al. (2014) found through foam rheological experiments that CO_2 foam fracturing fluid belongs to power-law fluid, whose viscosity increases with foam quality and pressure, and decreases with temperature and shear rate. Li et al. (2010) established a model of proppant flowing with foam. Through Reynolds number to calculate the friction coefficient of foam and proppant, and added them to obtain the friction coefficient of three-phase fluid. For the CO_2 injection process, Cheng et al. (2013), and Shen et al. (2010) proposed using coiled tubing to inject CO_2, which is more conducive to the transformation of CO_2 into a supercritical state. With the development of coiled tube fracturing technology, the coiled tube sandblasting perforating annulus fracturing is one of the most concerned and the most rapidly developing technologies (Yu et al., 2013). Compared with tubing injection, annulus injection can significantly reduce the friction caused by the flow of fracturing fluid in the wellbore (Wang et al., 2010).

At present, although a variety of models for CO_2 foam fracturing fluids have been established, most of them only consider the gas-liquid phase and ignore the influence of proppant on temperature and pressure. When the CO_2 foam fracturing fluid flows in the wellbore, the friction between the proppant and the pipe wall will cause serious frictional pressure loss, and the proppant will also change the density and viscosity of the fracturing fluid, so the two-phase model will produce large errors in the calculation of temperature and pressure of CO_2 foam fracturing fluid in the wellbore. In this paper, the gas, liquid, and solid three-phase flow model of CO_2 foam fracturing fluid in the wellbore was established to realize the accurate prediction of fluid temperature and pressure during the flow process, which provided a theoretical basis for the design of CO_2 foam fracturing parameters.

TEMPERATURE AND PRESSURE CALCULATION MODEL IN WELLBORE

Model Assumptions

To establish the temperature and pressure calculation model for the flow of CO_2 foam fracturing fluid in the wellbore, the following assumptions are proposed: 1) CO_2 foam fracturing fluid flow along the wellbore is treated as a one-dimensional flow; 2) The injection pressure, injection mass flow rate, and surface temperature are assumed to be constant; 3) The gas phase, liquid phase, and solid phase are present in the wellbore at the same time; 4) The annulus fluid only has heat conduction, and the effects of natural convection and radiation are ignored. According to the construction characteristics of CO_2 foam fracturing, a physical model is established as shown in **Figure 1** (Guo et al., 2015).

Numerical Model

Proppant has a great influence on the temperature and pressure of CO_2 foam fracturing fluid flowing in the wellbore, so the CO_2 foam two-phase flow equation needs to be corrected (Xu et al., 2019). In this paper, the solid phase is coupled to the CO_2 foam two-phase flow model by volume averaging method, and the governing equation of the steady state model of CO_2 foam fracturing fluid is established.

Heat Transfer Model

During CO_2 foam fracturing fluid injection, the temperature change depends on heat transfer down the tubing and heat exchange between the fluid and the tubing wall. Therefore, the energy conservation equation of CO_2 foam fracturing fluid in the tubing can be obtained (Sun X et al., 2017; Sun et al., 2018; Xu et al., 2018):

$$-\frac{\partial\left(\rho_{\mathrm{f}} C_{p,\mathrm{f}} Q_{\mathrm{f}} T_{\mathrm{f}}\right)}{\partial z}+2\pi r_{\mathrm{tu,i}} h_{\mathrm{f}}\left(T_{\mathrm{tu}}-T_{\mathrm{f}}\right)=0 \tag{1}$$

where the subscripts "f," "tu," and "i" represent the CO_2 foam fracturing fluid, tubing, and inner radius, respectively; ρ represents the density, kg/m^3; T represents the temperature, °C; C_p represents the specific heat capacity, J/(kg·°C); Q represent the mass flow rate, kg/s; h represents the heat transfer coefficient between CO_2 foam fracturing fluid and tubing, W/(m^2·°C).

Heat is transferred in the axial direction by conduction; the heat exchange between the tubing wall and the fluid, and the heat exchange between the tubing wall and the annulus fluid in the

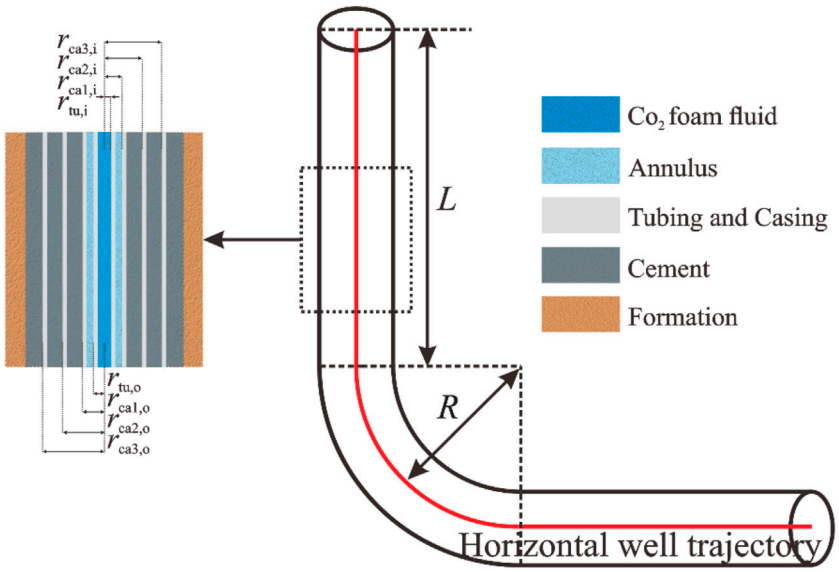

FIGURE 1 | Diagram of the wellbore-formation system for CO_2 foam fracturing fluid.

radial direction through conduction are factors that affect the tubing temperature. The energy conservation equation of the tubing is given by (Xu et al., 2019):

$$\lambda_{tu}\pi\left(r_{tu,o}^2 - r_{tu,i}^2\right)\frac{\partial^2 T_{tu}}{\partial z^2} + 2\pi r_{tu,i}h_f\left(T_f - T_{tu}\right) + 2\pi r_{tu,o}\frac{\lambda_{tu-an}}{\left(r_{ca1,i} - r_{tu,i}\right)/2}\left(T_{an} - T_{tu}\right) = 0 \tag{2}$$

where the subscripts "an" and "ca1" represent the annulus fluid and the production casing, respectively; $\lambda_{tu\text{-}an}$ represents the thermal conductivity between the tubing and the annulus fluid, W/(m·°C); the subscripts "o" represents the outer radius, respectively.

The temperature of the wellbore-formation system is determined by the heat transfer in the axial direction through conduction and the heat exchange between the phase layers.

$$\lambda_{an}\pi\left(r_{ca1,i}^2 - r_{tu,o}^2\right)\frac{\partial^2 T_{an}}{\partial z^2} + 2\pi r_{tu,o}\frac{\lambda_{tu-an}}{\left(r_{ca1,i} - r_{tu,i}\right)/2}\left(T_{tu} - T_{an}\right) + 2\pi r_{ca1,i}\frac{\lambda_{an-ca3}}{\left(r_{ca1,o} - r_{tu,o}\right)/2}\left(T_{ca1} - T_{an}\right) = 0 \tag{3}$$

$$\lambda_{ca1}\pi\left(r_{ca1,o}^2 - r_{ca1,i}^2\right)\frac{\partial^2 T_{ca1}}{\partial z^2} + 2\pi r_{ca1,i}\frac{\lambda_{an-ca1}}{\left(r_{ca1,o} - r_{tu,o}\right)/2}\left(T_{an} - T_{ca1}\right) + 2\pi r_{ca1,o}\frac{\lambda_{ca1-ce1}}{\left(r_{ca2,i} - r_{ca1,i}\right)/2}\left(T_{ce1} - T_{ca1}\right) = 0 \tag{4}$$

$$\frac{\lambda_{fo}}{r}\frac{\partial}{\partial r}\left(r\frac{\partial T_{fo}}{\partial r}\right) + \lambda_{fo}\frac{\partial^2 T_{fo}}{\partial z^2} = 0 \tag{5}$$

where the subscripts "ce1" and "fo" represent the cement layer and the formation, respectively; $\lambda_{an\text{-}ca1}$ represents the thermal conductivity between the annulus fluid and the production casing, W/(m·°C); $\lambda_{ca1\text{-}ce1}$ represents the thermal conductivity between the production casing and the cement layer, W/(m·°C).

Heat transfer of carbon dioxide foam fracturing fluid mainly includes thermal conductivity coefficient, heat transfer coefficient, and specific heat capacity, the calculation formula is as follows:

$$\lambda_f = \Gamma\left(1 - C_{sf}\right)\lambda_g + \left(1 - \Gamma\right)\left(1 - C_{sf}\right)\lambda_l + C_{sf}\lambda_s \tag{6}$$

$$h_f = \Gamma\left(1 - C_{sf}\right)h_g + \left(1 - \Gamma\right)\left(1 - C_{sf}\right)h_l + C_{sf}h_s \tag{7}$$

$$C_{p,f} = \left(\Gamma\left(1 - C_{sf}\right)\rho_g C_{p,g} + \left(1 - \Gamma\right)\left(1 - C_{sf}\right)\rho_l C_{p,l} + \rho_s C_{sf} C_{p,s}\right)/\rho_f \tag{8}$$

where the subscripts "g," "l," and "s" represent the internal phase and external phase and proppant, respectively; C_{sf} represents the proppant volumetric concentration; Γ represents the foam quality.

Pressure Model

$$\frac{\partial p}{\partial z} - \rho_f g\sin\theta + \frac{2f_f\rho_f v_f^2}{2r} - \rho_f v_f \Delta v_f = 0 \tag{9}$$

where p represents the pressure, MPa; g represents the gravity acceleration, m/s^2; θ represents the inclination angle; f represents the friction coefficient; v represents the velocity, m/s; r represents the radius, m; $\triangle v$ represents the speed difference between two positions, m/s (Xu et al., 2019).

The velocity equation of CO_2 foam fracturing fluid is given by:

$$v_f = \frac{q_g + q_l + q_s}{\pi r_{tu,i}^2} \tag{10}$$

where q represents the volume flow rate, m^3/s.

The foam quality and proppant volumetric concentration are given by:

$$\Gamma = \frac{V_g}{V_g + V_l} = \frac{q_g}{q_g + q_l} \tag{11}$$

$$C_{sf} = \frac{V_s}{V_g + V_l + V_s} \tag{12}$$

where V represents the volume, m^3.

The liquid phase density can be calculated as follows:

$$\rho_l = \rho_{ref} + \frac{\rho_{ref}}{\beta}(p - p_{ref}) - \rho_{ref}\alpha(T - T_{ref}) \tag{13}$$

where the subscript "ref" represent the reference condition (p_{ref} = 0.101325 MPa, T_{ref} = 20°C); β represents the isothermal volume modulus of the external phase, Pa; α represents the volume expansion coefficient, $°C^{-1}$. In this paper, the external phase of CO_2 foam fracturing fluid is water, ρ_{ref} = 1000 kg/m^3, $\beta = 2.2 \times 10^9$ Pa, α = 0.000207$°C^{-1}$ (Xu et al., 2019).

According to volume averaging, gas, liquid, and proppant mass are given by:

$$m_g = V_f \Gamma\left(1 - C_{sf}\right)\rho_g \tag{14}$$

$$m_l = V_f (1 - \Gamma)\left(1 - C_{sf}\right)\rho_l \tag{15}$$

$$m_s = V_f C_{sf} \rho_s \tag{16}$$

The density of CO_2 foam fracturing fluid is given by:

$$\rho_f = \left(m_g + m_l + m_s\right)/V_f \tag{17}$$

where m represents the mass, kg.

Substituting **Eqs. 14–16** into **Eq. 17**, the density of foam fracturing fluid can be obtained:

$$\rho_f = \Gamma\left(1 - C_{sf}\right)\rho_g + (1 - \Gamma)\left(1 - C_{sf}\right)\rho_l + C_{sf}\rho_s \tag{18}$$

CO_2 properties are calculated by S-W model (Span and Wagner 1996), because the model is more accurate.

$$\Phi(\delta, \tau) = \Phi^O(\delta, \tau) + \Phi^r(\delta, \tau) \tag{19}$$

where Φ represents the Helmholtz energy; Φ^O represents the ideal gas part of Helmholtz energy; Φ^r represents the residual fluid part of Helmholtz energy; δ and τ represent the reduced density and inverse reduced temperature, respectively.

Friction Calculation

For CO_2 foam fracturing fluid, whose flow pattern has a direct effect on the friction coefficient, when $Re \le Re_c$, it is laminar flow; otherwise, it is turbulent flow, where Re_c = 3470−1370 n (Li et al., 2010).

$$Re = \frac{\rho_f (2r_{tu,i})^n v_f^{2-n}}{\frac{K}{8}\left(\frac{6n+2}{n}\right)^n} \tag{20}$$

The friction coefficient of CO_2 foam fracturing fluid containing proppant is calculated by the sum of fluid friction coefficient and proppant friction coefficient.

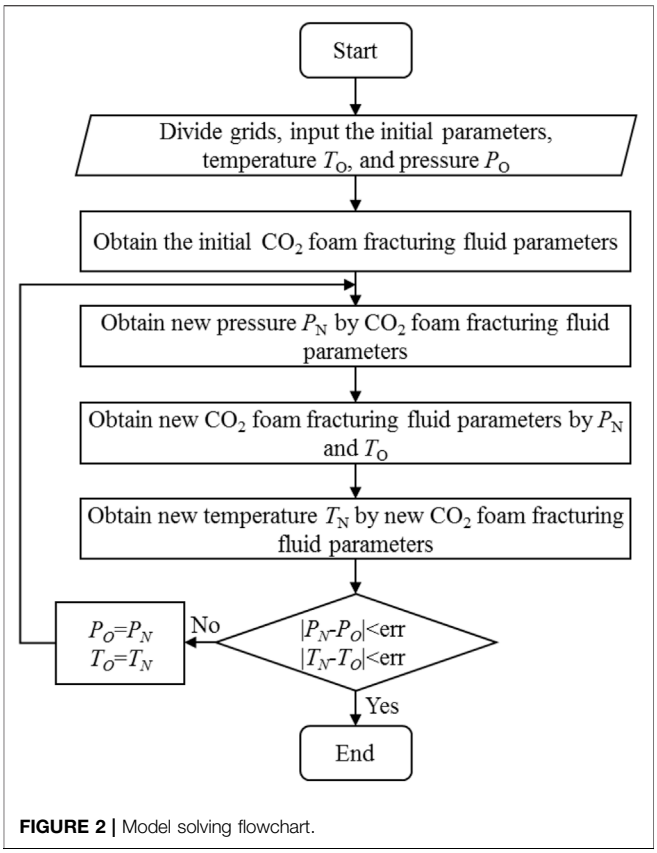

FIGURE 2 | Model solving flowchart.

$$\begin{cases} f_l = \dfrac{16}{Re}, & Re \le Re_c \\ \sqrt{\dfrac{1}{f_l}} = \dfrac{4}{n^{0.75}} \log\left[Re \cdot f_l^{(1-n/2)}\right] - \dfrac{0.4}{n^{1.2}}, & Re > Re_c \end{cases} \tag{21}$$

The calculation of the proppant friction coefficient is given by:

$$f_s = \frac{39.36}{Re^{0.9907}} \left(\frac{v_f^2}{g d_s}\right)^{0.02968} \left(\frac{\rho_s}{\rho_f}\right)^{0.1403} C_{sf}^{0.03844} \tag{22}$$

Then, the friction coefficient of CO_2 foam fracturing fluid containing proppant is $f_f = f_l + f_s$.

The friction of CO_2 foam fracturing fluid flowing in the wellbore is given by:

$$F_f = \frac{2 l \rho_f f_f v_f^2}{2r} \tag{23}$$

where F represents the friction, Pa; l represents the casing length, m.

Boundary Conditions

Boundary conditions of the model:

$$\begin{cases} Q_g = A \\ Q_l = B \\ C_{sf} = C \end{cases} \tag{24}$$

where A, B, and C are the initial values, respectively.

TABLE1 | The calculation parameters.

Parameters	Values	Parameters	Values
Well depth(H)/m	4000	Geothermal gradient (t_g)/°C m^{-1}	0.03
Tubing ID ($r_{tu,i}$)/m	0.1005	Tubing OD ($r_{tu,o}$)/m	0.1143
Production casing ID ($r_{ca1,i}$)/m	0.1594	Production casing OD ($r_{ca1,o}$)/m	0.1778
Technical casing ID ($r_{ca2,i}$)/m	0.2266	Technical casing OD ($r_{ca2,o}$)/m	0.2445
Surface casing ID ($r_{ca3,i}$)/m	0.3204	Surface casing OD ($r_{ca3,o}$)/m	0.3397
Wellbore diameter(D)/m	0.5080	Casing/tubing thermal conductivity (λ_{tc})/W m^{-1}°C^{-1}	44.7
Cement thermal conductivity (λ_{ce})/W m^{-1}°C^{-1}	0.52	Formation thermal conductivity (λ_{fo})/W m^{-1}°C^{-1}	2.09

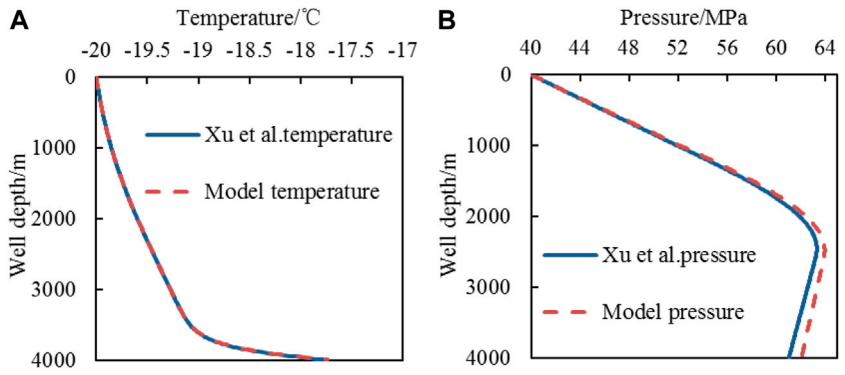

FIGURE 3 | Temperature and pressure distribution of CO_2 proppant gas-solid two phases in the wellbore [**(A)**: temperature profile; **(B)**: pressure profile].

The model solving process is shown in **Figure 2**. The model is divided into several elements, and it is assumed that the properties of the fracturing fluid in each element are constant. The initial fluid parameters such as phase state, density, and viscosity are calculated from the initial values of pressure and temperature. The new pressure distribution is obtained from the initial fluid parameters. New fluid parameters are obtained from the new pressure and initial temperature. The energy conservation equation of the wellbore-formation system is calculated with the new fluid parameters to obtain a new temperature. Finally, the new temperature and pressure distribution are compared with the old temperature and pressure distribution to verify the convergence.

MODEL VERIFICATION

In this paper, the two-phase fluid temperature and pressure calculation data of CO_2 proppant and CO_2 foam are used because of the lack of gas, liquid, and solid phase field measured data (Xu et al., 2019). The calculated data is compared with the calculated results of the model to verify the model's accuracy. The calculation parameters are shown in **Table 1**.

The model is validated with the CO_2 proppant two-phase model of Xu. The injection mass flow rate Q_w is 80 kg/s; the injection temperature t_i, proppant volumetric concentration C_{sf}, and injection pressure P_i are −20°C, 0.2, and 40 MPa, respectively. The comparison between the model calculation results of Xu et al. and the simulation results in this paper is shown in **Figure 3**.

The bottom hole temperature calculated result by the model of Xu and in this paper are −17.77°C and −17.74°C respectively, the temperature difference is 0.03°C, the error is 0.18%, and the average error of the whole well is 0.01%. The bottom hole pressure calculated result by the model of Xu and in this paper are 61.03 and 62.06 MPa, respectively, the pressure difference is 1.03 MPa, the error is 1.03%, and the average error of the whole well is 0.86%.

The model is validated with the CO_2 foam two-phase model of Xu. The injection mass flow rate Q_w is 60 kg/s; the injection temperature t_i, foam quality Γ, and injection pressure P_i are 5°C, 0.75, and 40 MPa, respectively.

As shown in **Figure 4**, the bottom hole temperature calculated result by the model of Xu et al. and in this paper are 11.26°C and 12.62°C respectively, the temperature difference is 1.36°C, the error is 12.03%, and the average error of the whole well is 1.47%. The bottom hole pressure calculated result by the model of Xu and in this paper are 36.79 and 37 MPa, respectively, the pressure difference is 0.21 MPa, the error is 0.58%, and the average error of the whole well is 0.49%.

The comparison of the calculation results proves that the model in this paper has good accuracy, indicating that the model is suitable for CO_2 foam fluid in the wellbore calculation.

COMPARISON OF INJECTION METHODS OF CO_2 FOAM FRACTURING FLUID

This section compares the temperature and pressure distribution in the wellbore of the two injection methods with tubing-carrying

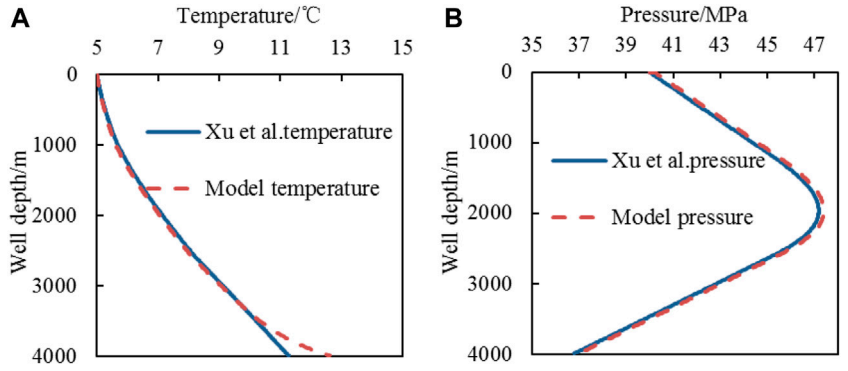

FIGURE 4 | Temperature and pressure distribution of CO_2 foam gas-liquid two phases in the wellbore [**(A)**: temperature profile; **(B)**: pressure profile].

TABLE 2 | The basic parameters of calculation.

Parameters	Values	Parameters	Values
Depth of kick off point(L)/m	1000	Geothermal gradient (t_g)/°C m^{-1}	0.03
Absolute tubing roughness(ε)/m	0.0000254	Formation surface temperature(t)/°C	20
Building radius(R)/m	1000	Well depth(H)/m	4000
Tubing ID ($r_{tu,i}$)/m	0.1005	Tubing OD ($r_{tu,o}$)/m	0.1143
Production casing ID ($r_{ca1,i}$)/m	0.1784	Production casing OD ($r_{ca1,o}$)/m	0.1937
Technical casing ID ($r_{ca2,i}$)/m	0.2502	Technical casing OD ($r_{ca2,o}$)/m	0.2731
Surface casing ID ($r_{ca3,i}$)/m	0.323	Surface casing OD ($r_{ca3,o}$)/m	0.3397
Wellbore diameter(D)/m	0.5080	Casing/tubing thermal conductivity (λ_{tc})/W m^{-1}°C^{-1}	44.7
Cement thermal conductivity (λ_{ce})/W m^{-1}°C^{-1}	0.52	Formation thermal conductivity (λ_{fo})/W m^{-1}°C^{-1}	2.09
Proppant density (ρ_s)/kg m^{-3}	2500	Proppant diameter (d_s)/m	0.0003
Proppant thermal conductivity (λ_s)/W m^{-1}°C^{-1}	10	Proppant specific heat capacity (C_s)/J kg^{-1}°C^{-1}	1000
Annulus fluid specific heat capacity (C_{an})/J kg^{-1}°C^{-1}	4190	Annulus fluid thermal conductivity (λ_{an})/W m^{-1}°C^{-1}	0.58

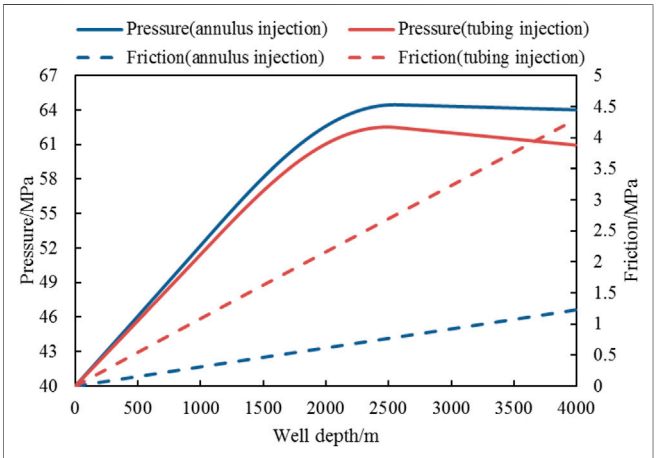

FIGURE 5 | Changes of pressure and friction under different injection methods.

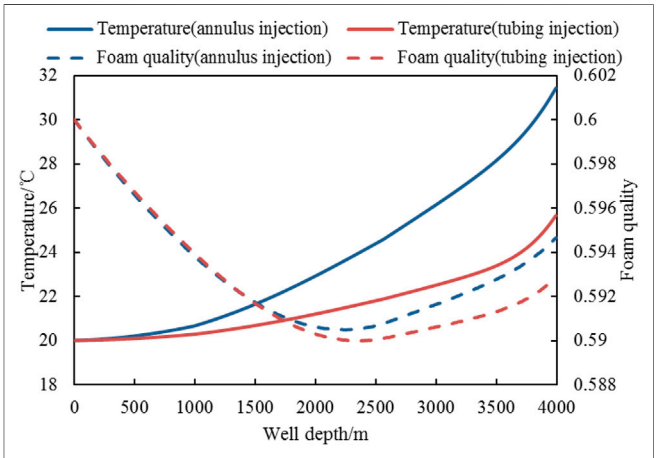

FIGURE 6 | Changes in temperature and foam quality under different injection methods.

proppant, annulus replenishes fracturing fluid, and annulus-carrying proppant, tubing replenishes fracturing fluid, to illustrate the impact of injection methods on wellbore fluid temperature and pressure. The basic parameters of the calculation are shown in **Table 2**.

The injection mass flow rate Q_w is 80 kg/s, the foam quality Γ is 0.6, and the injection temperature t_i, proppant volumetric concentration C_{sf}, and injection pressure P_i are 20°C, 0.2, and 40 MPa, respectively. **Figure 5** shows the pressure and friction changes of CO_2 foam fracturing fluid in the wellbore. **Figure 6**

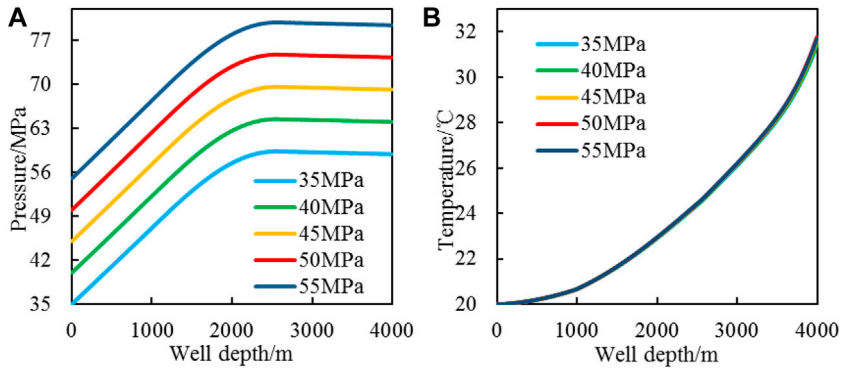

FIGURE 7 | CO_2 foam fracturing fluid pressure and temperature change with injection pressure [**(A)**: pressure profile; **(B)**: temperature profile].

shows the changes in the temperature and foam quality in the wellbore.

Figure 5 shows that the bottom hole pressure of annulus injections and tubing injection are 64.02 and 60.95 MPa, respectively. The bottom hole pressure of annulus injection is 3.07 MPa higher than that of tubing injection. The temperature curve of **Figure 6** shows that the bottom hole temperature is 31.43°C and 25.66°C, respectively. The bottom hole temperature of the annulus injection method is 5.77°C higher than that of the tubing injection. The annulus cross-section is larger than that of the tubing, so during the injection process, the friction of the annulus injection is smaller than that of the tubing injection. Therefore, under the same injection pressure, the annulus injection has a higher bottom hole pressure. Xu's study showed that the temperature increased with the increase of foam quality. The foam quality curve of **Figure 6** shows that the foam quality of the annulus injection is greater than that of the tubing injection after the wellbore reaches 2,000 m, so the temperature in the annulus injection wellbore is higher than that of the tubing injection. The above results show that the use of annulus injection can achieve higher pressure, temperature, and lower frictional pressure loss.

ANALYSIS OF THE FACTORS AFFECTING THE TEMPERATURE AND PRESSURE OF THE FLUID IN THE WELLBORE THROUGH ANNULUS INJECTION

The Influence of Injection Pressure

The injection mass flow rate Q_w is 70 kg/s, the foam quality Γ is 0.6, and the injection temperature t_i and proppant volumetric concentration C_{sf} are 20°C and 0.2, respectively. Change the injection pressure P_i increases from 35 to 55 MPa with an interval of 5 MPa, and analyze the influence of injection pressure on temperature and pressure. **Figure 7** shows the temperature and pressure changes of CO_2 foam fracturing fluid in the wellbore.

The pressure calculation results in **Figure 7** show that the wellbore pressure increases with the increase of well depth and stabilizes when CO_2 foam fracturing fluid reaches the horizontal section. Every 5 MPa increase in injection pressure, the pressure in the wellbore will increase by 5 MPa uniformly. The pressure change is mainly caused by the increase in injection pressure. As the well depth increases, the pressure of the CO_2 foam fracturing fluid in the wellbore also gradually increases. It can be seen from the temperature profile that the injection pressure increases by 20 MPa and the bottom hole temperature increase does not exceed 0.2°C, indicating that the temperature in the wellbore does not change with the pressure change.

The Influence of Foam Quality

The injection mass flow rate Q_w, injection temperature t_i, proppant volumetric concentration C_{sf}, and injection pressure P_i are 70 kg/s, 20°C, 0.2, and 40 MPa, respectively. Change the foam quality Γ to increase from 0.5 to 0.9 with an interval of 0.1.

The results in **Figure 8** show that changing the foam quality mainly has a greater impact on the temperature in the wellbore. The foam quality increases by 0.4, and the wellbore temperature increases by 3.8°C, a growth of 12.3%. Analysis of the reasons shows that the specific heat capacity of the gas phase is smaller than that of the liquid phase. As the foam quality increases, the specific heat capacity of CO_2 foam fracturing fluid decreases, and the heat required to increase the same temperature is reduced, increasing the temperature of CO_2 foam fracturing fluid in the wellbore. The increase in foam quality has little effect on pressure changes.

The Influence of Mass Flow Rate

The injection temperature t_i, proppant volumetric concentration C_{sf}, foam quality Γ, and injection pressure P_i are 20°C, 0.2, 0.6, and 40 MPa, respectively. Change the injection mass flow rate Q_w to increase from 70 to 230 kg/s with an interval of 40 kg/s. **Figure 9** shows the temperature and pressure changes of the CO_2 foam fracturing fluid in the wellbore.

It can be seen from **Figure 9** that the injection flow rate increases by 190 kg/s, the bottom hole pressure reduces 12.35 MPa, a decrease of 19.29%, and the bottom hole temperature reduces 7.42°C, a decrease of 23.61%. With the increase of the injection flow rate, the temperature and pressure decrease drastically, the pressure decrease rate increases with the increase of the injection flow rate, and the temperature decrease rate decreases with the increase of the injection flow rate. Analysis of the reasons shows that the increase of injection flow rate will lead to insufficient heat transfer and temperature drop because the

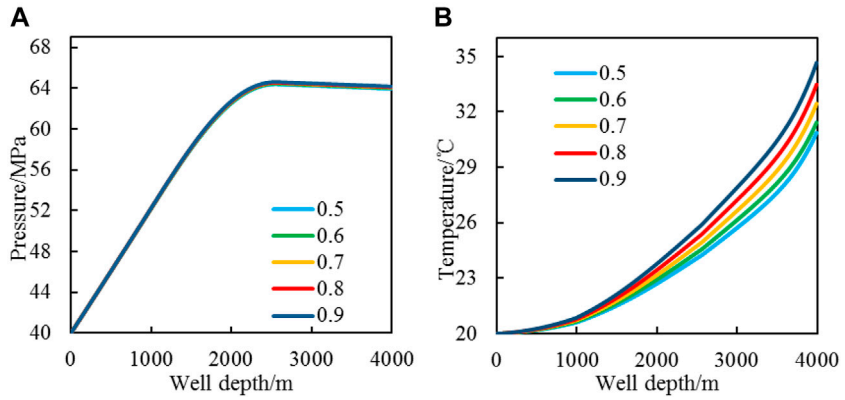

FIGURE 8 | CO_2 foam fracturing fluid pressure and temperature change with foam quality [**(A)**: pressure profile; **(B)**: temperature profile].

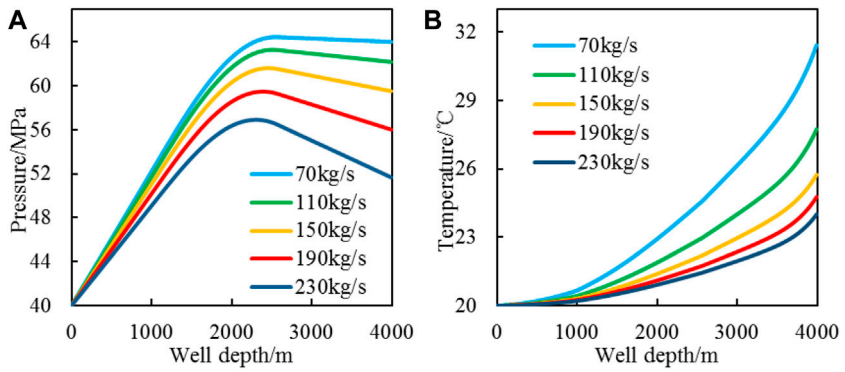

FIGURE 9 | CO_2 foam fracturing fluid pressure and temperature change with mass flow rate [**(A)**: pressure profile; **(B)**: temperature profile].

contact time between fracturing fluid and wellbore is reduced. The increase of injection flow rate will also lead to frictional pressure loss increase between fracturing fluid and wellbore, making the pressure drop.

The Influence of Proppant Volumetric Concentration

The injection mass flow rate Q_w, injection temperature t_i, foam quality Γ, and injection pressure P_i are 70 kg/s, 20°C, 0.6, and 40 MPa, respectively. Change the proppant volumetric concentration C_{sf} to increase from 0.1 to 0.3 with an interval of 0.05. The temperature and pressure changes of the CO_2 foam fracturing fluid in the wellbore after changing the proppant volumetric concentration are shown in **Figure 10**.

Figure 10 pressure profile shows that the increase of the proppant volumetric concentration causes the CO_2 foam fracturing fluid pressure to increase because the hydrostatic pressure and density of the fracturing fluid increase with the proppant volumetric concentration increase. The temperature calculation results show that the bottom hole temperature only increases 3.13°C as the proppant volumetric concentration increases 0.2 because the specific heat capacity of the proppant is lower than that of the CO_2 foam. As the proppant volumetric concentration increases, the CO_2 foam fracturing fluid absorbs the same heat from the environment to obtain a higher temperature, but the influence of proppant volumetric concentration on bottom hole temperature is small.

The Influence of Injection Temperature

The injection mass flow rate Q_w, proppant volumetric concentration C_{sf}, foam quality Γ, and injection pressure P_i are 70 kg/s, 0.2, 0.6, and 40 MPa, respectively. The injection temperature t_i is 24, 25, 26, 27, and 28°C. The influence of different injection temperatures on the temperature and pressure of the CO_2 foam fracturing fluid in the wellbore is shown in **Figure 11**.

Figure 11 shows that the higher the injection temperature, the higher the temperature in the wellbore. For every 1°C increase in the injection temperature, the bottom hole temperature increases by 0.8°C. Comparing the influence of injection temperature on the temperature distribution of CO_2 foam fracturing fluid in the wellbore, the pressure change of the CO_2 foam fracturing fluid in the wellbore is small.

The Influence of Geothermal Gradient

The injection mass flow rate Q_w, proppant volumetric concentration C_{sf}, injection temperature t_i, foam quality Γ, and injection pressure P_i are 70 kg/s, 0.2, 20°C, 0.6, and 40 MPa, respectively. Change the

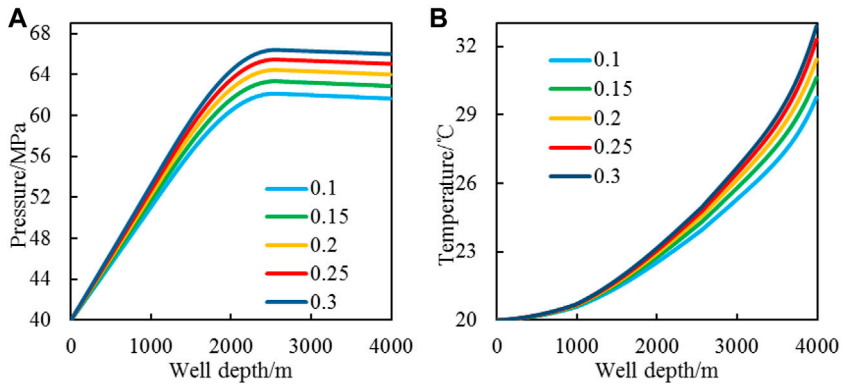

FIGURE 10 | CO_2 foam fracturing fluid pressure and temperature change with proppant volumetric concentration [**(A)**: pressure profile; **(B)**: temperature profile].

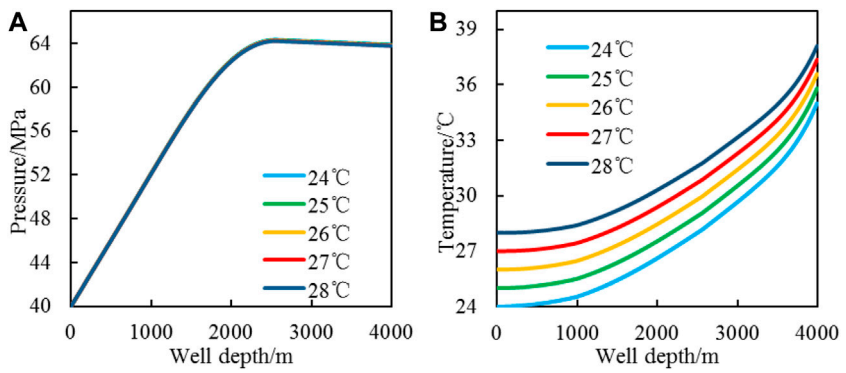

FIGURE 11 | CO_2 foam fracturing fluid pressure and temperature change with injection temperature [**(A)**: pressure profile; **(B)**: temperature profile].

geothermal gradient to increase from 0.03°C/m to 0.05°C/m with an interval of 0.005. **Figure 12** shows the temperature and pressure changes of CO_2 foam fracturing fluid in the wellbore.

The increase of the geothermal gradient will cause the formation temperature to rise. The temperature difference between formation and wellbore CO_2 foam fracturing fluid increases and heat transfer increases. From the temperature calculation results in **Figure 12**, the temperature in the wellbore gradually increases with the geothermal gradient increase and the bottom hole temperature increases by 1.4°C for every increase of the geothermal gradient by 0.005°C/m. The geothermal gradient has a small influence on the pressure distribution in the wellbore.

Study on the Phase State of CO_2 Foam Fracturing Fluid in the Wellbore

According to the previous study, the pressure and temperature of CO_2 foam fracturing fluid increase with the increase of well depth. When the pressure and temperature reach 7.38 MPa and 31.1°C, the CO_2 phase will change to a supercritical state (Zhang et al., 2017). Supercritical CO_2 is a dense, low-viscosity fluid with excellent hole cleaning capabilities. Kolle (2000) by studying the phase change of CO_2, the well depth when CO_2 changes into a supercritical state can be obtained, which provides a basis for the design of fracturing parameters in the field. In this paper, the injection pressure has exceeded 7.38 MPa. If the temperature exceeds 31.1°C, it can indicate that the CO_2 has reached the supercritical state. Through the random combination of the above six factors, the well depth when the CO_2 foam fracturing fluid reaches the critical temperature under different factors is obtained.

Through analysis of the influence of six factors on supercritical state, the main factors are proppant volumetric concentration C_{sf}, foam quality Γ, mass flow rate Q_w, injection temperature t_i and geothermal gradient t_g. These five factors are randomly combined to obtain the well depth data when the CO_2 foam fracturing fluid reaches the critical temperature, as shown in **Table 3**, where W is the well depth when the CO_2 foam fracturing fluid reaches the critical temperature, m.

After normalizing the above data, **Eq. 25** is obtained by fitting, where $R^2 = 0.997$.

$$W_n = -0.77t_{i,n} - 0.245\Gamma_n - 0.247t_{g,n} - 0.184C_{sf,n} + 0.11Q_{w,n} + 1.137 \quad (25)$$

It can be seen from **Eq. 25** that the well depth when reaching the critical temperature decreases with the increase of proppant

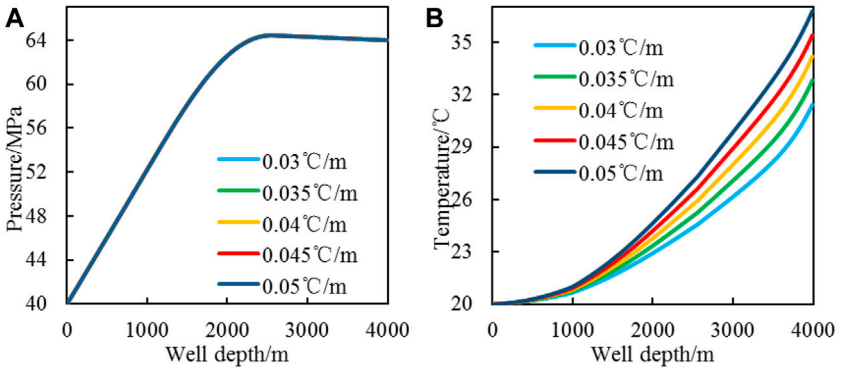

FIGURE 12 | CO_2 foam fracturing fluid pressure and temperature change with geothermal gradient [**(A)**: pressure profile; **(B)**: temperature profile].

TABLE 3 | Well depth at supercritical.

t_i/°C	t_g/°C/m	C_{sf}	Γ	Q_w/kg/s	W/m
22.69	0.038	0.16	0.85	71	3010
21.55	0.045	0.38	0.74	90	3160
24.06	0.032	0.34	0.94	72	2690
21	0.038	0.4	0.91	71	2880
23.79	0.036	0.32	0.68	77	3010
28.23	0.041	0.39	0.79	76	1730
24.76	0.047	0.19	0.98	83	2340
25.64	0.036	0.27	0.65	76	2910
21.22	0.036	0.21	0.65	73	3660
20.47	0.035	0.16	0.79	79	3920
25.22	0.049	0.35	0.59	86	2520
23.96	0.044	0.38	0.51	85	2960
25.2	0.042	0.36	0.72	77	2450
28.42	0.049	0.22	0.6	79	1760
28.29	0.032	0.11	0.52	85	2580
20.19	0.032	0.48	0.89	84	3480
26.66	0.041	0.24	0.51	81	2520
25.2	0.039	0.32	0.6	78	2720
23.12	0.045	0.22	0.6	73	2930
28.64	0.046	0.26	0.85	87	1640

volumetric concentration, injection temperature, foam quality, geothermal gradient, and injection temperature, and increases with the increase of injection mass flow rate. In the design of fracturing parameters, reducing the injection mass flow rate, increasing the injection temperature, proppant volumetric concentration, and foam quality, CO_2 can be transformed into a supercritical state in a shallow well depth to improve the fracturing effect.

CONCLUSION

Under the same conditions, compared with tubing injection, the annulus injection of CO_2 foam fracturing can effectively increase the pressure and temperature in the wellbore and reduce the frictional pressure loss during the flow of CO_2 foam fracturing fluid.

The pressure and temperature in the wellbore of the annulus injected CO_2 foam fracturing fluid decrease with the increase of the mass flow rate. The mass flow rate increased by 190 kg/s, and the bottom hole pressure and temperature decreased by 12.35 MPa and 7.42°C, respectively. The increase of mass flow rate is not conducive to the transformation of CO_2 into a supercritical state.

The proppant volumetric concentration, foam quality, injection temperature, and geothermal gradient are positively correlated with the temperature, while the injection flow rate is negatively correlated with the temperature. Under the permitting construction conditions, increasing the injection temperature, proppant volumetric concentration, and foam quality is conducive to the transition of CO_2 to a supercritical state.

DATA AVAILABILITY STATEMENT

The original contributions presented in the study are included in the article/Supplementary Material. Further inquiries can be directed to the corresponding author.

AUTHOR CONTRIBUTIONS

HL and GP contributed to conception and design of the study. GP conducts numerical model establishment, verification, and influencing factor analysis. HL wrote the manuscript. All authors contributed to manuscript revision and read and approved the submitted version.

FUNDING

This research was supported by the National Natural Science Foundation of China (No. 51874098).

REFERENCES

Ahmed, S., Elraies, K. A., Forooozesh, J., Bt Mohd Shafian, S. R., Hashmet, M. R., Hsia, I. C. C., et al. (2017). Experimental Investigation of Immiscible Supercritical Carbon Dioxide Foam Rheology for Improved Oil Recovery. *J. Earth Sci.* 28 (5), 835–841. doi:10.1007/s12583-017-0803-z

An, Z., Li, Z., Huang, S., Lv, Q., Jia, Z., et al. (2014). Flow Pattern of Nitrogen Foam Fracturing Fluid in Horizontal Pipe. *Sci. Technol. Eng.* 14 (35), 220–224. doi:10.7623/syxb202110011

Carter, R. H., Holditch, S. A., and Wolhart, S. L. (1996). "Results of a 1995 Hydraulic Fracturing Survey and a Comparison of 1995 and 1990 Industry Practices," in SPE Annual Technical Conference and Exhibition (Denver, Colorado: OnePetro).

Cheng, Y., Li, G., Wang, H., Shen, Z., and Fan, A. (2013). Feasibility Analysis on Coiled-Tubing Jet Fracturing with Supercritical CO2. *Oil Drilling Prod. Technol.* 35 (06), 73–77. doi:10.13639/j.odpt.2013.06.004

Cong, Z., Li, Y., Pan, Y., Liu, B., Shi, Y., Wei, J., et al. (2022). Study on CO2 Foam Fracturing Model and Fracture Propagation Simulation. *Energy* 238, 121778. doi:10.1016/j.energy.2021.121778

Faroughi, S. A., Pruvot, A. J.-C. J., and McAndrew, J. (2018). The Rheological Behavior of Energized Fluids and Foams with Application to Hydraulic Fracturing: Review. *J. Pet. Sci. Eng.* 163, 243–263. doi:10.1016/j.petrol.2017.12.051

Friehauf, K. E., and Sharma, M. M. (2009a). A New Compositional Model for Hydraulic Fracturing with Energized Fluids. *SPE Prod. Operations* 24 (04), 562–572. doi:10.2118/115750-pa

Friehauf, K. E., and Sharma, M. M. (2009b). "Fluid Selection for Energized Hydraulic Fractures," in SPE Annual Technical Conference and Exhibition (Calgary, Alberta: Society of Petroleum Engineers). doi:10.2118/124361-ms

Gu, M., and Mohanty, K. K. (2014). Effect of Foam Quality on Effectiveness of Hydraulic Fracturing in Shales. *Int. J. Rock Mech. Mining Sci.* 70, 273–285. doi:10.1016/j.ijrmms.2014.05.013

Guo, J., and Zeng, J. (2015). A Coupling Model for Wellbore Transient Temperature and Pressure of Fracturing with Supercritical Carbon Dioxide [J]. *Acta Petrolei Sinica* 36 (02), 203–209.

Guo, J., Zeng, J., Zhang, R., and Zhou, C. (2015). A Dual Transient Coupling Model for Wellbore of Carbon Dioxide Injection Well. *Acta Petrol. Sinica* 36 (08), 976–982. doi:10.7623/syxb201508008

Gupta, A. P., Gupta, A., and Langlinais, J. (2005). "Feasibility of Supercritical Carbon Dioxide as a Drilling Fluid for Deep Underbalanced Drilling Operation," in SPE Annual Technical Conference and Exhibition (Calgary, Alberta: Society of Petroleum Engineers). doi:10.2118/96992-ms

He, J., Afolagboye, L., Lin, C., and Wan, X. (2018). An Experimental Investigation of Hydraulic Fracturing in Shale Considering Anisotropy and Using Freshwater and Supercritical CO2. *Energies* 11 (3), 557. doi:10.3390/en11030557

He, Z., Li, G., Tian, S., Wang, H., Shen, Z., and Li, J. (2016). SEM Analysis on Rock Failure Mechanism by Supercritical CO 2 Jet Impingement. *J. Pet. Sci. Eng.* 146, 111–120. doi:10.1016/j.petrol.2016.04.023

Kolle, J. J. (2000). "Coiled-tubing Drilling with Supercritical Carbon Dioxide," in SPE/CIM international conference on horizontal well technology (Calgary, Alberta: Society of Petroleum Engineers). doi:10.2118/65534-ms

Li, C., Huang, Y., Sun, X., Gao, R., Zeng, F., Tontiwachwuthikul, P., et al. (2017). Rheological Properties Study of Foam Fracturing Fluid Using CO 2 and Surfactant. *Chem. Eng. Sci.* 170, 720–730. doi:10.1016/j.ces.2017.03.022

Li, S., Li, Z., Lin, R., and Li, B. (2010). Modeling of Sand Cleanout with Foam Fluid for Vertical Well. *SPE J.* 15 (03), 805–811. doi:10.2118/120449-pa

Li, Y., Jia, D., Rui, Z., Peng, J., Fu, C., and Zhang, J. (2017). Evaluation Method of Rock Brittleness Based on Statistical Constitutive Relations for Rock Damage. *J. Pet. Sci. Eng.* 153, 123–132. doi:10.1016/j.petrol.2017.03.041

Li, Z., Wang, D., and Huang, S. (2008). The Coupling Mathematical Model for Foam Fluid Flowing in Wellbore. *J. Southwest Pet. University(Science Technol. Edition)* 30 (06), 1–201. doi:10.3863/j.issn.1000-2634.2008.06.001

Luo, X., Wang, S., Wang, Z., Jing, Z., and Lv, M. (2014). Experimental Research on Rheological Properties and Proppant Transport Performance of GRF-CO2 Fracturing Fluid. *J. Pet. Sci. Eng.* 120, 154–162. doi:10.1016/j.petrol.2014.06.009

McAndrew, J., Cisternas, P., Pruvot, A., Kong, X., and Tong, S. (2017). "Water Consumption and Proppant Transport Aspects of Foam Fracturing Fluids," in Unconventional Resources Technology Conference, 24-26 July 2017 (Austin, Texas: Society of Exploration Geophysicists, American Association of Petroleum Geologists, Society of Petroleum Engineers), 1027–1034.

Moridis, G. (2018). *Literature Review and Analysis of Waterless Fracturing Methods*. Berkeley, CA (United States): Lawrence Berkeley National Lab. (LBNL).

Shao, Y., Liu, J., Xi, B., Sun, J., Qu, C., Song, H., et al. (2019). Drilling Fluid Invasion Law for Reservoir with Medium-Low Porosity and Permeability. *Well Logging Technol.* 43 (1), 70–74. doi:10.16489/j.issn.1004-1338.2019.01.013

Shen, Z., Wang, H., and Li, G. (2010). Feasibility Analysis of Coiled Tubing Drilling with Supercritical Carbon Dioxide. *Pet. Exploration Develop.* 37 (06), 743–747. doi:10.1016/s1876-3804(11)60008-6

Sherif, T., Ahmed, R., Shah, S., and Amani, M. (2016). Rheological Correlations for Oil-Based Drilling Foams. *J. Nat. Gas Sci. Eng.* 35, 1249–1260. doi:10.1016/j.jngse.2016.09.064

Song, W., Ni, H., Wang, R., Sun, B., and Shen, Z. (2017a). Pressure Transmission in the Tubing of Supercritical Carbon Dioxide Fracturing. *J. CO2 Utilization* 21, 467–472. doi:10.1016/j.jcou.2017.08.012

Song, W., Ni, H., Wang, R., and Zhao, M. (2017b). Wellbore Flow Field of Coiled Tubing Drilling with Supercritical Carbon Dioxide. *Greenhouse Gas Sci. Technol.* 7 (4), 745–755. doi:10.1002/ghg.1685

Song, Y., Li, Z., Jiang, Z., and Luo, Q. (2017). Progress and Development Trend of Unconventional Oil and Gas Geological Research. *Pet. Exploration Develop.* 44 (4), 638–648. doi:10.1016/s1876-3804(17)30077-0

Span, R., and Wagner, W. (1996). A New Equation of State for Carbon Dioxide Covering the Fluid Region from the Triple-Point Temperature to 1100 K at Pressures up to 800 MPa. *J. Phys. Chem. reference Data* 25 (6), 1509–1596. doi:10.1063/1.555991

Sun, F., Yao, Y., Chen, M., Li, X., Zhao, L., Meng, Y., et al. (2017). Performance Analysis of Superheated Steam Injection for Heavy Oil Recovery and Modeling of Wellbore Heat Efficiency. *Energy* 125, 795–804. doi:10.1016/j.energy.2017.02.114

Sun, F., Yao, Y., and Li, X. (2018). The Heat and Mass Transfer Characteristics of Superheated Steam Coupled with Non-condensing Gases in Horizontal wells with Multi-point Injection Technique. *Energy* 143, 995–1005. doi:10.1016/j.energy.2017.11.028

Sun, X., Du, M., Han, B., Sun, Y., Zhao, M., Guan, B., et al. (2017). Review on Carbon Dioxide Fracturing Technology. *Oilfield Chem.* 34 (02), 374–380. doi:10.19346/j.cnki.1000-4092.2017.02.035

Tan, K., and Qiao, J. (2020). Development History and prospect of Remote Sensing Technology in Coal Geology of China. *Int. J. Coal Sci. Technol.* 7 (2), 311–319. doi:10.1007/s40789-020-00323-2

Tang, J., Fan, B., Xiao, L., Tian, S., Zhang, F., Zhang, L., et al. (2021). A New Ensemble Machine-Learning Framework for Searching Sweet Spots in Shale Reservoirs. *SPE J.* 26 (01), 482–497. doi:10.2118/204224-pa

Tang, J., Wu, K., Zuo, L., Xiao, L., Sun, S., and Ehlig–Economides, C. (2019). Investigation of Rupture and Slip Mechanisms of Hydraulic Fractures in Multiple-Layered Formations. *SPE J.* 24 (05), 2292–2307. doi:10.2118/197054-pa

Tang, Y., Li, R., and Wang, S. (2020). Research Progress and Prospects of Coal Petrology and Coal Quality in China. *Int. J. Coal Sci. Technol.* 7 (2), 273–287. doi:10.1007/s40789-020-00322-3

Tong, S., Gu, M., Singh, R., and Mohanty, K. K. (2019). Proppant Transport in Foam Fracturing Fluid during Hydraulic Fracturing. *J. Pet. Sci. Eng.* 182, 106279. doi:10.1016/j.petrol.2019.106279

Tong, S., Singh, R., and Mohanty, K. K. (2017). "Proppant Transport in Fractures with Foam-Based Fracturing Fluids," in SPE Annual Technical Conference and Exhibition (Calgary, Alberta: Society of Petroleum Engineers).

Wang, H., Shen, Z., and Li, G. (2012). A Wellbore Flow Model of Coiled Tubing Drilling with Supercritical Carbon Dioxide. *Energy Sourc. A: Recovery, Utilization, Environ. Effects* 34 (14), 1347–1362. doi:10.1080/15567036.2010.520065

Wang, H., Shen, Z., and Li, G. (2011). Wellbore Temperature and Pressure Coupling Calculation of Drilling with Supercritical Carbon Dioxide. *Pet. Exploration Develop.* 38 (1), 97–102.

Wang, S., Sun, D., Du, W., Geng, D., Bai, R., and Wang, Y. (2020). Evaluation Method of Shale Brittleness index. *Well Logging Technol.* 44 (3), 294–299. doi:10.16489/j.issn.1004-1338.2020.03.015

Wang, T., Xu, Y., Jiang, J., et al. (2010). The Technology of Annulus Hydraulic-Jet Fracturing with Coiled Tubing. *Nat. Gas Industry* 30 (01), 65–143. doi:10.3787/j.issn.1000-0976.2010.01.018

Wanniarachchi, W. A. M., Ranjith, P. G., Perera, M. S. A., Rathnaweera, T. D., Zhang, D. C., and Zhang, C. (2018). Investigation of Effects of Fracturing Fluid on Hydraulic Fracturing and Fracture Permeability of Reservoir Rocks: An Experimental Study Using Water and Foam Fracturing. *Eng. Fracture Mech.* 194, 117–135. doi:10.1016/j.engfracmech.2018.03.009

Xie, J., Tang, J., Yong, R., Fan, Y., Zuo, L., Chen, X., et al. (2020). A 3-D Hydraulic Fracture Propagation Model Applied for Shale Gas Reservoirs with Multiple Bedding Planes. *Eng. Fracture Mech.* 228, 106872. doi:10.1016/j.engfracmech.2020.106872

Xu, Z., Song, X., Li, G., Wu, K., Pang, Z., and Zhu, Z. (2018). Development of a Transient Non-isothermal Two-phase Flow Model for Gas Kick Simulation in HTHP Deep Well Drilling. *Appl. Therm. Eng.* 141, 1055–1069. doi:10.1016/j.applthermaleng.2018.06.058

Xu, Z., Wu, K., Song, X., Li, G., Zhu, Z., and Sun, B. (2019). A Unified Model to Predict Flowing Pressure and Temperature Distributions in Horizontal Wellbores for Different Energized Fracturing Fluids. *SPE J.* 24 (02), 834–856. doi:10.2118/194195-pa

Yekeen, N., Padmanabhan, E., and Idris, A. K. (2018). A Review of Recent Advances in Foam-Based Fracturing Fluid Application in Unconventional Reservoirs. *J. Ind. Eng. Chem.* 66, 45–71. doi:10.1016/j.jiec.2018.05.039

Yi, L.-P., Li, X.-G., Yang, Z.-Z., and Li, Y. (2019). Wellbore Temperature and Pressure Calculation Model for Coiled Tubing Drilling with Supercritical Carbon Dioxide. *Energ. Sourc. Part A: Recovery, Utilization, Environ. Effects* 41 (8), 959–974. doi:10.1080/15567036.2018.1522394

Yu, D., Hu, Q., and Tan, D. (2013). Current Situation of Coiled Tubing Sandblast Perforation Sandpack Annular Fracture Technology. *China Pet. Machinery* 41 (12), 112–117. doi:10.3969/j.issn.1001-4578.2013.12.026

Zhang, J., Li, Y., Pan, Y., Wang, X., Yan, M., Shi, X., et al. (2021). Experiments and Analysis on the Influence of Multiple Closed Cemented Natural Fractures on Hydraulic Fracture Propagation in a Tight sandstone Reservoir. *Eng. Geology.* 281, 105981. doi:10.1016/j.enggeo.2020.105981

Zhang, X., Lu, Y., Tang, J., Zhou, Z., and Liao, Y. (2017). Experimental Study on Fracture Initiation and Propagation in Shale Using Supercritical Carbon Dioxide Fracturing. *Fuel* 190, 370–378. doi:10.1016/j.fuel.2016.10.120

Conflict of Interest: The authors declare that the research was conducted in the absence of any commercial or financial relationships that could be construed as a potential conflict of interest.

Publisher's Note: All claims expressed in this article are solely those of the authors and do not necessarily represent those of their affiliated organizations, or those of the publisher, the editors and the reviewers. Any product that may be evaluated in this article, or claim that may be made by its manufacturer, is not guaranteed or endorsed by the publisher.

NOMENCLATURE

A initial values

B initial values

C initial values

C_p specific heat capacity, J/(kg°C)

C_{sf} proppant volumetric concentration

d diameter, m

f friction coefficient

F friction, Pa

g gravity acceleration, m/s^2

h heat transfer coefficient, W/(m^2·°C)

H Well depth, m

ID inner diameter, m

K consistency index of power-law fluids, Pa·s^n

l casing length, m

L Depth of kick off point, m

m Mass, kg

n flow behavior index of power-law fluids

OD outer diameter, m

p fluid pressure, MPa

P_i injection pressure, MPa

q volume flow rate, m^3/s

Q mass flow rate, kg/s

Q_w injection mass flow rate, kg/s

r radius, m

Re Reynolds number

$\mathbf{Re}_c$ critical Reynolds number

t_g Geothermal gradient, °C/m

t_i injection temperature, °C

T temperature, °C

v fluid velocity, m/s

V volume, m^3

W well depth when the CO_2 foam fracturing fluid reaches the critical temperature, m

z one-dimensional coordinate along the wellbore trajectory, m

Subscripts

an annulus fluid

ca1 production casing

ca2 technical casing

ca3 surface casing

ce1 cement layer for production casing

ce2 cement layer for technical casing

ce3 cement layer for surface casing

f CO_2 foam fracturing fluid

fo formation

g internal phase

i inner radius

l external phase

n normalizing data

o outer radius

ref reference condition

s proppant

tu tubing

Greek letters

α volume expansion coefficient, °C^{-1}

β isothermal volume modulus of the external phase, Pa

$\lambda_{\mathbf{tu\text{-}an}}$ thermal conductivity between the tubing and the annulus fluid, W/(m·°C)

$\lambda_{\mathbf{an\text{-}ca1}}$ thermal conductivity between the annulus fluid and the production casing, W/(m·°C)

$\lambda_{\mathbf{ca1\text{-}ce1}}$ thermal conductivity between the production casing and the cement layer, W/(m·°C)

θ inclination angle

ρ density of CO_2 foam fracturing fluid, kg/m^3

Γ foam quality

Φ the Helmholtz energy

$\Phi^{\mathbf{o}}$ the ideal gas part of Helmholtz energy; represents

$\Phi^{\mathbf{r}}$ the residual fluid part of Helmholtz energy

δ the reduced density

τ the inverse reduced temperature

ε Absolute tubing roughness, m

frontiers in Earth Science

ORIGINAL RESEARCH
published: 31 January 2022
doi: 10.3389/feart.2021.784931

The Influence of the Distribution Characteristics of Complex Natural Fracture on the Hydraulic Fracture Propagation Morphology

Huan Zhao[1], Wei Li[1], Lei Wang[2], Jing Fu[3], Yun Long Xue[4], Jian Jun Zhu[2] and Si Qi Li[1]*

[1]College of Petroleum Engineering, Northeast Petroleum University, Daqing, China, [2]Daqing Oilfield Production Technology Institute, Daqing, China, [3]Colorado School of Mines, Golden, CO, United States, [4]Changqing Oilfield Exploration and Development Research Institute, Xian, China

Natural fractures are common in unconventional reservoirs (e.g., tight oil and gas, shale oil and gas), for which hydraulic fracturing is the main exploitation method. Natural fractures influence the propagation and final transformation effect of hydraulic fractures, which is an important factor for fracture optimization design. In this work, the method of globally embedding zero-thickness cohesive zone elements is applied to establish a dynamic propagation model of hydraulic fractures in naturally fractured reservoirs, and the influence of natural fracture development on the fracture propagation patterns is investigated. The results show that the hydraulic fracture propagation paths in fractured reservoirs are highly complex, and steering, branching, and merging of the propagation paths may occur. When the natural fracture development is small, the fracture propagation pattern is mainly influenced by the minimum horizontal principal stress. In contrast, when the natural fracture development is large, the fracture propagation pattern is influenced by the natural fracture distribution. With increasing natural fracture angle, hydraulic fractures can easily pass through natural fractures and form wide fracturs. Higher numbers of natural fracture groups and fractal dimensions increase the number of fracture propagation directions and communicating natural fractures, and the fractures tend to be narrow and complex.

Keywords: complex natural fracture, hydraulic fracture, dynamic propagation, cohesive zone element, fractal dimension

OPEN ACCESS

Edited by:
Jizhou Tang,
Tongji University, China

Reviewed by:
Jiawei Li,
Texas A&M University, United States
Giovanni Toscani,
University of Pavia, Italy

****Correspondence:***
Wei Li
liwei@nepu.edu.cn

Specialty section:
This article was submitted to Economic Geology, a section of the journal Frontiers in Earth Science

Received: *28 September 2021*
Accepted: *29 November 2021*
Published: *31 January 2022*

Citation:
Zhao H, Li W, Wang L, Fu J, Xue YL, Zhu JJ and Li SQ (2022) The Influence of the Distribution Characteristics of Complex Natural Fracture on the Hydraulic Fracture Propagation Morphology. Front. Earth Sci. 9:784931. doi: 10.3389/feart.2021.784931

INTRODUCTION

A large portion of global oil and gas resources occur in naturally fractured formations with low permeability. Hydraulic fracturing technology can improve the reservoir seepage characteristics, connect natural reservoir fractures, and improve the recovery of oil and gas, which are important for achieving economic benefits from fractured reservoirs (Tang et al., 2020; Xia et al., 2020; Jun et al., 2021; Ziyuan et al., 2022). However, the existence of natural fractures poses serious challenges in hydraulic fracturing design. Mayerhofer et al. first introduced the concept of a modified reservoir volume (Rahman and Rahman, 2010), and complex network structures have since become a common assumption in the predictions of the true state of hydraulic fractures in naturally fractured unconventional reservoirs. A quantification of the hydraulic fracture type at the field scale is difficult, but can be achieved by indirect measurements and observations and inter-well interference analysis, which can be used to infer the upper limits of the fracture size (Yuwei et al.,

2017; et al., 2019; Nan et al., 2020). The field conditions of naturally fractured reservoirs typically include extremely high peritectic stresses, which cannot be appropriately replicated in laboratory-scale experiments. Numerical simulations thus provide a useful method to measure the propagation behavior of hydraulic fractures in naturally fractured reservoirs.

Natural fractures place important constraints on mining operations. A comprehensive understanding of the propagation law of hydraulic fractures in the presence of natural fractures is therefore critical and has attracted extensive research attention in recent years. Zhang et al. (Zhang and Jeffrey, 2006; Zhang et al., 2007) established a hydraulic fracture propagation model with fully coupled fluid flow and stresses caused by fracture tension/slip and friction evolution based on the displacement discontinuity method, and numerically simulated the interactions between hydraulic and pre-existing fractures. Dahi-Taleghani et al. (Dahi-Taleghani and Olson, 2011) simulated the propagation process of multiple hydraulic fractures and considered the interaction between hydraulic and natural fractures. Chuprakov et al. (Chuprakov et al., 2011) used the displacement discontinuity method and Mohr–Coulomb criterion to explain natural fractures and the mechanical activation mechanism responsible for the interaction between pressurized hydraulic fractures. Kresse et al. (Kresse et al., 2013) developed a complex fracture network model based on a two-dimensional boundary element model using an unconventional fracture model, and proposed a method to calculate stress shadows during the propagation of multiple fractures. Hou et al. (Bing et al., 2015) used the displacement discontinuity method to establish a two-dimensional model of multi-fracture propagation in a destination reservoir based on the theory of linear elastic fracture mechanics, and analyzed the complex morphology of hydraulic fracture propagation in a formation considering the interference of randomly distributed natural fractures. Cottrell et al. (Cottrell et al., 2013) established a discrete fracture network numerical model to simulate hydraulic fracture propagation in a natural fracture network and the interaction between hydraulic and natural fractures, and compared the results with those obtained from finite element numerical simulations. Xia et al. (Lei et al., 2016) performed discrete-element numerical simulations to establish a two-dimensional model of single-crack propagation, and analyzed the stress shadow effect on the fracture propagation direction. Fatahi (Fatahi et al., 2017) simulated the interaction between hydraulic and natural fractures based on a discrete-element numerical model, and verified the simulation results with experimental data. Chen (Zhiqiang et al., 2018) developed a hydrodynamic coupled LBM-DEM (Boltzmann method-discrete element method) model to study hydraulic fracture propagation in rocks with natural colluvial fractures. Bruno (Bruno and Einstein, 2014) applied ABAQUS software based on the extended finite element method to numerically simulate the stress field near the fracture tip, and analyzed the variation of the maximum principal stress and maximum shear stress at the hydraulic fracture tip in the presence of natural fractures and their effect on fracture initiation and propagation. Dehghan et al. (Dehghan et al., 2016) established various three-dimensional numerical models based on hydraulic fracture experiments using ABAQUS software, simulated the propagation of hydraulic fractures at the intersection with natural fractures using the extended finite element method, and found that the energy release rate significantly affects the propagation behavior of hydraulic fractures. Liu (Fei et al., 2017) proposed a novel fully coupled hydraulic fracture model using the extended finite element method to reveal the interaction mechanism between hydraulic fractures with orthogonal and nonorthogonal anisotropic angles and natural nonintersecting fractures.

The above models analyzed the behavior of hydraulic fracture propagation in the presence of natural fractures to some extent, but certain limitations remain. In this study, the cohesion model is used, which simulates complex fracture propagation and interaction mechanisms (Haddad et al., 2016). This model was first proposed by Dugdale (Dugdale, 1960) and Barenblatt (Barrenblatt, 1962) and is more capable of representing the discontinuities of brittle materials (e.g., rocks) than traditional finite element models. This method uses cohesive elements to simulate fracture formation, which avoids the problem of fracture tip singularity, and is now extensively used to simulate cracking in brittle materials (e.g., crystals, rocks). Yang et al. (Yang et al., 2009) developed an algorithm to freely embed cohesive elements in solid finite element meshes, which provides a reference and basis for simulating the fracturing of complex structures. Mokryakov (Mokryakov, 2011) established a cohesive force model for hydraulic fracturing that considers a reservoir's plastic zone based on the fracture tip treatment presented in Barenblatt, developed a hydraulic fracture propagation model to improve the fitting accuracy of pressure logging, and applied the model to the problem of the intersection and propagation of hydraulic and natural fractures. Guo (Jianchun et al., 2015) established a coupled stress-percolation-damage model based on the cohesion method without introducing a fracture criterion, simulated the interaction between hydraulic and natural fractures, studied the intersection and propagation of hydraulic and natural fractures, and discussed the effects of stress field and pinch angle on fracture propagation. Wang (Wang, 2015; Wang, 2016) developed a hydraulic fracture model by considering pore elastic and pore plastic formations using the cohesion method, and analyzed the effect of plastic deformation near the fracture tip and inside the reservoir. Gonzalez and Dahi (Gonzalez and Dahi, 2015) investigated the intersecting hydraulic and natural fracture propagation process by modifying the intermediate nodes of the cohesion units embedded at the intersection of hydraulic and natural fractures. Chen (Chen et al., 2017) simulated the interaction between hydraulic and natural fractures using a cohesive finite element model. Dahi (Dahi et al., 2018) extended the cohesion model by introducing a fracture network, but the fracture propagation paths in the region needed to be predefined and the fractures could only propagate along predefined paths and weak planes. Wang (Wang, 2019) used the natural fracture distribution density, length, dip angle, and degree of cementation to develop a hydraulic fracture propagation model in a randomly fractured reservoir, and analyzed the effects of fracture size on proppant distribution and stress shading on fracture propagation.

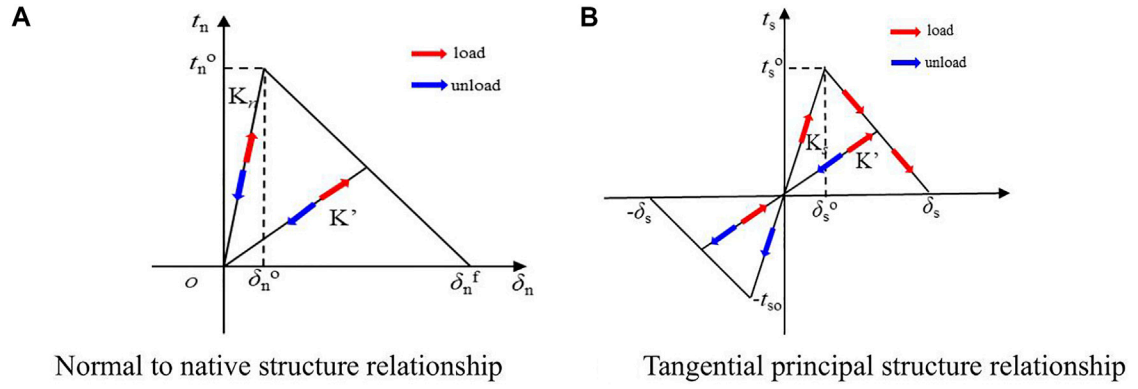

FIGURE 1 | Bilinear constitutive model **(A)** Normal to native structure relationship **(B)** Tangential principal structure relationship.

Nevertheless, only a limited number of studies have addressed the behavior of hydraulic fractures in reservoirs containing fracture networks. Furthermore, most previous studies included pre-existing fracture propagation paths, which make it difficult to portray a fracture system with a large amount of fracture sets differently oriented in a reservoir. To address these issues, this study 1) combines the natural fracture network and global embedded cohesive element methods to establish a dynamic model of hydraulic fracture propagation in a fractured reservoir in accordance with the formation's fractal characteristics; 2) analyzes the influence of different natural fracture system distributions on hydraulic fracture propagation; 3) eliminates the need for pre-existing fracture paths; and 4) more realistically reflects the hydraulic fracture propagation law of fractured formations.

MATHEMATICAL MODELS

Equilibrium Equation for Solid Deformation

To simulate the propagation of hydraulic and natural fractures, the proposed model involves the coupling of several physical processes, including 1) fracture propagation, 2) fluid flow within the fracture, 3) rock deformation near the fracture, and 4) fluid leakage in the porous medium. The theory of seepage is coupled with rock elastic deformation to describe the mechanical response of porous materials using the theory of pore elasticity.

The equilibrium equation of solid deformation can be described as follows (Diguang et al., 2016),

$$\begin{cases} \nabla\boldsymbol{\sigma} + \mathbf{b} = 0 \\ \varepsilon = \dfrac{\left[\nabla\mathbf{u} + (\nabla\mathbf{u})^T\right]}{2} \\ \boldsymbol{\sigma} = \mathbf{D}\boldsymbol{\varepsilon} \end{cases} \tag{1}$$

where **b** is the body force, N/m3. **σ** is the stress tensor, MPa. **ε** is the strain stress, m. **u** is the deformation displacement, m. **D** is Stiffness matrix in constitutive equation.

The basic theory of pore elasticity shows an explicit coupling between the propagation of a matrix skeleton and pressure of the diffusing pore fluid (Jianchun et al., 2015). The total stress (σ_{ij}) can be expressed as:

$$\sigma_{ij} = \sigma'_{ij} + \alpha p \delta_{ij}, \tag{2}$$

where σ'_{ij} is the effective stress, p is the pore pressure, α is the Biot constant, and δ_{ij} is the Kronecker delta.

Rock Damage Criterion

The rock tends to experience brittle damage and a cohesive unit is used to simulate the characteristics of the random fractures of rocky media. In this approach, a bilinear intrinsic model (**Figure 1**) is used to describe the relationship between traction force and displacement (Chen et al., 2009), i.e., linear elastic strengthening before damage and linear softening after damage. The area under the traction-displacement curve equals the critical fracture energy G^c (Wang, 2019).

$$G^c = \frac{K_{IC}^2}{E}\left(1 - \nu^2\right) \tag{3}$$

where K_{IC} is the stress intensity factor, E is the Young's modulus, υ is Poisson's ratio.

The quadratic nominal stress criterion was selected as the initial damage criterion, which states that damage starts when the ratio of the square of the nominal stress in each direction is equal to 1, which can be expressed as:

$$\left\{\frac{\langle t_n \rangle}{t_n^0}\right\}^2 + \left\{\frac{t_s}{t_s^0}\right\}^2 = 1, \tag{4}$$

where t_n^0 and t_s^0 are the peak nominal stresses when the normal and tangential deformations are perpendicular to the interface, respectively, t_n and t_s are the normal and tangential stress components, respectively, and the brackets indicate that damage is not caused by purely compressive deformation or the stress conditions.

In the bilinear constitutive relation, the cohesive unit follows the elastic constitutive relationship (Haddad and Sepehrnoori, 2015):

$$\text{i.e.t} = \begin{Bmatrix} t_n \\ t_s \end{Bmatrix} = \begin{bmatrix} K_{nn} & K_{ns} \\ K_{ns} & K_{ss} \end{bmatrix} = \text{K}\varepsilon,$$

where K denotes the stiffness matrix of the cohesive unit in the elastic phase. During loading, the material stiffness K' is determined by the initial stiffness K and damage variable D. The damage response can be defined as:

$$K' = (1 - D)K, \tag{5}$$

where D is the damage variable scalar, which increases monotonically. When $D = 0$, the material is not damaged; when $D = 1$, the material is completely damaged.

The Law of Liquid Flow

`We assume that the fracturing fluid is an incompressible Newtonian fluid and the fluid flow in the cohesive units is divided into tangential and normal flow. Normal flow indicates the leakage of fracturing fluid into the formation and tangential flow is the driving force for fracture propagation (Guo et al., 2017), as shown in **Figure 2**.

$$\frac{dq_f}{dx} - \frac{dw}{dt} + q_l = 0 \tag{6}$$

where is q_f is the average velocity per unit height, m2/s. w is fracture width, m. q_l is the fluid loss, m/s.

Normal flow in fractures is based on the following principles:

$$\begin{cases} q_t = c_t(p_i - p_t) \\ q_b = c_b(p_i - p_b) \end{cases} \tag{7}$$

where q_t and q_b denote the fluid flow rate into the upper and lower surfaces of a cohesion element, respectively, c_t and c_b indicate the filter loss coefficients of the upper and lower surfaces, respectively, p_i denotes the pressure in a cohesion element by virtual node interpolation, and p_i and p_b indicate the fluid pressure on the upper and lower surfaces of a cohesion element, respectively.

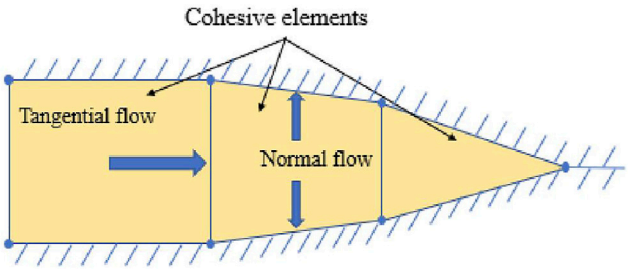

FIGURE 2 | Fracturing fluid flow pattern within the cohesive element. The fluid flow continuity equation in the fracture is (Zhilong et al., 2008).

GLOBAL COHESION MODEL

Global Embedded Cohesive Element Method

The strengths of natural fractures and rock media in a formation can substantially vary. During propagation, hydraulic fractures encounter natural fractures at a variety of interaction types (e.g., intersection, capture, blockage), and fracture propagation in rocks is difficult to predict. It is not possible to predetermine the location of embedded units within the model, and conventional models are required to prefabricate potential propagation paths. To gain insight into the influence of natural fractures on hydraulic fracture propagation and portray the propagation of simulated hydraulic fractures that intersect with natural fractures, the method of globally embedding zero-thickness cohesive units is implemented through secondary development. This approach assigns natural fractures and unit material rock properties, and simulates natural fractures and particle cementation in rocks. The fracture propagation process can thus be based on the judging criterion being free to expand in any unit.

The modeling method of zero-thickness viscous cohesion elements splits the nodes of the initial finite element mesh. **Figure 3** shows a schematic diagram of the finite element mesh before and after embedding the viscous cohesion elements, and the zero-thickness viscous cohesion elements are embedded on the boundary of each solid element.

The fracture direction is determined by the order of the nodes. The connecting units are numbered using the counterclockwise node numbering principle, and the first two node units are along the edges of the cohesive units. To avoid node number duplication, nodes at the same location are split, all units in the study area are traversed once, and the occurrence number of each node in the fractured area is recorded, the latter of which represents the number of times the node must be split. The node number is one number higher than the largest bit of the original maximum node number. The first value indicates the number of splits, followed by the original node number before the split, which forms a new cohesive unit node number. Similarly, the cohesive unit number is formed according to the new node number assignment.

Hydraulic Fracturing Model for Fractured Reservoirs

The natural fractures system in reservoirs are related to tectonic stresses. However, the direction of a natural fracture distribution is not necessarily related to the current stress field because the formation may have undergone multiple tectonic events in the past. The geometric distribution of natural fractures is therefore complex and difficult to describe. Studies performed at different fracture scales have shown that the distribution of multiple fracture properties (e.g., length, number, displacement) follows a power-law function (Bonnet et al., 2001). In many cases, fractal dimensions can be measured on a logarithmic map and used to evaluate the geometric characteristics of a fracture network (Bour and Davy, 1997; Gustafson and Fransson, 2005). The natural fracture system with the fractal geometric characteristics is

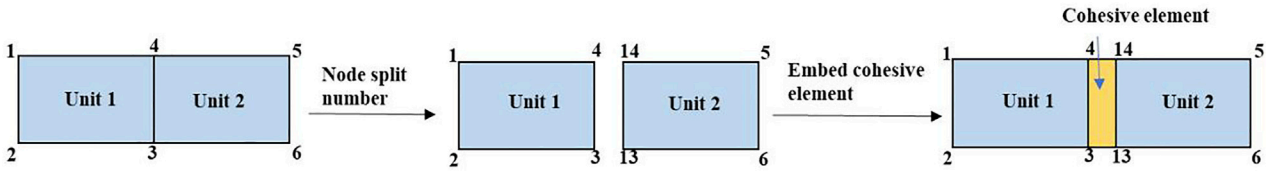

FIGURE 3 | Quadrilateral grid zero-thickness cohesive element embedding.

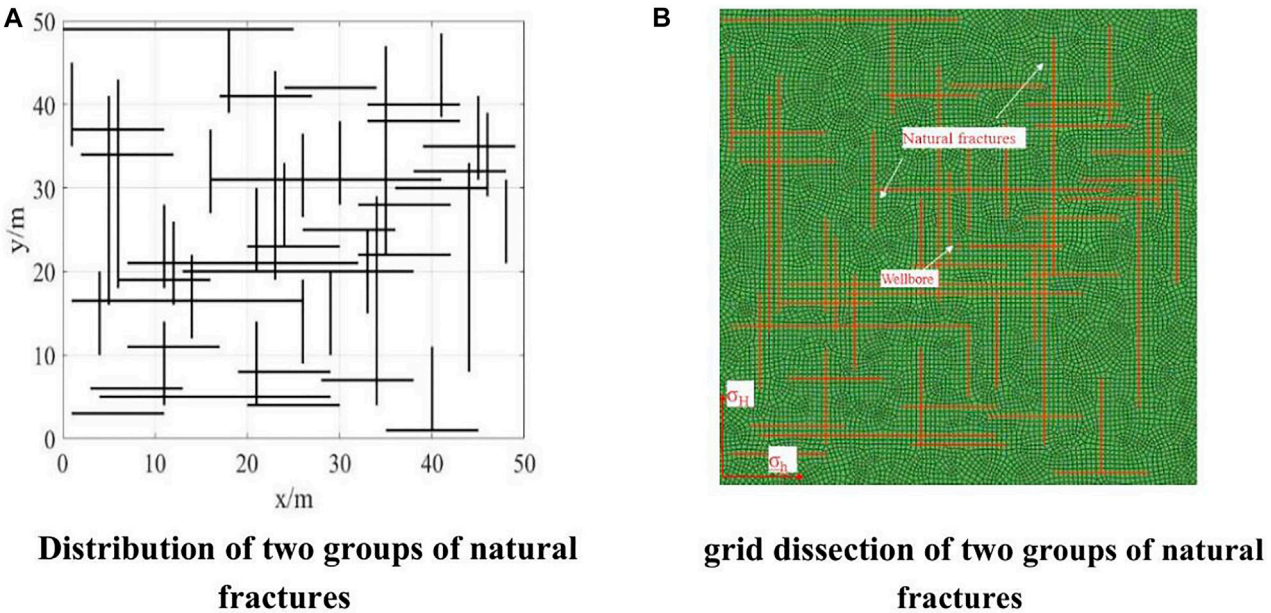

FIGURE 4 | The natural fracture distribution and grid dissection. **(A)** Distribution of two groups of natural fractures. **(B)** grid dissection of two groups of natural fractures.

generated by applying MATLAB coding. In the fracture network, there are m groups of fractures. Each group of fractures has the properties such as fracture length and fracture number (Wei et al., 2020).

$$r_{\alpha i} = \left[(1-\alpha_i) r_{min\,i}^{\ -D_{Ri}} + \alpha_i r_{max\,i}^{\ -D_{Ri}}\right]^{-1/D_{Ri}} (1 \le i \le m) \quad (8)$$

$$N_i(r_{\alpha i} \ge r_i) = \left(\frac{r_{max\,i}}{r_i}\right)^{D_{Ri}/2} (1 \le i \le m) \quad (9)$$

where $r_{\min i}$ is the lower limit value of the fracture size in the i group, $r_{\max i}$ is the upper limit value, L_i is the cumulative length of the fracture in the i group, N_i is the cumulative number of the fractal fracture, D_{Ri} is the cumulative length of fractal dimension.

Then, the reservoir with the natural fracture network is meshed, and the global cohesive elements are embedded in ABAQUS through secondary development technology. Different mechanical properties are given to rock elements and natural fracture elements.

An injection well is placed in the center of the simulated area. A model of hydraulic fracture propagation in the presence of two sets of natural fractures in a reservoir is developed by applying an autonomous natural fracture network model to form a randomly distributed natural fracture pattern where both fractal dimensions are equal to 1.2. The natural fracture distribution and grid dissection are shown in **Figure 4A**. The model size is 50 m × 50 m and the wellbore point is located at the center of the simulated area. The fracture propagation is based on the maximum circumferential stress criterion. The simulation parameters are listed in **Table 1** for the reservoir characteristics of block A.

Dynamic propagation model analysis of the fractured reservoir is used to obtain the stress distribution and fracture morphology at different time steps, as shown in **Figure 5**.

Figure 5A shows the hydraulic fracture propagation stage. The influence of natural fractures is not apparent and the fractures extend along the direction of the maximum principal stress. **Figure 5B** shows the propagation of the hydraulic fractures to the natural fracture boundary, which vertically intersects the natural fractures. The hydraulic fracture is captured by the natural fractures, and the fractures extend along the natural

TABLE 1 | Numerical simulation parameters of hydraulic fracturing in multi-fractured reservoirs.

Parameters	Value	Parameters	Value
Depth of strata (m)	1,648	Rock density (kg/m^3)	2,300
Modulus of elasticity (GPa)	22	Injection speed (m^3/min)	6
Poisson's ratio	0.3	Fracturing fluid viscosity (mPa·s)	100
Stratigraphic pressure (MPa)	17	Initial hole length (m)	0.2
Maximum horizontal principal stress (MPa)	30	Natural fracture angle (°)	90
Minimum horizontal principal stress (MPa)	27	Natural fractal dimension of fractures	1.2
Tensile strength of rock (MPa)	4.8	Number of natural fractures	62

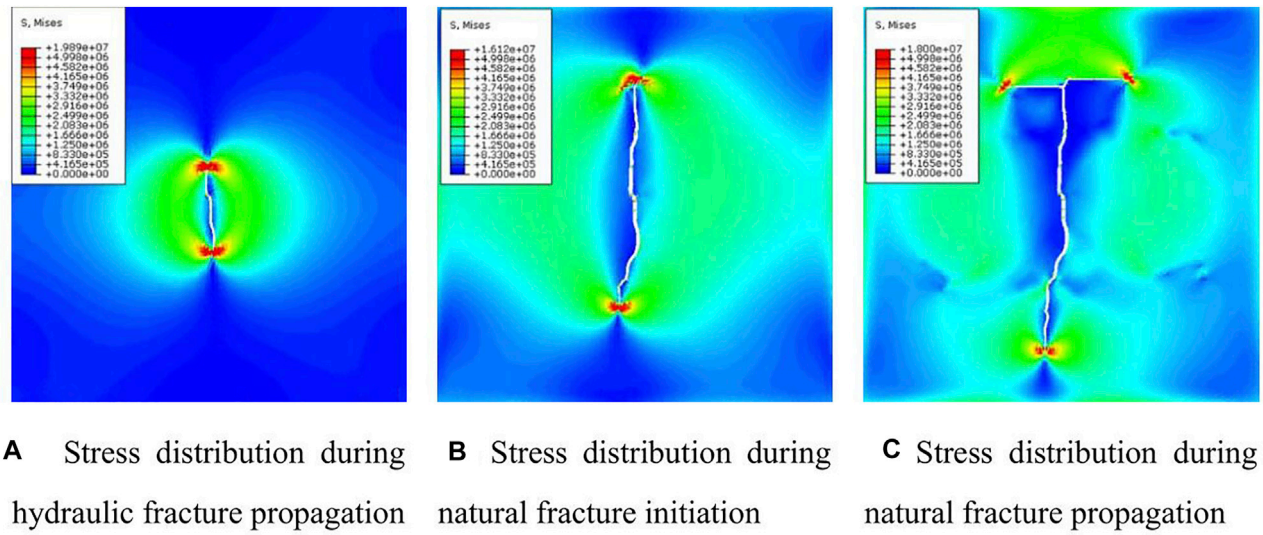

FIGURE 5 | Fracture propagation pattern at different time steps **(A)** Stress distribution during hydraulic fracture propagation. **(B)** Stress distribution during natural fracture initiation. **(C)** Stress distribution during natural fracture propagation.

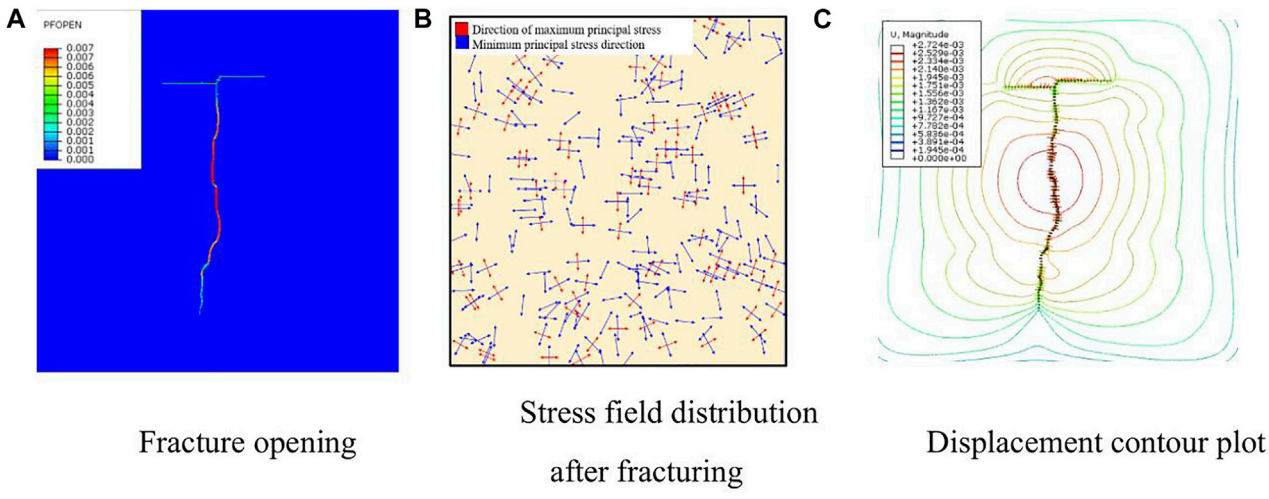

FIGURE 6 | The results of simulation. **(A)** Fracture opening. **(B)** Stress field distribution after fracturing. **(C)** Displacement contour plot.

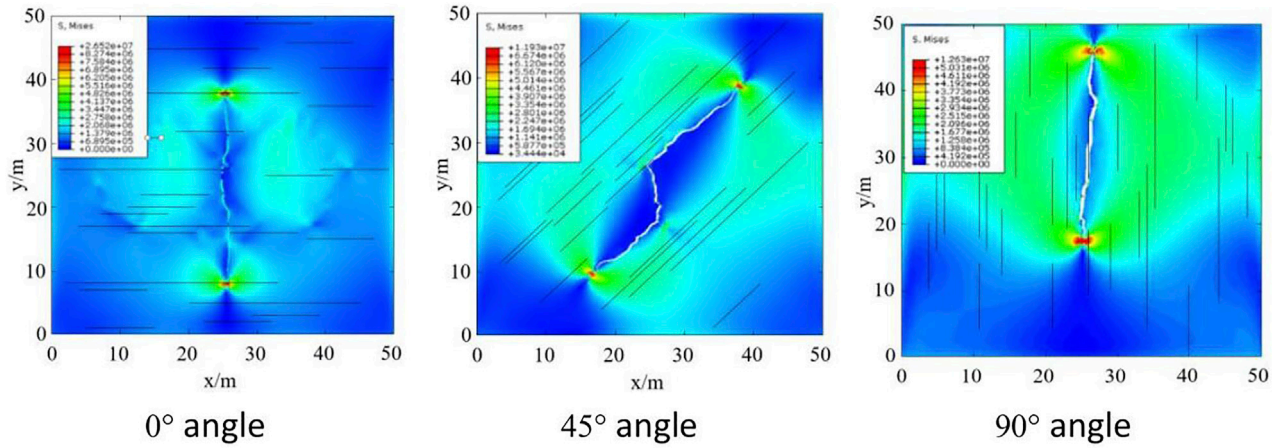

FIGURE 7 | Hydraulic fracture propagation pattern of different natural fracture angle.0° angle.45° angle.90° angle.

fracture direction. **Figure 5C** shows when the hydraulic fracture propagation meets the natural fractures and forms multiple fracture branches in three directions. The fracture propagation direction is mainly influenced by the natural fracture distribution, and the fracture complexity increases compared with a group of naturally fractured reservoirs.

Figure 6A shows that the hydraulic fractures form wider fractures near the borehole, whereas those at the end of the fracture are narrower. **Figure 6B** shows that hydraulic fracturing alters the *in-situ* stress field around the fracture. The stress field is also significantly deflected, which significantly influences the fracture propagation. Fracture propagation causes strain in the rock around the fracture (**Figure 6C**), and the displacement is larger near the borehole and smaller at the end of the fracture.

HYDRAULIC FRACTURE PROPAGATION PATTERN IN FRACTURED RESERVOIRS

The distribution of real natural fractures is complex, and hydraulic fracture propagation patterns differ when encountering different natural fracture networks. Combined with the natural fracture network model (Diguang et al., 2016), a hydraulic fracture propagation model is established for the case when two sets of natural fractures exist in a reservoir. The factors that influence the fracture propagation pattern are analyzed when a single well is hydraulically fractured.

Effect of Natural Fracture Angle on Hydraulic Fracture Propagation

The natural fracture network model is applied to form a randomly distributed natural fracture pattern with fracture angles of 0°, 45°, and 90° and a fractal dimension of 1.2. The numerical simulation method with globally embedded cohesion units is applied to simulate and analyze the fracture propagation law in fractured reservoirs with different distributions of natural fracture angles, and the simulation results are shown in **Figure 7**.

The fracture propagation pattern of the reservoir with a natural fracture distribution shows that a single fracture forms when the fracture angle is 0° or 90° and extends along the direction of the maximum horizontal principal stress. For a 0° fracture, the hydraulic fracture vertically intersects and easily crosses the natural fracture, which is controlled by the anisotropy of the stress field, and forms a more symmetrical hydraulic fracture. For a 45° fracture, the hydraulic fracture communicates with the natural fractures to form a fracture pattern that expands along the 45° direction and is less affected by the stress field anisotropy. For a 90° fracture, when the hydraulic fracture intersects with the natural fracture, the hydraulic fracture expands along the natural fracture direction. When the natural fracture is communicated, the pressure drops and the hydraulic fracture tends to expand in the direction of the pressure drop, which forms an asymmetrically expanding fracture pattern.

The fracture morphology form by hydraulic fracturing in reservoirs are compared in **Figure 8** for different natural fracture angles. The results show that when the natural fracture angle is 90°, the number of natural fractures and connected natural fractures are less and the fracture width is larger. When the natural fracture angle is 45°, the hydraulic fracture opens and communicates one natural fracture. When the natural fracture distribution is 0°, the hydraulic fracture opens and communicates five natural fractures. and the propagation width increase uniformly, and fluctuations occur in the growth curve because of certain resistances when passing through the natural fracture.

Effect of the Number of Natural Fracture Groups on Fracture Propagation

The natural fracture network model is applied to generate a fractal dimension of 1.2 using 1, 2, or 3 groups of natural fractures in the reservoir. The maxium number of natural fracture is 30 every group. The maxium length is 50 m and the factal dimension is 1.2. The fracture angle of the first group is 0°, the fracture angle

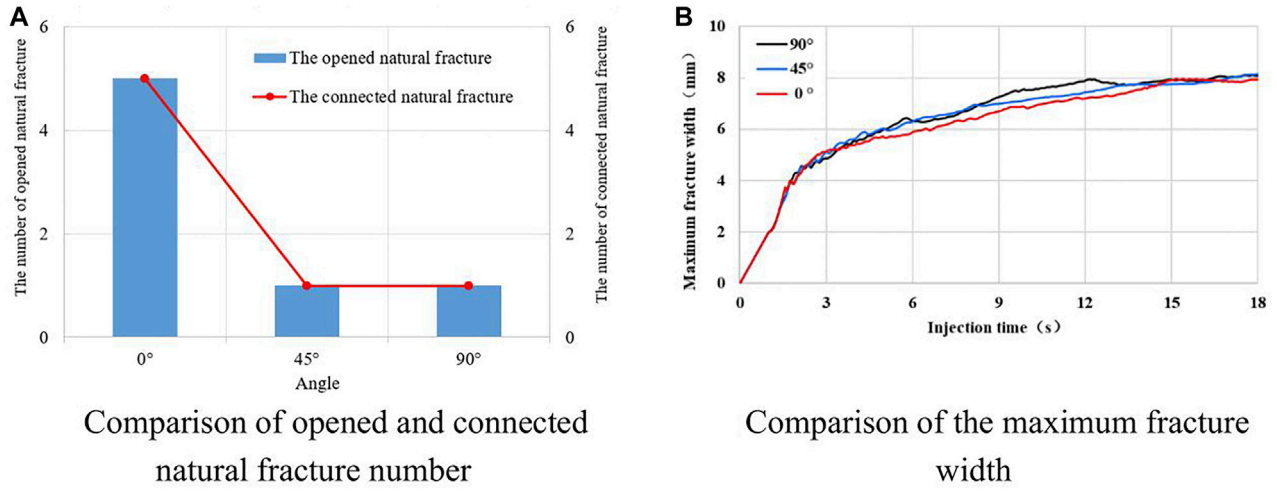

FIGURE 8 | The fracture morphology comparison of different natural fracture angle. **(A)** Comparison of opened and connected natural fracture number. **(B)** Comparison of the maximum fracture width.

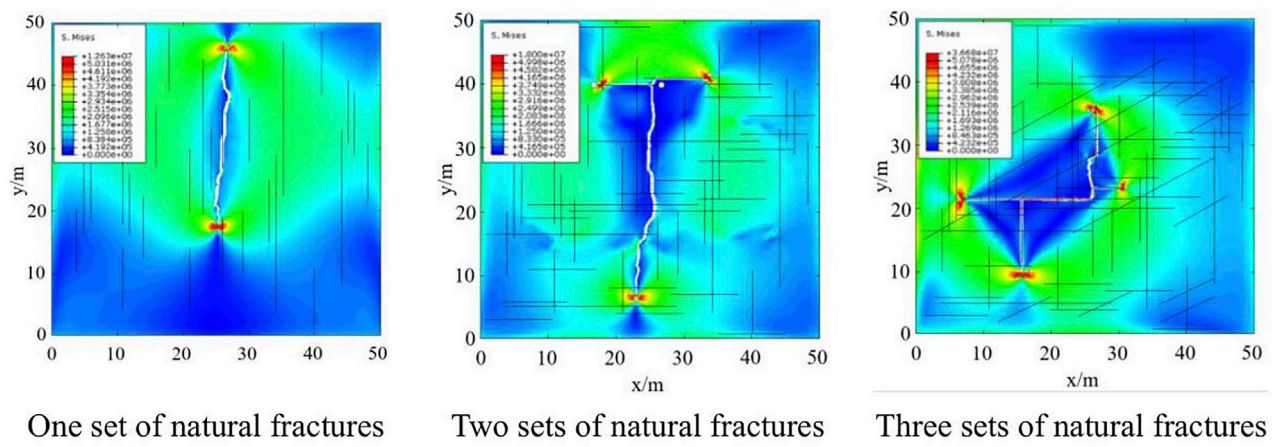

FIGURE 9 | Hydraulic fracture propagation pattern of different natural fracture group. One set of natural fractures. Two sets of natural fractures. Three sets of natural fractures.

of the second group is 90° and the fracture angle of third group is 45°. The simulations are analyzed using the globally embedded cohesion unit method, and the results are shown in **Figure 9**.

The fracture propagation morphology shows that when a group of natural fractures exists in the reservoir, the hydraulic fracture propagation morphology is singular and influenced by the stress field anisotropy. As the distribution direction of natural fractures in a reservoir increases, the hydraulic fracture propagation morphology becomes increasingly complex and forms multiple branching fractures, which are less influenced by the stress field.

Figure 10A compares the total of natural fractures that open and connect by hydraulic fracturing in reservoirs with different numbers of fracture groups. When the natural fracture group is one, the hydraulic fracture opens and connects 1 natural fracture. When the natural fracture group is two, the hydraulic fracture opens 3 natural fracture and connects 53 natural fractures. When the natural fracture group is three, the hydraulic fracture opens 5 natural fracture and connects 70 natural fractures. It can be seen that when the natural fracture is more complex, the number of opening and connecting natural fractures is more. The complex natural fractures are conducive to improve oil and gas recovery.

Figure 10B compares the maximum fracture widths that form by the propagation of hydraulic fracture in reservoirs with different numbers of fracture groups. The fracture widths are the same during the early propagation stage. Upon meeting natural fractures, the hydraulic fractures are affected differently because of different lengths and widths of the natural fractures. Fewer natural fracture groups tend to form larger fracture widths at a given injection time. Wide and short

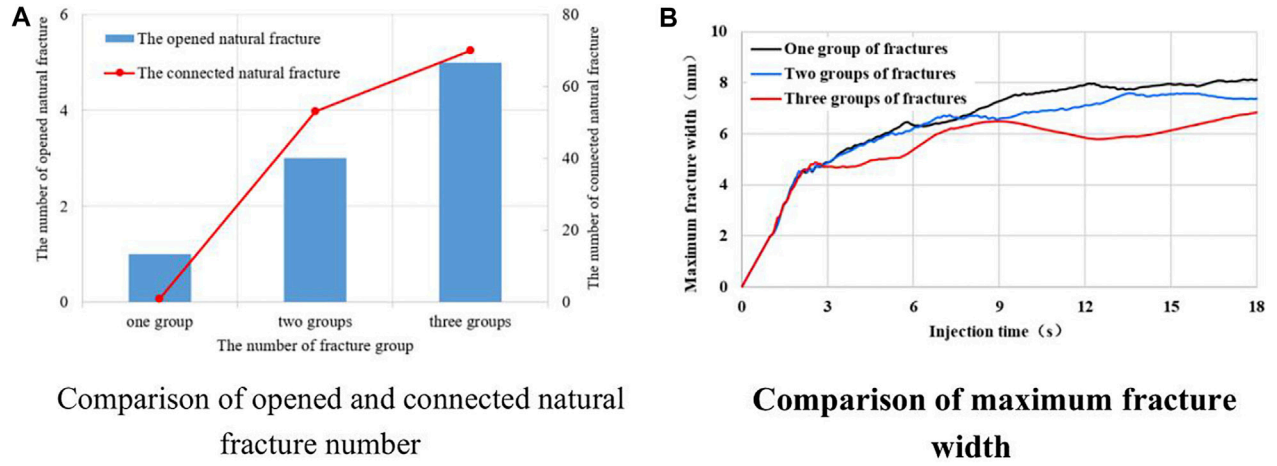

FIGURE 10 | The fracture morphology comparison of different natural fracture group. **(A)** Comparison of opened and connected natural fracture number. **(B)** Comparison of maximum fracture width.

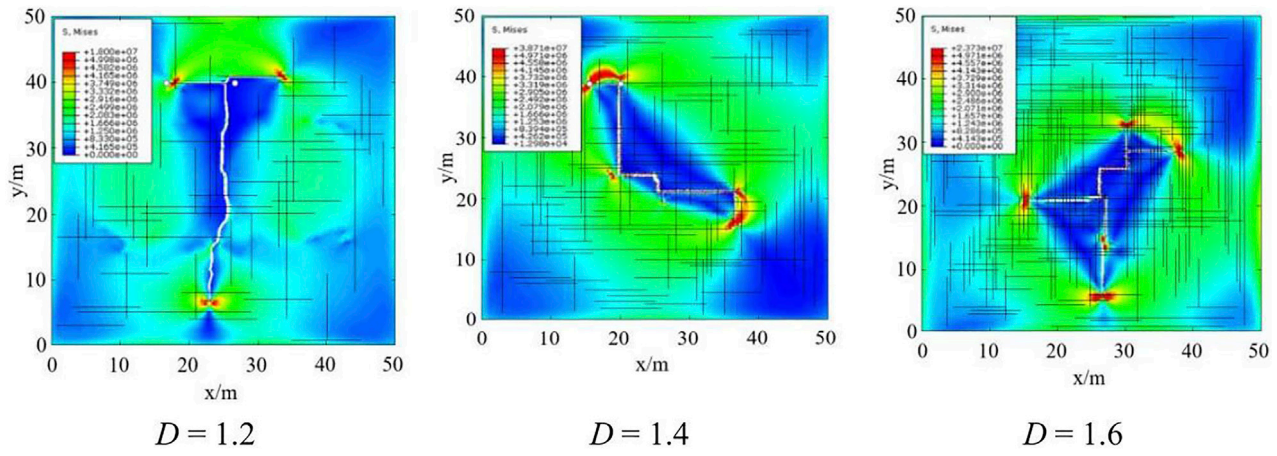

FIGURE 11 | Hydraulic fracture propagation pattern of different natural fracture dimension. *D* = 1.2. *D* = 1.4. *D* = 1.6.

fractures tend to form when a single group of fractures is present in the reservoir, whereas narrow and long fractures tend to form when multiple groups of fractures are present in the reservoir.

A comparison of the obtained fracture distributions shows that an increasing number of natural fracture groups results in more complex and lower maximum fracture width, and more fracture propagation directions. The hydraulic fractures are more likely to expand along the natural fractures and form a complex fracture network, and the fracture transformation effect is better.

Effect of Fractal Dimension of Natural Fractures on Fracture Propagation

The fractal dimension of natural fractures is an important parameter that can be used to characterize the fracture distribution. The maxium number of natural fracture is 30, the maxium length is 50 m and the factal dimension is 1.2 in model I. The maxium number of natural fracture is 60, the maxium length is 50 m and the factal dimension is 1.4 in model II. The maxium number of natural fracture is 110, the maxium length is 50 m and the factal dimension is 1.6 in model III. In every model, the fracture angle of first group is 0° and the fracture angle of second group is 90°. The globally embedded zero-thickness cohesive unit method is applied to simulate the hydraulic fracture propagation process and compare and analyze the effects of fracture modification in the reservoir for different fractal dimension distributions. The simulation results are shown in **Figure 11**.

The fracture propagation morphology shows that when the fractal dimension is 1.2, the hydraulic fracture propagation morphology is singular and influenced by the stress field anisotropy. With increasing fractal dimension, the natural fracture distribution becomes increasingly complex and the hydraulic fracture propagation process leads to turning,

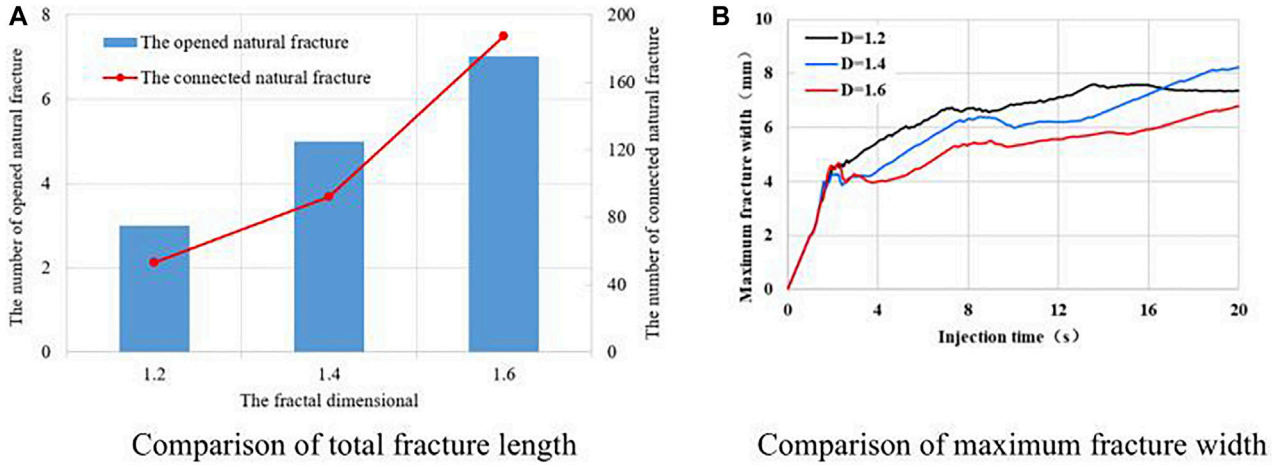

FIGURE 12 | The fracture morphology comparison of different natural fracture dimension. **(A)** Comparison of total fracture length. **(B)** Comparison of maximum fracture width.

branching, merging, and the formation of multiple branching fractures, which are less influenced by the stress field.

Figure 12 shows that once the injection energy reaches a certain value, the total fracture propagation length and width increase with increasing injection time. During the early hydraulic fracture propagation stage, the total fracture width grow at relatively consistent rates because they are not yet influenced by natural fractures. When the fractures meet natural fractures, the fracture width decreases for higher fractal dimension conditions, and the fracture propagation length tends to fluctuate. Reservoirs with a higher fractal dimension tend to open more natural fractures, fracturing fluid flows in multiple directions, less liquid exists in the main flow channel, and narrow and long natural fractures easily form that expand in multiple directions. When a hydraulic fracture expands along a natural fracture, the fracturing fluid velocity increases and the total fracture width decreases. When a hydraulic fracture expands through a natural fracture, it accumulates more energy and the fracture width rapidly increases.

A comparison of the fracture transformation effect shows that with increasing fractal dimension, the total natural fracture that opened and connected by hydraulic fracture increases, the maximum fracture width decreases, and the number of fracture propagation directions increases. A reservoir is more likely to form a complex fracture network that expands in multiple directions after hydraulic fracturing when the fractal dimension of the natural fracture distribution is higher, and the reservoir fracture transformation effect is better compared with that prior to fracturing.

CASE ANALYSIS

Natural fractures are the main seepage channel and important storage space of shale reservoir, and the communication of natural fractures is mainly used to improve the fracturing effect during the exploitation process. The rock outcrops is

FIGURE 13 | The nature fracture distribution.

the best way to obtain the discontinuous structure such as fractures, joints. Take the outcrop of the Longmaxi formation in south Sichuan as an example to analyze the effect of hydraulic fracture technology of shale reservoir. As shown in the **Figure 13**, the outcrop of the measurement point develops two groups of intersecting fractures mainly. The fracture length is 0.5~6 m, the fracture angle is 13° and 93° respectively, the fracture density is 3.26 m/m^2. The nature fractures have the characteristics of grouping and parallelism. Many of the nature fractures have been broken and cleaved, and the natural fracture network is complex. Therefore, hydraulic fracturing technology is proposed to connect the complexity natural fracture and improve the oil and gas recovery.

In order to analyze the development characteristics of fracture network and the hydraulic fracturing effect in Longmaxi shale, MATLAB script files were used to simulate the distribution characteristics and connectivity of shale fractures according to the statistical data of shale

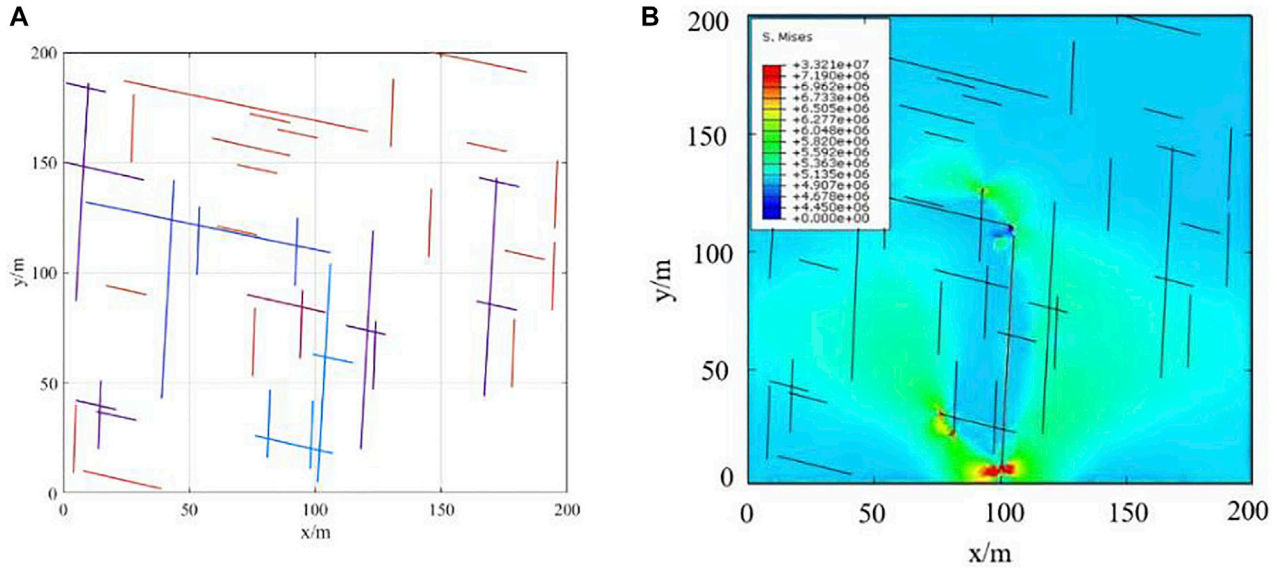

FIGURE 14 | The fracture morphology before and after hydraulic fracturing. **(A)**The connectivity and fracture distribution of nature fracture. **(B)**The fracture morphology after hydraulic fracturing.

outcrops in Longmaxi Formation. The fractal dimension of the first group is 1.6 and the fractal dimension of the second group is 1.5. The fracture angle of the first group is 13° and the fracture angle of the second group is 93°. Based on the natural fracture system, the ABAQUS was used to simulate hydraulic fracture propagation.

The natural fracture system distribution and the connectivity of the natural fracture of Longmaxi using the fracture network model is shown in **Figure 14A**. The connected natural fracture clusters are shown by different colors. It can be seen from that the dis-connected natural fracture account for 45.24% and the connected natural fracture account for 54.76%. The maximum connected fracture cluster contains 5 natural fractures and account for 11.90%. The hydraulic fracture process is stimulated applying the global embed cohesive elements method. The fracture morphology of this well is shown in **Figure 14B**. Hydraulic fracturing can connect different fracture clusters. The maximum connected fracture cluster contains 9 natural fractures and the proportion of connected fractures increased from 11.90 to 21.43% after hydraulic fracturing. The connectivity of the entire fracture and the effect of development will be greatly improved.

CONCLUSION

1) A dynamic hydraulic fracture propagation model is established that uses globally embedded cohesive elements and considers a reservoir with complex distributed natural fractures. The model can be used to simulate the rock and propagation behavior of hydraulic fractures and investigate the complex fracture system morphology.
2) The hydraulic fracture propagation characteristics of naturally fractured reservoirs are investigated. The hydraulic fracture propagation of fractured reservoirs is influenced by a combination of the natural fracture distribution, which determines the overall fracture propagation path direction. The fracture geometry in near-borehole areas tends to be more complex than in the far field, and the fracture size is larger.
3) The influence of different factors on the propagation of hydraulic fractures in naturally fractured reservoirs is analyzed. With increasing natural fracture angle, the hydraulic fractures easily pass through the natural fractures, the propagation form is singular, and the fractures are wider. Higher numbers of natural fracture groups tend to more readily form complex fracture forms with multiple directions, and the opened and connected natural fractures are more, and the fractures are narrow. With increasing fractal dimension, multi-directional complex fractures more easily form and the fractures are narrow, the opened and connected natural fractures are more.
4) The case study shows that connected fractures account for 54.76% of the total fractures in the outcrop shale fracture network of the Longmaxi formation and the proportion of connected fractures increased from 11.90 to 21.43% after hydraulic fracturing.

DATA AVAILABILITY STATEMENT

The original contributions presented in the study are included in the article/Supplementary Material, further inquiries can be directed to the corresponding author.

AUTHOR CONTRIBUTIONS

HZ contributed to the conception and design of the study, writing–original draft; WL contributed to the conception and funding acquisition; LW and JF contributed to the writing checking and editing; YLX and JJZ, project administration; SQL, data analysis.

FUNDING

The research was supported by the National Natural Science Foundation of China (No. 51774093) and Northeast Petroleum University introduces the talented person scientific research start funds subsidization project (No.13051202008).

REFERENCES

Barrenblatt, G. I. (1962). The Mathematical Theory of Equilibrium Cracks in Brittle Fracture. *Adv. Appl. Mech.* 7, 55–125.

Bing, H., Mian, C., Baowei, Z., and Sang, Y. (2015). Propagation of Multiple Hydraulic Fractures in Fractured Shale Reservoir. *Chin. J. Geotechnical Eng.* 37 (6), 1041–1046. doi:10.11779/CJGE201506010

Bonnet, E., Bour, O., Odling, N. E., Davy, P., Main, I., Cowie, P., et al. (2001). Scaling of Fracture Systems in Geological media. *Rev. Geophys.* 39, 347–383. doi:10.1029/1999rg000074

Bour, O., and Davy, P. (1997). Connectivity of Random Fault Networks Following a Power Law Fault Length Distribution. *Water Resour. Res.* 33, 1567–1583. doi:10.1029/96wr00433

Bruno, G. D. S., and Einstein, H. H. (2014). Finite Element Study of Fracture Initiation in Flaws Subject to Internal Fluid Pressure and Vertical Stress. *Int. J. Sol. Structures* 51 (23), 4122–4136. doi:10.1016/j.ijsolstr.2014.08.006

Chen, Z., Bunger, A. P., Zhang, X., and Jeffrey, R. G. (2009). Cohesive Zone Finite Element-Based Modeling of Hydraulic Fractures. *Acta Mechanica Solida Sinica* 22 (5), 443–452. doi:10.1016/s0894-9166(09)60295-0

Chen, Z., Jeffrey, R., G., and Zhang, X. (2017). Finite-element Simulation of a Hydraulic Fracture Interacting with a Natural Fracture. *SPE J.* 22 (1), 219–234. doi:10.2118/176970-pa

Chuprakov, D. A., Akulich, A. V., and Siebrits, E. (2011). Hydraulic-fracture Propagation in a Naturally Fractured Reservoir. *SPE Prod. Operations* 26 (1), 88–97. doi:10.2118/128715-pa

Cottrell, M., Hosseinpour, H., and Dershowitz, W. (2013). "Rapid Discrete Fracture Analysis of Hydraulic Fracture Development in Naturally Fractured Reservoirs," in Proceedings of the Unconventional Resources Technology Conference, Denver, CO, August 2013. doi:10.1190/urtec2013-245

Dahi, T., A., Gonzalez, M., and Hao, H. (2018). Numerical Simulation of Hydraulic Fracture Propagation in Naturally Fractured Formations Using the Cohesive Zone Model. *J. Pet. Sci. Eng* 165, S0920410518300755. doi:10.1016/j.petrol.2018.01.063

Dahi-Taleghani, A., and Olson, J. E. (2011). Numerical Modeling of Multistranded-Hydraulic-Fracture Propagation: Accounting for the Interaction between Induced and Natural Fractures. *SPE J.* 16 (03), 575–581. doi:10.2118/124884-pa

Dehghan, A. N., Goshtasbi, K., and Ahangari, K. (2016). 3D Numerical Modeling of the Propagation of Hydraulic Fracture at its Intersection with Natural (Pre-existing) Fracture. *Rock Mech. Rock Eng.* 50, 1–20. doi:10.1007/s00603-016-1097-7

Diguang, G., Zhanqing, Q., Jianxiong, L., and Qu, G. Z. (2016). Extended Finite Element Simulation of Hydraulic Fracture Based on ABAQUS Platform. *Rock Soil Mech.* 37 (5), 302–310. doi:10.16285/j.rsm.2016.05.036

Dugdale, D. S. (1960). Yielding of Steel Sheets Containing Slits. *J. Mech. Phys. Sol.* 8, 100–104. doi:10.1016/0022-5096(60)90013-2

Fatahi, H., Hossain, M. M., and Sarmadivaleh, M. (2017). Numerical and Experimental Investigation of the Interaction of Natural and Propagated Hydraulic Fracture. *J. Nat. Gas Sci. Eng.* 37, 409–424. doi:10.1016/j.jngse.2016.11.054

Fei, L., Zhifeng, L., Yu, S., and Changlin, Z. (2017). Deformation Behavior between Hydraulic and Natural Fractures Using Fully Coupled Hydromechanical Model with XFEM. *Math. Probl. Eng.*, 1–12. doi:10.1155/2017/6373957

Gonzalez, M., and Dahi, T., A. (2015). "A Cohesive Model for Modeling Hydraulic Fractures in Naturally Fractured Formations[C]," in Proceedings of the SPE hydraulic fracturing technology conference, Woodlands, TX (Woodlands, TX: HFTC), 3–5.

Guo, J., Luo, B., Lu, C., Lai, J., and Ren, J. (2017). Numerical Investigation of Hydraulic Fracture Propagation in a Layered Reservoir Using the Cohesive Zone Method. *Eng. Fracture Mech.* 186, 195–207. doi:10.1016/j.engfracmech.2017.10.013

Gustafson, G., and Fransson, Å (2005). The Use of the Pareto Distribution for Fracture Transmissivity Assessment. *Hydrogeol J.* 14, 15–20. doi:10.1007/s10040-005-0440-y

Haddad, M., Du, J., and Vidal-Gilbert, S. (2016). "Integration of Dynamic Microseismic Data with a True 3D Modeling of Hydraulic Fracture Propagation in Vaca Muerta Shale[C]," in Proceedings of the SPE hydraulic fracturing technology conference (Woodlands, TX: HFTC), 9–11.

Haddad, M., and Sepehrnoori, K. (2015). Simulation of Hydraulic Fracturing in Quasi-Brittle Shale Formations Using Characterized Cohesive Layer: Stimulation Controlling Factors. *J. Unconventional Oil Gas Resour.* 9, 65–83. doi:10.1016/j.juogr.2014.10.001

Jianchun, G., Xing, Z., Haiyan, Z., and Rui, P. (2015). Numerical Simulation of Interaction of Hydraulic Fracture and Natural Fracture Based on the Cohesive Zone Finite Element Method. *J. Nat. Gas Sci. Eng.* 25, 180–188. doi:10.1016/j.jngse.2015.05.008

Jun, Z., Yuwei, L., Yishan, P., and Xiangyang, W. (2021). Experiments and Analysis on the Influence of Multiple Closed Cemented Natural Fractures on Hydraulic Fracture Propagation in a Tight Sandstone Reservoir. *Eng. Geology.* 281, 105981.

Kresse, O., Weng, X., Gu, H., and Wu, R. (2013). Numerical Modeling of Hydraulic Fractures Interaction in Complex Naturally Fractured Formations. *Rock Mech. Rock Eng.* 46 (3), 555–568. doi:10.1007/s00603-012-0359-2

Lei, X., Yawu, Z., Lei, Ji., and Ye, Y. (2016). Research on Influence of Initial Horizontal Principal Stress on Stress Shadow. *Chin. J. Rock Mech. Eng.* S1, 2819–2825. doi:10.13722/j.cnki.jrme.2015.1555

Mokryakov, V. (2011). Analytical Solution for Propagation of Hydraulic Fracture with Barenblatt's Cohesive Tip Zone. *Int. J. Fract* 169, 159–168. doi:10.1007/s10704-011-9591-0

Nan, Z., Tan, M., and Liu, Z. (2020). Quantitative Fracture Evaluation Method Using Microspherically Focused Logging Data. *Well Logging Technology* 44 (1), 61–66. doi:10.1016/j.engeos.2021.08.005

Rahman, M. M., and Rahman, M. K. (2010). A Review of Hydraulic Fracture Models and Development of an Improved pseudo-3D Model for Stimulating Tight Oil/gas Sand. *Energy Sourc. A: Recovery, Utilization, Environ. Effects* 32 (15), 1416–1436. doi:10.1080/15567030903060523

Tang, J., Fan, B., Xiao, L., Tian, S., Zhang, F., Zhang, L., et al. (2020). A New Ensemble Machine-Learning Framework for Searching Sweet Spots in Shale Reservoirs. *SPE J.* 26 (1). doi:10.2118/204224-pa

Wang, H. (2019). Hydraulic Fracture Propagation in Naturally Fractured Reservoirs: Complex Fracture or Fracture Networks. *J. Nat. Gas Sci. Eng.* 68, 102911. doi:10.1016/j.jngse.2019.102911

Wang, H. (2016). Numerical Investigation of Fracture Spacing and Sequencing Effects on Multiple Hydraulic Fracture Interference and Coalescence in Brittle and Ductile Reservoir Rocks. *Eng. Fracture Mech.* 157, 107–124. doi:10.1016/j.engfracmech.2016.02.025

Wang, H. (2015). Numerical Modeling of Non-planar Hydraulic Fracture Propagation in Brittle and Ductile Rocks Using XFEM with Cohesive Zone Method. *J. Pet. Sci. Eng.* 135, 127–140. doi:10.1016/j.petrol.2015.08.010

Wei, L., Huan, Z., and Hongjun, W. (2020). A Novel Approach of Two-Dimensional Representation of Rock Fracture Network Characterization and Connectivity Analysis. *J. Pet. Sci. Eng.* 184, 106507. doi:10.1016/j.petrol.2019.106507

Wen, R., Yang, X., and Liu, D. (2019). Comprehensive Evaluation of Fracture Distribution by Near-And Far-Well Logging and Monitoring Technology. *Well Logging Technology* 43 (5), 531–535. doi:10.16489/j.issn.1004-1338.2019.05.017

Xia, H., Han, L., and Li, G. (2020). New Method for Calculating Fracturing Pressure of TIV Formation in Horizontal Wells. *Well Logging Technology* 44 (2), 116–121.

Yang, Z. J., Su, X. T., Chen, J. F., and Liu, G. H. (2009). Monte Carlo Simulation of Complex Cohesive Fracture in Random Heterogeneous Quasi-Brittle Materials. *Int. J. Sol. Structures* 46 (17), 3222–3234. doi:10.1016/j.ijsolstr.2009.04.013

Yuwei, L., Dan, J., Zhenhua, R., and Jun, Z. (2017). Evaluation Method of Rock Brittleness Based on Statistical Constitutive Relations for Rock Damage. *J. Pet. Sci. Eng.* 153, 123–132. doi:10.1016/j.petrol.2017.03.041

Zhang, X., and Jeffrey, R. G. (2006). The Role of Friction and Secondary Flaws on Deflection and Re-initiation of Hydraulic Fractures at Orthogonal Pre-existing Fractures. *Geophys. J. Int.* 166 (3), 1454–1465. doi:10.1111/j.1365-246x.2006.03062.x

Zhang, X., Jeffrey, R. G., and Thiercelin, M. (2007). Deflection and Propagation of Fluid-Driven Fractures at Frictional Bedding Interfaces: A Numerical Investigation. *J. Struct. Geology.* 29 (3), 396–410. doi:10.1016/j.jsg.2006.09.013

Zhilong, L., Jin, Z., and Heng'an, W. (2008). A Simulation Study of Hydraulic Fracturing Propagation with a Solid-Fluid Coupling Model. *Rock Soil Mech.* 29 (11), 138–143.

Zhiqiang, C., Zhengming, Y., and Moran, W. (2018). Hydro-mechanical Coupled Mechanisms of Hydraulic Fracture Propagation in Rocks with Cemented Natural Fractures. *J. Pet. Sci. Eng.* 163, 421–434. doi:10.1016/j.petrol.2017.12.092

Ziyuan, C., Yuwei, L., and Yishan, P. (2022). Study on CO_2 Foam Fracturing Model and Fracture Propagation Simulation. *Energy* 238, 121778. doi:10.1016/j.energy.2021.121778

Conflict of Interest: WL and ZJ were employed by the company Daqing Oilfield Production Technology Institute.

The remaining authors declare that the research was conducted in the absence of any commercial or financial relationships that could be construed as a potential conflict of interest.

Publisher's Note: All claims expressed in this article are solely those of the authors and do not necessarily represent those of their affiliated organizations, or those of the publisher, the editors and the reviewers. Any product that may be evaluated in this article, or claim that may be made by its manufacturer, is not guaranteed or endorsed by the publisher.

frontiers in Earth Science

ORIGINAL RESEARCH
published: 09 February 2022
doi: 10.3389/feart.2021.802842

Studies and Applications of Dual Pore Saturation Model Based on Pore Structure Classification in Tight Reservoirs

Liu Tangyan[1], *Li Qingfeng*[2], *Zhang Cuihua*[2], *Yang Wentao*[3], *Liu Shiqiong*[4]* *and Zhao Wenjun*[1]

[1]State Key Laboratory of Marine Geology, Tongji University, Shanghai, China, [2]Daqing Branch, China Petroleum Logging Co. Ltd., Daqing, China, [3]College of Chemistry, Nankai University, Tianjin, China, [4]State Key Laboratory of Oil and Gas Reservoir Geology and Exploitation, Southwest Petroleum University, Chengdu, China

The complex pore structure of rock may influence resistivity logs and make it challenging to perform saturation estimations with better precision. For example, water saturation may go higher or lower when Archie's formulae are used to obtain the saturation as the logging resistivity may become greater or smaller, due to the influences of complex pore structures in the reservoirs. In this paper, having considered the influences of pore structure on logging resistivity, we have developed a different algorithm to improve the equivalent rock element model (EREM, a rock conduction model) to have better water saturation. First of all, the nuclear magnetic resonance (NMR) echo data of cores are inverted by using the optimized inversion to calculate pore parameters, such as the average radius of spherical pore tubular pore, Cd path, and sorting coefficient. Secondly, according to the parameters derived from the optimization inversions, the pore structures of the core are divided into different groups. Based on the classifications of the pore structure, the conduction parameters of rock for different pore structures are determined by fitting the experimental conduction data of rock with a damping factor. Finally, the working flow of calculating fluid saturation according to the EREM model is determined for different conduction parameters. The key feature of the improved EREM saturation model is to eliminate the influence of pore structure on rock conduction, highlight the influence of pore fluid on rock conduction, and then improve the calculation accuracy of saturation in it. The applications of our research show that the saturation estimations derived from the improved EREM model appear to be more reasonable in terms of the saturation value and its numerical trend. Thus, the improved EREM model has potential in petroleum exploration and exploitation.

Keywords: pore structure, NMR (nuclear magnetic resonance), echo inversion, water saturation, logging interpretation, rock conduction

OPEN ACCESS

Edited by:
Yuwei Li,
Liaoning University, China

Reviewed by:
Yanchun Ling,
University of North Carolina at Chapel Hill, United States
Qiwei Zhan,
Zhejiang University, China
Xinlei Shi,
China National Offshore Oil Corporation, China

***Correspondence:**
Liu Shiqiong
531855036@qq.com

Specialty section:
This article was submitted to Economic Geology, a section of the journal Frontiers in Earth Science

Received: *27 October 2021*
Accepted: *24 December 2021*
Published: *09 February 2022*

Citation:
Tangyan L, Qingfeng L, Cuihua Z, Wentao Y, Shiqiong L and Wenjun Z (2022) Studies and Applications of Dual Pore Saturation Model Based on Pore Structure Classification in Tight Reservoirs. Front. Earth Sci. 9:802842. doi: 10.3389/feart.2021.802842

Abbreviations: C_0, the initial pore structure efficiency (dimensionless); C_F, the initial pore structure efficiency (dimensionless); R_o, the resistivity of rock completely saturated with water (Ω.m); R_w, the resistivity of formation water (Ω.m); R_t, the resistivity of rock (Ω.m); R_F, the porosity scaling factor (dimensionless); R_I , the saturation scaling factor (dimensionless); F, the formation resistivity factor; I, the formation resistivity factor; c, d, the coefficients related to pore structure; V_c, the volume of fracture pore in μm^3; V_s, the volume of spherical pore in μm^3; e, f, the coefficients related to hydrocarbon saturation and pore fluid distributions; C_I, the saturation structure efficiency (dimensionless); ϕ, porosity, total porosity; S_w, water saturation.

INTRODUCTION

The exploration and development of complex oil-bearing reservoirs are becoming increasingly important in the petroleum industry worldwide. It has become challenging for petroleum engineers to find a solution to perform oil exploitation economically and efficiently. Moreover, many research reports have confirmed that pore structure and pore fluid distribution may influence the resistivity of rocks. Even if the porosity and saturation are identical, the resistivity of the rock may change evidently when the pore structure changes significantly and/or the fluid shape in the pore changes significantly. In this case, the classic Archie formula (Archie., 1942) cannot be applied in the complex reservoir. In addition, many studies suggested that the excessive usage of the Archie formulae could result in a significant error of saturation estimation, even when the qualified logging data are available. In the classic Archie formulae, petroleum engineers cannot distinguish if the resistivity responses are induced by pore structure or by pore fluids (Aguilera and Aguilera, 2003; Azar and Javahenrian, 2008; Allori et al., 2011; Bauer and Youssef, 2011; Shi et al., 2020). The pore structure of the reservoir is so complex that it is almost impossible to characterize it by any analytic equation.

Furthermore, pore-throat-size distribution (PSD) may control numerous fundamental petrophysical properties, such as rock resistivity, permeability, and fluid flow in the pore and impact the characterization of water and hydrocarbon reserves (Garcia and Heidari, 2021; Tang et al., 2021). Nevertheless, to have higher accuracy of saturation estimation, we must develop some quantitative models or/and methods to eliminate the influences of pore structure on rock resistivity (Zhan et al., 2020; Zhan et al., 2021). Abousrafa et al. (2009) designed a spherical pore to connect three tubular pores. When the tubular pores connect the spherical pore at different angles, Abousrafa studied the influences of pore structure on rock resistivity using an analytical method. His research is of great value to understanding the influence of pore structure on rock resistivity. However, developing a practical model to obtain the saturation in tight reservoirs is still a problem. Bryan and Pallatt (1996) noted that the applicability of the Archie formula in complex reservoirs was limited before the research by Abousrafa. It is suggested that the conductivity of rock is closely related to the pore shape and pore fluid distribution, and a specific cement index was proposed in the research by Bryan. For example, when the pore porosity is less than 10%, the classical Archie formula does not apply to a tight reservoir. Still, it may be suitable for the tight reservoir after data correction. To confirm his views, Bryan and Pallatt (1996) developed a particle accumulation model to simulate the dolomitization compaction process and quartz cementation process on rock resistivity.

The model by Bryan can predict rock formation factors and the resistivity index, and all the predictions show excellent consistency with the experimental data. The predictions of this model can be used to calculate oil saturation in consolidated and unconsolidated sandstone. However, it still is a problem to describe the pore structure by field logging data. Suman, Man, and other researchers have also carried out a series of practical research on the mechanism of rock conduction. Suman and Knight (1997) proposed a network model to study the relationships between pore structure, skeleton wettability, and rock conduction in partially fluid-saturated rock. After comparing the water wetting rock with the oil wetting rock, he believed that the oil wetting rock has a larger saturation index (n). The wettability of rock influences their conduction, mainly through the film thickness of wettable water. Suman pointed out that the saturation index decreases when larger and simpler pores exist in rocks. Man and Jing (2000) also paid attention to the relationship between rock wettability and conduction. He argued that rock wettability seems variable in analyzing experimental data, and the non-Archie phenomena exist in different samples. To understand these relationships, Man proposed a new pore network model according to the pore morphology and the shape combinations of the different pores. The theoretical model comprehensively considered the geometric characteristics of pores, including the pore shape factor, pore size distribution, and pore coordination number (connectivity of pores). The influence of wetting history and saturating history on rock resistivity and capillary force is also considered (Ramamoorthy et al., 2021). The experimental data of Man show that the wettability of the same pore may change due to the difference in saturating history (Shi et al., 2021). In this paper's research, the influence of pore structure on rock conduction is attributed to the background factor, and the background factor is characterized by the model parameters (Huang et al., 2020; Tang et al., 2021; Valagiannopoulos, 2021). For different pore structures in the reservoir, the model parameters corresponding to the different pore structures are determined for each model (Newgord et al., 2020; Zhang et al., 2020). Therefore, it can be considered that the pore structure does not constitute any influence on rock conduction in the reservoir with the same or similar pore structures, and the rock resistivity is entirely dependent on the response of pore fluids. Based on these considerations, the accuracy of saturation estimations is then improved.

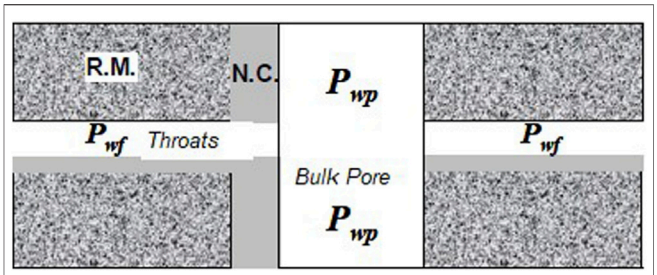

FIGURE 1 | Conduction model of complex pore structure (Shang et al., 2003).

IMPROVEMENT OF THE EQUIVALENT ROCK ELEMENT MODEL MODEL

Shang et al. (2003) proposed the equivalent rock element model (EREM) model to study the influence of rock pore structure on rock conductivity. To objectively describe and quantitatively evaluate the influence of rock conductive path and fluid

distribution on rock conduction and understand how the conductive path and fluid distribution influenced rock resistivity, research has been performed in the paper to improve the EREM model. Consequently, a better evaluation of oil saturation is expected. The original EREM model with a complex pore structure suggested by Shang et al. (2003) is presented in **Figure 1** and **Eqs 1–7**.

$$\log(R_F) = c\log(\phi) + d\left[\log(\phi)\right]^2 \tag{1}$$

$$C_0 = \frac{V_c}{V_s} \tag{2}$$

$$C_F = \frac{C_0 R_F}{1 + (1 - R_F)C_0} \tag{3}$$

$$F = \frac{R_0}{R_w} = \frac{(1-\phi)^2}{C_F\phi} + \frac{1}{\phi} \tag{4}$$

$$\log(R_I) = e\log(S_w) + f\left[\log(S_w)\right]^2 \tag{5}$$

$$C_I = \frac{C_F R_I}{1 + (1 - R_I)C_F} \tag{6}$$

$$I = \frac{R_t}{R_0} = \frac{(1-S_w)^2}{C_I S_w} + \frac{1}{S_w} \tag{7}$$

Where:

- R_F is the porosity scaling factor with no dimension, reflecting the influence of pore structure on the conductivity of rock.
- c and d are the coefficients related to pore structure.
- C_0 is the initial dimensionless pore structure efficiency, and the parameter characteristics that influence the pore morphology on the conductivity of rock. C_0 can be determined with the distribution curve of the spherical fracture model. In this research, the ratio of the potential value of the cumulative distribution curve of the spherical pore and fracture pore in the spherical-fracture model is assigned as C_0.
- C_F is the initial pore structure efficiency, and it has no dimension.
- V_c is the volume of fracture pore in μm^3.
- V_s is the volume of spherical pore in μm^3;
- R_I is the dimensionless saturation scaling factor, reflecting the influences of hydrocarbon content and fluid distributions on the conductivity of rock;
- *e* and *f* are the coefficients related to hydrocarbon saturation and pore fluid distributions.
- C_I is the dimensionless saturation structure efficiency, reflecting the influence of hydrocarbon distribution and pore structure on rock conduction.

The other symbols are in accordance with the definitions of the classical Archie formula. The main feature of **Eqs 1–7** is that, in the double logarithmic coordinate system, the relationship between porosity and formation factors shows as nonlinear and plotting water saturation against resistivity increase index also presents the nonlinear equation. If only straight tubular pores exist in the rock model, the equation of formation factor versus resistivity increase index can be expressed in **Eqs 8, 9** (Liu et al., 2013).

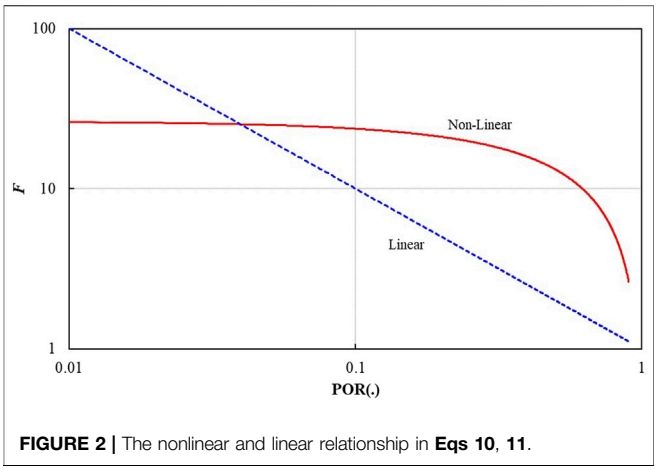

FIGURE 2 | The nonlinear and linear relationship in **Eqs 10, 11**.

$$F = \frac{R_0}{R_w} = \frac{1}{\phi} \tag{8}$$

$$I = \frac{R_t}{R_0} = \frac{1}{S_w} \tag{9}$$

After comparing the improved EREM model with **Eqs 8, 9**, we can find that the linear terms of $(1/\varphi)$ and $(1/S_w)$ appear in both **Eqs 1–7** and **Eqs 8, 9**. The expression of *F* in **Eqs 1–7** is separated into two equations (**Eqs 10, 11**), then F is plotted against porosity (φ) for the two equations in the dual-logarithm coordinate frame (**Figure 2**). There are a nonlinear relationship and a linear relationship shown in **Figure 2**. The non-linear and linear ones are derived from F_c (φ) and F_d (φ), respectively.

$$F_c(\phi) = \frac{(1-\phi)^2}{C_F\phi} \tag{10}$$

$$F_d(\phi) = \frac{1}{\phi} \tag{11}$$

Eqs. 8–9 have demonstrated that the linear term $(1/\phi)$ is relative to the straight tubular pore (simple pore, Liu et al., 2013). Thus, the non-linear term $((1-\phi)^2/C_F\phi)$ is assigned as the contribution of the bend tubular pore (complex pore). Therefore, the total conduction contributions in the improved EREM model are composed of bent tubular pores and straight tubular pores.

Strictly speaking, when only the isolated pores exist in rock, the rock sample will be an isolator for current. The classical Archie formula, however, fails to conclude this. Meanwhile, the improved EREM model is suitable for the isolated pores, and it is equivalent to the case of $C_0 = 0$. Thus, it can be concluded that the rock sample has no conductivity. Furthermore, the improved EREM model is also valid for conductive rocks with only straight tubular pores, equivalent to $C_F = \infty$, $C_I = \infty$.

By solving the quadratic equations for the variable of S_W in the improved EREM model (**Eq. 1**), the calculation formula of S_W is obtained (**Eqs 12, 13**).

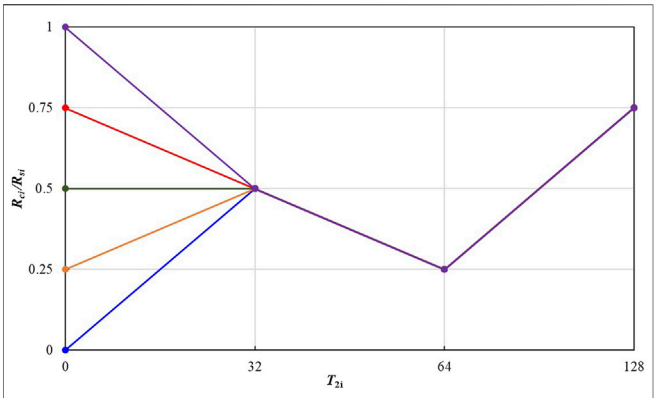

FIGURE 3 | The C_d path composed of C_d values and the order number of T_2 binsets.

$$DLT = (2 + C_I I)^2 - 4(C_I + 1) \tag{12}$$

$$S_w = \frac{(2 + C_I I) \pm \sqrt{DLT}}{2} \tag{13}$$

RESERVOIR CLASSIFICATIONS BASED ON PORE STRUCTURE

Based on the reservoir classifications of pore structure, the equations of the improved EREM are suggested in our research. Thus, it is necessary to develop a practical method to fulfill the reservoir classification in terms of pore structure before the improved EREM can be put into saturation estimations. Xue et al. presented a method to perform reservoir classifications in terms of pore structure by using the sphere–cylindrical model (2017). We will use the method to fulfill the reservoir classifications.

In studies by Xue et al., (2017), the C_d value and C_d path are employed to characterize pore structure. The C_d value is defined as the radius ratio of the tubular pore to the spherical pore, as shown in **Eq. 14**. The C_d path is the plot composed of C_d values and the order numbers of T_2 binsets (**Figure 3**). In each T2 binset, the combinations of tubular pore and spherical pore are ruled by the C_d values, so the entire C_d paths of the spherical tube model describe the configurations between spherical pores and tubular pores in reservoirs. It means that the pore structures are similar in rock if they have the same and/or similar C_d paths (Xue et al., (2017)). Therefore, in this study, the C_d path can be used to judge a similar degree of pore structure. Then we can classify reservoirs into different groups according to pore structure. The classifications of C_d path express the ratio between the fracture width of and the radius of spherical pores in each group. Therefore, the C_d paths and their distribution describe the structural characteristics of pores in rock.

$$C_d = \frac{R_c}{R_s} \tag{14}$$

A great many publications have stated, at home and abroad, including Kennedy and Herrick (2011), Song et al. (2012), and Haro (2017), that the conductivity of rock is closely related to pore structure. In other words, only on the premise of a consistent pore structure background can we have a better relationship between rock conductivity and oil-bearing properties to improve the estimations of oil saturation further. Therefore, when determining the parameters of the EREM, the data of the same working area are divided into different groups according to the classifications of pore structure. All the rock samples possess the same or similar pore structures in the same data group. Then, the improved EREM model parameters are determined for each data group (**Figure 4**).

In the working area, the experiments of nuclear magnetic resonance (NMR) had been performed for 19 samples, and the samples were collected from Well GC10, GC13, and GC16, respectively. The spin echoes of NMR were inversed using the optimizing inversion of a spherical-fracture model (Liu et al., 2006). The C_d paths of the 19 cores were obtained in terms of NMR data (Wang and Liu, 2017). The mean square errors between every two C_d paths were calculated. The smaller the mean square error is, the more similar the C_d path is, and all the samples with fewer mean square errors are put into the same group. It should be noted that, when the parameters c and d in the EREM model are determined with the conduction data of water saturation, or the parameters e and f in the EREM model are determined with the conduction data of oil injection, at least three samples should be involved in each classification group of C_d path because there are two unknown parameters for the conduction data of water saturation. There are two further unknown parameters for the conduction data of oil injection. According to the rules above, the 19 C_d pathways in **Figure 2** were divided into three groups with the less minimum mean square deviation (**Table 1**; **Figure 5**).

DETERMINING PARAMETERS FOR THE IMPROVED EQUIVALENT ROCK ELEMENT MODEL

The constant cement and saturation indices are abandoned in the improved EREM model presented in **Eq. 1**. The parabolic functions characterize the influences of pore structure and fluid distribution on the conductivity of rock, making a clear physical sense. Furthermore, it is fairly simple to determine the parameters for the improved EREM model. There are four critical parameters contained in the improved EREM model, "c, d, e, f."

To determine the parameters of c and d, it is necessary to measure the samples' resistivity when they are fully saturated by brine for at least three or more cores. The process of parameter determination is suggested as follows:

First, the C_F value of the core is calculated according to the $F = R_0/R_W$ expression in **Eqs 1–7**.

Second, according to the calculations of the sphere-fracture model, the volumes of fracture and sphere, V_{FI} and V_{SI}, are calculated and C0 = VFI/VSI can obtain the value of C0. Our research showed that the median value of C_0 is a good coefficient suitable for the EREM model. For example, $C_0 = 0.0318$ for the working zone.

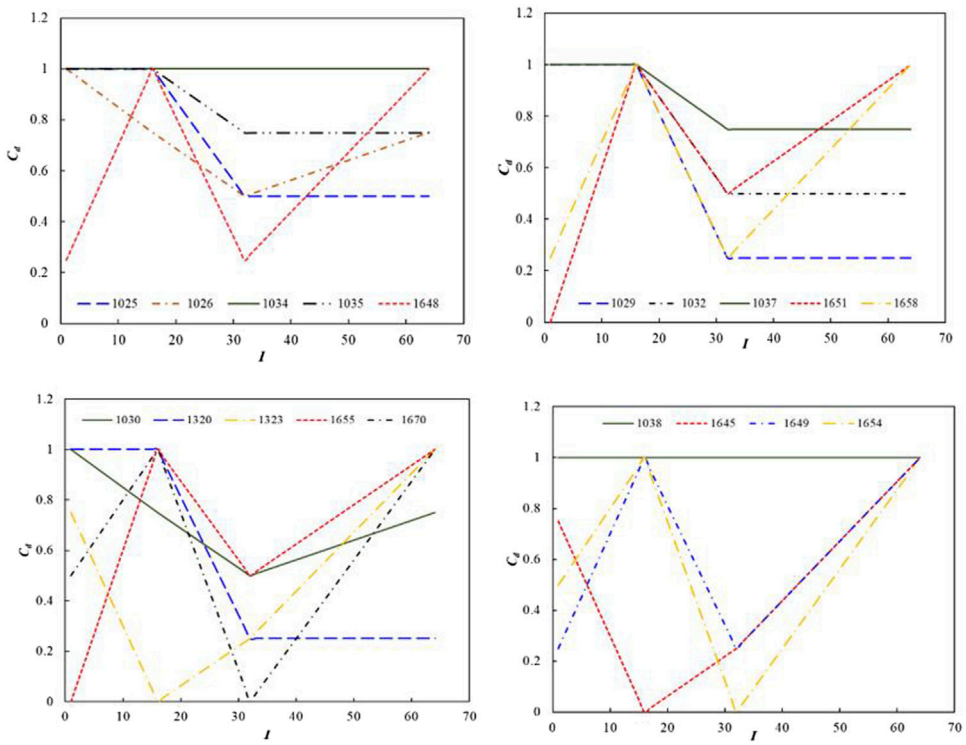

FIGURE 4 | Determination of rock pore structure (C_d path) by core NMR experiments.

TABLE 1 | Cd path classifications of NMR data in the GC working area.

Group-1	σ	0	0.194	0	0.388	0.194	0.194	0.194
	Cores	1,025	1,029	1,032	1,034	1,035	1,037	1,320
Group-2	σ	0	0	0.381	0.381			
	Cores	1,323	1,645	1,026	1,030			
Group-3	σ	0	0	0.146	0.146	0.146	0	0.146
	Cores	1,648	1,649	1,651	1,654(No)	1,655	1,658	1,670(No)

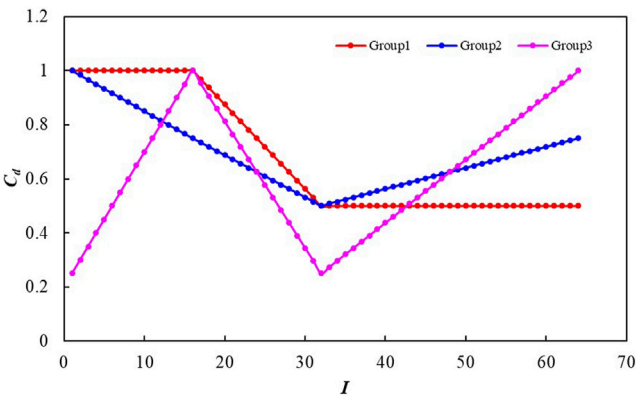

FIGURE 5 | Three groups of all the 19 Cd paths.

Third, the matrix *YF* (**Eq. 15**) is calculated according to the R_F expression in **Eqs 1–7**.

$$YF = \begin{pmatrix} \log(R_{F1}) \\ \log(R_{F2}) \\ .... \\ \log(R_{Fn}) \end{pmatrix} \tag{15}$$

Fourth, the matrix *AF* (**Eq. 16**) is calculated according to the porosity of the cores.

$$AF = \begin{pmatrix} \log(\phi_1) & \log^2(\phi_1) \\ \log(\phi_2) & \log^2(\phi_2) \\ .... & .... \\ \log(\phi_n) & \log^2(\phi_n) \end{pmatrix} \tag{16}$$

Fifth, the parameters c and d with the matrix equation in **Eq. 17** are calculated,

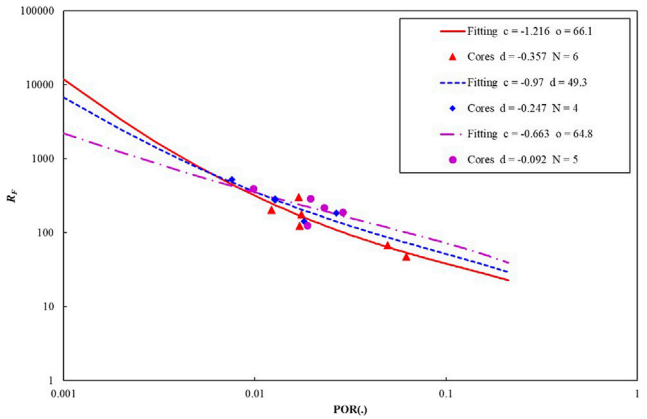

FIGURE 6 | Parameters of c and d for the improved EREM model in group1, group2, and group3.

TABLE 2 | Parameters of the improved EREM model and C_d path determined by the grouping samples.

Group	λ	C	d	λ	e	f
Group 1 Parameters	0	−1.216	−0.357	0	0.168	0.012
Group 2 Parameters	0	−0.97	−0.247	0	0.168	0.012
Group 3 Parameters	0	−0.663	−0.092	0	0.168	0.012

$$\begin{pmatrix} c \\ d \end{pmatrix} = \left(AF^T \times AF + \lambda I\right)^{-1} AF^T \times AF \tag{17}$$

where I is the 2×2 unit diagonal matrix and λ is the damping factor by which we can obtain the better stability and rationality of the calculation for **Eq. 17**. Suppose there is no maximum in the relationship of formation factor versus porosity; in other words, the curve of F versus φ keeps a monotonic increasing trend in the process of porosity decreasing. In that case, the damping factor λ can be taken to zero, or it is necessary to increase the value of λ gradually from zero until the bulge disappears. The parameters of the EREM model are determined by the grouping samples based on the data of 19 cores in the working area (**Figures 5**, **6** and **Table 2**).

After the classifications with the C_d paths, as shown in **Table 2**, each core data group has a typical C_d path and the corresponding parameters of c, d, e, and f. In other words, all the cores in the same group have the same or similar C_d path. Thus, all the cores in the same group will have the same or similar pore structure. Consequently, the influence of pore structure on rock conductivity in the same group can be eliminated because of the same or similar pore structure. Furthermore, the influence of porosity on rock conductivity can be highlighted. Under this condition, the formation factor is a single-valued function of porosity, meaning that the formation factor is determined by the porosity and only the porosity, as shown in **Figure 5**.

In the improved EREM model, the parameters of e and f are mainly utilized to characterize the distribution influence of pore fluid on rock resistivity. The determination of e and f is similar to the one of c and d. Due to the tight lithology in the study area, it is complicated to conduct displacement experiments for the shale cores. In this study, the general parameters of e and f in a similar tight gas-bearing reservoir are adopted (**Table 2**).

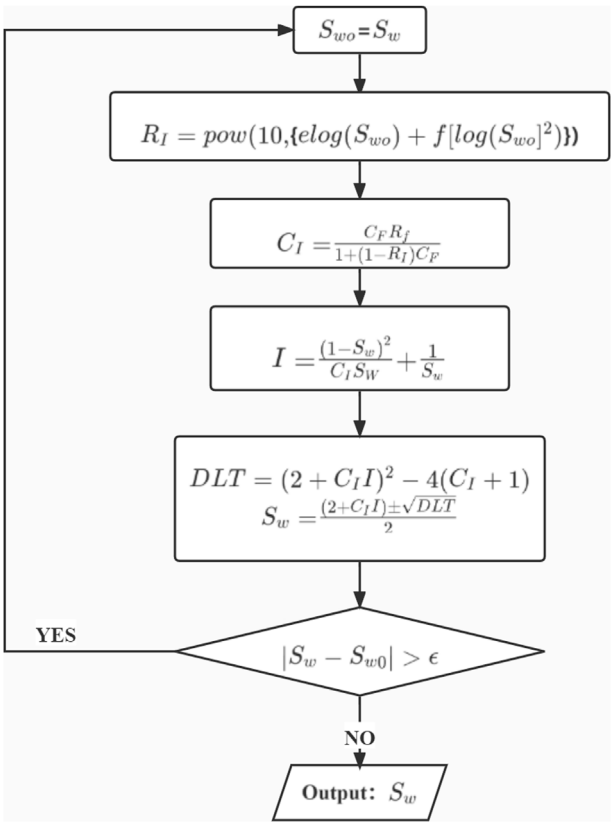

FIGURE 7 | Workflow of saturation estimation of iterative calculation.

APPLICATIONS OF THE IMPROVED EQUIVALENT ROCK ELEMENT MODEL MODEL

This study used an iterative process to perform water saturation estimations. The iterative process is perfectly convergent after the logging calculations are completed in the working area, as shown in the chart below (**Figure 7**).

Using the improved EREM model developed in the research, we performed logging processes in 10 boreholes in the GC working area. Compared with the classical Archie formula, the saturation estimations derived from the improved EREM model tend to be more reasonable on the calculating value and number changing trend. Subsequently, the improved EREM has better application potential. Taking Well xx3 as an example in the

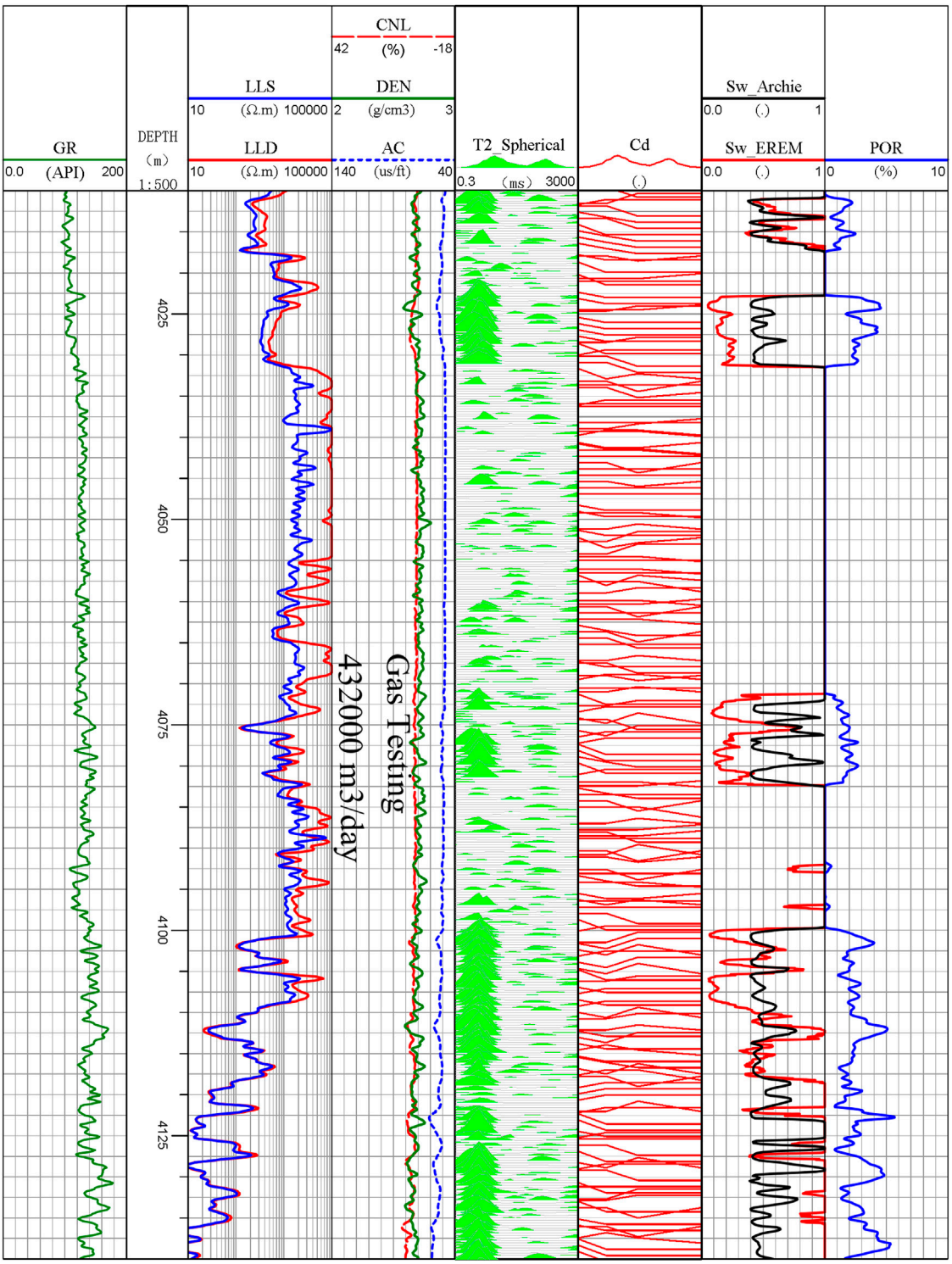

FIGURE 8 | Comparison of saturation estimation between the improved EREM model and Archie model in Well XX3.

working area, the saturation estimations are presented in **Figure 8**. Gas testing was carried out in the interval section from 4,011 to 4,160 m, and the daily production of natural gas was 432,000 m^3. The water saturation in the same interval was between 30% and 55%, showing an excellent alignment with the gas testing data.

Comparing the saturation estimations from the improved EREM model with the one from the classical Archie model, the saturation estimation from the former displays better alignment with the gas-testing production in the calculating value and changing trend (**Figure 8**). Conclusively, the improved EREM model has better application potential in the petroleum industry to locate the right gas reserves. In addition, the variation trend of gas saturation from the former in different depths is more consistent with the natural status of pore fluids in the formation profile. On the other hand, the gas saturation derived in the classical Archie model changes sharply in the same interval section. Still, no physical mechanism of fluid existence can support such gas existence like this in reservoirs.

CONCLUSION AND DISCUSSION

Complex pore structure may have various effects on the rock conductivity in oil-bearing and/or gas-bearing reservoirs, including the effects of increasing or decreasing resistivity, which significantly reduces the accuracy of saturation estimation in the classical saturation model. This paper developed an improved EREM model to obtain the saturation estimations with better precision. In the improved EREM model, all pores are divided into different groups according to their structures. The pore structures are characterized by four parameters. An optimization inversion was performed for the echo data of NMR in terms of the improved EREM to gain the C_d pathways which describe the pore structures. The data processing in our research shows that the saturation estimations from the improved EREM model seem to be in good alignment with the gas production. Based on the research above, the main conclusions of this paper can be summarized as the following three points (Leung et al., 2021Spangenberg, 2001Zhang et al., 2015).

1) The improved EREM model presents a better description of the conductivity characteristics of rocks in a nonlinear way, which objectively reveal the real conductivity mechanism of complex reservoirs.
2) Based on the classifications of pore structure, the saturation parameters are determined according to different pore structures. Its essence is to peel off the influence of pore structure and fluid distribution on rock resistivity, highlighting pore fluids' influence. Consequently, the saturation estimations are obtained with better precision for complex reservoirs.
3) Compared with the saturation estimations from the classical model, the improved EREM model shows more consistency with the physical occurrence mechanism of fluids in both the value and variation trend.

DATA AVAILABILITY STATEMENT

The original contributions presented in the study are included in the article/Supplementary Material, further inquiries can be directed to the corresponding author.

AUTHOR CONTRIBUTIONS

All authors listed have made a substantial, direct, and intellectual contribution to the work and approved it for publication.

FUNDING

This work is supported by the National 13th 5-Year Plan of Oil and Gas Program of China (No. 2017ZX05019-001), CNPC Research Project (No. 2017 F-16), National Natural Science Foundation of China (No. 41476027), and PetroChina Key Technological Program (No. 2016E-0503), all the research support funds are greatly appreciated.

REFERENCES

Abousrafa, E. M., Somerville, J. M., Hamilton, S. A., Olden, P. W. H., Smart, B. D. G., and Ford, J. (2009). Pore Geometrical Model for the Resistivity of Brine Saturated Rocks. *J. Pet. Sci. Eng.* 65, 113–122. doi:10.1016/j.petrol.2008.12.009

Aguilera, M. S., and Aguilera, R. (2003). Improved Models for the Petrophysical Analysis of Dual-Porosity Reservoir. *Petrophysics* 44 (1), 21–35.

Allori, D., Bartoli, G., and Miguel, A. F. (2011). "Wind Tunnel Similitude Criteria for Fluid Flow in Macro-Porous Materials," in *Proceedings of 7th International Conference on Diffusion in Solids and Liquids*, Vilamoura, Portugal, 312–313.

Archie, G. E. (1942). The Electrical Resistivity Log as an Aid in Determining Some Reservoir Characteristics. *Pet. Technol. Am. Inst. Mining Metallurgical Eng.* 146, 54–62. doi:10.2118/942054-g

Azar, J. H., Javaherian, A., Pishvaie, M. R., and Nabi-Bidhendi, M. (2008). An Approach to Defining Tortuosity and Cementation Factor in Carbonate Reservoir Rocks. *approach defining tortuosity cementation Factor carbonate reservoir rocksJournal Pet. Sci. Eng.* 60, 125–131. doi:10.1016/j.petrol.2007.05.010

Bauer, D., Youssef, S., Han, M., Bekri, S., Rosenberg, E., Fleury, M., et al. (2011). From Computed Microtomography Images to Resistivity index Calculations of Heterogeneous Carbonates Using a Dual-Porosity Pore-Network Approach: Influence of Percolation on the Electrical Transport Properties. *Phys. Rev. E Stat. Nonlin Soft Matter Phys.* 84, 11133. doi:10.1103/PhysRevE.84.011133

Bryant, S., and Pallatt, N. (1996). Predicting Formation Factor and Resistivity Index in Simple Sandstones. *J. Pet. Sci. Eng.* 15, 169–179. doi:10.1016/0920-4105(95)00066-6

Garcia, A. P., and Heidari, Z. (2021). Non-invasive Quantification of Throat-Size Distribution and Corresponding Capillary Pressure. *JOURNAL PETROLEUM SCIENCE ENGINEERING* 96, 1–9. doi:10.1016/j.petrol.2020.108019

Haro, C. F. (2006). "Permeability Modeling. Setting Archie and Carman-Kozeny Right," in *Paper Presented at the SPE Europec/EAGE Annual Conference and Exhibition*, Vienna, Austria. doi:10.2118/100200-MS

Huang, H., Tsang, L., Colliander, A., Shah, R., Xu, X., and Yueh, S. (2020). Multiple Scattering of Waves by Complex Objects Using Hybrid Method of T-Matrix and Foldy-Lax Equations Using Vector Spherical Waves and Vector Spheroidal Waves. *Pier* 168, 87–111. doi:10.2528/pier20080409

Kennedy, W. D., and Herrick, D. C. (2011). Conductivity Models for Archie Rocks. *GEOPHYSICS* 77 (3), WA109–WA128. doi:10.1190/geo2011-0297.1

Leung, T., Tien-Hao, L., and Shurun, T. (2021). Calculations of Bands and Band Field Solutions in Topological Acoustics Using the Broadband Green's Function-Kkr-Multiple Scattering Method. *Prog. Electromagnetics Res.* 171, 137–158. doi:10.2528/pier21081706

Liu, T., Zhou, C., and Zaitian, M. A., (2006). Restricted and Optimized Conditions of Sphere-Cylinder Model and its Applications [J]. *Journal of Tongji University (Natural Science)*. doi:10.1016/S1872-2032(06)60021-8

Liu, T. Y., Tang, T. Z., Du, H. H., Zhang, H-N., and Wang, H-T. (2013). The Study of Conductive Rock Mechanism Based on Pore Structure. *Chin. J. Geophys.* 56 (8), 2818–2826. (in Chinese). doi:10.1002/cjg2.20062

Man, H. N., and Jing, X. D. (2000). Pore Network Modelling of Electrical Resistivity and Capillary Pressure Characteristics. *Transport in Porous Media* 41, 263–285. doi:10.1023/a:1006612100346

Newgord, C., Garcia, A. P., and Heidari, Z. (2020). Joint Interpretation of Electrical Resistivity and T2 NMR Measurements to Estimate Wettability and Water Saturation. *SPE RESERVOIR EVALUATION ENGINEERING*, 23, 772–782. doi:10.2118/200499-pa

Ramamoorthy, R., Ramakrishnan, T. S., Dasgupta, S., and Raina, I. (2021). Towards a Petrophysical Consistent Implementation of Archie's Equation for Heterogeneous Carbonate Rocks. *PETROPHYSICS* 61 (5), 450–472. doi:10.30632/pjv61n5-2020a4

Shang, B. Z., Hamman, J. G., and Caldwell, D. H. (2003). "A Physical Model to Explain the First Archie Relationship and beyond, SPE 84300," in SPE Annual Technical Conference and Exhibition held in Denver, Colorado, USA, 5-8 October 2003 (Denver, Colorado: Society of Petroleum Engineers Inc.), 1–12.

Shi, X., Wang, P., Xu, J., Yang, H., and Xu, S. (2020). "Discovery of New Oil Reserves by Combining Production Logging with Open Hole Log Interpretation in Low Resistivity Pay," in Paper presented at the Offshore Technology Conference, Houston, Texas, USA, May 06, 2020. doi:10.4043/30644-MS

Shi, X., Zhang, J., Lu, Y., Han, Z., and He, Y. (2021). "Quantitative Evaluation of Water Flooding in a Low Resistivity Heavy Oil Reservoir with NMR and Conventional Logs," in Paper presented at the SPE Annual Technical Conference and Exhibition, Dubai, UAE, September 23, 2021. doi:10.2118/205928-MS

Song, Y. J., Wang, X. Y., and Tang, X. M. (2012). A Saturation Interpretation Model for Low Porosity and Permeability Reservoirs Based on the Pore Geometric Conduction Theory. *Logging Tech.* 36 (2), 124–129. (in Chinese). doi:10.16489/.issn.1004-1338.2012.02.004

Spangenberg, E. (2001). Modeling of the Influence of Gas Hydrate Content on the Electrical Properties of Porous Sediments. *J. Geophys. Res.* 106 (4), 6535–6548. doi:10.1029/2000jb900434

Suman, R. J., and Knight, R. J. (1997). Effects of Pore Structure and Wettability on the Electrical Resistivity of Partially Saturated Rocks-A Network Study. *Geophysics* 62 (4), 1151–1162. doi:10.1190/1.1444216

Tang, J., Fan, B., Xiao, L., Tian, S., Zhang, F., Zhang, L., et al. (2021). A New Ensemble Machine-Learning Framework for Searching Sweet Spots in Shale Reservoirs. *SPE J.* 26 (01), 482–497. doi:10.2118/204224-PA

Valagiannopoulos, C. (2021). Designing Nanoinclusions for Quantum Sensing Based on Electromagnetic Scattering Formalism (Invited Paper). *Prog. Electromagnetics Res.* 170, 1–15. doi:10.2528/pier20112306

Wang, H., and Liu, T., (2017). Derivation of Archie's Law Based on a Fractal Pore Volume. *Geophys. J. Int.* 209 (3), 1403–1407. doi:10.1093/gji/ggx095

Xue, M., Zhang, H., and Liu, T., (2017). Novel Method to Quantitatively Evaluate Pore Structures by Sphere-cylinder Model [J]. *Well Logging Technology*. doi:10.3969/j.issn.1004-1338.2014.01.009

Zhan, Q., Wang, Y., Fang, Y., Ren, Q., Yang, S., Yin, W.-Y., et al. (2021). "An Adaptive High-Order Transient Algorithm to Solve Large-Scale Anisotropic Maxwell's Equations," in Proceeding of the IEEE Transactions on Antennas and Propagation, September 2021 (IEEE), 1. doi:10.1109/tap.2021.3111639

Zhan, Q., Zhuang, M., Mao, Y., and Liu, Q. H. (2020). Unified Riemann Solution for Multi-Physics Coupling: Nisotropic Poroelastic/elastic/fluid Interfaces. *J. Comput. Phys.* 402, 108961. doi:10.1016/j.jcp.2019.108961

Zhang, H. N., Tang, T. Z., Liu, T. Y., Sun, P., and Jiang, L-M. (2015). Saturation Evaluating Method Based on Pore Structure. *Prog. Geophysta* 30 (2), 0709–0717. doi:10.6038/pg20150231

Zhang, L., Abbaspourrad, A., Parsa, S., Tang, J., Cassiola, F., Zhang, M., et al. (2020). "Core-Shell Nanohydrogels with Programmable Swelling for Conformance Control in Porous Media," in *ACS Appl. Mater. Inter.*, 12, 34217–34225. doi:10.1021/acsami.0c09958

Conflict of Interest: The authors declare that the research was conducted in the absence of any commercial or financial relationships that could be construed as a potential conflict of interest.

Publisher's Note: All claims expressed in this article are solely those of the authors and do not necessarily represent those of their affiliated organizations, or those of the publisher, the editors, and the reviewers. Any product that may be evaluated in this article, or claim that may be made by its manufacturer, is not guaranteed or endorsed by the publisher.

frontiers in Earth Science

METHODS
published: 11 February 2022
doi: 10.3389/feart.2022.808183

Numerical Analysis of Zipper Fracturing Using a Non-Planar 3D Fracture Model

Zhen Wang[1,2]*, *Lifeng Yang*[1,2], *Rui Gao*[1,2], *Guanshui Xu*[3], *Zhe Liu*[1,2], *Shaoyuan Mo*[1,2], *Meng Fan*[1,2] *and Xin Wang*[1,2]

[1]CNPC Key Laboratory of Oil and Gas Reservoir Stimulation, Langfang, China, [2]Research Institute of Petroleum Exploration and Development, PetroChina, Beijing, China, [3]University of California, Riverside, Riverside, CA, United States

Zipper fracturing has become one of the routine reservoir stimulation methods for developing unconventional resources such as shale oil and gas. A non-planar 3D fracture propagation model is used to study the fracture propagation behavior of zipper fracturing. The effects of stage time lag, staggered perforation cluster spacing, and horizontal principal stress contrast on the fracture geometry are analyzed through numerical simulation. The simulation results show that increasing the stage time lag can increase the fracture length and improve inter-well stimulation. For the formation with higher horizontal principal stress contrast, the staggered perforation cluster spacing has a minimum effect on the fracture configuration of zipper fracturing. For the formation with lower horizontal principal stress contrast, the fractures follow the curved paths and intersect with each other, which potentially has adverse effects on the stimulation of the subsequent stages.

Keywords: zipper fracturing, stress interference, frac hit, 3D fracture propagation, proppant transport

OPEN ACCESS

Edited by:
Shengnan Chen,
University of Calgary, Canada

Reviewed by:
Fengshou Zhang,
Tongji University, China
Jiawei Li,
Texas A&M University, United States

***Correspondence:**
Zhen Wang
wangzhen69@petrochina.com.cn

Specialty section:
This article was submitted to Economic Geology, a section of the journal Frontiers in Earth Science

Received: *03 November 2021*
Accepted: *11 January 2022*
Published: *11 February 2022*

Citation:
Wang Z, Yang L, Gao R, Xu G, Liu Z, Mo S, Fan M and Wang X (2022) Numerical Analysis of Zipper Fracturing Using a Non-Planar 3D Fracture Model. Front. Earth Sci. 10:808183. doi: 10.3389/feart.2022.808183

1 INTRODUCTION

The development of hydraulic fracturing technology for unconventional petroleum resources has been a subject of considerable interest in recent years (Soliman et al., 2008; Li et al., 2017; Zhang et al., 2017; Zhang et al., 2019; Xie et al., 2020; Zhang et al., 2021a; Zhang et al., 2021b). Multistage, multicluster fracturing (MMF) of horizontal wells has become widely used to produce hydrocarbon from unconventional reservoirs, such as shales and tight sandstones. As shown in **Figure 1A**, the consecutive-fracturing sequence is the most commonly used fracturing sequence of MMF for a single horizontal well. In consecutive fracturing, fractures are created sequentially stage by stage along the same wellbore. Another fracturing sequence of MMF in a single horizontal well, referred to as "alternate fracturing," was proposed to decrease fracture spacing and generate additional fracture complexity (Roussel and Sharma 2011). This strategy places the second fracture at the location of what would traditionally be the third fracture, followed by the propagation of a "middle fracture" (**Figure 1B**). However, due to the limitations of fracturing tools and fracturing technique levels, the alternate fracturing method is rarely used for practical hydraulic-fracturing treatments. Zipper fracturing is also proposed as a method to improve production performance in wells in pad-drilling applications. Specifically, this method refers to fracturing two or more parallel horizontal wells. The fracturing treatment is performed stage by stage alternatively along the two wells. The method saves the pump-down and plug-and-perf standby time and, therefore improves operational efficiency compared with consecutive fracturing in one well. It is also expected that the treatment further

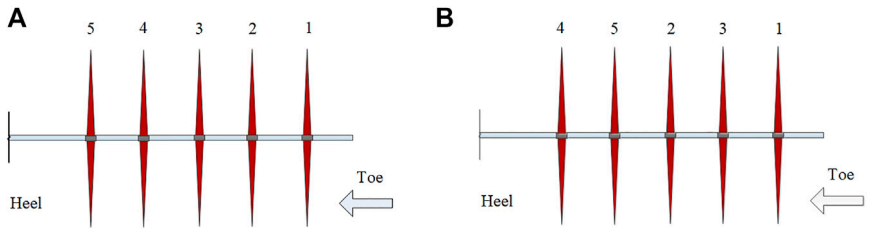

FIGURE 1 | Sketch of two fracturing sequence in the single horizontal well. **(A)** Consecutive sequence (1-2-3-4-5); **(B)** alternate sequence (1-3-2-4-5).

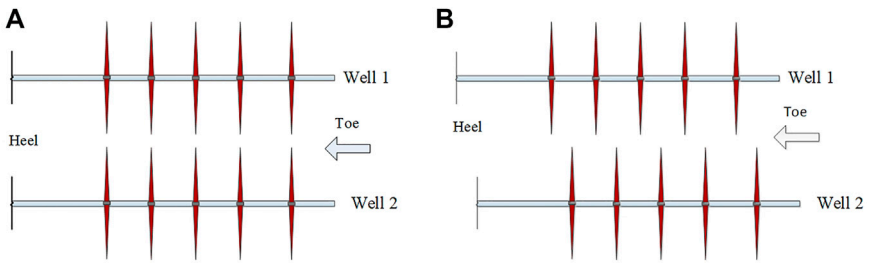

FIGURE 2 | Sketch of two completion scenarios of zipper fracturing in two horizontal wells. **(A)** Tip-to-tip zipper fracturing configuration; **(B)** staggered zipper fracturing configuration.

promotes fracture network complexity to improve production performance (Qiu et al., 2015). **Figure 2** illustrates the two completion scenarios of zipper fracturing. The so called "tip-to-tip" zipper fracturing is shown in **Figure 2A**, and staggered zipper fracturing is shown in **Figure 2B**. In a practical stimulation treatment, it is nearly impossible to guarantee the precise tip-to-tip fracture placement in two horizontal wells. Therefore, we consider the tip-to-tip configuration as the special case of staggered zipper fracturing. Only staggered zipper fracturing is studied in this paper.

Various mathematical models have been used to evaluate the effectiveness and performance of zipper fracturing. Rafiee et al. (2012) estimated both tip-to-tip and staggered zipper in terms of the fracture geometry, stress interference, and production performance through an analysis of different predefined planar fractures. The results demonstrated that the staggered zipper fracturing improves the performance of fracturing treatment compared with the tip-to-tip zipper fracturing due to increased contact area. Using a poroelastic model, Manchanda et al. (2014) studied the time-dependent stress interference behavior of induced unpropped fractures in both consecutive and zipper fracturing. The results showed that the time interval between adjacent fractures in a wellbore is a key parameter for the design of treatments. The longer time interval leads to stress shadow shrinking from the closure of the induced unpropped fractures, resulting in less fracture interference and improved performance. The model also assumed the predefined planar fracture in the numerical analysis. Shen (2014) investigated the influence of neighboring stimulation stages on generating the stimulated reservoir volume (SRV) with a continuum damage model based on a hydro-mechanical finite element method (FEM). The results indicated that the SRV generated by the sequential injection method is significantly less than that generated by the simultaneous injection method. Nagel et al. (2014) presented a study of multiwell completion using a hydromechanical coupled discrete element model. The results showed that the improvement in well stimulation using the zipper-fracturing completion technique is highly dependent on the *in situ* pore pressure, *in situ* stresses, and natural fracture characteristics. Sierra and Mayerhofer (2014) reviewed and discussed numerical reservoir-modeling results of zipper fracturing and demonstrated that the benefits of zipper fracturing could be maximized by generating proper fracture geometry and properly staggering the perforation/fracture system. Qiu et al. (2015) studied zipper fracturing using an unconventional fracture model capable of simulating branched fracture propagation. The quantitative results show that zipper fracturing may not deliver an obvious production benefit compared with sequential fracturing, depending on well spacing and perforation cluster spacing. Shi et al. (2018) applied the extended finite element method (XFEM), which is based on the cohesive zone method (CZM), to model fracture propagation at a reservoir with different mechanical homogeneities. The numerical studies confirmed that a staggered zipper fracturing scenario could assist hydraulic fracture propagation along a straight path.

The displacement discontinuity method (DDM) is widely used in dealing with fracture deformation problems for its high computational efficiency (Tang et al., 2018; Tang et al., 2019; Cong et al., 2021a; Cong et al., 2021b; Li et al., 2021). In this paper,

we adopt a nonplanar 3D fracture model, based on 3D DDM, to investigate the fracture propagation behavior of zipper fracturing. The effects of the stage time lag, staggered perforation cluster spacing, and stress contrast will be studied in detail. Here the stage time lag refers to the time interval between the adjacent two fracturing stages. The nonplanar 3D fracture model simulates fracture propagation, fluid flow, and proppant transportation in a fully coupled hydromechanical manner (Xu and Wong 2013). The special feature of this model includes fracture closure in shut-in and curved fracture intersection, which makes quantitative analysis of time-dependent fracture interference and intersection possible.

2 NON-PLANAR 3D FRACTURE MODEL

Mathematical formulations

The adopted non-planar 3D fracture model assumes that all fractures are vertical and can turn in the horizontal direction. The fractures are discretized into structured rectangular elements, and all field variables, such as fracture opening, shear displacement, fluid pressure, and proppant volumetric concentration, are registered and associated with these elements. Fractures are assumed to be filled with slurry (the mixture of fracturing fluid and proppants), and fluid lag at the crack tip region is neglected.

Specifically, the fracture deformation is described by the 3D displacement discontinuity method (Shou 1994):

$$\begin{cases} -\sigma_{sl}^{i} = \sum_{k=1}^{N} K_{sl,sl}^{ik} D_{sl}^{k} + \sum_{k=1}^{N} K_{sl,sh}^{ik} D_{sh}^{k} + \sum_{k=1}^{N} K_{sl,nn}^{ik} D_{nn}^{k} \\ -\sigma_{sh}^{i} = \sum_{k=1}^{N} K_{sh,sl}^{ik} D_{sl}^{k} + \sum_{k=1}^{N} K_{sh,sh}^{ik} D_{sh}^{k} + \sum_{k=1}^{N} K_{sh,nn}^{ik} D_{nn}^{k} \\ p - \sigma_{nn}^{i} = \sum_{k=1}^{N} K_{nn,sl}^{ik} D_{sl}^{k} + \sum_{k=1}^{N} K_{nn,sh}^{ik} D_{sh}^{k} + \sum_{k=1}^{N} K_{nn,nn}^{ik} D_{nn}^{k} \end{cases} \tag{1}$$

where D_{nn} is the normal displacement discontinuity; D_{sl}, D_{sh} is the shear displacement discontinuity in the fracture length and height direction, respectively; p is the fluid pressure; and σ_{nn}, σ_{sl}, and σ_{sh} are the effective formation normal and shear stress, which can be calculated from the remote *in situ* stress through the principle of superposition. The nine matrices Ks are the boundary influence matrices related to the element size, location, and orientation, as well as the elastic constants. The superscripts i and k represent the element index; N is the total number of elements.

The fluid flow and proppant transport within a fracture are represented by the volume conservation equations (Adachi et al., 2007):

$$\frac{\partial w}{\partial t} = \nabla \cdot \left[w(1-c)\mathrm{v}^{f} + wc\mathrm{v}^{p} \right] + \delta(x,y) q_0 - q_l \tag{2}$$

$$\frac{\partial (cw)}{\partial t} = \nabla \cdot (cw\mathrm{v}^{p}) + \delta(x,y) c_0 q_0 \tag{3}$$

where t is the time; w is the fracture width, namely, normal displacement discontinuity D_{nn}; c is the volume concentration of the proppants; q_0 is the fluid injection rate; c_0 is the specified proppant volume concentration in fluid injection; $\delta(x, y)$ is the Dirac delta function; and q_l corresponds to the fluid leak-off rate following a one-dimensional Carter type leak-off model:

$$q_l = \frac{2C_L}{\sqrt{t - \tau(x,y)}} \tag{4}$$

where $\tau(x, y)$ is the time at which the surface position is first exposed to the fracturing fluid, and C_L is the Carter leak-off coefficient.

v^f and v^p are volume averaged velocities of the fracturing fluid and proppant, respectively, described as:

$$\mathrm{v}^{f} = \frac{w^2}{12\mu^{f}} Q^{f}\left(c, \frac{w}{a}\right)\left(\nabla p - \rho^{f}\mathbf{g}\right) \tag{5}$$

$$\mathrm{v}^{p} = Q^{p}\left(c, \frac{w}{a}\right)\left(\mathrm{v}^{f} + \mathrm{v}^{s}\right) \tag{6}$$

where p is the fluid pressure, $\mathbf{g}$ is the gravity vector, a is the proppant radius, μ^f is the apparent viscosity of fracturing fluid, ρ^f is the fracturing fluid density, and v^s is the proppant settling velocity, given by:

$$\mathrm{v}^{s} = \frac{a^2}{12\mu^{f}}\left(\rho^{p} - \rho^{f}\right)\mathbf{g} \tag{7}$$

where ρ^p is the proppant density.

Function $Q^f(c, \frac{w}{a})$ reflects the effects of proppant concentration on the fracturing fluid viscosity and captures the transition from Poiseuille's flow to Darcy's filtration flow when the concentration reaches the maximum value, which can be written as (Dontsov and Peirce 2015):

$$Q^{f}\left(c, \frac{w}{a}\right) = \left(1 - \frac{c}{c_{max}}\right)^{\beta} + \frac{a^2}{w^2}\frac{c}{c_{max}}\tilde{D} \tag{8}$$

where $\beta = 1.5$, $\tilde{D} = 8(1 - c_{max})^{\alpha}/3c_{max}$, $\alpha = 4.1$, and $c_{max} = 0.585$.

Blocking function $Q^p(c, \frac{w}{a})$ is equal to 0 when proppant bridging appears or proppant concentration arrives at the maximum value, and 1 otherwise, which can be evaluated from experimental data for specific fracturing materials.

To include the limited entry technique, the perforation pressure drop p_r is modeled by the Bernoulli equation (Long and Xu 2017):

$$p_r = \frac{8\rho}{\pi^2 C_d^2 d_p^4}\left(\frac{q_{ri}}{n}\right)^2 \tag{9}$$

where C_d is the dimensionless discharge coefficient; d_p is the perforation diameter; q_{ri} is the volumetric injection rate at a specific injection location; n the number of perforations at the specific injection location; ρ is the slurry density, and $\rho = (1 - c)\rho^f + c\rho^p$. It is assumed that the pressure at the perforation in the wellbore is equal everywhere.

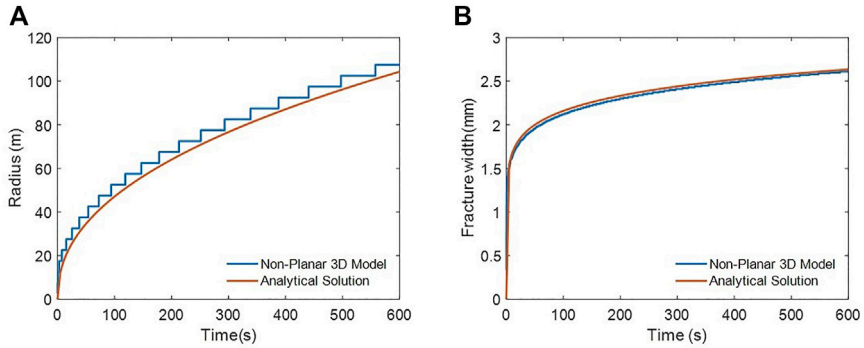

FIGURE 3 | Comparisons between nonplanar 3D model and analytical solutions. **(A)** Radius; **(B)** fracture width.

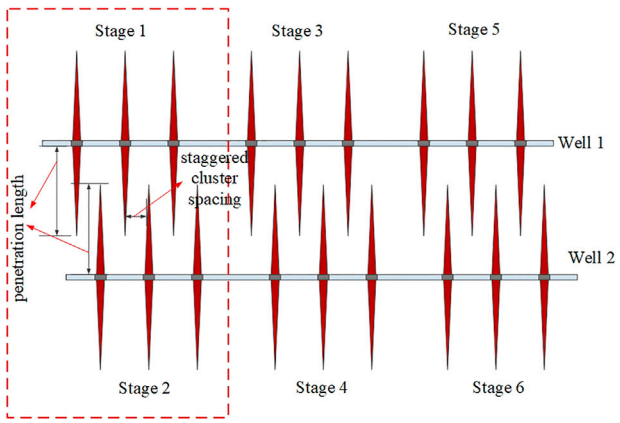

FIGURE 4 | Sketch of zipper fracturing.

Numerical procedure

The volume conservation **Eqs. 2** and **3** for fluid and proppant are discretized by the finite volume method as follows:

$$w^{t+\Delta t} = w^t + \left(\sum_M l_{nm} q_{nm}\right)\frac{\Delta t}{A_n} + q_0\frac{\Delta t}{A_n} - 4C_L\left(\sqrt{t+\Delta t - t_0} - \sqrt{t - t_0}\right) \quad (10)$$

$$c^{t+\Delta t} = c^t + \left(\sum_M l_{nm} q^p_{nm}\right)\frac{\Delta t}{w_n A_n} + c_0 q_0 \frac{\Delta t}{w_n A_n} \quad (11)$$

where Δt is the time step, A_n is the area of element n, t_0 is the time at which the element position is first exposed to the fracturing fluid, l_{nm} is the length of the intersection line between elements n and m, and M is the number of surrounding elements of element n. The subscript nm indicates the interface between element n and m. The interface slurry flux q_{nm} is expressed as:

$$q_{nm} = q^f_{nm} + q^p_{nm} \quad (12)$$

The interface fluid flux q^f_{nm} is given by:

$$q^f_{nm} = (1 - c_{nm})\frac{w^3_{nm}}{12\mu^f_{nm}} Q^f_{nm}\left(c, \frac{w}{a}\right)\left(\frac{p_n - p_m}{D_{nm}} - \rho^f_{nm} g_{nm}\right) \quad (13)$$

The interface proppant flux q^p_{nm} is:

$$q^p_{nm} = c_{nm} Q^p_{nm}\left(c, \frac{w}{a}\right)\left(\frac{w^3_{nm}}{12\mu^f_{nm}} Q^f_{nm}\left(c, \frac{w}{a}\right)\left(\frac{p_n - p_m}{D_{nm}} - \rho^f_{nm} g_{nm}\right) + w_{nm}\frac{a^2_{nm}}{12\mu^f_{nm}}\left(\rho^p_{nm} - \rho^f_{nm}\right) g_{nm}\right) \quad (14)$$

where D_{nm} is the distance between the two central nodes of element n and m. The interface variables a, c, w, ρ^f, ρ^p, μ^f are determined by upwind scheme.

The elasticity **Eq. 1** and volume conservation **Eqs 10–11** form a set of transient nonlinear coupled equations, with the fracture width w, fluid pressure p, and proppant

TABLE 1 | Basic input parameters.

Fluid properties		Proppant properties	
Viscosity (Pa.s)	**Density (kg/m^3)**	**Diameter (mm)**	**Density (kg/m^3)**
0.1	1,000	0.2	2,500
Formation properties			
Young's modulus (GPa)	Poission's ratio	Toughness (MPa·m$^{0.5}$)	Leak-off (m/s$^{0.5}$)
20	0.25	1	2×10^{-5}
Injection parameters			
Perforation diameter (mm)		Dimensionless discharge coefficient Cd	No. of perforations
10		0.6	12

TABLE 2 | Pumping schedule.

Injection rate (m^3/min)	Injection time (min)	Proppant volume fraction	Proppant weight fraction (kg/m^3)	Stage
12	10	0	0	1
12	10	0.05	131.579	1
12	10	0.1	277.778	1
12	10	0.15	441.176	1
12	10	0.2	625	1
12	10	0.25	833.333	1
0	60	0	0	1
12	10	0	0	2
12	10	0.05	131.579	2
12	10	0.1	277.778	2
12	10	0.15	441.176	2
12	10	0.2	625	2
12	10	0.25	833.333	2
0	120	0	0	2

concentration c as the primary variables. The coupled nonlinear equations are solved in an explicit time-stepping method with an adaptive time integration algorithm. For a given time step Δt, substituting the known w, p, and c of the last time step into **Eqs. 1**, **10**, and **11**, the primary variables of the current time step can be easily obtained.

Fracture advances when the mode I (opening) stress intensity factor K_I of the crack tip element exceeds the fracture toughness K_{Ic} of the rock, namely:

$$K_I \geq K_{Ic} \tag{15}$$

where $K_I = 0.806\frac{\sqrt{\pi}E}{4(1-\upsilon^2)\sqrt{\Delta a}}D_{nn}$, and Δa is the crack tip element length; E is Young's modulus, and υ is Poisson's ratio.

The direction of fracture growth is oriented along with the maximum horizontal principal stress, which is expressed by:

$$\theta = \begin{cases} 2\tan^{-1}\left(\frac{1}{4}\frac{K_I}{K_{II}} + \frac{1}{4}\sqrt{\left(\frac{K_I}{K_{II}}\right)^2 + 8}\right), & when\ \frac{K_I}{K_{II}} < 0 \\ 2\tan^{-1}\left(\frac{1}{4}\frac{K_I}{K_{II}} - \frac{1}{4}\sqrt{\left(\frac{K_I}{K_{II}}\right)^2 + 8}\right), & when\ \frac{K_I}{K_{II}} > 0 \end{cases} \tag{16}$$

where θ is the propagation angle, which is in the polar coordinate system with the origin at the crack tip; K_{II} is the stress intensity factor of mode II (shearing) in the length direction and given by $K_{II} = 0.806\frac{\sqrt{\pi}E}{4(1-\upsilon^2)\sqrt{\Delta a}}D_{sl}$.

The model is validated by comparing with existing asymptotic analytical solutions of penny-shaped hydraulic fracture propagation (Dontsov 2016), where the viscosity-dominated fracture configuration is described by:

$$r(t) = 0.6944\left(\frac{q_0^3 E t^4}{12\mu(1-\upsilon^2)}\right)^{\frac{1}{9}}$$
$$w_{in}(t) = 0.1901\left(\frac{(12\mu)^2(1-\upsilon^2)^2 q_0^3 t}{E^2}\right)^{\frac{1}{9}} \tag{17}$$

where r is the fracture radius, and w_{in} is the fracture width at the inlet. The input parameters are listed as $q_0 = 5\ m^3$/min, $\mu = 5$ mPa·s, $E = 30$ GPa, $\nu = 0.20$, $K_{Ic} = 0.2$ MPa·$m^{0.5}$, $C_L = 0$ m/$s^{0.5}$, $t = 10$ min. The results (**Figure 3**) show a good agreement between our non-planar 3D model and analytical solutions.

3 MODELING DETAILS AND RESULTS

Basic inputs

This section presents a detailed study of the effects of various parameters on zipper fracturing, including the stage time lag, perforation cluster spacing, and stress contrast. A typical two-horizontal-well zipper fracturing with staggered fractures is considered as shown in **Figure 4**. Each stage has three perforation clusters. Without loss of generality, only stage 1 and stage 2 are selected to be analyzed. Here we define the length of the part of a fracture between two horizontal wells as penetration length, which can reflect the interwell stimulation effectiveness to some extent. The staggered perforation cluster spacing is also shown in **Figure 4** as the spacing between two adjacent perforation clusters in the two horizontal wells. We assume that the perforation cluster has an even spacing in the single horizontal well.

The basic inputs of the simulations, such as treatment, reservoir and completion parameters, are listed in **Table 1**. The formation is assumed to have three layers. The thickness of the perforated zone is 60 m and sandwiched by two stress-barrier zones with 5 MPa *in situ* stress confinement. The stress confinement contains the vertical height of the fracture; as a result, we can focus on the fracture-width distribution and length

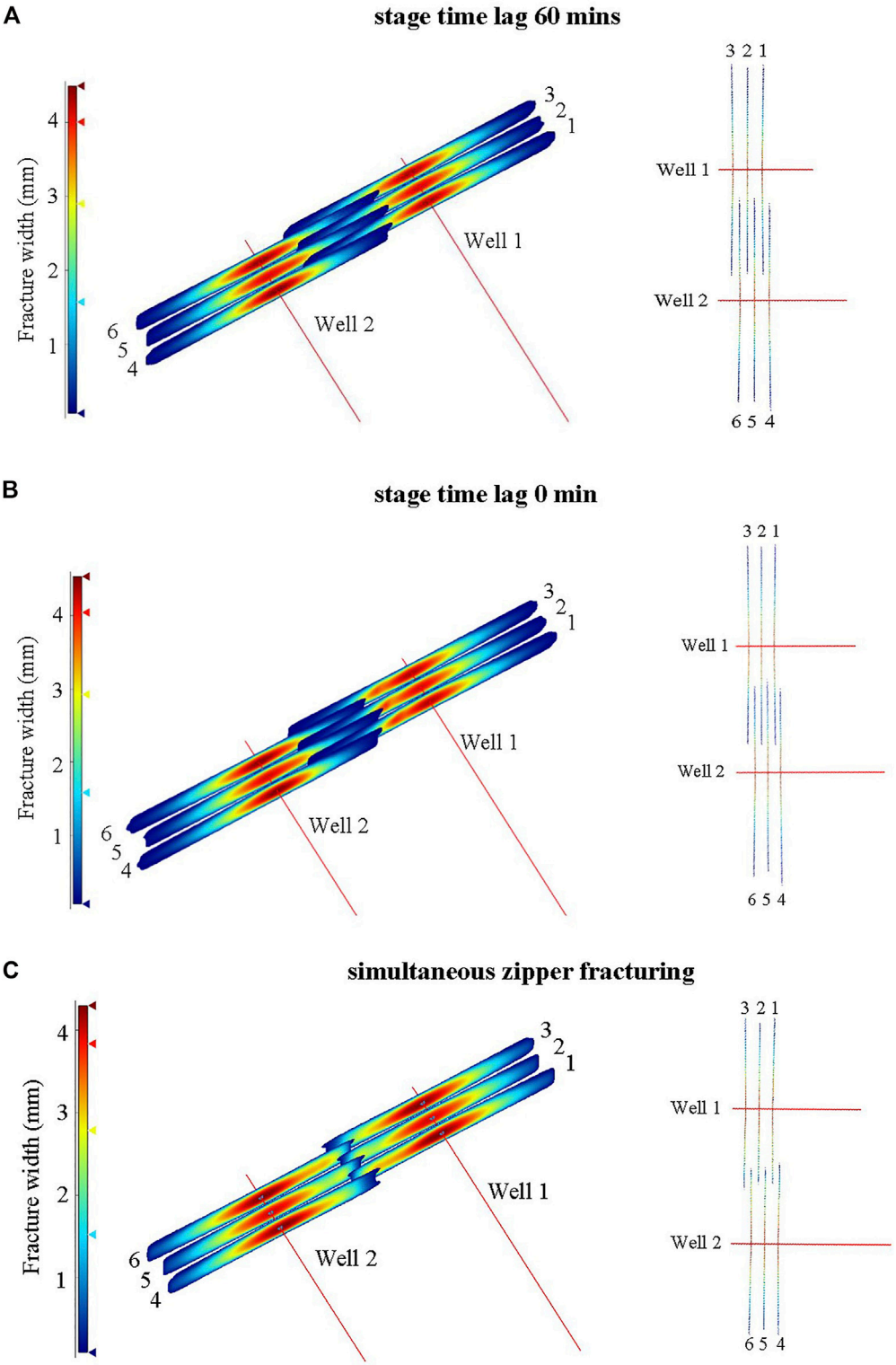

FIGURE 5 | Fracture configuration of different well completions. **(A)** Side view (left) and top view (right) of sequential zipper fracturing, stage time lag 60 min; **(B)** side view (left) and top view (right) of sequential zipper fracturing, stage time lag 0 min; **(C)** side view (left) and top view (right) of simultaneous zipper fracturing.

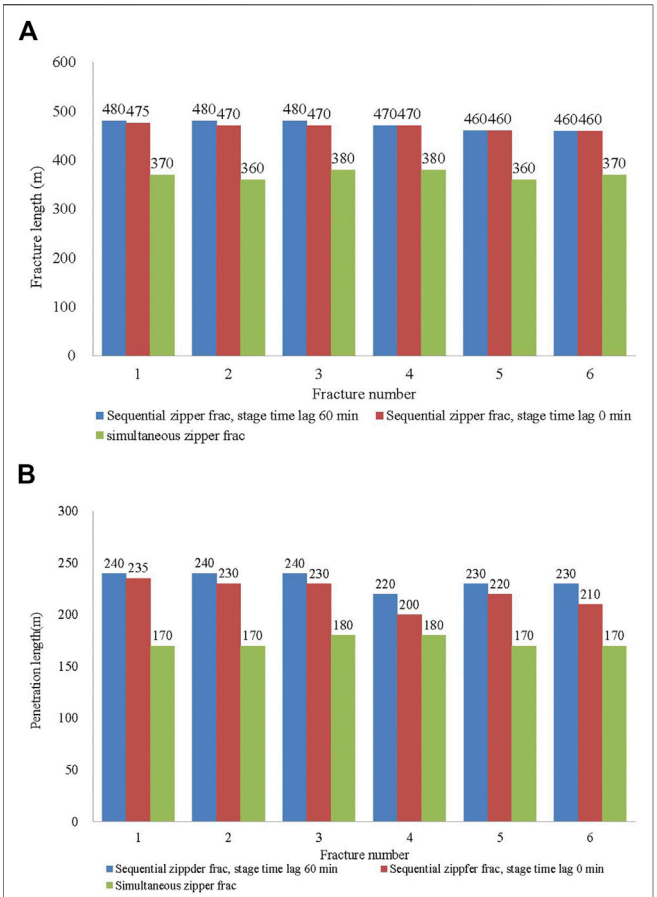

FIGURE 6 | Fracture length and penetration length of different well completions. **(A)** Fracture length; **(B)** penetration length.

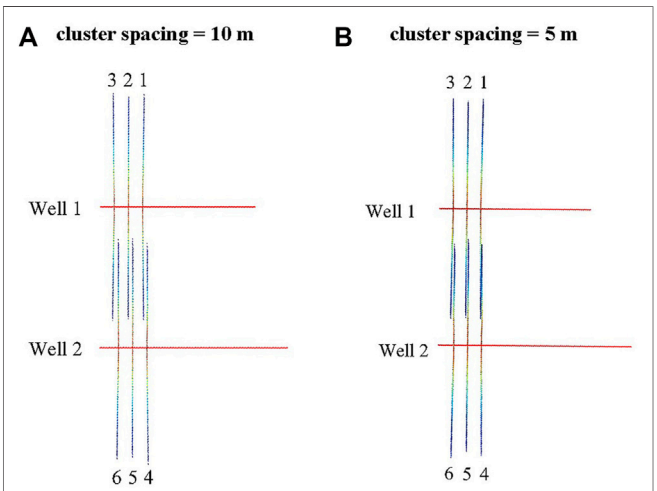

FIGURE 7 | Fracture configuration of irregular staggered zipper fracturing. **(A)** Top view of fracture configuration with staggered perforation cluster spacing 10 m; **(B)**: top view of fracture configuration with staggered perforation cluster spacing 5 m.

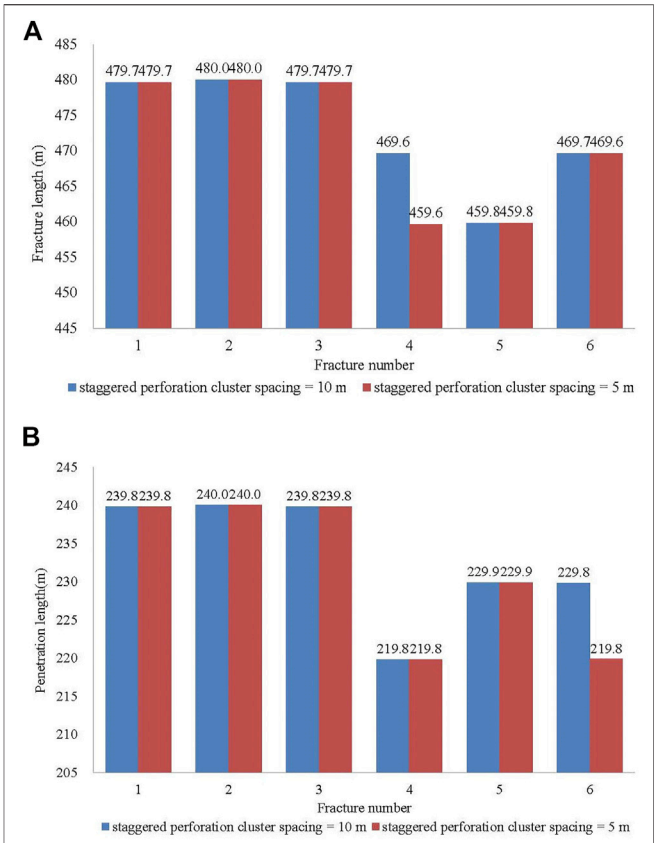

FIGURE 8 | Fracture size of irregular staggered zipper fracturing. **(A)** Fracture length; **(B)** penetration length.

when performing sensitivity analysis. The horizontal principal stress contrast is 10 MPa, and the well spacing is 300 m. The perforation cluster spacing of both wells is 30 m, and the staggered perforation cluster spacing is 15 m. **Table 2** presents the pumping schedule. The slurry injection rate is 12 m^3/min, and the total injection time is 60 min for one stage with a total proppant of 277 tons. The time lag between stage 1 in well 1 and stage 2 in well 2 is 60 min. The two stages use the same pumping schedule. After slurry injection, a 120-min shut-in time ensures that the fracturing fluid can leak off adequately and release the fluid pressure thoroughly. If not specified, the above-mentioned parameters are used for all the simulations.

Influence of stage time lag

Three zipper fracturing scenarios are presented and analyzed to investigate the influence of the stage time lag of a two-horizontal-well zipper fracturing on fracture growth. **Figure 5** shows the fracture configurations of different well completions. **Figure 5A** is side and top view of the basic model of sequential zipper fracturing with a 60-min stage time lag, as shown in the section 3.1. **Figure 5B** is side and top view of a sequential zipper fracturing without the stage time lag. **Figure 5C** is side and top view of a case of simultaneous zipper fracturing. Especially, for simultaneous zipper fracturing, the pumping schedule merges to one stage for the two wells, and the

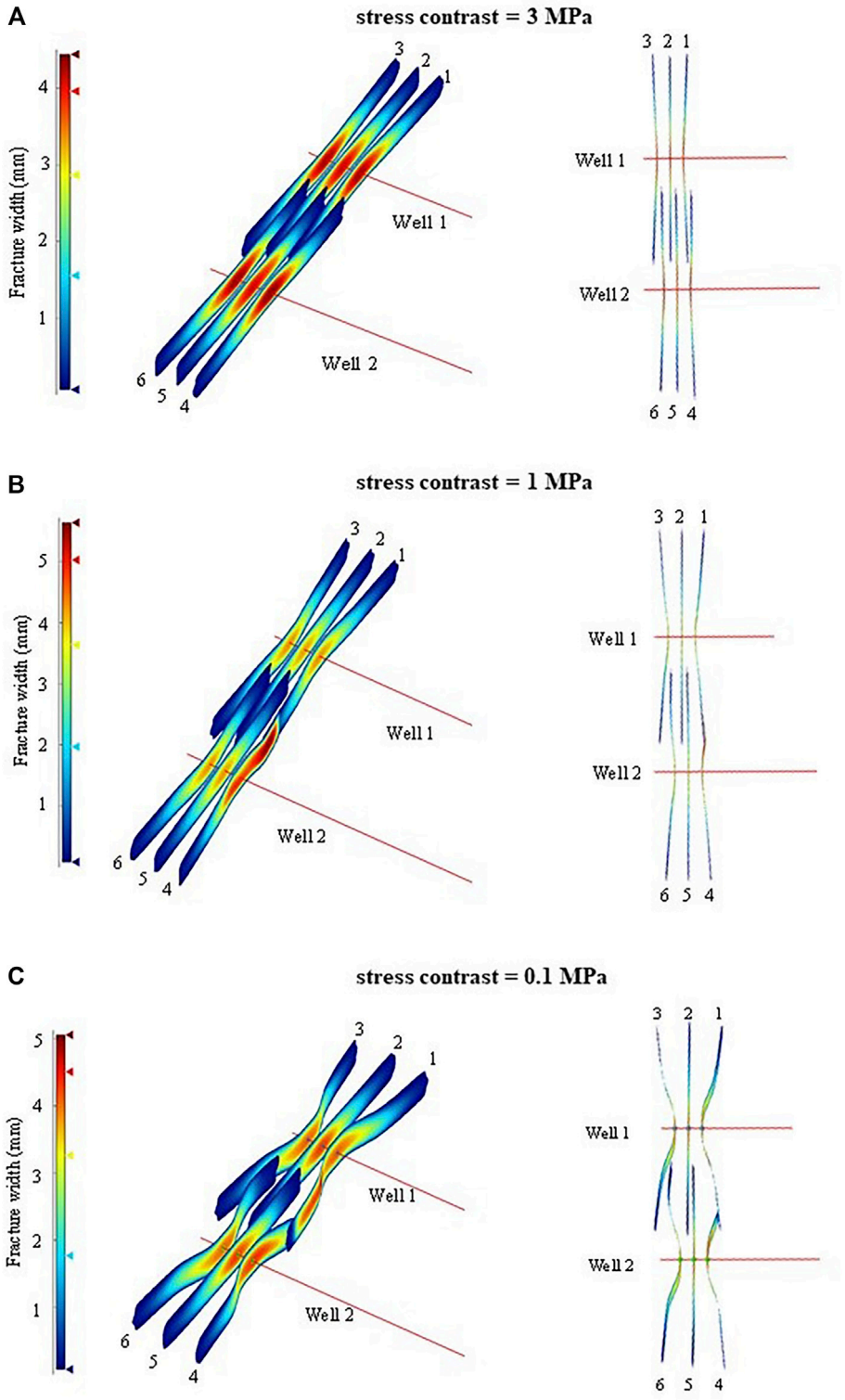

FIGURE 9 | Fracture configuration of different stress contrast scenarios. **(A)** Side view (left) and top view (right), stress contrast 3 MPa; **(B)** side view (left) and top view (right), stress contrast 1 MPa; **(C)** side view (left) and top view (right), stress contrast 0.1 MPa.

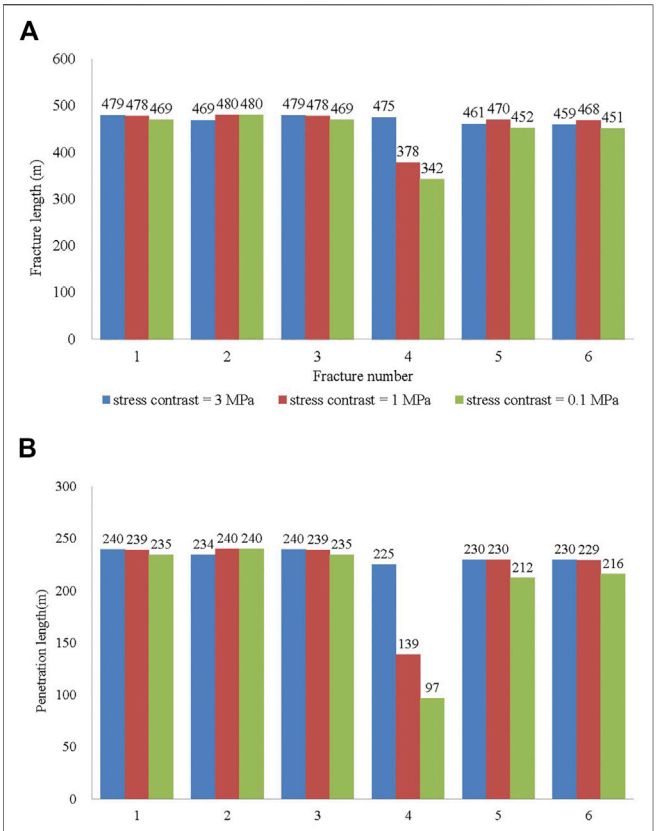

FIGURE 10 | Fracture size under different stress contrast scenarios. **(A)** Fracture length; **(B)**: penetration length.

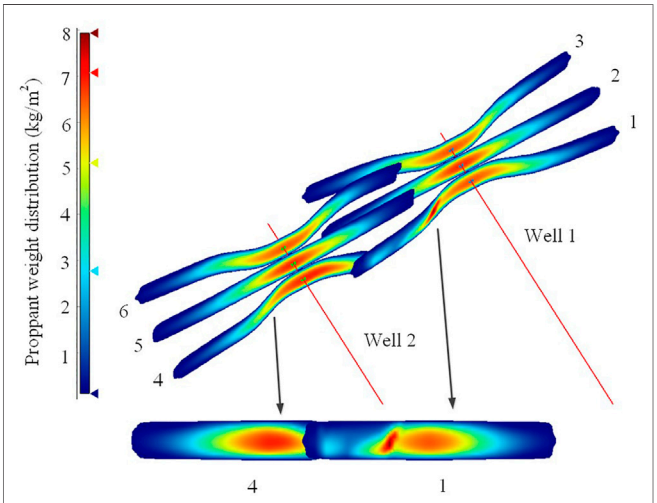

FIGURE 11 | Proppant weight distribution in fractures under 0.1-MPa stress contrast condition.

injection time doubles. **Figure 6** presents the fracture length and penetration length of hydraulically induced fractures of the corresponding well completion.

FIGURE 12 | Rod tubing filled with proppant sand during a frac-hit; cited from Jacobs (2017).

The results in **Figures 5**, **6** indicate that the stage time lag substantially influences fracture configuration. For the sequential zipper fracturing, as the stage time lag reduces, both the fracture length and the penetration length of well 1 decrease, as shown in **Figures 5A**,**B**, **6**. This implies that during the stage time lag, the fractures in well 1 continue propagating while leak-off, and this is caused by the rebalancing of fluid pressure in the fracture even though there is no fluid injection. Although the two stages employ the same pumping schedule, the induced fractures of stage 1 changed the local stress field around fractures, so the hydraulically induced fractures of stage 2 in well 2 are suppressed, to some extent, by the fractures of stage 1 in well 1. When the stage time lag reduces to zero, the fracture growth of stage 2 influences the rebalancing of fluid pressure of fractures in stage 1 and, thus, suppresses the further growth of fractures in stage 1. This is why the fracture length of well 1 with no stage time lag is less than the fracture length of well 1 with a 60-min stage time lag as shown in **Figure 6**. It is noteworthy that interwell/interstage interference is mutual, i.e., all of the fracture propagation in stage 1 and stage 2 are influenced by each other. The fracture length of well 2 does not seem to change for the two scenarios of the sequential zipper fracturing, but the penetration length decreases for the well with less stage time lag. The fracture tends to propagate away from the interwell region, which may result in inefficient interwell stimulation. The simultaneous zipper fracturing has the most severe interwell/interstage interference; the fracture length and penetration length decrease about 20% compared with sequential zipper fracturing, as shown in **Figures 5C**, **6**. The corresponding inter-well stimulation effectiveness is worst.

Influence of staggered perforation cluster spacing

To study the influence of staggered perforation cluster spacing on zipper fracturing, we decrease the staggered perforation cluster spacing to 10m and 5 m. Compared with **Figure 5A**, **Figure 7**

shows that the fracture configuration still keeps nearly straight under the 10MPa horizontal principal stress contrast, even for the 5m perforation cluster spacing. Compared with **Figure 6**, **Figure 8** shows that the fracture length and penetration length remain almost the same in the three scenarios. Decreasing the staggered perforation cluster spacing has virtually no effect on the fracture configuration of zipper fracturing in this stress contrast condition. Consequently, we may conclude that one can design small perforation cluster spacing in one stage and small staggered perforation cluster spacing of two wells to further improve interwell stimulation effectiveness under high stress contrast conditions.

Influence of horizontal principal stress contrast

To study the influence of horizontal principal stress contrast on zipper fracturing, we decreased the horizontal principal stress contrast to 3MPa, 1MPa, and 0.1 MPa. Compared with **Figure 5A**, **Figures 9**, **10** show that fracture-induced stress interference and inter-well interference significantly affect the fracture configuration. As shown in **Figure 9**, the two outer fractures of well 1 curve more as the stress contrast decreases. After some curved distance, the two outer fractures propagate again along the direction of in situ maximum horizontal principal stress. This is due to the less stress interference with the increase in fracture spacing. The inner fracture always keeps straight propagation because of the balance of two opposite stress interference caused by the outer fractures. Overall, the three fractures of well 1 for different scenarios present a uniform propagation pattern. The fracture length difference is less than 4% as shown in **Figure 10A**. The propagation of the three fractures of well 2 are affected by the interwell interference of well 1 and their own interfracture interference. Hence, the fractures grow shorter than the ones of well 1 and curve noticeably. It is worth noting that fracture 4 intersects with fracture 1 of well 1 under 1 and 0.1 MPa stress contrast, resulting in "frac hits" between the two wells. The fracture width and proppant weight distribution (**Figures 9C**, **11**) show that after frac hits, the fracturing fluid and proppant of fracture 4 enter fracture 1, which causes fracture 1 to reopen and proppant transport toward the wellbore of well 1. This may result in a negative effect on the successive stimulation treatment and production. The simulation results in this section also confirm the proppant sand production phenomenon during a frac-hit in a practical treatment, as shown in **Figure 12** cited from Jacobs (2017).

4 CONCLUSION

In this paper, we investigate the effects of the stage time lag, staggered perforation cluster spacing, and horizontal principal stress contrast on the behavior of zipper fracturing. Based on our analyses, we have the following specific conclusions:

1) The stage time lag significantly affects the fracture configuration of zipper fracturing. The stress interference of simultaneous zipper fracturing is most severe, and hence, the fracture length and penetration length are affected the most, leading to the worst inter-well stimulation effectiveness. With the increase in the stage time lag, the pressurized fractures of the previous stage have more time to complete the final fracture propagation through rebalance of fluid pressure and fluid leak-off. The local stress field recovers to some extent, which leads to a weaker stress interference impact on the next stage. This may ensure that the fractures of the next stage grow longer and penetrate deeper between wells and, hence, improve interwell stimulation effectiveness.
2) For a formation with higher horizontal principal stress contrast, stress contrast dominates the fracture propagation. Decreasing the staggered perforation cluster spacing has almost no effect on the fracture configuration of zipper fracturing. One may design small perforation cluster spacing to improve interwell stimulation effectiveness.
3) For a formation with lower horizontal principal stress contrast, interfracture stress interference significantly affects fracture configurations of zipper fracturing. The treatment job may cause "frac hits" and sand production, which will result in an adverse effect on the successive stimulation treatment and production.

DATA AVAILABILITY STATEMENT

The original contributions presented in the study are included in the article/Supplementary Material, further inquiries can be directed to the corresponding author.

AUTHOR CONTRIBUTIONS

ZW and LY proposed the research. RG and ZL prepared figures and tables, and interpreted the structural data. ZW, LY, and XW developed the main ideas. GX, SM, and MF participated in the numerical simulation work. ZW, LY, and GX contributed to the writing the original manuscript. SM, MF, and XW contributed to revising the manuscript. All co-authors actively contributed to manuscript with comments, ideas, and suggestions.

FUNDING

This work was financially supported by Research and Application of Key Technical Equipment for Major Engineering (Phase II) of CNPC Scientific Research and Technology Development Project (2018E-2105), Software Development Project of CNPC on Volume Fracturing Optimization & Design (2020B-4118).

ACKNOWLEDGMENTS

The authors would like to thank the editor and the reviewers of this article for their valuable comments that helped improve the quality of the paper.

REFERENCES

Adachi, J., Siebrits, E., Peirce, A., and Desroches, J. (2007). Computer Simulation of Hydraulic Fractures. *Int. J. Rock Mech. Mining Sci.* 44 (5), 739–757. doi:10.1016/j.ijrmms.2006.11.006

Cong, Z., Li, Y., Pan, Y., Liu, B., Shi, Y., Wei, J., et al. (2021b). Study on CO2 Foam Fracturing Model and Fracture Propagation Simulation. *Energy* 238, 121778, doi:10.1016/j.energy.2021.121778

Cong, Z., Li, Y., Liu, Y., and Xiao, Y. (2021a). A New Method for Calculating the Direction of Fracture Propagation by Stress Numerical Search Based on the Displacement Discontinuity Method. *Comput. Geotechnics* 140, 104482. doi:10.1016/j.compgeo.2021.104482

Dontsov, E., and Peirce, A. (2015). Proppant Transport in Hydraulic Fracturing: Crack Tip Screen-Out in KGD and P3D Models. *Int. J. Sol. Structures*. 63, 206–218, doi:10.1016/j.ijsolstr.2015.02.051

Dontsov, E. V. (2016). An Approximate Solution for a Penny-Shaped Hydraulic Fracture that Accounts for Fracture Toughness, Fluid Viscosity and Leak-Off. *R. Soc. Open Sci.* 3, 160737. doi:10.1098/rsos.160737

Jacobs, T. (2017). Oil and Gas Producers Find Frac Hits in Shale wells a Major challenge. *J. Pet. Tech.* 69 (04), 29–34. doi:10.2118/0417-0029-jpt

Li, J., Liu, Y., and Wu, K. (2021). A New Higher Order Displacement Discontinuity Method Based on the Joint Element for Analysis of Close-Spacing Planar Fractures. *SPE J.* doi:10.2118/208614-PA

Li, Y., Jia, D., Rui, Z., Peng, J., Fu, C., and Zhang, J. (2017). Evaluation Method of Rock Brittleness Based on Statistical Constitutive Relations for Rock Damage. *J. Pet. Sci. Eng.* 153, 123–132. doi:10.1016/j.petrol.2017.03.041

Long, G B., and Xu, G S. (2017), The Effects of Perforation Erosion on Practical Hydraulic-Fracturing Applications, *SPE J.*, 22 (2). 645–659, SPE-185173-PA. doi:10.2118/185173-pa

Manchanda, R., Sharma, M. M. M., and Holzhauser, S. (2014). Time-Dependent Fracture-Interference Effects in Pad Wells. *SPE Prod. Operations* 29 (04), 274–287. doi:10.2118/164534-pa

Nagel, N., Sheibani, F., Lee, B., Agharazi, A., and Zhagn, F. (2014). "Fully-Coupled Numerical Evaluations of Multiwell Completion Schemes: The Critical Role of *In-Situ* Pressure Changes and Well Configuration," in SPE Hydraulic Fracturing Technology Conference (The Woodlands, Texas: Society of Petroleum Engineers) USASPE-168581-MS. doi:10.2118/168581-ms

Qiu, F., Porcu, M. M., Xu, J., Malpani, R., Pankaj, P., and Pope, T. L. (2015). "Simulation Study of Zipper Fracturing Using an Unconventional Fracture Model," in SPE/CSUR Unconventional Resources Conference (Calgary, Alberta, Canada: Society of Petroleum Engineers). SPE-175980-MS. doi:10.2118/175980-MS

Rafiee, M., Soliman, M. Y., and Pirayesh, E. (2012). "Hydraulic Fracturing Design and Optimization: A Modification to Zipper Frac," in SPE Annual Technical Conference and Exhibition (San Antonio, Texas, USA: Society of Petroleum Engineers). SPE-159786-MS. doi:10.2118/159786-ms

Roussel, N. P., and Sharma, M. M. (2011). Optimizing Fracture Spacing and Sequencing in Horizontal-Well Fracturing. *Spe Prod. Operations* 26 (02), 173–184. doi:10.2118/127986-pa

Shen, X. (2014). "Numerical Analysis on the Interaction between Two Zipper Frac Wells Using the Continuum Damage Method," in Offshore Technology Conference-Asia (Kuala Lumpur, Malaysia: Offshore Technology Conference). OTC-24975-MS. doi:10.2118/24975-ms

Shi, X., Li, D. J., Liu, Y., Xu, H. X., and Du, Y. K. (2018). "Hydraulic Fracture Propagation in Horizontal Wells With Modified Zipper Fracturing in Heterogeneous Formation," in 52nd U.S. Rock Mechanics/Geomechanics Symposium (Seattle, Washington: American Rock Mechanics Association). ARMA-2018-189.

Shou, K. (1994). Three-Dimensional Displacement Discontinuity Method with Application to Bonded Half-Space Problems. Ph.D. Dissertation. University of Minnesota.

Sierra, L., and Mayerhofer, M. (2014). "Evaluating the Benefits of Zipper Fracs in Unconventional Reservoirs," in SPE Unconventional Resources Conference, April 1–3, 2014 (The Woodlands, Texas, USA: Society of Petroleum Engineers). SPE-168977-MS.

Soliman, M. Y., East, L. E., and Adams, D. L. (2008), 23. Geomechanics Aspects of Multiple Fracturing of Horizontal and Vertical Wells, *SPE Drilling & Completion*, 217–228. SPE-86992-PA. doi:10.2118/86992-PA

Tang, J., Wu, K., Zeng, B., Huang, H., Hu, X., Guo, X., et al. (2018). Investigate Effects of Weak Bedding Interfaces on Fracture Geometry in Unconventional Reservoirs. *J. Pet. Sci. Eng.* 165, 992–1009. doi:10.1016/j.petrol.2017.11.037

Tang, J., Wu, K., Zuo, L., Xiao, L., Sun, S., and Ehlig–Economides, C. (2019). Investigation of Rupture and Slip Mechanisms of Hydraulic Fractures in Multiple-Layered Formations. *SPE J.* 24 (05), 2292–2307. doi:10.2118/197054-PA

Xie, J., Tang, J., Yong, R., Fan, Y., Zuo, L., Chen, X., et al. (2020). A 3-D Hydraulic Fracture Propagation Model Applied for Shale Gas Reservoirs with Multiple Bedding Planes. *Eng. Fracture Mech.* 228, 106872. doi:10.1016/j.engfracmech.2020.106872

Xu, G. S., and Wong, S. W. (201317043). "Interaction of Multiple Non-planar Hydraulic Fractures in Horizontal wells," in International Petroleum Technology Conference, 26–28, 2013 (Beijing, China: IPTC). doi:10.2523/17043-ms

Zhang, F., Damjanac, B., and Maxwell, S. (2019). Investigating Hydraulic Fracturing Complexity in Naturally Fractured Rock Masses Using Fully Coupled Multiscale Numerical Modeling. *Rock Mech. Rock Eng.* 52 (12), 5137–5160. doi:10.1007/s00603-019-01851-3

Zhang, F., Dontsov, E., and Mack, M. (2017). Fully Coupled Simulation of a Hydraulic Fracture Interacting with Natural Fractures with a Hybrid Discrete-Continuum Method. *Int. J. Numer. Anal. Meth. Geomech.* 41 (13), 1430–1452. doi:10.1002/nag.2682

Zhang, F., Wang, X., Tang, M., Du, X., Xu, C., Tang, J., et al. (2021b). Numerical Investigation on Hydraulic Fracturing of Extreme Limited Entry Perforating in Plug-And-Perforation Completion of Shale Oil Reservoir in Changqing Oilfield, China. *Rock Mech. Rock Eng.* 54, 2925–2941. doi:10.1007/s00603-021-02450-x

Zhang, J., Li, Y., Pan, Y., Wang, X., Yan, M., Shi, X., et al. (2021a). Experiments and Analysis on the Influence of Multiple Closed Cemented Natural Fractures on Hydraulic Fracture Propagation in a Tight Sandstone Reservoir. *Eng. Geology.* 281, 105981. doi:10.1016/j.enggeo.2020.105981

Conflict of Interest: Authors ZW, LY, RG, ZL, SM, MF, and XW were employed by the company Research Institute of Petroleum Exploration and Development, PetroChina.

The remaining author declares that the research was conducted in the absence of any commercial or financial relationships that could be construed as a potential conflict of interest.

frontiers in Earth Science

ORIGINAL RESEARCH
published: 23 March 2022
doi: 10.3389/feart.2022.824352

Analysis of the Influencing Factors on Electrical Properties and Evaluation of Gas Saturation in Marine Shales: A Case Study of the Wufeng-Longmaxi Formation in Sichuan Basin

Fujing Sun[1,2], *Jianmeng Sun*[1,2]*, *Xin Zeng*[1,2]*, *Weiguo Yuan*[3], *Jinyan Zhang*[4], *Wei Yan*[3] and *Weichao Yan*[1,2]

[1]Key Laboratory of Deep Oil and Gas, China University of Petroleum (East China), Qingdao, China, [2]School of Geosciences, China University of Petroleum (East China), Qingdao, China, [3]Sinopec Exploration Company, Chengdu, China, [4]Well Logging Company of Sinopec Shengli Oilfield Service Corporation, Dongying, China

OPEN ACCESS

Edited by:
Yuwei Li,
Liaoning University, China

Reviewed by:
Qiang Guo,
China Jiliang University, China
Jun Zhang,
Northeast Petroleum University, China
Jiawei Li,
Texas A&M University, United States

***Correspondence:**
Xin Zeng
zengxinupc@tom.com
Jianmeng Sun
sunjm@upc.edu.cn

Specialty section:
This article was submitted to Economic Geology, a section of the journal Frontiers in Earth Science

Received: 29 November 2021
Accepted: 07 March 2022
Published: 23 March 2022

Citation:
Sun F, Sun J, Zeng X, Yuan W, Zhang J, Yan W and Yan W (2022) Analysis of the Influencing Factors on Electrical Properties and Evaluation of Gas Saturation in Marine Shales: A Case Study of the Wufeng-Longmaxi Formation in Sichuan Basin. Front. Earth Sci. 10:824352. doi: 10.3389/feart.2022.824352

Accurate gas saturation calculations are critical to evaluating the production of marine shale gas reservoirs. As a high-resolution exploration method, geophysical resistivity well-logging technology has been widely applied in almost all types of oil/gas reservoirs to evaluate formation fluid saturation. Although the calculated saturations are accurate for conventional reservoirs, it is a challenging task to acquire the gas saturation of shale gas reservoirs due to the presence of complex rock compositions and fluid types. It is necessary to analyze different influencing factors on electrical properties to establish a more applicable gas saturation model for marine shales. In this work, we make full use of geological data, well logging data, and rock experiment data to analyze the influencing factors of electrical properties in the Wufeng-Longmaxi Formation in the Sichuan Basin, China. Six conductive factors are studied, including stratigraphic structures, clay minerals, pyrite, organic matter, pore structures, and formation fluids. Then, a shale conductivity model is developed, in which high- and low-resistivity layers are connected in parallel. Based on the conductivity model, a new method for influencing factors of stepwise stripping conductivity is proposed to calculate shale gas saturation. Finally, by interpreting the well logging data of two shale gas wells, we compared the saturation calculation results of different methods to demonstrate the accuracy of the new method. The results show that thin, low-resistivity layers, clay minerals, pyrite and overmature carbonized organic matter reduce the resistivity of shale and weaken the contribution of fluids to the measured shale resistivity. Moreover, the calculation accuracy of this new method is better than that of Archie's equation, Simandoux's equation, and the neutron-density porosity overlay method. The findings of this paper will help gain insight into the mechanism of resistivity responses for marine shale reservoirs and improve the accuracy of the estimated gas saturation.

Keywords: marine shale, resistivity, conductivity model, gas saturation, Sichuan Basin

INTRODUCTION

Due to the influence of the "peak oil" theory (Brandt et al., 2013), researchers have gradually focused on unconventional oil and gas resources for the advancement of technological breakthroughs in exploration and development (Yasin et al., 2019; Dong et al., 2020; Du et al., 2021; Golsanami et al., 2021). Among the unconventional resources, shale gas has become one of the most promising fossil resources since the advancement of multistage hydraulic technology and horizontal drilling processes (Soeder, 2018; Bakhshi et al., 2020; Wang et al., 2021). Compared with conventional sandstone gas, shale gas has unique characteristics, such as nanosized storage pore spaces (Wu et al., 2020a), unusual gas flow mechanisms (Li et al., 2019) and different existing states (free gas and adsorbed gas) (Zhu et al., 2021). In addition, a high content of organic matter exists in marine shales (Zhu et al., 2019). Because of the high cost of shale gas production, gas saturation must be accurately calculated in advance to determine whether a shale gas well is worthy of commercial production.

As a fine exploration method, geophysical resistivity well logging technology has been widely applied in almost all types of oil/gas reservoirs to evaluate the fluid saturation of formations (Golsanami et al., 2020). The most classical saturation model is Archie's equation (Archie, 1942), which is expressed as follows:

$$S_w = \left(\frac{abR_w\phi^m}{R_t}\right)^{\frac{1}{n}} \quad (1)$$

where S_w represents the water saturation, decimal; R_t is the logging resistivity, Ω·m; R_w is the formation water resistivity, Ω·m; ϕ is porosity, decimal; m represents the cementation index; n represents the saturation index; and a and b are lithologic coefficients. Although Archie's equation has been applied in conventional reservoirs for decades, it only considers the influence of the conductivity of water in pores. However, based on X-ray diffraction (XRD) analysis, it is known that marine shales usually contain quartz, feldspar, carbonate, clay and pyrite (Zhang et al., 2019). Pyrite and some clay minerals have an inherently high electrical conductivity, which affects rock resistivity (Hamada et al., 2001; Savage et al., 2008). It is a challenging task to acquire the gas saturation of shale gas reservoirs due to their complex rock compositions and fluid types. Therefore, a full understanding of the influences of different factors on shale resistivity is needed. Although there are many studies using laboratory electrical experiments to study shale resistivity (Zhong et al., 2021; Han et al., 2015; Senger et al., 2020), the resistivity index is still hard to determine due to difficulties associated with the drainage process. Recently, some scholars have used digital rock simulations to study the effects of different components on shale resistivity (Wu et al., 2020b), which provides a new description of the electrical mechanisms of shale. However, their conclusions are not entirely consistent. Nie et al. (2016) used the finite element method to simulate the resistivity of shale gas reservoir rock and found that the clay mineral content and pyrite content reduced the shale resistivity substantially, while organic matter had little influence on resistivity. Zhang et al. (2017a) fitted the gas saturation and density, neutron, apparent density porosity and apparent neutron porosity difference of rock samples respectively, and established the calculation formula of gas saturation by using non electric logging information. Wu et al. (2020c) verified the negative relationship between clay minerals and resistivity, but they believed that organic matter could reduce shale resistivity. There is still a lack of systematic analysis of the influencing factors on the electrical properties of marine shale.

Due to the many factors affecting shale resistivity and the complex conductivity mechanism, the effective resistivity-based marine shale gas saturation calculation method is seldom used. Most oil service companies in China use shaly sand models [e.g., Simandoux's equation (Simandoux, 1963)] to calculate the gas saturation of shale, but the calculated saturation results have large errors associated with the core analysis values. Kadkhodaie and Rezaee (2016) proposed a new correlation method for water saturation calculations in gas shale reservoirs, but they did not take the effects of thin, low-resistivity layers and pyrite into consideration in the saturation model. Nonelectric logging data can also be used to calculate gas saturation. Zhao et al. (2020) constructed digital cores with different fracture widths and found that when the fracture width is narrow, the fracture has no significant effect on the resistance increase coefficient. When the fracture width is wide, there is a nonlinear relationship between resistance increase coefficient and water saturation in double logarithmic coordinates. Sun et al. (2018) studied the abnormal low resistance of the reservoir in the exploration and development of shale gas in the Yangtze region, and obtained six main factors causing the low resistance of shale reservoir: high clay content, over mature organic matter, high pyrite content, high water salinity, poor reservoir physical properties and excellent geological conditions. According to the relationships among the total water saturation, V_P-to-V_S ratio and total porosity, Liu et al. (2018) developed a method for calculating the water saturation of shale gas reservoirs. Zhang et al. (2017b) proposed the neutron-density porosity overlay method to calculate gas saturation, which worked well in their studied marine shale gas wells. However, to make full use of resistivity logging data, the conductive influencing factors need to be considered comprehensively before proposing a gas saturation model.

In this study, we took the Wufeng-Longmaxi Formation in the Sichuan Basin [the most promising shale gas plays in China (Chen et al., 2020)] as a typical example to analyze the influencing factors of electrical properties and develop a new resistivity-based gas saturation model. The resistivity logging results show that high-resistivity layers (> 100 Ω m), medium-resistivity layers (5–100 Ω m) and low-resistivity layers (< 5 Ω m) coexist in marine shale gas wells. We first utilized geological data, well logging data, and rock experiment data to analyze six influencing factors (stratigraphic structure, clay, pyrite, organic matter, pore structure, and formation fluid) of electrical properties in the Wufeng-Longmaxi Formation. Then, according to the formation types and conductive components, we proposed a new shale conductivity model. A procedure employing the stepwise stripping of conductivity influencing factors was also

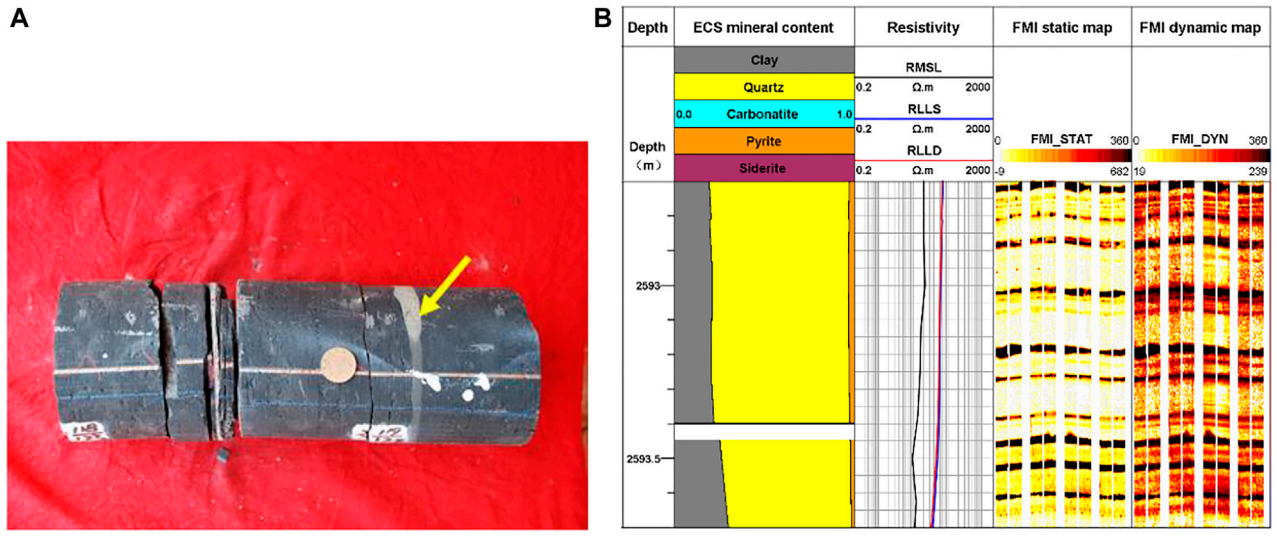

FIGURE 1 | Core characteristics and FMI image of the thin, low-resistivity layer: **(A)** core sample; **(B)** FMI image.

proposed to calculate the shale gas saturation. Finally, we applied different saturation models to two shale gas wells and verified the accuracy of the new method.

ANALYSIS OF INFLUENCING FACTORS ON ELECTRICAL PROPERTIES FOR MARINE SHALE

Stratigraphic Structure

During the bottom deposition period of the Wufeng-Longmaxi Formation in the Sichuan Basin, several large-scale volcanic eruptions occurred, and tuff materials from the volcanic eruptions were deposited, formed and altered in a marine alkaline environment to form potassium bentonite (Chen et al., 2019). The coring report shows that there are more than 20 thin layers of potassium bentonite in the bottom strata of the Wufeng-Longmaxi Formation, with a single layer thickness of 1–2 cm, even reaching up to 30 cm in some locations. **Figure 1A** shows a thin layer in a full diameter core sample. Bentonite is a claystone whose main composition consists of smectite, illite and illite-smectite mixed layers (Wang et al., 2019). According to the literature, these clay minerals have high cation exchange capacity (CEC) values, which decrease the resistivity of the rock (Yan et al., 2018). Therefore, the potassium bentonite layers are thin, low-resistivity layers, which appear as dark bands on the image collected from the formation micro imager (FMI) logging tool, as shown in **Figure 1B**.

The vertical resolution of the deep lateral resistivity (RLLD) logging tool is approximately 0.9 m, and the shale resistivity has high anisotropy in the range of vertical resolution affected by thin, low-resistivity layers. Controlled by a shield electrode and loop electrode, deep lateral logging currents flow horizontally into the layer, and the measured resistivity is more notably influenced by the horizontal resistivity. However, the horizontal resistivity is obviously smaller than the vertical resistivity (Klein and Martin, 1997). Therefore, the measured resistivity is too low, which leads to the underestimation of the actual gas saturation of marine shale reservoirs based on traditional fluid saturation calculation models. When the thin, low-resistivity layer is not developed and the FMI image shows bright blocky characteristics, the resistivity of shale is high due to the discontinuous conductive pathway.

In addition to the macroscopic characteristics of thin, low-resistivity layers, there are different types of microlaminations. By combining the thin section analysis and quantitative evaluation of minerals with SCANning electron microscopy (QEMSCAN) techniques, organic-rich lamination (**Figure 2A**), silt lamination (**Figures 2B,F**), clay lamination (**Figures 2E**, **3C**) and pyrite lamination (**Figure 2D**) are observed. The lamination shows patchy, vein-like, lenticular or linear distribution shapes, with thicknesses of approximately 0.1–1 mm. The continuous microscopic distribution of clay lamination, pyrite lamination and organic lamination can provide a continuous conductive pathway for electric current, which reduces the resistivity of shale.

Moreover, the marine organic-rich shale in the studied formation has unique depositional patterns, similar to those of stable ocean basins with low subsidence rates and low sedimentation rates (Zou et al., 2015). At the shale deposition stage, when periodic changes in energy, temperature and salinity exist, parallel shale beddings are readily developed. Shale bedding forms mechanically weak surfaces that usually alter under induced fracturing when encountering tectonic stress concentrations or excessive formation pressures. In addition, high silica contents, high organic matter contents and high hydrocarbon generation pressures can also cause shale bedding fractures. During the drilling process, these fractures are filled with highly saline mud filtrate, which decreases shale resistivity.

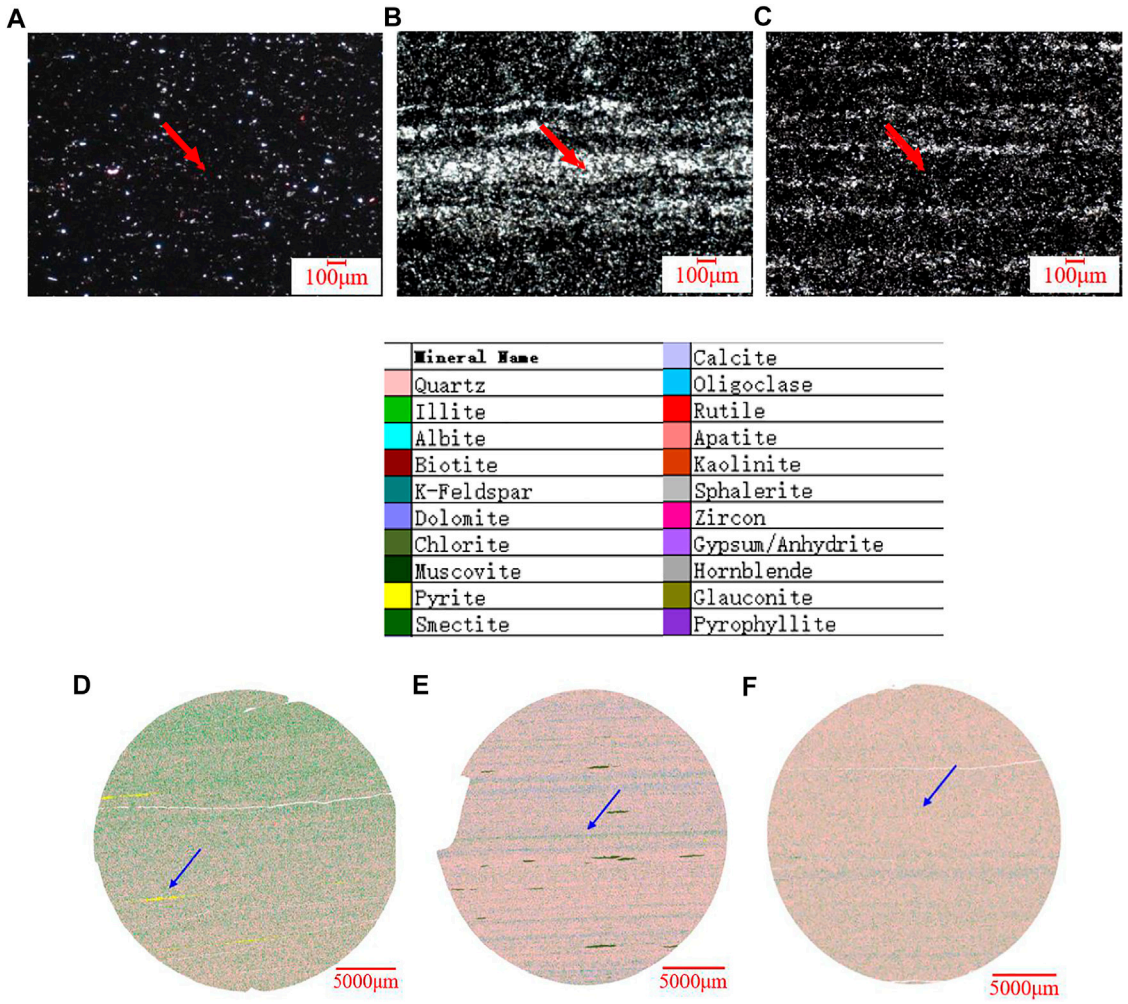

FIGURE 2 | Microlamination characteristics of shale: **(A–C)** thin sections of organic-rich lamination, silt lamination and clay lamination; **(D–F)** QEMSCAN images of pyrite lamination, clay lamination and silt lamination.

Clay Minerals

In our study, clay minerals refer to fine-grained (less than 2 μm in diameter) aqueous aluminosilicate minerals with a layered crystalline structure. The X-ray diffraction (XRD) results show that the total clay mineral content of shale samples taken from the Wufeng-Longmaxi Formation is between 16 and 63%, and the clay minerals are mainly composed of illite-smectite mixed layers, illite and chlorite. Clay minerals have obvious influences on the resistivity of shale for two reasons. First, some clay minerals have high cation exchange effects, which increase the electrical conductivity. Smectite has the strongest cation exchange capacity, with CEC values ranging from 0.4 to 1.5 meq/g. The average CEC value of illite is 0.25 meq/g, and the low CEC value of chlorite is close to 0.05 meq/g (Silva et al., 2018). When the content of mixed layer is high, the additional conductivity of montmorillonite and mixed layer is the most obvious, which leads to the significant reduction of reservoir resistivity (Xie et al., 2019). In addition, the negative charges present on clay surfaces can adsorb polar water molecules and form conductive water bounds. Smectite and illite adsorb a large number of water molecules due to their large specific surface area, which decreases the resistivity of rock.

Figure 3A shows the well logging data (gamma spectra, lithology curves, porosity curves and resistivity curves) of conventional logging tools and elemental capture spectroscopy (ECS) logging data of the Longmaxi (abbreviated as Long) Formation in marine gas well J1. The uranium curve (U) illustrates that both the total organic matter contents and the associated pyrite contents are low, which cannot have caused the resistivity difference between Long *A New Shale Conductivity Model* and Long *Gas Saturation Calculation Procedure*. However, the average shale resistivity of Long *Gas Saturation Calculation Procedure* is 35 Ω m, which is much smaller than that of the Long *A New Shale Conductivity Model* (50–1,000 Ω m). According to the interpreted clay content curve from the ECS data, the clay content of Long *A New Shale Conductivity Model* is higher than that of Long *Gas Saturation Calculation Procedure*, resulting in the resistivity difference observed between the two sections.

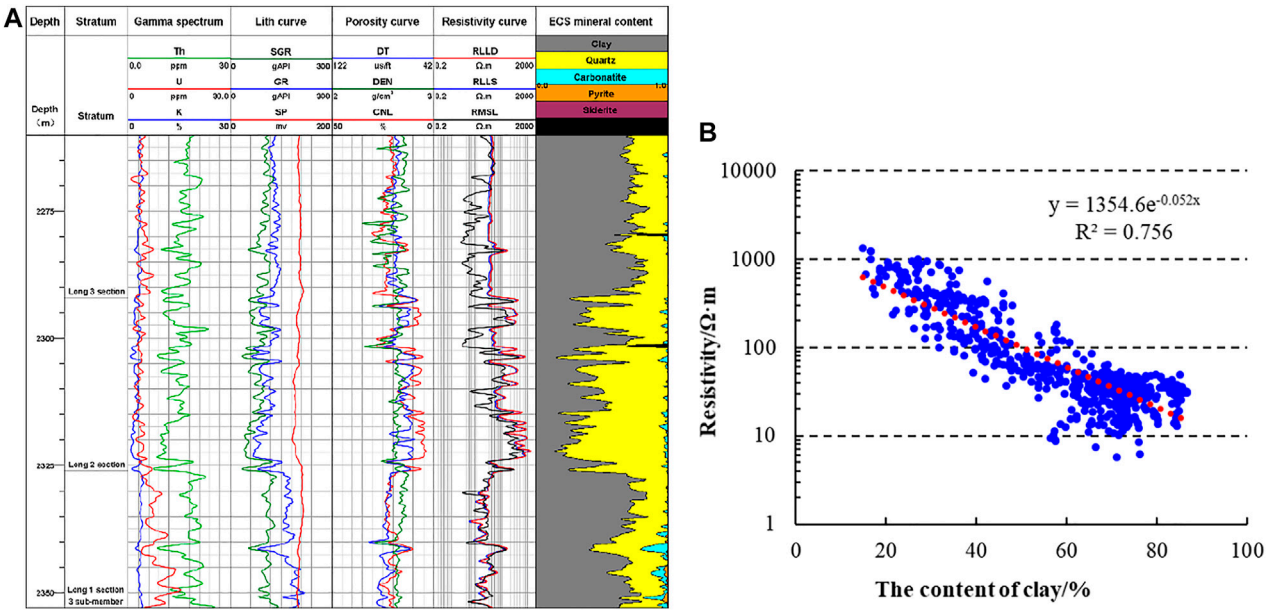

FIGURE 3 | (A) Well logging data of the Longmaxi Formation in well J1; **(B)** the relationship between resistivity and clay content.

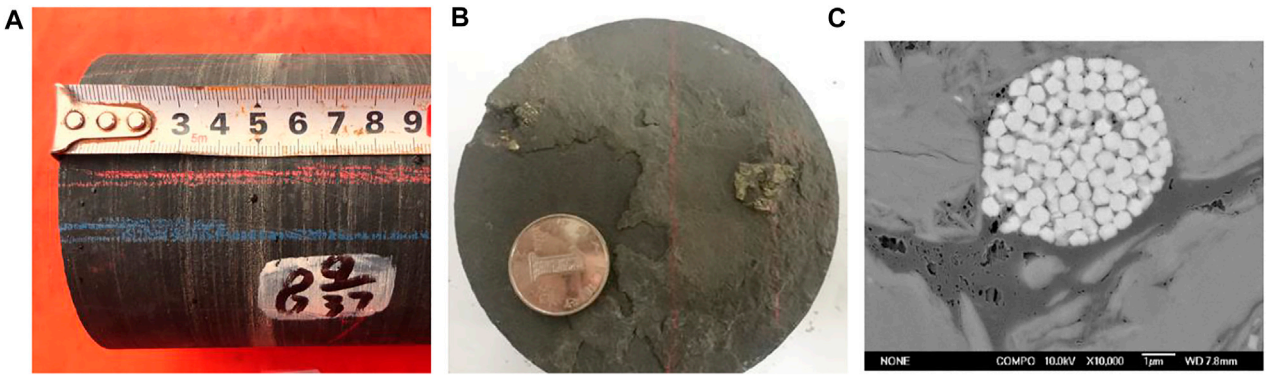

FIGURE 4 | Different types of pyrites: **(A)** striped pyrite; **(B)** patchy pyrite; and **(C)** strawberry-shaped pyrite.

Figure 3B shows the relationship between the measured resistivity (RLLD) and clay content. There is a strong negative correlation between the resistivity and the clay content, which is expressed as **Eq. 2**, indicating that clay is one of the main factors affecting resistivity.

$$R_t = 1354.6 \times e^{-0.052V_{sh}} \quad (2)$$

where R_t is the deep lateral resistivity, Ω·m; and V_{sh} is the clay content, %.

Pyrite

Pyrite is a metal sulfide (FeS_2) with a high density (4.9–5.2 g/cm^3) and a low resistivity (10^{-5}~1 Ω m) (Kennedy, 2004). Unlike the ionic conductivity of formation water, the charge carrier of pyrite is electrons. The regular arrangement of iron and sulfur atoms in the crystal structure explains the very high conductivity of pyrite. Clavier et al. (1976) found that when the pyrite content of a rock sample was greater than 7.0%, the conductivity of dry rock was also high. Especially when pyrite was distributed in strips to form a continuous conductive pathway, the resistivity decreased in a spike shape. Clavier et al. according to the experimental study on the influence ability of dispersed pyrite under the condition of resistivity measurement at different frequencies, it is found that the content of pyrite increases and the correction coefficient of electric logging increases (Sun et al., 2018). Marine shale in the Wufeng-Longmaxi Formation was deposited in deep water, and a stable and anoxic depositional environment assisted in the formation and preservation of pyrite. At the large-scale level, there are two main types of pyrites, including striped pyrite (**Figure 4A**) and patchy pyrite (**Figure 4B**). These pyrite

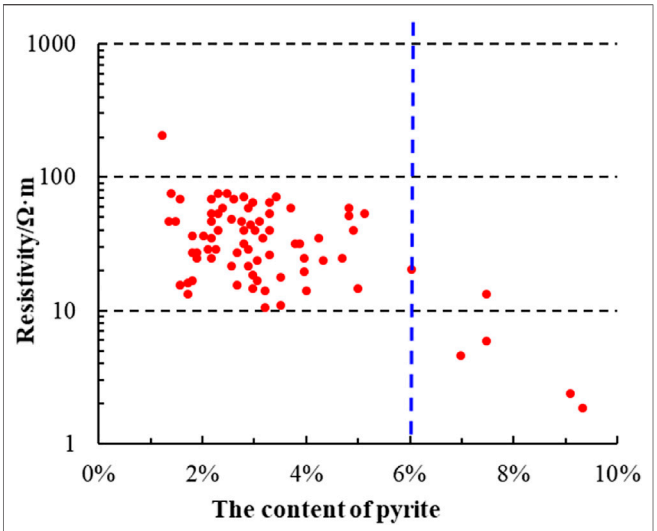

FIGURE 5 | The relationship between shale resistivity and pyrite content.

aggregates can be identified in the FMI image. With scanning electron microscopy (SEM) analysis, we can see that pyrite usually forms in a strawberry shape on the microscale (**Figure 4C**).

Figure 5 shows the relationship between the laboratory-measured pyrite content and the resistivity of the shale samples collected from several marine shale gas wells. It is concluded that when the pyrite content is less than 6.0%, there is no obvious correlation between the shale resistivity and pyrite content. However, when the pyrite content is greater than 6.0%, the shale resistivity decreases significantly.

Organic Matter

As an important source rock, gas-bearing shale contains organic matter. During the early formation stage, the resistivity of immature shale is low (Hinds and Berg, 1990). With increasing thermal maturity, the amount of hydrocarbons generated from organic matter increases, and the low-resistivity water in the pore space is replaced by nonconductive oil and gas. Theoretically, the shale resistivity should be high in the highly mature or overmature stage. However, although the average vitrinite reflectance (R_o) of the studied shale is greater than 2.0%, the shale resistivity is not high. The main factor preventing the shale resistivity from rising is the carbonization of organic matter. With increasing thermal maturity, the H/C ratio decreases, and the aromaticity of organic matter increases (Mao et al., 2010). The structure of carbon-rich and aromatized organic matter is similar to that of graphite (resistivity ranges from $8 \times 10^{-6}\,\Omega\,m$ to $13 \times 10^{-6}\,\Omega\,m$), which is a semiconductor or conductor. Wang et al. (2018) studied organic matter carbonization in Longmaxi Formation shale and found that the lower limit of R_o for carbonization was 3.5%. Shale with an R_o less than 3.4% does not show organic matter carbonization, while shale with an R_o between 3.4 and 3.5% may show weak organic matter carbonization. Xie et al. (2017) through the comparative analysis of coring data and logging curves of many wells pointed out that there is a good negative correlation between TOC content and density. With the decrease of density, TOC increases and maturity becomes higher. After the hydrocarbon with low hydrogen content turns into graphite, the conductivity increases, the resistivity decreases and the gas content becomes worse. Therefore, overmature carbonized organic matter reduces the resistivity of shale.

To analyze the effect of total organic carbon (TOC) on shale resistivity, we measured the TOC contents of shale samples from Long *Analysis of Influencing Factors on Electrical Properties for Marine Shale* in well J1 and established the relationship between resistivity and the TOC content (**Figure 6A**). The resistivities and TOC contents in well logging curves of well J1 are shown in **Figure 6B**. As shown in **Figure 6A**, the correlation between TOC content and resistivity is poor and the influence of organic matter content on shale resistivity is not obvious. Therefore, TOC content is not added to the model.

Pore Structures

In a previous study, we utilized SEM images to describe different types of pores in marine shale gas samples, including dissolved inorganic pores, pores between strawberry pyrite crystals, organic pores and microfractures (Zeng et al., 2020), but the effect of pore structure on shale resistivity was unclear. The porosity of shale in the Wufeng-Longmaxi Formation is generally less than 8.0%, and the permeability is less than 0.1 mD. To analyze the effect of porosity on shale resistivity, the relationship between the porosity and resistivity (RLLD) of the shale from well J1 is analyzed, as shown in **Figure 7A**. There is no correlation between the shale porosity and the measured resistivity and dry sample porosity can not effectively characterize the change of resistivity. The shale resistivity is measured by well logging tools, and nonconductive gas fills the pore space of shale. Therefore, there are many other factors controlling resistivity. To solve this problem, we performed resistivity experiments on 27 fully water saturated shales and then investigated the relationship between resistivity and porosity (**Figure 7B**). There is a weak negative correlation between the porosity and shale resistivity under the water-saturated state. The correlation is better when the porosity is greater than 3.0%, which indicates that water saturated porosity is also an influencing factor of electrical properties.

Pore structure refers to the geometry and size of pores and throats in rocks and their configuration relationships, which has been demonstrated to be an important factor affecting resistivity (Wang et al., 2018). However, research on the relationship between the pore structure and resistivity of marine shale is still limited. As an advanced nondestructive technology, nuclear magnetic resonance (NMR) has been widely used in studying pore structures of both conventional (Golsanami et al., 2019; Li et al., 2017) and unconventional rocks (Yan et al., 2017; Yan et al., 2019; Dong et al., 2020). In this work, we applied NMR and

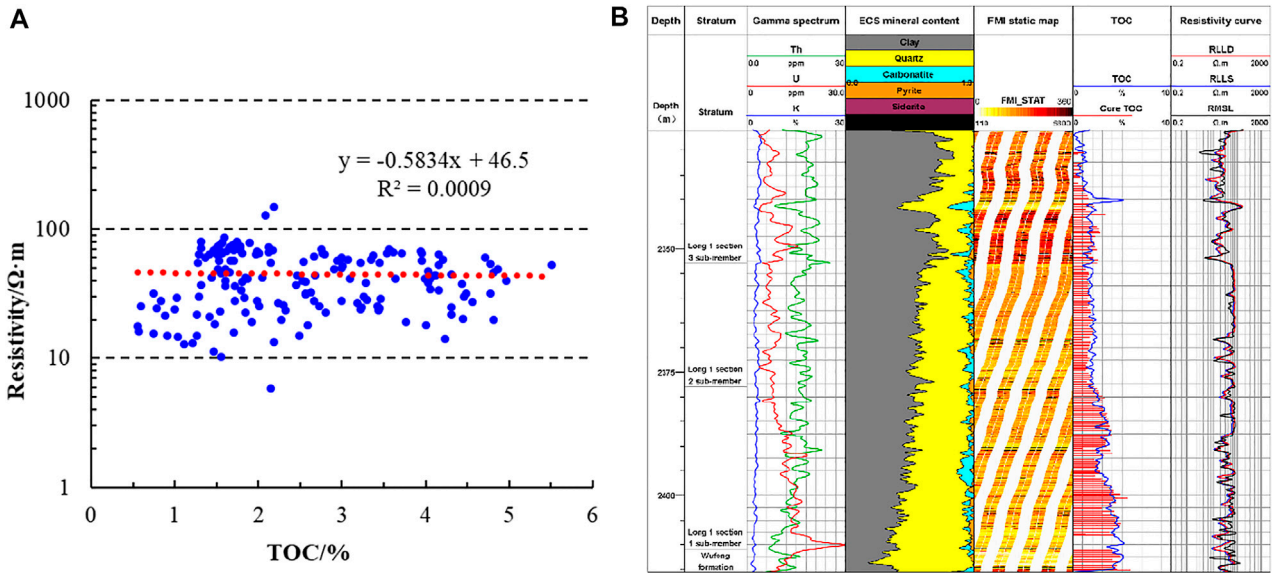

FIGURE 6 | (A) Relationship between TOC content and resistivity; **(B)** well logging data in well J1.

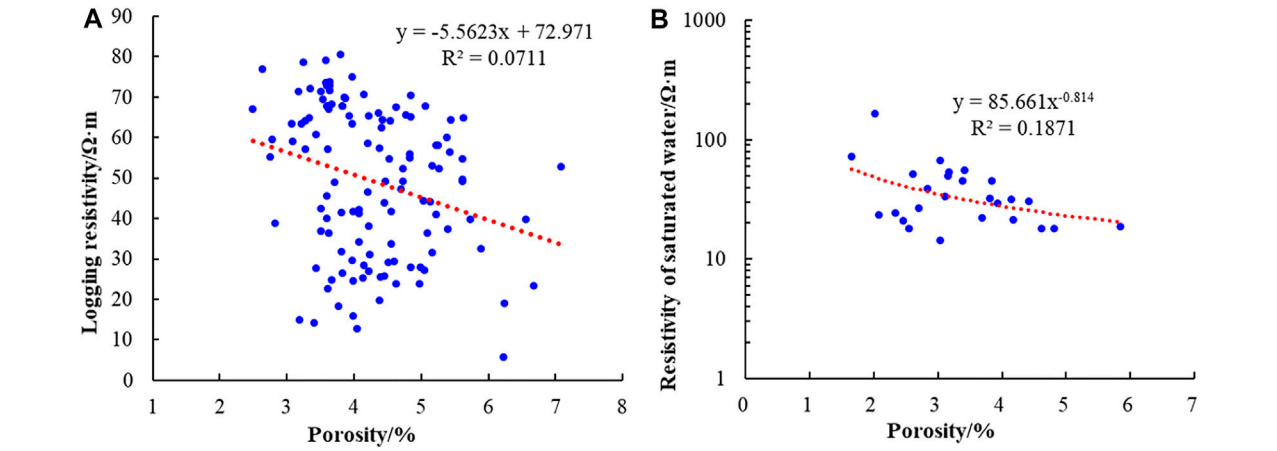

FIGURE 7 | Relationship between porosity and resistivity: **(A)** porosity and logging resistivity (RLLD); **(B)** porosity and resistivity of shale in a water-saturated state.

resistivity measurements to water-saturated shale samples to study the influence of pore structure on electrical properties. The T_2 spectra of shale samples with similar porosities are compared, as shown in **Figure 8**. The porosities of shale samples J7-1 and J7-2 are 2.34 and 2.46%, respectively, and their resistivities are 24.46 Ω m and 20.48 Ω m, respectively. Through the comparisons of T_2 spectra (**Figure 8A**), we can see that shale J7-2 has a high first peak amplitude (short transverse relaxation time). Shale samples J5-3 and D3-5 have the same porosity of 3.16%, and their resistivities are 53.65 Ω m and 49.8 Ω m, respectively. **Figure 8B** shows that the T_2 of the highest peak of shale D3-5 is longer than that of shale J5-3. For shale samples, Gao et al. (2018) verified that a long T_2 represents large pores, and a short T_2 represents small pores. Therefore, it is concluded that the larger the proportion of large pores is, the lower the resistivity of the shale.

Formation Fluids

Formation Water

Highly saline formation water is considered to be one of the most important factors forming low-resistivity oil and gas layers (Pan et al., 2001). The marine shale in the study area was deposited in a marine environment with a seawater salinity of 35,000 mg/L. After deposition, compaction and hydrocarbon generation, the partial free formation water in shale is expelled or consumed, which increases the salinity of the remaining formation water. In

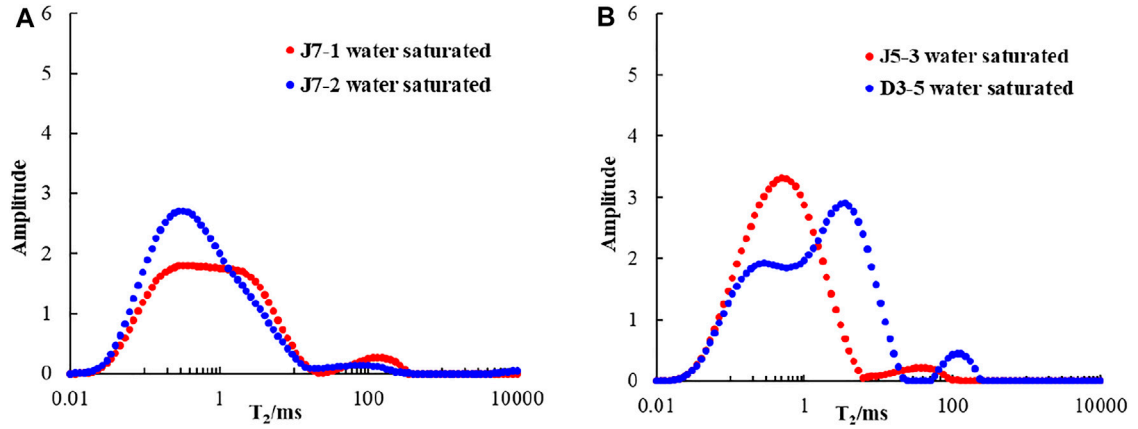

FIGURE 8 | Comparisons of T_2 spectra of different shale samples: **(A)** J7-1 and J7-2; **(B)** J5-3 and D3-5.

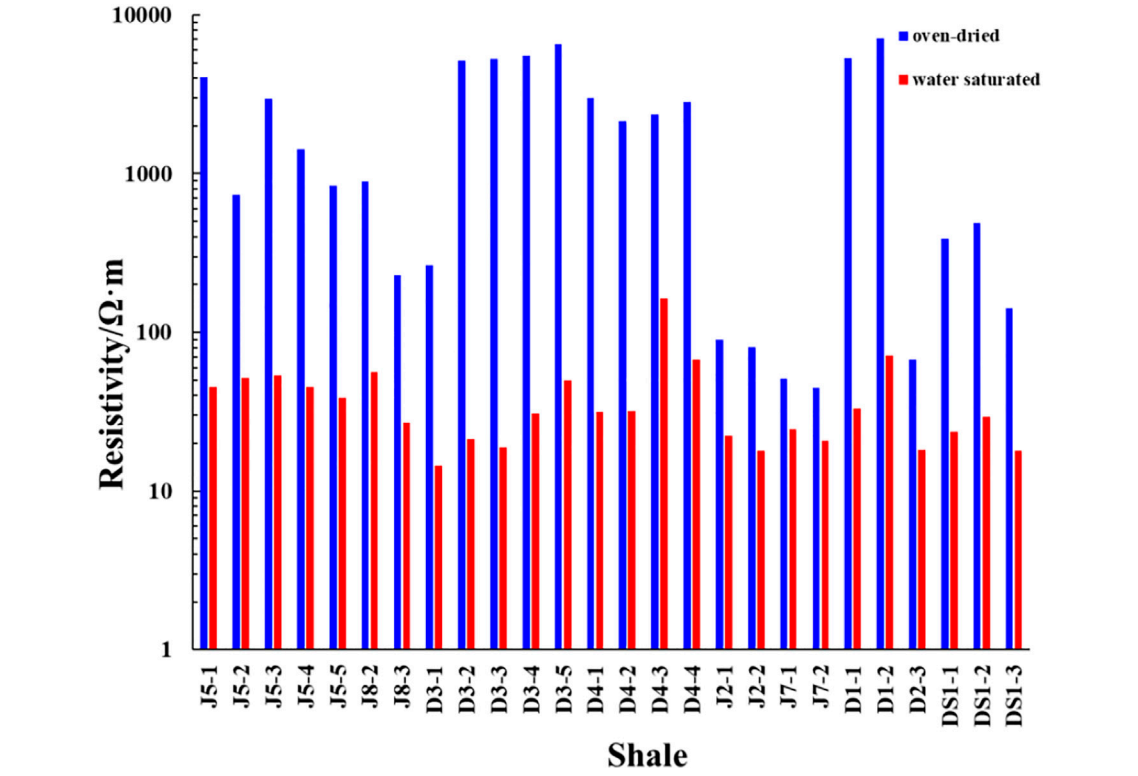

FIGURE 9 | Resistivities of 26 shale samples in an oven-dried and water-saturated states.

the absence of original formation water data, the water analysis data of the adjacent Ordovician Baota Formation (O_2b) are used as a reference for shale formation water. The formation water type of O_2b is $CaCl_2$ with an average equivalent NaCl salinity of 72,925 mg/L. According to the calculation of formation depth and temperature, the equivalent resistivity of formation water is 0.034–0.041 Ω m.

To analyze the effect of formation water salinity on shale resistivity, we first dried 26 shale samples by using a high-temperature oven instrument and then saturated them with 70,000 mg/L NaCl solution. Resistivity experiments were performed on shales with different fluid saturation states. **Figure 9** shows that the resistivity of water-saturated shale is 1–2 orders of magnitude lower than that of dry shale, which also

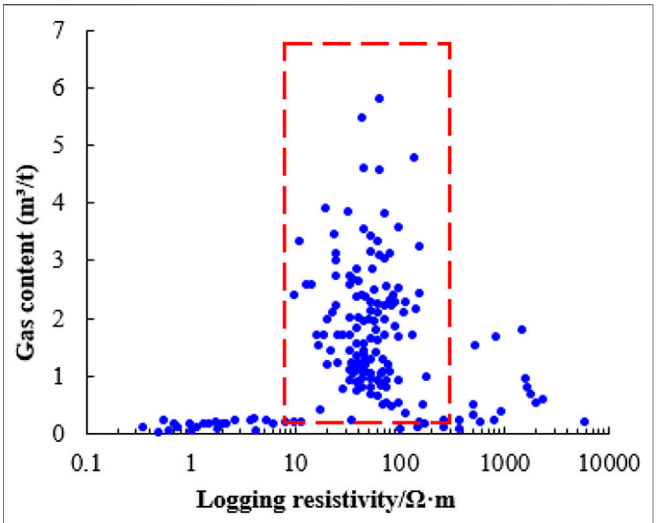

FIGURE 10 | A cross-plot of shale gas content and logging resistivity, Blue dots are data points, within the red circle is medium-resistivity and high-production.

illustrates that high salinity formation water has an obvious effect on shale resistivity.

Total Natural Gas

Although shale resistivity is subject to the combined effects of multiple factors, natural gas still has a significant influence on shale resistivity. Based on the gas desorption volumes and resistivities of shales from 10 gas production wells, we made a cross-plot of gas content and logging resistivity, as shown in **Figure 10**.

The above figure can be divided into three parts: low-resistivity and low-production, medium-resistivity and high-production, and high-resistivity and low-production.

1) Low-resistivity and low-production. When the shale resistivity is between 0.1 and 7 Ω m, the shale reservoir does not produce gas, or it produces a small amount of gas. The reason is that when the shale resistivity is low, regardless of whether it is caused by high water saturation or overmature carbonized organic matter, the shale contains little organic matter, which lacks sufficient conditions for gas production.
2) Medium-resistivity and high-production. When the shale resistivity is in the medium range (7–200 Ω m), the shale reservoir produces a large quantity of gas. Shale contains a high proportion of large size pores. Shale has sufficient and necessary conditions for encouraging gas production, which is referred to as the "resistivity window."
3) High-resistivity and low-production. If shale develops with poor pore structures, the shale resistivity is over 200 Ω m, which lacks sufficient conditions for gas production.

Adsorbed Gas

In addition to free gas, there is adsorbed gas (accounting for more than 30% of the total porosity) in shale. Unlike free gas, which generally occupies the center of pores, adsorbed gas is adsorbed on the surface of shale pores and changes the fluid distribution (Memon et al., 2021). To analyze the effect of adsorbed gas on shale resistivity, a self-developed combined isothermal adsorption and resistivity measurement device (**Figure 11A**) was used to measure changes in shale resistivity by placing resistivity probes at both ends of the plunger sample while conducting isothermal adsorption experiments. We also compared the effects of methane and helium on shale resistivity. The experimental results show (**Figure 11B**) that the shale resistivity decreases with increasing pore gas pressure under a constant water saturation content. The shale resistivity decreases rapidly under low pressure and stabilizes under high pressure.

It is also concluded that shale resistivity with methane is greater than shale resistivity with helium under the same pore gas pressure. We use a schematic diagram of the pore fluid distribution in shale to explain it, as shown in **Figure 12**. The yellow, blue and red circles represent solid matrix molecules,

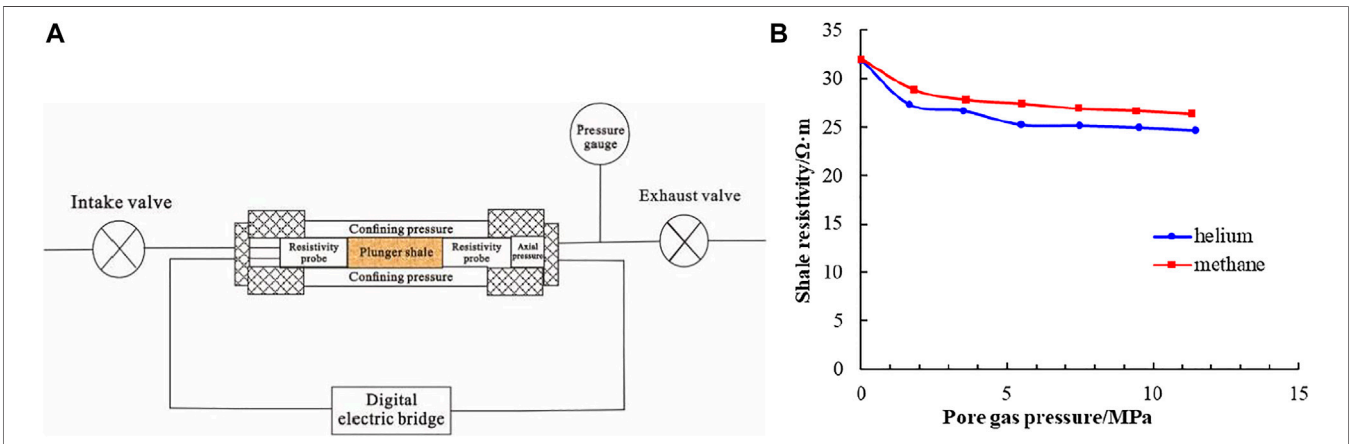

FIGURE 11 | (A) A self-developed combined isothermal adsorption and resistivity measurement device; **(B)** the relationships between pore gas pressures and shale resistivities.

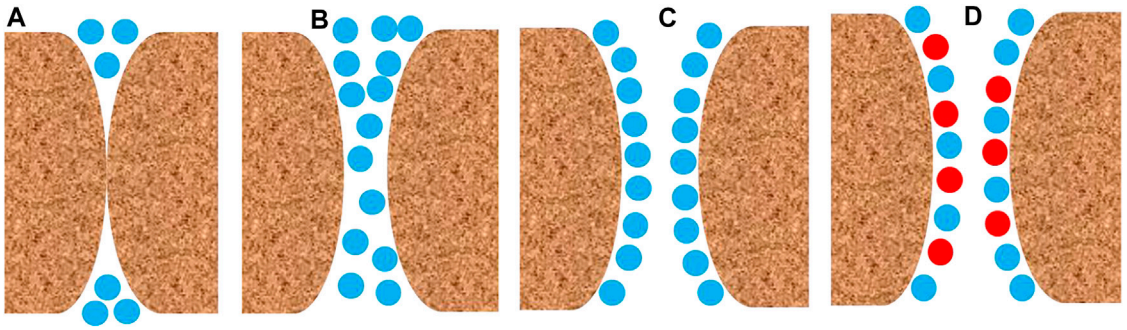

FIGURE 12 | A schematic diagram of pore fluid distribution in shale: **(A)** before gas injection; **(B)** after gas injection; **(C)** helium injection; **(D)** methane injection.

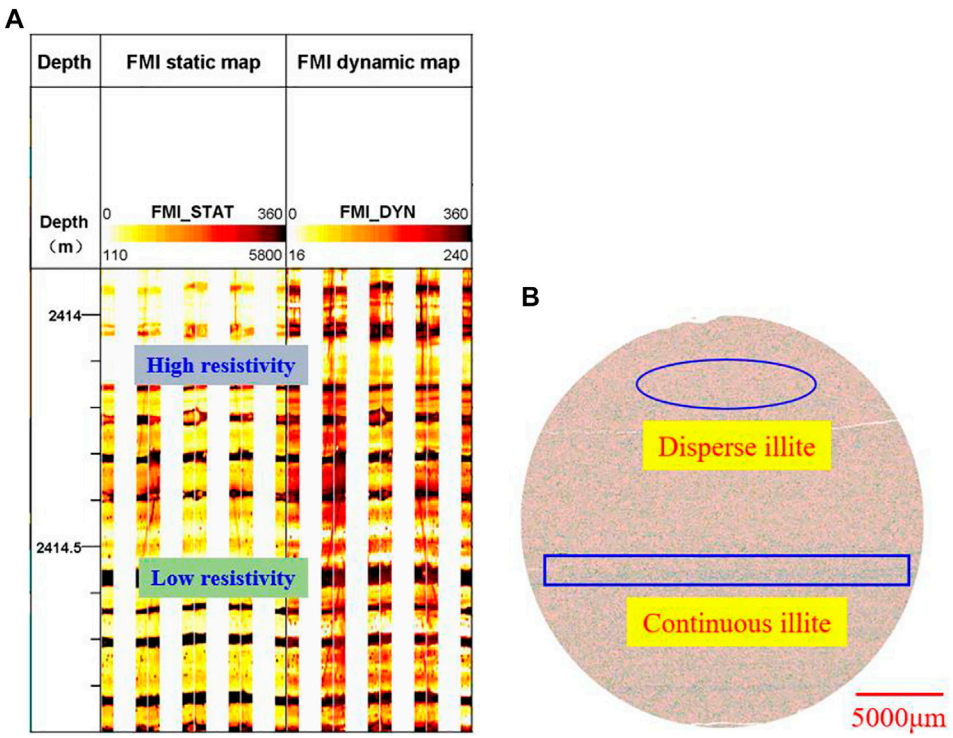

FIGURE 13 | (A) High-resistivity and low-resistivity layers in the FMI image; **(B)** Mineral image.

helium molecules and methane molecules, respectively. Under a low electric field strength, gas is nonconductive, and only extremely weak currents pass through methane and helium. Therefore, the electrical properties of the shale depend mainly on the solid matrix and pore water distribution. When helium is injected, with increasing gas pressures, the effective stress on the shale decreases, and some microfractures and pore throats exist (**Figure 12B**). Adjacent pore water molecules enter the pore space, which decreases the shale resistivity. In addition, the free gas molecules squeeze the solid matrix particles, making the particles more tightly bound, which also enhances the electrical conductivity of shale. Compared with helium, methane has a stronger adsorption capacity. Partial methane molecules are adsorbed on organic matter and clay surfaces, and some conductive water molecules are replaced by nonconductive methane molecules. The continuity of the shale electric current is affected, which increases the shale resistivity.

A NEW SHALE CONDUCTIVITY MODEL

The conductivity model is a comprehensive reflection of the conductive factors and conductive patterns. Before carrying out gas saturation evaluations, the shale conductivity model

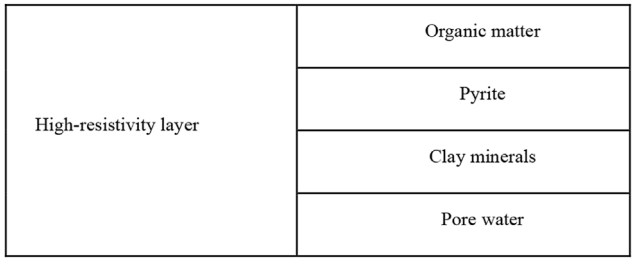

FIGURE 14 | Shale conductivity model.

should be constructed. Based on the analysis of influencing factors on electrical properties, it is concluded that both high-resistivity and low-resistivity layers exist within the resistivity logging detection range (**Figure 13A**). In addition, pore water is continuously distributed, and pyrite, clay and organic matter are both continuously distributed in a dispersed manner (**Figure 13B**).

The presence of thin, low-resistivity layers, overmature carbonized organic matter, clay minerals and pyrite crystals reduce the shale resistivity, which decreases the contribution of pore fluids to the resistivity but the correlation between TOC and resistivity is poor. The direct application of resistivity curves to calculate the gas saturation of shales may lead to large errors. Therefore, a suitable shale conductivity model needs to be developed to calculate the gas saturation. According to the formation types and conductive components, the shale conductivity model is constructed, as shown in **Figure 14**.

There are two types of shale layers, namely, a low-resistivity layer and a high-resistivity layer. Although organic matter, pyrite and clay may exist in a low-resistivity layer, the electric current is usually continuous. Therefore, we regard the low-resistivity layer as a large conductive component rather than a separation component. However, electric currents in a high-resistivity layer are not continuous, and we believe that organic matter, pyrite, clay and pore water have special influences on shale resistivity. The final shale resistivity is expressed as:

$$\frac{1}{R_t} = \frac{1 - f_L}{R_H} + \frac{f_L}{R_L} \tag{3}$$

$$R_L = R_i \tag{4}$$

$$\frac{1}{R_H} = \alpha \frac{V_{cl}^{p_1} S_w}{R_{cl}} + \beta \frac{V_{py}^{p_2}}{R_{py}} + \gamma \frac{V_k^{p_3}}{R_k} + \frac{\phi^m S_w^n}{abR_w} \tag{5}$$

where R_L is the resistivity of the low-resistivity layer, Ω·m; R_H is the resistivity of the high-resistivity layer, Ω·m; f_L represents the proportion of the low-resistivity layer in the resistivity logging detection range; R_i is the resistivity of the conductive component in the low-resistivity layer, Ω·m; R_{cl} is the clay resistivity, Ω·m; R_{py} is the pyrite resistivity, Ω·m; R_k is the resistivity of organic matter, Ω·m; V_{cl} represents the clay volume content, decimal; V_{py} represents the volume content of pyrite, decimal; V_k represents the volume content of organic matter, decimal; and α, β and γ are the mixing coefficients of clay, pyrite and organic matter, respectively. The mixing coefficient is generally less than one, which is related to the content and distribution of components. p_1, p_2, and p_3 represent the influence coefficients of clay, pyrite and organic matter, respectively, which are generally between one and two.

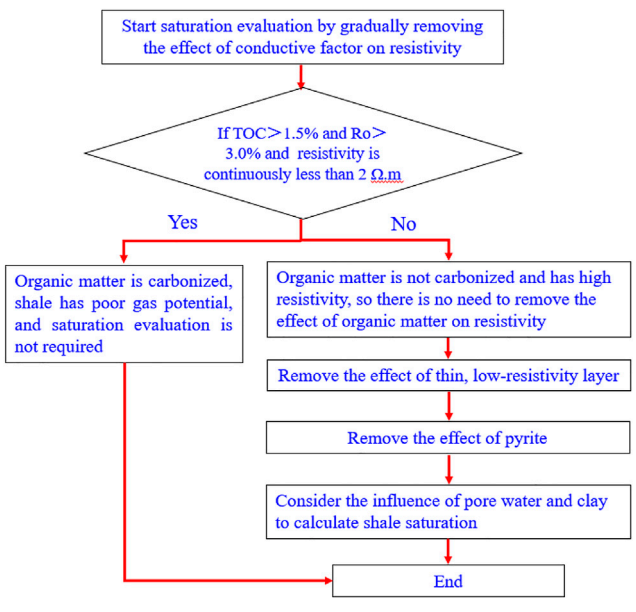

FIGURE 15 | Flow chart of the new procedure with stepwise stripping of conductivity influencing factors.

GAS SATURATION CALCULATION PROCEDURE

Well logging resistivity is affected by many factors, but only clay conductivity and pore water conductivity are related to gas saturation. To accurately calculate the gas saturation of shale, it is necessary to remove the influence of organic matter, thin, low-resistivity layers and pyrite crystals on the resistivity. In this study, a new procedure with stepwise stripping of conductivity influencing factors is proposed for calculating gas saturation.

The Process of Organic Matter

When the organic matter is overmaturely carbonized and conductive, the well logging resistivity of organic-rich shale shows an ultralow resistivity characteristic (Wang and Zhang, 2018), which is usually less than 2 Ω m. The hydrocarbon-generating ability of organic matter decays after carbonization, and the formation pressure coefficient is low under the condition of no gas source supply. Then, organic pores and intergranular pores are greatly reduced or even disappear. The pore radius and pore volume decrease, and the porosity is only 1/3–1/2 of the normal level (Wang et al., 2013). In addition, the desorption gas content is less than 1.0 m^3/t. Therefore, we believe that shale reservoirs with carbonized organic matter have extremely limited gas production and storage capacities, and it is useless to evaluate gas saturation. If the organic matter is not carbonized, the organic

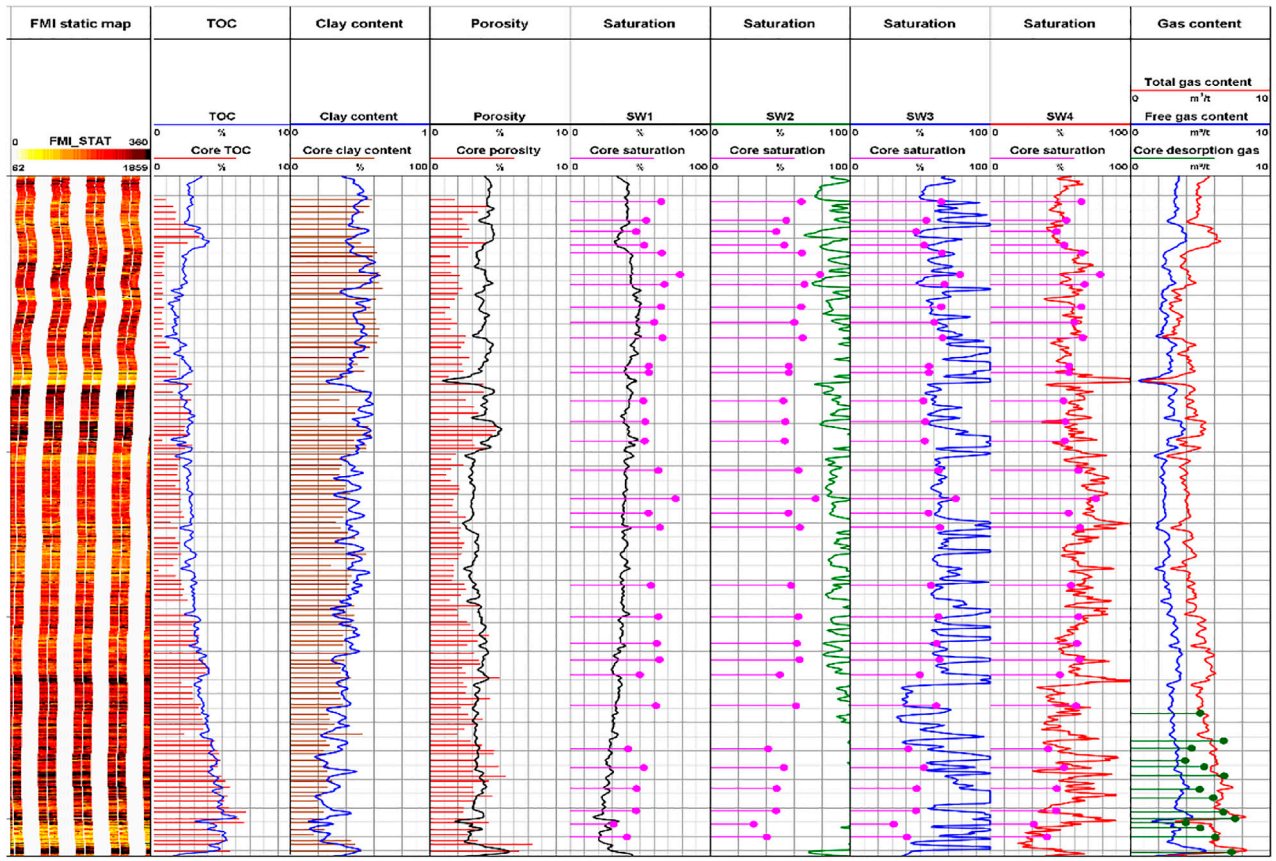

FIGURE 16 | Well logging interpretations of marine shale gas well J9, Sw4 is new model, Sw1-Sw3 are old models.

matter has little influence on the logging resistivity, and it is unnecessary to strip the influence of organic matter on shale resistivity for calculating the gas saturation.

The Process of Thin, Low-Resistivity Layer

When a thin, low-resistance layer exists, the deep lateral resistivity shale is low. To improve the accuracy of logging interpretation, two methods are used to strip the influence of the thin, low-resistivity layer.

The first method is to use high-resolution resistivity logging data. Shale gas wells in the study area have produced FMI data, and the longitudinal resolution of the FMI logging tool reaches as high as 2.54 mm. The FMI image can clearly reflect the stratigraphic structures present around the well. A high-resolution resistivity curve, namely, the scaled synthetic resistivity curve (SRES), can be obtained by combining the shallow lateral resistivity with a high-resolution FMI image (Bastia and RadhaKrishna, 2012). The SRES curve not only has a high resolution (2.54 mm) but also reflects the true resistivity of the formation. Therefore, we can use SRES instead of RLLD data to calculate the water saturation, which reduces the influence of the low-resistivity layer on shale resistivity.

The second method is used to calculate the resistivity of the high-resistivity layer based on the horizontal resistivity model of the thin interlayer and then remove the influence of the thin, low-resistivity layer on the shale resistivity. We first counted the SRES resistivity distribution of the Wufeng-Longmaxi Formation and used a certain cutoff value R_{cut} as the resistivity limit of the high- and low-resistivity layers. Then, we used the longitudinal resolution of RLLD as the window length (0.9 m), and the number of data points count_H for SRES curve values greater than R_{cut} and count_L for data points less than R_{cut} within the window length were counted. The proportion of the low-resistivity layer in the window length (f_L) and the resistivity of the high-resistivity layer can be expressed as:

$$f_L = \frac{count_L}{count_L + count_H} \tag{6}$$

$$R_H = \frac{(1 - f_L)R_t R_L}{R_L - f_L R_t} \tag{7}$$

The Process of Pyrite

When the pyrite content reaches a certain percentage, the log resistivity decreases sharply. The relationship between the pyrite content and the resistivity in **Figure 5** shows that when the pyrite content is less than 6%, the effect of pyrite on shale resistivity is not obvious. Otherwise, the shale resistivity decreases significantly. It is worth mentioning that the pyrite content rarely exceeds 10%.

Because of the irregular distribution of pyrite, its effect on the shale resistivity is not simply acting in series or parallel. Pyrite has a mixed effect on shale resistivity and should be stripped. Based on the shale conductivity model, the resistivity without the influence of pyrite (R_F) is expressed by the following:

$$\frac{1}{R_F} = \frac{1}{R_H} - \delta\frac{V_{py}^{\beta}}{R_{py}} \tag{8}$$

$$\delta = \begin{cases} 0 & , v_{py} < 5\% \\ p \times v_{py} + q & , v_{py} > 5\% \end{cases} \tag{9}$$

where δ is the pyrite mixing effect coefficient and p and q are parameters of the linear equation. Through digital rock simulations, we found that when the pyrite content is less than 5%, δ is near 0. When the pyrite content is greater than 5%, δ has a linear relationship with the pyrite content.

The Process of Formation Water and Clay

Clay minerals have various distribution forms in shale, such as striated and dispersed, and it is difficult to describe the influence of clay minerals on shale resistivity in a simple way. In muddy sandstone, Simandoux (1963) proposed a fluid saturation model without considering the specific clay distribution form; however, it worked well. In this paper, we used Simandoux's equation by considering that the influences of pore water and clay on shale resistivity were both controlled by the water saturation, which can be expressed as:

$$\frac{1}{R_F} = \frac{\phi^m S_w^2}{abR_w} + \frac{V_{cl}}{R_{cl}} S_w \tag{10}$$

$$S_w = \frac{-\frac{V_{cl}}{R_{cl}} + \sqrt{\left(\frac{V_{cl}}{R_{cl}}\right)^2 + 4\frac{\phi^m}{abR_wR_F}}}{2 \times \frac{\phi^m}{abR_w}} \tag{11}$$

$$S_g = 1 - S_w \tag{12}$$

where S_g represents for gas saturation, decimal.

Summary of the Whole Procedure

The flow chart of the new procedure with stepwise stripping of conductivity influencing factors is shown in **Figure 15**. The first step is to determine whether the organic matter is overmaturely carbonized. If it is carbonized, then the shale is considered to have a poor gas potential, and it is unnecessary to carry out gas saturation calculations. Otherwise, there is no need to strip the effect of organic matter because of its small effect on shale resistivity. The next step is to combine high-resolution

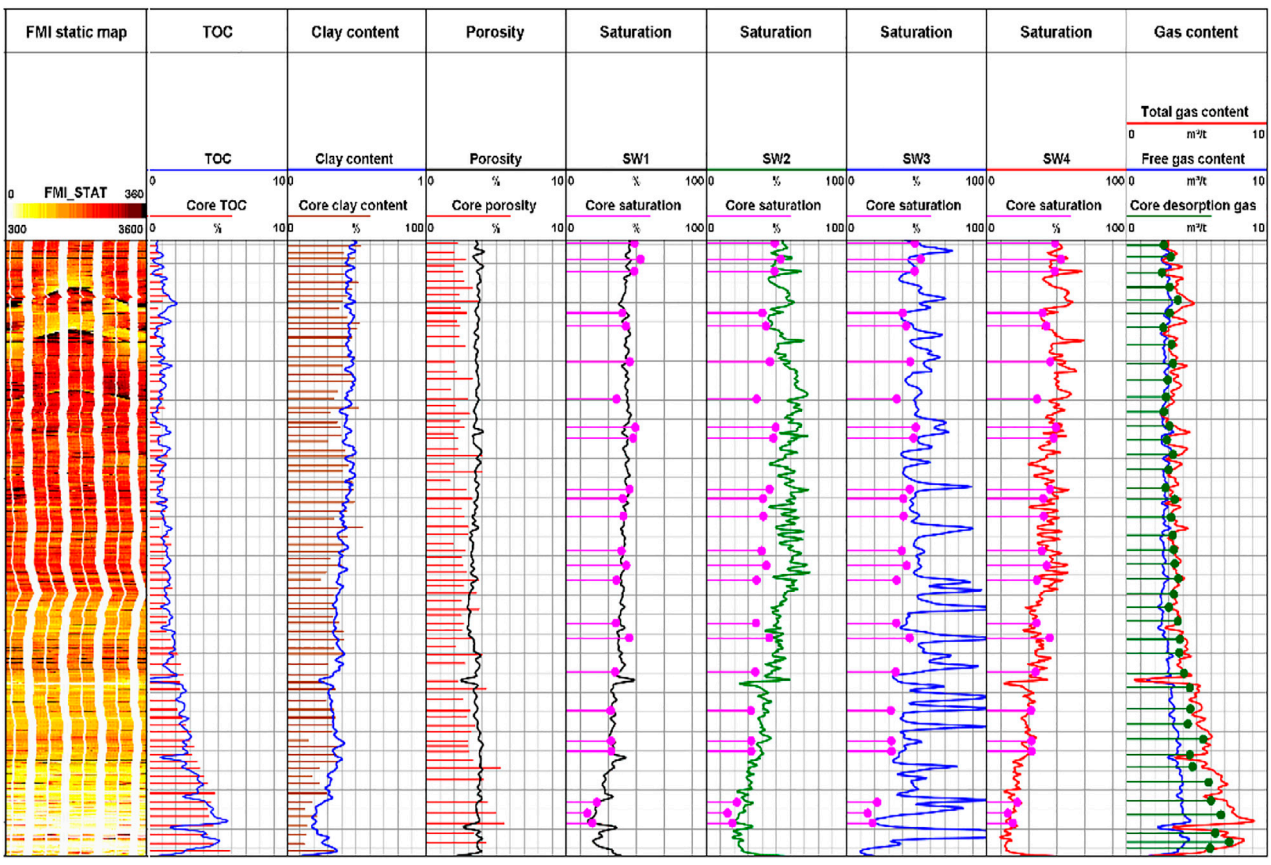

FIGURE 17 | Well logging interpretations of marine shale gas well D4, Sw4 is new model, Sw1-Sw3 are old models.

resistivity logging data and a horizontal resistivity model to strip the influence of thin, low-resistivity layers. Then, the pyrite content was calculated, and the effect of pyrite was stripped. Finally, the effects of water and clay on shale resistivity are considered to calculate the shale gas saturation. It should be noted that the gas saturation calculated based on the above processes is free gas saturation. To evaluate the total gas saturation of shale, adsorbed gas saturation needs to be calculated (Zeng et al., 2014).

EXAMPLE OF GAS SATURATION EVALUATION OF MARINE SHALE GAS WELLS

This paper utilized the new procedure with stepwise stripping of conductivity influencing factors to calculate the shale gas saturation of marine shale gas wells. The gas saturation results calculated by the neutron-density porosity overlay method, Archie's equation and Simandoux's equation were also compared. **Figures 16**, **17** show the calculated water saturations in the Wufeng-Longmaxi Formation for wells J9 and D4, respectively. In these well logging interpretation figures, the first channel shows the depth; the second channel shows the stratum; the third channel shows the FMI static image; the fourth channel shows the original and corrected resistivities; the fifth channel shows the TOC content; the sixth channel shows the pyrite content; the seventh channel shows the clay content; the eighth channel shows the porosity; the ninth channel shows the water saturation calculated by the neutron-density porosity overlay method (SW1); the 10th channel shows the water saturation calculated by Archie's equation (SW2); the 11th channel shows the water saturation calculated by Simandoux's equation (SW3); the 12th channel shows the water saturation calculated by our new method (SW4); the 13th channel shows the calculated gas content, including the free gas content, the total gas content and the desorption gas contents of the shale samples. The TOC content, clay content and porosity calculated by conventional logging curves agree well with the core analysis results, which provides reliable parameters for calculating marine shale gas saturation.

Most of the TOC contents in well J9 are greater than 1.5%, and the vitrinite reflectance of each shale sample is smaller than 3.0%. In addition, the logging resistivity is approximately 20 Ω m. Therefore, organic matter is not carbonized, which does not necessarily strip the effect of organic matter on resistivity. From the FMI static image, we can see that the Wufeng-Longmaxi Formation develops many thin, low-resistivity layers, and their influences on resistivity should be removed. ECS logging data show that the vast majority of the pyrite content is less than 5.0%, and there is no spike-like low-resistivity characteristic where the pyrite content is high, which indicates that pyrite has little effect on resistivity for well J9. Therefore, the main conductivity influencing factors are the thin, low-resistivity layer, clay and pore water. After stripping the influence of the thin, low-resistivity layer, the resistivity increases.

By comparing the results of rock analysis, it can be seen that the accuracies of the four water saturation calculation methods are different. The water saturation results calculated by both the neutron-density porosity overlay method and Archie's equation are higher than the actual water saturations, which means that these two methods are not applicable in this well. The water saturations calculated by Simandoux's equation agree well with the core analysis results in some layers. However, the water saturations are inconsistent with the actual saturations in this, low-resistivity layers. Among the calculated water saturation results, our new method provides the most accurate results. In addition, the total gas content calculated from the well logging data is in good agreement with the core desorption gas content, which also illustrates the accuracy of our method.

The vitrinite reflectance of shale in well D4 is between 2.1 and 2.8%, and the logging resistivity is approximately 40 Ω m, which indicates that there is no need to strip the effect of organic matter on resistivity. Thin, low-resistivity layers are determined by analyzing the FMI static image. Comparing the original logging resistivity with the ECS pyrite content, we can see that pyrite has an effect on shale resistivity, which should be stripped when calculating the gas saturation. Therefore, the main conductive influencing factors of this well are the presence of thin, low-resistivity layers, pyrite crystals, clay particles and pore water volumes. The corrected resistivity is higher than the original resistivity. The water saturations calculated by Archie's equation and Simandoux's equation are greater than core saturations. Our new method and the neutron-density porosity overlay method have good application results in this well. The calculated total gas content agrees well with the core desorption gas content, which also proves the accuracy of our method. At the same time, in the process of calculation, different influencing factors are quantitatively calculated, and different influencing factors are reasonably selected according to the model, so that the model has higher accuracy.

CONCLUSION

This research utilized geological data, well logging data, and rock experiment data to analyze the influencing factors of electrical properties in the Wufeng-Longmaxi Formation in the Sichuan Basin, China. The effects of stratigraphic structure, clay, pyrite, organic matter, pore structure, and formation fluid on shale resistivity were investigated. In addition, we proposed a new procedure which utilizes the stepwise stripping of conductivity influencing factors to calculate the shale gas saturation (At present, the application scope is only applicable to the shale in the study area, and the shale in other areas has not been verified. At the same time, in order to use this model, there must be electrical imaging logging data). Based on the results, the following conclusions can be drawn:

1) The resistivity of marine shale is affected by multiple factors. Thin, low-resistivity layers, high clay contents, pyrite crystals, overmature carbonized organic matter, larger proportions of

large pores and highly saline water volumes can reduce shale resistivity. Moreover, we summarized some upper and lower limit values. When the pyrite content is less than 6.0%, there is no obvious correlation between the shale resistivity and the pyrite content, and the shale resistivity decreases significantly after the pyrite content is greater than 6.0%. When R_o is greater than 3.5% and the shale resistivity is extremely low (less than 2 Ω m), the organic matter is over carbonized.

2) We made a cross-plot of gas content and logging resistivity, which could be divided into a low-resistivity (0.1–7 Ω m) and low-production part, a medium-resistivity (7–200 Ω m) and high-production part, and a high-resistivity (> 200 Ω m) and low-production part. By using a self-developed combined isothermal adsorption and resistivity measurement device, we found that the shale resistivity decreased with increasing pore gas pressures under a constant water saturation content. In addition, shale resistivity with methane was greater than shale resistivity with helium under the same pore gas pressure.
3) We developed a new shale conductivity application model for both low-resistivity layers and high-resistivity layers. Based on this model, a new procedure utilizing the stepwise stripping of conductivity influencing factors was proposed for calculating gas saturation. It is necessary to remove the influences of organic matter, thin, low-resistivity layers and pyrite on well logging resistivities to acquire the corrected resistivity, which only reflects clay and pore water.

4) By analyzing the well logging interpretations of two wells, the accuracies of different water saturation methods were compared. Archie's equation is not applicable to marine shale reservoirs because it does not take some conductive influencing factors into the equation. Simandoux's equation is suitable for shale only when there is no thin, low-resistivity layer. The application capability of the neutron-density porosity overlay method is unclear because it provides good calculation results for well D4, but the results of well J9 are poor. We will investigate the neutron-density porosity overlay method deeper in future studies. Among these methods, our new method shows the best water saturation calculation capability, and the calculated gas contents agree well with the core desorption gas contents.

DATA AVAILABILITY STATEMENT

The original contributions presented in the study are included in the article/Supplementary Material, further inquiries can be directed to the corresponding authors.`

AUTHOR CONTRIBUTIONS

FjS: Conceptualization, Data curation, Formal analysis, Methodology, Investigation, and Writing-original draft. XZ: Data curation, Formal analysis, Methodology, Investigation, Writing-original draft. JS: Supervision, Validation, Resources, Writing-review and editing. WgY: Methodology, and Investigation. JZ: Methodology, and Investigation. WY: Methodology, and Investigation. WcY: Methodology, and Investigation.

FUNDING

This work was supported in part by the National Science and Technology Major Project (No. 2017ZX05036-005-003), Natural Science Foundation of Shandong Province (No. ZR2020QD054), and Fundamental Research Funds for the Central Universities (No. 20 CX06026A).

REFERENCES

Archie, G. E. (1942). The Electrical Resistivity Log as an Aid in Determining Some Reservoir Characteristics. *Am. Inst. Mech. Eng.* 146, 54–62. doi:10.2118/942054-g

Bakhshi, E., Golsanami, N., and Chen, L. (2020). Numerical Modeling and Lattice Method for Characterizing Hydraulic Fracture Propagation: A Review of the Numerical, Experimental, and Field Studies. *Arch. Comput. Method. E* 28 (5), 3329–3360. doi:10.1007/s11831-020-09501-6

Bastia, R., and Radhakrishna, M. (2012). Exploration in the Indian Offshore Basins-Some Challenging Issues Related to Imaging and Drilling. *Dev. Pet. Sci.* 59, 319–359. doi:10.1016/b978-0-444-53604-4.00007-7

Brandt, A. R., Millard-Ball, A., Ganser, M., and Gorelick, S. M. (2013). Peak Oil Demand: The Role of Fuel Efficiency and Alternative Fuels in a Global Oil Production Decline. *Environ. Sci. Technol.* 47 (14), 8031–8041. doi:10.1021/es401419t

Chen, L., Wang, G., Yang, Y., Jing, C., Chen, M., and Tan, X. (2019). Geochemical Characteristics of Bentonite and its Influence on Shale Reservoir Quality in Wufeng-Longmaxi Formation, South Sichuan Basin, China. *Energy Fuels* 33 (12), 12366–12373. doi:10.1021/acs.energyfuels.9b03510

Chen, Y., Xu, J., and Wang, P. (2020). Shale Gas Potential in China: A Production Forecast of the Wufeng-Longmaxi Formation and Implications for Future Development. *Energy Policy* 147, 111868. doi:10.1016/j.enpol.2020.111868

Clavier, C., Heim, A., and Scala, C. (1976). "Effect of Pyrite on Resistivity and Other Logging Measurements," in SPWLA 17th Annual Logging Symposium.

Dong, H., Sun, J., Arif, M., Golsanami, N., Yan, W., and Zhang, Y. (2020). A Novel Hybrid Method for Gas Hydrate Filling Modes Identification via Digital Rock. *Mar. Pet. Geology.* 115, 104255. doi:10.1016/j.marpetgeo.2020.104255

Du, P., Cai, J., Liu, Q., Zhang, X., and Wang, J. (2021). A Comparative Study of Source Rocks and Soluble Organic Matter of Four Sags in the Jiyang Depression, Bohai Bay Basin, NE China. *J. Asian Earth Sci.* 216, 104822. doi:10.1016/j.jseaes.2021.104822

Gao, F., Song, Y., Li, Z., Xiong, F., Chen, L., Zhang, X., et al. (2018). Quantitative Characterization of Pore Connectivity Using NMR and MIP: A Case Study of the Wangyinpu and Guanyintang Shales in the Xiuwu basin, Southern China. *Int. J. Coal Geology.* 197, 53–65. doi:10.1016/j.coal.2018.07.007

Golsanami, N., Bakhshi, E., Yan, W., Dong, H., and Mahbaz, B. (2020). Relationships between the Geomechanical Parameters and Archie's Coefficients of Fractured Carbonate Reservoirs: a New Insight. *Energ. Source. Part. A.* (2). doi:10.1080/15567036.2020.1849463

Golsanami, N., Sun, J., Liu, Y., Yan, W., Lianjun, C., Jiang, L., et al. (2019). Distinguishing Fractures from Matrix Pores Based on the Practical Application of Rock Physics Inversion and NMR Data: A Case Study from an Unconventional Coal Reservoir in China. *J. Nat. Gas Sci. Eng.* 65, 145–167. doi:10.1016/j.jngse.2019.03.006

Golsanami, N., Zhang, X., Yan, W., Yu, L., Dong, H., Dong, X., et al. (2021). NMR-based Study of the Pore Types' Contribution to the Elastic Response of the Reservoir Rock. *Energies* 14 (5), 1513. doi:10.3390/en14051513

Hamada, G. M., Al-Blehed, M. S., Al-Awad, M. N., and Al-Saddique, M. A. (2001). Petrophysical Evaluation of Low-Resistivity sandstone Reservoirs with Nuclear Magnetic Resonance Log. *J. Pet. Sci. Eng.* 29 (2), 129–138. doi:10.1016/s0920-4105(01)00095-x

Han, T., Best, A. I., Sothcott, J., North, L. J., and MacGregor, L. M. (2015). Relationships Among Low Frequency (2Hz) Electrical Resistivity, Porosity, clay Content and Permeability in Reservoir Sandstones. *J. Appl. Geophys.* 112, 279–289. doi:10.1016/j.jappgeo.2014.12.006

Hinds, G. S., and Berg, R. R. (1990). Estimating Organic Maturity from Well Logs, Upper Cretaceous Austin Chalk, Texas Gulf Coast. *Trans. Gulf. Coast. Assoc. Geol. Soc.* 40, 295–300. doi:10.1306/20b230c5-170d-11d7-8645000102c1865d

Kadkhodaie, A., and Rezaee, R. (2016). A New Correlation for Water Saturation Calculation in Gas Shale Reservoirs Based on Compensation of Kerogen-clay Conductivity. *J. Pet. Sci. Eng.* 146, 932–939. doi:10.1016/j.petrol.2016.08.004

Kennedy, M. C. (2004). "Gold Fool's: Detecting, Quantifying and Accounting for the Effects of Pyrite on Modern Logs," in SPWLA 45th Annual Logging Symposium.

Klein, J. D., and Martin, P. R. (1997). The Petrophysics of Electrically Anisotropic Reservoirs. *The Log Analyst* 38 (3), 25–36.

Li, M., Vashaee, S., Romero-Zerón, L., Marica, F., and Balcom, B. J. (2017). A Magnetic Resonance Study of Low Salinity Waterflooding for Enhanced Oil Recovery. *Energy Fuels* 31 (10), 10802–10811. doi:10.1021/acs.energyfuels.7b02166

Li, Z., Jun Yao, J., and Kou, J. (2019). Mixture Composition Effect on Hydrocarbon-Water Transport in Shale Organic Nanochannels. *J. Phys. Chem. Lett.* 10 (15), 4291–4296. doi:10.1021/acs.jpclett.9b01576

Liu, K., Sun, J., Zhang, H., Liu, H., and Chen, X. (2018). A New Method for Calculation of Water Saturation in Shale Gas Reservoirs Using VP-To-VS Ratio and Porosity. *J. Geophys. Eng.* 15, 153–163. doi:10.1088/1742-2140/aa83e5

Mao, J., Fang, X., Lan, Y., Schimmelmann, A., Mastalerz, M., Xu, L., et al. (2010). Chemical and Nanometer-Scale Structure of Kerogen and its Change during thermal Maturation Investigated by Advanced Solid-State 13C NMR Spectroscopy. *Geochimica et Cosmochimica Acta* 74, 2110–2127. doi:10.1016/j.gca.2009.12.029

Memon, A., Li, A., Memon, B. S., Muther, T., Han, W., Kashif, M., et al. (2021). Gas Adsorption and Controlling Factors of Shale: Review, Application, Comparison and Challenges. *Nat. Resour. Res.* 30, 827–848. doi:10.1007/s11053-020-09738-9

Nie, X., Zou, C., Li, Z., Meng, X., and Qi, X. (2016). Numerical Simulation of the Electrical Properties of Shale Gas Reservoir Rock Based on Digital Core. *J. Geophys. Eng.* 13, 481–490.

Pan, H., Wang, J., Fan, Z., Ma, Y., Liu, J., and Li, M. (2001). Low Resistivity Oil(gas)-Bearing Reservoir Conductive Model. *Sci. China Ser. D-earth Sci.* 44, 346–355. doi:10.1007/bf02907105

Savage, K. S., Stefan, D., and Lehner, S. W. (2008). Impurities and Heterogeneity in Pyrite: Influences on Electrical Properties and Oxidation Products. *Appl. Geochem.* 23 (2), 103–120. doi:10.1016/j.apgeochem.2007.10.010

Senger, K., Birchall, T., Betlem, P., Ogta, K., Ohm, S., Olaussen, S., et al. (2020). Resistivity of Reservoir Sandstones and Organic Rich Shales on the Barents Shelf: Implications for Interpreting CSEM Data. *Geosci. Front.*, 101063.

Silva, M. L. d., Martins, J. L., Ramos, M. M., and Bijani, R. (2018). Estimation of clay Minerals from an Empirical Model for Cation Exchange Capacity: an Example in Namorado Oilfield, Campos basin, Brazil. *Appl. Clay Sci.* 158, 195–203. doi:10.1016/j.clay.2018.02.040

Simandoux, P. (1963). Dielectric Measurements of Porous media: Application to the Measurement of Water Saturations, Study of the Behavior of Argillaceous Formations. *Rev. Fr. Petrol.* 18 (S1), 193–215.

Soeder, D. J. (2018). The Successful Development of Gas and Oil Resources from Shales in North America. *J. Pet. Sci. Eng.* 163, 399–420. doi:10.1016/j.petrol.2017.12.084

Sun, J., Xiong, Z., Luo, H., Zhang, H., and Zhu, J. (2018). Mechanism Analysis and Logging Evaluation of Low Resistivity in Lower Paleozoic Shale Gas Reservoirs of Yangtze Region. *J. China Univ. Pet. (Edition Nat. Science)* 42 (5), 47–56.

Wang, D., Wang, Y., Dong, D., Wang, S., Huang, J., Huang, Y., et al. (2013). Quantitative Characterization of Reservoir Space in the Lower Cambrian Qiongzhusu Shale, Southern Sichuan Basin. *Natur. Gas. Ind.* 33 (7), 1–10.

Wang, J., and Zhang, S. (2018). Pore Structure Differences of the Extra-low Permeability sandstone Reservoirs and the Causes of Low Resistivity Oil Layers: a Case Study of Block Yanwumao in the Middle of Ordos Basin, NW China. *Pet. Exploration Dev.* 45, 273–280. doi:10.1016/s1876-3804(18)30030-2

Wang, T., Tian, S., Zhang, W., Ren, W., Li, G., and Li, G. (2021). Production Model of a Fractured Horizontal Well in Shale Gas Reservoirs. *Energy Fuels* 35 (1), 493–500. doi:10.1021/acs.energyfuels.0c03787

Wang, Y., Li, X., Chen, B., Wu, W., Dong, D., Zhang, J., et al. (2018). Lower Limit of thermal Maturity for the Carbonization of Organic Matter in marine Shale and its Exploration Risk. *Pet. Exploration Dev.* 45, 402–411. doi:10.1016/s1876-3804(18)30045-4

Wang, Y., Li, X., Wang, H., Jiang, S., Chen, B., Ma, J., et al. (2019). Developmental Characteristics and Geological Significance of the Bentonite in the Upper Ordovician Wufeng - Lower Silurian Longmaxi Formation in Eastern Sichuan Basin, SW China. *Pet. Exploration Dev.* 46 (4), 687–700. doi:10.1016/s1876-3804(19)60226-0

Wu, Y., Lin, C., Yan, W., Liu, Q., Zhao, P., and Ren, L. (2020b). Pore-scale Simulations of Electrical and Elastic Properties of Shale Samples Based on Multicomponent and Multiscale Digital Rocks. *Mar. Pet. Geology.* 117, 104369. doi:10.1016/j.marpetgeo.2020.104369

Wu, Y., Tahmasebi, P., Lin, C., and Dong, C. (2020c). A Comprehensive Investigation of the Effects of Organic-Matter Pores on Shale Properties: a Multicomponent and Multiscale Modeling. *J. Nat. Gas Sci. Eng.* 81, 103425. doi:10.1016/j.jngse.2020.103425

Wu, Y., Tahmasebi, P., Yu, H., Lin, C., Wu, H., and Dong, C. (2020a). Pore-scale 3D Dynamic Modeling and Characterization of Shale Samples: Considering the Effects of thermal Maturation. *J. Geophys. Res-sol. Ea.* 125 (1). doi:10.1029/2019jb018309

Xie, H., Li, H., Yuan, W., Feng, M., Yan, W., and Sun, J. (2019). Calculation Method of Gas Saturation in Low-Resistivity Shale Reservoirs of Longmaxi Formation. *Well Logging Tech.* 43 (02), 161–166.

Xie, X., Luo, B., Yin, L., Liang, H., and Li, Y. (2017). Influence Factors of Low Resistivity Shale Gas Reservoir. *Acta Geologica Sichuan* 37 (03), 433–437.

Yan, W., Sun, J., Cheng, Z., Li, J., Sun, Y., Shao, W., et al. (2017). Petrophysical Characterization of Tight Oil Formations Using 1D and 2D NMR. *Fuel* 206, 89–98. doi:10.1016/j.fuel.2017.05.098

Yan, W., Sun, J., Golsanami, N., Li, M., Cui, L., Dong, H., et al. (2019). Evaluation of Wettabilities and Pores in Tight Oil Reservoirs by a New Experimental Design. *Fuel* 252, 272–280. doi:10.1016/j.fuel.2019.04.130

Yan, W., Sun, J., Zhang, J., Yuan, W., Zhang, L., Cui, L., et al. (2018). Studies of Electrical Properties of Low-Resistivity Sandstones Based on Digital Rock Technology. *J. Geophys. Eng.* 15, 153–163. doi:10.1088/1742-2140/aa8715

Yasin, Q., Du, Q., Ismail, A., and Shaikh, A. (2019). A New Integrated Workflow for Improving Permeability Estimation in a Highly Heterogeneous Reservoir of Sawan Gas Field from Well Logs Data. *Geomech. Geophys. Geo-energ. Geo-resour.* 5, 121–142. doi:10.1007/s40948-018-0101-y

Zeng, X., Sun, J., and Cui, H. (2014). Shale Adsorbed Gas Volume Calculation Model under Varied Temperature. *Well Log. Tech.* 38 (3), 286–291.

Zeng, X., Sun, J., Yan, W., Cui, R., Yuan, W., Yan, W., et al. (2020). New Insight into the Petrophysical Characterization of Shales with Different Fluid Saturation States Based on Nuclear Magnetic Resonance Experiments. *Energy Fuels* 34 (5), 5599–5610. doi:10.1021/acs.energyfuels.0c00093

Zhang, J., Li, R., Wang, L., Chen, F., and Geng, B. (2017a). A New Method for Calculating Gas Saturation of Low-Resistivity Shale Gas Reservoirs. *Nat. Gas Industry* 37 (04), 34–41. doi:10.1016/j.ngib.2017.09.004

Zhang, J., Li, S., Wang, L., Chen, F., and Geng, B. (2017b). A New Method for Calculating Gas Saturation of Low-Resistivity Shale Gas Reservoirs. *Nat. Gas Industry B* 4 (5), 346–353. doi:10.1016/j.ngib.2017.09.004

Zhang, L., Xiao, D., Lu, S., Jiang, S., and Lu, S. (2019). Effect of Sedimentary Environment on the Formation of Organic-Rich marine Shale: Insights from Major/trace Elements and Shale Composition. *Int. J. Coal Geology.* 204, 34–50. doi:10.1016/j.coal.2019.01.014

Zhao, J., Cui, L., Chen, H., Li, N., Wang, Z., Ma, Y., et al. (2020). Quantitative Characterization of Rock Microstructure of Digital Core Based on CT Scanning. *Geoscience* 34 (06), 1205–1213.

Zhong, Z., Rezaee, R., Esteban, L., Josh, M., and Feng, R. (2021). Determination of Archie's Cementation Exponent for Shale Reservoirs; an Experimental Approach. *J. Pet. Sci. Eng.* 201, 108527. doi:10.1016/j.petrol.2021.108527

Zhu, L., Ma, Y., Zhang, C., Wu, S., and Zhou, X. (2021). New Parameters for Charactering the Gas-Bearing Properties of Shale Gas. *J. Petrol. Sci. Eng.* 201:108290. doi:10.1016/j.petrol.2020.108290

Zhu, L., Zhang, C., Zhang, Z., Zhou, X., and Liu, W. (2019). An Improved Method for Evaluating the TOC Content of a Shale Formation Using the Dual-Difference ΔlogR Method. *Mar. Pet. Geology.* 102, 800–816. doi:10.1016/j.marpetgeo.2019.01.031

Zou, C., Dong, D., Wang, Y., Li, X., Huang, J., Wang, S., et al. (2015). Shale Gas in China: Characteristics, Challenges and Prospects (I). *Pet. Exploration Dev.* 42, 753–767. doi:10.1016/s1876-3804(15)30072-0

Conflict of Interest: Authors WgY and WY were employed by the Sinopec Exploration Company. Author JZ was employed by the Well Logging Company of Sinopec Shengli Oilfield Service Corporation.

The remaining authors declare that the research was conducted in the absence of any commercial or financial relationships that could be construed as a potential conflict of interest.

frontiers in Earth Science

ORIGINAL RESEARCH
published: 29 March 2022
doi: 10.3389/feart.2022.850023

Lithology Classification and Porosity Estimation of Tight Gas Reservoirs With Well Logs Based on an Equivalent Multi-Component Model

Zhenyang Wang[1,2], *Xin Nie*[1,2]*, *Chong Zhang*[1,2], *Mingrui Wang*[1,2], *Junwei Zhao*[3] and *Longde Jin*[4]

[1]Cooperative Innovation Center of Unconventional Oil and Gas, Yangtze University (Ministry of Education & Hubei Province), Wuhan, China, [2]Key Laboratory of Exploration Technologies for Oil and Gas Resources (Yangtze University), Wuhan, China, [3]Institute of Mud Logging Technology and Engineering, Yangtze University, Jingzhou, China, [4]Golder Associates, Atlanta, GA, United States

Tight gas makes up a significant portion of the natural gas resources. There are tight gas reservoirs with great reserve and economic potential in the west Sichuan Basin, China. Due to the complex mineral component and heterogeneity of the thick tight sand formations, the reservoir parameters are challenging to evaluate from well logs using conventional methods, even the fundamental porosity. The mineral components must be considered. In this study, based on the analysis of different logging responses of varying lithologies, we introduced the complex reservoir analysis (CRA) method. CRA is always used in the carbonate reservoirs to calculate the different rock component volume fractions and can be used to classify the lithology and calculate the porosity simultaneously. By analyzing the component, a new equivalent component method (CRAE) is proposed based on the CRA method in this paper. In this method, the AC-CNL equation-calculated porosity is calibrated according to the core porosity data to set the rock components' physical parameters. After calibration, the rock component fractions and porosity can be calculated accurately. Also, according to the relationship between the grain size and natural gamma-ray, a granularity median model was established. Six lithology types, including coarse-grained quartz sandstone and coarse-grained lithic sandstone, are distinguished, and the porosity is estimated in the study area. The identification results are compared with the mud logging data and other methods. It shows that this method is very well adequate in the tight sandstone gas reservoirs in the study area.

Keywords: tight gas, lithology identification, well logging, complex reservoir analysis, MD model

OPEN ACCESS

Edited by:
Yuwei Li,
Liaoning University, China

Reviewed by:
Qiang Guo,
China Jiliang University, China
Jing Ba,
Hohai University, China

***Correspondence:**
Xin Nie
niexin_cugb@126.com

Specialty section:
This article was submitted to Economic Geology, a section of the journal Frontiers in Earth Science

Received: *07 January 2022*
Accepted: *04 March 2022*
Published: *29 March 2022*

Citation:
Wang Z, Nie X, Zhang C, Wang M, Zhao J and Jin L (2022) Lithology Classification and Porosity Estimation of Tight Gas Reservoirs With Well Logs Based on an Equivalent Multi-Component Model. Front. Earth Sci. 10:850023. doi: 10.3389/feart.2022.850023

INTRODUCTION

Unconventional reservoirs have become the research hotspot (Gao et al., 2018; Cong et al., 2022). As an essential source of unconventional natural gas, the tight sandstone reservoirs have attracted extensive attention (Bai et al., 2013; He et al., 2020). These reservoirs in China have excellent resource potential and are characterized by low porosity, low permeability, and complex pore structure (Li et al., 2017). Stratigraphic lithology classification and identification are essential for evaluating fine modeling reservoir parameters (Li and Li, 2013; Alzubaidi et al., 2021). Accurate evaluation of

reservoir properties such as lithology identification and porosity calculation is the basis of exploration and development, as well as the basis for calculation of reservoir parameters (Yuan et al., 2018; Zhou et al., 2018). Their accuracy is very important for predicting, exploring, and developing rich areas of oil and gas resources. However, typical characteristics such as complex lithology, low maturity of sandstone, strong diagenesis, and substantial heterogeneity bring difficulties and challenges to the accurate identification of the lithologic zone and become the main constraints for practical exploration of this type of reservoir (Pang et al., 2019; Xiong et al., 2020; Bai et al., 2021; Wei et al., 2021).

Previous research mainly focused on improving the identification accuracy of lithologic types by using logging curves by various methods (Tan et al., 2017; Liu et al., 2020). Traditional lithologic identification methods include debris logging, core logging, and cross plot (Zhao and Gao, 2003). Gupta et al. (2012) used natural gamma-ray logging, high-resolution resistivity logging, lithologic density logging, and other logging data cross-mapping techniques to evaluate the lithologic and physical property parameters of the reservoir profile from two wells of fractured basalt. Cheng et al. (2016) established the cross-plot method and logging curve calculation method to identify sandstone, siltstone, etc. Zhou et al. (2017) proposed a lithologic classification method based on thin sections, logging curves, and core physical property data. Das and Chatterjee (2018) identified gas sand, saltwater sand, carbonate rock, and shales by analyzing vertical and horizontal impedance diagrams. Khamees et al. (2021) used neutron-density cross plot, acoustic-density cross plot, M–N cross plot, etc. The results show that they are well applied in lithology identification of Jeribe formation in a field in northern Iraq. For the unique strata with strong heterogeneity and complex structure, the traditional lithology identification method is challenging to ensure identification accuracy (Sun et al., 2019).

With the re-emergence of deep learning in recent years, many machine learning methods have been applied to lithology identification using logging data. The combination of machine learning algorithm and lithological classification model mainly includes support vector machine (Sebtosheikh and Salehi, 2015), neural network (Han et al., 2018), and decision tree (Duan et al., 2016). Sebtosheikh et al. (2015) adopted the support vector machine (SVM) classification method to predict the lithology of a heterogeneous carbonate reservoir in Iran based on core analysis data. Zhao et al. (2017) proposed a multivariate membership function discriminant method, which regarded lithology identification as a linear model in the fuzzy domain and obtained target results by establishing a multivariate membership function. Wang et al. (2018) proposed a KNN clustering optimization method based on weighted cosine distance to fit the lithologic model better. Xiang et al. (2020) presented the application of deep learning to establish a deep trust network (DBN) based on logging data in lithology. However, the combination of machine learning methods with geological data is less, and the results may not conform to the general geological laws, resulting in unsatisfactory identification results. Also, most of these methods are limited to lithology identification and rarely combine with reservoir physical property data. Moreover, machine learning methods may be affected by drilling fluid (Chen et al., 2020).

Based on the geological data of the target interval, we classify the lithology of the reservoir by integrating the thin-section information, core analysis data, and well logging data in this paper. The lithology of these reservoirs is mainly coarse-, medium-, and fine-grained quartz sandstone and lithic sandstone. By analyzing the relationship between rock compositions, reservoir parameters, and logging response, we proposed a new method based on the complex reservoir analysis method (CRA) with equivalent components (CRAE). We used the acoustic transit time (AC) log and compensated neutron porosity log (CNL) to estimate formation porosity and set the parameters of the matrix components to make the results agree with the core data. Then, the fractions of the mineral components are calculated. Also, we used the natural gamma-ray log (GR) to calculate the granularity median. By combining the component fractions and granularity median, we can accurately identify the formation lithology of the Xu 2 Member tight gas reservoir in CX depression, West Sichuan Basin. The second part of this article gives the geological background. The third part introduces the data and methods of the study. The fourth and fifth present the application results and comparison and discuss the effect. Finally, conclusions are drawn in the sixth section.

GEOLOGICAL SETTINGS

The West Sichuan Depression is located west in the Sichuan Basin, east to the Longmenshan orogenic belt, and northwest to the Yangtze block. It is a part of the western Sichuan foreland basin (**Figure 1**), and the area is about 3.1×10^4 km^2. It was formed during the transition from the marine cratonic basin to the continental basin in the Sichuan Basin in the Late Triassic. There is a set of the coal-bearing clastic rock group from bottom to top from marine facies to continental facies and dominated by continental facies. The thickness of this set of formations does not change much, with a slight decrease from west to east. CX depression is a part of the west Sichuan Depression. From bottom to top, it includes Xu 1, Xu 2, Xu 3, Xu 4, and Xu 5. The section of interest of this study is Xu 2.

The Xu 2 member in the boreholes of the research area has a depth of 4,300–6,000 m and a thickness of about 400–500 m. It is dominated by gas-bearing lithic sandstone and lithic quartz sandstone. There are primarily argillaceous siltstone and black silty shale, interbedded with different thicknesses and with carbonaceous shale and coal lines. Detrital materials, mostly sedimentary and metamorphic debris with a small number of volcanic debris, are abundant. The reservoirs generally contain clay minerals and calcareous minerals such as calcite and dolomite. They are dense. The porosity distribution of the reservoir is shown in **Figure 2**, with an average porosity of 3.7% and a permeability of less than 0.1 micro-Darcy (mD). The reservoirs are affected by multiple structures, formation temperature, pressure, and cemented calcium and mud. The frontal sedimentary subfacies of the braided river delta are

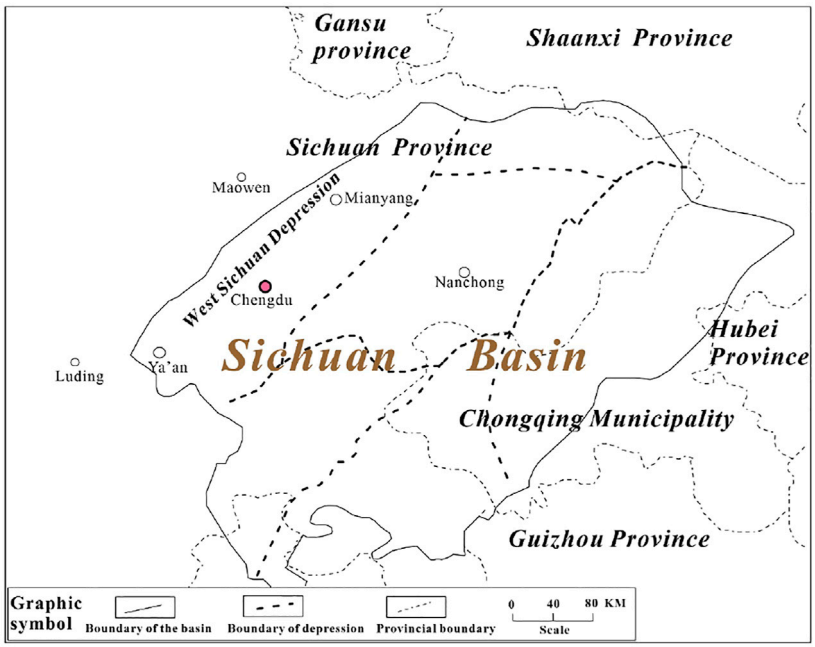

FIGURE 1 | Location of the West Sichuan depression.

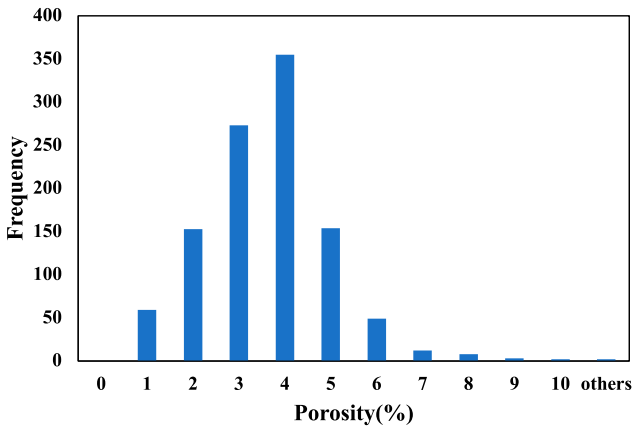

FIGURE 2 | Porosity distribution histogram.

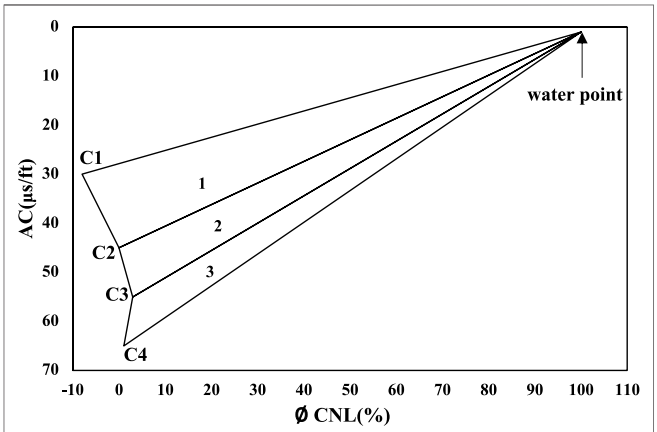

FIGURE 3 | Triangle diagram of the CRA Method.

relatively developed. The porosity is low, and the lithology is complicated, making it challenging to identify the lithology and calculate the porosity accurately.

METHODOLOGY AND DATA

CRA Method

Usually, the CRA method is used to analyze the lithological composition of carbonate formations and allows porosity calculation. The interpreter can specify the number and attributes of the mineral components according to geological conditions, but to no more than four minerals. According to the cross-plot diagram of two porosity logs (**Figure 3**), C1, C2, C3, and C4 are the porosity log intersections of four minerals set according to the analysis requirements of stratigraphic components. The junction of the framework values of each two adjacent minerals can form a lithological triangle with the water point. According to their position on the intersection diagram, the triangles from top to bottom are called the first, second, and third triangles. If the data point falls into a particular triangle, it is considered a rock composed of the two minerals forming this triangle. The interpreter can set the minerals according to the formation component analysis results from the thin casting sections. Then, a combination of any two

porosity logging response equations of AC, CNL, or density log (DEN) can be used for lithology analysis (Yong and Zhang, 2002). The calculation steps are as follows:

1) Calculation of shale content by using GR or SP. Generally, we choose GR to calculate the shale content. The equations are as follows (Nie et al., 2017):

$$SH = \frac{GR - GR_{MIN}}{GR_{MAX} - GR_{MIN}}, \tag{1}$$

$$V_{SH} = \frac{2^{GCUR \times SH} - 1}{2^{GCUR} - 1}, \tag{2}$$

where the SH is the original shale content; GR_{MAX} is the GR values of maximum and GR_{MIN} is the GR values of minimum in the formation, and V_{SH} is the calculated shale content. The GCUR is the correction coefficient.

2) The bulk model of the formations is **Eqn. 3**, and the log response equations are **Eqn. 4–6**:

$$V_{SH} + V_{QZ} + V_{Feld} + V_{\mathrm{Deb}} + \varnothing = 1, \tag{3}$$

$$V_{SH}CNL_{SH} + V_{QZ}CNL_{QZ} + V_{Feld}CNL_{Feld} + V_{\mathrm{Deb}}CNL_{\mathrm{Deb}} + \varnothing CNL_f = CNL, \tag{4}$$

$$V_{SH}AC_{SH} + V_{QZ}AC_{QZ} + V_{Feld}AC_{Feld} + V_{\mathrm{Deb}}AC_{\mathrm{Deb}} + \varnothing AC_f = AC, \tag{5}$$

$$V_{SH}DEN_{SH} + V_{QZ}DEN_{QZ} + V_{Feld}DEN_{Feld}V_{\mathrm{Deb}}DEN_{\mathrm{Deb}} + \varnothing DEN_f = DEN, \tag{6}$$

where $\varnothing$ is the porosity; V_{SH}, V_{QZ}, V_{Feld}, and V_{Deb} are the contents of shale, quartz, feldspar, and rock debris; CNL_{SH}, CNL_{QZ}, CNL_{Feld}, and CNL_{Deb} are the CNL skeleton values of shale, quartz, feldspar, and rock debris; AC_{SH}, AC_{QZ}, AC_{Feld}, and AC_{Deb} are the AC skeleton values of shale, quartz, feldspar, and rock debris; DEN_{SH}, DEN_{QZ}, DEN_{Feld}, and DEN_{Deb} are the DEN skeleton values of shale, quartz, feldspar, and rock debris; and $\varnothing CNL_f$ $\varnothing AC_f$, and $\varnothing DEN_f$ are the response value of CNL, AC, and DEN of porosity fluid.

3) The volume content of each mineral is calculated with these equations, and an optimum formation lithologic result is found which contains shale and one or two mineral components.

CRAE Parameter Analysis

There are quartz, feldspar, rock debris, and less mud content in the formations of the study area identified from the thin casting section data. Since the feldspar content in the XC area is basically below 10% and the physical properties are unstable, we choose to ignore it in the bulk model. We only consider quartz, the physical properties of which are stable, and a large number of metamorphic rocks and igneous rocks in the debris with low AC value are treated as an equivalent component. Also, because the DEN log is greatly affected by the borehole enlargement, we choose the AC-CNL cross plot to calculate the lithology profile. Therefore, the formations are considered to consist of shale, quartz, and rock debris, and GR, AC, and CNL logs are used. According to the abovementioned analysis, due to the limitation of research lithology types, the CRA method is not applicable in this study; we can simplify the CRA model and propose the CRAE model as follows:

$$V_{SH} + V_{QZ} + V_{Deb} + \varnothing = 1, \tag{7}$$

$$V_{SH}CNL_{SH} + V_{QZ}CNL_{QZ} + V_{Deb}CNL_{Deb} + \varnothing CNL_f = CNL, \tag{8}$$

$$V_{SH}AC_{SH} + V_{QZ}AC_{QZ} + V_{Deb}AC_{Deb} + \varnothing AC_f = AC. \tag{9}$$

We used the AC-CNL ensemble average value to calculate the porosity. Taking the triangle formed by quartz and rock debris as an example, reference for relevant equation derivation (Yong and Zhang, 2002), the calculation equation is as follows:

1) Calculation of triangle coefficients:

$$V_{QZ} + V_{Deb} + \varnothing = 1, \tag{10}$$

$$V_{QZ}CNL_{QZ} + V_{\mathrm{Deb}}CNL_{\mathrm{Deb}} + \varnothing CNL_f = CNL, \tag{11}$$

$$V_{QZ}AC_{QZ} + V_{\mathrm{Deb}}AC_{\mathrm{Deb}} + \varnothing AC_f = AC. \tag{12}$$

We make $CNL_{QZ} = Y_1$, $CNL_{Deb} = Y_2$, $CNL_f = Y_3$, $CNL = Y$, $AC_{QZ} = X_1$, $AC_{Deb} = X_2$, $AC_f = X_3$, $AC = X$, $V_{QZ} = V_1$, $V_{Deb} = V_2$, and $\varnothing = V_3$. Then, its mathematical transformation is

$$V_1 + V_2 + V_3 = 1, \tag{13}$$

$$V_1Y_1 + V_2Y_2 + V_3Y_3 = Y, \tag{14}$$

$$V_1X_1 + V_2X_2 + V_3X_3 = X. \tag{15}$$

It is solved as

$$V_1 = A_1X + B_1Y + C_1, \tag{16}$$

$$V_2 = A_2X + B_2Y + C_2, \tag{17}$$

$$V_3 = 1 - V_1 - V_2, \tag{18}$$

where $B_1 = (X_2 - X_3)/D_1$, $A_1 = B_2(Y_3 - Y_2)/(X_2 - X_3)$, $C_1 = -(A_1X_2 + B_1Y_2)$, and $D_1 = (X_2 - X_3)(Y_1 - Y_2) - (Y_2 - Y_3)(X_1 - X_2)$. $B_2 = (X_1 - X_3)/D_2$, $A_2 = B_2(Y_3 - Y_1)/(X_1 - X_3)$, $C_2 = -(A_2X_1 + B_2Y_1)$, and $D_2 = (X_1 - X_3)(Y_2 - Y_3) - (Y_1 - Y_3)(X_2 - X_3)$. When $X_2 = X_3$, $D_1 = -(Y_2 - Y_3)(X_1 - X_2)$, $B_1 = 0$, $A_1 = 1/(X_1 - X_2)$, and $C_1 = -A_1X_2$. When $X_1 = X_3$, $D_2 = -(X_2 - X_3)(Y_1 - Y_3)$, $B_2 = 0$, $A_2 = 1/(X_2 - X_3)$, and $C_2 = -A_2X_1$.The coefficients A_1, B_1, and C_1 and A_2, B_2, and C_2 in the equation are called the triangular coefficients of the intersection diagram, which can be calculated according to the abovementioned equations according to the known parameters of the fluid and the two minerals.

2) Shale correction for porosity log data:

According to the following equation, the shale correction is performed on the porosity log.

$$CNL = N_{SH} - (N_{SH} - CNL)/OMSH, \tag{19}$$

$$AC = T_{SH} - (T_{SH} - AC)/OMSH, \tag{20}$$

$$OMSH = 1 - V_{SH}, \tag{21}$$

TABLE 1 | Correspondence between median grain size and Ø-value size.

Natural grain size standard (mm)	ø-value size standard	Terrigenous debris names	Source debris names
≥ 128	**≤ -7**	**Boulders**	**Boulder-grained crumbs**
128 ~ 32	**–7 ~ –5**	**Coarse-grained gravel**	**Coarse-grained gravel**
32 ~ 8	**–5 ~ –3**	**Medium-grained gravel**	**Medium -grained gravel**
8 ~ 2	**–3 ~ –1**	**Fine-grained gravel**	**Fine-grained gravel**
2 ~ 0.5	**–1 ~ 1**	**Coarse-grained sand**	**Coarse-grained sand**
0.5 ~ 0.25	**1 ~ 2**	**Medium-grained sand**	**Medium-grained sand**
0.25 ~ 0.06	**2 ~ 4**	**Fine-grained sand**	**Fine-grained sand**
0.06 ~ 0.03	**4 ~ 5**	**Coarse-grained silt**	**Coarse-grained silt**
0.03 ~ 0.004	**5 ~ 8**	**Fine-grained silt**	**Fine-grained silt**
< 0.004	**> 8**	**Mud**	**Mud debris**

Bold value represent a corresponding relationship between particle size and median particle size.

where T_{SH} is the AC value of the surrounding mudstone read from the logging information, N_{SH} is the CNL value of the surrounding mudstone read from the log data, the OMSH is the volume percentage of mud removed.

3) Mineral volume content and porosity calculation:

According to **Equations 16–18**, the data points are solved with triangles, respectively, and the mineral volume and porosity of the layer where the data points are located.

Median Grain Size Model

The median grain size, namely, MD (Ø50), refers to the abscissa value corresponding to the frequency of 50% on the cumulative frequency curve of the grain diameters. It represents the grain diameter size in the middle of the population and is always represented by the Ø-value size (**Table 1**). The median particle size can indicate the size of the grains in a clastic formation.

The natural gamma-ray is a reflection of radioactive materials, and its morphological changes are effected by the content of mud and other radioactive materials in the formation. The smaller the particle size, the stronger the adsorption performance for radioactive materials; from the perspective of the natural gamma baseline deviation from large to small, it can reflect the change in particle size from coarse to fine (Song et al., 2009). Therefore, the natural gamma-ray can reflect the relative instability of the shale content in the clastic rock formation and the change of the clastic grain size. From a geological point of view, the higher the rock mud content, the smaller the particle size. These two have a good corresponding relationship, and the natural gamma is less disturbed by other factors. Therefore, the continuous longitudinal characteristics of the ΔGR defined as **Eqn. 22** can be used to predict the MD (Sima et al., 2017).

$$\Delta GR = \frac{GR - GR_{MIN}}{GR_{MAX} - GR_{MIN}}. \quad (22)$$

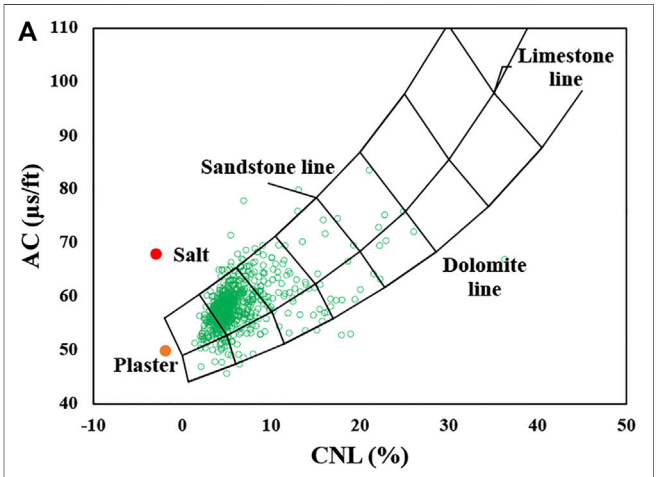

FIGURE 4 | Cross plot of porosity log. **(A)** Cross plot of CNL and AC. **(B)** Cross plot of CNL and DEN.

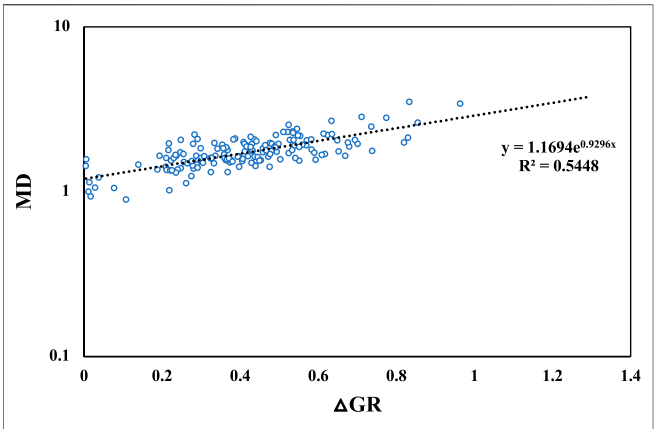

FIGURE 5 | Cross plot of Δ GR and median grain size.

Data Collection

In this study, we collected the conventional well logging data, core casting thin-section analysis data, and ΔGR value of 184 samples of 46 wells. Most of these wells have lithological logs including the spontaneous potential (SP), GR, wellbore caliper (CAL), the dual lateral resistivity logs including deep resistivity (LLD) and shallow resistivity (LLS), and the porosity logs, including CNL, DEN, and AC. Also, the casting thin-section analysis data provide the volume content of the shale, quartz, rock debris, and feldspar.

Analysis of Logging Response Characteristics and Parameter Setting

Due to the known complexity of the rock components, we introduced the porosity log cross plots, which are used to determine the lithology in **Figure 4**. **Figure 4A** is the AC-CNL cross plot. It shows most of the logging data points are under the sandstone line, which means some components are with very low AC in the formations. Also, **Figure 4B** is the DEN-CNL cross plot. It also reveals that there are high-density components. Those components with relatively low AC and high DEN might be the volcanic or metamorphic debris, which have calcium minerals or other elements with high density and wave speed. Therefore, we introduced the CRA method to this study.

The median particle size and ΔGR value of 184 samples were statistically analyzed, as shown in **Figure 5**. The result indicates that the MD and ΔGR are with an exponential relationship, shown as follows:

$$MD = 1.1694 \cdot e^{0.9262 \cdot \Delta GR}. \quad (23)$$

According to the abovementioned cross-plot analysis, we can conclude that the formations contain calcite, dolomite, and other calcareous minerals and siliceous materials. Meanwhile, in the well section with more rock debris, AC is lower, and CNL is higher than sandstone, indicating that the rock debris has lower AC and relatively high CNL. The AC of this debris is 43–49 μs/ft. Under the action of calcareous cementation, the AC is reduced.

The Xu2 member is dominated by tight sandstone. The AC is smaller than that of the more porous rocks. One reason for this is the heavy mineral components. In addition, the depth of burial also affects the response value of AC. As the depth increases, the overburden pressure on the rock layer increases, which changes the particle density, elastic modulus, and fluid density in the pores of the rock. More importantly, the porosity of the rock formation decreases regularly with the increase in the depth of the overlying rock layer, which increases the acoustic velocity of the rock formation. The AC of the same lithology formation decreases (Zhang et al., 2009).

We tried to find the best parameters for the CNL and AC of shale, quartz, and rock debris by calculating the formation's porosity with different parameters and comparing it with the core analysis result. When the calculated porosity agrees well with the core data, the parameters are adequate. Different from the previous quartz parameter CNL and AC which are −2%, 55 μs/ft, we adjusted the quartz's parameter to −2%, 50 μs/ft, and the rock debris was adjusted to 0% and 43 μs/ft for CNL and AC, respectively. At the same time, we set up the AC-CNL physical parameters required for the equations to calculate porosity and lithological components. The process of lithology identification and porosity estimation is shown in **Figure 6**.

APPLICATION RESULTS

According to the abovementioned analysis, applications were carried out in the study area. The application results in well 1 are shown in **Figure 7**. In **Figure 7**, the first three tracks are the original conventional logs, and the fourth track is the depth track. The fifth track is the lithological component profile we calculated by using the CRAE workflow. The sixth track is the lithological profile

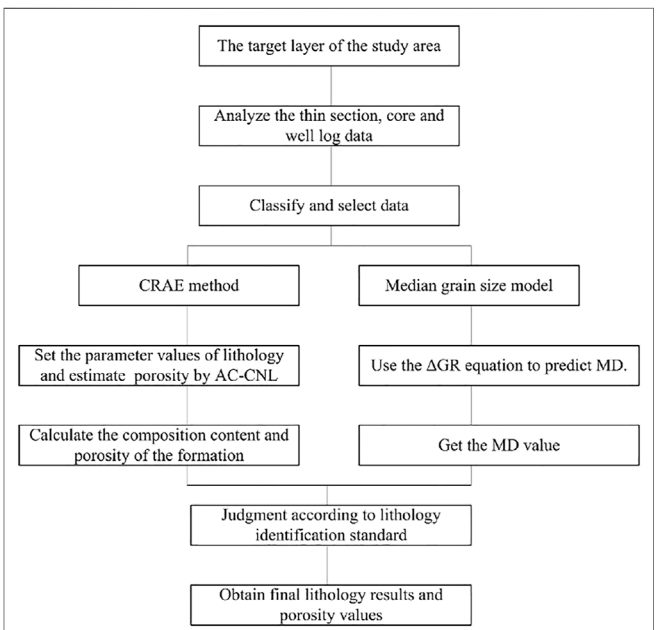

FIGURE 6 | Flowchart of lithology identification and porosity estimation.

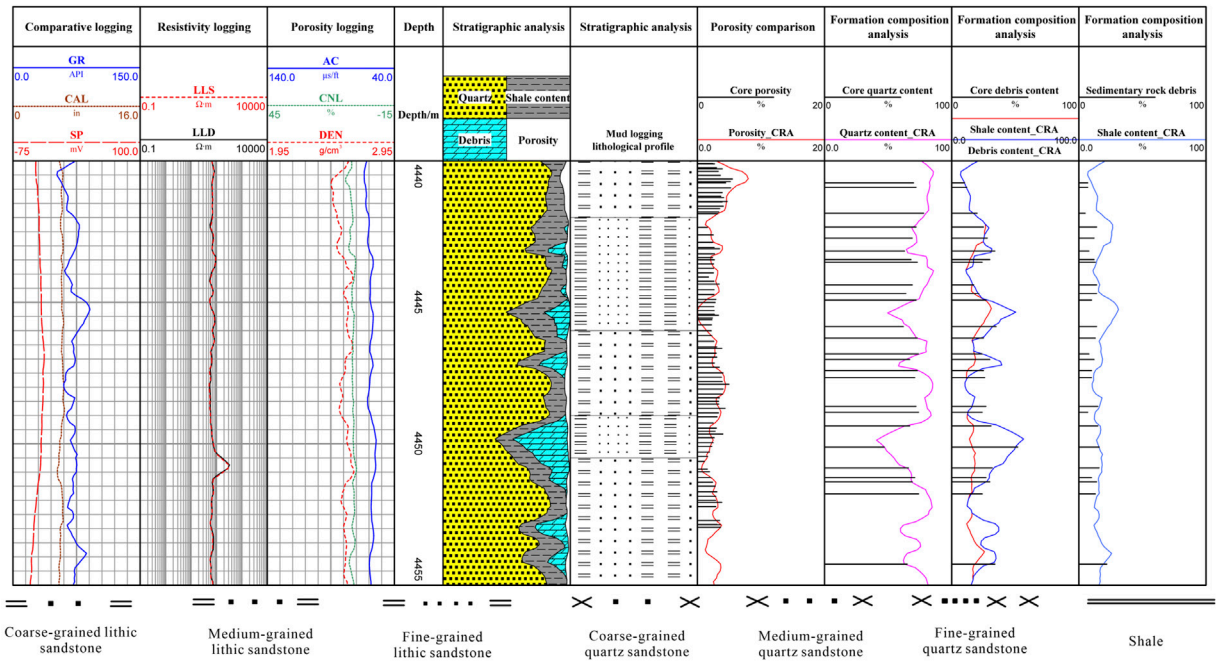

FIGURE 7 | Comparison of the lithological profile and formation composition of 4,440–4,455 m in well 1.

TABLE 2 | Lithologic classification standard.

Quartz + flint (%)	Rock debris content (%)	Median grain size ø	Category of lithology
> 90		ø < 1	Coarse-grained quartz sandstone
		1 < ø < 2	Medium-grained quartz sandstone
		ø > 2	Fine-grained quartz sandstone
< 75	> 25	ø < 1	Coarse-grained lithic sandstone
		1 < ø < 2	Medium-grained lithic sandstone
		ø > 2	Fine-grained lithic sandstone

They are the basis for dividing lithology by component content.

from mud logging. The right four tracks are the calculated porosity, quartz, rock debris, and so-called shale content. The black horizontal lines are the core analysis results. It can be seen that the porosity calculated by AC-CNL is consistent with the core porosity. Also, in the last three tracks, the component content of quartz, rock debris, and shale content calculated by the response equation is compared with the thin-section analysis results. It reveals that the calculated quartz content is in good agreement with the core thin-section data. The total volume fraction of the calculated shale content and rock debris is consistent with the rock debris from the core analysis result. Also, the computed shale content corresponds to the composition of sedimentary debris from the core thin-section data. This means there are tiny silty debris and clay minerals in the sedimentary debris, and this part contributes most of the GR radiation. The calculation and discrimination results confirm the correctness of the profile calculated.

According to the sandstone classification standard shown in **Table 2**, the geological survey and lithologic composition of the study area were classified. The final lithological classification result can be obtained after adding the MD calculation result into the lithology component profile. The MD was calculated by using the ΔGR model. A classification result is shown in **Figure 8**. The final classification results are compared with the Fisher discriminant and the mud logging results. The last four tracks in this figure are the mud logging, the Fisher discriminant and the calculated lithological profile, and the calculated MD. From the figure, we can see the lithological results of this well are consistent with the lithology in the mud logging profile and more refined. The correct rate is 89.96% of the calculated lithological profile by the CRAE method, and it is higher than the Fisher discriminant (it is 78.62%), which shows that this workflow has applicability in the study area.

DISCUSSIONS

The CRA method uses the GR or SP log to obtain the shale content and two other porosity logs to determine the mineral composition of the lithological composition. This method is

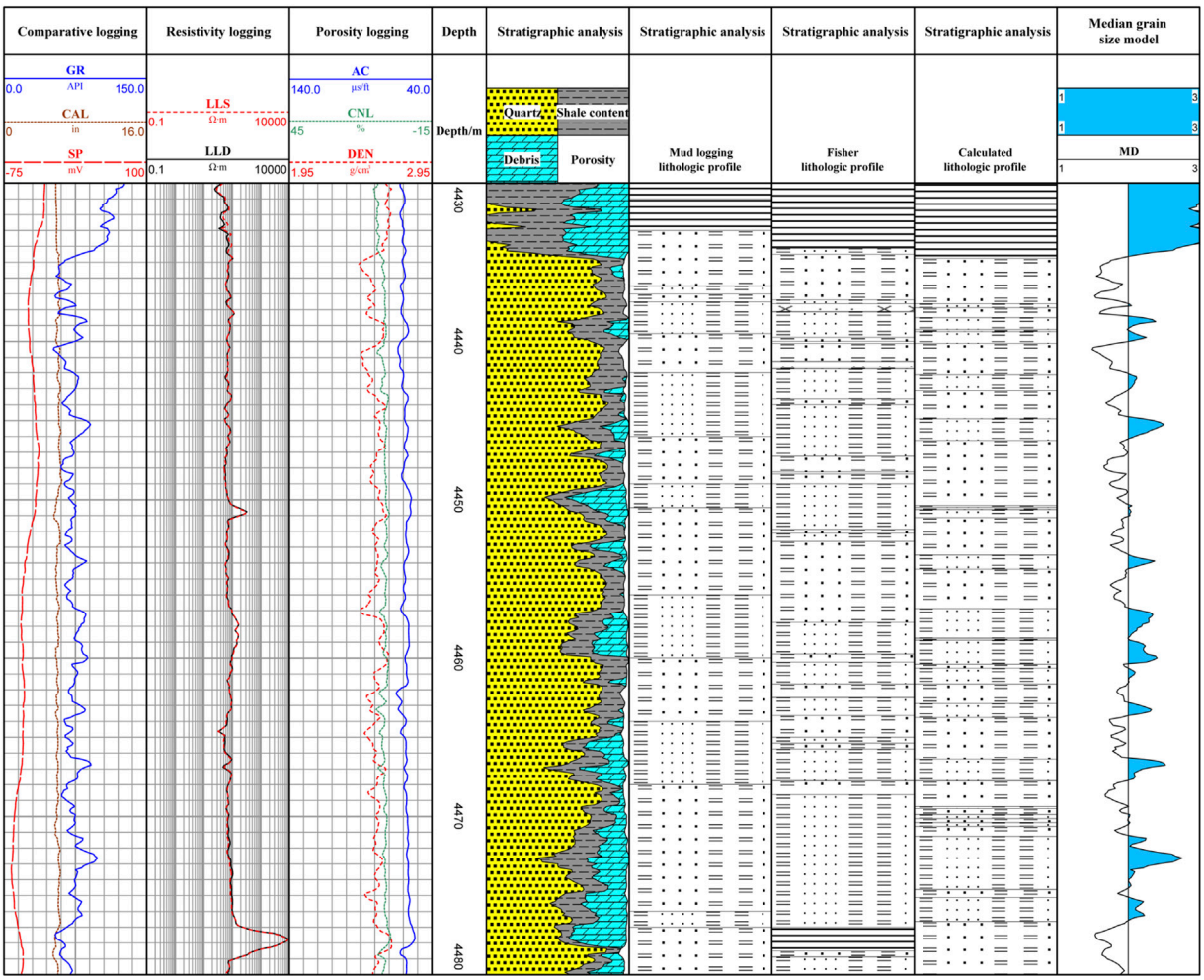

FIGURE 8 | Comparison of mud logging, Fisher discriminant, and the calculated lithological profile of formation mineral composition at 4,430–4,480 m in well 1.

aimed at carbonate rocks, in which the calcite and dolomite develop. As the minerals of calcite and dolomite have stable physical properties, including acoustic wave velocity and neutron porosity, the calculated mineral composition content is always accurate. However, the CRA method is rarely used in sandstone formations. One reason is that normally in the conventional sandstones, the lithology is simple; the other is the tight sandstones with complex mineral components. In this study area, we propose the CRAE method, in which we treat the tight gas reservoir rock as a mixture of quartz, debris, and pores, ignoring the relatively low volume fraction of the unstable mineral feldspar. The rock debris includes sedimentary, metamorphic, and igneous rocks. The sedimentary rocks can be calculated from the GR log for their radioactivity. Also, the metamorphic and igneous rock debris are combined and set a parameter. Meanwhile, the calculated shale contents in different formations have different meanings. The shale content calculated in the tight sandstone formation is a reflection of the sedimentary debris. Also, in shale and other formations, it represents the actual shale content in the formation.

In summary, this method is simple to select parameters. The accuracy meets production needs, and the workflow is easy to popularize. The determination of parameters is the most crucial step. When this workflow is used in a new study area, we should calibrate with core analysis data to select accurate parameters. In other words, when the lithological composition of the study area is different, the components can be replaced. The matrix parameter value of the lithology can be calculated according to the practical value of the study area and calibrated by core porosity.

CONCLUSION

The complex geological structure and lithological categories of tight sandstone gas reservoirs have posed challenges for logging lithological identification and porosity calculation. This article introduces a CRAE and MD calculation workflow to identify six

different lithologies and estimate porosity. The conclusions are as follows:

1) The GR, CNL, and AC logs contain the lithological information and can be used to reveal the components of the formations.
2) Based on the component analysis, the rock bulk volume can be equivalent to three parts: quartz, rock debris, and porosity. The CNL and AC log parameters are selected and used in the CRAE method. The calculated profiles reveal the effeteness of the CRAE method. The agreement of the calculated shale content from GR and the sedimentary debris reveals the radioactive contributions are mainly from the sedimentary debris.
3) The GR log and the MD of the formation have a good relationship, and the ΔGR can be used to predict the MD after the statistical modeling. The rocks can then be divided into coarse, medium, and fine grained through their grain sizes.
4) The proposed lithology identification method and porosity estimation have achieved good application results, providing a new effective workflow for lithology identification in tight areas. Parameters should be recalibrated when used in a new study area.

DATA AVAILABILITY STATEMENT

The raw data supporting the conclusions of this article will be made available by the authors, without undue reservation.

AUTHOR CONTRIBUTIONS

ZW processed the data and wrote the first version of this manuscript. XN introduced the whole workflow and made revisions on the manuscript. CZ provided suggestions on the methodology. JZ provided the data and gave suggestions. LJ reviewed the language and revised the manuscript.

FUNDING

This study was financially supported by the Open Foundation of Cooperative Innovation Center of Unconventional Oil and Gas, Yangtze University (Ministry of Education and Hubei Province, No. UOG 2022-09), the National Natural Science Foundation of China (No. 41504094), and the Open Foundation of Top Disciplines in Yangtze University (No. 2019KFJJ0818009).

REFERENCES

Alzubaidi, F., Mostaghimi, P., Swietojanski, P., Clark, S. R., and Armstrong, R. T. (2021). Automated Lithology Classification from Drill Core Images Using Convolutional Neural Networks. *J. Pet. Sci. Eng.* 197, 107933. doi:10.1016/j.petrol.2020.107933

Bai, B., Zhu, R., Wu, S., Yang, W., Gelb, J., Gu, A., et al. (2013). Multi-scale Method of Nano(Micro)-CT Study on Microscopic Pore Structure of Tight sandstone of Yanchang Formation, Ordos Basin. *Pet. Exploration Develop.* 40, 354–358. doi:10.1016/S1876-3804(13)60042-7

Bai, X., Li, Z., Lai, F., Wang, L., and Wu, D. (2021). Method for Evaluation of Engineering Sweet Spots Tight sandstone Reservoir Production wells. *Arab. J. Geosci.* 14, 1–12. doi:10.1007/s12517-021-09216-3

Chen, G., Chen, M., Hong, G., Lu, Y., Zhou, B., and Gao, Y. (2020). A New Method of Lithology Classification Based on Convolutional Neural Network Algorithm by Utilizing Drilling String Vibration Data. *Energies* 13, 888. doi:10.3390/en13040888

Cheng, D., Yuan, X., Zhou, C., Tan, C., and Wang, M. (2016). Logging-lithology Identification Methods and Their Application: A Case Study on the Chang 7 Member in the central-western Ordos Basin, NW China. *China Pet. Explor.* 21, 117–126. doi:10.3969/j.issn.1672-7703.2016.05.0016

Cong, Z., Li, Y., Pan, Y., Liu, B., Shi, Y., Wei, J., et al. (2022). Study on CO2 Foam Fracturing Model and Fracture Propagation Simulation. *Energy* 238, 121778. doi:10.1016/j.energy.2021.121778

Das, B., and Chatterjee, R. (2018). Well Log Data Analysis for Lithology and Fluid Identification in Krishna-Godavari Basin, India. *Arab. J. Geosci.* 11, 231. doi:10.1007/s12517-018-3587-2

Duan, H., Deng, Z., Deng, F., and Wang, D. (2016). Assessment of Groundwater Potential Based on Multicriteria Decision Making Model and Decision Tree Algorithms. *Math. Probl. Eng.* 2016, 1–11. doi:10.1155/2016/2064575

Gao, L., Yang, Z., and Shi, Y. (2018). Experimental Study on Spontaneous Imbibition Chatacteristics of Tight Rocks. *Adv. Geo-energy Res.* 2, 292–304. doi:10.26804/ager.2018.03.07

Gupta, S. D., Chatterjee, R., and Farooqui, M. Y. (2012). Formation Evaluation of Fractured Basement, Cambay Basin, India. *J. Geophys. Eng.* 9, 162–175. doi:10.1088/1742-2132/9/2/162

Han, L., Fuqiang, L., Zheng, D., and Weixu, X. (2018). A Lithology Identification Method for continental Shale Oil Reservoir Based on Bp Neural Network. *J. Geophys. Eng.* 15, 895–908. doi:10.1088/1742-2140/aaa4db

He, M., Gu, H., and Wan, H. (2020). Log Interpretation for Lithology and Fluid Identification Using Deep Neural Network Combined with MAHAKIL in a Tight sandstone Reservoir. *J. Pet. Sci. Eng.* 194, 107498. doi:10.1016/j.petrol.2020.107498

Khamees, L. A., Alhaleem, A. A., and Alrazzaq, A. (2021). Different Methods for Lithology and Mineralogy Recognition. *Mater. Today Proc.* 5. [In press]. doi:10.1016/j.matpr.2021.04.531

Li, X., and Li, H. (2013). A New Method of Identification of Complex Lithologies and Reservoirs: Task-Driven Data Mining. *J. Pet. Sci. Eng.* 109, 241–249. doi:10.1016/j.petrol.2013.08.049

Li, Y., Jia, D., Rui, Z., Peng, J., Fu, C., and Zhang, J. (2017). Evaluation Method of Rock Brittleness Based on Statistical Constitutive Relations for Rock Damage. *J. Pet. Sci. Eng.* 153, 123–132. doi:10.1016/j.petrol.2017.03.041

Liu, Y., Xian, C., Li, Z., Wang, J., and Ren, F. (2020). A New Classification System of Lithic-Rich Tight sandstone and its Application to Diagnosis High-Quality Reservoirs. *Adv. Geo-energy Res.* 4, 286–295. doi:10.46690/ager.2020.03.06

Nie, X., Wan, Y., and Bie, F. (2017). Dual-shale-content Method for Total Organic Carbon Content Evaluation from Wireline Logs in Organic Shale. *Open Geosci.* 9, 133–137. doi:10.1515/geo-2017-0011

Pang, M., Ba, J., Carcione, J. M., Picotti, S., Zhou, J., and Jiang, R. (2019). Estimation of Porosity and Fluid Saturation in Carbonates from Rock-Physics Templates Based on Seismic Q. *Geophysics* 84, M25–M36. doi:10.1190/GEO2019-0031.1.–M36

Sebtosheikh, M. A., Motafakkerfard, R., Riahi, M. A., Moradi, S., and Sabety, N. (2015). Support Vector Machine Method, a New Technique for Lithology Prediction in an Iranian Heterogeneous Carbonate Reservoir Using Petrophysical Well Logs. *Carbonates Evaporites* 30, 59–68. doi:10.1007/s13146-014-0199-0

Sebtosheikh, M. A., and Salehi, A. (2015). Lithology Prediction by Support Vector Classifiers Using Inverted Seismic Attributes Data and Petrophysical Logs as a New Approach and Investigation of Training Data Set Size Effect on its Performance in a Heterogeneous Carbonate Reservoir. *J. Pet. Sci. Eng.* 134, 143–149. doi:10.1016/j.petrol.2015.08.001

Sima, L., Wang, C., Wu, F., Wang, L., Ma, L., and Wang, Z. (2017). Calculation of Moblie Water Saturation in Tight sandstone Reservoirs of Penglaizhen

Formation, Western Sichuan Basin. *Well Logging Technol.* 40, 199–204. doi:10.16489/j.issrL.1004-1338.2017.02.01

Song, Z., Li, W., Tang, C., Li, W., Pang, Z., and Wang, Y. (2009). Dividing Sedimentary Facies and Reservoir Distributions by Using Natural Potential and Natural Gamma ray Logging Curves. *Prog. Geophys.* 24, 651–656. doi:10.3969/j.issn.1004-2903.2009.02.038

Sun, J., Li, Q., Chen, M., Ren, L., Huang, G., Li, C., et al. (2019). Optimization of Models for a Rapid Identification of Lithology while Drilling - A Win-Win Strategy Based on Machine Learning. *J. Pet. Sci. Eng.* 176, 321–341. doi:10.1016/j.petrol.2019.01.006

Tan, Z., Wang, W., Li, W., Lu, S., and He, T. (2017). Controlling Factors and Physical Property Cutoffs of the Tight Reservoir in the Liuhe basin. *Adv. Geo-energy Res.* 1, 190–202. doi:10.26804/ager.2017.03.06

Wang, X., Yang, S., Zhao, Y., and Wang, Y. (2018). Lithology Identification Using an Optimized KNN Clustering Method Based on Entropy-Weighed Cosine Distance in Mesozoic Strata of Gaoqing Field, Jiyang Depression. *J. Pet. Sci. Eng.* 166, 157–174. doi:10.1016/j.petrol.2018.03.034

Wei, Y., Ba, J., Carcione, J. M., Fu, L.-Y., Pang, M., and Qi, H. (2021). Temperature, Differential Pressure, and Porosity Inversion for Ultradeep Carbonate Reservoirs Based on 3D Rock-Physics Templates. *Geophysics* 86, M77–M89. doi:10.1190/GEO2020-0550.1

Xiong, F., Sun, W., Ba, J., and Carcione, J. M. (2020). Effects of Fluid Rheology and Pore Connectivity on Rock Permeability Based on a Network Model. *J. Geophys. Res. Solid Earth* 125 (3), e2019JB018857. doi:10.1029/2019JB018857

Xiang, M., Qin, P., and Zhang, F. (2020). Research and Application of Logging Lithology Identification for Igneous Reservoirs Based on Deep Learning. *J. Appl. Geophys.* 173, 103929. doi:10.1016/j.jappgeo.2019.103929

Yong, S., and Zhang, C. (2002). *Logging Date Processing and Comprehensive Interpretation*. Dongying: China University of Petroleum Press.

Yuan, C., Ma, M., Zhou, C., Feng, Z., and Shi, Y. (2018). An Improved Method to Evaluate Porosity with the Combination of Formation Elemental Logging and Density. *Well Logging Technol.* 42, 145–148. doi:10.16489/j.issn.1004-1338.2018.02.004

Zhang, C., Jiang, W., and Pan, H. (2009). *Acoustic Logging Principle and Application*. Beijing: Petroleum Industry Press.

Zhao, J., and Gao, F. (2003). Application of Crossplots Based on Well Log Data in Identifying Volcanic Lithology. *Glob. Geol.* 22, 136–140. doi:10.1016/S0955-2219(02)00073-0

Zhao, J., Wang, F., and Lu, Y. (2017). Application of Multivariate Membership Function Discrimination Method for Lithology Identification. *Jsm* 46, 2223–2229. doi:10.17576/jsm-2017-4611-24

Zhou, X., Zhang, Z., Zhang, C., Nie, X., Zhang, C., and Zhu, L. (2017). A New Lithologic Classification Method for Tight sandstone Reservoirs Based on Rock Components and Logging Response Characteristics. *J. Geophys. Eng.* 14, 1599–1607. doi:10.1088/1742-2140/aa8eb5

Zhou, Y., Jing, C., Li, Z., and Zhang, Z. (2018). Porosity Modeling of Tight Reservoir Based on Diagenetic Reservoir Facies Classification. *Well Logging Technol.* 42, 175–180. doi:10.16489/j.issn.1004-1338.2018.02.009

Conflict of Interest: Author LJ is employed by Golder Associates. The remaining authors declare that the research was conducted in the absence of any commercial or financial relationships that could be construed as a potential conflict of interest.

frontiers | Frontiers in Earth Science

METHODS
published: 01 April 2022
doi: 10.3389/feart.2022.863773

Quantification of the Fracture Complexity of Shale Cores After Triaxial Fracturing

Yonghao Zhang[1,2†], Jinfeng Ma[1†], Yang Wang[3†], Fei Wang[4†], Xin Li[2†] and Luanxiao Zhao[5†]*

[1]National and Local Joint Engineering Research Center of Carbon Capture and Storage Technology, Department of Geology, Northwest University, Xi'an, China, [2]CNPC Logging Company Limited, Xi'an, China, [3]SINOPEC Geophysical Research Institute, Nanjing, China, [4]College of Geology Engineering and Geomatics, Chang'an University, Xi'an, China, [5]State Key Laboratory of Marine Geology, Tongji University, Shanghai, China

Diagnosing fractures under compression is of great importance in optimizing hydraulic fracturing stimulation strategies for unconventional reservoirs. However, a lot of information, such as fracture morphology and fracture complexity, is far from being fully excavated in the laboratory limited by the immature fracture identification techniques. In the current study, we propose a set of methods to analyze the fracture complexity of cylindrical cores after triaxial fracturing. Rock failure under conventional compression tests is real-time controlled by monitoring the stress–strain evolutions to ensure that the cores remain cylindrical after failure. The lateral surface of the core cylinders is scanned with a 2D optical scanner to extract the fracture parameters, surface fracture rate, and inclination dispersion, which are normalized and averaged to derive the fracture complexity. After analyzing the data for 24 shale gas reservoir cores from the Sichuan Basin, the fractal dimension of fracture images shows a good linear correlation with the surface fracture rate but has no correlation with the dip dispersion. The calculated fracture complexity has nearly no relationship with the E-v–based brittleness index but demonstrates a positive correlation with the mineral content–based brittleness index. Moreover, the fracture complexity is associated with the core mineralogical compositions. The fracture complexity is positively correlated with the content of quartz, calcite, and dolomite and negatively correlated with the content of clay minerals and has no obvious relationship with the content of feldspar. The proposed method provides an experimental basis for the evaluation of fracturability of unconventional oil and gas reservoirs.

Keywords: triaxial compression, fracability, fracture morphology, fractal dimension, fracture complexity

Edited by:
Yuwei Li,
Liaoning University, China

Reviewed by:
Junxin Guo,
Southern University of Science and Technology, China
Ken Ikeda,
C3.ai, United States
Jun Zhang,
Northeast Petroleum University, China

****Correspondence:***
Yang Wang
ywang0605@hotmail.com
orcid.org/0000-0002-5792-9852

†These authors have contributed equally to this work and share first authorship

Specialty section:
This article was submitted to Economic Geology, a section of the journal Frontiers in Earth Science

Received: *27 January 2022*
Accepted: *08 March 2022*
Published: *01 April 2022*

Citation:
Zhang Y, Ma J, Wang Y, Wang F, Li X and Zhao L (2022) Quantification of the Fracture Complexity of Shale Cores After Triaxial Fracturing. Front. Earth Sci. 10:863773. doi: 10.3389/feart.2022.863773

1 INTRODUCTION

Unconventional shale gas or oil reservoirs are frequently characterized with extremely low permeability (Vernik, 2016; Zhao et al., 2018; Wang Y. et al., 2021). Extracting economic gas or oil flow from such reservoirs requires the use of horizontal drilling and staged hydraulic fracturing techniques (Barree et al., 2015; Ma et al., 2017; Li J. et al., 2018; Li et al., 2021).

The brittleness index has long been used to evaluate the reservoir fracability (Ishii et al., 2011; Tarasov and Potvin, 2013; Nejati and Ghazvinian, 2014; Holt et al., 2015; Zhang et al., 2016; Akinbinu, 2017; Li et al., 2017; Li et al., 2019; Feng et al., 2020; Wang Y. et al., 2020). The brittleness index, to some extent, can reflect the fracture complexity after the reservoir fracturing treatment.

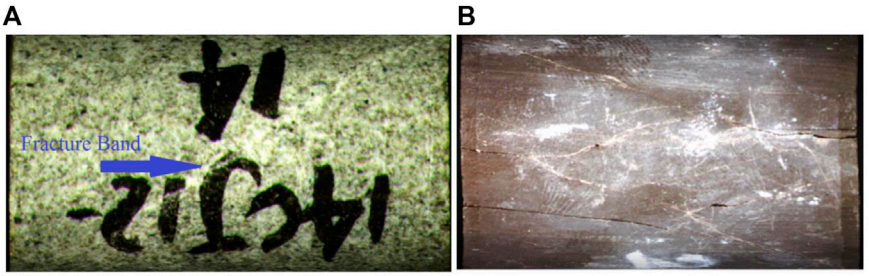

FIGURE 1 | Core photos after triaxial fracturing. **(A)** A post-frac sandstone. The fractures are barely opened and distributed in the form of faint bands. **(B)** A post-frac shale. Some fractures are filled with fragmental products, appearing white. The unfilled fractures are black.

Reservoirs with high brittleness index can quickly form complex fracture networks, while reservoirs with low brittleness index can easily form double-wing fractures (Rickman et al., 2008). In geo-engineering applications, the mineral content–based (**Eq. (1)**, Jarvie et al., 2007) and the *E*-ν–based (**Eq. (2)**, Rickman et al., 2008) methods are frequently used to derive the reservoir brittleness index (Qin and Yang, 2019; Wang Y. et al., 2020).

$$BI = \frac{Q}{Q + C + Cl}, \tag{1}$$

where *BI* is the brittleness index, *Q* is the silicic mineral content (e.g., quartz, feldspar), *C* is the carbonate mineral content (e.g., calcite, dolomite, ferrodolomite), and *Cl* is the clay content.

$$BI = \left(\frac{E - E_{\min}}{E_{\max} - E_{\min}} \times 0.5 + \frac{\nu - \nu_{\max}}{\nu_{\min} - \nu_{\max}} \times 0.5 \right) \times 100, \tag{2}$$

where $E_{\max}$ and $E_{\min}$ are the maximum and minimum Young's moduli, respectively; and $\nu_{\max}$ and $\nu_{\min}$ are the maximum and minimum Poisson's ratios, respectively.

However, those empirical methods are established based on practical productions and are limited by the experimental data support. In addition, dozens of brittleness index calculation methods based on stress–strain relation, strength, and energy evolution are proposed in the material mechanics (Ai et al., 2016; Bai, 2016; Wen et al., 2020). However, these methods are essentially describing the fracture extension and do not depict the capability of forming complex fracture networks.

Quantitatively describing the fracture complexity of rocks after laboratory fracturing is a key technique in the reservoir fracability research (Jin et al., 2015). Currently, there are three post-compression fracture analysis methods. The first one is based on acoustic emission signals generated by the failure of the rock structure during the fracturing process (Stanchits et al., 2015; Li et al., 2017; Li N. et al., 2018). However, the acoustic emission response is an indirect fracture analysis method and cannot obtain the specific parameters of each fracture. The second one is to analyze the rock fragmentation characteristics based on counting the fragment size after fracturing (Akinbinu, 2017; Li et al., 2017; Li X. et al., 2018). The result of this method is relatively rough, which is strongly affected by the artificial factors. The third method is quantitatively analyzing the fractures based on image processing after rock fracturing. The most used method is the fractal geometric method (Mandelbrot, 1967; Xie, 1992). This method is based on the premise of identifying fractures in the image, and only describes the amount of fractures but cannot describe the complexity of fracture angles (Guo et al., 2014).

Axial compression fracturing is a common method for obtaining rock mechanical properties in the laboratory (Brace et al., 1966; Jaeger et al., 1969; Iyare et al., 2021; Li et al., 2020; Zhang et al., 2021). During the measurements, the cylindrical rock samples are axially compressed until the samples are fractured. Through such measurements, we can obtain the rock mechanical parameters, such as compressive strength, Young's modulus, and Poisson's ratio. In addition, the fracture morphology contains a lot of information (**Figure 1**). **Figure 1A** shows the image of tight sandstone with single-shear fractures. **Figure 1B** is a shale after fracturing treatments, accompanied by different fracture angles and sizes. The information reflected by the sample images is far from being excavated. From a technical point of view, there are two main reasons. One is that the fracture morphology after uniaxial fracturing is highly affected by the degree of fracturing; the other is that the fracture discrimination using the color difference in the images is low. As shown in **Figure 1A**, the degree of fracture opening is relatively low. The fractures are distributed in the form of faint bands, which makes it difficult to evaluate the fracture width. As shown in **Figure 1B**, some fractures are filled with fragmental products and appear white, while the unfilled fractures are black, which brings great difficulties in extracting fracture information using the color difference threshold. Therefore, there exist inherent shortages in the quantitative fracture analysis using fractal geometry methods (Zhang et al., 2014).

In this study, we propose a set of experimental methods, including core sample fracturing, image acquisition, and fracture analysis, to quantitatively analyze fracture complexity. We attempt to keep the fractured rocks not scattered by controlling a constant strain rate during the triaxial compression. In addition, we summarize a set of fracture grading methods for cylindrical samples after triaxial fracturing. Subsequently, we can conveniently extract the characteristic parameters of each fracture, such as fracture length, width, and dip angle. Based on the extracted parameters, we propose a calculation method for the fracture complexity after triaxial fracturing treatment.

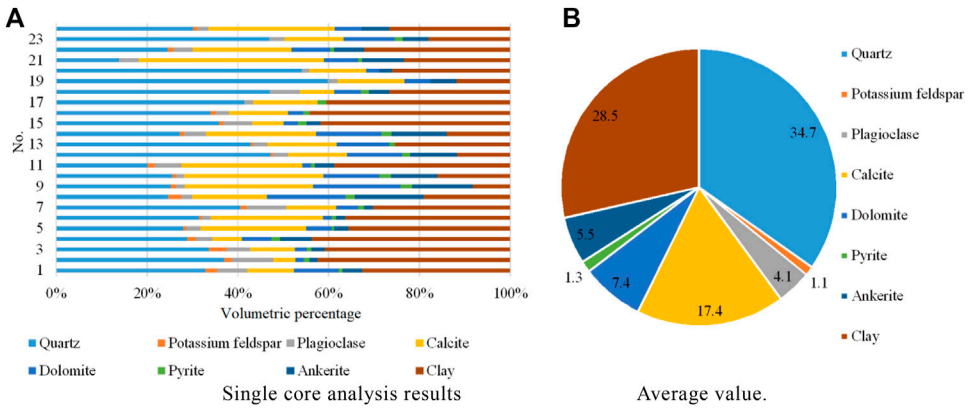

FIGURE 2 | X-ray diffraction (XRD) analysis results for 24 shale samples. **(A)** Single-core analysis results. **(B)** Average value.

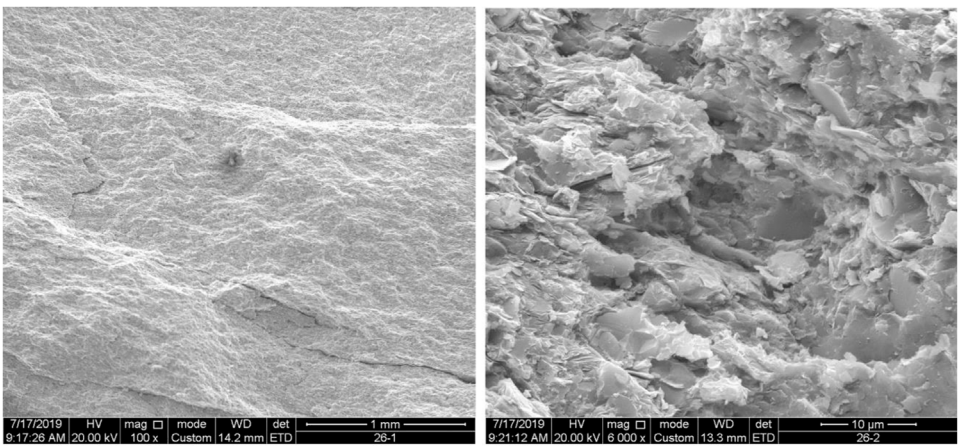

FIGURE 3 | Scanning electron microscope (SEM) images for #15 sample.

2 EXPERIMENTAL METHODOLOGY

2.1 Sample Description

In this research study, we select 24 gray–black mud shale samples drilled from Longmaxi and Wufeng formations in the Zhaotong area of the Sichuan Basin. All drilled samples are cut in the direction parallel to the bedding planes and machined to cylinders with a diameter of 2.54 cm and a length ranging from 4.5 to 5.0 cm. **Figure 2** shows the results of the X-ray diffraction (XRD) analysis, which indicate that the quartz content ranges from 13.9% to 59.9%, the feldspar content ranges from 1.6% to 10.9%, the carbonate mineral (e.g., calcite, dolomite, and ferrodolomite) content ranges from 8.4% to 60.9%, and the clay content ranges from 8.2% to 44.1%. **Figure 3** shows the scanning electron microscope (SEM) images for #15 sample at two different scales. The fractures are relatively developed in the direction parallel to the bedding plane. The clay minerals display a sheet-like structure and are distributed in directional orientation sub-parallel to the bedding plane.

2.2 Experimental Setup

2.2.1 Servo-Hydraulically Controlled Triaxial Testing System

We carry out the triaxial tests on all 24 samples using a servo-hydraulically controlled triaxial testing system, AutoLab 1,500 manufactured by New England Research Inc., as shown in **Figure 4A**. The triaxial testing system comprises a load cell, pressure intensifier that allows applying the confining pressure up to 68 MPa, pore pressure system, and digital recording system. The sample, wrapped with a Viton rubber, is placed between the top and bottom endcaps, as shown in **Figure 4B**. The contacting area between the buffer and sample is twined by copper wires to ensure good alignment and avoid potential sliding during the measurements. The axial strain (ε_a) is recorded by mounting a pair of linear variable differential transformers (LVDTs) between the top and bottom endcaps. The radial strain (ε_r) is measured by placing another LVDT at the middle of the sample. The precision of strain measurements is about 0.01 µm. Given that the selected shales have visible bedding planes in the direction of axial

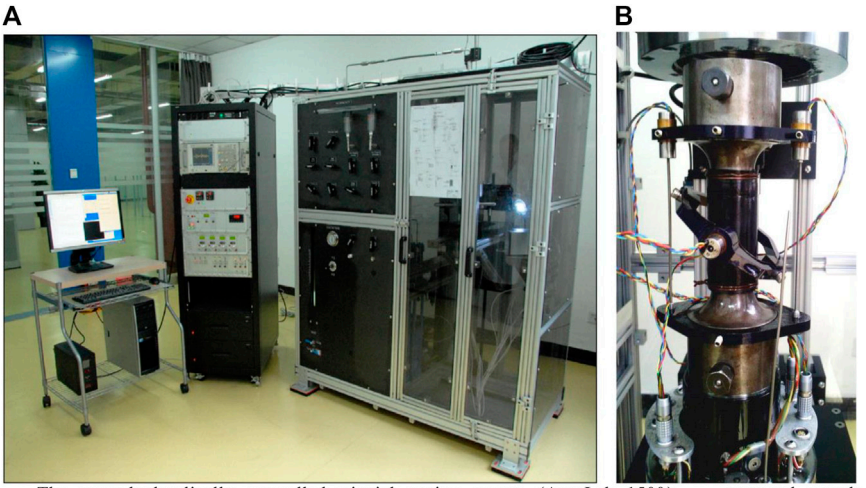

FIGURE 4 | Triaxial testing system and prepared sample. **(A)** Servo-hydraulically controlled triaxial testing system (AutoLab 1500); **(B)** prepared sample assembly placed between two endcaps and inserted into the confining vessel.

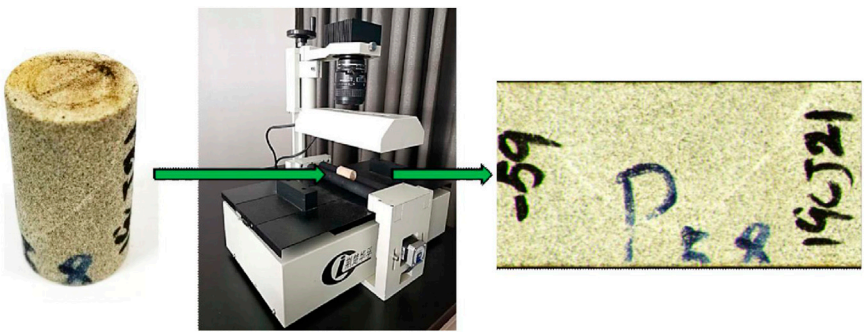

FIGURE 5 | JB-PDC core optical image scanner and its principle.

loading, the radial LVDT is fixed in the direction perpendicular to the bedding plane.

2.2.2 JB-PDC Core Optical Image Scanner

In this study, the main equipment used for collecting core images after triaxial compression is the JB-PDC core optical image scanner developed by Huafu Company (**Figure 5**). The equipment mainly comprises a camera and sample carrier. The camera is a line-array camera with a resolution of 2000 dpi. The sample carrier is capable of loading samples with a flat surface or a sample tray with flat particles. The sample carrier can be driven to scan the sample horizontally. It can also load a cylindrical sample, which drives the sample to roll *in situ* under the camera by the rotation of two rollers. **Figure 5** shows that the side surface of a cylindrical sample is unfolded into a rectangular image after rolling the sample in the scanner. The rectangular image can be restored to a cylindrical shape, as shown in **Figures 1**, **2**.

2.3 Experimental Procedures and Methodologies

The experimental procedures for quantitatively analyzing the fracture complexity after triaxial fracturing treatment of 24 shale samples include five steps:

1) Carrying out triaxial fracturing experiments to achieve a state of "fractured without scattering";
2) Scanning the core images after triaxial fracturing treatment and acquiring the fracture information;
3) Preprocessing the core images and conducting fracture classification;
4) Extracting the fracture parameters, such as length, width, and dip angle;
5) Calculating the surface fracture rate and fracture dip dispersion. Subsequently, calculating the fracture complexity.

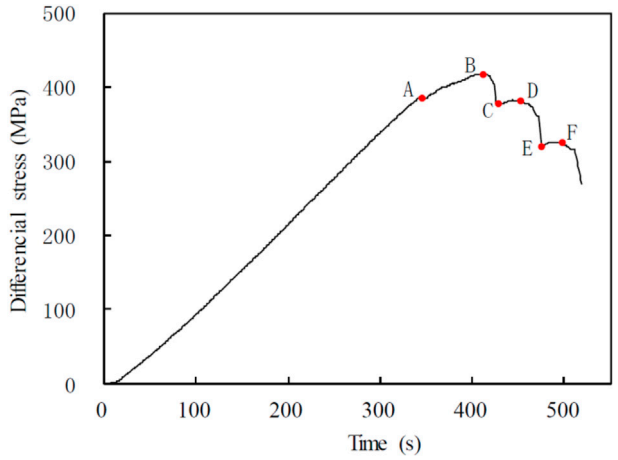

FIGURE 6 | Differential stress and strain vs. time in triaxial fracturing.

2.3.1 Triaxial Fracturing Experiment With Controlling the Fracturing Degree

The sample assemblage is mounted inside the confining vessel. The vessel is, subsequently, filled with mineral oil by driving the confining pump. Then, we move the hydraulic piston downward to touch the top endcap and apply axial stress on the rock sample. To ensure the comparability of the fracture complexity of 24 shale samples, a uniform fracturing degree must be controlled during the measurements. First, the confining pressure is set to a value simulating the *in situ* horizontal effective stress at the original buried depth. Second, the axial loading is controlled with a constant strain rate, that is, lowering the hydraulic piston at a constant speed to avoid squashing the cores. After fracturing, the hydraulic piston slowly lowers with a constant speed, and the axial stress is released automatically. Thus, we can monitor the stress–strain evolution to determine the fracturing degree.

A large number of experimental observations have revealed that the fracture would develop with different stages under conditions of controlling a constant strain rate. **Figure 6** shows the applied stress as a function of time in the process of triaxial fracturing for a shale sample. When the hydraulic piston lowers downward, the axial stress increases and the stress inside the rock accumulates. When the axial stress is beyond point A, the internal microstructure inside the rock starts getting destroyed. When the axial stress reaches the compressive strength, point B, the microstructural fractures accumulate to form a macro-fracture, and the axial stress quickly decreases. With the macro-fracture extension, the internal stress quickly releases. The stress release rate is greater than the stress increase rate caused by lowering the hydraulic piston. The first-level fracture extension would stop when the fracture front stress is lower than the residual strength of the rock. Subsequently, the axial stress begins to accumulate again. Therefore, we can observe point C in the stress–time curve. As the hydraulic piston continues to be lowered, the stress accumulation inside the rock continues. When the first-level residual strength (point D) is reached, the internal structure of the rock is destroyed again, accompanied by fracture extension or newborn fractures. The stress is released again and decreases by showing the second-level residual strength (point E). With such periodical processes, the rock sample is shattered completely. The segment from points C to D represents the development of the first-level fractures. To ensure similar fracturing degree for all 24 samples, we uniformly compress all samples to point D.

2.3.2 Fracture Information Collection

As shown in **Figure 5**, the post-fractured sample is placed on the JB-PDC core optical image scanner. The fractures on the side surface of the cylindrical sample are displayed on a planar graph. For a cylindrical sample with a diameter of 1.0 inch, the resolution of the scanner is about 0.04 mm.

2.3.3 Pre-Processing the Core Images

Even if the triaxial fracturing experiment described in **Section 2.3.1** is used to control the degree of fracturing, most of the post-fractured images are still difficult to be identified due to the low fracture opening degree, background interference, and insufficient acquisition accuracy. It is necessary to preprocess the core images to make the fractures recognizable. Although the traditional image processing software has poor results in brightness, contrast, and other color difference processing, it is still easy to be used for observing the fractures in actual core samples. We summarize a set of fracture classification methods by analyzing the core fracturing process and observing the post-fractured core images. The fracture images are preprocessed accordingly to make the fractures easy to be identified and extracted.

The fracture classification method is summarized in **Table 1**. The fractures are classified into four levels according to the fracture morphology (extension degree, penetration degree, width, and dip angle of each fracture) and fracture generation mechanism.

According to the aforementioned classification method, the fractures with different levels are redrawn with lines of different thicknesses, as shown in **Figure 7**. In **Figure 7A**, the original core image after fracturing has a low fracture opening degree and is highly affected by the artificial markers. In **Figure 7B**, through the image preprocessing in **Section 2.3.3**, the fractures after triaxial compression are clearly identified.

2.3.4 Fracture Parameter Extraction

We extract the length of each fracture and the height and width pixel values of the circumscribed rectangle. The length is subsequently converted into the actual length:

$$l_i = l_p \times \frac{h}{h_p}, \tag{3}$$

where l_i is the actual length of the ith fracture (mm), l_p is the fracture's pixel length (pixel), h is the actual height of the sample (mm), and h_p is the sample's pixel height (pixel). The fracture width is the product of each pixel length and the corresponding pixel value.

TABLE 1 | Post-fractured core fracture classification method.

Grade	Name	Main Features
I	Major fracture	The core splits first along the main fracture. Generally, it has the longest extension and the largest width and runs through the core. Therefore, the major fractures distribute axis-symmetrically on the scroll image. Generally, there is only one main fracture in the core; brittle rock can have multiple main fractures, which need to be confirmed with the end face of the core
II	Secondary fracture	The elongation and width of secondary fractures are large, but the penetration is weak, so there is no symmetrical fracture on the scroll image
III	Branch fracture	The elongation and penetration of the branch fractures are weak, but they are obvious on the image, and the occurrence of them is not consistent with the major or the secondary fractures; they can be extended through the major fracture or secondary fracture
IV	Associated fracture	Small fishbone fractures associated with the major or the secondary fractures; they have weak elongation, penetration, and width

The dip angle of each fracture can be calculated with the height and width of the circumscribed rectangle:

$$A = Arc\tan\frac{H}{W}, \tag{4}$$

where A is the fracture dip angle (degree), ranging between 0° and 90°; and H and W are the height and width of the circumscribed rectangle (pixel), respectively.

2.3.5 Fracture Complexity

The complex fracture network after triaxial fracturing treatment has three characteristics: large number, large fracture, and complex morphology. Therefore, the fracture complexity is a function of the number, size, and morphology of the fractures. The fracture number can be directly counted from the fracture image. The fracture size can be characterized by the fracture area in the image. The more discrete the fracture dip angle after core compression, the closer the fracture is to a network. As a result, the fracture morphology can be characterized by the disorder degree of the fracture dip angle. We propose the concepts of surface fracture rate and fracture dip dispersion.

The surface fracture rate is the area sum of all fractures divided by the sum of the side surfaces.

$$R_f = \sum_{i=1}^{n}\frac{S_i}{S_l} \times 100, \tag{5}$$

where R_f is the surface fracture rate (dimensionless), S_i is the area of the ith fracture (mm^2), and S_l is the area of the side surface (mm^2).

The fracture dip dispersion is calculated by **Eq. (6)**.

$$D_a = \sqrt{\frac{\sum_{i=1}^{n}\left(A_i - \bar{A}\right)^2}{n}} \times 100, \tag{6}$$

where D_a is the fracture dip dispersion (dimensionless), $\bar{A}$ is the weight average of fracture dips (degree); the weight is assigned by the fracture grade, and A_i is the dip angle of the ith fracture (degree).

The surface fracture rate and fracture dip dispersion contain information of the number, size, and morphology of the generated fractures. According to the statistical analysis method, the surface fracture rate and fracture dip dispersion are averaged to represent the fracture complexity (F_c). The surface fracture rate and fracture dip dispersion are necessary to be normalized because the values in different samples are quite different.

$$F_c = \left(\frac{R_f - R_{f\min}}{R_{f\max} - R_{f\min}} + \frac{D_a - D_{a\min}}{D_{a\max} - D_{a\min}}\right)\Big/2, \tag{7}$$

where F_c is the fracture complexity. According to the theoretical and empirical analyses of cylindrical samples with a diameter of 1 inch, the maximum and minimum surface fracture rates are 3 and 0, respectively. The maximum and minimum fracture dip dispersion is 45° and 0°, respectively. Hence, **Eq. 7** can be simplified as follows:

$$F_c = \frac{R_f}{6} + \frac{D_a}{90}. \tag{8}$$

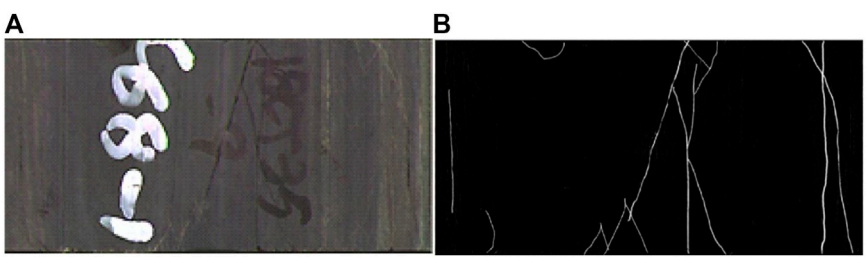

FIGURE 7 | (A) An original post-frac core image. Fractures are difficult to be identified due to the image resolution. **(B)** A post-frac core image preprocessed with the method in Section 2.3.3. The fractures are clearly identified.

FIGURE 8 | Photos of 24 post-fractured core samples.

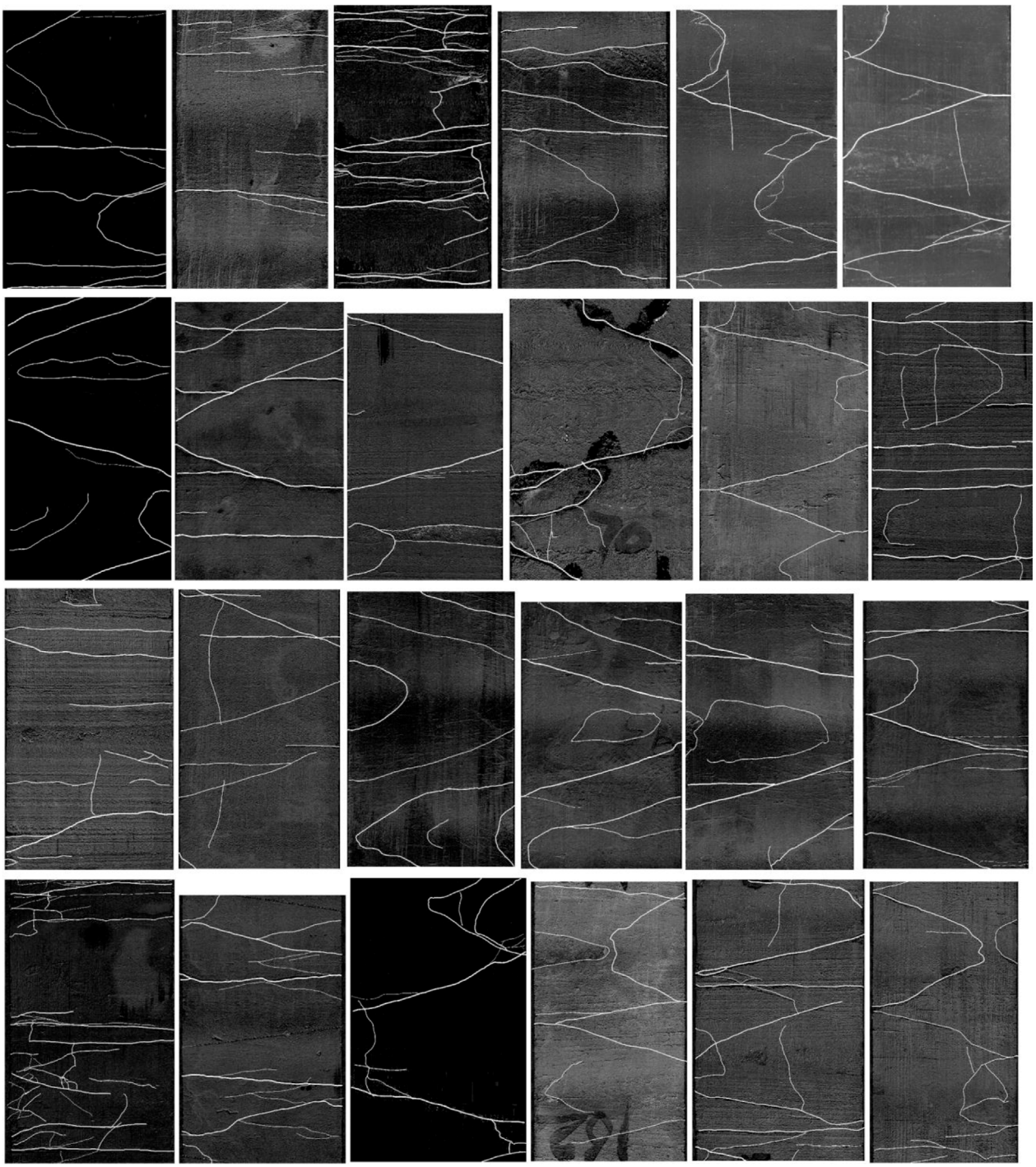

FIGURE 9 | Crack extraction results of the lateral surface expansion map of 24 cores after compression test.

3 EXPERIMENTAL RESULTS

3.1 Quantitative Analysis Results of Fracture Complexity

The 24 core samples were subjected to triaxial fracturing according to the method described in **Section 2.3.1**. After fracturing, the samples remained cylindrical (partially split into two halves and bonded with glue), and then optical scroll scanning was performed according to the method described in **Section 2.3.2**. **Figure 8** shows the photos of the post-fractured cores arranged by sample number.

Figure 9 is a group photo of the unfolded side surface of the 24 cores (sorted by NO.), preprocessed according to the method

TABLE 2 | Fracturing and fracture analysis results of 24 cores after compression test.

No	No. of major fractures	No. of secondary fractures	No. of branch fractures	No. of associated fractures	Normalized D_a	Normalized R_f	F_c
1	2	2	2	2	75.8	33.1	54.4
2	2	2	4	4	45.9	23.5	34.7
3	4	5	4	20	46.2	64.1	55.2
4	2	4	1	0	50.9	36.0	43.4
5	2	2	4	8	42.7	30.6	36.7
6	2	3	2	0	57.3	31.1	44.2
7	2	2	5	1	34.6	28.9	31.8
8	6	2	1	0	76.3	41.6	58.9
9	2	2	2	4	88.5	24.9	56.7
10	2	2	4	3	43.5	26.2	34.9
11	3	3	0	0	59.7	27.6	43.7
12	4	2	7	3	95.0	47.6	71.3
13	2	1	11	0	83.3	26.6	54.9
14	2	2	6	0	76.4	33.7	55.0
15	2	4	1	0	6.8	33.4	20.1
16	2	3	3	2	44.0	35.1	39.6
17	4	2	5	1	78.7	33.3	56.0
18	2	3	2	8	54.4	36.4	45.4
19	2	6	15	20	63.0	49.5	56.2
20	3	2	2	11	43.0	35.0	39.0
21	2	1	6	6	51.8	29.0	40.4
22	2	3	3	1	66.7	34.9	50.8
23	3	4	8	4	62.6	45.4	54.0
24	1	4	7	0	65.9	35.1	50.5

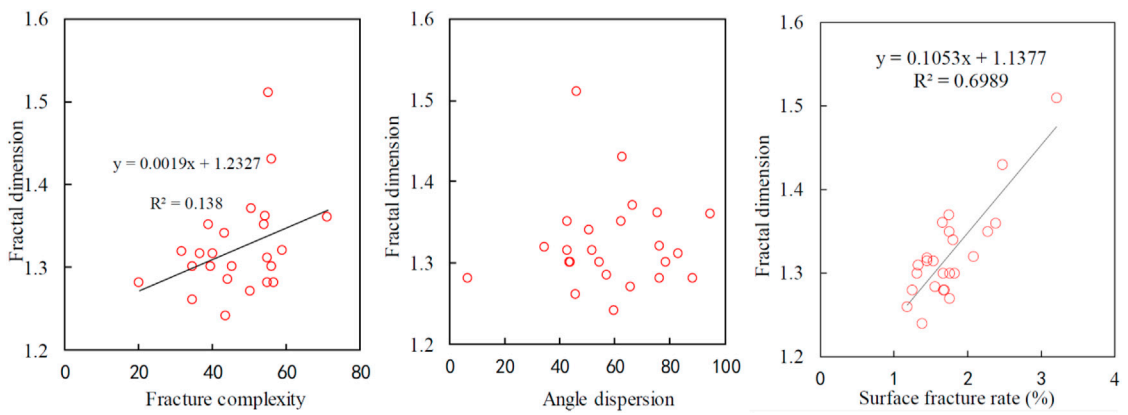

FIGURE 10 | Relationship between the fractal dimension and fracture complexity, angle dispersion, and surface fracture rate.

described in **Section 2.3.3**, and the parameters of each fracture were extracted according to the method described in **Section 2.3.4**. Then, the fracture rate (R_f) and the dip angle dispersion (D_a) of each core were calculated according to the method described in **Section 2.3.5**, and finally, the fracture complexity (F_c) was calculated. **Table 2** shows the results of the fracture quantitative analysis of the 24 post-fractured core samples. The confining pressure in the table is the confining pressure of the triaxial fracturing experiment, which simulates the effective stress calculated according to the core depth and formation pressure. The sorting result shows that F_c is in good agreement with the actual core fracture complexity.

3.2 Contrast Between Fracture Complexity and Fractal dimension

The fractal theory was proposed by Mandelbrot (1967). It is one of the important branches of modern nonlinear science and is widely used in many fields such as mathematics, physics, chemistry, biology, medicine, geography, and geology. Xie (1992) first combined the fractal theory with rock mechanics and studied the relationship between fracture fractals and mechanical properties of fracture structure planes. Later, numerous researchers studied the relationship between a large number of fractures and fractal dimensions and achieved good results. At present, the commonly

TABLE 3 | Calculated brittleness indices.

No	Dynamic Young's modulus (GPa)	Dynamic Poisson's ratio	Static Young's modulus (GPa)	Static Poisson's ratio	Fractal dimension	BI-Mi	BI-Ac	BI-Me
1	40.0	0.33	31.4	0.12	1.361	36.6	74.6	0.0
2	54.5	0.15	23.6	0.08	1.260	42.1	65.6	54.2
3	61.2	0.17	16.2	0.34	1.510	37.5	0.0	62.6
4	43.4	0.29	24.0	0.17	1.340	31.2	49.6	11.7
5	59.2	0.26	35.3	0.18	1.315	29.3	71.6	44.0
6	54.0	0.29	36.5	0.23	1.284	32.7	64.9	29.7
7	56.6	0.25	30.8	0.12	1.318	45.9	74.7	41.8
8	51.3	0.24	29.6	0.22	1.320	26.6	51.1	34.6
9	57.3	0.29	35.7	0.19	1.280	26.8	70.3	36.0
10	66.0	0.21	36.1	0.18	1.300	27.1	73.8	63.4
11	63.2	0.27	35.9	0.23	1.240	22.0	62.6	47.6
12	50.5	0.23	29.5	0.19	1.360	50.1	57.6	34.0
13	56.7	0.16	31.5	0.16	1.310	45.1	67.2	56.5
14	48.3	0.25	28.2	0.20	1.280	29.7	53.4	27.0
15	60.9	0.24	34.0	0.21	1.280	39.5	63.5	49.8
16	52.0	0.29	37.3	0.12	1.300	36.0	87.3	25.8
17	53.7	0.29	36.3	0.21	1.300	43.1	68.7	29.5
18	43.1	0.13	26.2	0.13	1.300	51.4	62.9	40.1
19	65.1	0.15	35.4	0.19	1.430	61.2	71.0	71.9
20	59.5	0.12	33.2	0.11	1.350	55.1	80.5	68.6
21	70.2	0.24	39.8	0.18	1.315	14.7	80.7	64.6
22	63.8	0.15	32.3	0.10	1.370	26.2	81.4	69.3
23	50.7	0.17	31.7	0.14	1.350	49.6	70.9	44.7
24	52.3	0.20	31.1	0.15	1.270	31.2	68.0	41.9

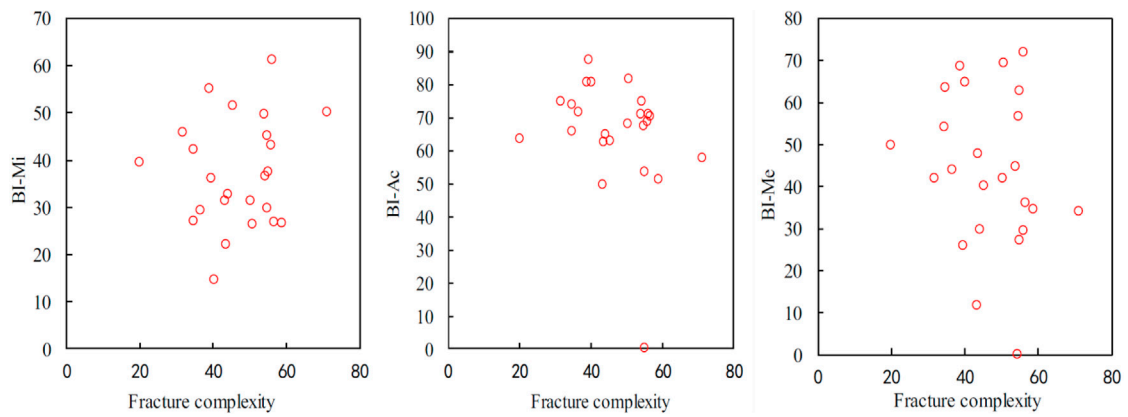

FIGURE 11 | Relationship between the brittleness index and fracture complexity.

used fractal description methods for rock fractures include the area perimeter method (Miller and Ross, 1993), box dimension method (Peng et al., 2004), and variogram method. The box dimension method is widely used due to operation convenience. The box dimension method uses the fracture fractal dimension to characterize the irregularity of fractures.

In this study, after preprocessing the core images of 24 shales, the box dimension method is used to calculate the fractal dimension. The square grid with a length of r is used to cover the entire core. The number of square grids [N(r)] containing the fractures is counted. The side length of the square grid (r) is gradually changed to obtain N(r). In the double-logarithmic coordinate system, the least square is used to make regression analysis on the statistical data (r and N(r)). The slope of the regression line is the fractal dimension (D). The calculation results are shown in **Table 2**. The parameters in **Tables 1**, **2** are cross-plotted, as shown in **Figure 10**. The fractal dimension is positively correlated with fracture complexity, but the correlation is weak. The fractal dimension does not show correlation with the fracture dip dispersion, but has a good linear correlation with the surface fracture rate. This is because the fractal dimension only considers the proportion of abnormal points in the binarized

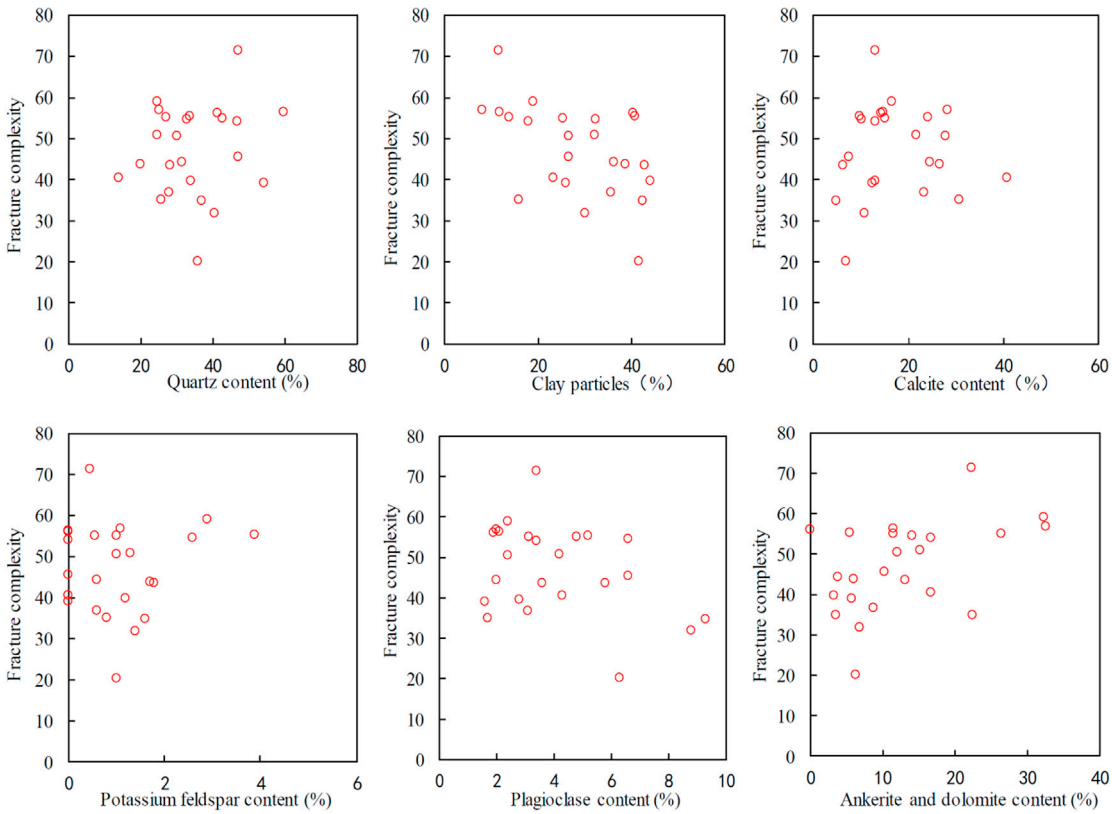

FIGURE 12 | Relationship between mineral content and fracture complexity.

image, which is essentially the same as the surface fracture rate. However, the image noise has an effect on the fractal dimension but has no effect on the surface fracture rate. Therefore, in contrast, it is more advantageous in describing the complex fractures after triaxial fracturing treatment by using the fracture complexity than by using the fractal dimension.

3.3 Contrast Between Fracture Complexity and Brittleness Index

Table 3 shows the rock mechanical parameters for all 24 shale samples. We use **Eq. 1** to calculate the brittleness index (BI-Mi). According to the ultrasonic velocity data, we calculate the dynamic Young's modulus and Poisson's ratio, which are subsequently used to calculate the brittleness index (BI-Ac), according to **Eq. 2**. The maximum and minimum values of Young's modulus and Poisson's ratio are from the empirical values of the target reservoirs, which are 70.2 GPa and 40.0 GPa and 0.33 and 0.04, respectively. The static Young's modulus and Poisson's ratio obtained in the triaxial fracturing experiment are used to calculate the rock mechanical brittleness index (BI-Me), according to **Eq. 2**. **Figure 11** shows the comparisons of brittleness index from three methods. The fracture complexity (F_c) and brittleness index (BI-Mi) show a positive correlation. There is no obvious correlation between F_c and BI-Ac or BI-Me.

3.4 Relationship Between Fracture Complexity and Mineral Compositions

Figure 12 shows the correlations between mineral contents and fracture complexity. The fracture complexity has a positive correlation with the quartz, calcite, and dolomite content. The fracture complexity has a negative correlation with clay content. The fracture complexity has no obvious relationship with feldspar content.

4 DISCUSSION

4.1 Impact of Fracturing Methods

In this study, the cores are broken by the axial compression method, which would finally result in shear fracturing. In practice, reservoirs are broken by increasing the pore pressure in hydraulic fracturing, which would result in tensile fracturing. Although the fracturing methods are different, due to the microscopic heterogeneity and anisotropy of the rock, the fractures of the two fracturing methods are preferentially generated or extended along the weak planes of the internal microstructure. The number and morphology of fractures and the fracturing strength are all determined by the weak planes at micro scale. Therefore, the rock mechanical properties obtained from the triaxial compression experiment can be applied to

hydraulic fracturing to analyze the fracability of oil and gas reservoirs (Jin et al., 2015; Li N. et al., 2018).

4.2 Insufficiency of the Method

The quantification of the fracture complexity proposed in this study is a new technology. Many new problems have risen in practical applications and are still being improved. For example, the verticality and flatness of the cylindrical core end face has a serious impact on fracture morphology, which puts forward higher requirements for core processing accuracy than the current industry level. The F_c calculation method is still being optimized. For example, the calculation of fracture dip dispersion in **Eq. (4)** does not consider the influence of fracture size. In addition, the image preprocessing software is being developed to formulate rules to realize automatic fracture classification and reduce the artificial influences. The microscopic mechanism that affects the surface fracture rate and fracture dip dispersion also needs to be studied.

4.3 Fracability

The post-fracturing fracture complexity describes the complexity of the primary fractures generated after core fracturing. A larger F_c represents a better fracturing result but it does not fully represent the fracability of the rock. To fully analyze the fracability of rocks, the fracturing process can be divided into three stages: In the first stage, the internal microstructures are continuously destroyed until the axial stress increases to the compressive strength. In the second stage, the microscopic fractures are connected to form macroscopic fractures, and the strength of the rock decreases. In the third stage, the macroscopic fractures continue to extend along the weak planes, and the energy of fracturing is also reduced until it is insufficient to support the fracture extension. Through the aforementioned analysis, in addition to the fracture complexity, a complete description of the fracturing process requires rock strength and fracture extensibility. Less rock strength means that a smaller stress is required for hydraulic fracturing. Therefore, the rock strength and fracability are negatively correlated. In addition, a faster fracture extension after fracturing means a faster hydraulic fracturing speed, resulting in less proppant, shorter soaking time, and lower cost. Therefore, the fracture extensibility is positively related to the fracability. For the triaxial fracturing experiment in this study, the strength can be described by the triaxial compressive strength, and the extensibility of the fracture produced after compression can be described by the analysis of the stress–strain curve. Through the triaxial fracturing experiment, the rock fracability can be completely analyzed.

5 CONCLUSION

We propose a set of methods for quantitatively analyzing the fracture complexity of rocks after triaxial fracturing. The results suggest that

1) Fracture complexity can represent the complex fracture characteristics of mud shales after triaxial fracturing;
2) The fractal dimension of fractures has a good linear correlation with the surface fracture rate and has no correlation with the fracture dip dispersion. By comparison, the fracture complexity is more suitable for describing the complex fracture network than the fractal dimension;
3) Fracture complexity has no obvious relationship with the brittleness index based on Young's modulus and Poisson's ratio and has a positive correlation with the brittleness index based on mineral compositions;
4) Fracture complexity is positively correlated with the content of quartz, calcite, and dolomite and negatively correlated with the content of clay minerals and has no obvious relationship with the content of feldspar.

The quantitative analysis method for the fracture complexity calculation after triaxial fracturing is a new technology. There are still many problems to be solved. However, this technology provides a solution to the bottleneck problem in the fracturing evaluation of unconventional oil and gas reservoirs and has good application prospects.

DATA AVAILABILITY STATEMENT

The original contributions presented in the study are included in the article/Supplementary Material, further inquiries can be directed to the corresponding author.

AUTHOR CONTRIBUTIONS

All authors listed have made a substantial, direct, and intellectual contribution to the work and approved it for publication.

FUNDING

This work is supported by the Scientific Research and Technology Development Project of the China National Petroleum Corporation (2021DJ4003).

REFERENCES

Ai, C., Zhang, J., Li, Y., Zeng, J., Yang, X., and Wang, J. (2016). Estimation Criteria for Rock Brittleness Based on Energy Analysis during the Rupturing Process. *Rock Mech. Rock Eng.* 49 (12), 4681–4698. doi:10.1007/s00603-016-1078-x

Akinbinu, V. A. (2017). Relationship of Brittleness and Fragmentation in Brittle Compression. *Eng. Geology.* 221, 82–90. doi:10.1016/j.enggeo.2017.02.029

Bai, M. (2016). Why Are Brittleness and Fracability Not Equivalent in Designing Hydraulic Fracturing in Tight Shale Gas Reservoirs. *Petroleum* 2 (1), 1–19. doi:10.1016/j.petlm.2016.01.001

Barree, R. D. D., Cox, S. A. A., Miskimins, J. L. L., Gilbert, J. V. V., and Conway, M. W. W. (2015). Economic Optimization of Horizontal-Well Completions in Unconventional Reservoirs. *SPE Prod. Operations* 30 (04), 293–311. doi:10.2118/168612-pa

Brace, W. F., Paulding Jr., B. W., and Scholz, C. (1966). Dilatancy in the Fracture of Crystalline Rocks. *J. Geophys. Res.* 71 (16), 3939–3953. doi:10.1029/jz071i016p03939

Feng, R., Zhang, Y., Rezagholilou, A., Roshan, H., and Sarmadivaleh, M. (2020). Brittleness Index: From Conventional to Hydraulic Fracturing Energy Model. *Rock Mech. Rock Eng.* 53 (2), 739–753. doi:10.1007/s00603-019-01942-1

Guo, T., Zhang, S., Qu, Z., Zhou, T., Xiao, Y., and Gao, J. (2014). Experimental Study of Hydraulic Fracturing for Shale by Stimulated Reservoir Volume. *Fuel* 128, 373–380. doi:10.1016/j.fuel.2014.03.029

Holt, R. M., Fjær, E., Stenebråten, J. F., and Nes, O.-M. (2015). Brittleness of Shales: Relevance to Borehole Collapse and Hydraulic Fracturing. *J. Pet. Sci. Eng.* 131, 200–209. doi:10.1016/j.petrol.2015.04.006

Ishii, E., Sanada, H., Funaki, H., Sugita, Y., and Kurikami, H. (2011). The Relationships Among Brittleness, Deformation Behavior, and Transport Properties in Mudstones: An Example from the Horonobe Underground Research Laboratory, Japan. *J. Geophys. Res. Solid Earth* 116 (B9), 1–15. doi:10.1029/2011jb008279

Iyare, U. C., Blake, O. O., and Ramsook, R. (2021). Brittleness Evaluation of Naparima Hill Mudstones. *J. Pet. Sci. Eng.* 196, 107737. doi:10.1016/j.petrol.2020.107737

Jaeger, J. C., Cook, N. G., and Zimmerman, R. (1969). *Fundamentals of Rock Mechanics*. London: Methuen.

Jarvie, D. M., Hill, R. J., Ruble, T. E., and Pollastro, R. M. (2007). Unconventional Shale-Gas Systems: The Mississippian Barnett Shale of North-Central Texas as One Model for Thermogenic Shale-Gas Assessment. *AAPG Bull.* 91 (4), 475–499. doi:10.1306/12190606068

Jin, X., Shah, S. N., Roegiers, J.-C., and Zhang, B. (2015). An Integrated Petrophysics and Geomechanics Approach for Fracability Evaluation in Shale Reservoirs. *SPE J.* 20 (03), 518–526. doi:10.2118/168589-pa

Li, J., Li, Y., and Wu, K. (2021). "An Efficient Higher Order Displacement Discontinuity Method with Joint Element for Hydraulic Fracture Modeling," in 55th US Rock Mechanics/Geomechanics Symposium (OnePetro, Virtual, June 2021).

Li, J., Yu, W., Guerra, D., and Wu, K. (2018). Modeling Wettability Alteration Effect on Well Performance in Permian basin with Complex Fracture Networks. *Fuel* 224, 740–751. doi:10.1016/j.fuel.2018.03.059

Li, N., Zhang, S., Zou, Y., Ma, X., Wu, S., and Zou, Y. (2018). Experimental Analysis of Hydraulic Fracture Growth and Acoustic Emission Response in a Layered Formation. *Rock Mech. Rock Eng.* 51 (4), 1047–1062. doi:10.1007/s00603-018-1547-5

Li, X., Wang, S., Ge, S., Reza, M., and Li, Z. (2018). Investigation on the Influence Mechanism of Rock Brittleness on Rock Fragmentation and Cutting Performance by Discrete Element Method. *Measurement* 113, 120–130. doi:10.1016/j.measurement.2017.07.043

Li, Y., Long, M., Tang, J., Chen, M., and Fu, X. (2020). A Hydraulic Fracture Height Mathematical Model Considering the Influence of Plastic Region at Fracture Tip. *Pet. Exploration Develop.* 47 (1), 184–195. doi:10.1016/S1876-3804(20)60017-9

Li, Y., Jia, D., Rui, Z., Peng, J., Fu, C., and Zhang, J. (2017). Evaluation Method of Rock Brittleness Based on Statistical Constitutive Relations for Rock Damage. *J. Pet. Sci. Eng.* 153, 123–132. doi:10.1016/j.petrol.2017.03.041

Li, Y., Long, M., Zuo, L., Li, W., and Zhao, W. (2019). Brittleness Evaluation of Coal Based on Statistical Damage and Energy Evolution Theory. *J. Pet. Sci. Eng.* 172, 753–763. doi:10.1016/j.petrol.2018.08.069

Ma, X., Li, N., Yin, C., Li, Y., Zou, Y., Wu, S., et al. (2017). Hydraulic Fracture Propagation Geometry and Acoustic Emission Interpretation: A Case Study of Silurian Longmaxi Formation Shale in Sichuan Basin, SW China. *Pet. Exploration Develop.* 44 (6), 1030–1037. doi:10.1016/s1876-3804(17)30116-7

Mandelbrot, B. (1967). How Long Is the Coast of Britain? Statistical Self-Similarity and Fractional Dimension. *Science* 156 (3775), 636–638. doi:10.1126/science.156.3775.636

Miller, K. S., and Ross, B. (1993). *An Introduction to the Fractional Calculus and Fractional Differential Equations*. New York: Wiley.

Nejati, H. R., and Ghazvinian, A. (2014). Brittleness Effect on Rock Fatigue Damage Evolution. *Rock Mech. Rock Eng.* 47 (5), 1839–1848. doi:10.1007/s00603-013-0486-4

Peng, R. D., Xie, H. P., and Ju, Y. (2004). Computation Method of Fractal Dimension for 2-D Digital Image. *J. China Univ. Mining Technol.* 33 (1), 19–24. doi:10.1023/B:APIN.0000033637.51909.04

Qin, H., and Yang, X. (2019). Log Interpretation Methods for Measuring the Brittleness of Tight Reservoir. *Well Logging Technol.* 43 (5), 509–513+530. doi:10.16489/j.issn.1004-1338.2019.05.013

Rickman, R., Mullen, M. J., Petre, J. E., Grieser, W. V., and Kundert, D. (2008). "A Practical Use of Shale Petrophysics for Stimulation Design Optimization: All Shale Plays Are Not Clones of the Barnett Shale," in SPE annual technical conference and exhibition (Denver, Colorado, USA, September 2008: Society of Petroleum Engineers). doi:10.2118/115258-ms

Stanchits, S., Burghardt, J., and Surdi, A. (2015). Hydraulic Fracturing of Heterogeneous Rock Monitored by Acoustic Emission. *Rock Mech. Rock Eng.* 48 (6), 2513–2527. doi:10.1007/s00603-015-0848-1

Tarasov, B., and Potvin, Y. (2013). Universal Criteria for Rock Brittleness Estimation under Triaxial Compression. *Int. J. Rock Mech. Mining Sci.* 59, 57–69. doi:10.1016/j.ijrmms.2012.12.011

Vernik, L. (2016). *Seismic Petrophysics in Quantitative Interpretation*. Society of Exploration Geophysicists, Tulsa. doi:10.1190/1.9781560803256

Wang, Y., Li, H., Mitra, A., Han, D.-H., and Long, T. (2020). Anisotropic Strength and Failure Behaviors of Transversely Isotropic Shales: An Experimental Investigation. *Interpretation* 8 (3), SL59–SL70. doi:10.1190/INT-2019-0275.1

Wang, Y., Zhao, L., Han, D.-H., Mitra, A., Li, H., and Aldin, S. (2021). Anisotropic Dynamic and Static Mechanical Properties of Organic-Rich Shale: The Influence of Stress. *Geophysics* 86 (2), C51–C63. doi:10.1190/geo2020-0010.1

Wen, T., Tang, H., and Wang, Y. (2020). Brittleness Evaluation Based on the Energy Evolution throughout the Failure Process of Rocks. *J. Pet. Sci. Eng.* 194, 107361. doi:10.1016/j.petrol.2020.107361

Xie, H. (1992). Fractal Geometry and its Application in Rock and Soil Mechanics. *Chin. J. Geotechnical Eng.* 14 (1), 14–24.

Zhang, D., Ranjith, P. G., and Perera, M. S. A. (2016). The Brittleness Indices Used in Rock Mechanics and Their Application in Shale Hydraulic Fracturing: A Review. *J. Pet. Sci. Eng.* 143, 158–170. doi:10.1016/j.petrol.2016.02.011

Zhang, J., Li, Y., Pan, Y., Wang, X., Yan, M., Shi, X., et al. (2021). Experiments and Analysis on the Influence of Multiple Closed Cemented Natural Fractures on Hydraulic Fracture Propagation in a Tight sandstone Reservoir. *Eng. Geology.* 281, 105981. doi:10.1016/j.enggeo.2020.105981

Zhang, S., Guo, T., Zhou, T., Zou, Y., and Mu, S. (2014). Fracture Propagation Mechanism experiment of Hydraulic Fracturing in Natural Shale. *Acta Petrolei Sinica* 35 (3), 496–503. doi:10.7623/syxb201403011

Zhao, L., Qin, X., Zhang, J., Liu, X., Han, D.-H., Geng, J., et al. (2018). An Effective Reservoir Parameter for Seismic Characterization of Organic Shale Reservoir. *Surv. Geophys.* 39 (3), 509–541. doi:10.1007/s10712-017-9456-9

Conflict of Interest: YZ and XL were employed by the CNPC Logging Company Limited. Author YW was employed by the SINOPEC Geophysical Research Institute.

The remaining authors declare that the research was conducted in the absence of any commercial or financial relationships that could be constructed as a potential conflict of interest.

Publisher's Note: All claims expressed in this article are solely those of the authors and do not necessarily represent those of their affiliated organizations, or those of the publisher, the editors, and the reviewers. Any product that may be evaluated in this article, or claim that may be made by its manufacturer, is not guaranteed or endorsed by the publisher.

frontiers | Frontiers in Earth Science

ORIGINAL RESEARCH
published: 05 May 2022
doi: 10.3389/feart.2022.853082

Discovery of Early Mesozoic Magmatism in the Northern Muglad Basin (Sudan): Assessment of Its Impacts on Basement Reservoir

Jian Zhao[1,2] *and Lirong Dou*[1,2]*

[1]Research Institute of Petroleum Exploration and Development, PetroChina, Beijing, China, [2]China National Oil and Gas Exploration and Development Company Ltd., Beijing, China

The crystalline basement in the Central African Rift System (CARS) has been confirmed as a good unconventional reservoir in the surrounding basins of the Muglad area, Sudan. This study has recognized at least five Early Mesozoic intrusions for the first time at the northern margin of the Muglad Basin. Field and petrographic investigations show that they are mainly granite, syenite, diorite, and monzonite, with dominant alkali feldspar, plagioclase, quartz, and minor hornblende, biotite, and magnetite. Zircon internal structures, Th/U ratios, and rare earth element (REE) patterns indicate their magmatic origin. A total of 210 zircons from five samples were analyzed using LA-ICP-MS and they yielded U-Pb ages from 195.0 ± 6 to 225.0 ± 3 Ma, belonging to the Late Triassic-Early Jurassic. These results suggest that the Muglad Basin basement is not universally Precambrian as previously considered. The older basement was intruded and modified by Early Mesozoic magmas as evidenced by field contacts and our dating results. These magmatic events produced diverse Mesozoic igneous rocks prior to the formation of the Muglad Basin (Early Cretaceous), becoming new members of the crystalline basement. This composite basement then experienced prolonged weathering and fracturing for 65–95 Ma, resulting in porous and permeable weathered layers or fractured zones, making the basement a good unconventional reservoir for oil and gas.

Keywords: Zircon U-Pb age, lithological characteristics, Mesozoic intrusions, Precambrian basement, unconventional reservoir, Muglad Basin, Sudan

OPEN ACCESS

Edited by:
Jizhou Tang,
Tongji University, China

Reviewed by:
Hao Xiong,
Yale University, United States
Aishwarya Srinivasan,
Texas A&M University, United States

***Correspondence:**
Lirong Dou
doulirong@cnpcint.com

Specialty section:
This article was submitted to Economic Geology, a section of the journal Frontiers in Earth Science

Received: *12 January 2022*
Accepted: *24 February 2022*
Published: *05 May 2022*

Citation:
Zhao J and Dou L (2022) Discovery of Early Mesozoic Magmatism in the Northern Muglad Basin (Sudan): Assessment of Its Impacts on Basement Reservoir. Front. Earth Sci. 10:853082. doi: 10.3389/feart.2022.853082

INTRODUCTION

Basement rocks are key in studying the formation and evolution of rift basins, and their lithological characteristics, generation, and homogeneity also directly affect their exploration potential and economic values, such as the bearing of metals or the development of oil and gas reservoirs. The Central African Rift System (CARS) is an intracontinental Cretaceous–Paleogene rift system with dozens of well-known prolific basins, such as the Bongor, Doba, Doseo, Salamat, Melut, and Muglad basins, where encouraging oil and gas resources have been successively discovered. These trans-extensional or extensional basins were mainly formed during the Early Cretaceous on the Precambrian crystalline basement (Fairhead J. D., 1988; Binks and Fairhead, 1992; Guiraud and Maurin, 1992; Genik, 1993; Fairhead et al., 2013). Regionally, these rift basins have experienced the Precambrian-Late Jurassic pre-rift stage (the craton), the Early Cretaceous- Late Cretaceous rift stage

(evolution of fault sags and depressions), and the Paleogene-current post-rift stage (Schull, 1988; Genik, 1992; McHargue et al., 1992; Genik, 1993). The Precambrian-Late Jurassic craton stage has been generally regarded as the main period of the regional basement formation. Although the latter two stages were respectively dominated by intraplate rifting and depression sedimentation, the basement has been mostly inherited and preserved, without significant changes in lithology. As a result, it has been widely accepted that the basements across the Central African Rift System (CARS) should be similar or homogeneous, and comparable among different basins (Fairhead J. D., 1988; Schandelmeier and Pudlo, 1990; Guiraud et al., 1992; Guiraud and Maurin, 1992).

Previously, both regional geological surveys and intensive oil and gas exploration activities in the CARS have proved and even addressed that the basement in the CARS only consists of ancient Precambrian rocks. For example, the basement in southwestern Chad is composed of Precambrian granite, granodiorite, and granitic gneisses (Penaye et al., 2006). Some Precambrian marble was also discovered locally and reported by Penaye et al. (2006), which added a new rock member to the granitic basement. In the neighboring Melut basin in Sudan, the granite, granodiorite, and gneisses in the basement have consistent geological ages of ca. 540 Ma (Schull, 1988; Awad, 2015). Likewise, in the Bongor basin (Chad), at least two major groups of rocks were identified, including magmatic rocks with ages between 621 Ma and 525 Ma and metamorphic rocks between 616 Ma and 526 Ma (Dou et al., 2015; Li et al., 2017; Dou et al., 2018).

In 2018, high oil flows were tested from basement buried hills in the Bongor Basin (Chad), providing a new perspective of basement study that greatly boosted the related research not only for fundamental geology but also for evaluation of unconventional reservoirs. The basement reservoirs in the Bongor Basin are classic buried hills where the reservoir is a combination of the weathered, leached, and fractured basement. The exposure and weathering of the fractured basement provide good conditions for storing and transporting hydrocarbons (Dou et al., 2018). The lithology of the basement has fundamental impacts on the development of the unconventional reservoir. The buried hills' morphology, their burial depth, and their relationship to major faults will also affect the degree of reservoir development (Dou et al., 2015; Li et al., 2017; Dou L. et al., 2018). Besides, time also plays a key role in reservoir development. The longer duration of the basements was weathered and fractured, the better a basement reservoir could be developed.

However, our current understanding of the Muglad Basin, such as the fundamental lithology of the basement, and the potential as an unconventional reservoir, are still very limited compared to other CARS basins. Vail (1972) suggested that the basement of the Muglad Basin was composed of Precambrian

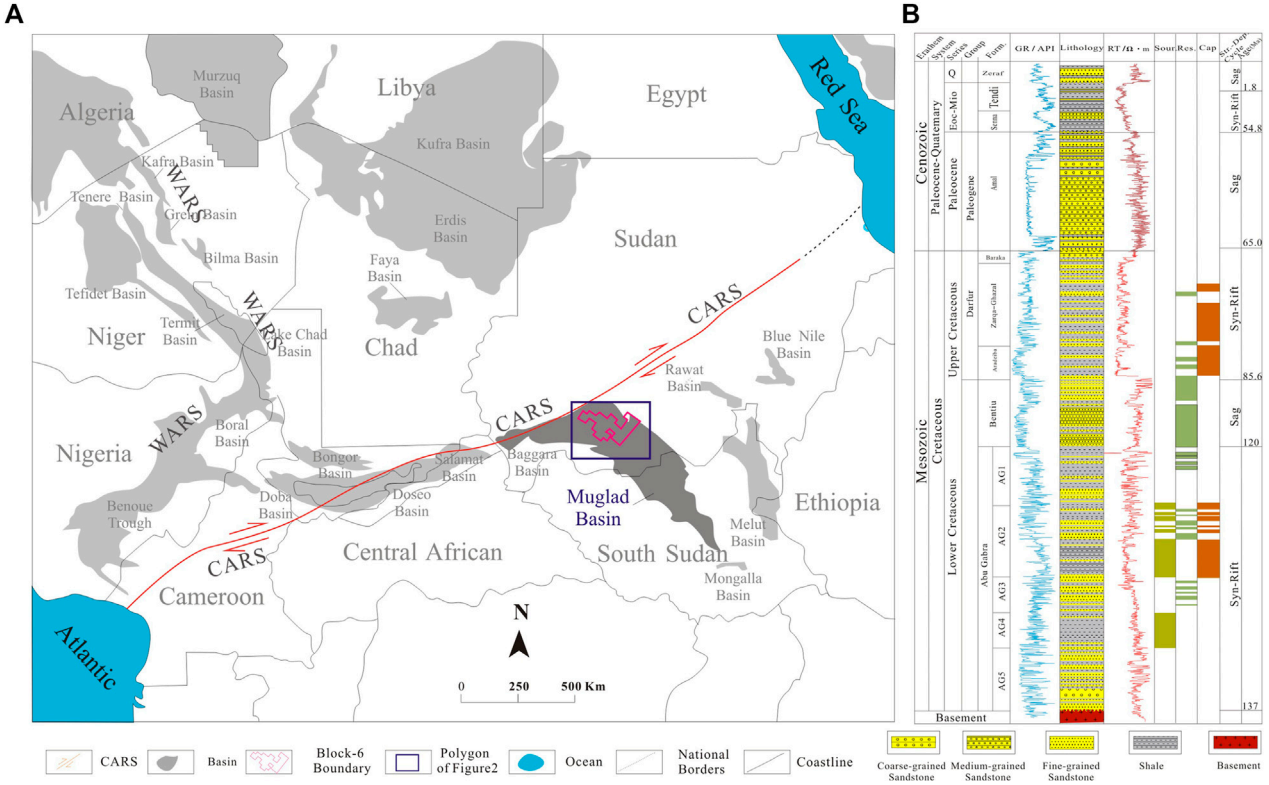

FIGURE 1 | Structural location and main lithostratigraphy of the Muglad Basin, Sudan (modified from Genik 1993) **(A)** Location of the Muglad basin in Central African Rift System (CARS), blue square showing the polygon of **Figure 2** and the red polygon outlines Block-6, Sudan. **(B)** Main lithostratigraphy and structural evolution cycles of the Muglad Basin.

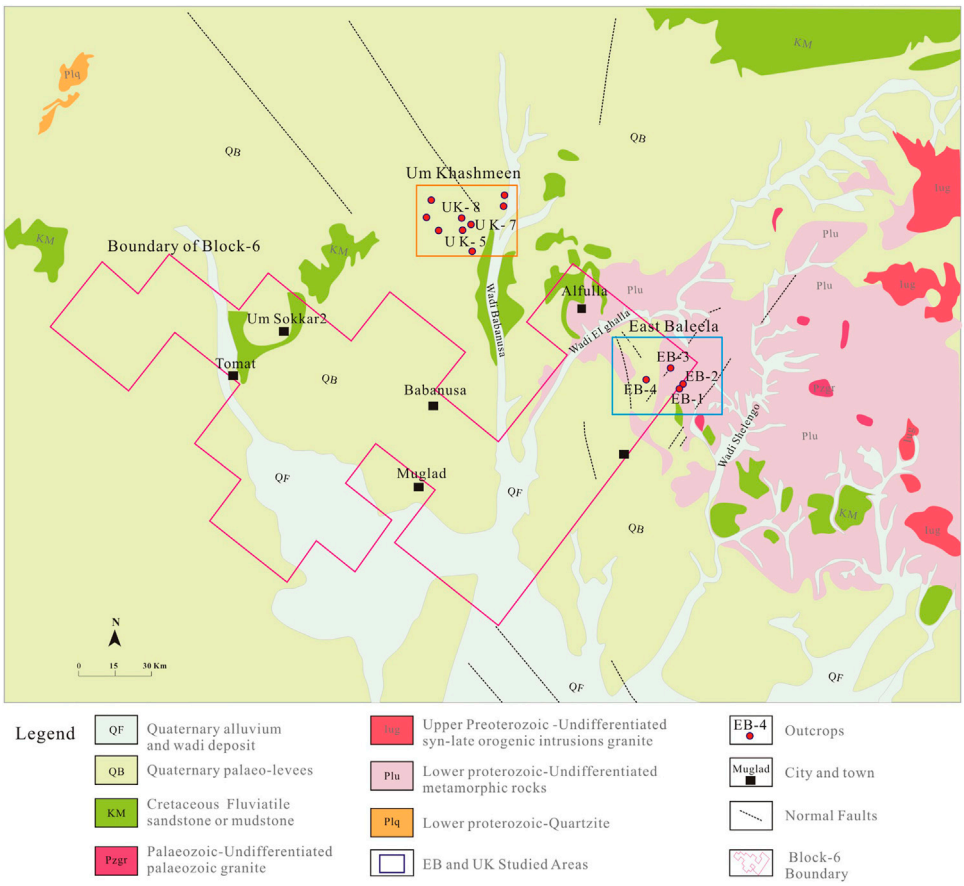

FIGURE 2 | Studied outcrops in the geological map of Sudan (modified from GRAS, 2005). The two studied areas (EB and UK) are outlined by a blue square and a yellow square, respectively.

rocks, including granite, granodiorite, granitic gneiss, and amphibolite, etc, without providing ages of these rocks. Zhao et al. (2020) further documented the dominated granitoids of the Muglad Basin basement underwent variable degrees of regional metamorphism, but no ages were available.

In this study, we conducted a detailed geological survey and collected samples along the north margin of the Muglad basin to study the lithology diversity and chronology of the basement rocks. The results will help to assess whether the basement of the Muglad basin is a potential target for a good unconventional reservoir.

GEOLOGICAL SETTINGS

Muglad Basin lies in the southern part of the Republic of Sudan, crossing Sudan and the Republic of South Sudan. It extends about 800 km long and 200 km wide, covering an area of more than 12×10^4 km^2. This basin is a Cretaceous rift basin developed on the Precambrian crystalline basement (Fairhead J. D., 1988; Fairhead J. D., 1988; Schandelmeier and Pudlo, 1990; Fairhead, 1992; Guiraud et al., 1992; Guiraud and Maurin, 1992; Tong et al., 2004; Yassin et al., 2017), and located on the south part of the Central African Rift System (CARS). The NW-SE trending basin extends towards the northwest where it terminates at the CARS and gradually converges toward the southeast (Genik, 1992; Genik, 1993) (**Figure 1A**). In terms of the Exploration & Production (E&P) block division, the northern part of the Muglad basin is in Block-6 (outlined in red in **Figure 1A**), which was operated by China National Petroleum Company (CNPC).

Throughout the tectonic evolution of the CARS, three major rifting-sagging cycles have been identified in the Muglad Basin (Fairhead, 1988; Schull, 1988; Genik, 1992; Genik, 1993). *1*) Abu Gabra-Bentiu cycle, with strong rifting and faulting movement, the Abu Gabra Formation (Fm.) is the earliest syn-rift sequence and consists of conglomerates at the bottom, sandstone and mudstone, and organic-rich shale in the upper intervals. After that, a thick layer of sandstone was deposited in the Bentiu Fm. as the first sag system. *2*) Darfur-Amal cycle, with relatively weaker tectonic movement, the shaly sedimentary sequence was developed in the Darfur Group and was followed by a thicker layer of sandstone in Amal. *3*) Eocene-present period, with the weakest rifting stage in the Early Paleogene, is characterized by interbedded sandstone and shale with uneven distribution in different areas (**Figure 1B**).

FIGURE 3 | Overview photographs of outcrops. **(A)** Outcrop covered by plant and broken dispersed sandstones (EB -3); **(B)** Outcrop covered by a thin layer of Quaternary loess (UK-5); **(C)** Outcrop partially covered by low shrub (UK-9); **(D)** Outcrop as giant igneous bodies (UK-8); **(E)** Outcrop with dispersed granite bodies (UK-4); **(F)** Outcrops with joints and fractures (UK-4).

All the three sedimentary cycles overly the basement. Up to now, a total of 19 wells have been drilled into the basement in Block-6, with rock penetration thickness ranging from 17 to 257 m. The penetrated intervals are mainly composed of granite or granodiorite that experienced regional metamorphism in different degrees (Zhao et al., 2020).

The studied areas of this work include the East-Baleela-Low-High (EB) in the east margin of Block-6 and the Um-Khashmeen (UK) in the north margin of Block-6, covering nearly 2,700 km^2 (**Figure 2**). They are in a transition zone between the Nuba mountains and the Muglad basin (GRAS, 2005). Due to the uplift of the Nuba Mountain, the strata in the Muglad Basin were tilted towards the mountain, which provided ideal sections and "windows" for basement investigation (**Figure 2**).

MATERIALS AND METHODS

Sample Collection and Description in Field

At least 20 locations were investigated during the whole field trip, of which 15 outcrops (4 in EB area, 11 in UK area) were observed and described in detail (**Figure 2**). For each outcrop, orientation data, as well as photos and some quick sketches, for all the strata, sedimentary structures, fault planes, joints, and fractures were collected. At each outcrop, we sampled different types of rocks and recorded their GPS coordinates, occurrences, and contact relationships with their country rocks.

Laboratory Analysis

About 120 samples were collected in the field and then examined in the laboratory. Samples were named after outcrop and sampling number. For example, EB3-2 is a sample that was collected at the second sampling location at the EB-3 outcrop.

Around 100 thin sections from a total of 80 hand specimens were studied. Petrology and mineralogy were systemically described in terms of rock types, micro-textures, structures, mineral assemblages, mineral species, mineral contents, and mineral alternation.

Zircon geochronology study was conducted on five representative samples from five outcrops, including zircon internal structures, Th and U contents, rare earth elements (REE), and U-Pb dating on more than 200 zircons.

Cathodoluminescence (CL) images were taken on these zircons before analysis to reveal the internal structure and determine the analytical positions. All these obtained data were combined to determine the origin of zircons.

Zircon U-Pb Dating Methods

The single-zircon U-Pb dating method was utilized to estimate the ages of these rocks. Sample preparation and age dating were conducted in the State Key Laboratory of Continental Dynamics at Northwest University, China. The equipment used was a Laser Ablation Inductively Coupled Plasma Mass Spectrometry (LA-ICP-MS) produced by Agilent with a GeoLas200 M laser ablation system produced by MicroLas. The laser ablation system consisted of a Compex102 ArFexcimer laser (operated at a wavelength of 193 nm) from Lambda Physik, with a MicroLas optical system.

Single spot laser ablation was used for sampling, with a spot diameter of 30 μm and a frequency of 10 Hz. The carrier gas for the ablated materials was high-purity argon and helium. Standard zircon 91,500 and synthetic glass NIST610 were used as standards, with one analysis on zircon 91,500 every five spots and one analysis on NIST610 every 10 spots. The background acquisition time for each spot was 30 s and the signal acquisition time was 40 s. GLITTER software (ver. 4.0, Macquarie University) was used for data processing. The zircon standard 91,500 was adopted as the external standard for isotopic ratio fractionation correction during age calculation.

RESULTS

Field Investigations

The outcrops can be roughly divided into two types, covered, and uncovered. The former type of outcrops is usually covered by plants, sparse vegetation (**Figure 3A**), or overlying sedimentary strata such as Quaternary flood deposits (**Figures 3B,C**). Uncovered outcrops have no vegetation cover, and the rocks are completely and directly exposed, appearing as a single giant granite body (**Figure 3D**) or multiple continuous low-amplitude hills (**Figures 3E,F**). Many outcrops have clear broken zones, fractured belts, or joint systems (**Figures 3E,F**).

At least dozens of rock types, either igneous or metamorphic, were identified in the field at different outcrops. The igneous rocks include granite, syenite, diorite, and monzonite and they are relatively fresh (**Figures 4A–C,F**). The metamorphic rocks contain metasandstone, quartzite, gneiss, and mylonite (**Figures 4D,E**). Most outcrops are dominated by igneous rocks (85 vol%), followed by gneiss and quartzite (around 10%), and minor mylonite (less than 5%).

Field Occurrence and Petrology of the Representative UK-7 Outcrop

In this study, the UK-7 outcrop was selected to represent the rock types and their occurrences of the studied outcrops. The rocks at the UK-7 outcrop are directly exposed to the surface (**Figure 5A**) and are typically granite and syenite (**Figure 5A**). Spheroidal weathering is widespread, with hundreds of ball-shaped granites distributed randomly. Fractures often transect veins, joints, and other fractures (**Figures 5A,B**). The rocks are usually flesh red, dense, and massive, with a medium-coarse-grained texture. Aggregates of K- feldspar or hornblende crystals are visible in hand specimens (**Figure 5C**).

Sample UK7-1 is medium-to-coarse-grained syenite, with a subhedral granular texture and grain sizes from 1.0 to 4.0 mm. It is composed of alkali feldspar, plagioclase, and quartz. The dominant alkali feldspar (69%) occurs in both subhedral-tabular and wide-tabular shapes, within which plagioclase commonly appears as metasomatic relicts, suggesting intensive alkalization (**Figures 6A,B**). The plagioclase (10%) is tabular, with some polysynthetic twinning. The hornblende (20%), sometimes occurring as aggregates, are subhedral, euhedral granular, and columnar grains, with good cleavages, partial chlorination, and magnetite precipitation. The quartz, with varied contents, is xenomorphic-granular and infilled between tabular feldspar crystals (**Figures 6C,D**). Except for some metasomatic minerals, almost all the mineral crystals are in good shape with sharp boundaries, indicating a weak degree of hydrothermal alteration.

We studied all the collected samples from the 15 outcrops and found that they are more commonly composed of granite, syenite, and diorite, with a minor volume of metasandstone, mylonite, gneiss, and quartzite (**Table 1**). They have similar mineral assemblages of alkali feldspar, plagioclase, quartz, and amphibole (or hornblende). In igneous rocks, alkali feldspar and plagioclase are principal minerals, and their contents could reach as high as 75%. Residual plagioclases are usually developed within alkali feldspar, indicating strong alkalization. The contents of quartz vary from 10% to 25%. And the hornblende is usually with magnetite. These minerals seem fresh without significant alternation, but the micro-fractures and veins are usually developed among them. Metamorphic rocks have various mineral assemblages, and serious mineral alteration. Metasandstone and quartzite are mainly composed of quartz and lithic fragments. Similarly, the mylonite is also composed of the quartz-dominated matrix, showing strong recrystallization and orientation, while gneiss is constituted by biotite, feldspar, and quartz. Most of these minerals are underwent partly to completely alternation (**Table 1**).

Zircon CL Imaging, REE Patterns, and U-Pb Dating Results of Sample UK7-1

Zircon Cathodoluminescence (CL) Characteristics

Cathodoluminescence (CL) imaging is an effective method to reveal the morphology, internal structures of zircons and helps to determine their origin. For example, magmatic zircons typically display oscillatory zoning or fan-shaped zoning structures, while metamorphic zircons have different internal structures, including no zoning, weak zoning, or cloud-like zoning (Wu and Zheng, 2004). Thus, identifying the origin of zircons by CL images could assist to get more geological meaningful ages. CL imaging was conducted on nearly fifty zircons from sample UK7-1. These zircons are large euhedral grains (100–300 μm), with generally

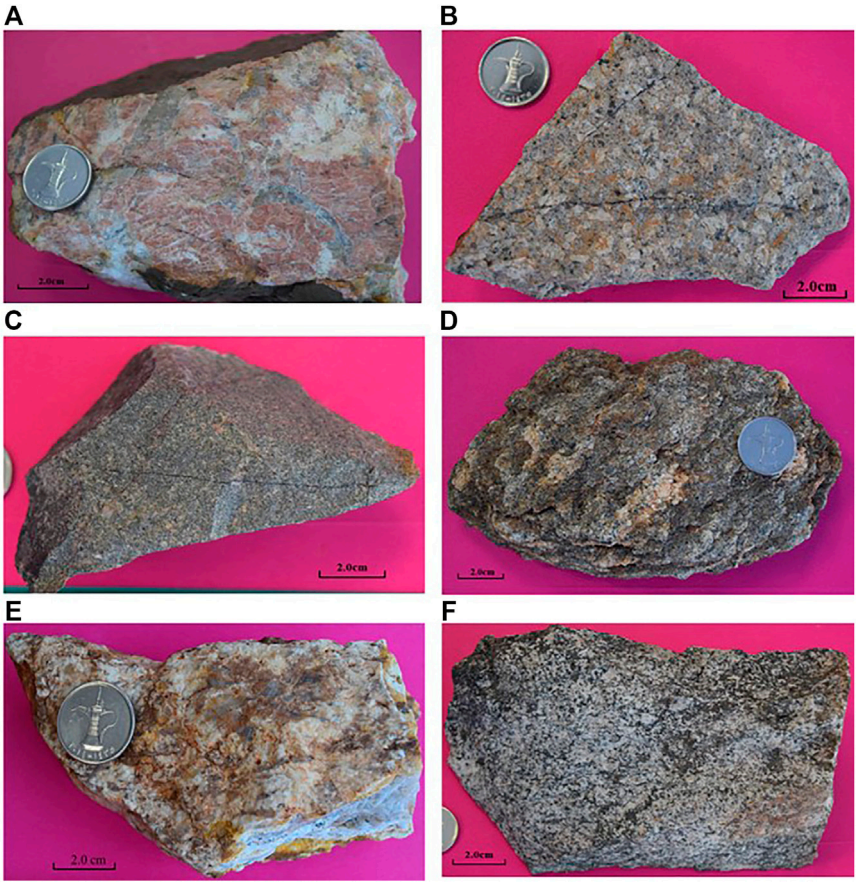

FIGURE 4 | Photographs of different types of rocks from outcrops. **(A)** Alkaline granite pegmatite, with K-feldspar phenocrysts and quartz veins (EB3-5); **(B)** Porphyritic quartz syenite, alkali feldspar phenocrysts (UK 5-1); **(C)** Silicified fine-grained monzonite (UK9-2). **(D)** Altered biotite gneiss, gneissic structure (UK 15-1); **(E)** Mylonite in gray color with high quartz content and certain orientation (UK14-1); **(F)** Fine-grained K-feldspar diorite, with local hornblende aggregates and high content of plagioclase (UK6-1).

strong luminescence showing obvious oscillatory zoning structures (**Figure 7**), indicating their magmatic origin.

Zircon REE Patterns

Zircon grains from sample UK7-1 have low Th (18–509 ppm; mean = 170 ppm) and U contents (40–495 ppm, mean = 186 ppm), with variable Th/U ratios ranging from 0.5 to 1.3, diagnostic of unaltered igneous zircons (Th/U ≥ 0.5) (**Supplementary Appendix S1**). They have relatively high total REE contents (ΣREE = 938–21,853 ppm; mean = 10,758 ppm). The chondrite-normalized REE patterns of zircons from this sample display significant enrichment of heavy REEs relative to light REEs (**Figure 8** and **Supplementary Appendix S2**), with significant positive Ce and negative Eu anomalies, all of which indicate a magmatic origin (Hoskin and Schaltegger, 2003).

Zircon U-Pb Dating of Sample UK7-1

Thirty-six spots were also analyzed on zircons for sample UK7-1 (**Supplementary Appendix S3**). The U-Pb Concordia diagrams suggest that most ages are clustered in a narrow range between 210 Ma and 250 Ma, mainly around 230 Ma. A weighted mean age of 224 ± 2 Ma was obtained and is a reliable crystallization age of the syenite (**Figure 9**).

Zircon REE Patterns and U-Pb Dating Results of Other Samples

Zircon grains from the sample UK5-2 display low Th (29–131 ppm; mean = 61 ppm) and U contents (76–204 ppm, mean = 131 ppm), with a limited Th/U ratio range of 0.3–0.5 (mean = 0.5). In sample UK6-1, zircons show variable Th (24–4,968 ppm; mean = 939 ppm) and U contents (385–1,460 ppm, mean = 835 ppm), with largely variable Th/U ratios of 0.1–3.4 (mean = 0.9). The Th and U contents of zircon grains from sample UK6-2 are much higher with values of 257–3,281 ppm (mean = 817) and 342–1,688 ppm (mean = 1,076 ppm), respectively. The Th/U ratios of zircons from this sample (mean = 0.8) are mostly higher than 0.5, similar to those of typical igneous zircons. Zircon grains from sample UK11-3 show extremely variable Th (54–5,399 ppm; mean = 1796 ppm) and U contents (106–1,277 ppm; mean = 501 ppm), resulting in largely variable Th/U ratios of 0.5–8.5. All these zircon

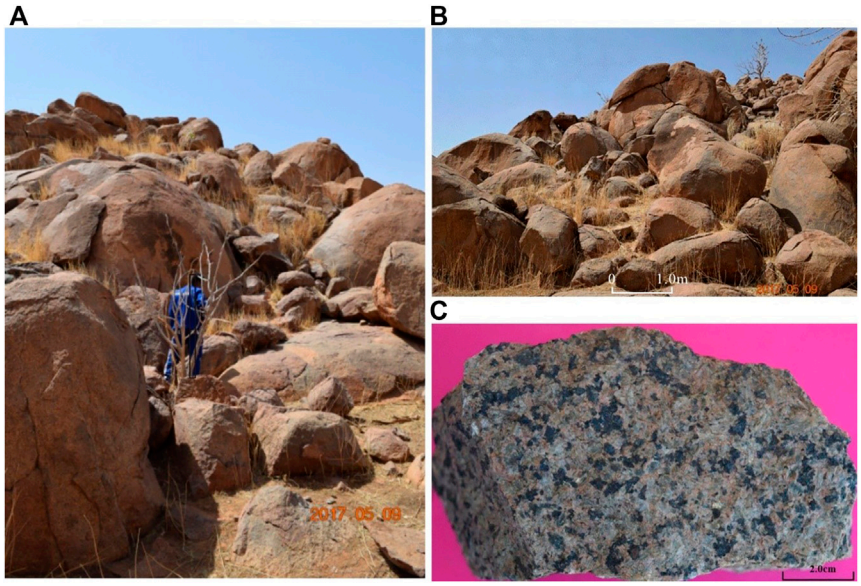

FIGURE 5 | Overview of UK-7 outcrop and sampling. **(A)** Overview of the UK-7 outcrop and apparent spheroidal weathering; **(B)** Fractured and spheroidal weathered granite bodies; **(C)** Hand specimen of basement (ID UK7-1) rock for laboratory test. The UTM geographic coordination of sample UK7-1 is X:598492; Y: 1328369.

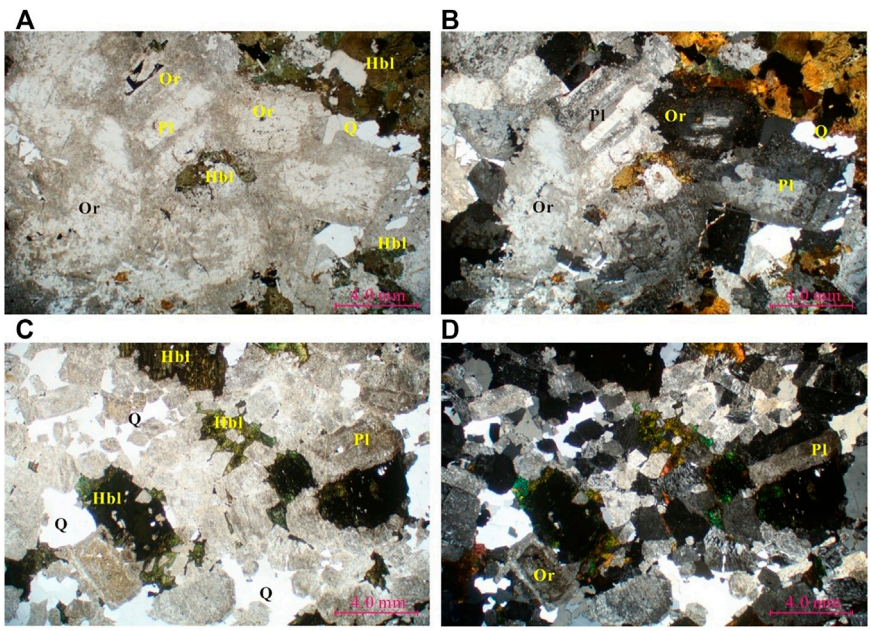

FIGURE 6 | Photomicrographs illustrating the mineral assemblage and typical micro-texture of sample UK7-1. **(A)** Principal minerals, alkali feldspar, plagioclase, and hornblende; **(B)** Wide-tabular alkali feldspar with metasomatized plagioclase; **(C)** Granular, short columnar amphibole with chlorite rims; **(D)** Granular quartz infilled between feldspar and hornblende. Pl, Plagioclase; Or, K-Felspar; Hbl, Hornblende; Q, Quartz.

Th-U data indicate the zircons from these samples are of magmatic origin.

The zircon REE pattern diagrams were also generated. The chondrite-normalized REE patterns of zircons from sample UK5-2 display enrichment of heavy REEs relative to light REEs, with significant positive Ce and negative Eu anomalies (**Figure 10A**). Comparatively, in sample UK6-1, the rising slopes from LREE to HREE are much weaker.

TABLE 1 | Rock types and mineral assemblages of basement rocks in the studied outcrops.

Rock type	Sub type	Rock name	Micro-texture and micro-structure	Mineral assemblages and typical characteristics	Outcrops and location
Igneous rocks	Granite	Alkaline feldspar granite, granite porphyry, medium-fine-grained alkali feldspar granite, fine-grained hornblende feldspar granite, silicified alkali feldspar granite	Granite structure, porphyritic structure, massive structure	Alkaline feldspar 60%, plagioclase 15%, quartz 25%; phenocrysts are mainly quartz and alkaline feldspar	EB3, UK4, UK5, UK8, UK10
	Syenite	Porphyry quartz syenite, medium-coarse-grained syenite, medium-fine-grained quartz syenite, silicified fine-grain monzonite	Hypidiomorphic-granular texture, porphyritic texture, massive structure	Alkaline feldspar 74%, plagioclase 5%, amphibole 7%, magnetite 4%, quartz 10%. Residual plagioclase in alkaline feldspar indicates strong alkalization	UK4, UK5, UK6, UK7,UK9
	Diorite	Fine-grained diorite, fine-grained quartz diorite	Hypidiomorphic-granular texture, massive structure	Plagioclase 57%, hornblende 43% (precipitating magnetite), or plagioclase 50%, hornblende 37%, quartz 13%	UK6
Metamorphic rocks	Metamorphic sandstone	Coarse-grained metamorphic conglomerate sandstone, metamorphic fine-grained quartz sandstone	palimpsest texture, massive structure, local quartzite	Quartz 60%, lithic fragment 40%	EB3, UK11
	Mylonites	Mylonite	Mylonitic structure, ocellar structure	composed of fragments and groundmass, fragments 10%, eyeball-like distribution, completely altered to clay; the quartz groundmass underwent strong recrystallization, oriented and in striped distribution	UK14
	Gneiss	Altered biotite gneiss	lepidoblastic texture, gneiss structure	biotite 30%, altered feldspar 30%, quartz 30%	UK15
	Quartzite	Quartzite, silicified rock	Coarse-large-grained crystalloblastic texture, massive structure	Mainly composed of quartz, with undulose extinction	UK16, UK11

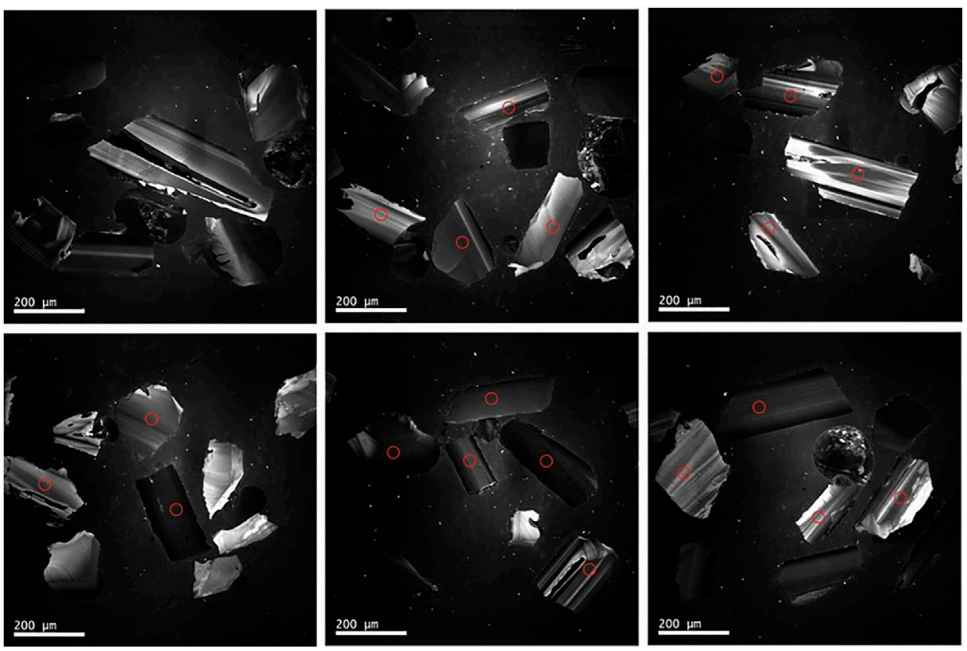

FIGURE 7 | CL images of zircons from sample UK7-1. CL images show strong luminance with obvious oscillatory zoning structures. (Red circles representing analytical points).

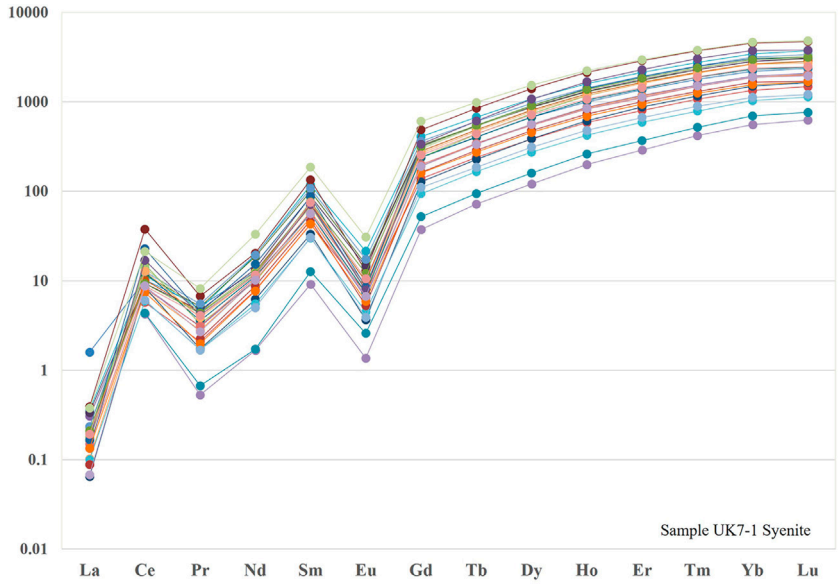

FIGURE 8 | REE distribution pattern of zircons of sample UK7-1. Enrichment of heavy REEs relative to light REEs, with significant positive Ce and negative Eu anomalies.

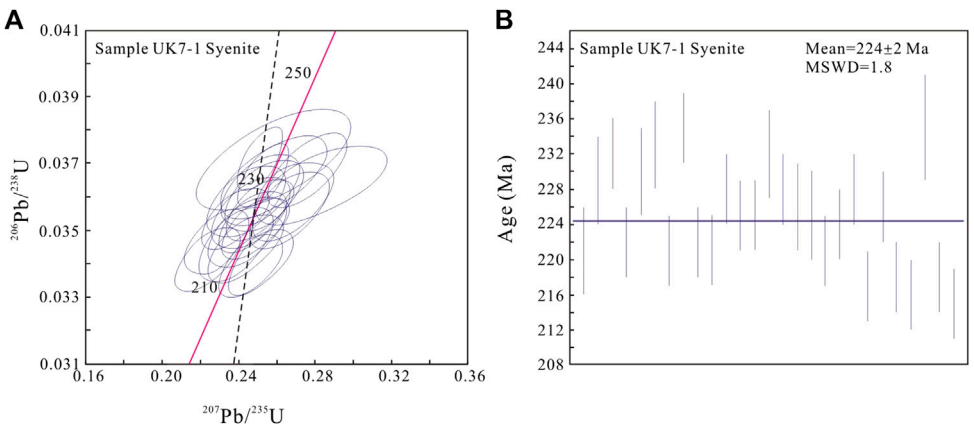

FIGURE 9 | Zircon U-Pb ages of UK7-1. **(A)** Concordia diagram showing the ages between 210 and 250 Ma. **(B)** Weighted mean age indicating the age of 224 ± 2 Ma.

However, the positive Ce and negative Eu anomalies remain obvious (**Figure 10B**). For sample UK 6-2, the zircons also display a steeply rising slope but relatively weak positive Ce anomalies and negative Eu anomalies among other samples (**Figure 10C**). Sample UK 11-3 also show significant positive Ce and negative Eu anomalies (**Figure 10D**). All these characteristics of zircon trace elements indicate the zircons are of magmatic origin (Hoskin and Schaltegger, 2003).

Using the same dating method and following the same procedure as those of sample UK7-1, we tested another 144 individual zircon grains from samples UK5-2, UK 6-1, UK6-2, and UK11-3. The sample ages were obtained either from the Concordia graph, weighted mean age, or both. Sample UK5-2 has a Concordia age of 217.8 ± 1.7 Ma, consistent with the weighted mean age of 218 ± 2 Ma (**Figures 11A,B**). The Concordia diagram of UK 6-1 revealed an age of 224.8 ± 3 Ma (**Figure 11C**), while the sample UK6-2 shows an intercept age at 207.2 ± 5.9 Ma (**Figure 11D**). The ages from sample UK 11-3 are a little dispersed and give a mean age of 195 ± 6 Ma (**Figures 11E,F**). All these ages were summarized in **Table 2**.

DISCUSSIONS

Based on the mineral assemblage, zircon CL imaging, and U-Pb dating data, we speculate that most outcrops are mainly composed of

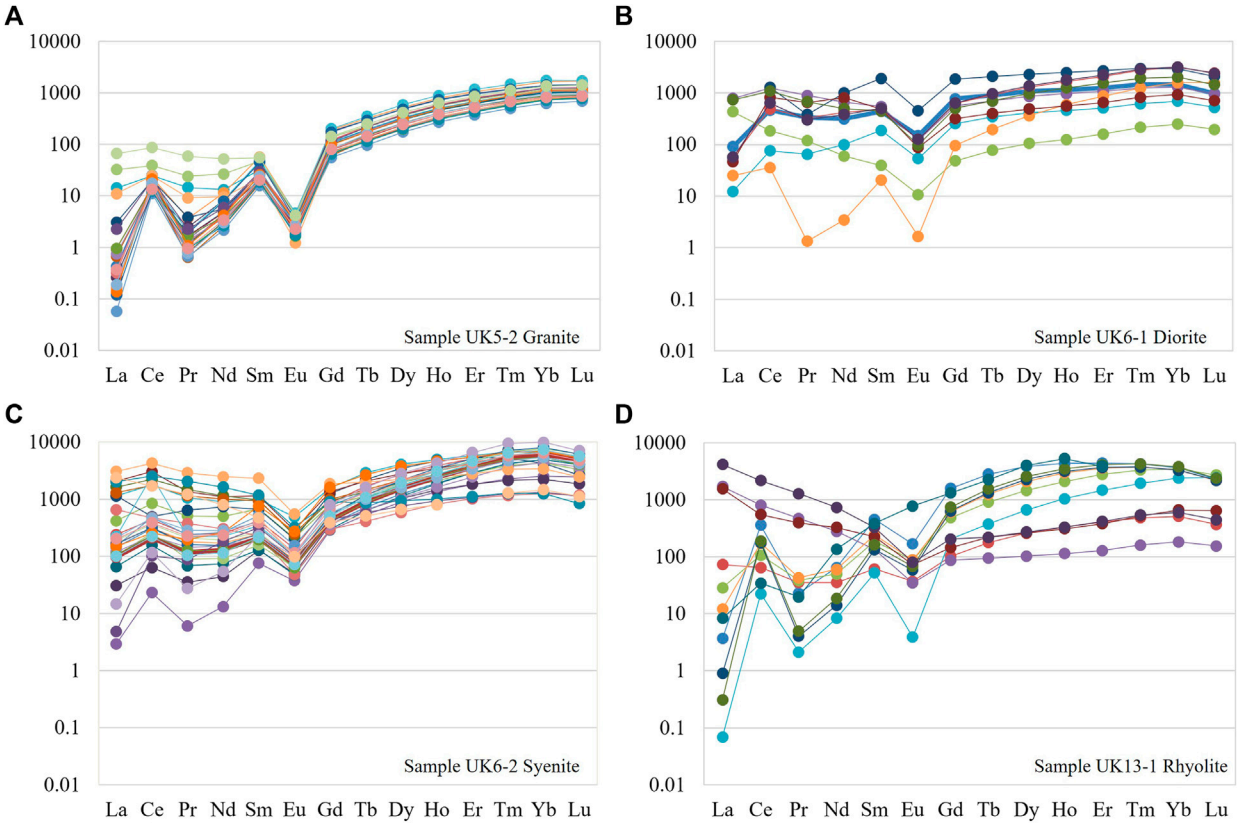

FIGURE 10 | REE distribution patterns of zircons in other samples. **(A)** REEs of sample UK5-2. **(B)** REEs of sample UK6-1; **(C)** REEs of sample UK6-2; **(D)** REEs of sample UK13-1.

granite and granodiorite, with similar mineral associations, micro-textures, and structures. The zircon oscillatory zoning, the Th/U ratios, and REE patterns all indicate their magmatic origin.

The obtained U-Pb ages are reliable and robust, revealing these rocks were formed in Late Triassic-Early Jurassic. For the first time, the Late Triassic-Early Jurassic magmatic events have been identified in the basement of the Muglad Basin area and the whole CARS.

New Member of the Basement of the Muglad Basin

Before the basin-rifting stage, from Precambrian to Late Jurassic, the CARS rarely experienced large-scale intraplate magmatic events, so the Precambrian granite intrusions are very limited in the basin basement. However, since the beginning of basin-rifting in the Cretaceous, the CARS have undergone frequent and intensive magmatic events due to intraplate extension. At least three regional magmatic events took place, i.e., the Early Cretaceous (147–106 Ma), Late Cretaceous (95–75 Ma), and Paleogene (66–52 Ma) events. The main igneous rocks are basalt and diorite, and they are common in the Bongor, Termit, and Doba Basins (**Table 3**; Wilson et al., 1992; Guiraud and Maurin, 1992, Guiraud et al., 1992; Janssen et al., 1995; Maluski et al., 1995; Coulon et al., 1996; Kamdem et al., 2002; Lu et al., 2009).

The identification of the Late Triassic-Early Jurassic intrusions in addition to the Later Cretaceous intrusions indicates that some local thermal or magmatic events also occurred in the Early Mesozoic. These intrusions resulted in changes in rock association and basement morphology. These Early Mesozoic intrusions are therefore a new member to the basement of the Muglad Basin in addition to the Precambrian rocks.

A New Candidate for Basement Reservoir

As mentioned above, the lithology of the basement has fundamental impacts on the development of an unconventional reservoir (Hu et al., 1981; Dou et al., 2015; 2018). The primary minerals of the Late Triassic-Early Jurassic igneous rock in the Muglad Basin are feldspars (both potassic and plagioclase) and quartz, with various amounts of dark minerals (mainly hornblende and biotite). These mineralogical compositions of felsic rocks with inherent susceptibility to alteration and diagenesis makes them better candidates for basement reservoirs. Adjacent to these outcrops, drilled wells and three-dimension seismic data (3D seismic) in Block-6 have revealed a double-layer structure for the basement. The shallow layer is the weathered crust, and the middle-deep layer is mainly fractured zones (Zhao et al., 2020). The crust is mainly constituted by these granitoids and has very good porosity and permeability. Its thickness varies from area to area and is

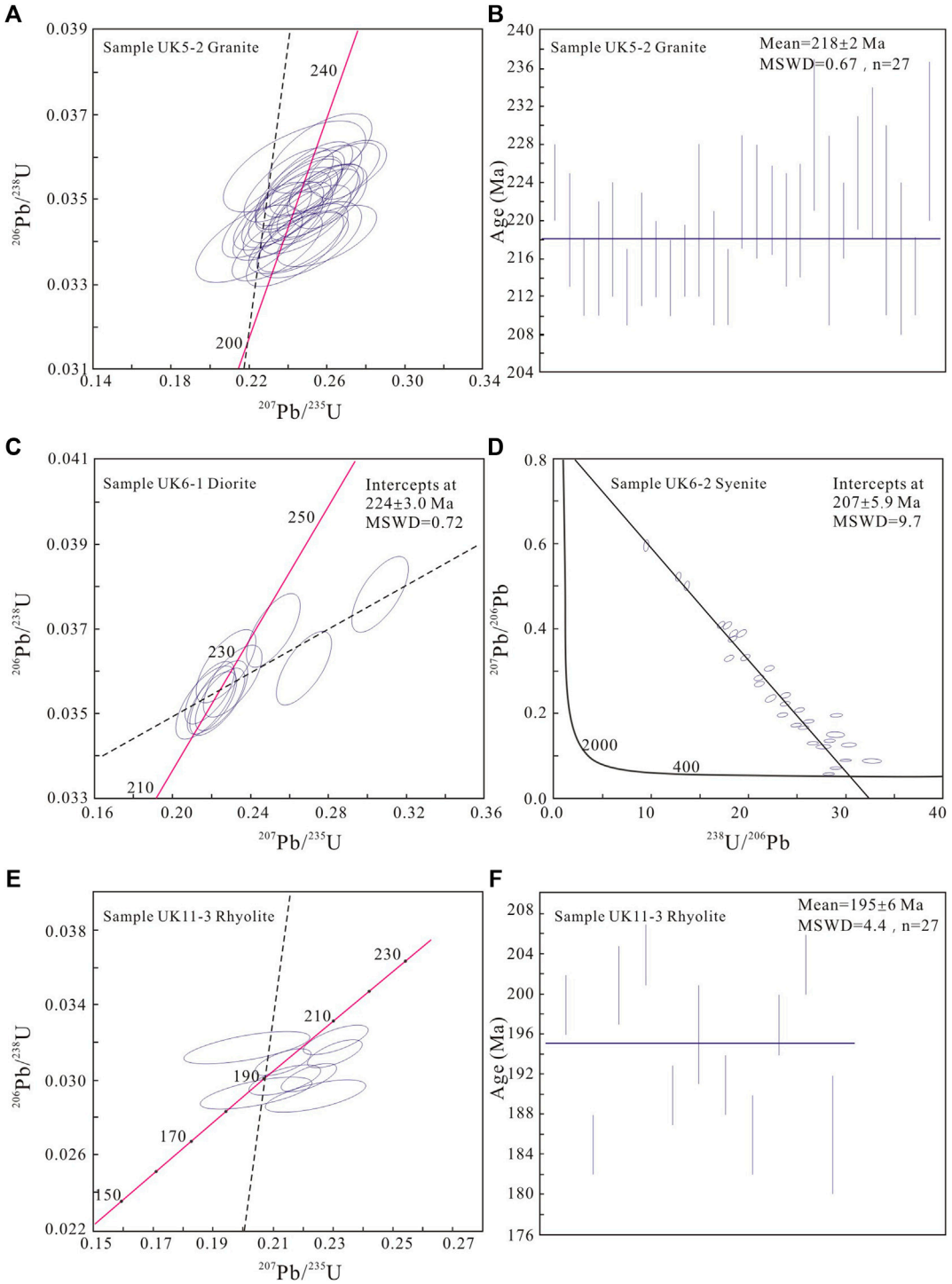

FIGURE 11 | Zircon U-Pb ages of samples. **(A)** Concordia diagram and **(B)** weighted mean age for Sample UK5-2; **(C)** Concordia diagram for Sample UK6-1; **(D)** Concordia diagram for Sample UK6-2; **(E)** Concordia diagram and **(F)** weighted mean age for Sample UK11-3.

usually less than 50 m (Zhao et al., 2020). Similarly, in the Bongor basin (Chad), the thickness of the weathered crust could reach up to hundreds of meters with excellent porosity and permeability, and they are also the product of granitic basement weathering (Dou et al., 2015; 2018; Dou et al., 2018).

In addition, these intrusive rocks were formed as early as in the Early Mesozoic. After that, they experienced regional uplifting, mechanical breaking, physical weathering, and leaching for as long as 65 Ma – 95 Ma during and after the basin formation. This long-time duration of weathering and leaching would

TABLE 2 | Summary of LA-ICP-MS U-Pb zircon ages of all samples.

Sample	Sample ID	Lithology	Age	Stage
1	UK5-2	porphyritic alkali feldspar granite	218 ± 2 Ma	Norian of Triassic
2	UK6-1	fine grained k-feldspar quartz diorite	225 ± 3 Ma	
3	UK6-2	fine-grained quartz syenite	207 ± 5 Ma	Rhaetian of Triassic
4	UK11-3	rhyolite (creolite)	195 ± 6 Ma	Sinemurian of Jurassic
5	UK7-1	medium-coarse syenite	224 ± 2 Ma	Norian of Triassic

TABLE 3 | Magmatic events and geochronology in the basins across the CARS (After Dou et al., 2018).

Basin	Well	Depth/m	Occurrence and location	K-Ar Age/Ma	Geological chronology
Bongor	Ronier-1	1895–1900	Intrusive rock in lower Cretaceous	65.6 ± 2.4	Paleogene
		1950–1955	Intrusive rock in lower Cretaceous	65.3 ± 3.1	Paleogene
		1980–1985	Intrusive rock in lower Cretaceous	59.6 ± 2.1	Paleogene
Termit	Acacia-1	1,490–1,495	Intrusive rock in upper Cretaceous	63.1 ± 2.2	Paleogene
		1,550–1,555	Intrusive rock in upper Cretaceous	62.8 ± 1.8	Paleogene
Doba	Nere-1	940–945	Intrusive rock in upper Cretaceous	79.0 ± 2.3	Later Cretaceous
		1,625–1,630	Intrusive rock in lower Cretaceous	93.5 ± 2.9	Later Cretaceous
	Figuier-1	50–60	Intrusive rock in upper Cretaceous/partly exposed basement	95.0 ± 2.0	Later Cretaceous
		1,680–1,685	Intrusive rock in lower Cretaceous	88.4 ± 2.5	Later Cretaceous

significantly improve their porous and permeable properties and form weathering-leaching zone or fissures-fracture zone of considerable scale and thickness. The exploration practice in the Bongor basin (Chad) revealed that the weathered crust in high buried hills is much thicker than that in low buried hills. This is mainly because the weathering time of high buried hills is longer than that of low buried hills before they were buried, indicating the impact of weathering time on basement reservoir development (Dou et al., 2018).

Finally, the outcrops are adjacent to the CARS, with strong tectonic activities and frequent changes in the tectonic stress regime, which provide external conditions for the formation of fractures and the improvement of reservoir properties (Genik, 1992; Fairhead et al., 2013). The geological field investigations found multi-stage fractures in these outcrops. Meanwhile, millimeter-sized fractures can also be seen in thin sections (Zhao et al., 2020).

Further Research on the Mesozoic Intrusions

Although the Mesozoic intrusions are first discovered and reported in this study, we do not know their regional distribution due to the limited study area compared to the Muglad Basin. Based on our field investigation and laboratory analysis, we intend to believe that these intrusive bodies are sills exposed at these outcrops. They may come from the same magma chamber in deep layer because they all share similar mineral assemblages, ages, and chemical compositions. It is anticipated that these intrusions may be developed in a much larger area, and more and more discoveries will be made in the future. To clarify their types and scales, additional geological surveys and geophysical work should be conducted in the future. Then their representativeness should be further demonstrated across the basin.

Besides, magmatism and its implication for tectonic evolution would be one major part of the next-stage research. Because magmatism is probably related to regional rifting. The volcanic activities in Chad basins were reported as the products of the intraplate extensional stress regime, corresponding to the tectonic setting of the whole West and the Central during the Cretaceous (Lu et al., 2009). A comprehensive study of these topics will help understand the scientific significance of this episode of magmatism and shed light on future regional geological surveys and oil and gas exploration.

CONCLUSIONS

The Late Triassic-Early Jurassic rocks in the Muglad Basin are mainly intermediate-acid intrusive rocks, including granite, syenite, diorite, and monzonite, with principal minerals of alkali feldspar, plagioclase, quartz, and minor hornblende, biotite, and magnetite. The oscillatory zoning in CL images, Th/U ratios, and REE patterns of zircons from these intrusions indicate their magmatic origin. These intrusions have zircon U-Pb ages ranging from 195.0 ± 6 to 225.0 ± 3 Ma.

For the first time, the Late Triassic-Early Jurassic intrusive rocks were identified in the CARS region, indicating that the old basement was subjected to younger magmatic intrusion. Therefore, the Muglad Basin consists of at least two major generations of basement rocks: Precambrian rocks and Early Mesozoic intrusions, and thus the basement in the CARS is unlikely a “uniform craton” as traditionally considered.

Together with the Precambrian basement, the Early Mesozoic igneous rocks experienced at least 65–95 Ma of weathering and fracturing during the formation and evolution of the Muglad basin, which may have formed an unconventional reservoir. As a new target for hydrocarbon exploration, the potential of the

basement in the Muglad Basin and the whole CARS is probably underestimated.

DATA AVAILABILITY STATEMENT

The original datasets presented in the study are included in the article/**Supplementary Material**, further inquiries can be directed to the corresponding author.

AUTHOR CONTRIBUTIONS

JZ, conducted the field trip and collected the samples for laboratory tests and analysis. LR-D, fully in charge of this comprehensive research project, providing academic guidance and technical supervision.

FUNDING

The field work was financially supported by Petro-Energy company, CNPC. The research was funded by the China National Petroleum Corporation (CNPC)/2019D-4306 and the Major State Basic Research Development Program of China (2016ZX05029).

ACKNOWLEDGMENTS

The authors thank the Petro-Energy Company, CNPC, OEPA, and Sudapet for their supporting, guidance, and supervision. The authors thank Petro-Energy for permitting the use and publication of the data in this research. The authors are also grateful to the specialists in the State Key Laboratory of Continental Dynamics at Northwest University, China, for providing the laboratory test. We also acknowledge the editor and the reviewers of this manuscript for their constructive comments and suggestions that have greatly improved this manuscript.

SUPPLEMENTARY MATERIAL

The Supplementary Material for this article can be found online at: https://www.frontiersin.org/articles/10.3389/feart.2022.853082/full#supplementary-material

REFERENCES

Awad, M. Z. (2015). *Petroleum Geology and Resource of Sudan*. Berlin: Geozon Science Dedia UG, 427.

Binks, R. M., and Fairhead, J. D. (1992). A plate tectonic setting for the Mesozoic rifts of Western and Central Africa, in P. A. Ziegler, ed., Geodynamics of rifting, volume II. Case history studies on rifts, North and South America: Tectonophysics: Amsterdam, Elsevier. 213, 141–151. doi:10.1016/0040-1951(92)90255-5

Coulon, C., Vidal, P., Dupuy, C., Baudin, P., Popoff, M., Maluski, H., et al. (1996). The Mesozoic to Early Cenozoic Magmatism of the Benue Trough (Nigeria); Geochemical Evidence for the Involvement of St Helena Plume. *J. Petrol.* 37 (6), 1364–1358. doi:10.1093/petrology/37.6.1341

Dou, L. R., Wei, X. D., Wang, J. C., Li, J. L., Wang, R. C., and Zhang, S. H. (2015). Characteristics of Granitic Basement Reservoir in Bongor Basin (In Chinese with English Abstract). *Acta Petrolei Sinica* 36 (8), 898–903. doi:10.7623/syxb201508001

Dou, L. R., Xiao, K. Y., and Wang, J. C. (2018). *Petroleum Geology and Exploration Practice in Intensive Inversion Rift basin (In Chinese)*. Beijing, China: Petroleum Industry Press.

Dou, L. R., Wang, J. D., Wang, R., Wei, X., and Shrivastava, C. (2018). Precambrian Basement Reservoirs: Case Study from the Northern Bongor Basin, the Republic of Chad. *AAPG Bull.* 102 (9), 1803–1824. doi:10.1306/02061817090

Fairhead, J. D., Green, C. M., Masterton, S. M., and Guiraud, R. (2013). The Role that Plate Tectonics, Inferred Stress Changes and Stratigraphic Unconformities Have on the Evolution of the West and Central African Rift System and the Atlantic continental Margins. *Tectonophysics* 594, 118–127. doi:10.1016/j.tecto.2013.03.021

Fairhead, J. D. (1988b). "Late Mesozoic Rifting in Africa," in *Triassic-Jurassic Rifting, continental Breakup and the Origin of the Atlantic Ocean and Passive Margins*. Editor W. Manspeizer (New York: Elsevier), 998. doi:10.1016/b978-0-444-42903-2.50038-5

Fairhead, J. D. (1988a). Mesozoic Plate Tectonic Reconstructions of the central South Atlantic Ocean: The Role of the West and Central African Rift System. *Tectonophysics* 155, 181–191. doi:10.1016/0040-1951(88)90265-x

Fairhead, J. D. (1992). The West and Central African Rift Systems: Foreword. *Tectonophysics* 213 (1-2), 139–140. doi:10.1016/b978-0-444-89912-5.50033-8

Genik, G. J. (1993). Petroleum Geology of Cretaceous-Tertairy Rift Basins in Niger, Chad and the Central African Republic [J]. *AAPG Bull.* 77 (8), 1405–1434. doi:10.1306/bdff8eac-1718-11d7-8645000102c1865d

Genik, G. J. (1992). Regional Framework, Structural and Petroleum Aspects of Rift Basins in Niger, Chad and the Central African Republic (C.A.R.). *Tectonophysics* 213 (1/2), 169–185. doi:10.1016/b978-0-444-89912-5.50036-3

GRAS (2005). *Geological Map of the Sudan, Scale 1*. Sudan: Ministry of Energy & Mines, Geological & Mineral Resources Department, Khartoum, 20000000. [M].

Guiraud, R., Binks, R. M., Fairhead, J. D., and Wilson, M. (1992). Chronology and Geodynamic Setting of Cretaceous-Cenozoic Rifting in West and Central Africa. *Tectonophysics* 213, 227–234. doi:10.1016/0040-1951(92)90260-d

Guiraud, R., and Maurin, J.-C. (1992). Early Cretaceous Rifts of Western and Central Africa: an Overview. *Tectonophysics* 213 (1-2), 153–168. doi:10.1016/b978-0-444-89912-5.50035-1

Hoskin, P. W. O., and Schaltegger, U. (2003). 2. The Composition of Zircon and Igneous and Metamorphic Petrogenesis. *Rev. mineralogy Geochem.* 53 (1), 27–62. doi:10.1515/9781501509322-005

Hu, J. Y., Tong, X. G., and Xu, S. B. (1981). Regional Distribution of Buried-hill Reservoirs in Bohai Bay Basin, China (In Chinese with English Abstract). *Pet. exploration Dev.* 5, 1–9.

Janssen, M. E., Stephenson, R. A., and Cloethingh, S. (1995). Temporal and Spatial Correlations between Changes in Plate Motions and the Evolution of Rifted Basins in Africa. *Geol. Soc. Am. Bull.* 107 (11), 1217–1322. doi:10.1130/0016-7606(1995)107<1317:tascbc>2.3.co;2

Kamdem, J. B., Kraml, M., Keller, J., and Henjes-Kunst, F. (2002). Cameroon Line Magmatism: Conventional K/Ar and Single-crystal Laser Ages of Rocks and Minerals from the Hossere Nigo Anorogenic Complex, Cameroon. *J. Afr. Earth Sci.* 35, 99–105. doi:10.1016/s0899-5362(02)00002-7

Li, W., Dou, L. R., Wen, Z. G., Zhang, G. Y., Cheng, D. S., Du, Y. B., et al. (2017). Buried-hill Hydrocarbon Genesis and Accumulation Process in Bongor Basin, Chad (In Chinese with English Abstract). *Acta Petrolei Sinica* 38 (11), 1253–1262. doi:10.7623/syxb201711004

Lu, Y., Liu, J., Lirong, D., Guo, Z., Xiao, K., Hu, Y., et al. (2009). K-ar and 39 Ar-40 Ar Geochronology of Basalts from the Chad Basin, Africa and its Geodynamics Setting (In Chinese with English Abstract). *Acta Geologica Sinica* 83 (8), 1125–1133.

Maluski, H., Coulon, C., Popoff, M., and Baudin, P. (1995). 40Ar/39Ar Chronology, Petrology and Geodynamic Setting of Mesozoic to Early Cenozoic Magmatism from the Benue Trough, Nigeria. *J. Geol. Soc.* 152, 311–326. London. doi:10.1144/gsjgs.152.2.0311

McHargue, T. R., Heidrick, T. L., and Livingston, J. E. (1992). Tectonostratigraphic Development of the Interior Sudan Rifts, Central Africa. *Cent. Africa: Tectonophysics* 213 (1–2), 187–202. doi:10.1016/b978-0-444-89912-5.50037-5

Penaye, J., Kröner, A., Toteu, S. F., Van Schmus, W. R., and Doumnang, J.-C. (2006). Evolution of the Mayo Kebbi Region as Revealed by Zircon Dating: An Early (Ca. 740Ma) Pan-African Magmatic Arc in Southwestern Chad. *J. Afr. Earth Sci.* 44, 530–542. doi:10.1016/j.jafrearsci.2005.11.018

Schandelmeier, H., and Pudlo, D. (1990). The Central African Fault Zone (CAFZ) in Sudan-a Possible continental Transform Fault. *Berl Geowiss Abh A* 120 (1), 31–44.

Schull, T. J. (1988). Rift Basins of interior Sudan: Petroleum Exploration and Discovery. *AAPG Bull.* 72 (10), 1128–1142. doi:10.1306/703c9965-1707-11d7-8645000102c1865d

Tong, X.-G., Lirong, D., Tian, Z.-J., Pan, X.-H., and Zhu, X.-D. (2004). Geological Mode and Hydrocarbon Accumulating Mode in Muglad Passive Rift basin, Sudan (In Chinese with English Abstract). *Acta Petrolei Sinica* 25 (1), 19–24.

Vail, J. R. (1972). Pre-Nubian Tectonic Trends in Northeastern Sudan. *J. Geol. Soc.* 128 (1), 21–31. doi:10.1144/gsjgs.128.1.0021

Wilson, M., Guiraud, R., and Guiraud, R. (1992). Magmatism and Rifting in Western and Central Africa, from Late Jurassic to Recent Times. *Tectonophysics* 213 (1-2), 203–225. doi:10.1016/b978-0-444-89912-5.50038-7

Wu, Y. B., and Zheng, Y. F. (2004). Mineralogy of Zircon and its Constraints on the Interpretation of U-Pb Age (In Chinese with English Abstract). *China Acad. J.* 49 (16), 1589–1604. doi:10.1007/bf03184122

Yassin, M. A., Hariri, M. M., Abdullatif, O. M., Korvin, G., and Makkawi, M. (2017). Evolution History of Transtensional Pull-Apart, Oblique Rift basin and its Implication on Hydrocarbon Exploration: A Case Study from Sufyan Sub-basin, Muglad Basin, Sudan. *Mar. Pet. Geology.* 79, 282–299. doi:10.1016/j.marpetgeo.2016.10.016

Zhao, J., Zhang, G., Liu, A., Ke, W., Shi, Y., Zou, Q., et al. (2020). Development Characteristics and Exploration Significance of Basement Reservoirs in Block-6 of the Muglad Basin, Sudan (In Chinese with English Abstract). *China Pet. exploration* 25 (4), 133–142. doi:10.3969/j.issn.1672-7703.2020.04.014

Conflict of Interest: The authors JZ, LD were employed by Research Institute of Petroleum Exploration and Development (RIPED), PetroChina and China National Oil and Gas Exploration and Development Company Ltd.(CNODC), CNPC.

The authors declare that the research was conducted in the absence of any commercial or financial relationships that could be construed as a potential conflict of interest.

frontiers | Frontiers in Earth Science

ORIGINAL RESEARCH
published: 12 May 2022
doi: 10.3389/feart.2022.863730

Application of GPR System With Convolutional Neural Network Algorithm Based on Attention Mechanism to Oil Pipeline Leakage Detection

Jiadai Li[1†], Ding Yang[1†], Cheng Guo[1], Chenggao Ji[2], Yangchao Jin[1], Haijiao Sun[3] and Qing Zhao[1]*

[1]School of Resources and Environment, University of Electronic Science and Technology of China, Chengdu, China, [2]CNPC Logging Company Limited Tianjin Branch, Tianjin, China, [3]Institute of Petroleum Engineering Technology, SINOPEC Northwest Company, Urumqi, China

High-efficiency and high-quality detection of oil pipeline will significantly reduce environmental pollution and economic loss, so an unconventional oil pipeline anomaly detection convolutional neural network (CNN) algorithm based on attention mechanism is proposed in this article. By taking the simulated ground-penetrating radar (GPR) data as prior knowledge, the structure of the convolutional neural network based on the attention mechanism is constructed, and finally, the location and working condition of the underground oil pipeline are recognized in the simulation data and measured data. The simulation results show that after using the new optimized convolutional neural network, the accuracy rates of the leakage discrimination from horizontal data acquired along the oil pipeline and the classification of the target from longitudinal data acquired perpendicular to the oil pipeline are 94.5% and 84.6%, respectively. Compared with the original convolutional neural network without an attention mechanism, the accuracy rates of the leakage discrimination and the classification of the target are improved by 6.2% and 7.8%, respectively. We further train measured data with an optimized convolutional neural network, results show that compared with a conventional network, the new network can increase the corresponding accuracy rates of the leakage discrimination and the targets classification by 5.4% and 6.9%, reaching 92.3% and 84.4%, respectively. According to our study, the ground-penetrating radar oil pipeline recognition algorithm based on an attention mechanism can well accomplish the identification of underground oil pipelines.

Keywords: unconventional detection, convolutional neural network, ground-penetrating radar, oil pipeline leakage, attention mechanism

OPEN ACCESS

Edited by:
Jizhou Tang,
Tongji University, China

Reviewed by:
Anyong Qing,
Southwest Jiaotong University, China
Xingqiu Yuan,
Argonne National Laboratory (DOE), United States

***Correspondence:**
Cheng Guo
guocheng@uestc.edu.cn

†These authors share first authorship

Specialty section:
This article was submitted to Economic Geology, a section of the journal Frontiers in Earth Science

Received: *27 January 2022*
Accepted: *06 April 2022*
Published: *12 May 2022*

Citation:
Li J, Yang D, Guo C, Ji C, Jin Y, Sun H and Zhao Q (2022) Application of GPR System With Convolutional Neural Network Algorithm Based on Attention Mechanism to Oil Pipeline Leakage Detection. Front. Earth Sci. 10:863730. doi: 10.3389/feart.2022.863730

INTRODUCTION

The rapid development of the petroleum industry makes the research on the safety of oil storage and transportation meaningful (Hu et al., 2021). The oil pipeline has become an important choice for oil transportation because of its high safety, high speed, and reasonable cost (Chen et al., 2018). Under the influence of external factors, the oil pipeline running for a long time is prone to leakage problems.

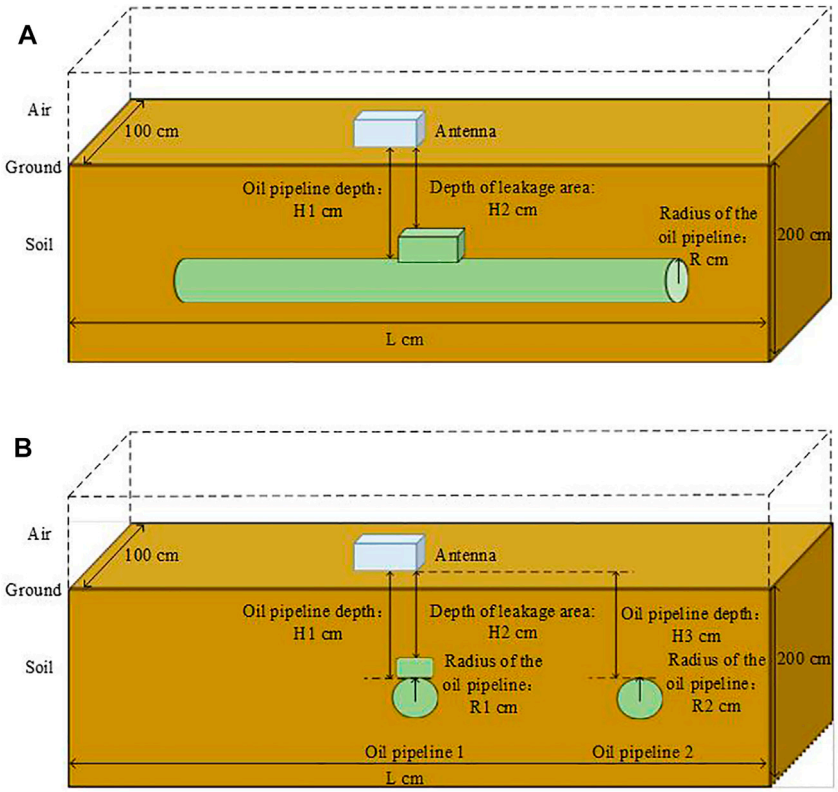

FIGURE 1 | Experiment configuration when obtaining oil pipeline B-scan data by GPR. **(A)** Acquisition model of horizontal B-scan data along oil pipeline; **(B)** acquisition model of longitudinal B-scan data perpendicular to the oil pipeline.

After the oil pipeline leaks, it will not only waste a lot of resources and cause economic loss, but also seriously pollute the environment and affect human life. Efficient and high-quality detection of oil pipelines will be able to monitor leakage in time and effectively reduce resource waste and environmental pollution (Wang et al., 2014). Therefore, an unconventional oil pipeline anomaly detection algorithm based on the attention mechanism is proposed.

Up to now, there are many detection methods for oil pipeline leakage. For example, the negative pressure wave method, ultrasonic detection method, optical fiber detection method, etc. Negative pressure wave method is safe and simple. It also has a wide detection range and fast response. However, this method is difficult to successfully detect small and slow leakage (Liang et al., 2010). The ultrasonic detection method is complex and needs to fill the coupling agent between the probe and the pipe wall (Yang et al., 2021). The optical fiber detection method has good security and high sensitivity, but it needs to add appropriate isolation materials and has a high cost (Zhou et al., 2019; Zhao et al., 2021). Instead, the ground-penetrating radar(GPR) has the characteristics of being nondestructive, high efficiency, having high imaging resolution, and penetrability (Cao et al., 1996). It is widely used in road and bridge detection, building quality analysis as well as underground target detection and classification (Hinton and Salakhutdinov, 2006; Vargas et al., 2017). After comprehensive consideration, the unconventional method of ground-penetrating radar is proposed to detect the state of the underground oil pipeline.

Interpretation of ground-penetrating radar (GPR) section data highly depends on the subjective judgment of experts, which takes a long time and has the risk of misjudgment (Kunihiko and Sei, 1982; Lu and Zhang, 2016; Wanjun et al., 2016). Therefore, it is of great significance to explore an efficient automatic underground target recognition algorithm. Several research studies have been carried out to realize the automatic recognition of GPR section features (Jia et al., 2007; Liu et al., 2017). The most classic image recognition algorithm in GPR is Hough transform, mainly used to identify hyperbola in GPR images (Windsor et al., 2013; Li et al., 2016). However, due to the diversity of detected targets, the corresponding signals of targets in GPR images are not limited to hyperbola but complex and diverse. Dictionary learning method and template matching method are also commonly used GPR image recognition algorithms (Sagnard and Tarel, 2016; Terrasse et al., 2016). But those similar approaches rely heavily on dictionary models and templates, requiring a lot of parameter configurations.

With the gradual maturity of deep learning, it has been widely used in exploration techniques in recent years, such as fracturing design optimization, sweet spot detection, production forecasting, GPR data interpretation, etc, (Wang and Chen, 2019; Tang et al., 2020; Xiong et al., 2020). Lei W et al. (2019) used the R-CNN network to identify hyperbolic features in GPR B-scan images. It can

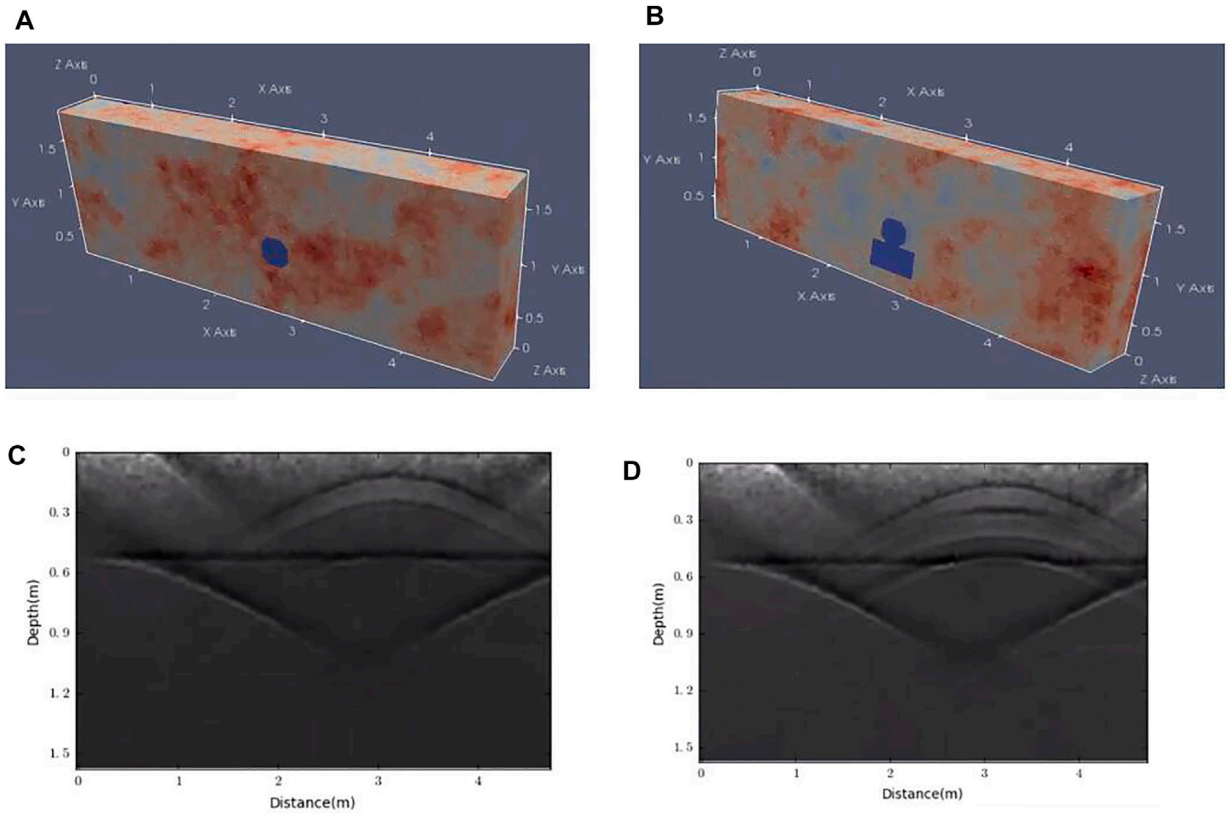

FIGURE 2 | 3D and B-scan images of oil pipeline simulation model. **(A)** 3D image of normal operation; **(B)** 3D image of leakage; **(C)** B-scan image under normal operation; **(D)** B-scan under leaking condition.

determine whether there are buried objects in the detected underground space. Kang et al. (2020) constructed 3D radar data of underground targets, and then put it in the deep convolutional neural network for training. The accuracy of cavity and pipeline classification was 92% and 98%, and the false alarm rate was 8% and 2%, respectively. Lei et al. (2020) combined the convolutional neural network and the long-short-term memory artificial neural network to extract the hyperbola in the B-scan image of the ground-penetrating radar. However, the existing research mainly focuses on the data processing of the whole B-scan image. Classification output often stays in the recognition of the whole image, and its main research objectives are the existence of underground targets and the recognition of target materials. Further exploration of the geometric features, size, condition, and position of the target is still insufficient. Therefore, a novel convolutional neural network based on the attention mechanism is proposed for further feature recognition of the underground oil pipelines.

Numerical Simulation Mechanism and Realization of Underground Oil Pipeline

A GPR oil pipeline recognition system based on the attention mechanism requires a lot of training and test data, which need to be real data or close to them. The data obtained by electromagnetic simulation can be generated in batches with simple locations. Moreover, the target location is clear from the data, and the actual situation can be accurately represented. Therefore, a large amount of electromagnetic simulation data is initially obtained in this study to provide data support for neural network construction. Furthermore, these simulation data help a lot for the acquisition, processing, and network structure adjustment of measured data.

To achieve a reasonable numerical simulation of underground pipeline objects in an interested environment, a direct relationship between soil physical properties and the overall dielectric response of soil components (soil particles, water, and air) is established using dielectric mixing models. According to a semi-empirical model proposed by Peplinski et al. (1995), the soil simulation model is constructed to simulate the electromagnetic properties of real soil. In this model, the soil is composed of clay, silt, and sand. The diameter of clay, silt and sand is below 0.002, 0.002–0.02 mm, and 0.02–2 mm, respectively. Different soil types can be constructed by changing the proportions of different components. Soil water content also has a certain influence on its electromagnetic properties. Therefore, the complex permittivity of soil $\varepsilon(\omega)$ can be expressed as **Eq. 1**:

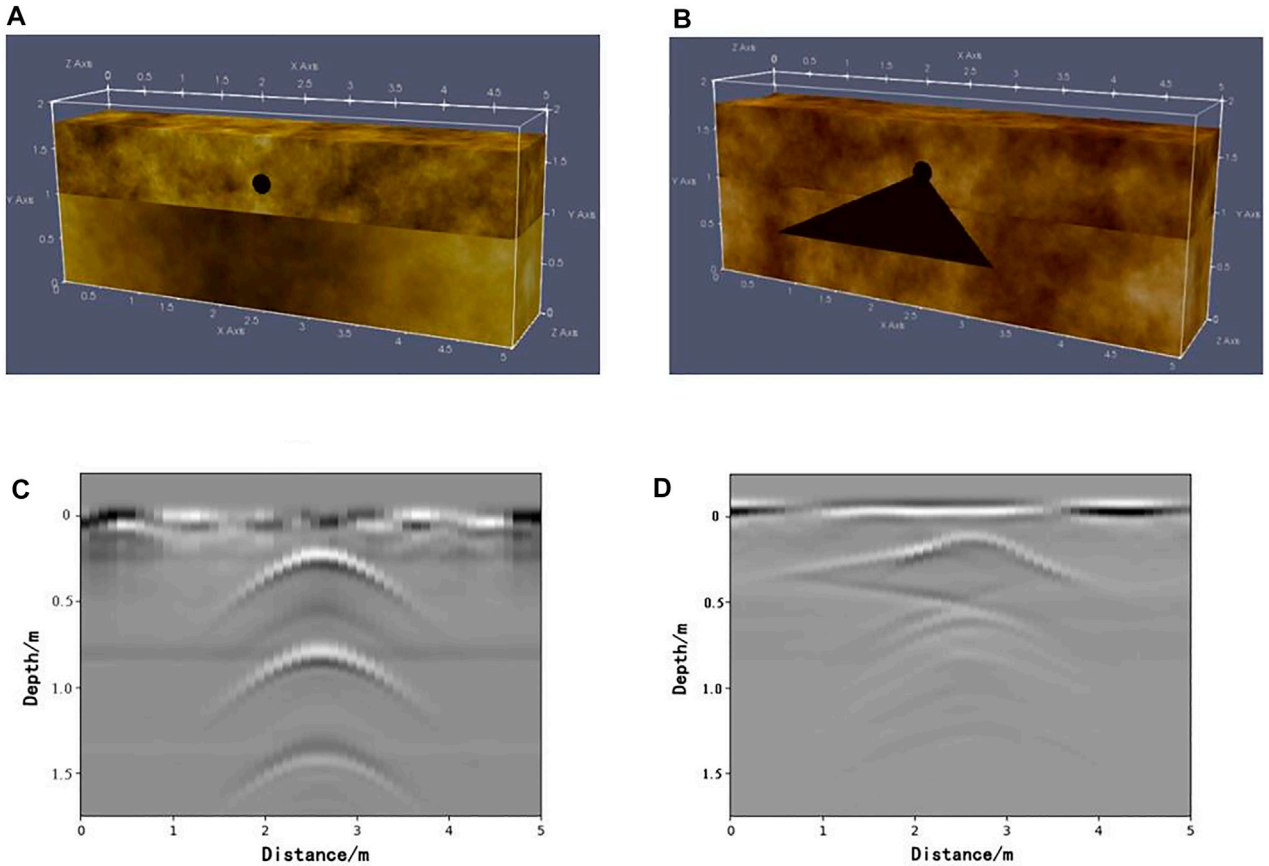

FIGURE 3 | 3D and B-scan images of water pipeline simulation model. **(A)** 3D image of normal operation; **(B)** 3D image of leakage; **(C)** B-scan image under normal operation; **(D)** B-scan under leaking condition.

$$\varepsilon(\omega) = \varepsilon'(\omega) - j\varepsilon''(\omega) \tag{1}$$

$$\varepsilon'(\omega) = 1.15\left[1 + \frac{\rho_b}{\rho_s}\left(\varepsilon_s^{\alpha}\right) + m_v^{\beta'}\varepsilon'^{\alpha}_{fw} - m_v\right]^{1/\alpha} - 0.68 \tag{2}$$

$$\varepsilon''(\omega) = \left[m_v^{\beta''}\varepsilon''^{\alpha}_{fw}\right] \tag{3}$$

In the aforementioned formula, $\varepsilon'(\omega)$ and $\varepsilon''(\omega)$ are the real and imaginary parts of the complex dielectric constant $\varepsilon(\omega)$, respectively. ρ_b and ρ_s are the total density of soil and the density of sandy soil composition (unit: g/cm3), respectively. a is an empirical constant with a value of 0.65. β' and β'' are the constants related to soil composition, and their expressions are:

$$\beta' = 1.2748 - 0.519S - 0.152C \tag{4}$$

$$\beta'' = 1.33797 - 0.603S - 0.166C \tag{5}$$

where S and C are the proportions of sand and clay, respectively ($0 < S < 1$, $0 < C < 1$).

In **Eqs 2**, **3**, ε'_{fw} and ε''_{fw}, respectively, represent the real and imaginary parts of free water in the soil, and their expressions are:

$$\varepsilon'_{fw} = \varepsilon_{w\infty} + \frac{\varepsilon_{w0} - \varepsilon_{w\infty}}{1 + \left(2\pi f\tau_w\right)^2} \tag{6}$$

$$\varepsilon''_{fw} = \frac{2\pi f\tau_w\left(\varepsilon_{w0} - \varepsilon_{w\infty}\right)}{1 + \left(2\pi f\tau_w\right)^2} + \frac{\sigma_{eff}}{2\pi\varepsilon_0 f}\frac{\left(\rho_s - \rho_b\right)}{\rho_s m_v} \tag{7}$$

$\varepsilon_{w\infty}$ is the limit of ε''_{fw} at high frequencies. τ_w is the relaxation time constant of free water. ε_{w0} is the static relative permittivity of water, and its value is 80.1. σ_{eff} is the effective conductivity, which is given by the empirical **Eq. 8**:

$$\sigma_{eff} = 0.0467 + 0.2204\rho_b - 0.4111S + 0.6614C \tag{8}$$

Through the aforementioned mechanism, the real soil environment can be simulated and fitted. **Figure 1** shows the experimental configuration when using GPR to obtain B-scan data of the oil pipeline. We set the length of the entire space as L, ranging from 500 to 2500 cm, the height to 200 cm, the width to 100 cm, and the diameter of the single grid to 2 cm. Soil consists of variable sand and clay with a density of 2.66 and 2 g/cm^3, respectively. Its water content varied from 0.1% to 1%. The frequency of the antenna is selected from 100 to 600 Mhz. The initial position of the antenna is 20 cm from the left edge of the model, and the distance between transmit and receive antennas is 5 cm. The acquisition of the horizontal B-scan data along the oil pipeline is shown in **Figure 1A**. The radius of the oil pipeline is set

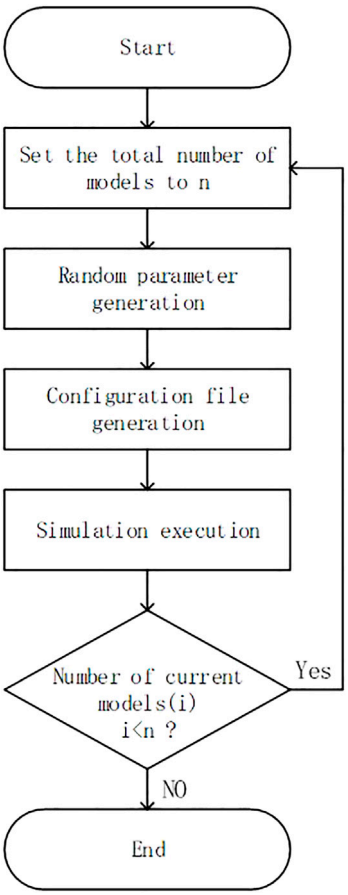

FIGURE 4 | Flow chart of the program generating bulk simulation data.

as R, ranging from 10 to 72 cm. The depth of the oil pipeline is H1 with the range of 0 to (200-2R) cm. When the oil pipeline leaks, the depth of leakage area is depicted as H2, changing from 0 to 200 cm according to the position of the oil pipeline. Similarly, the acquisition of longitudinal B-scan data perpendicular to the oil pipeline is shown in **Figure 1B**. The radius of oil pipeline 1 is R1, varying from 10 to 72 cm. The depth of 1 is H1 with the range of 0 to (200-2R) cm. When leakage occurs, the depth of leakage area is H2, ranging from 0 to 200 cm according to the position of the oil pipeline. The depth of oil pipeline 2 is H3 and the radius is R2, which is consistent with those of oil pipeline 1.

The simulated B-scan data of the oil pipeline are obtained using the experimental setup for the field measurement with GPR. **Figures 2A and B** show the three-dimensional (3D) simulation model of the oil pipeline under the condition of normal operation and leakage, respectively. The pipeline is full of oil with a buried depth of 0.65m, a horizontal coordinate of 2.75 m, and a radius of 0.3 m. The leak area is filled with oil, directly below the oil pipeline. And its length, height, and width are set to 50, 30, and 50 cm, respectively. The soil is composed of 50% sand and 50% clay.

Figures 2C and D show the corresponding simulation results of the two models in **Figures 2A andB**. A great difference exists in the B-scan image when leakage occurs or not. Concretely, the hyperbolas of the pipeline without leakage are more clear and non-intersecting, as shown in **Figure 2C**. Because the leakage area overlaps with the pipeline, a portion of the hyperbola representing leakage will intersect the original hyperbola of the pipeline, as shown in **Figure 2D**. Therefore, the GPR can clearly identify underground targets. However, due to the continuous reflection of electromagnetic waves among the leakage area, the pipeline area, and the stratum surface, the pipeline and leakage can only be clearly characterized at the top of the B-scan image. The hyperbolas superimpose on each other in **Figure 2D** and become too disordered to extract their representations.

Because no appropriate leaking oil pipelines exist, water is selected to replace oil to simulate leakage due to environmental pollution and safety issues. **Figures 3A and B** show 3D simulation model under the condition of normal operation and water leakage, respectively. The water pipeline has a buried depth of 0.4 m, a horizontal coordinate of 2.5 m, and a radius of 0.1 m. The leakage is a mixture of water and soil, with an area of about 0.06 m^2. The leftmost and rightmost horizontal coordinates of the leakage are 2.1 and 2.7 m, respectively. Both models use the stratified soil with a surface part composed of a mixture of sand and silt (70%) as well as clay (30%), and a bottom half composed of a mixture of sand and silt along with clay each accounting for 50%.

Figures 3C and D show the corresponding simulation results of the two models in **Figures 3A and B**. Similar to the B-scan images of oil pipelines, a great difference exists between water pipelines with and without leakage. The multiple disjoint and vertically distributed hyperbolas in **Figure 3C** are caused by the back and forth bounces of electromagnetic waves between the pipeline and the stratum surface. A horizontal line will also be generated at the formation interface due to the reciprocating reflections of electromagnetic waves between the formation interface and the surface. While in **Figure 3D**, the hyperbolas superimposed on each other and the characteristic echo at the formation interface is also not obvious.

In the batch generation of simulation data, parameters of each simulation model, such as soil composition, the shape, size, and working state of the target, and the obtained simulation results should be different. The simulation data generator replaces the random key parameters that need to be adjusted with placeholders and sets the predetermined range of the parameters. The process for producing bulk simulation data are demonstrated in **Figure 4**. Each time the program runs, the first step is to generate a model configuration file. During this procedure, parameters represented by placeholders will first generate and input data of a limited range into the configuration file. After saving the file, the program will realize the corresponding simulation operation.

Detection Model of Underground Oil Pipeline Based on Attention Mechanism

The attention model is divided into soft attention and hard attention. When choosing information, soft attention does not extract just one information from multiple information, but calculates the weighted average of this information and then

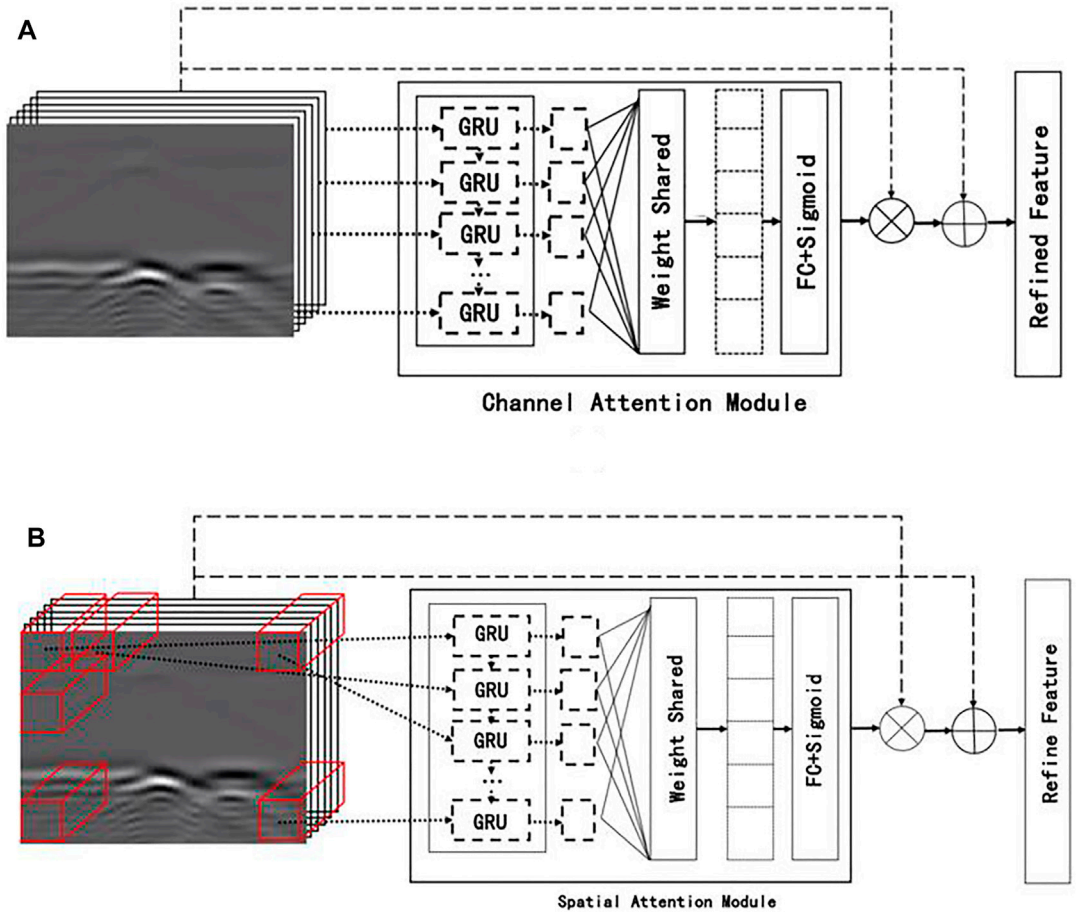

FIGURE 5 | Structure diagram of attentional mechanism model. **(A)** Structure of channel domain attention model; **(B)** structure of spatial attention model.

inputs it into the neural network for calculation. Hard attention is to select a certain piece of multiple information, which can be selected according to the magnitude of the probability. Generally, the soft attention model is used to deal with neural network problems of its differentiable nature. There are three types of attention domain models in soft attention, namely the spatial domain model, the channel domain model, and the mixed domain model of them (Convolutional Block Attention Module, CBAM), which can extract attention in the channel and spatial dimensions (Woo et al., 2018). Compared with the attention mechanism that only focuses on one separate domain, it can achieve better results.

When the input feature is $F \in R^{L\times W\times C}$, and the three-dimensional information of the input feature map is L, W, and C. The final output feature map F'' is obtained after the input feature map F passes through the spatial attention module $M_S \in R^{L\times W\times 1}$ and the channel attention module $M_c \in R^{1\times 1\times C}$.

$$F' = M_c(F) \otimes F \tag{9}$$

$$F'' = M_s(F) \otimes F' \tag{10}$$

Because the input features and refined features are of a consistent size, the original parameters of the neural network remain unchanged after extraction by the CBAM module. The new features extracted by the convolutional neural network contain multiple channels representing different kinds of original ones, which have different effects on the final content identified by a convolutional neural network. While channel domain attention model is to generate the weight of each channel according to its degree of importance, and finally emphasizes attention to key channels as well as reduces attention to non-key ones. The structure of the channel domain attention model is shown in **Figure 5A**.

The channel attention module initially uses the average and maximum pooling operations to aggregate the information of the feature map on each channel, and generates two different channel context descriptors F^c_{mea} and $F^c_{\max}$, as shown in **Eqs 11**, **12**:

$$F^c_{mea} = \frac{1}{L\times W}\sum_{i=1}^{L}\sum_{j=1}^{W} x_c(i,j) \tag{11}$$

$$F^c_{\max} = Max(x_c(i,j)), i \in [1,L], j \in [1,W] \tag{12}$$

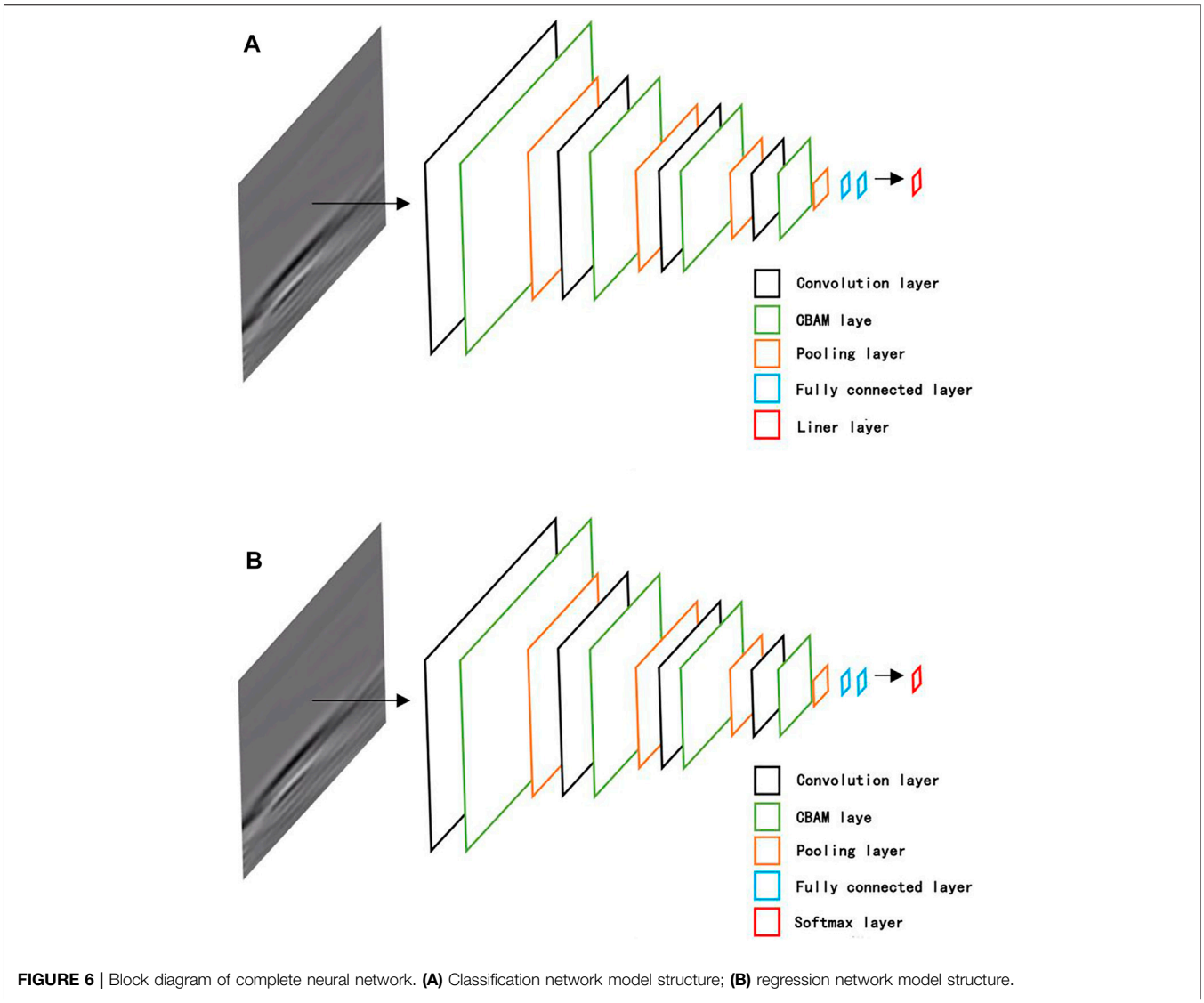

FIGURE 6 | Block diagram of complete neural network. **(A)** Classification network model structure; **(B)** regression network model structure.

TABLE 1 | Parameters of underground target recognition classification network structure.

Layer	Type	Parameter
1	Convolution layer	32 6 × 6 filters; ReLu activated
2	CBAM layer	32 input and output features
3	Convolution layer	64 4 × 4 filters; ReLu activated
4	CBAM layer	64 input and output features
5	Convolution layer	128 4 × 4 filters; ReLu activated
6	CBAM layer	128 input and output features
7	Convolution layer	256 4 × 4 filters; ReLu activated
8	CBAM layer	256 input and output features
9	Fully connected layer	128 neurons; ReLu activated
10	Dropout layer	Dropout rate: 0.5
11	Fully connected layer	64 neurons; ReLu activated
12	Dropout layer	Dropout rate: 0.5
13	Fully connected layer	6 neurons; softmax activated

where $F^c_{\max}$ and F^c_{mea} are the maximum and average pooling features on channel C, respectively. The length and width of the feature map are L and W, respectively. x_c represents channel C.

Then average and maximum pooling features are input into the multilayer perceptron network, respectively. Combining the output values of them, the weight parameters of combined output feature can be obtained. The calculation formula is as follows:

$$\begin{aligned} M_c(F) &= \sigma\left(mlp\left(P_{mea}\ (F)\right) + mlp\left(P_{max}\ (F)\right)\right) \\ &= \sigma\left(w_1\left(w_0\left(F^c_{mea}\right)\right) + w_1\left(w_0\left(F^c_{\max}\right)\right)\right) \end{aligned} \tag{13}$$

where $P_{max}\ (F)$ and $P_{mea}\ (F)$ represent maximum and average pooling operations, respectively. w_0 and w_1 are the weight values of multi-layer perceptron. σ represents the activation function.

There are various interferences when using GPR B-scan imaging, and the image content is complicated. It is

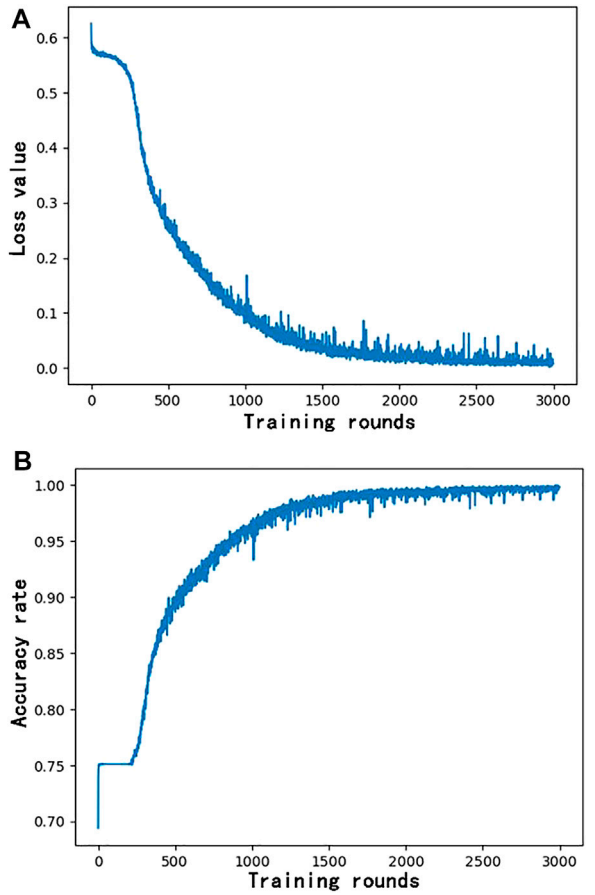

FIGURE 7 | Results of 3,000 training rounds. **(A)** Loss rate function curve; **(B)** accuracy rate curve.

particularly important to focus on and classify the regions with prominent features. Based on the features extracted by the convolutional neural network, the spatial domain attention model further explores the connections between features of different regions. In this way, weights of different regions are generated to highlight critical regions and weaken unimportant ones. The spatial attention module, delineated in **Figure 5B**, mainly focuses on the spatial relations among features and plays as a supplement to channel attention.

After average and maximum pooling of input features, two independent feature maps, $F^s_{mea} \in R^{L\times W\times 1}$ and $F^s_{\max} \in R^{L\times W\times 1}$, are generated.

$$F^s_{mea} = \frac{1}{N}\sum_{c=1}^{N} s_{ij}(c) \tag{14}$$

$$F^s_{\max} = Max\left(s_{ij}(c)\right), c \in [1, N] \tag{15}$$

where N represents the number of feature channels, $s_{ij}(c)$ is the element at coordinates (i, j) on the cth feature map. $F^s_{\max}$ and F^s_{mea} are the maximum and average fusion feature on each channel, respectively. After putting the two merged feature maps into the convolutional layer, we can get the attention weight in spatial dimension. Where σ is the activation function, f is the convolution operation, and $n\times n$ is the size of convolution kernel.

$$\begin{aligned} Ms(F) &= \sigma\left(f^{n\times n}\left(\left[P_{\text{mea}}(F); P_{\max}(F)\right]\right)\right) \\ &= \sigma\left(f^{n\times n}\left(\left[F^{mea}_s; F^{\max}_s\right]\right)\right) \end{aligned} \tag{16}$$

In order to identify the location and working state of an underground oil pipeline, the initial convolutional neural network structure is composed of a convolution layer, pooling layer, and full connection layer. The generalization ability of the network is weak, and the calculated accuracy rates of the horizontal pipeline leakage identification and longitudinal target location are low. In order to solve the problem of weak generalization ability and improve the accuracy rates, dropout technology is introduced. Dropout technology can mitigate overfitting and regularize. The core idea of dropout is to discard some neurons with a certain probability during network training. Then the over-fitting of the network is reduced and the generalization ability of the model is enhanced. In order to further improve the accuracy rates of the horizontal pipeline leakage identification and longitudinal target location, a convolutional attention module CBAM is introduced. The convolutional pooling operation in a convolutional neural network defaults to the same importance of each channel in the feature map. However, the amount of information carried by each channel is different, so it is unreasonable to assign the same importance to each channel.

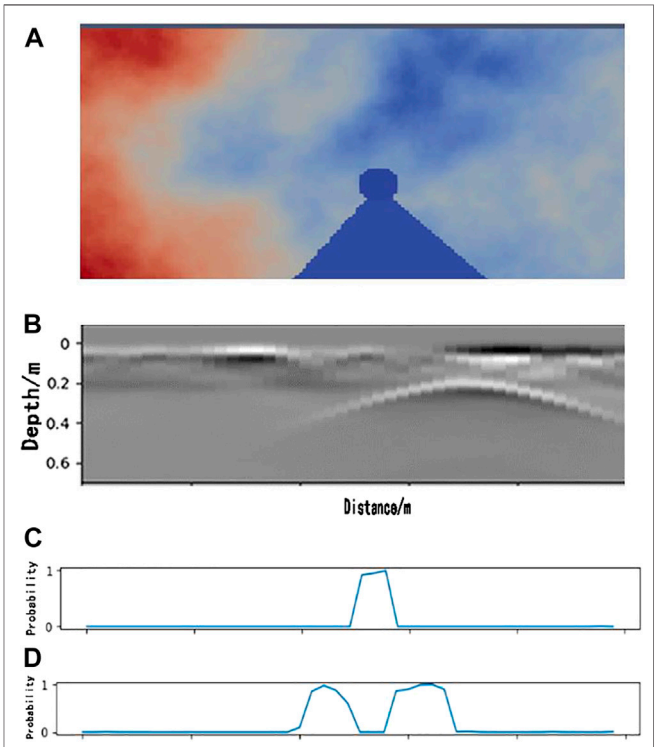

FIGURE 8 | Classification network identification results. **(A)** Pipeline leakage model; **(B)** pipeline leakage B-scan diagram; **(C)** pipeline discrimination probability; **(D)** leak discrimination probability.

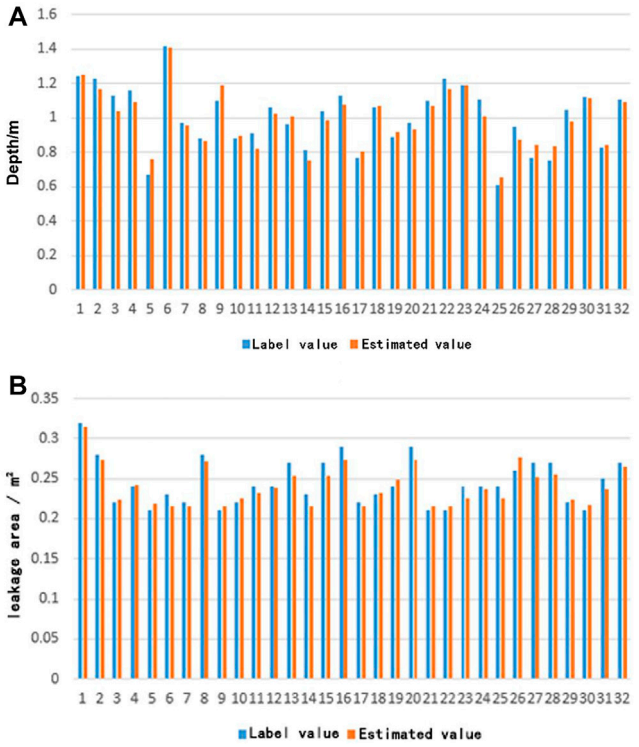

FIGURE 9 | Results of pipeline depth. **(A)** and leakage area; **(B)** identification

The convolutional attention module CBAM, based on the mechanism of the human visual system, will place more attention on important areas and reduce the weight of unimportant factors. Therefore, different feature maps and different regions of feature maps have different degrees of attention. Finally, the accuracy rates of the horizontal pipeline leakage identification and longitudinal target location are further improved.

Finally, in order to better recognize the horizontal position, state, depth, and cross-sectional area of the underground target, two convolutional neural networks based on the attention mechanism are proposed. They are the classification network for target horizontal position and state recognition, and the regression network for target depth and cross-sectional area detection.

Classification Network

The initial classification network and its relevant parameters are shown in **Figure 6A** and **Table 1**, respectively. However, the CBAM layer and dropout operation are not used. The network contains 4 convolutional layers, and the size of the convolution kernel in the first layer is set to 6×6 to modularize corresponding data features with high efficiency. The size of the following convolution kernel decreases with the progressively smaller feature map, which can increase the fitting expression ability of the network. Through these four convolution layers, the network can reduce the parameters and the amount of calculation while retaining the characteristics, and greatly improving the calculation efficiency. After each convolutional network layer, an attention module CBAM layer is added, which does not change the size and quantity of data but increases the weight of the key areas of the image. Add a pooling layer after the CBAM layer is to reduce data size and increase channel number. Then, two full connection layers and one output layer are designed. These three layers help classify the data extracted by the convolutional neural network. The last output layer is proposed to determine whether the output result is no target, pipeline, or pipeline leakage in the case of pipeline leakage detection. The activation function of this layer is softmax, which is suitable for data classification and can enable the network to represent the probability of each attributed type through machine learning. The maximum probability is set as the output target classification to further accomplish the classification and discrimination of the B-scan images.

Regression Network

The initial classification network its relevant parameters are shown in **Figure 6B**, but the CBAM layer and dropout operation are not used. For the prediction of target depth, the output function needs to be adjusted to give the discrete output value. Transformation is made on the basis of a classification network to construct the regression network. The target cross-

FIGURE 10 | Measurements in different directions. **(A)** Horizontal detection line; **(B)** longitudinal detection line.

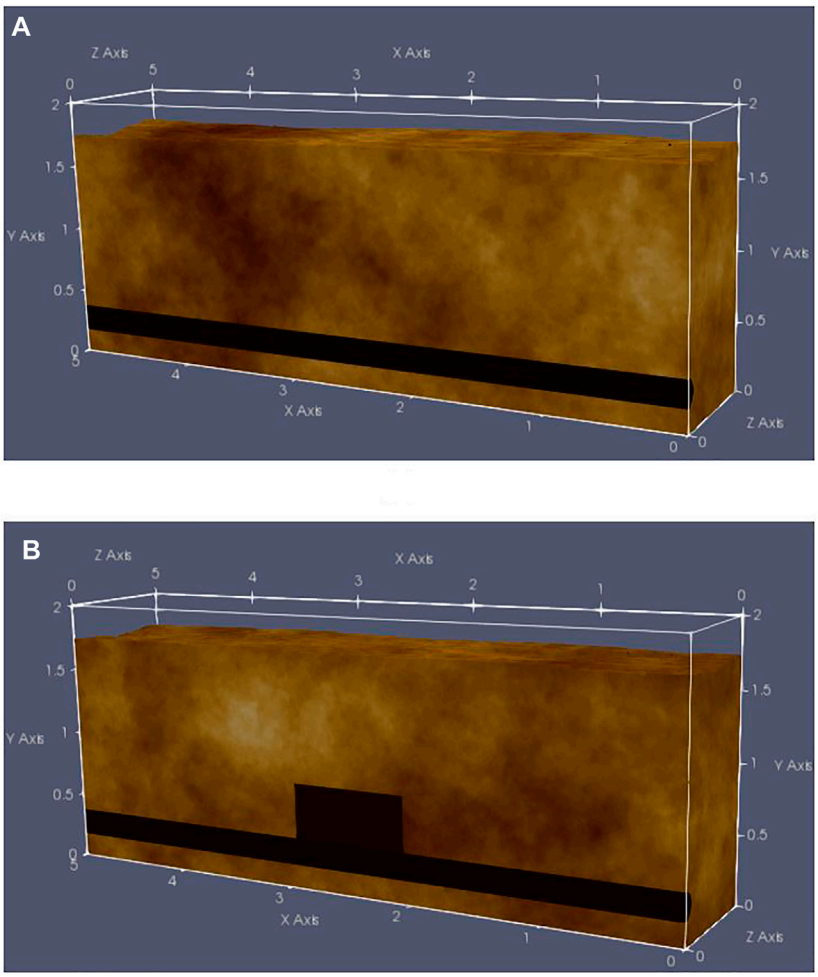

FIGURE 11 | Cross-sectional models of actual oil pipeline detection **(A)** and simulated oil pipeline leakage area **(B)**.

sectional area and depth prediction can be carried out by changing the output layer function from softmax to liner, the output results of which are continuous real numbers. The front part of the regression network structure is the same as that of the classification network, and relevant parameters are adjusted during training to improve the recognition accuracy.

Simulation Results and Analysis

The convolutional neural network based on the attention mechanism is used to train the simulation data at first. GPU parallel acceleration and a GeForce GTX 1080 Ti graphics card are employed during training. When training the network, Adam is selected by the optimizer, where the learning rate is 0.0001, the loss function is "categorical_crossentropy," and the accuracy rate is "keras.metrics_accuracy." The batch size is set as 90, and each training round consequently takes 32 s. As demonstrated in **Figure 7A**, the loss rate function declines rapidly at the initial stage, from 0.65 to 0.1 after 1,000 rounds of learning. After that, it gradually slows down and approaches 0 in oscillation. In **Figure 7B**, the accuracy rate increased rapidly from 0.7 to 0.95 at first, and then it is infinitely close to 1. This is similar to the normal learning process, indicating that our network keeps improving in learning so that the recognition result keeps approaching the given label. The gradually improving recognition ability of the designed network makes it more suitable for the identification of test data.

An identification result of pipeline leakage together with the corresponding model and the B-scan image are displayed in **Figure 8**. Obviously, the network proposed in this study can accurately distinguish pipelines, leakage areas and untargeted areas. Compared with given data labels, the accuracy of simulated training results reaches about 93%, implying that this classification network is well competent for underground oil pipeline classification and recognition. Furthermore, comparing the recognition results of the simulation data with their input labels, the calculated accuracy of the horizontal pipeline leakage identification, and longitudinal target location are 94.5% and 84.6%, respectively. Using the initial convolutional neural network without the attention module for training, the calculated accuracy rates of the horizontal pipeline leakage identification and longitudinal target location is 88.3% and

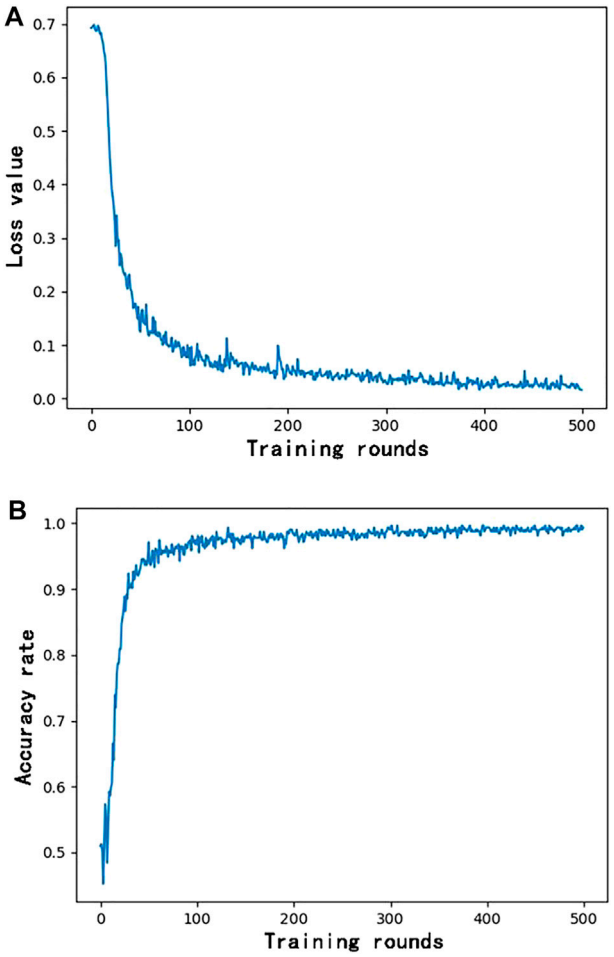

FIGURE 12 | Results after 500 times of training with horizontal test data. **(A)** Loss rate function curve; **(B)** accuracy rate curve.

76.8%, respectively. The optimized network improves the accuracy rates of the horizontal pipeline leakage identification and longitudinal target location by 6.2% and 7.8%, respectively. It can be seen that the optimized networks with attention modules can greatly improve the recognition results.

As for the judgments of depth and leakage area, the designed network can get results with an average accuracy rate of 95.1% (**Figure 9A**) and 96.4% (**Figure 9B**), respectively.

Measured Results and Analysis

In order to verify the applicability of the underground target recognition method based on the attention mechanism to real data, we went to the Tahe Oilfield in Xinjiang to provide measured data support for a neural network. According to the prior knowledge obtained from simulation, the measured parameters of GPR are set as follows. The antenna is 250 Mhz, the time window is 100 ns, the sampling interval is 0.4 ns, and the antenna step is 0.05 m. With the aforementioned parameter settings, the effective detection depth is 3 m and the resolution is 0.2 m.

As shown in **Figure 10**, the experiment was mainly conducted in a desert environment with undulating topography. The soil within the detection depths is composed of gray-white fine sand and silt sand layers with a yellow-gray clay layer. The oil pipeline is buried in the soil to a depth of about 1–2 m. Considering the conditions of the test environment and oil pipeline laying, both longitudinal and horizontal detection lines were adopted. A horizontal line was set to collect relatively comprehensive information along the oil pipeline laying direction. The longitudinal line is perpendicular to the oil pipeline laying direction, which can supplement the detection of abnormal sites and extract the reflection characteristics of an oil pipeline.

The actual detection area is roughly modeled in **Figure 11A**. As for the lack of leaking oil pipeline, simulated leakage points were set up along the oil pipeline line. As the cross-section of the simulating leakage model shown in **Figure 11B**, two 50 × 50 × 60 cm sandpits were excavated directly above the simulated leakage points and filled with water. These sandpits were backfilled and tamped after the natural infiltration of water. GPR was used for longitudinal and horizontal detections before and after simulating leakage. The different characteristics of reflected waves received by radar before and after the change of physical properties of the surrounding medium are analyzed from the obtained data.

The experiment data are grouped according to the horizontal and longitudinal lines and input into the neural network for learning after being associated with their respective label data. This indicates that the network is running properly. Take the loss value function curve and accuracy curve of data from the horizontal line as examples. When training the network, Adam is selected by the optimizer, where the learning rate is 0.0001, the loss function is "categorical_crossentropy," and the accuracy rate is "keras.metrics_accuracy." After 500 rounds of training, namely 500 epochs, the loss value gradually decreases, while the accuracy rate gradually increases and approaches 1, as shown in **Figure 12**. The loss value and accuracy of the longitudinal line are similar to those of the horizontal line, indicating that the network is running properly.

The measured data may output three cases, including oil pipeline, leakage and no target. Results are given in terms of the probability of each type being present at a certain location. In the aforementioned three cases, the case with the highest probability is output as the final recognition result. The discrimination time of artificial intelligence method for single GPR data is about 20 s, which is greatly improved compared with manual interpretation method. Notably, for the case that leakage and oil pipeline exist simultaneously, the output discrimination result of proposed network will be leakage, because the simulated leakage area is located above the oil pipeline.

Selecting a set of oil pipeline leakage identification results from horizontal detection data for further discussion. The cross-section of the experimental area is modeled in **Figure 13A**, and the identification result, as well as the B-scan image, are shown in **Figure 13B**. There are multiple echoes in the B-scan image (**Figure 13B**), which strongly interfere with the results of manual discrimination. Instead, thetraining results of the novel

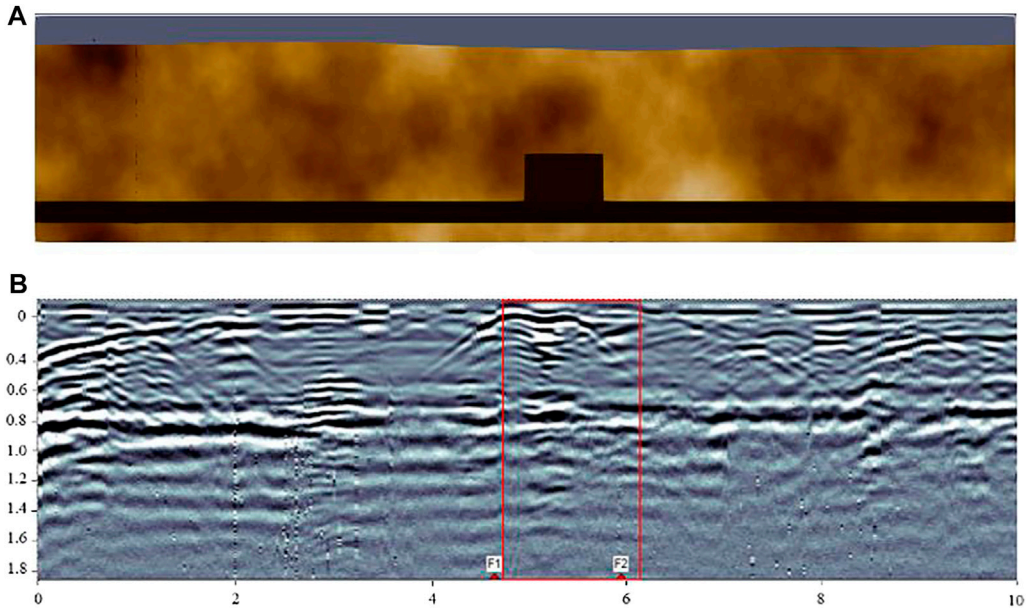

FIGURE 13 | (A) Cross-section of simulated model for horizontal oil pipeline leakage detection. **(B)** Corresponding leakage identification results.

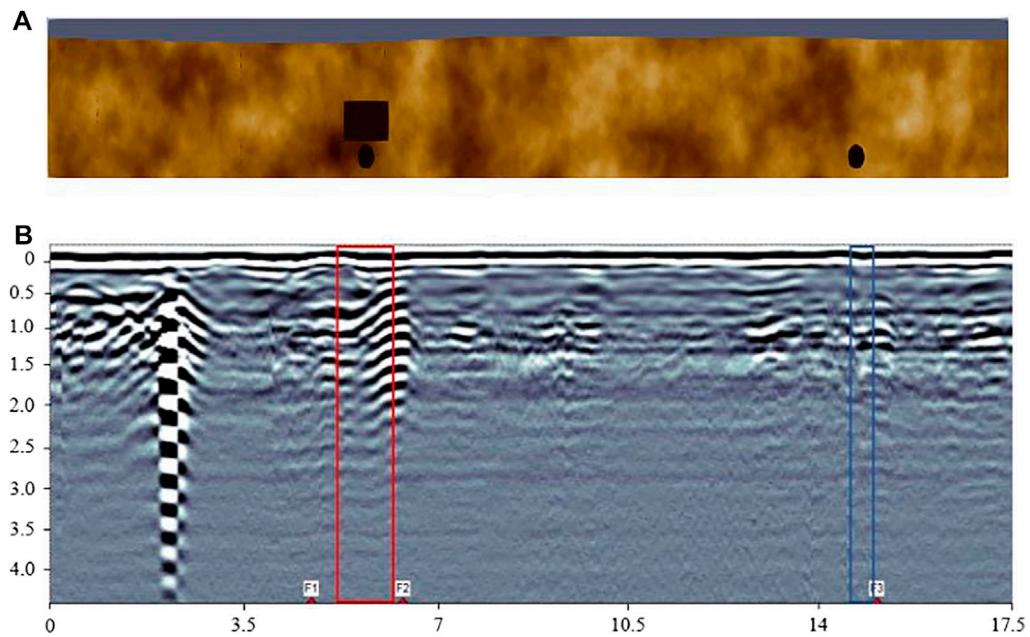

FIGURE 14 | (A) Cross-section of simulated model for longitudinal oil pipeline leakage detection. **(B)** Identification results of simulated leakage and oil pipeline under normal working condition.

network in this study can be perfectly matched with the labeled experimental data. During the detection, marks were made at F1 and F2 to indicate the occurrence of leakage with the abscissa ranging from about 4.67 to 5.94 m. As marked with a red frame in **Figure 13B**, the proposed network gives the classification with the highest probability from 4.74 to 6.14 m, corresponding well to the marked area. This implies that our network can avoid distractions and output the results only representing targets of interest.

Similarly, a set of longitudinal oil pipeline leakage identification results is also chosen for analysis. The cross-section of the simulated experimental model and the result of the B-scan image after network

identification are successively shown in **Figure 14**. The simulated leakage is marked from 5.4 to 6.2 m along X-coordinate, and an oil pipeline is marked at 14.8 m. After network training, the identified leakage section, represented by the red frame in **Figure 14B**, locates at 4.7 and 6.5 m on the horizontal axis, and the identified oil pipeline part, represented by the blue frame in **Figure 14B** , is 14.4–15 m. The output results are in good agreement with the given labels. In addition, there are some interferences at about 2 and 9.4 m in the B-scan image. However, our network does not take these interferences as target signals and the identification results exclude them from the targets of concern.

Comparing the identification results of the test data after network training with their input labels, the calculated accuracy rates of the horizontal oil pipeline leakage data and longitudinal target data are 92.3% and 84.4%, respectively. Using the initial convolutional neural network without the attention module for training, the calculated accuracy rates of the horizontal pipeline leakage identification and longitudinal target location are 86.9% and 77.5%, respectively. The optimized network improves the accuracy rates of the horizontal pipeline leakage identification and longitudinal target location by 5.4% and 6.9%, respectively. The optimized networks with the attention module help improve the recognition results. To sum up, the constructed network in this article can be well applied to the measured GPR data.

CONCLUSION

Through the optimized convolutional neural network based on the attention mechanism, the key information of the target of the underground oil pipeline can be identified. The simulation results show that after using the optimized new convolutional neural network, the accuracy rates of the leakage discrimination from horizontal data acquired along the oil pipeline and the classification of the target from longitudinal data acquired perpendicular to the oil pipeline are 94.5% and 84.6%, respectively. Compared with the original convolutional neural network without an attention mechanism, the corresponding accuracy rates are improved by 6.2% and 7.8%, respectively. Furthermore, the field measured results show that after using the optimized network, the accuracy rates of the leakage discrimination and the classification of the target are 92.3% and 84.4%, respectively. Compared with that of the conventional network, the accuracy rates of the leakage discrimination and the targets classification are improved by 5.4% and 6.9%, respectively. The research results show that the proposed network models are competent for the underground oil pipeline targets recognition with the simulated and measured data with high accuracy.

DATA AVAILABILITY STATEMENT

The raw data supporting the conclusion of this article will be made available by the authors, without undue reservation.

AUTHOR CONTRIBUTIONS

JL is responsible for the field experimental design, measured data acquisition, and article writing. DY is responsible for data processing, network construction, and article writing. CG is responsible for the experimental design. CJ is responsible for high quality data processing of measurement data. YJ is responsible for data processing. HS is responsible for the acquisition and processing of high quality simulation data. QZ is responsible for the overall design scheme.

FUNDING

This work was financially supported by fundings from the Subtopics of National Key R&D Program (No. 2018YFC0603303), the Sichuan Science and Technology Program (Grant No. 2021YFH0057 and 2021YFG0369) and the SINOPEC Northwest Oil Field Company (No. 34400007-19-ZC0607-0234).

REFERENCES

Cao, Zhenfeng., Yang, Shifu., Song, Shirong., and Zhou, Jian. (1996). Ground Penetrating Radar Data Processing Method and its Application[J]. *Geology. Exploration* 32 (01), 34–42. (in Chinese with English abstract).

Chen, J., Wang, S., Liu, Z., and Guo, Y. (2018). Network-based Optimization Modeling of Manhole Setting for Pipeline Transportation. *Transportation Res. E: logistics transportation Rev.* 113, 38–55. doi:10.1016/j.tre.2018.01.010

Hinton, G. E., and Salakhutdinov, R. R. (2006). Reducing the Dimensionality of Data with Neural Networks. *science* 313 (5786), 504–507. doi:10.1126/science.1127647

Hu, C., Wang, F., and Ai, C. (2021). Calculation of Average Reservoir Pore Pressure Based on Surface Displacement Using Image-To-Image Convolutional Neural Network Model. *Front. Earth Sci.* 9, 712681. doi:10.3389/feart.2021.712681

Jia, L., Guo, C., Wang, F., and Zhang, J. (2007). The Summary of the Surface Ground Penetrating Radar Applied in Subsurface Investigation[J]. *Prog. Geophys.* 22 (02), 629–637. (in Chinese with English abstract). doi:10.3969/j.issn.1004-2903.2007.02.043

Kang, M.-S., Kim, N., Lee, J. J., and An, Y.-K. (2020). Deep Learning-Based Automated Underground Cavity Detection Using Three-Dimensional Ground Penetrating Radar. *Struct. Health Monit.* 19 (1), 173–185. doi:10.1177/1475921719838081

Kunihiko, F., and Sei, M. (1982). Neocognitron: A New Algorithm for Pattern Recognition Tolerant of Deformations and Shifts in Position[J]. *Pattern Recognition* 15 (6), 455–469.

Lei, W., Hou, F., Xi, J., Tan, Q., Xu, M., Jiang, X., et al. (2019). Automatic Hyperbola Detection and Fitting in GPR B-Scan Image. *Automation in Construction* 106, 102839. doi:10.1016/j.autcon.2019.102839

Lei, W., Luo, J., Hou, F., Xu, L., Wang, R., and Jiang, X. (2020). Underground Cylindrical Objects Detection and Diameter Identification in GPR B-Scans via the CNN-LSTM Framework. *Electronics* 9 (11), 1804. doi:10.3390/electronics9111804

Li, W., Cui, X., Guo, L., Chen, J., Chen, X., and Cao, X. (2016). Tree Root Automatic Recognition in Ground-Penetrating Radar Profiles Based on

Randomized Hough Transform. *Remote Sensing* 8 (5), 430. doi:10.3390/rs8050430

Liang, S., Jianlin, W., and Liqiang, Z. (2010). Analysis on Detectable Leakage Ratio of Liquid Pipeline by Negative Pressure Wave Method. *Acta Petrolei Sinica* 31 (4), 654–658. doi:10.7623/syxb201004026

Liu, Q., Zhang, N., Yang, W., Wang, S., Cui, Z., Chen, X., et al. (2017). "A Review of Image Recognition with Deep Convolutional Neural Network," in International Conference on Intelligent Computing, Liverpool, UK, August 7–10, 2017 69–80. doi:10.1007/978-3-319-63309-1_7

Lu, H., and Zhang, Q. (2016). Application of Deep Convolutional Neural Network in Computer Vision[J]. *J. Data Acquisition Process.* 31 (01), 1–17. (in Chinese with English abstract). doi:10.16337/j.1004-9037.2016.01.001

Peplinski, N. R., Ulaby, F. T., and Dobson, M. C. (1995). Dielectric Properties of Soils in the 0.3-1.3-GHz Range. *IEEE Trans. Geosci. Remote Sensing* 33 (3), 803–807. doi:10.1109/36.387598

Sagnard, F., and Tarel, J.-P. (2016). Template-matching Based Detection of Hyperbolas in Ground-Penetrating Radargrams for Buried Utilities. *J. Geophys. Eng.* 13 (4), 491–504. doi:10.1088/1742-2132/13/4/491

Tang, J., Fan, B., Xiao, L., Tian, S., Zhang, F., Zhang, F., et al. (2020). A New Ensemble Machine-Learning Framework for Searching Sweet Spots in Shale Reservoirs[J]. *SPE J.* 26 (1), 482–497. doi:10.2118/204224-pa

Terrasse, G., Nicolas, J. M., Trouvé, E., and Drouet, É. (2016). "Automatic Localization of Gas Pipes from GPR Imagery[C]," in 2016 24th European Signal Processing Conference (EUSIPCO), Budapest, Hungary, August 29–September 2, 2016, 2395–2399.

Vargas, R., Mosavi, A., and Ruiz, R. (2017). Deep Learning: A Review[J]. *Adv. Intell. Syst. Comput.* 5, 1–11.

Wang, L., Wang, H., and Xiong, M. (2014). Technical Analysis and Research Suggestions for Long-Distance Oil Pipeline Leakage Monitoring. *Oil Gas Storage and Transportation* 33 (11), 1198–1201. doi:10.6047/j.issn.1000-8241.2014.11.010

Wang, S., and Chen, S. (2019). Insights to Fracture Stimulation Design in Unconventional Reservoirs Based on Machine Learning Modeling. *J. Pet. Sci. Eng.* 174, 682–695. doi:10.1016/j.petrol.2018.11.076

Wanjun, Liu., Xuejian, Liang., and Haicheng, Qu. (2016). Learning Performance of Convolutional Neural Networks with Different Pooling Models[J]. *J. Image Graphics* 21 (9), 1178–1190. (in Chinese with English abstract). doi:10.11834/jig.20160907

Windsor, C. G., Capineri, L., and Falorni, P. (2013). A Data Pair-Labeled Generalized Hough Transform for Radar Location of Buried Objects[J]. *IEEE Geosci. Remote Sensing Lett.* 11 (1), 124–127. doi:10.1109/LGRS.2013.2248119

Woo, S., Park, J., Lee, J.-Y., and Kweon, I. S. (2018). "CBAM: Convolutional Block Attention Module," in Proceedings of the European conference on computer vision (ECCV), Munich, German, September 8–14, 2018, 3–19. doi:10.1007/978-3-030-01234-2_1

Xiong, H., Kim, C., and Fu, J. (2020). "A Data-Driven Approach to Forecasting Production with Applications to Multiple Shale Plays[C]," in SPE Improved Oil Recovery Conference, Tulsa, USA, August 31–September 4, 2020 (Society of Petroleum Engineers (SPE)).

Yang, D., Hou, N., Lu, J., and Ji, D. (2021). Novel Leakage Detection by Ensemble 1DCNN-VAPSO-SVM in Oil and Gas Pipeline Systems. *Appl. Soft Comput.*, 115, 108212. doi:10.1016/j.asoc.2021.108212

Zhao, Y. Z., Su, Y. L., Hou, X. Y., and Hong, M. H. (2021). Directional Sliding of Water: Biomimetic Snake Scale Surfaces. *Opto-Electronic Adv.* 4 (4), 04210008. doi:10.29026/oea.2021.210008

Zhou, Z., Zhang, J., Huang, X., and Guo, X. (2019). Experimental Study on Distributed Optical-Fiber cable for High-Pressure Buried Natural Gas Pipeline Leakage Monitoring. *Opt. Fiber Tech.* 53, 102028. doi:10.1016/j.yofte.2019.102028

Conflict of Interest: CJ was employed by CNPC Logging Company Limited Tianjin Branch. HS was employed by SINOPEC Northwest Company.

The remaining authors declare that the research was conducted in the absence of any commercial or financial relationships that could be construed as a potential conflict of interest.

frontiers | Frontiers in Earth Science

ORIGINAL RESEARCH
published: 23 May 2022
doi: 10.3389/feart.2022.861091

Data Governance Facilitate Digital Transformation of Oil and Gas Industry

Jian Su[1,2], *Shanglin Yao*[2]* *and He Liu*[1,2]

[1]School of Economics and Management, China University of Petroleum, Qingdao, China, [2]Research Institute of Petroleum Exploration and Development, Beijing, China

Data gradually becomes a critical concern for the strategic resources in enterprises. Massive amounts of data with different types involved in the oil and gas industry can be obtained through IoT (Internet of Things) devices, supported by Blockchain technology with characteristics of immutability and credibility in distributed storage. Hence, credible data will be rationally used in Big Data analysis and Artificial Intelligence implementation. The global mutual trust protocol of Blockchain technology is the bridge among IoT devices, Big Data analysis and Artificial Intelligence implementation, and enables effective coordination of participation of multiple parties and ultimately break isolated island of information. Data governance is the prerequisite for data sharing. As a basic project, Data Sharing breaks data islands and business barriers, improving Data Governance capabilities in Digital Transformation and promoting high-quality development of the oil and gas industry) From the perspective of Digital Transformation, this paper reviews the current situation and problems of Data Governance by evaluating the Data Governance ability of oil and gas enterprises. Furthermore, a proposal is put forward to apply Blockchain technology to improve the Data Governance system and capabilities as the overall program of the oil and gas industry Data Governance system.

Keywords: data governance, digital transformation, oil and gas industry, exploration and development, data sharing, governance capabilities, block chain, shale gas

OPEN ACCESS

Edited by:
Yuwei Li,
Liaoning University, China

Reviewed by:
Yanchun Ling,
University of North Carolina at Chapel Hill, United States
Wei Yu,
University of Texas at Austin, United States
Zhangxing Chen,
University of Calgary, Canada

***Correspondence:**
Shanglin Yao
yaoshanglin@petrochina.com.cn

Specialty section:
This article was submitted to Economic Geology, a section of the journal Frontiers in Earth Science

Received: *24 January 2022*
Accepted: *31 March 2022*
Published: *23 May 2022*

Citation:
Su J, Yao S and Liu H (2022) Data Governance Facilitate Digital Transformation of Oil and Gas Industry. Front. Earth Sci. 10:861091. doi: 10.3389/feart.2022.861091

PREFACE

Recently the digital economy has embarked on a major era of transformation. The in-depth integration of industrial technology and information technology innovates production organization and operation methods, triggering industrial resolution and traditional industrial upgrading with new industries, new formats and new models continuing to emerge. As a traditional industry, the oil and gas industry faces a new situation of the energy revolution to be accelerated. Digital technologies, such as Cloud Computing, Internet of Things (IoT), 5G, Big Data, Artificial Intelligence and Blockchain, should be adopted effectively to drive business model restructuring, management model reform, business model innovation and core competence enhancement to achieve industrial transformation and upgrading with value growth. At the same time, only when oil and gas companies systematically and thoroughly redefine their business, including all aspects of the organization, process, business model and employee capabilities, can Digital Transformation succeed.

In 2013, Tallon considered data to be a special asset (Tallon, 2013). With the advent of the Big Data era, "data as an asset" has become the core trend of the industry. The definition of data assets in the "Data Asset Management Practice White Paper 4.0": What is owned or controlled by an enterprise includes not only the internal data of the enterprise, but also the external data obtained by

the enterprise through purchase, which can bring future economic benefits to the enterprise, or data resources recorded electronically. The core of Digital Transformation is data sharing, and data sharing requires Data Governance as the foundation. Therefore, Data Governance has become an important basic project related to Digital Transformation and high-quality development.

URGENT REQUIREMENTS FOR DATA GOVERNANCE IN DIGITAL TRANSFORMATION OF OIL AND GAS INDUSTRY

The Core of Digital Transformation is to Achieve Full Data Sharing

With the rapid development of Informatization, Big Data, and Intelligence, people usually compare cash flow to the blood of an enterprise. Data is an information record that identifies various resources and activities of an enterprise, with each datum as a neuron of an enterprise. Data has become a significant strategic resource that enterprises and society pay attention to as an important carrier of production, operation and management activities with highlights from all people. If data cannot be fully shared and used efficiently, other sharing will be impossible, and Digital Transformation will not be realized. For the oil and gas industry, data sharing has huge space, great potential and great value, including the business data such as internal enterprise planning, procurement, production, sales, and finance, and the oil and gas value chain data such as production, refining, transportation, sales, storage and marketing, as well as other data from all aspects of data on changes in external market supply and demand, price adjustments, and policy environment. Through full sharing of these data, the value of data assets is comprehensively improved, and business operations and decision-making methods are transformed from traditional manual statistical calculation and empirical analysis to accurate analysis based on systems, data and models, which effectively supports the optimal allocation of resources, efficient market operation forecasts, and Scientific connection of production, refining, transportation, sales, storage, and trade links to maximize the company's overall benefits (Liu, 2019; Dai, 2020).

Data sharing embodies three aspects of value in the oil industry. Firstly, it contributes to oil exploration and development management, realizing the most scientific decision-making and efficient productivity. Then, data sharing could analyze the trend and potential demand of oil resource consumers. Thus it encourages the industry to innovate pragmatically and develop potential markets steadily. For instance, data analysis and detection systems are set up in gas and petrol stations to record every customer demand in the country. It could formulate timely service and new product suggestions to retain high-quality customers and expand the market. Finally, data sharing could monitor the production and safety of oil fields through network detection. After all, intelligent detection is more efficient and safer than manual detection.

The Premise and Foundation of Data Sharing is Scientific and Effective Data Governance

As information technology continues to deepen application integration and innovation, various applications have gradually penetrated all walks of life. The authority, authenticity, validity, and compliance of data with business requirements are critical to cross-business data analysis. Data management with the unified criterium and quality will be the institutional guarantees for sharing applications among various businesses. Bhansali also elaborated on the value of Data Governance in the book,

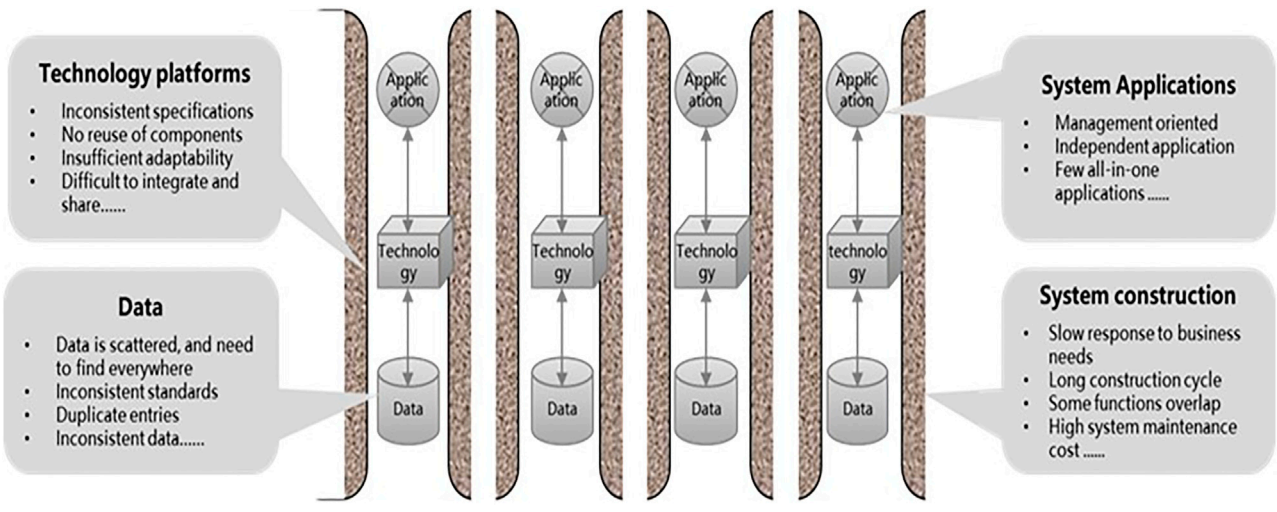

FIGURE 1 | Current system status of data sharing.

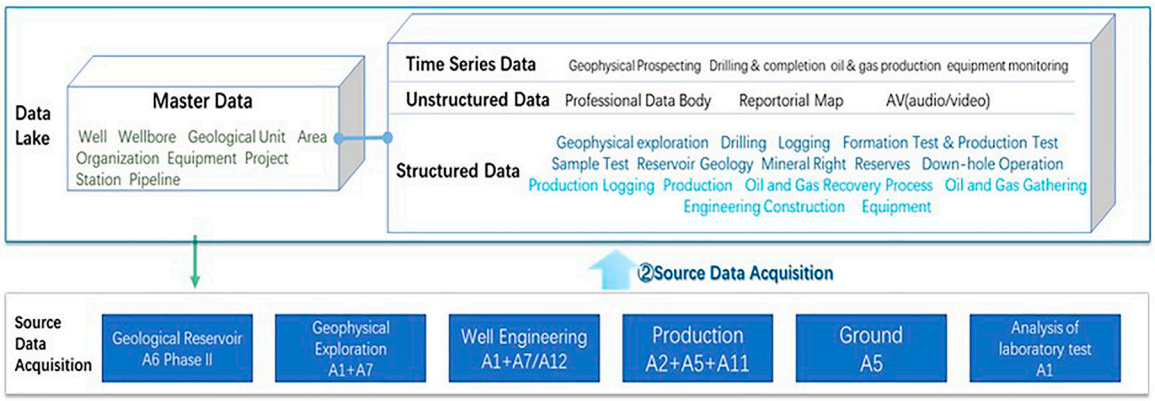

FIGURE 2 | Source collection of exploration and development data.

believing that the norms of Data Governance can help organizations manage data more effectively, reduce the cost of information use, improve the effectiveness of law compliance and control, and promote the generation of high-quality data (Bhansali, 2013). Only through Data Governance can the high quality of data be improved. The main purpose of Data Governance is to improve the effectiveness of data sharing applications and work around how data is transformed into assets. Trope, etc. all believe that Data Governance should be integrated with various business departments (Trope and Power, 2005), not just the IT department. At present, the business information systems of oil and gas companies have multiple data collections, repeated data entry, inconsistent data standards, and low data quality, which severely restrict the level of data sharing and application of oil and gas companies and hinder the company's Digital Transformation (Dai, 2020).

Technology platforms have inconsistent specifications, no reuse of components, insufficient adaptability, and are difficult to integrate and share.

Data is scattered and need to find everywhere, inconsistent standards, duplicate entries and inconsistent data.

System applications are management-oriented, independent applications and few all-in-one applications.

The following phenomena exist in system construction: slow response to business needs、long construction cycle、some functions overlap、high system maintenance costs. As shown in **Figure 1**, the realization path of consistency, integrity, authenticity and validity of business data is the implementation of Data Governance.

Data governance helps to identify the current situation and problems of data management. Unify the enterprise business system's data governance system, data structure, and data standards to form a company-level data resource directory. Guided by the concept of data co-construction, sharing and co-governance, Data Governance advocates data management of standard, quality, security and sharing. It guarantees the operation of organization, system and process. It is also crucial to organize relevant parties to carry out Data Governance activities together, promote all parties to build the company's Data Governance system jointly, and improve Data Governance capabilities. Data governance activities should be divided into front-line information systems and data warehouses, embedded in the whole life cycle of the system, jointly manage and highlight data problems, improve the quality of data resources from the source. In this way, all parties involved could share high-quality Data Governance achievements and create a new enterprise Data Governance model of "co-construction, co-management and sharing".

THE CONNOTATION OF DATA GOVERNANCE IN THE OIL AND GAS INDUSTRY AND THE KEY ISSUES TO BE ADDRESSED

The Connotation of Data Governance in the Oil and Gas Industry

Informatic defines Data Governance as "the functional alignment and definition of processes, policies, standards, technologies and people across the organization to manage data as a corporate asset, enabling the availability of accurate, consistent, secure and timely data and controlled growth to make better business decisions, reduce risk and improve business processes".

The essence of Data Governance in the oil and gas industry is to treat data as an asset of the company, and to develop a set of systems for the "collection, storage, management and application" of data across the organization, including both decision-making and executive levels, and both business and IT departments. Data governance is a long-term process that integrates business and IT throughout the business process.

All data sources are generated by its business front-end transaction process, and those who generate data and input data. In other words, all data depends on the business, and it is meaningless to discuss data governance and business separately. Therefore, the analysis of data sources and their business distribution is the foundation of Data Governance.

Key Issues in Data Governance at Oil and Gas Industry

The dynamic and static data of oil and gas field enterprises are massive. Taking the unified upstream system as an example, the data management mode segmented from A1 to An has accumulated massive data resources, including exploration and production technology data management system, oil and gas water well production data management system, oil recovery and surface engineering operation management system, engineering technology production operation management system, exploration and production scheduling command system, oil and gas production IoT system, engineering technology IoT system, etc. It has built nine major types of data asset libraries, covering nearly 450,000 exploration and evaluation development wells, managing more than 1.08 million logging data body files, 600 oil and gas reservoirs, more than 7,000 work areas of seismic data, more than 3.67 million documents, etc., and storing more than 1.7 petabytes of data in total. As shown in **Figure 2**, with such a huge amount of data and the continuous growth of data diversity, "data island" are growing, and data quality varies, greatly hindering the digital transformation process, and Data Governance is urgently needed to address the following issues.

The First question lies in the management mode of compartmentalization that caused a large number of "data island". At present, oil and gas field enterprises contain several compartmentalized departments or systems, each of which has its own data, and the data of each department or system is often stored separately, forming its own system. The raw data of the same study may exist in multiple systems, multiple databases, and even in the computers of various researchers. It cannot ensure the authority of the raw data in each study, affecting the accuracy of the research results and failing to guide E&P research and production effectively. The core problem of such data is that there are many databases, platforms and isolated applications, leading to the serious problem of "data island". Firstly the data standards are not uniform, and the data patterns do not match. There is no unified, timely updated and shared oil and gas well geological database and engineering foundation database, which is easy to cause data conflicts and data redundancy, and there is no consulting service company with compatibility and neutrality to classify and secondary development, which is later applied to data sharing, mining and analysis. Secondly, the specifications of the technical platform are inconsistent. The components are not reusable, have insufficient adaptability, and are difficult to integrate and share. Thirdly the number of system applications is large, and there are many management-oriented independent applications but few integrated applications. Fourthly, system construction is slow in response to business needs with a long construction cycle, duplication of some functions, and high system maintenance costs (Li et al., 2019).

There are two main direct negative effects brought by data silos: First, investment waste. Geological data has multiple interpretations, and the results need to be verified according to the back-end works, with continuously revised and optimized geological model and parameters should be to gradually approach the real underground situation. If the back-end engineering construction results cannot be fed back to the geological department timely, the reservoir model will not be corrected in time. If some ideas that have been proved to be wrong by predecessors are tried again by others, low-level mistakes will be repeated continuously, which resulting in extreme waste.

The second is reduced efficiency. The multi-solution of geological knowledge also causes different disciplines and different teams to choose inconsistent parameter parameters when working on the same reservoir, which makes the research results lack uniformity and comparability. Different disciplines or teams often repeat simple and low-level data collection, data screening and understanding and digestion after taking over the same target work, which seriously affects work efficiency.

The second issue is data quality. It is necessary to verify the authenticity and integrity of the data, because of the inconsistency of data collection methods, statistical methods and control measures over the past 60 years. In particular, the current IoT in the old upstream oil fields is not fully covered, and the degree of automated data collection is not yet high, which affects the validity and accuracy of data. Moreover, data comes from various sources and involves multiple participating subjects in their life cycle. Issues such as whether data are authentically generated, data tampering, and inconsistent standards and types of data from multiple sources can affect data quality and, thus, the data decision outcomes of data users. Therefore, Data Governance needs to support the traceability of big data throughout its lifecycle.

GOALS AND DIRECTIONS OF DIGITAL TRANSFORMATION IN THE OIL AND GAS INDUSTRY

As a traditional industry, the oil and gas industry faces an opportunity of accelerated energy revolution and energy transformation. It requires to make effective use of digital technologies (such as cloud computing, Internet of Things, 5G, big data, artificial intelligence) to promote business model reconstruction, management model reform, business model innovation and core competency enhancement, so as to achieve industrial transformation, upgrading and value growth. At the same time, digital transformation can only succeed if oil and gas companies systematically and thoroughly redefine their business, including all aspects of the organization, processes, business models and employee capabilities.

Overall Objectives

It is necessary to use automatic sensing to collect real-time operation data in the oil and gas industry chain, use comprehensive interconnection to widely obtain internal and external data, and use digital technology to optimize business execution and operational efficiency continuously. We will build a closed-loop system for the integration and interaction between the physical oil and gas enterprise and the digital twin, and promote the two-way connection between the physical business

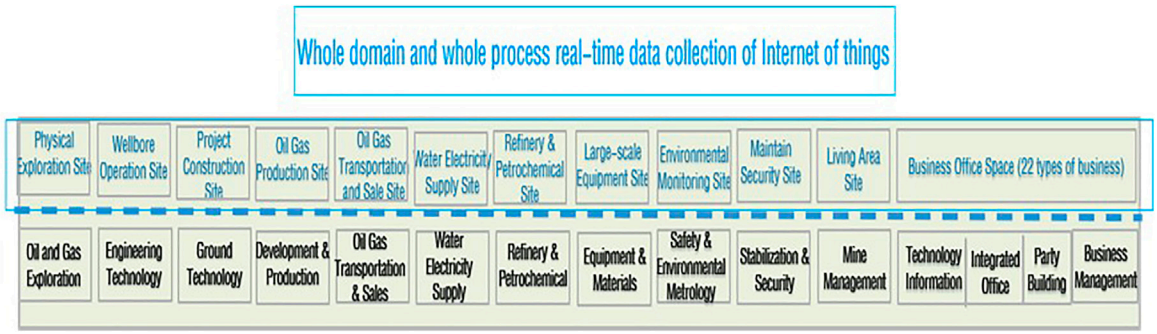

FIGURE 3 | Whole domain and whole process real-time data collection of Internet of things.

and the digital world, so as to form an internal and external connection, sharing and collaboration mechanisms, and finally realize cost reduction and efficiency increase, collaboration and sharing, continuous innovation, risk pre-control and intelligent decision-making, and continuously improve the productivity of all employees and the ability to create assets.

Main Directions

It is important to integrate digital technology into the products, services and processes of the oil and gas industry chain, thus promoting changes in the company's development philosophy, working model, operation and management, scientific and technological research and development and management system mechanism to build new capabilities such as intelligent production, networked collaboration and personalized services and create new business models, new production methods and new industrial ecologies driven by users, data and innovation.

INTERNET OF THINGS, BLOCKCHAIN TECHNOLOGY IN DATA GOVERNANCE

Data Integrity, Accuracy, Consistency and Timeliness Guaranteed by IoT Technologies

The oil and gas industry is characterized by high asset density, long operating distances and dangerous production environments. Establishing an industrial IoT can effectively streamline processes, enrich decision-making tools and improve operational efficiency. The IoT of the oil and gas industry usually consists of three layers: sensing, transmission, and application. The sensing layer consists of sensors and radio identification frequency devices (RIFD) installed in each key production link, which is used to collect data information in oil and gas exploration, development and production in real-time. The transmission layer is composed of networks such as the Internet and mobile communication networks, which are responsible for data transmission. And the application layer refers to the system management platform, which realizes the analysis and processing of oil and gas data. It establishes a comprehensive, interconnected information network among reservoirs, wellbores, individual wells, field stations, pipeline networks, equipment and personnel, realizes the comprehensive sensing capability of the oil and gas exploration, development and production management system, and provides a basic platform for intelligent production and decision management of oil and gas systems.

The IoT technology enables a unified automatic and standardized collection of data sources through data quality control tools. These tools guarantee data quality by building a high-quality data mode, allowing collected data to directly flow into the lake to realize the standardized docking of data lake and sensors. In this way, redundant data like repeated and multiple collections are avoidable. So that the data quality control tools could not only ensure the integrity, accuracy, consistency, and timeliness of data acquisition, enrichment, conversion, storage, and application.

IoT collects production data formed "four unification". Unification of data entrance - is a uniform data acquisition interface that allows automatic production data collection and guarantees uniqueness and timeliness. Unification of the data model—provides developing and producing functions and facilitates data sharing. Unification of data quality control - equips by combining big data, artificial intelligence algorithm judgment and manual sampling to ensure accuracy, and improves efficiency while reducing the labour intensity and workload of data entry personnel. Unification of data services—provides reliable data services for unified construction systems and personalized oilfield systems through cloud platforms to ensure data consistency and integrity.

The IoT system construction of oil and gas fields has created significant economic and social benefits in optimizing the production process and organizational structure, improving production efficiency and management level, and reducing labour intensity (especially for front-line workers) and production costs and safety risk. It has generated a cumulative direct economic benefit of 1.16 billion yuan and cut 24660 in the number of front-line workers.

The Changning shale gas field, which is the first in China in terms of daily shale gas production, is a typical case of successful digital transformation empowered by Data Governance with IoT technology as a grip, As shown in **Figure 3**.

IoT technology supports a lot in oil and gas production process management. It realizes real-time data collection, transmission and monitoring of oil and gas production sites,

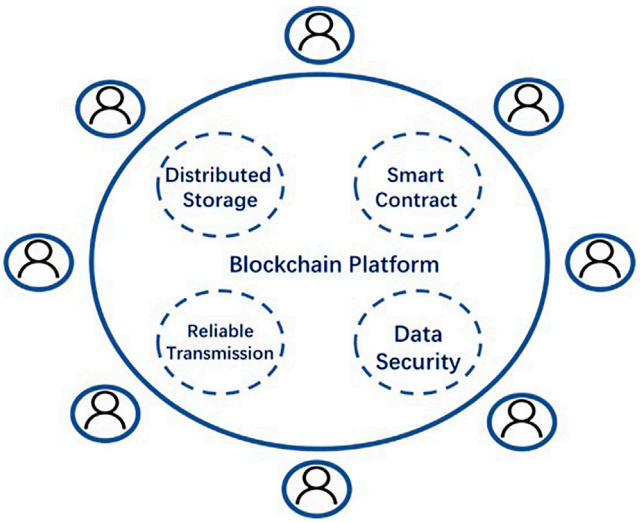

FIGURE 4 | Blockchain-based data storage sharing platform.

including wells, workshops, stations and processing plants. Besides, it promotes the transformation of production methods—optimizes production processes, management processes, and organization and improves production efficiency and management level. Furthermore, IoT technology energizes intelligent analysis of production devices, electrical facilities, energy consumption and self-control equipment during the production process. The production process realizes intelligent application of data in four fields, covering intelligent analysis of production devices, intelligent analysis of power facilities, intelligent analysis of energy consumption correlation, and intelligent analysis of self-control equipment, to realize lean and safe production with high timeliness and considerable economy. Timeliness is reflected in the automatic data collection at the minute level and early warning at the hourly level. The economy is reflected in the timely detection of abnormalities in plant conditions, accurate prediction of the probability of accidents and events, scientific evaluation of the health of key plants and reduction of plant daily management costs by more than 20%.

Elimination of "Data Island" by Blockchain Technology to Ensure True and Safe Data Sharing

Blockchain integrates cryptography and distributed database technologies, which can effectively and securely solve the problem of data sharing across organizations and eliminate the phenomenon of "data island". With its decentralized, open, transparent, and tamper-evident characteristics, Blockchain is compatible with the transparency requirement of Big Data value realization and can overcome the authenticity problem of current Data Governance, providing a new solution for Data Governance.

Blockchain technology can be used during data circulation to strengthen data quality control and ensure data traceability and immutability. The distributed storage can be used to realize data sharing, break "data island", and promote integrated data integration.

Data decision-making permeates all aspects of production and operation. Due to the involvement of multiple stakeholders, there are problems such as data tampering, data falsification, and differences in the types and standard rules of data from different sources in the process of storage, processing and sharing, which will affect the quality of decision-making data. Therefore, data users need to audit the decision data. Blockchain, as a decentralized distributed database, enables data storage and processing that supports auditing. In addition, by building a decentralized distributed database system among different interest subjects based on Blockchain, data is quickly broadcasted to each interest subject through the whole network, ensuring the authenticity and timeliness of data sharing and circulation.

Each node in the Blockchain network stores data, and once the data is stored in the Blockchain, it will not be tampered with or lost. Even if there are problems such as communication failures and deliberate attacks, the correctness of the data storage can still be guaranteed, and the data users can audit it. In addition, storing data in the Blockchain also supports the audibility of the data treatment process and results.

As a decentralized distributed database, Blockchain supports historical status query of data to confirm whether the current data status is correct. For a traditional database management system, the current data state is stored and maintained in the database, and only the information such as the data processing process is stored in the database log for failure recovery, and does not support the historical state query of data.

Blockchain technology allows data to be stored and shared more conveniently and safely, which is of great significance in the oil and gas field with high data integrity requirements. Blockchain technology has strong practicality for data protection and management. By building a Blockchain-based data storage and sharing platform, the data can be safely stored on the chain, but all data can be kept interrelated and connected with each other. As shown in **Figure 4**, in the data storage sharing platform, relevant business organizations will join the data storage sharing platform as nodes in the Blockchain system to realize the utilization and sharing of data resources. At the same time, the distributed storage, consensus mechanism and smart contracts in Blockchain technology provide guarantees for data management, safe storage and sharing and data users can audit decision data and perform analysis and make decisions on trusted data (He et al., 2017; Zhao et al., 2018; Fu, 2019; Gong et al., 2019).

For problems such as inconsistent types and standard rules for data from different sources, uniform data types and standard rules can be developed based on the Blockchain and smart contracts. Smart contracts will be stored and synchronized in various nodes of the Blockchain, and the Blockchain will automatically execute validation based on the code on the smart contracts. Since the execution process of smart contracts is open and transparent, the execution process and execution results are audible, which can improve the efficiency of multi-source data sharing and there is no single point of failure.

TABLE 1 | Blockchain data storage item of shale gas.

Geophysical prospecting	Seismic acquisition results, VSP logging, production management
Well Drilling	Well History of Drilling Well, Production Management
Mud Logging	Basic Data, Engineering Logging, Geological Logging, Comprehensive Analysis, Production Management
Well logging	Construction Data, One-dimensional and two-dimensional Curve Data, Graph of Conventional Logging, Variable Density, New Technology Logging, Reservoir Interpretation Conclusion, Logging Production Management
Oil Testing	Oil Test, Testing, Special Construction, Production Management
Analysis and Testing	Conventional Core Analysis, Special Core Analysis, Fluid Property Analysis, Geochemical Analysis, Oil Recovery Laboratory Analysis, Stratigraphical Paleontology Analysis
Reserve Management	Oil and Gas Field Information, Block Element Information, Development Unit Information
Reservoir Geology	Basic Geological Data, Oil and Gas Field Production, Development Logging, Development Well Testing, Program, Economic evaluation, Production Plan, Conventional Analysis of Oil and Gas Wells
Oil Recovery Technology	Artificial Lift Equipment, Equipment Operation, Process Management, Logistics Management
Borehole Operation	Construction Preparation, Shaft Construction, Special Construction, Construction Summarization
Oil-gas Gathering and Transportation	Oil Depot and Gas Station Data, Equipment Operation, Pipeline Data
Surface Construction	Electricity, Bridges, Roads and Communications

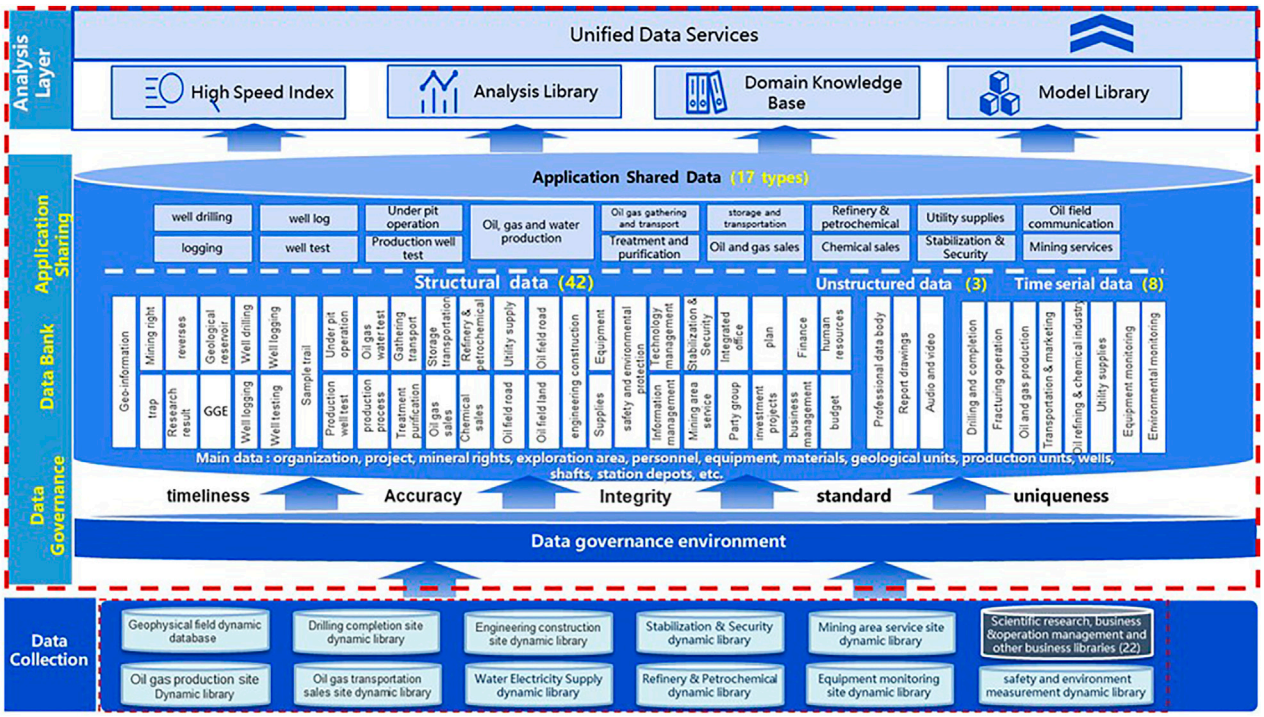

FIGURE 5 | *oil field Regional data lake.

At present, in * oilfield, Blockchain technology supports various E&P business fields of shale gas to store the structured raw data. These data cover 12 categories: geophysical exploration, drilling, mud logging, well logging, oil testing, analysis and testing, reserve management, reservoir geology, oil recovery technology, borehole operation, oil-gas gathering and transportation and surface construction, as shown in **Table 1**.

On account of the authenticity data before uploading the chain, a Blockchain-based data management platform is established to record the site data and operation information of reservoir exploration, oil and gas extraction and other aspects in real-time and accurately. In addition, this platform digitizes real-time and data sharing of site supervision, significantly improves data security, site supervision effectiveness, and production risk control. It also optimizes the construction process and supervision measures and takes full advantage of Blockchain. The advantages of Blockchain technology will drive the oil and gas industry towards digital business innovation and provide a guarantee for safe and efficient production and cost reduction and efficiency in the oil and gas sector.

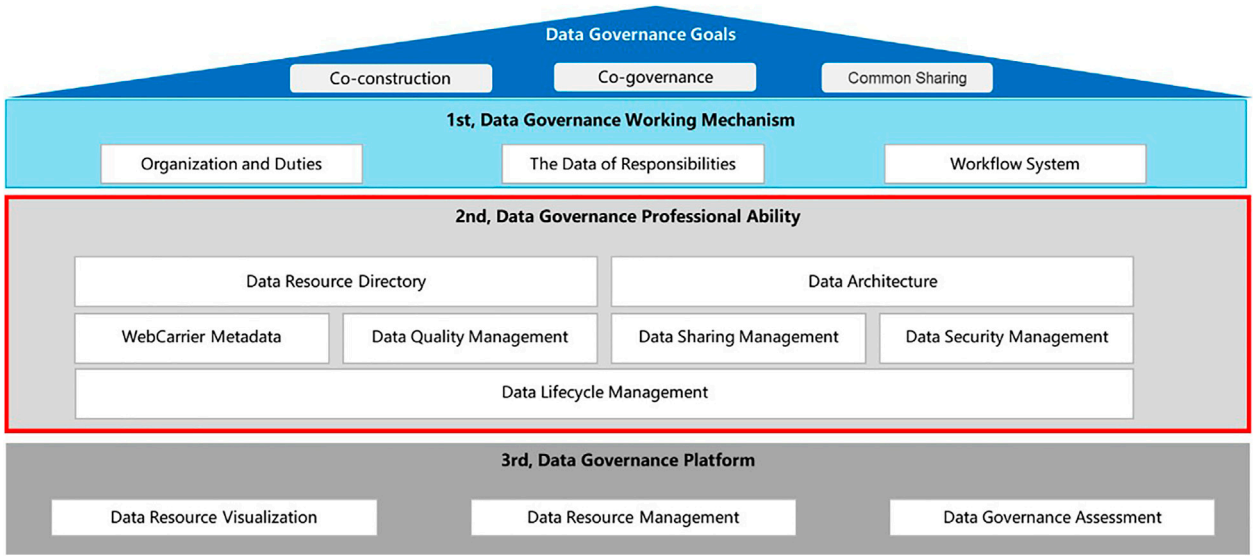

FIGURE 6 | Framework of oil and gas data governance system.

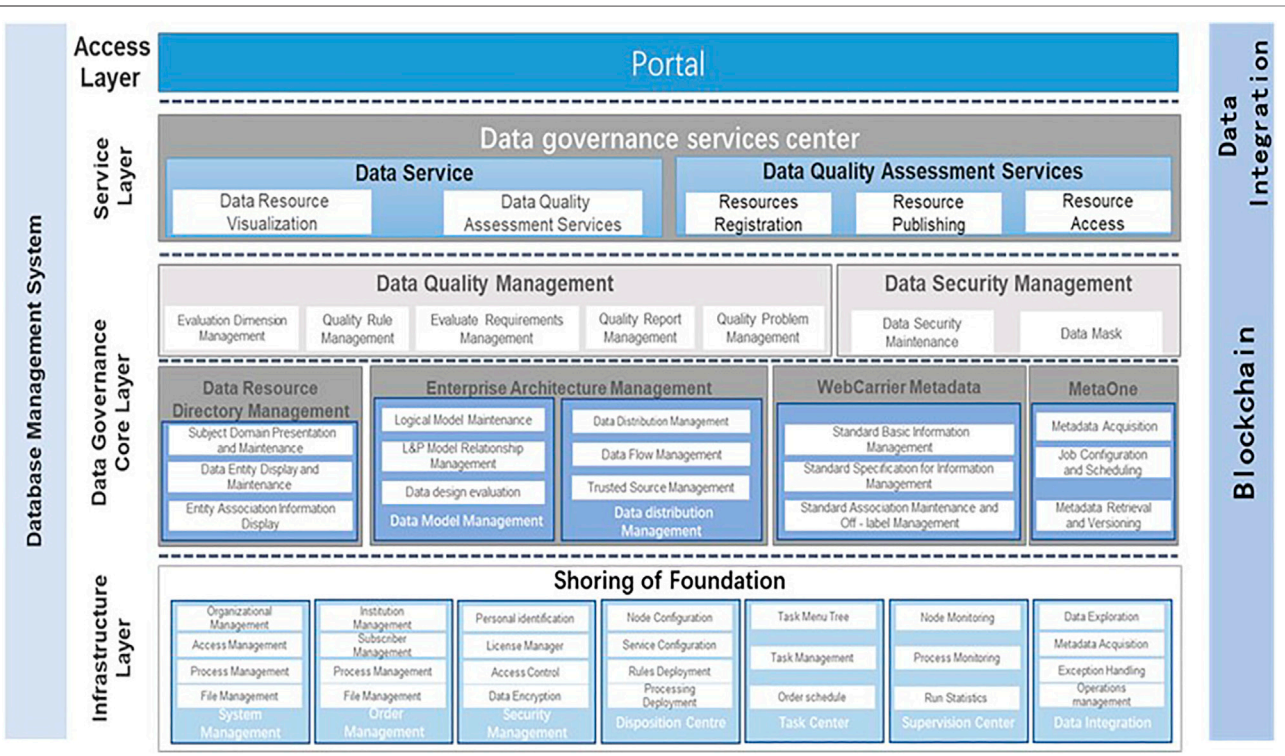

FIGURE 7 | Data governance platform.

The shale gas master Data Governance based on Blockchain is the core task to realize centralized management and sharing of shale gas data. Master data refers to relatively static, core and high-value data shared by multiple application systems across the enterprise, also known as enterprise benchmark data. Master data can create and maintain the consistency, completeness, relevance and accuracy of data of each business and system in the related fields.

Master data scope determination: the use of shale gas business data in each business system is sorted out, and then analyzed by

the Data Governance expert group in conjunction with actual shale gas data use and shale gas characteristic business to form consistent, complete and accurate company-wide core business data of shale gas.

Master data standard specification: based on Blockchain and Smart Contracts, unified data types and standard rules can be established for master data naming specification of shale gas, model standard specification, coding specification, master data association relationship and master data accuracy and integrity business logic rules to develop a quality management in the whole life cycle process.

The Data Governance technical team can load the confirmed authoritative master data information from the temporary environment to the Blockchain through the ETL tool, and distribute the master data information of shale gas to all business systems. So far, the integrity, uniqueness, standardization, consistency and correlation of shale gas master data of all company business systems were realized; the data-sharing mechanism was realized and improved, thus helping the oilfield reduce cost and improve efficiency through data analysis and reuse.

THE OVERALL PLAN FOR A DATA GOVERNANCE SYSTEM

At present, the oil and gas industry has many problems in the process of data generation, processing, and application due to many reasons. It is necessary to accelerate the construction of the Data Governance system from a group lever, including the clarification of the centralized Data Governance department, the data management of standardization, metadata and master data and regular evaluation of data maturity of governance capabilities. It is necessary to strengthen the dynamic data collection of the entire industry chain and establish a data collection, transmission and aggregation system covering the entire business chain. In order to improve Data Governance capabilities comprehensively, we should adopt systematic thinking and systematic solutions, and implement policies from the concept, organization, management, and technology dimensions. A comprehensive Data Governance system could provide high-quality data foundation guarantees for the Digital Transformation of the oil and gas industry.

Most foreign scholars have proposed a Data Governance framework system during their research. For example, the draft framework model proposed by Wende defined various decision-making fields and corresponding role divisions (Wende, 2007). The most significant contribution of this framework model is to help organizations build data quality responsibilities. The decision domains and roles it proposed can be used as the structural configuration of Data Governance, but there is still a lack of use verification under different organizational scenarios. Among them, the most influential is the decision domain model of Data Governance proposed by Khatri and Brown (Khatri and Brown, 2010). Their framework includes five decision domains: data criteria, quality, metadata, access, and life cycle, and expounds the type and scope of decision domains. This model proposed different centralized, decentralized and shared decision-making power levels in the same organizational decision-making domain. At the same time, it provides a common framework of standard terms, which makes it widely adopted in subsequent studies.

Combined with foreign design concepts and the characteristics of the oil and gas industry (Fisher, 2008), the author summarizes the Data Governance system elements as follows. Under the data co-construction, sharing and co-governance guidelines, the Data Governance system concentrates on data standards, quality, security and sharing, and guarantees the operation of organizations, institutions and processes. Supported by the Data Governance platform, this system innovates the data integration analysis and sharing exchange mechanism. So that, Blockchain technology is able to promote the construction of Data Governance systems and governance capabilities in the oil and gas industry. *Oil field regional data lake as shown in **Figure 5**.

Framework of Oil and Gas Data Governance System

Data management activities should be carried out with all relevant parties jointly in combination with "top-level design plus partial landing" with effective results to promote the company's Data Governance system, as shown in **Figure 6**, to improve data management capabilities. The Data Governance activities should fall into the front-line information system, data warehouse and be embedded in the full life cycle of the system to jointly manage outstanding data problems to improve the quality of data resources from the source. As a result, all parties involved can share high-quality Data Governance results, and create a new Data Governance pattern of "co-construction, co-governance, and sharing" for the company.

Data Governance Platform

Martijn et al. proposed a Data Governance platform that includes a three-tier system of technical architecture, process architecture, and business architecture (Martijn et al., 2015); and Seine proposed a five-tier system that includes executive tier, strategic tier, tactical tier, operation tier and support tier (Seiner, 2016). The system's Data Governance platform also elaborated on the respective roles, processes, communication, indicators and tools at the five levels. With reference to the above design ideas, combined with the characteristics of the oil and gas industry's entire industry chain, a Data Governance platform for the oil and gas industry has been built to follow the Data Governance system and implement relevant policies, procedures and methods as platform functions, realizing data consolidation, data maintenance and data application to improve the efficiency and effectiveness of all aspects of Data Governance. As shown in **Figure 7**, the data management platform can be divided into the database, data management core, data service, and user access layers.

Application Effectiveness of Data Governance Platform Pilot Construction

The pilot construction of *oilfield Data Governance platform covers the core activities and data management in shale gas

exploration and production (E&P), reaching a plethora of achievements in multiple dimensions.

- Established an integrated data model covering *oilfield E&P core activities, to fundamentally realize the transparent sharing of cross-professional data;
- Established a unified data resource management system, to implement asset-based exploration and exploration data management;
- Established a unified data acquisition system based on Iot, to achieve unique source site, one-time acquisition and global shared;
- Established a unified E&P Data Blockchain storage system, to scientifically preserve valuable data assets which obtained at great expense;
- Established a unified E&P Data Governance platform, to realize the integrated application of E&P data;
- Automatic data quality check with high availability rate;
- Data application across departments and professions, integration and collaboration;
- Comprehensive research "one-click access" and significant improvement in work efficiency.

With oil and gas reservoir as the core, it realizes parameter interaction and optimization adjustment, professional mutual synergy and promotion, and builds connections for different professions and departments to communicate and break obstacles. Furthermore, it records instantly during the run process, gradually accumulates experience, continuously learns and iterates, forms efficient templates, and finally achieves maximum benefits.

*Oilfield Data Governance platform has stored the primary data of five business domains and 41 businesses of E&P, which fully supports all applications of E&P. Currently, the data content covers 608 exploratory wells and 575 development wells in 29 oil and gas fields, with a total of 1994 categories, more than 160 million entries, and about 1T data information (excluding seismic body data). Overall data normalization reaches more than 90%, providing use for seven professional databases and application systems, including dynamic exploration database, development production database, mud logging database, well logging database, geological reservoir library, target database and logging decision support system.

CONCLUSION

In the Digital Transformation development of the oil and gas industry, it is necessary to support the research and development of Blockchain technology vigorously, continuously upgrade and improve it through iterative construction, create a "sample room", ensure the quality and efficiency of Data Governance and advocate the formation of a concept and culture of data co-construction, sharing and co-governance. The Digital Transformation of the industry can be carried out from the three aspects: technology development, scenario application, and standard formulation to promote the standardized and large-scale application of Blockchain technology in the oil and gas industry, and continue to implement all elements of the Data Governance system in place. Each element of the Data Governance system should be executed continuously to a full extent one by one with multi-party coordination, comprehensive policy implementation and long-term contributions to achieve collaborative innovation, efficient operation and value enhancement of the entire business chain of the oil and gas industry.

DATA AVAILABILITY STATEMENT

The original contributions presented in the study are included in the article/Supplementary Material, further inquiries can be directed to the corresponding author.

AUTHOR CONTRIBUTIONS

JS: performed the data analyses and wrote the manuscript; SY: contributed significantly to analysis and manuscript preparation; HL: helped perform the analysis with constructive discussions.

FUNDING

National Natural Science Foundation of China/Basic Science Center Project "The theory and application of resource and environment management in the digital economy era" (72088101).

REFERENCES

Autonomous, Author. (2012). All the Ingredients for success: Data Governance, Data Quality and Master Data Management. Available at: https://tdwi.org/whitepapers/2012/03/all–the–ingredients–for–success–data–governance–data–quality–and–master–data–management.aspx.

Autonomous, Author. (2010). See Course Materials from EWSolutions, enterprise Data Governance and Stew Ardship[EB/OL]. Available at: http://www.EW-Solutions.com.

Bhansali, N. (2013). *Data Governance: Creating Value from Information Assets*. CRC Press, 28–122.

Dai, H. (2020). *PetroChina: Drive the High-Quality Development of the Oil and Gas Industry with Digital Transformation*. Website of State-owned Assets Supervision and Administration Commission of the State Council.

Fisher, T. (2008). The Four Stages of Data Maturity, Data Flux[EB/OL]. Available at: http://www.sas.com/news/sascom/2007q4/column_tech.html (Accesssed 10 05, 2008).

Fu, Rao. (2019). *When the Oil and Gas Industry Meets the Block Chain*. Ta Kung Pao, 11–13.

Gong, R., Yang, R., and Lan, M. (2019). Application Prospects of Block Chain Technology in the Petroleum Industry[J]. *Inf. Syst. Eng.* (11), 62–65.

He, P., Yu, G., Zhang, Y. F., et al. (2017). Survey on Blockchain Technology and its Application Prospect[J]. *Comput.Sci* 44 (4), 1–7.

IBM Data governance council (2008). IBM Data Governance council. Available at: http://www–01.ibm.com/software/tivoli/governance.

Khatri, V., and Brown, C. V. (2010). Designing Data Governance. *Commun. ACM* 53 (1), 148–152.

Li, G., Wang, F., Xuejun, P., and Liu, H. (2019). Optimized Application of Geology-Engineering Integration Data of Unconventional Oil and Gas Reservoirs[4]. *China Petroleum Exploration* 24 (1), 147–152.

Liu, S. (2019). Research on Data Governance System in "Share China Petroleum. *[J]* No.6, 21–29.

Martijn, N., Hulstijn, J., Bruijne, M., and Tam, Y.-H. (2015). "Determining the Effects of Data Governance on the Performance and Compliance of Enterprises in the Logistics and Retail Sector," in Conference on e-Business, e-Services and e-Society, 454–466.

Seiner, R. S. (2016). Noninvasive Framework for Data Governance Implementation: Details, Part 2[EB/OL]. Available at: http://tdan.com/non–invasive–framework–for–datagovernance–implementation–details–part–2/20130 (Accesssed 01 24, 2016).

Tallon, P. (2013). Corporate Governance of Big Data Perspectives on Value, Risk and Cost. *Computer* (46), 32–38.

Trope, R. L., and Power, M. (2005). Lessons in Data Governance: A Survey of Legal Developments in Data Management, Privacy and Security. *Business Lawyer* 61, 471–516.

Wende, K. (2007). "A Model for Data Governance–organizing Accountabilities for Data Quality Management," in 18th Australasian Conference on Information Systems, 417–425.12

Zhao, G., Sun, J., Wang, M., et al. (2018). Block Chain Technology Boosts the Digital Transformation of Oil and Gas Exploration and Development[J]. *Sinopec* 397 (10), 72–74.

Conflict of Interest: The authors declare that the research was conducted in the absence of any commercial or financial relationships that could be construed as a potential conflict of interest.

Publisher's Note: All claims expressed in this article are solely those of the authors and do not necessarily represent those of their affiliated organizations, or those of the publisher, the editors and the reviewers. Any product that may be evaluated in this article, or claim that may be made by its manufacturer, is not guaranteed or endorsed by the publisher.

frontiers | Frontiers in Earth Science

ORIGINAL RESEARCH
published: 30 June 2022
doi: 10.3389/feart.2022.862710

Adaptability Analysis of Full Height Mining at One Time of Deep Soft Thick Coal Seam

Qinghai Li[1], Haonan Wang[1], Xuejun Zheng[2], Kaixin Li[3], Yonghu Ji[2] and Zijun Wang[1]*

[1]College of Energy and Mining Engineering, Shandong University of Science and Technology, Qingdao, China, [2]Shandong Lilou Coal Industry Co., Ltd., Heze, China, [3]College of Geodesy and Geomatics, Shandong University of Science and Technology, Qingdao, China

With the improvement of technology and equipment, it is preferred to adopt full-height mining at one time when conditions permit. According to the specific geological conditions of no. 3 coal seam in Lilou Coal Industry, the feasibility of full-height mining and top-caving mining method for soft thick coal seam with large buried depth is analyzed by means of theoretical analysis, numerical simulation and field application analysis, which provides basis for the subsequent improvement of field mining method. Through the establishment of cantilever beam mechanical model of basic roof, the influence of two mining methods on the energy response of basic roof is analyzed. Based on the energy storage characteristics of coal seam, roof and floor measured in the field, the intensity of energy released from disturbed strata by two coal mining methods is analyzed. PFC2D numerical simulation was used to compare the roof failure of the two mining methods, to monitor the change of the stress in the coal seam after excavation, and to calculate the coal seam burial depth suitable for a full mining height by adjusting the *in-situ* stress. The results show that compared with top-coal mining, the elastic strain energy accumulated in the full-height roof beam is more, and the energy release intensity of disturbed rock is greater. The roof crack extension height is 9.1 m and the coal wall failure depth is 5.46 m under the condition of full mining height at one time. The roof crack extension height is 1.19 m and the coal wall failure depth is 2.19 m under the caving coal mining method. In the caving coal mining method, the stress level of the original rock is restored at 3 m in front of the coal wall, and the stress level of the original rock is restored at 5 m in front of the coal wall when the full mining height is once taken. It is safer to adopt full-height mining method when the buried depth of coal seam is less than 380 m. The research results can provide reference for mining soft thick coal seam with large buried depth.

Keywords: full height mining at one time, top caving mining, cantilever beam model, elastic strain energy, coal wall stability

OPEN ACCESS

Edited by:
Yuwei Li,
Liaoning University, China

Reviewed by:
Tong Zhao,
Taiyuan University of Technology, China
Meng Li,
China University of Mining and Technology, China

****Correspondence:***
Qinghai Li
liqinghai@sdust.edu.cn

Specialty section:
This article was submitted to Economic Geology, a section of the journal Frontiers in Earth Science

Received: *26 January 2022*
Accepted: *18 May 2022*
Published: *30 June 2022*

Citation:
Li Q, Wang H, Zheng X, Li K, Ji Y and Wang Z (2022) Adaptability Analysis of Full Height Mining at One Time of Deep Soft Thick Coal Seam. Front. Earth Sci. 10:862710. doi: 10.3389/feart.2022.862710

1 INTRODUCTION

China is rich in coal resources, and thick coal seam resources account for about 44.8% of the total coal reserves in China. The annual output of thick coal seam accounts for 40 ~ 50% of the national coal output, which provides energy guarantee for China's economic development. At present, there are three main methods for thick coal seam mining: slicing mining, full height mining at one time

and top coal caving mining. Slicing mining has some shortcomings, such as complex technology, low efficiency and poor economic benefits. At present, it has been basically eliminated in domestic mines, but the full height mining at one time process and mining equipment are relatively mature, which has been widely popularized and applied in China, and the mining height has increased from the earliest 4.5 m to over 8.0 m. Typical intelligent fully mechanized mining face with over 8.0 m mining height in Shangwan Coal Mine of Shendong Coal Group has been successfully put into operation (Wang et al., 2021; He et al., 2021; Zhang, 2020). Top coal caving mining method has strong adaptability to coal seam occurrence conditions, and has the advantages of full thickness mining at one time, high production efficiency, high economic benefits, etc. However, for hard roof, the rock strata integrity is strong and it is not easy to fall, and the coal recovery rate is low, so auxiliary measures such as hydraulic fracturing technology and loose blasting can be used to enhance caving property of top coal, and now caving property of top coal mining method is also widely used (Hubbret and Wills, 1957; Wong et al., 2002; Zhang et al., 2010; Wang and Pang 2018).

Although the theoretical mining height of top coal caving mining is the same as that of full height mining at one time, the working procedure of top coal caving mining is different from that of full height mining at one time, and there are some differences in the influence of the two methods on the stability of the working face (Kong et al., 2019; Hu et al., 2018; Zhang et al., 2016). In recent years, scholars at home and abroad have done a lot of research on the failure mechanism of the working face with full height mining at one time: Hu and Jin (2006) summarized the law and characteristics of rock pressure behavior in full height mining at one time stope by analyzing the field rock pressure data of the working face. Ning (2009) established a compression bar model with one end rigidly fixed and one end elastically fixed, and obtained the failure mechanism of coal wall in full height mining at one time working face. Gong and Jin (2008) established the mechanical model of roof with full height mining at one time according to the mechanical characteristics of rock structural plane, and put forward the control mechanism of roof conditions in different rock strata. Hao et al. (2004) obtained the interaction mechanism between overlying rock movement and support in full height mining at one time stope by studying the equilibrium structure of overlying rock mass. Xu et al. (Xu and Ju 2011; Liang et al., 2017) found in the research that when the mining height is increased, the fracture form of the first key layer above the coal seam changes from "masonry beam" structure to "cantilever beam" structure, and it is easy to collapse suddenly to the goaf. Under the conditions of "three soft", thick alluvium and extra-thick hard coal seam, the "cantilever beam" model of roof provides theoretical basis for the stability control of coal wall and roof in full height mining at one time working face (Liang et al., 2019; Zhang et al., 2020). At the same time, Ju et al. (2013, 2014, 2012) found that the collapse form of "cantilever beam" structure of roof strata would increase the periodic weighting interval of the working face through similar simulation experiments, field measurement and theoretical analysis. Yang et al. (2020) found through similar simulation and numerical analysis that the increase of suspended ceiling area will lead to the increase of cohesive energy of roof, and cohesive energy of roof is the main reason for the failure of coal and rock mass. Feng et al. (2019) combined theoretical analysis with on-site monitoring, and revealed the response mechanism of mining speed to the energy release from roof rock breaking, and found that the energy released from hard roof breaking was positively correlated with mining speed.

At present, the technology of full height mining at one time of shallow coal seams in China is mature, and its application is mainly concentrated in western mining areas, for example, the fully mechanized working face with large mining height of 1-2 coal seams in 12,401 working face of Shangwan Coal Mine in Shendong Mining Area (Xu et al., 2020; Yang and Liu 2020; Zhao et al., 2021), the buried depth of coal seams is 124–244 m, the thickness of coal seams is 7.56–10.97 m (average 9.26 m), and the Platts coefficient of coal seams is $f = 2 \sim 4$. However, for the coal seam with large buried depth, the coal seam bears the high static load of overlying strata. Under the disturbance of mining with full height mining at one time, roof instability and coal wall spalling will become more frequent. When coal and rock mass have impact tendency, the threat of dynamic disasters such as rock burst induced by overlying high static load superimposed with full height mining at one time disturbance is further increased (Dou et al., 2005; Xia et al., 2013; Liu et al., 2014; Pan 2019). At present, China is still in the trial stage for full height mining at one time with large buried depth, especially when the coal seam is soft, it is a challenge to successfully implement full height mining at one time.

In this paper, taking No. 3 coal seam of Lilou Coal Industry as the engineering background, the energy response mechanism of the roof is analyzed by establishing a cantilever beam model of the roof, the stored energy of the roof of different mining methods is compared, and the disturbed rock range of full height mining at one time and top caving mining is analyzed based on the field parameters. Furthermore, PFC^{2D} numerical software is used to simulate and analyze the instability process of roof and coal wall in full height mining at one time and top coal caving mining. By adjusting the *in-situ* stress value of the numerical model, the crack range of roof and coal wall is compared, and the buried depth of coal seam suitable for full height mining at one time is analyzed by inversion. Combined with the characteristics of on-site ground pressure behavior in No. 3 coal seam of Lilou Coal Industry, the adaptability of full height mining at one time in No. 3 coal seam of Lilou Coal Industry was determined, which provided a basis for selecting mining methods of coal seams under similar conditions.

2 CHARACTERISTICS OF STRATA BEHAVIOR IN WORKING FACE

The No. 1303 working face (Mining No. 3 Coal Seam) of Lilou Coal Industry is located in the middle and lower part of Shanxi

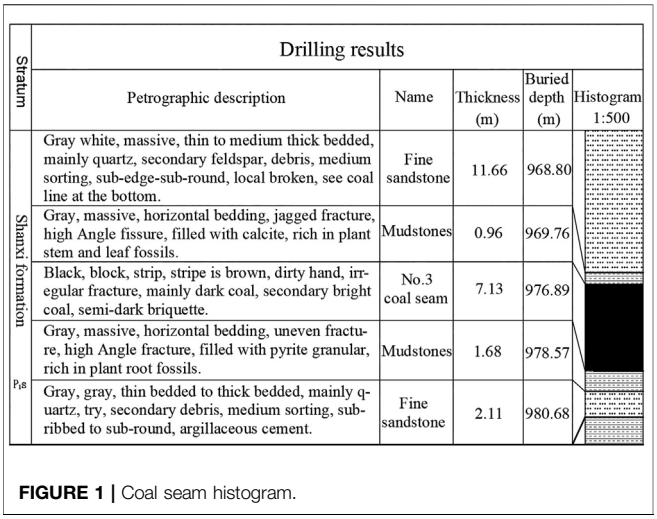

Stratum	Drilling results				
	Petrographic description	Name	Thickness (m)	Buried depth (m)	Histogram 1:500
Shanxi formation P_1s	Gray white, massive, thin to medium thick bedded, mainly quartz, secondary feldspar, debris, medium sorting, sub-edge-sub-round, local broken, see coal line at the bottom.	Fine sandstone	11.66	968.80	
	Gray, massive, horizontal bedding, jagged fracture, high Angle fissure, filled with calcite, rich in plant stem and leaf fossils.	Mudstones	0.96	969.76	
	Black, block, strip, stripe is brown, dirty hand, irregular fracture, mainly dark coal, secondary bright coal, semi-dark briquette.	No.3 coal seam	7.13	976.89	
	Gray, massive, horizontal bedding, uneven fracture, high Angle fracture, filled with pyrite granular, rich in plant root fossils.	Mudstones	1.68	978.57	
	Gray, gray, thin bedded to thick bedded, mainly quartz, try, secondary debris, medium sorting, sub-ribbed to sub-round, argillaceous cement.	Fine sandstone	2.11	980.68	

FIGURE 1 | Coal seam histogram.

formation, and the occurrence of coal seam (No. 3 Coal Seam) is mostly stable and its structure is relatively simple. The coal seam thickness is 6.70 ~ 7.31 m, the average coal thickness is 7.03 m, and the dip angle of coal seam is 4 ~ 16°, with an average of 13°. According to the field drilling histogram, the elevation of No. 3 coal floor in 1,303 working face is -994 ~ -890m, and the buried depth of coal seam is between 1,035 ~ 933 m. The immediate roof thickness of coal in working face 3 is 0.96 m, and the basic roof thickness is 8.12 m, the roof is mainly composed of medium and fine sandstone rock groups, with siltstone and mudstone rock groups locally. The immediate floor thickness of No.3 coal seam is 1.68 m, and the basic bottom thickness is 8.65 m, the floor is mainly composed of medium and fine sandstone rock groups, with siltstone mudstone rock groups locally. The coal seam histogram is shown in **Figure 1**. See **Table 1** for mechanical parameters of No.3 coal seam and roof and floor strata. From the mechanical parameters of coal seam No. 3 and roof and floor strata, it can be found that the strength of coal seam No. 3 is low, while the strength of roof and floor is high, which belongs to soft and thick coal seam.

Top coal caving mining is adopted in 1,303 working face of Lilou Coal Industry. In the process of mining, the hardness of the immediate roof strata is low, and the strength is weak. In the process of mining advancement, the caving increases with mining, and the basic roof periodic weighting rule is that the periodic weighting distance is between 20 and 22 m. During weighting, obvious weak vibration signals can be detected in the range of 0–150 m in front of the coal wall. After weighting, when the working face is advanced for 4–5 m, obvious spalling phenomenon occurs in the coal wall. Based on the above data, the analysis shows that the fracture span of the basic roof is 20–22 m, and the fracture position is about 4–5 m in front of the coal wall. When the working face is advanced for 4–5 m after the end of periodic weighting, the coal wall is at the fracture position, and the roof stress is concentrated on the coal wall at this time, which leads to the phenomenon of coal wall spalling. According to the appearance of on-site ore pressure, the schematic diagram of the pressure process is determined as shown in **Figure 2**. According to the appearance of on-site ore pressure, the schematic diagram of the pressure process is determined as shown in **Figure 2**. In the process of coal seam mining, the immediate roof caving along with mining, the basic roof forms a dynamic balance under the combined action of its own weight, overlying load and the supporting force of hydraulic support, and breaks and collapses in a cantilever beam structure.

3 COMPARISON ANALYSIS OF ENERGY RELEASE INTENSITY OF DIFFERENT MINING METHODS

3.1 Comparison Analysis of Bending Strain Energy of Basic Roof Rock Beam

The stress analysis of the basic roof in different mining methods is shown in **Figure 3**. The bending strain energy of the basic roof is analyzed by establishing a "cantilever beam" model, and the bending strain energy in the rock beam is compared between full height mining at one time and top coal caving mining. Under the condition of top coal caving mining, the top-coal is released, and the immediate roof fell as it was mined, so it is difficult for the top coal caving mining support to exert supporting force on the basic roof (Figure 3A), while under the condition of full height mining at one time, the support directly exerts stress on the direct top, and then can exert supporting force on the basic roof (Figure 3B). Under the action of self-weight stress and uniformly distributed load of overlying strata, the basic roof will undergo bending deformation, and when the tensile stress at the end of the rock beam reaches the tensile strength of the rock strata, the rock beam will break. therefore

$$R_t = \frac{M}{W} \tag{1}$$

TABLE 1 | Mechanical parameters of coal seam and roof and floor strata in 1,303 working face.

Items ground layer	Compressive strength σ_c (MPa)	Elastic modulus E (GPa)	Poisson's ratio μ	Tensile strength σ_t (MPa)	Cohesion c (MPa)	Friction angle φ (°)
Basic roof	103.99	21.65	0.24	7.15	29.97	34.30
Immediate roof	23.22	26.17	0.33	4.83	7.50	29.87
No.3 coal seam	14.65	1.33	0.22	0.59	0.56	38.89
Immediate floor	35.57	26.78	0.21	3.82	6.52	26.80
Basic bottom	128.12	32.81	0.24	8.31	26.04	37.60

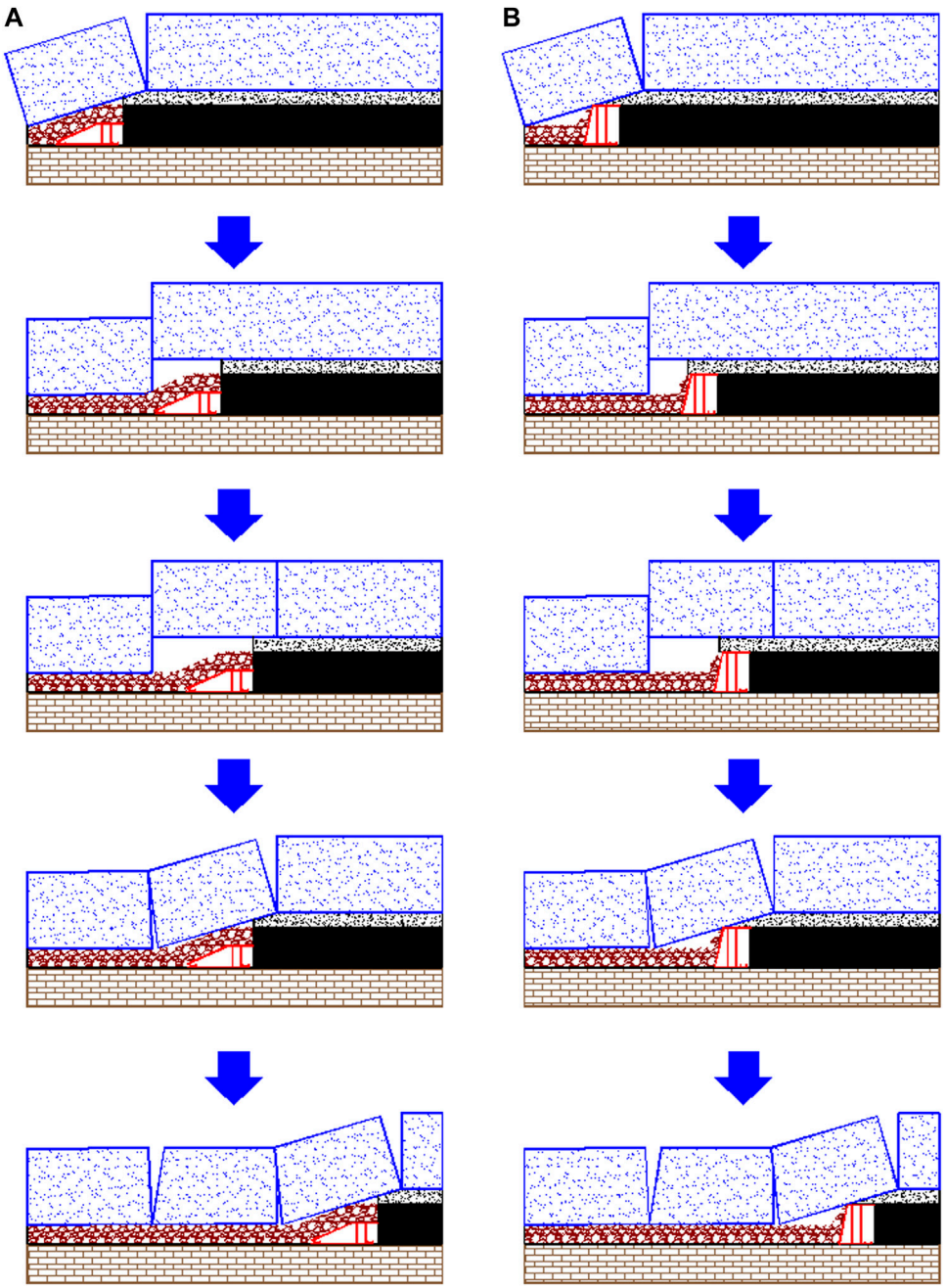

FIGURE 2 | Schematic diagram of periodic weighting process. **(A)** Top coal caving mining. **(B)** full height mining at one time.

In which: R_t -tensile strength of basic roof rock beam; M -bending moment of rock beam; W -bending stiffness of rock beam.

Contrasting the two mining methods, the bending stiffness W and tensile strength R_t of the basic roof are consistent, so the bending moment required for rock beam fracture under the two mining methods is consistent.

Under the condition of top coal caving mining:

$$M_T = \frac{1}{2}q_1 l_1^2 + \frac{1}{2}Ql_1 \tag{2}$$

In which: M_T- bending moment of rock beam under top coal caving mining condition; q_1- overburden load under top coal caving mining condition; l_1- Periodic weighting step under the condition of top coal caving mining; Q- Dead weight stress of fractured rock block.

Under the condition of full height mining at one time:

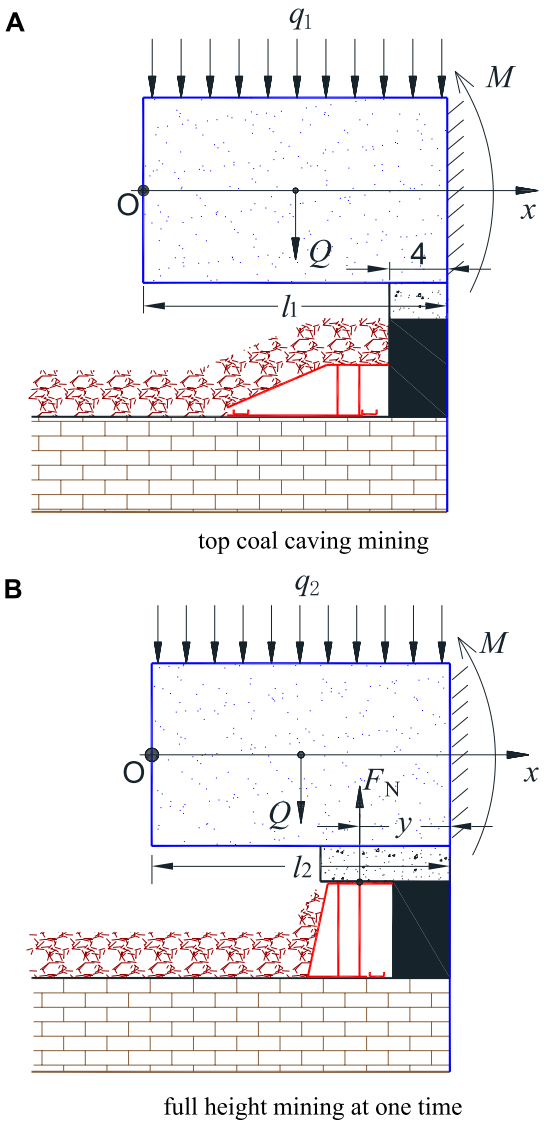

FIGURE 3 | Schematic diagram of stress on basic top rock beam. **(A)** top coal caving mining. **(B)** full height mining at one time.

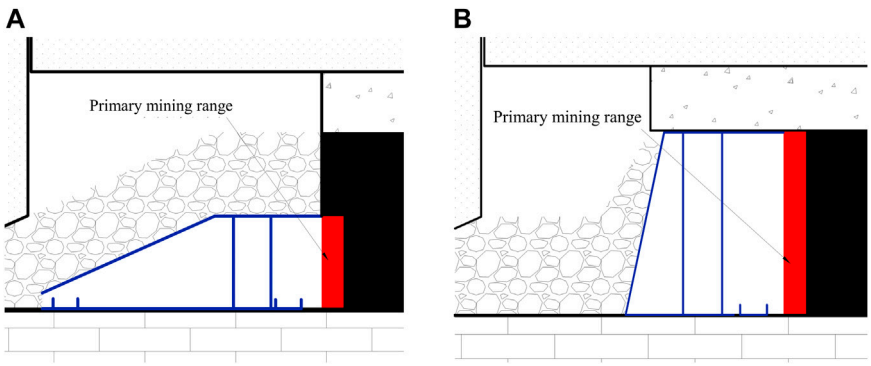

FIGURE 4 | Comparison of primary mining range of coal seam. **(A)** top coal caving mining. **(B)** full height mining at one time.

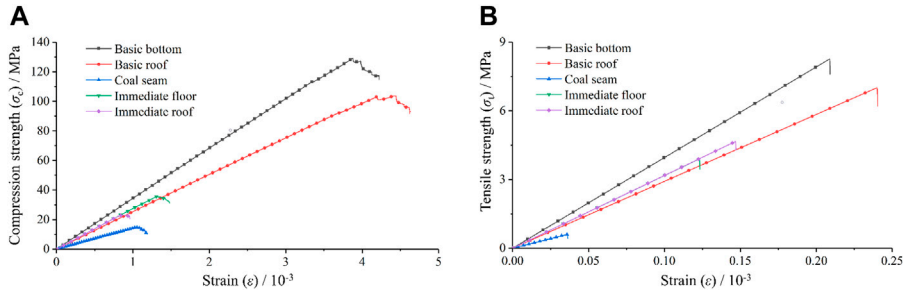

FIGURE 5 | Experimental results of various strata simulation. **(A)** Model compressive strength curve. **(B)** Model tensile strength curve.

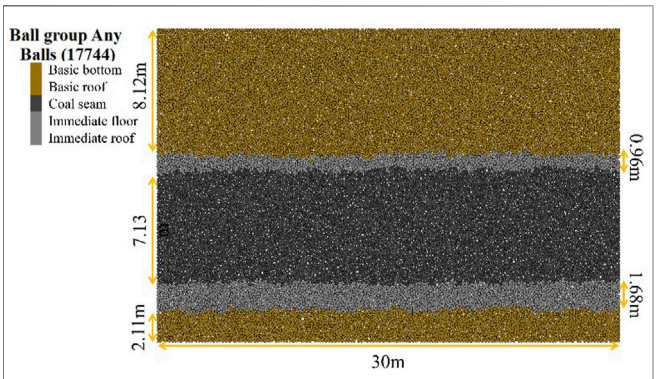

FIGURE 6 | Numerical model diagram of stope.

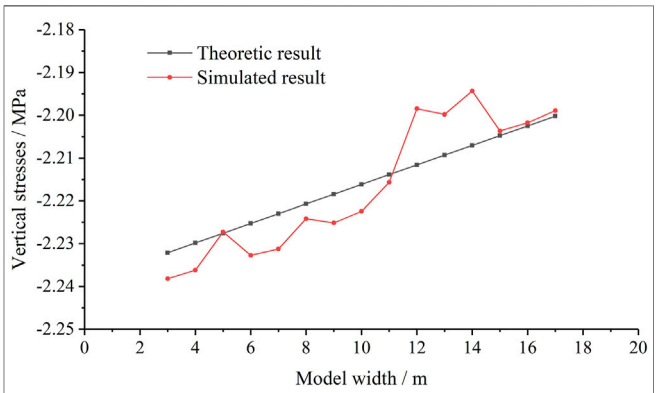

FIGURE 7 | Comparison of theoretical calculation and numerical simulation results of vertical stress.

$$M_F = \frac{1}{2}q_2 l_2^2 + \frac{1}{2}Ql_2 - F_N y \tag{3}$$

In which: M_F- bending moment of rock beam under the condition of full height mining at one time; q_2- overburden load under the condition of full height mining at one time; l_2- the periodic weighting step under the condition of full height mining at one time; y- the distance between the center of hydraulic support with full height mining at one time and the fracture position of roof rock beam, F_N- the supporting force of hydraulic support on the basic roof.

Due to the same bending moment required for rock beam fracture in the two mining methods, therefore

$M_T = M_F$then

$$\frac{1}{2}q_1 l_1^2 + \frac{1}{2}Ql_1 = \frac{1}{2}q_2 l_2^2 + \frac{1}{2}Ql_2 - F_N y \tag{4}$$

The coordinate system established in the basic top rock beam is shown in **Figure 3**. Before the basic roof breaks, the formula for calculating the bending strain energy in the rock beam is:

$$V_\varepsilon = \int_0^l \frac{M^2(x)}{2EI}dx \tag{5}$$

In which: V_ε- bending strain energy; E- elastic modulus; I- moment of inertia.

Calculation formula of bending strain energy under top coal caving mining condition is:

TABLE 2 | Input parameters of PFC^{2D} model for each rock stratum.

Ground layer	Surface gap g_s/mm	Effective modulus E^*/ GPa	Normal-to-shear stiffness ratio k^*	Tensile strength σt/ MPa	Cohesion c/ MPa	Density ρ/kg/m3
Basic roof	0.07	18.3	1.0	8.123	58.8	2,470
Immediate roof	0.07	19.9	1.0	5.4	10.56	2,340
Coal seam	0.07	1.05	1.0	0.7	8.0	1,350
Immediate floor	0.07	19.88	1.0	4.52	17.89	2,340
Basic bottom	0.07	24.8	1.0	9.58	72.4	2,470

TABLE 3 | Comparison between numerical simulation results and field mechanical parameters.

Ground layer	Numerical simulation results			Field mechanical parameter		
	Compressive strength σ_c/MPa	Elastic modulus *E*/GPa	Tensile strength σ_t/MPa	Compressive strength σ_c/MPa	Elastic modulus *E*/GPa	Tensile strength σ_t/MPa
Basic roof	103.77	21.91	7.01	103.99	21.65	7.15
Immediate roof	23.17	26.17	4.66	23.22	26.17	4.83
Coal seam	14.66	1.31	0.604	14.65	1.33	0.59
Immediate floor	35.69	26.93	39.03	35.57	26.78	3.82
Basic bottom	129.2	32.4	8.26	128.12	32.81	8.31

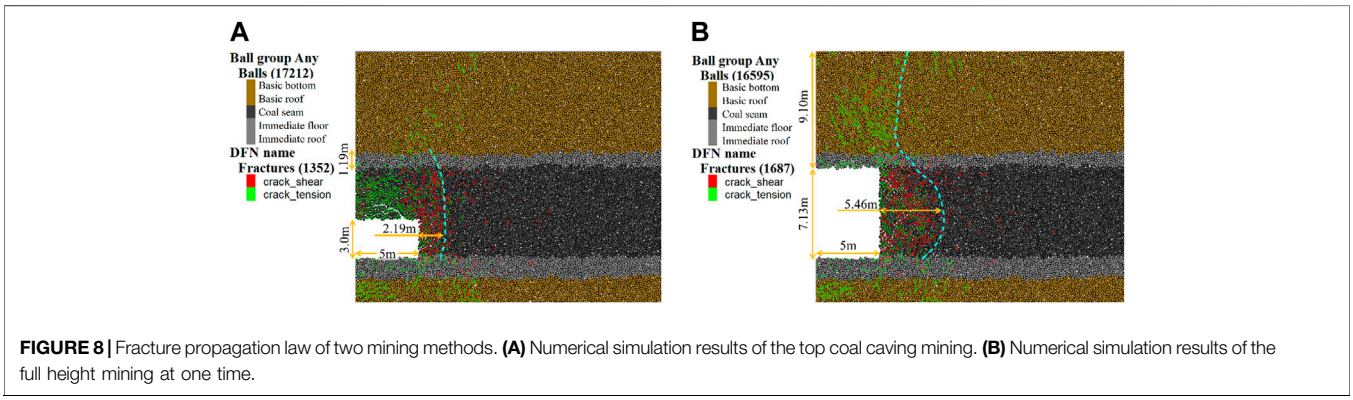

FIGURE 8 | Fracture propagation law of two mining methods. **(A)** Numerical simulation results of the top coal caving mining. **(B)** Numerical simulation results of the full height mining at one time.

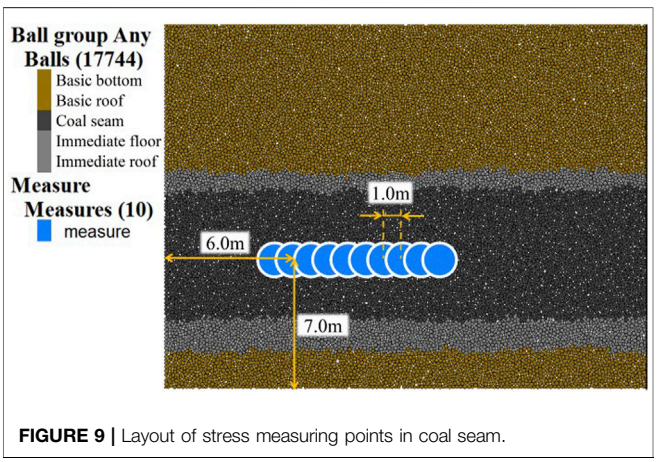

FIGURE 9 | Layout of stress measuring points in coal seam.

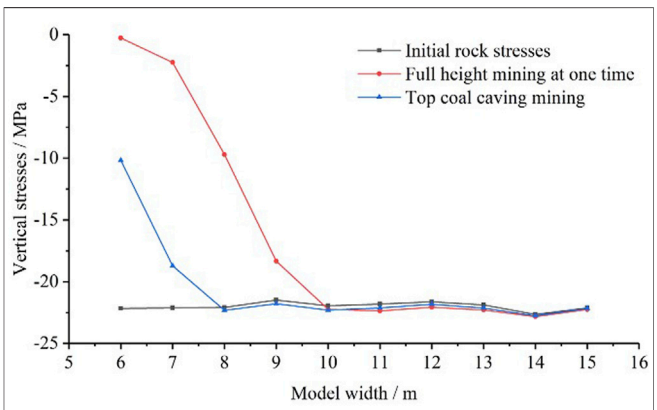

FIGURE 10 | Comparison of advanced stress after excavation.

$$V_{\varepsilon 1} = \int_0^{l_1} \frac{\left[q_1 x\left(\frac{x}{2}\right)\right]^2}{2EI} dx + \int_{\frac{l_1}{2}}^{l_1} \frac{\left[Q\left(x - \frac{l_1}{2}\right)\right]^2}{2EI} dx \quad (6)$$

In which: $V_{\varepsilon 1}$- bending strain energy of rock beam under top coal caving mining condition.

The formula for calculating bending strain energy under the condition of full height mining at one time is:

$$V_{\varepsilon 2} = \int_0^{l_2} \frac{\left[q_2 x\left(\frac{x}{2}\right)\right]^2}{2EI} dx + \int_{\frac{l_2}{2}}^{l_2} \frac{\left[Q\left(x - \frac{l_2}{2}\right)\right]}{2EI} dx \int_{l2-y}^{l_2} \frac{\{F_N[x - (l_2 - y)]\}^2}{2EI} dx \quad (7)$$

In which: $V_{\varepsilon 2}$- bending strain energy of rock beam under full height mining at one time condition.

Because the distance y between the center point of the hydraulic support with full height mining at one time and the fracture position of the roof rock beam is small, and the overlying immediate roof is soft and broken, the work done by the hydraulic support with full height mining at one time on the basic roof is mainly absorbed by the broken rock layer of the immediate roof, the supporting force of the hydraulic support will not displace in the basic roof, so the work done by the hydraulic support on the basic roof can be ignored, that is, **Eq. 7** can be simplified as follows:

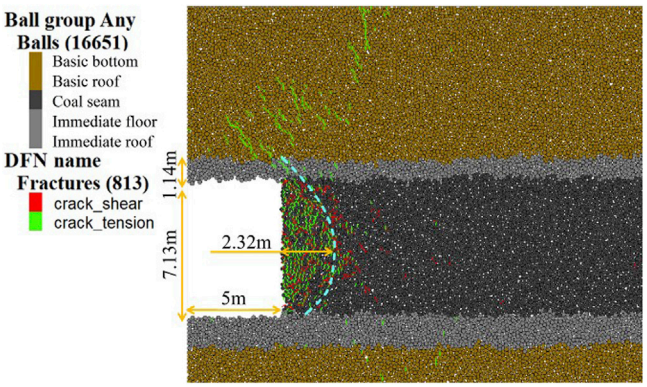

FIGURE 11 | Fracture propagation form of full height mining at one time after stress debugging.

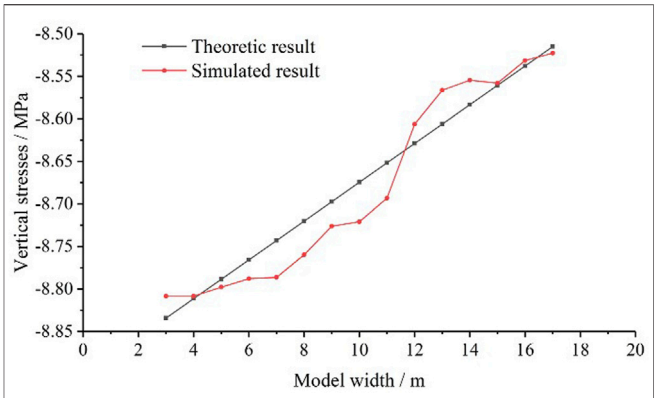

FIGURE 12 | Comparison of debugging stress debugging results of full height mining at one time.

$$V_{\varepsilon 2} = \int_0^{l_2} \frac{\left[q_2 x\left(\frac{x}{2}\right)\right]^2}{2EI} dx + \int_{\frac{l_2}{2}}^{l_2} \frac{\left[Q\left(x - \frac{l_2}{2}\right)\right]^2}{2EI} dx \quad (8)$$

According to the calculation **Eq. 4**, when the weighting steps of the two mining methods are the same ($l_1 = l_2$), then $q_2 > q_1$; When the overburden load of the two mining methods is the same ($q_1 = q_2$), then $l_2 > l_1$.

Because $q_2 > q_1$ or $l_2 > l_1$, substituting into **formulas (6)** and **(8)**, the bending strain energy stored in the basic roof rock layer is $V_{\varepsilon 2} > V_{\varepsilon 1}$, that is, the energy released when the basic roof breaks in full height mining at one time is greater than that in top coal caving mining.

3.2 Comparative Analysis of Mining Disturbance Range

In the process of top coal caving mining, the range of mining is small, the range of rock disturbed by primary mining is relatively small, and the primary release strength of bending strain energy stored in disturbed rock is relatively small. However, in the process of full height mining at one time, the range of mining is large, the rock strata disturbed by mining is relatively large, and the bending strain energy stored in the disturbed rock strata has relatively large one-time release strength. The primary mining range of different mining methods is shown in **Figure 4**.

At the same time, when the mining disturbance is large and there is more energy released at one time (for example, periodic weighting), the top coal in top coal caving mining is low in strength and easy to break, which can play a good role in energy absorption and buffering (Wang 2007). However, there is no coal seam buffer layer when the full height mining at one time, and the energy released at one time will directly act on the hydraulic support and coal wall when the roof breaks, further increasing the risk of coal wall spalling.

4 COAL WALL STABILITY COMPARATIVE ANALYSIS

4.1 Calibration of Meso-parameters of Numerical Model

In order to compare the stability of coal wall between the two mining methods, numerical simulation is used for analysis. Considering the advantages of PFC software in fracture propagation simulation, this paper chooses PFC software for simulation analysis. See **Table 1** for mechanical parameters of coal seam and roof and floor strata in Lilou Coal Industry. Because there is a certain difference between the input parameters and the output parameters in the numerical model, before the simulation analysis, first check the input parameters of the rock strata (Chen et al., 2018; Feng 2020).

A standard block of 100 × 50 mm is established, the model contains 1,481 particles, and the Flat-joint contact model is adopted among the particles, which mainly checks the uniaxial compressive strength σ_c, elastic modulus E and tensile strength σ_t of the rock strata. By debugging the particle surface gap, effective modulus, normal-to-shear stiffness ratio, tensile strength, cohesion and particle density in the numerical model, the mechanical parameters of the numerical model correspond to the laboratory experimental values, and the input parameters in the numerical model of each rock strata are determined as shown in **Table 2**. The simulation results of uniaxial compressive strength and tensile strength of each rock strata are shown in **Figure 5**. See **Table 3** for comparison of simulation results of various rock parameters with field mechanical parameters. from **Table 3**, it can be seen that numerical simulation results of compressive strength, elastic modulus and tensile strength of test block are close to field mechanical parameters, so all parameters can be used for subsequent simulation of coal seam excavation.

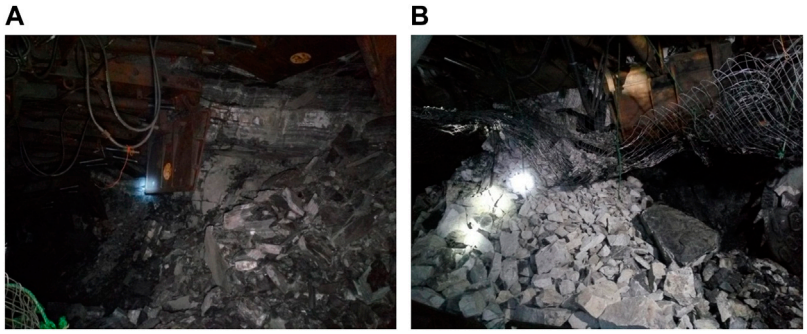

FIGURE 13 | Status of 103 fully mechanized top coal caving face. **(A)** Serious coal spalling. **(B)** Roof crushing and gangue leakage.

4.2 Establishment of Numerical Model

In order to prominent the failure process of surrounding rock and stress evolution law of coal seam after coal seam excavation, the model stope should be as large as possible, and the model should be as small as possible on the basis of eliminating boundary effect. After repeated debugging, the model height should be 20 m and the model strike length should be 30 m. According to geological histogram **Figure 1**, the thickness of each rock strata included in the model is determined as follows: basic roof 8.12 m, immediate roof 0.96m, coal seam 7.13 m, immediate floor 1.68 m and basic bottom 2.11 m. The model contains 17,744 particles. See **Table 3** for various parameters of coal strata, and the established model is shown in **Figure 6**.

4.3 Debugging of Stress Applied by Numerical Model

The basic roof buried depth is 960.68 m, the average density of overlying fine sandstone and mudstone is 2280 kg/m^3, and the gravity acceleration is 10 m/s^2. It is calculated that the stress on the upper surface of the model is about 21.89MPa, and the stress increases by 0.0228 MPa for every 1 m increase in depth. In the middle of the trend of the numerical model, vertical stress measuring points are set from the bottom of the model to the top of the model within 3–17 m, and the evolution law of vertical stress in the middle of the model is monitored. Repeated debugging confirms that 3.66×10^5 N downward pressure is applied in the upper part of the model within 18–20 m, while 2×10^3 N downward uniform pressure (simulated stress gradient) is applied in the upper part of the model within 0–20 m. The comparison between theoretical estimation results ($\sigma = \gamma h$) and simulated results is shown in **Figure 7**. The overall trend of the two results is close, but the stress in the simulated results fluctuates. The reason for the fluctuation is that the rock density is selected according to the average value in the theoretical calculation, while different rock layers are calculated according to different densities in the simulated results. In summary, it can be seen that the modeling method, parameter selection and external force applied of the numerical model are reasonable, which can be used for subsequent analysis.

4.4 Analysis of Numerical Simulation Results

4.4.1 Analysis of Failure State of Coal Wall and Roof Strata

Coal seam excavation starts from the left side of the model, referring to the field stope range, which is 5 m. In the process of mining, the coal seam mining height is 3.0 m when the top coal caving mining is carried out, and the coal body of 7.13 m is fully extracted when the full height mining at one time. PFC5.0 software automatically determines the running timestep of the model as 1 according to the contact stiff-ness and particle size between particles, and stops running when cracks in the roof of the numerical simulation model are through. In the process of simulation, it was found that the roof cracks were firstly connected when the full height mining at one time numerical simulation model ran 430 timesteps, so the two numerical simulation models stopped after running 430 timesteps. **Figure 8** shows the fracture propagation patterns obtained by simulating two mining methods.

It can be seen from Figure 8A that during top coal caving mining, under the action of initial rock stress and mining disturbance stress, cracks occur in the coal body, and the cracks form obvious up-and-down through cracks at 2.19 m in front of the coal wall, which extend to 1.19 m above the coal seam, and the integrity of the basic roof strata upward is good, with only a few micro cracks. It can be seen from Figure 8B that the cracks in the coal body form obvious up-and-down through cracks at 5.46 m in front of the coal wall, which extend to the top of the model, and the basic roof is fractured and damaged. the cracks range of coal wall under the condition of full height mining at one time is much larger than that during top coal caving mining, and the damage depth of coal wall during full height mining at one time is 2.5 times of that during top coal caving mining, and the phenomenon of coal wall spalling is serious.

4.4.2 Comparison of Stress in Coal Seam After Excavation

In order to compare the evolution law of coal advanced stress during top coal caving mining and full height mining at one time, 10 stress measuring points are arranged at an interval of 1.0 m at a distance of 7 m from the bottom of the model (at a height of 3.2 m in coal seam). The radius of measuring point is 1m, and from left

to right, measuring point 1 is located 6 m away from the leftmost side of the model (the left edge of measuring point 1 is located at the coal wall), and the layout of measuring points is shown in **Figure 9**. The comparison of advanced stress after excavation is shown in **Figure 10**.

It can be seen from **Figure 10** that stress reduction occurs near the coal wall after top coal caving mining and full height mining at one time. After full height mining at one time, under the action of overburden load and excavation disturbance load, the coal wall collapses and loses its bearing capacity. The vertical stress obtained by monitoring the coal wall position is 0.27 MPa. With the increase of the distance from the coal wall, the coal stress gradually recovers, and the coal stress is restored to the original at 5 m from the coal wall (about 10 m from the leftmost side of the model). After top coal caving mining, the vertical stress obtained by monitoring the coal wall position is about 10.2 MPa, so the coal wall has not completely lost its bearing capacity at this time, that is, the coal wall has not collapsed, and the coal stress has returned to the original rock stress level at 3 m away from the coal wall (about 8 m away from the leftmost side of the model). It can be seen that the damage degree of coal wall in top coal caving mining is far less than that in full height mining at one time. When full height mining at one time occurs, the coal wall collapses, and the stress of coal body is basically reduced to 0. However, although a large number of cracks are developed in the coal wall during top coal caving mining, the bearing capacity is not lost, that is, the coal wall does not collapse. Combined with the law of crack propagation, it is further verified that the stability of coal wall is poor when the full height mining at one time under this large buried depth condition, which is not conducive to on-site safety production.

4.5 Adaptability Analysis of Full Height Mining at One Time

In order to study the adaptability of the full height mining at one time, reduce the overlying load of the numerical model, and the microscopic parameters and running time of rock particles are kept unchanged, so as to realize that the cracks range of coal seam and roof at the full height mining at one time after stress debugging is similar to the damage result of full height mining at one time under the original rock stress condition, the coal seam depth at the full height mining at one time is applicable under this coal seam strength through stress inversion analysis. After debugging, the model applies a downward pressure of 1.4×10^5 N in the range of 18–20 m and a downward uniform pressure of 500N in the range of 0–20 m, and obtains the rock strata failure range when the full height mining at one time, as shown in **Figure 11**. At this time, the maximum failure depth of coal reaches 2.32 m in front of the coal wall, and the through fracture inside the coal body extends to 1.14 m above the coal seam, which is close to the fracture expansion when the top coal caving mining under the initial rock stress condition.

The vertical stress in the middle position of the monitored model strike is shown in **Figure 12**. By comparison, it is found that the theoretical value of overlying load of coal seam is about 8.65 MPa, and the corresponding burial depth at this time is about 380 m (the average density of overlying strata is 2280 kg/m^3, and the gravity acceleration is 10 m/s^2, $h = \sigma/\gamma$). Under this coal seam strength condition, when the buried depth of coal seam is less than 380m, the stability of coal wall and roof strata can be ensured by adopting full height mining at one time.

4.6 Field Application Analysis

In the process of site mining, the 1,303 fully mechanized caving face has a mining height of 3.0 m and a coal drawing height of 4.13 m. In the middle of the face, ZF15000/23/42 top coal caving hydraulic support and ZFG15000/25/42H top coal caving transition hydraulic support are used for support. Although top coal caving mining is adopted in 1,303 working face, the phenomenon of coal wall splints is still serious in the mining process, with severe ore pressure, poor stability of coal wall, and serious breakage and leakage of gangue in roof, as shown in **Figure 13**Figure 13A and Figure 13B. At the same time, weak vibration events often occur in the working face, which affects the working face advance speed and production efficiency. It can be seen that it is still difficult to maintain the stability of roof and coal wall in 1,303 working face caving coal mining, and further it can be seen that full height mining at one time is not suitable.

5 THE CONCLUSION

1) By establishing the mechanical model of the basic roof "cantilever beam" for comparative analysis of bending strain energy, it is determined that the energy released when the basic roof breaks is greater than that of the top coal caving mining. Further comparison shows that the rock strata disturbed by the first mining is relatively small in the top coal caving mining, and the energy release intensity of disturbed rock strata is relatively small.
2) It is found that through cracks appear in the roof of simulated full height mining at one time, the coal wall failure depth reaches 5.46 m, and the coal wall collapses and loses its bearing capacity. During top coal caving mining, the roof crack extends to 1.19 m above the coal seam, and the coal wall failure depth is 2.19 mm. The coal wall can still exert part of its bearing capacity, and its bearing stress is 10.2 MPa.
3) In order to study the adaptability of the full height mining at one time in the field, by reducing the overlying load of numerical simulation model, make the development degree of full height mining at one time coal seam and roof crack after coal seam excavation match with top coal caving mining. By comparing the simulated vertical stress with the theoretical stress, it is determined that the full height mining at one time is reliable when the buried depth is less than 380 m.

DATA AVAILABILITY STATEMENT

The raw data supporting the conclusion of this article will be made available by the authors, without undue reservation.

AUTHOR CONTRIBUTIONS

QL provided ideas and theoretical analysis for the paper. YJ and XZ provided field data for the paper. HW, KL and ZW conducted numerical simulation and data analysis. All members participate in writing articles.

FUNDING

The research is supported by the key project of natural science foundation of Shandong province (Grant Numbers ZR2020KE030). Supported by NSFC Youth Fund (Grant Numbers 52104136). The field information from the study site was provided by the Lilou Coal Mine.

ACKNOWLEDGMENTS

The author expresses his gratitude for this support.

REFERENCES

Chen, P. Y., Kong, Y., and Yu, H. M. (2018). Research on the Calibration Method of Microparameters of a Uniaxial Compression PFC^{2D} Model for Rock. *Chin. J. Undergr. Space Eng.* 14 (05), 1240–1249.

Dou, L. M., Lu, C. P., Mou, Z. L., Qin, Y. H., and Yao, J. M. (2005). Intensity Weakening Theory for Rockburst and its Application. *J. China Coal Soc.* (06), 690–694. doi:10.3321/j.issn:0253-9993.2005.06.003

Feng, K. W. (2020). Research on Calibration of Micro Parameters of PFC^{2D} Model in Uniaxial Compression of Coal Similar Materials. *Saf. Coal Mines* 51 (04), 5–9.

Feng, L. F., Dou, L. M., Wang, X. D., Jin, D. W., Cai, W., Xu, G. G., et al. (2019). Mechanism of Mining Advance Speed on Energy Release from Hard Roof Movement. *J. China Coal Soc.* 44 (11), 3329–3339. doi:10.13225/j.cnki.jccs.2018.1671

Gong, P. L., and Jin, Z. M. (2008). Mechanical Model Study on Roof Control for Fully-Mechanized Coalface with Large Mining Height. *Chin. J. Rock Mech. Eng.* 2008 (01), 193–198. doi:10.3321/j.issn:1000-6915.2008.01.027

Hao, H. J., Wu, J., Zhang, Y., and Yuan, Z. B. (2004). The Balance Structure of Main Roof and its Action to Immediate Roof in Large Cutting Height Workface. *J. China Coal Soc.* (02), 137–141. doi:10.3321/j.issn:0253-9993.2004.02.003

He, X., Zhao, Y., Yang, K., Zhang, C, and Han, P (2021). Development and Formation of Ground Fissures Induced by an Ultra Large Mining Height Longwall Panel in Shendong Mining Area[J]. *Bull. Eng. Geol. Environ.* (9), 2021. doi:10.1007/s10064-021-02429-6

Hu, G. W., and Jin, Z. M. (2006). Study on Mining Pressure Observation and its Developing Law of Fully Mechanized Mining Face with Large Mining Height. *J. Taiyuan Univ. Technol.* (02), 127–130.

Hu, S. X., Ma, L. Q., Guo, J. S., and Yang, P. J. (2018). Support-surrounding Rock Relationship and Top-Coal Movement Laws in Large Dip Angle Fully-Mechanized Caving Face. *J] Int. J. Min. Sci. And Technol.* 28 (3), 533–539. doi:10.1016/j.ijmst.2017.10.001

Hubbret, M. K., and Wills, D. G. (1957). Mechanics of Hydraulic Fracturing[J]. *Transcations Soc. Petroleum Eng. AIME* 210, 153–168.

Ju, J. F., Xu, J. L., and Zhu, W. B. (2014). Influence of Key Strata Cantilever Structure Motion on End-Face Fall in Fully-Mechanized Face with Super Great Mining Height. *J. China Coal Soc.* 39 (07), 1197–1204. doi:10.13225/j.cnki.jccs.2013.1000

Ju, J. F., Xu, J. L., Zhu, W. B., Wang, Q. X., and Hao, X. J. (2012). Strata Behavior of Fully-Mechanized Face with 7.0 M Height Support. *J. Min. Saf. Eng.* 29 (03), 344–350+356.

Ju, J., and Xu, J. (2013). Structural Characteristics of Key Strata and Strata Behaviour of a Fully Mechanized Longwall Face with 7.0m Height Chocks. *Int. J. Rock Mech. Min. Sci.* 58, 46–54. doi:10.1016/j.ijrmms.2012.09.006

Kong, D. Z., Pu, S. J., Zheng, S. S., Wang, C. H., and Lou, Y. H. (2019). Roof Broken Characteristics and Overburden Migration Law of Upper Seam in Upward Mining of Close Seam Group[J]. *Geotechnical Geol. Eng.* 2019 (4). doi:10.1007/s10706-019-00836-x

Liang, Y. P., Li, B., Yuan, Y., Zou, Q. L., and Jia, L. X. (2017). Moving Type of Key Strata and its Influence on Ground Pressure in Fully Mechanized Mining Face with Large Mining Height. *J. China Coal Soc.* 42 (06), 1380–1391. doi:10.13225/j.cnki.jccs.2016.1320

Liang, Y. P., Li, B., and Zou, Q. L. (2019). Movement Type of the First Subordinate Key Stratum and its Influence on Strata Behavior in the Fully Mechanized Face with Large Mining Height. J]*Arabian J. Geosciences* 12 (2). doi:10.1007/s12517-018-4208-9

Liu, S. H., Mao, D. B., Qi, Q. X., and Li, F. M. (2014). Under Static Loading Stress Wave Propagation Mechanism and Energy Dissipation in Compound Coal-Rock. *J. China Coal Soc.* 39 (S1), 15–22. doi:10.13225/j.cnki.jccs.2013.0411

Ning, Y. (2009). Mechanism and Control Technique of the Rib Spalling in Fully Mechanized Mining Face with Great Mining Height. *J. China Coal Soc.* 34 (01), 50–52.

Pan, J. F. (2019). Theory of Rockburst Start-Up and its Complete Technology System. *J. China Coal Soc.* 44 (1), 173–182.

Wang, G. F., and Pang, Y. H. (2018). Full-mechanized Coal Mining and Caving Mining Method Evaluation and Key Technology for Thick Coal Seam. *J. China Coal Soc.* 43 (01), 33–42. doi:10.13225/j.cnki.jccs.2017.4200

Wang, H., Liu, Y., Tang, Y., Gong, H., and Xu, G. (2021). Failure Mechanisms and the Control of a Longwall Face with a Large Mining Height within a Shallow-Buried Coal Seam. *Shock Vib.* 2021 (7), 1–11. doi:10.1155/2021/8494913

Wang, J. C. (2007). Mechanism of the Rib Spaling and the Controlling in the Very Soft Coal Seam. *J. China Coal Soc.* 155 (8), 785–788. doi:10.3321/j.issn:0253-9993.2007.08.001

Wong, R. H. C., and Wang, S. W. (2002). "Experimental and Numerical Study on the Effect of Material Property, Normal Stress and the Position of Joint on the Progressive Failure under Direct Shear[A]," in *Narms-tac2002, Mining and Tunneling Innovation and Opportunity[C* (Toronto, 1009–1016.*]*

Xia, Y. X., Lan, H., and Mao, D. B. (2013). Rock-burst Start Conditions and Prevention Technology under Static and Dynamic Load Action. *J. Min. And Strata Control Eng.* 18 (05), 83–86.

Xu, H. Z., Li, Q. S., Li, X. B., Zhang, G. J., Yang, Y. L., He, W. R., et al. (2020). Structural Evolution of Overburden and Surface Damage Caused by High-Intensity Mining with Shallow Depth. *J. China Coal Soc.* 45 (08), 2728–2739.

Xu, J. L., and Ju, J. F. (2011). Structural Morphology of Key Stratum and its Influence on Strata Behaviors in Fully-Mechanized Face with Supper-Later with Supper-Large Mining Height. *Chin. J. Rock Mech. Eng.* 30 (08), 1547–1556.

Yang, J. Z., and Liu, Q. J. (2020). Analysis and Measured of Strata Behavior Law and Mechanism of 8.8 Multra-High Mining Height Working Face. *Coal Sci. Technol.* 45 (08), 2728–2739.

Yang, J. Z., Zhang, K. G., Wang, Z. R., and Pang, N. Y. (2020). Technology of Weakening and Danger-Breaking Dynamic Disasters by Hard Roof. *J. China Coal Soc.* 45 (10), 3371–3379. doi:10.13225/j.cnki.jccs.2020.0599

Zhang, C., Zhao, Y., He, X., Guo, J, and Yan, Y (2020). Space-sky-surface Integrated Monitoring System for Overburden Migration Regularity in Shallow-Buried High-Intensity Mining[J]. *Bull. Eng. Geol. Environ.*, 1–15. doi:10.1007/s10064-020-02026-z

Zhang, C. W., Jin, Z. X., Song, X. M., Feng, G. R., Li, Z., Gao, R., et al.(2020) Failure Mechanism and Fracture Aperture Characteristics of Hard Thick Main Roof

Based on Voussoir Beam Structure in Longwall Coal Mining[J]*Energy Sci. Eng.*; 2020, 8(2)doi:10.1002/ese3.492

Zhang, G. Q., and Chen, M. (2010). Dynamic Fracture Propagation in Hydraulic Refracturing[J]. *J. Petroleum Sci. Eng.* (70), 266–272. doi:10.1016/j.petrol.2009.11.019

Zhang, N. B., Liu, C. Y., and Yang, P. J. (2016). Flow of Top Coal and Roof Rock and Loss of Top Coal in Fully Mechanized Top Coal Caving Mining of Extra Thick Coal Seams. *[J] Arabian J. Geosciences* 9 (6). doi:10.1007/s12517-016-2493-8

Zhao, Y. X., Ling, C. W., Liu, B., and He, X. (2021). Fracture Evolution and Energy Dissipation of Overlying Strata in Shallow-Buried Underground Mining with Ultra-high Working Face. *J. Min. Saf. Eng.* 38 (01), 9–30. doi:10.13545/j.cnki.jmse.2020.0212

Conflict of Interest: XZ and YJ was employed by the company Shandong Lilou Coal Industry Co., Ltd.

The remaining authors declare that the research was conducted in the absence of any commercial or financial relationships that could be construed as a potential conflict of interest.

Publisher's Note: All claims expressed in this article are solely those of the authors and do not necessarily represent those of their affiliated organizations, or those of the publisher, the editors and the reviewers. Any product that may be evaluated in this article, or claim that may be made by its manufacturer, is not guaranteed or endorsed by the publisher.

Advantages of publishing in Frontiers

OPEN ACCESS
Articles are free to read for greatest visibility and readership

FAST PUBLICATION
Around 90 days from submission to decision

HIGH QUALITY PEER-REVIEW
Rigorous, collaborative, and constructive peer-review

TRANSPARENT PEER-REVIEW
Editors and reviewers acknowledged by name on published articles

Frontiers
Avenue du Tribunal-Fédéral 34
1005 Lausanne | Switzerland

Visit us: www.frontiersin.org
Contact us: frontiersin.org/about/contact

REPRODUCIBILITY OF RESEARCH
Support open data and methods to enhance research reproducibility

DIGITAL PUBLISHING
Articles designed for optimal readership across devices

FOLLOW US
@frontiersin

IMPACT METRICS
Advanced article metrics track visibility across digital media

EXTENSIVE PROMOTION
Marketing and promotion of impactful research

LOOP RESEARCH NETWORK
Our network increases your article's readership